Physical characterisation of ionic liquid solutions and their potential applications as media for nanoparticle formation or batteries

by

Claire Boudie, BSc, MSc,

Presented to the School of Chemistry and Chemical Engineering,

The Queen's University Belfast

for the Degree of

Doctor of Philosophy

The Queen's University Belfast,

December 2016

Acknowledgements

First of all, I would like to thanks Dr Peter Nockemann and Dr Johan Jacquemin, my supervisors. Both were very helpful finding new ideas and funding, allowing me to go deeper into my research and gain access to the Synchrotrons in Oxford and Grenoble. I am also very grateful to Professor Ken Seddon and Professor Kim Swindall, founders of QUILL (Queens' University Ionic Liquid Laboratories) and Professor Chris Hardacre (former Head of School at Queen's University) where my project was based. My work at QUILL provided me with many exciting opportunities to travel such as the trip to the Gordon Research Conference (GRC) in Hong-Kong.

Chapter 6 of this thesis wouldn't have been possible without the support of the JSPS-London "Postdoctoral Fellowships Short-term for Foreign Researchers" which I was awarded in February 2015. This fellowship took place in partnership between QUILL and TUS (Tokyo University of Science), and enabled me to undertake a new project related to my Ph.D. I would like to "*arigatou gozaimasu*" (thank-you in japanese) to Prof. Shinichi Komaba and Dr. Mouad Dahbi as well as to the TUS students and friends I made there (Kiso san, Wanjie san and Xiaofei san, Hajars, Melek, Chistian and Romain) who made my time in Japan unforgettable.

My sincere thanks also goes to Dr Nimal Gunaratne, Dr Tristan Young, Dr Peter Goodrich, Dr Rebecca Taylor, Dr Erwan Coadou, Hannah Dunckley, Sinead Murphy and Alex Neale for help with the synthesis and characterisation of my Ionic-Liquids. In QUILL, we are very lucky to work in collaboration with technicians and administrative staff (Dr Sarah Thompson, Fiona Blakley, Angela and Suzie). I am very thankful to them all. I am also grateful to Stephen McFarland in Physics who was very patient and truly helpful. I also want to mention Clarisse Bloyet, now doing her Ph.D in France, who was a great MSc student to supervise.

In my hard days, I really did appreciate the support of my dear Ph.D colleagues for their positive attitude: Ena, Corina, Yulia, Katherine & Chris, Yoan, Anne, Eadaoin, and Jorge; as well as Natalia and Geeta. I particularly thank my "wee" friends and colleagues Sonia and Sophie with whom I had the chance to share

great memories. My lovely friends Marion, Sophie & Jorge, Lucie, Alix, Mary & Jorge, Quentin, Nicolas, Florence, Eloise, Anne-Heloise, Sasha & Geoffrey also helped to make the experience memorable.

Last but not least, I would like to thank my family: Mum, Dad and Laure, my sister, and also Floride & Stan for supporting me spiritually throughout writing this thesis and my life in general.

This thesis is dedicated to my lovely family and friends.

"Il est dans la nature humaine de penser sagement

Et d'agir de façon absurde" _ Anatole France

Abstract

Ionic liquid solutions of 1-ethyl-2-methylimidazolium alkyl-carboxylates in binary mixture with water have been investigated in function of the temperature and composition with the aim to investigate potential aggregation by increasing the carbon chain-length of the alkyl-carboxylate anions, and the effect on the *in-situ* growth of nanoparticles.

First of all, the synthetic route of each ionic liquid has been optimised and discussed in order to avoid impurities and obtain pure compounds (Chapter 2). The intra- and intermolecular interactions between cation–anion, individual ion–water, and IL ion pairs–water in solution have been carried out in two main chapters that include the macroscopic and microscopic study of all IL-systems studied.

Chapter 3 consists of a macroscopic study that includes the characterisation of the physical properties for each composition due to volumetric properties (densities, excess molar volumes and apparent & partial molar volumes) and to the transport properties (viscosity and conductivity), which has been carried out with the aim to classify those solutions using the Walden rule.

In chapter 4, in order to complete the macroscopic study, binary mixtures were analysed regarding their microscopic properties using ^{1}H, ^{13}C and 2D-(^{1}H/^{13}C)-HSQC NMR-spectroscopy, as well as X-Ray and neutron scattering techniques. The two latter techniques were used at the ISIS facility at the Appleton Laboratories and the ILL and ESFR facilities. The outcome of those two studies have provided relevant information on the interaction behaviour with the pure IL and the binary mixture and the impact of water has been discussed as well as the chain-length of the alkyl carboxylate anion.

In the next chapters, two different applications using both the presence of ionic liquids have been carried out in order to explore two main fields in which ionic liquids could provide beneficial properties or replace current compounds in a safer way.

Chapter 5 describes the first application of the previously used IL solutions for the *in-situ* synthesis of copper(II) oxide nanoparticles, which has been carried out using copper complexes as precursors dissolved in ionic liquids. The aim of this study was to gain a better understanding of the metal oxide nanoparticle formation and morphology control. In this study, the nanoparticle solutions were investigated *via* their physical and microscopic properties (TEM, XPS, X-Ray scattering). Single crystal diffraction was also used to identify the starting materials and the intermediate materials before the formation of nanoparticles. Potential applications of these novel nanofluids are heat transfer fluids or as catalysts.

In chapter 6, a second application of new ionic liquid solutions was investigated as electrolytes for sodium-ion batteries. This had the aim to provide safer electrolytes, since these offer several advantages over conventional electrolytes such as non-volatility, non-flammability and large electrochemical windows, which results in better long-term stability. By using novel functionalized ILs it could be demonstrated that these ILs are suitable potential electrolytes in this type of battery.

Contexte scientifique et résumé en français

De nos jours, les chimistes se focalisent sur l'amélioration de la chimie verte et essaient de trouver de nouvelles alternatives pour diminuer l'utilisation de solvants et pour optimiser les nouveaux outils technologiques en termes d'écologie, de rendement, de performance et de sécurité.

Ainsi l'utilisation des liquides ioniques pour remplacer certains solvants et pour optimiser certains systèmes est devenue le sujet propice à de nouvelles recherches. En effet, les liquides ioniques sont connus pour avoir la particularité d'être des sels liquides formés d'anions et de cations et donc d'avoir un point de fusion inférieur à 100°C. De plus ils ont la faculté de ne pas s'évaporer ce qui les rend utilisables pour des projets spatiaux par exemple ou encore pour remplacer des solvants inflammables et donc dangereux notamment dans le cas de la formulation d'électrolytes pour batterie, comme nous le verrons dans ce travail. Les liquides ioniques sont aussi appelés « designer solvents » du fait du nombre immense de combinaisons possibles entre l'anion et le cation qui permettent au chimiste de moduler leurs propriétés physico-chimiques. Ainsi des liquides ioniques aux propriétés hydrophobes, ou encore hydrophiles ou plus ou moins visqueux peuvent être créés ainsi que bien d'autres fonctionnalités. Les liquides ioniques sont utilisés dans le secteur de la pétrochimie comme catalyseur, mais aussi dans la capture de gaz toxiques comme le carbone de dioxyde et le mercure. Souvent il est même possible de recycler le liquide ionique alors que les solvants sont souvent rejetés dans l'atmosphère à cause de leur point d'ébullition souvent inférieur à 100°C (Chapitre 1).

Un autre sujet en grande évolution est le monde de la nanotechnologie. En effet, il a été reconnu que les nanoparticules engendrent de nouvelles propriétés souvent plus intéressantes du fait de leur petite taille. Il a été reconnu que l'ajout de nanoparticules dans certains systèmes, comme dans les électrolytes par exemple, pouvaient augmenter la conductivité du système. Il est aussi connu que diminuer la taille d'une particule augmente de façon exponentielle sa surface de réactivité ; ce qui est extrêmement important en catalyse. Récemment, de nouvelles investigations sont élaborées sur un nouveau matériau se composant d'un liquide plus ou moins visqueux dans lequel sont dispersés des nanoparticules. Ces nouveaux liquides sont appelés nano-fluides et sont souvent utilisés comme fluides caloporteurs dans le monde de l'automobile ; par exemple pour les systèmes de refroidissements. Les liquides ioniques peuvent ainsi être utilisés comme fluides caloporteur et ont été reconnus comme stabilisateurs de nanoparticules et comme précurseurs étant impliqués dans la taille des nanoparticules (Chapitre 1).

En parallèle de nombreuses études se concentrent sur l'optimisation des électrolytes pour les batteries métal-ions. En effet l'utilisation de solvants inflammables dans la fabrication de ces batteries est souvent l'élément déclencheur d'une source de risques pouvant aller jusqu'à l'explosion si les mesures de sécurité n'ont pas été prises correctement. Ainsi, le remplacement de ces solvants par des liquides ioniques comme électrolytes pourraient jouer un rôle clef pour limiter les risques d'échauffement des batteries. En effet les liquides ioniques sont des composés ininflammables de par leurs points d'ébullitions nettement supérieures au solvant et peuvent donc offrir une batterie potentiellement plus stable. De plus, de nouvelles études tentent de remplacer le Lithium de métal par le sodium de métal. Ce dernier est nettement plus abondant que son prédécesseur et nettement moins cher. En outre l'utilisation du sodium de métal redouble les risques d'inflammabilité et d'explosion de la batterie, ainsi l'utilisation des liquides ioniques pourrait s'avérer une option certainement plus adaptée et prometteuse (Chapitre 1).

Dans ce projet de thèse de chimie, des nanoparticules de cuivre ont été synthétisées *in-situ* par le biais de liquides ioniques (Chapitre 5). Pour ce faire, de nombreux outils ont été utilisés de façon à comprendre tout d'abord les interactions entre le mélange binaire réactionnelle utilisé dans la synthèse des nanoparticules. L'analyse des propriétés macroscopiques du mélange binaire a été réalisée tenant compte de la viscosité, densité, conductivité et des propriétés thermales du système (Chapitre 3), suivie de l'analyse des propriétés microscopiques des mixtures par des méthodes de spectroscopies (Chapitre 4). Ensuite l'analyse des nanoparticules a été faite par le biais du microscope électronique en transmission ainsi que d'instruments à base de rayon X (Chapitre 5). Ainsi, le but de cette recherche fut de comprendre comment la synthèse de ces nanoparticules a lieu, comment ces nanoparticules ont été formées, et ainsi de comprendre le rôle du liquide ionique dans la formation des nanoparticules. De ces résultats l'objectif était de montrer qu'il serait possible de contrôler la morphologie de nanoparticules par l'utilisation d'une gamme de liquides ioniques aux fonctionnalités chimiques bien spécifiques.

Un autre point de cette recherche fut de développer de nouveaux liquides ioniques ininflammables qui remplaceraient les électrolytes classiques utilisés pour les batteries au sodium et ainsi de comprendre l'impact provenant du design des liquides ioniques utilisés dans cette étude (Chapitre 6).

Abbreviations

[C$_2$MIm]$^+$ = 1-ethyl-2-methylimidazolium cation

[C$_3$H$_7$CO$_2$]$^-$ = butanoate anion

[C$_7$H$_{15}$CO$_2$]$^-$ = octanoate anion

[CH$_3$CO$_2$]$^-$ = acetate anion

ESS = Energy Storage Systems

EV = Electrical Vehicles

HEV = Plug-in Electric Vehicles

IL = Ionic liquid

ILs = Ionic liquids

LIBs = lithium-ions batteries

NMR spectroscopy = Nuclear Magnetic Resonance spectroscopy

SAXS = Small Angle X-ray Scattering

SEI = Solid Electrolyte Interphase

SIBs = Sodium-ions batteries

TEM = Transmission Electron Microscopy

WAXS = Wide Angle X-ray Scattering

XPS = X-ray Photoelectron Spectroscopy

Table of Content

Chapter 1 _ Introduction

1.1 Introduction

In this study, solutions of 1-ethyl-2-methylimidazolium alkyl-carboxylate ILs in binary mixtures with water will be investigated with the aim to investigate the effect of aggregation by increasing the carbon chain lengths from 2 to 8 carbons of the alkyl-carboxylate anion. A wide range of techniques will be applied, starting from the characterisation of their physical properties as well as spectroscopic techniques in function of temperature and mixture compositions in order to gain a full understanding of their interaction behaviour.

Furthermore, these carboxylate ionic liquids will be used in two separate applications. The first application will use those solutions to make copper(II) oxide nanoparticles by an *in-situ* method and to investigate the role of ILs and the presence of water in the nanoparticle formation. The second application will use ILs in binary mixture with a new solvent; propylene carbonate (PC), to investigate the role of these ILs in terms of overcoming current safety-issues with electrolytes for sodium-ion batteries. Those two applications are supported by a comprehensive study on the IL binary mixtures with water which will lead to gain a better understanding of the role of these ILs as "*designer solvent*".

In this chapter, a definition of ionic liquid will be reviewed, as well as the role of water in binary mixture with ionic liquid in terms of aggregation. Then the techniques that will be used in this study will be presented. Finally, some general background in the field of ionic liquid uses regarding the two applications undertaken in this work will be detailed, especially nanoparticle formation and the use as electrolytes for ion-batteries.

1.2 Ionic liquids

The field of ionic liquid (IL) started in 1914 with the work of Paul Walden, who reported on the ethylammonium nitrate ($[EtNH_3][NO_3]$) by the neutralisation of ethylamine with concentrated nitric acid[1,2]. This new species was studied intensively and has led to some important outcomes due to its unique physicochemical properties.[3]

1.2.1 Definition

From Walden's work, ILs can be defined as chemical composed entirely of cations and anions having melting points below 373 K (100°C).[1] In other words, they are liquid-salts, also called *molten salts*, made entirely of ions. Some common cations and anions of ionic liquids are shown in Figure 1-1 and Figure 1-2. According to Seddon,[4] there are about 10^{18} possible IL combinations which make them tuneable and therefore interesting for a range of applications. Indeed, they often referred to as "*designer-solvents*" since ILs can be tuned by changing the cation or either the anion with different functionalized group, such as hydrophilic or hydrophobic groups, which will also tune the physical properties of the new IL synthesis (viscosity, density, conductivity, thermal properties).
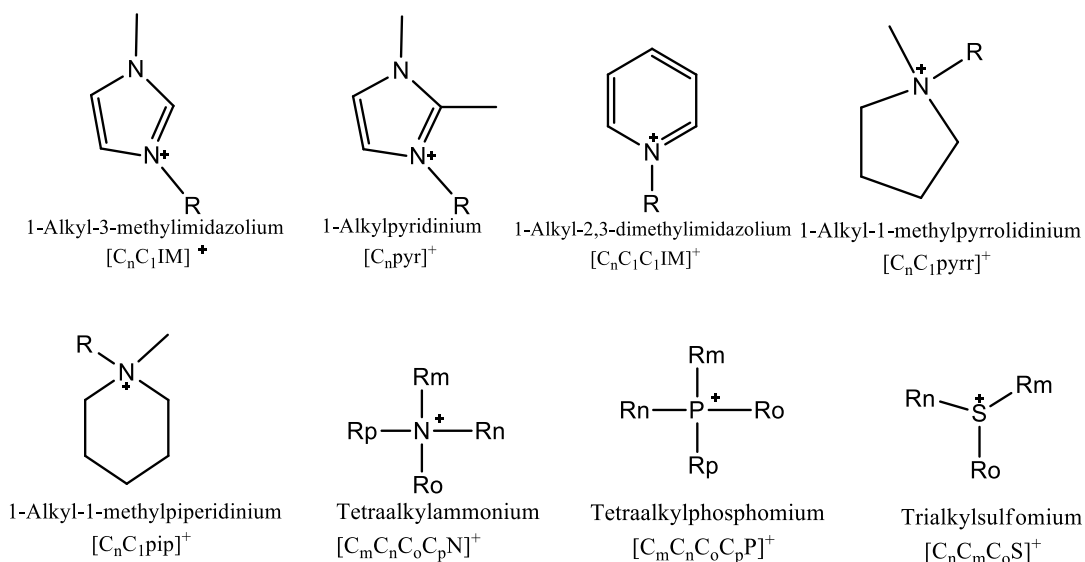
Figure 1-1. Common cations used for ionic liquids
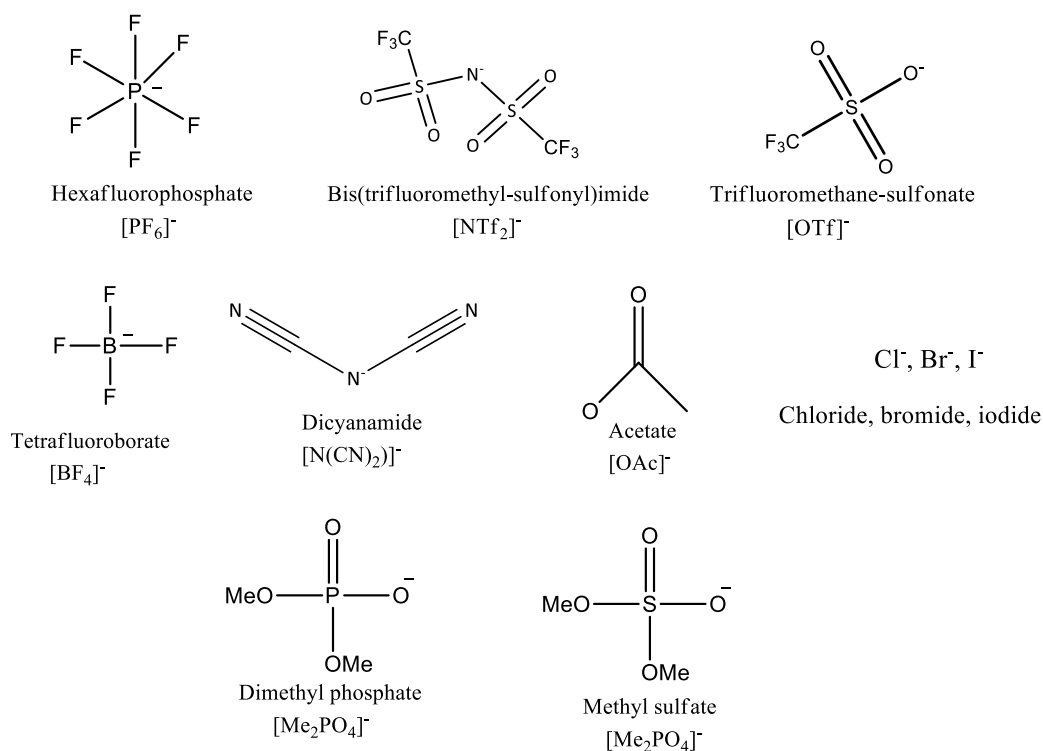
Figure 1-2. Common anions used for ionic liquids

1.2.2 Properties of ionic liquids

Ionic liquids exhibit unique properties such as a low vapour pressure, wide liquid-phase range and a high thermal and chemical stability.[3]

The reason why ILs are salts that remain liquid in the liquid state is due to their large and asymmetric cations and anions that keep moving around each other and therefore remain liquid below 373 K. In comparison, solid salts, such as NaCl which has a melting point of 1074.15 K (801 °C), are being solid due to the small and spherical shapes of the cations and anions that allows for efficient packing when cooling, and therefore leads to crystallisation.

Another relevant and attractive point with regard to ILs is their ability to have negligible vapour pressures. They are therefore non-flammable compounds. In fact, IL cations and anions are hold together by coulombic interactions. Those typical interactions are very hard to break below 673.15 K. In contrary, common solvent, such as water and alcohol are molecules interacting with each other by van der Waals forces and hydrogen bonds. These latter forces are easy to break

3

and will lead to the evaporation of the solvent at lower temperature (below 473.15 K).

Therefore, from all those unique and specific properties, ILs is used in many applications. Often these are used to replace volatile solvents, since they can be used under vacuum due to their low vapour pressure,[5] but also as electrolytes (for batteries, solar cells etc.) due to their ionic properties, to absorb/desorb gases such as CO_2, to capture harmful chemicals, such as mercury,[6,7] to extract precious metals from waste (Al, Zn, Ga, lanthanides...),[8] to dissolve different chemicals and materials, such as waste, cellulose, lignin or chitin into new-polymer, in catalysis or to produce shaped nanoparticles.[9]

1.2.3   Quantifying water content in ionic liquid

Water is known to be present in both hygroscopic and hydrophobic ILs due to ineffective drying after preparation or due to absorption from the moisture present in the atmospheric air. Even small amount of water content found in ILs can affect the structure of IL by, for instance formed new hydrogen-bonds complex with water.[4] Therefore, before investigating new reaction that involves IL, it is very important to consider the water content already present within the IL.

The determination of water content in ILs was achieved by a coulometric titration according to Karl Fisher, where iodine is generated by electrochemical oxidation in the cell. The coulometric cell consists of two parts, the anode and the cathode compartments as displayed in the Figure 1-3.[10] This process is based on the reaction described by R.W Bunsen:[11]

(Eq. 1)

$$I_2 + SO_2 + 2H_2O \longrightarrow 2HI + H_2SO_4$$
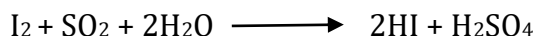
This reaction occurs in a non-aqueous system, where an alcohol is used as solvent (methanol is a suitable solvent in which IL are miscible with).
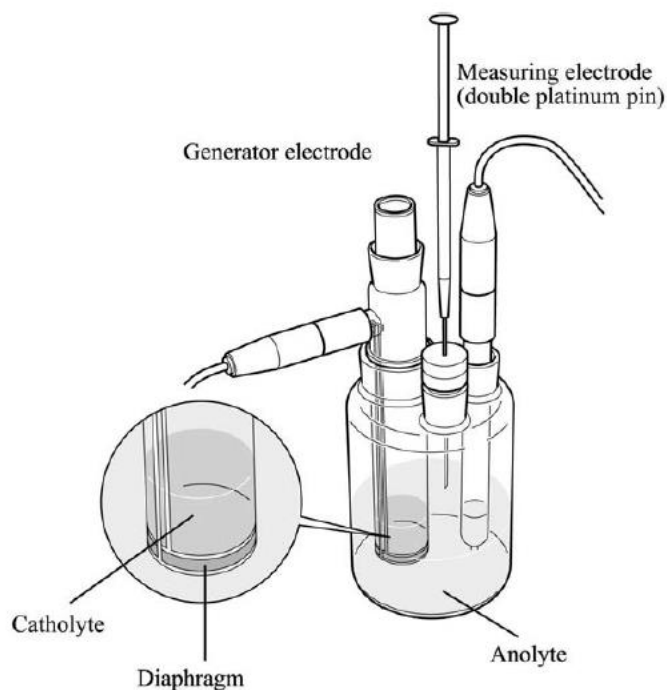
Figure 1-3. Schematic view of a coulombic titration Karl-Fisher.

At the anode, iodine (I_2) is generated from iodide ions (I^-) by electrochemical oxidation. Then the (I^-) ions release electrons at the anode and form iodine: (Eq. 2)

$$2\ I^- \longrightarrow I_2 + 2\ e^-$$
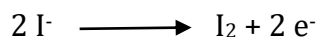
Iodine formed reacts immediately with water as show in (Eq. 1).

At the beginning and during the titration, iodine reacts with water. However, as soon as all the water in the sample has reacted with iodine, the now free iodine would increase the conductivity of the solution. This would lead to a drop in the voltage, which is used to indicate the end of the titration. Therefore, the water content in the sample tested can be calculated by knowing the number of mole of iodine that has reacted with the water during the reduction-oxidation reaction, as well as the introduced mass of the tested sample.

1.3 Ionic liquid and water binary mixtures

Binary mixture of ionic liquids and solvents under different conditions (i.e., concentration, temperature) are commonly used in electrochemistry. ILs are non-volatiles and therefore could increase the safety of battery for instance if used as electrolytes. However, their efficiency won't be as good as common electrolytes' solvent due to their high viscosity. Therefore, mixing ILs with an appropriate solvent would normally decrease their viscosity, resulting in better electrolyte performance. However, the addition of another fluid into ILs would also change its interionic and intermolecular interactions and thus its properties.[12-15]

Therefore, to support the understanding of those kind of mixtures it is important to find out their intermolecular interaction behaviour. Indeed, intermolecular interactions would depend on the nature of the IL cation and anion as well as the solvent used and the concentration used. Also, another interesting part of this study is to figure out how water is directly interacting with ILs over the whole composition range. In fact, ILs, either hydrophobic or hydrophilic, are known to absorb water from the moisture in air, which would affect the IL properties.[16-21] Therefore, it is important to understand the effect of water at any composition in ILs to avoid any problems when used in application, such as electrolytes for metal ion battery as it will be explain in more detail in Chapter 6 of this thesis.

In this work, thee IL mole fraction (χ_{IL}) and mass fraction (ω_{IL}) were including the initial water content left in the dried IL and added to the additional water incorporated in the binary mixture as seen in the (Eq. 3)and (Eq. 4):

(Eq. 3)

$$\chi_{IL} = \frac{n_{IL}}{n_{IL} + n_{water}}$$

(Eq. 4)

$$\omega_{IL} = \frac{m_{IL}}{m_{IL} + m_{water}}$$

where n_{IL} and n_{water} are the respective number of mole of IL and water obtained from the Karl-Fisher titration and where m_{IL} and m_{water} are the respective mass of IL and water.

1.3.1 Aggregation behaviour of alkyl-carboxylate anion-based ionic liquids in water

Alkyl carboxylates are well-known in the world of surfactant. In fact, the aggregation behaviour of imidazolium alkylcarboxylates protic ionic liquids ([Im][$C_nH_{2n+1}COO$]) in water has already been studied by Anouti *et al.*, as a function of the alkyl chain length (from n= 5 to 8) by using surface tensiometry and conductivity. In this study, it was shown that imidazolium alkyl carboxylates exhibit a higher ability to aggregate in aqueous solutions than classical anionic surfactants, proving the potential applicability as surfactant of these ILs.[22]

In the case of the ethanoate (n = 2), Hall *et al.*, have shown that [C_2MIm][CH_3CO_2] and water binary mixture do not form emulsions. To prove it, they have used proton, carbon and 2D-NMR spectroscopy (H-H between anion, cation and water correlation). By determining the chemical shifts ($\Delta\delta$ (ppm)), they were able to highlight where the hydrogen bonds were stronger between the anion and the cation of the pure ionic liquid and then which hydrogen ring would be disturbed by the addition of water and thus where the water would compete the most.

For the H^1-NMR spectroscopy, these authors found a $\Delta\delta$ (ppm) < 0, which means the protons have stronger hydrogen bonding than those having a positive $\Delta\delta$ (ppm). However, even though there are negative $\Delta\delta$ (ppm) in the case of the [C_2MIm][CH_3CO_2] their shifts were still too smooth to be classified as an emulsion. And therefore, by combining density and viscosity information, this paper had proven that there was no emulsion formed in the case of the [C_2MIm][CH_3CO_2] mixed with water. However, by increasing the alkyl chain length of the anion, a better aggregation of the mixture would be expected to lead to an emulsion formation as it was proven elsewhere.[22]

1.3.2 Intra- and intermolecular interactions of pure water

Before investigating the pure ILs and their mixtures with water it is important to gain a better understanding on the interaction behaviour of the pure water itself; an easy system to study and well known in the literature. A molecule of water is constituted of one atom of oxygen linked from both sides to two atoms of hydrogen *via* covalent bonds.

In a liquid system of pure water, the molecules are also linked to each other *via* intermolecular interactions, the *Van der Waals forces* and more particularly in this system by *hydrogen bonding*. Indeed, hydrogen atoms form weak interactions with other oxygens due to the basicity of the oxygen and the acidity of the hydrogen (interaction acid-basic or also called *dipole-dipole*).

However, since the temperature decrease, the intermolecular interactions between the molecules of water become stronger and stronger until water molecules become solid (ice). Unlike, when the temperature increases, intermolecular interactions between the molecules of water become weaker and weaker until the water molecules evaporate.

Covalent bonds are very strong; 464 kJ·mol^{-1} of energy is needed to break the H-O bond, whereas intermolecular interactions are weak in comparison, since only 19 kJ·mol^{-1} of energy is needed to break the bonds between molecules of water. The table below summarises the definition of inter and intramolecular interactions and their type of interactions associated and used in this work later.

Table 1-1. Intermolecular and intramolecular interactions definition.

	Intermolecular forces	Intramolecular forces
Meaning:	*Inter* = between Bonds which occur between atoms within different molecule.	*Intra* = inside Bonds which occur between atoms within the same molecule.
Strength of forces:	Weak	Strong
Type of bonds:	- Ion-Induced dipole forces - Ion-Dipole forces - Van der Waals forces (= London dispersion force and dipole-dipole force) - Hydrogen bonding (weakest)	- Non-Polar Covalent Bonds - Polar Covalent Bonds - Ionic Bonds

1.4 Characterisation of structure and interactions of mixtures

The structure of liquids has been studied for many years.[1,2] Investigations have, in general, been focussed on the arrangements in molecular solvents such as water, *t*-butanol, and simple chlorinated solvents.[4] In contrast, interest in the structure of ionic liquids (ILs) has only been developed significantly in the last decade.[23] In fact, a variety of experimental techniques has been used to investigate IL structures including neutron diffraction, X-ray scattering and NMR spectroscopy.[23-30]

These experimental techniques are generally coupled with theoretical work in order to access specific structures and interactions in IL solutions. This interest stems from the need to understand solvation and physico-chemical properties of these materials in order to design new ILs for particular applications. ILs have a wide range of valuable engineering properties (including effectively zero vapour pressure at ambient temperature) and their physical properties may be varied systematically leading to materials which can be tailored for a given process rather than the solvent dictating the process.[31,32]

 This understanding is critical since there are many cation-anion combinations available giving an IL with a melting point close to room temperature, and without some predictability, the wide solvent choice is problematic.[31]

The techniques that will be used in this study will be presented here thanks to the aim of this study.

1.4.1 NMR-Spectroscopy

The Nuclear Magnetic Resonance (NMR) spectroscopy is a preeminent analytical technique to determine the content and purity of a sample as well as its molecular structure.[33,34] This technique is performing on the nuclei of atoms only. All nuclei are electrically charged and many have spin that causes them to behave like a magnet (due to constant spinning).

Therefore, when an external magnetic field (called B_0) is applied, an energy transfer is possible between the spin of base energy (-1/2) to the spin of higher energy level (+1/2) of the nuclei. When the spin returns to its base level, the same energy is emitted and can be measured and processed in order to give an NMR spectrum for the nucleus concerned. A schematic view of the Figure 1-4:
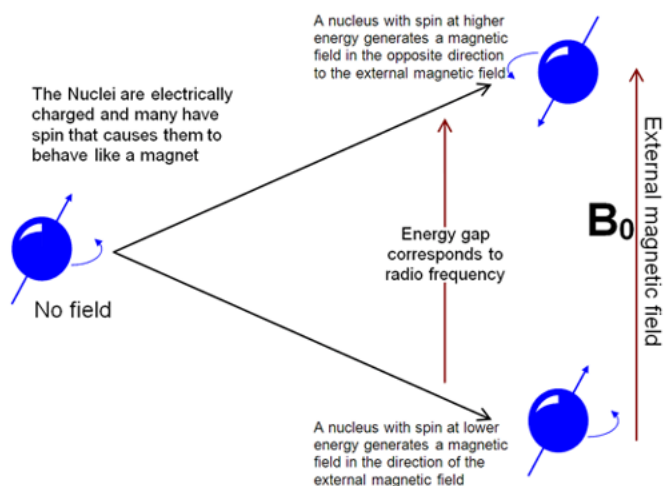
Figure 1-4. The case of the spin -1/2 nucleus, that included proton (^{1}H) and carbon (^{13}C) before and after exposition to a magnetic field B_0 (this schema was taken from a website page).[33]

1.4.1.1   Chemical shift variation background

What is called *chemical shift* (noted $\delta_i(x)$) is the strength of the magnetic field that the nucleus of an atom feels within the molecule in its environment. It is the difference between the external magnetic field and the field felt by the nucleus called "shielding" and measured in *ppm* (part per million).

In spectroscopy, *shielding* also called *upfield* shift is used when the nucleus feels weaker magnetic field and therefore would have a decrease of its chemical shift due to the addition of electron density, magnetic induction, or other effects to the considered atom. In the opposite, *deshielding* or *downfield* shift is used when the nucleus feels stronger magnetic field, having an increase of its chemical shift due to the removal of electron density, magnetic induction, or other effects.

In ^{1}H-NMR spectroscopy, a proton will be downfield when it is linked with an atom having a high electronegativity, whereas it will be an upfield shift when the proton is linked to an atom having a low electronegativity. As a remember,

electronegativity values of some main atoms are cited here: F = 4.0, O = 3.5, N = 3.0; Cl = 3.0, Br = 2.8, I = 2.5; S = 2.5; C = 2.5, P = 2.2, H = 2.1 and silicon has an electronegativity value of 1.9, even smaller than hydrogen.

1.4.1.2 *Chemical shift referencing issues*

Unfortunately, there is no common model to assess the study of chemical shifts using NMR spectroscopy in the literature, where different chemical shift referencing techniques has been used. Therefore, it is difficult to compare the data with the literature. Indeed, some studies have used *internal referencing* (a compound added directly to the mixture which would act as a reference).[35-41] However, this method should assume there are no intermolecular interactions with the internal referencing, which seems very unlikely. Fortunately, most of the other studies use an *external reference*, where a capillary containing the reference compound and a deuterated solvent are inserted into the NMR tube containing the IL mixture (this latter method is used in this work). Although, it was found that using only a deuterated solvent as reference can be inaccurate as it is mentioned in the *convention for chemical shifts* in the IUPAC Recommendation 2001 and 2008. [42,43]

1.4.1.3 *Relative and absolute chemical shift to study concentration effect on binary mixture*

In the literature, the impact of the solvent concentration in IL *via* NMR spectroscopy can be studied by comparing the chemical shift of all peaks in the NMR spectra for different IL solution compositions. To do so, all NMR spectra for each IL-solutions have to be on the same scale by using an external reference in order to compare the chemical shift variation of each peaks taken at different concentration.[44] Then, the **relative or absolute chemical shift** of each atom targeted (^1H, ^{13}C, ^{15}N, etc.) in IL-solutions at different concentration can be calculated. The relative chemical shift is noted **$\Delta\delta_i(x)$** and is found by the subtraction of the corresponding values of chemical shift of the IL-solvent mixture to the corresponding chemical shift of the pure IL scaled by using the same external reference as it is written below:

$$\Delta\delta_i(x) = \Delta\delta_i(x)_{\text{mixture}} - \Delta\delta_i(x)_{\text{pure IL}}$$

Again, in some studies, different references to subtract the mixture have been reported to determine their $\Delta\delta_i(x)$ as it can be chosen arbitrarily (i.e., the lowest concentration mixture, the neat IL or an intermediate concentration). So far, the most relevant reference concentration is the neat IL compound which is also used in this work.

In conclusion, by looking at the impact of the solvent concentration in the IL solutions, negative values of the relative chemical shift for a corresponding atom corresponds to an upfield shift; whereas positive values of the relative chemical shift correspond to a downfield shift.

1.4.2   The diffraction experiment

As explained in the Gudrun manual from ISIS (Rutherford Appleton Laboratory)[45], diffraction methods, such as small-angle X-ray scattering (SAXS) or neutron scattering used in this work, are used to study atomic structures of sample such as single crystal, polycrystalline powder, glass, liquid or gas. In fact, from neutron scattering, it is possible to obtain information about the location of atoms within a sample using neutron as beam source. In opposite, results from X-ray diffraction give information on the positions of atoms within the unit cell of a crystal.

A diffraction experiment requires a source of radiation, an incident beam monochromator and collimator, a sample to be investigated, a scattered beam collimator, a radiation detector(s), a data acquisition electronic to collect the detectors' information and data analysis software to convert raw data to differential cross section data. In the Figure 1-5 below, the basic of X-Ray and neutron diffraction are described. Every distance is measured relatively to the wavelength of the applied radiation, where scattering patterns are presented as function of Q:

(Eq. 5)

$$Q = \frac{4\pi}{\lambda} \cdot \sin\theta$$

When the particles show a highly ordered and periodic arrangement, such as interaction, aggregation or nanoparticle formation; the scatters show pronounced peak that is called the Bragg peak. The position of its maximum (Q_{max}) indicates the distance (d_{Bragg}) between the aligned particles by using Bragg's law:

(Eq. 6)

$$d_{Bragg} = \frac{2\pi}{Q_{max}} \ (nm)$$
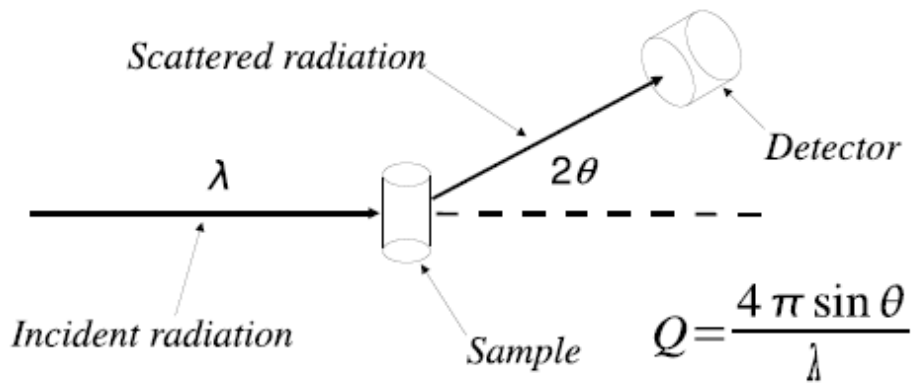
Figure 1-5: Primary layout of X-Ray or neutron diffractometer. [45]

1.4.2.1 Small-Angle X-Ray scattering (SAXS)

SAXS is an analytical method to determine the structure of particle systems in terms of averaged particle sizes or shapes. The materials can be solid or liquid and can contain solid, liquid or gaseous domains. X-rays are sent through the sample, and every particle inside the beam will send out a signal. This was, the average structure of all illuminated particles is measured.[46]

X-Ray are electro-magnetic waves similar to visible light. However, the wavelength is much shorter (<0.3 nm) than that of visible light (around 500 nm).

SAXS is a non-destructive, accurate and only requires a minimum of sample. The particle or structure sizes that can be resolved range from 1 to 100 nm but can be extended on both side by measuring at smaller (Ultra Small-Angle X-Ray Scattering, USAXS) or larger angles (Wide-Angle X-Ray Scattering, USAXS which is also called X-Ray Diffraction, XRD). However, small particles are hardly visible

in the presence of big particles or aggregation, but is very sensitive to the formation or growth of large particles.

1.4.2.2 *Neutron scattering*

A neutron is an electrically neutral subatomic particle with a mass 1,839 times larger than the electron.[47] Neutrons will interact with the nucleus of an atom rather than electron used in the process of X-ray diffraction. Unlike X-rays, the scattering power (called cross-section) of an atom is not related to the atomic number in the case of neutron scattering. Therefore, neutron diffraction allows to sense light atoms (such as hydrogen) and isotopes of the same elements within heavier atoms, and also to easily distinguish each elements in the sample due to their respective different scattering cross sections. However, one disadvantage of using neutrons instead of X-ray is cost and access, since synchrotrons are rare and need huge maintenance due to the nuclear reactor.
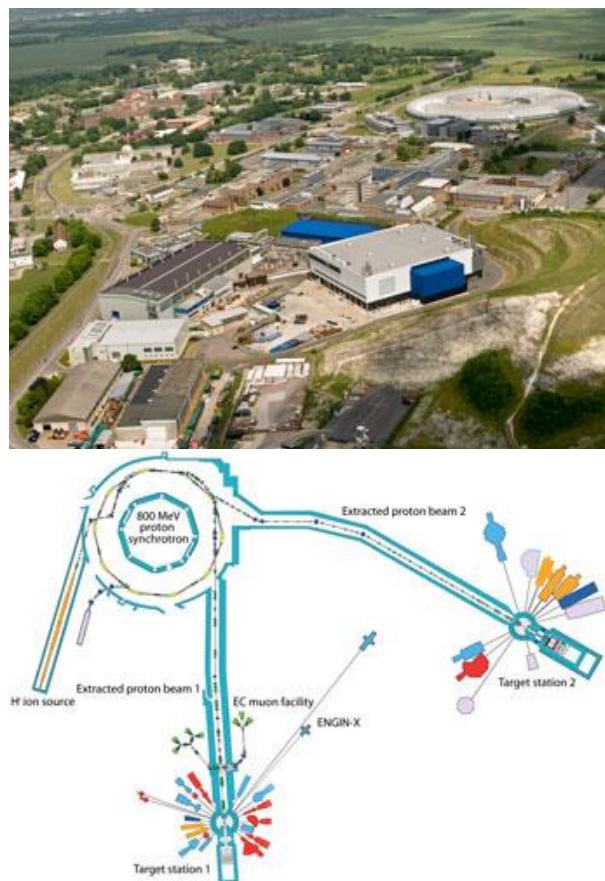
Figure 1-6. Synchrotron, ISIS Pulsed Neutron and Muon Source, Rutherford Appleton Laboratory in England.[45]

1.5 Applications of ionic liquids in Metal oxide nanoparticle formation

Ionic liquids have been found to be used in nanoparticle (NPs) formation in a large amount of study.[48,49]

In this part, the role of IL as well as some example of NPs synthesis without and with the use of IL will be investigate.

1.5.1 Role of ionic liquids as stabiliser for nanoparticles' formation

Ionic liquids can play different role in the nanoparticle formation process, such as their role as stabiliser of NPs. In fact, most of the time the cation plays a role as stabilising agent but can also play a role as a templating agent due to his tuneable surface tension. This can lead to an emulsion process and thus influence the size of the NPs. The role of emulsions as a template for NPs formation has been well described in the synthesis of spherical silica particles without the use of IL.

Furthermore, IL viscosity is known to affect the NPs size due to a slower mass transport in higher viscous liquids. In fact, the more viscous the IL, the smaller will be the nanoparticles and *vice-versa*.

1.5.2 Applications of Metal oxides

Metal oxides are used in catalysis, sensing, energy storage such as hydrogen storage,[50] optics, and electronics. Metal oxide nanoparticles especially are used in solar cells,[51] gas sensing,[52] magnetic storage media,[53] nanodevices,[54] heterogeneous catalysis,[55] and superconductor.[56]

Transforming metal oxides into nanoscale is opening new applications that are important in industry and daily life. In fact, when convert metal oxides into nanomaterials, new properties have in comparison to the bulk materials been found such as changes in their electronic properties, mechanical plasticity, magnetic behaviour and phase-transition temperature. Major industrial application for nanoparticles in the past ten years are found in the area of catalysts, polymer composites, paints/coatings and cosmetics.[57]

For instance, the liquid electrolyte in dye-sensitized solar cells is still a challenge in terms of stability. However, promising studies have shown that nanosized

particles can enhance these systems. For instance, the electrical conductivity of the electrolyte for a dye-sensitized solar cell can be improved by using copper encapsulated within carbon shell nanoparticles dispersed in ionic liquids at room temperature.[58] In fact, the electrical conductivity of the IL electrolyte seems to enhance due to the electron-rich carbon shell surfaces of these new nanosized systems. The electron transport was also found to be favoured by the CuO layer on the surface of the nanosize core system copper-carbon.

1.5.3 Synthesis of metal oxide nanoparticles

1.5.3.1 Common synthetic routes

Several processes are used to produce metal oxide nanoparticles such as high temperature processes, soft-chemistry routes and especially sol-gel processes.[59] A sol-gel process can be defined as the conversion of a precursor solution into an inorganic solid, where an inorganic metal salt or metal organic species (such as metal alkoxide) is used as precursor. It has been found that non-aqueous sol-gel processes were suitable for metal-oxide nanoparticles synthesis instead of using aqueous sol-gel processes. However, aqueous sol-gel processes are limited with regards to the control over the nanoparticle morphology.

In fact, three main reactions occur due to the high reactivity of the metal oxide and the water used as ligand and solvent: hydrolysis, condensation and aggregation which are difficult to control. It is also difficult to gain control over the crystallisation process of these metal oxide NPs. It was found that non-aqueous sol-gel processes in organic solvents are suitable to gain control over these previous reactions.

In fact, organic solvents are influencing the particle size, shape, surface and assembly properties, composition and crystal structure of the metal oxide NPs. This is due to the slow reaction rates, caused by the C-O bond, in association with the stabilizing effect of the organic solvent which lead to uniform crystallite particle morphologies in a range of a few nanometres.
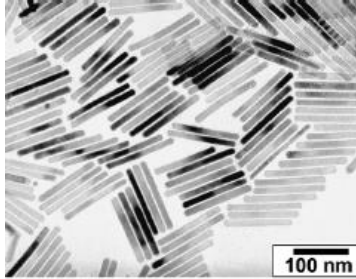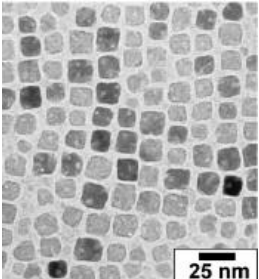
1.5.3.2   Ionic liquids used in metal oxide nanoparticles synthesis

It is well known that ionic liquid are suitable stabilisers of nanoparticles. [60,61]This is why in the past several years, ionic liquids have been used as solvents to produce nanoparticles, where a range of strategies have been reported regarding the control of the nanoparticle sizes and shapes. There is a large amount of papers reported on iron oxide nanoparticles, which is in high demand for biological applications. Only a few reports on copper oxide, magnesium oxide, silver oxide, lithium oxide, titanium oxide and zinc complex nanoparticles can be found in the literature.

In this thesis, the focus has been especially on iron and copper oxide, and zinc complex nanoparticles. Metal oxide nanomaterials can be prepared following three different methods, which includes first the use of capping agents, and furthermore new synthetic methodologies applying microwaves. Some examples are explained below to get a good understanding in these synthetic processes.

Wang *et al.*; have been using surface capping agents in order to control the morphology of iron oxide nanoparticles.[62,63] They were using 1-butyl-3-methylimidazolium bis(trifluoromethyl-sulfonyl) imide ($[C_4MIm][Tf_2N]$) ionic liquid to synthesis well-defined shapes of iron oxide nanostructures such as rods, cubes and spheres. To control the shape of the particles, oleic acid, oleylamine and 1,2-hexacandiol were used as surfactants. The size of the nanoparticles found was influenced by the temperature and the capping agent concentration. Table 1-2 below details the proportion of reagents used and the conditions applied to obtain specific shape and size.

Table 1-2. Table of reagent used to make different shape of iron oxide nanoparticles.

Shape of NPs	Nanorod		Nanocube (9nm)		Nanocube (13nm)	
Reagents	n/mmol	conditions	n/mmol	conditions	n/mmol	conditions
[C₄MIm][Tf₂N]	5mL	**RT:** dark red solution	5mL	**RT:** light yellow solution	3mL	**RT:** light yellow solution
Oleic acid	0.13	**140°C:** dark black solution	0.25		0.15	
Oleylamine	0.09		None	**230°C:** black solution	None	**210°C:** black solution
1,2-hecande candiol	0.34	**310°C:** reached in 2hrs and kept for 1 hr	None	**280°C:** reached in 2hrs and kept for 1hr	None	**280°C:** reached in 2hrs and kept for 1hr
Iron penta carbonyl	0.75		0.25		0.45	
TEM results[62]						
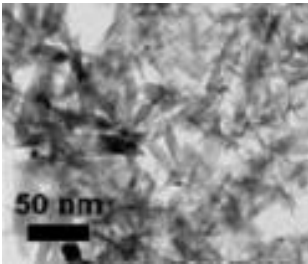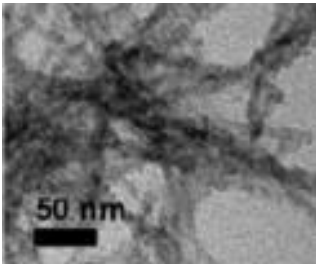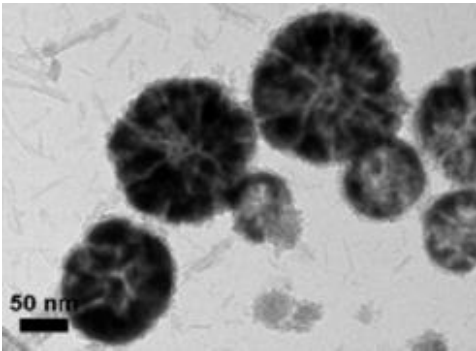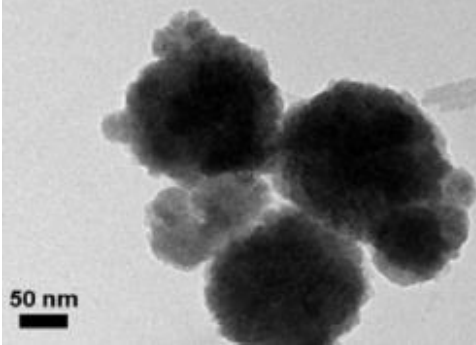
With the aim to characterise the NPs formed, they first extracted the NPs using hexane as a solvent to wash the particles from the ionic liquid. And then, the hexane solutions containing the products were centrifuged.[63]

Another study demonstrated that iron oxide nanoparticles can be also synthesized directly by thermal decomposition of $Fe(CO)_5$ using only a mix of ILs and co-solvent.[64] The morphology of the NPs has been controlled in this work, despite the absence of stabilising surfactant as seen previously.

The synthesis was made mixing 1mL of 1-octyl-3-methylimidazolium tetrafluoroborate [C₈MIm][BF₄] ionic liquid with 1.9 mL of dimethyl formamide (DMF) co-solvent and 0.1 mL of $Fe(CO)_5$. Iron compound was first dissolved in DMF and then added to the mixture of IL/DMF at 60 °C where the solution appeared bright-orange. Then the solution was heated at 90 °C for 1 hr where the solution became dark black. Iron oxide nanoparticles were separated from the IL using a magnet and the rest was washed with ethanol and water. IL and co-solvent effect on the nanoparticles was studying by changing the IL/co-solvent ratio.

The results have been observed then by TEM as shown in Table 1-3 below.

Table 1-3. Iron oxide nanoparticles synthesis using ILs and co-solvent. [64]

Effect of [omim][BF$_4$] IL and co-solvent:[64]				
[C$_6$MIm] [BF$_4$] /DMF ratio	1:0	1:1.5	1:3	0:1
Results n = 6	No particles formed	Nanobars formation	Anisotropic wirelike NPs	No particles formed

Effect of the carbon chain length of the cation imidazolium-based IL[64]:		
IL name	ratio	TEM result
[C$_{14}$MIm][BF$_4$] n = 14	1:1.5	
[C$_4$MIm][BF$_4$] n = 4	1:1.5	

These results demonstrated that the shape and the size of anisotropic iron oxide NPs can be controlled during the synthesis by changing the IL/co-solvent ratio and the carbon chain length of IL's cation.

1.6 Applications of ionic liquids in Safer Sodium-ion batteries

1.6.1 General context

In recent years, producing energies coming from fossil fuels and nuclear plants has several issues with supply and environment, and therefore many researchers worldwide are investigating renewable energies that allow the use of inexhaustible energy resources such as sun and wind. Renewable energies such as solar plants and wind turbines can produce more energy than we need daily, depending on the weather conditions (night time, storms, drought, etc.).[65]

Therefore, there is plenty of energy wasted if part of the energy cannot be used up when it is produced. Furthermore, since fossil fuels are becoming more and more critical, industry and academia are targeting electrical cars in replacement of motor cars for a better future.[65] Therefore, we need devices that can store electrical energy in order to generate electricity where and when it is needed. Accumulators and rechargeable batteries are the best devices so far that can store the electrical energy in a chemical form.[65]

So far, there are two types of batteries; primary and secondary batteries.[66] Primary batteries cannot be recharged due to the chemical energy in the electrolytes which is irreversibly transformed to electrical energy, such as in the case of alkaline batteries and zinc-carbon batteries. Those types of batteries are used in remote controls, clocks, toys, etc. They have only one-time use and are much cheaper than the secondary batteries, however, these are not environmentally friendly. In fact, those batteries have often high toxicity levels coming from the electrolyte decomposition after their use.

In contrast, secondary batteries are rechargeable batteries, such as lead-acid batteries (first rechargeable battery), nickel-cadmium (NiCd), nickel metal hydride (NiMH) and lithium-ion batteries. These are used in laptops computer, cell phones, MP3 player, electrical cars etc. These are much more expensive than primary batteries but then can be used for years since they are rechargeable.[66]

Nowadays, Li-ion batteries have reached the best performance among all the existing rechargeable batteries. These started in the 1970s when the chemist John Goodenough and his colleagues from Oxford University invented and developed Li_xCoO_2 as the cathode material of choice for the Li-ion rechargeable battery.[67] From their research, Sony commercialised the first LIB in 1991. Up to date, Li-ion batteries are found to be the best materials in the development of green technology in the field of electric vehicles (EV), hybrid electric vehicles (HEV), plug-in hybrid vehicles (PHEV) and green grid energy storage.[68]

Indeed, lithium metal is known to be the lighter-weight metal and as a metal-ion battery, it has the best electrochemical potential and provides the largest specific energy per weight. Up to date, a LIB can store almost twice as much energy as NiCd rechargeable batteries.[69] It is also a non-toxic material (compared to the toxic cadmium metal) as it is used as a natural product for treatment of bipolar disorders and to cure depression.[70-72]

However, there are serious concerns about the sustainability of lithium supplies as it is a rarely found metal on earth (with a relative abundance in the earth's crust of 20 ppm),[65] and therefore, its costs have prompted researchers to consider other anodic metals such as sodium, magnesium and zinc, which are significantly more abundant. Increasing numbers of electric vehicles and the application of lithium-based batteries for large scale stationary energy storage, involving load levelling and storage for intermittent renewable electricity generation, will undoubtedly put pressure on the supply and cost of lithium.

Thus, other technologies, including Na–ion, Mg–air and Zn–air batteries, whilst not providing the same energy density as lithium, may be potential alternatives for certain applications.[73-76] Therefore, in this chapter, sodium-ion batteries (SIBs) will be investigated as a replacement for LIBs.

Table 1-4. Comparison of Lithium and Sodium physical properties for rechargeable batteries, after reference.[65]

	Li+	Na+	K+	Mg+
Relative atomic mass	6.94	23.00	39.10	24.31
Mass-to-electron ratio	6.94	23.00	39.10	12.16
E (vs SHE)/V	-3.04	-2.71	-2.93	-1.55
Melting point/°C	180.5	97.7	63.4	650.0
Theoretical capacity of metal electrodes/ mAh·g^{-1}	3861	1166	685	2205
Coordination preference	Octahedral and tetrahedral	Octahedral and prismatic		Octahedral and tetrahedral

1.6.2 Sodium-ion batteries

Sodium metal is the sixth most abundant element on earth (2.6% of the earth's crust) and thus inexpensive. It is also non-toxic and environmentally friendly.
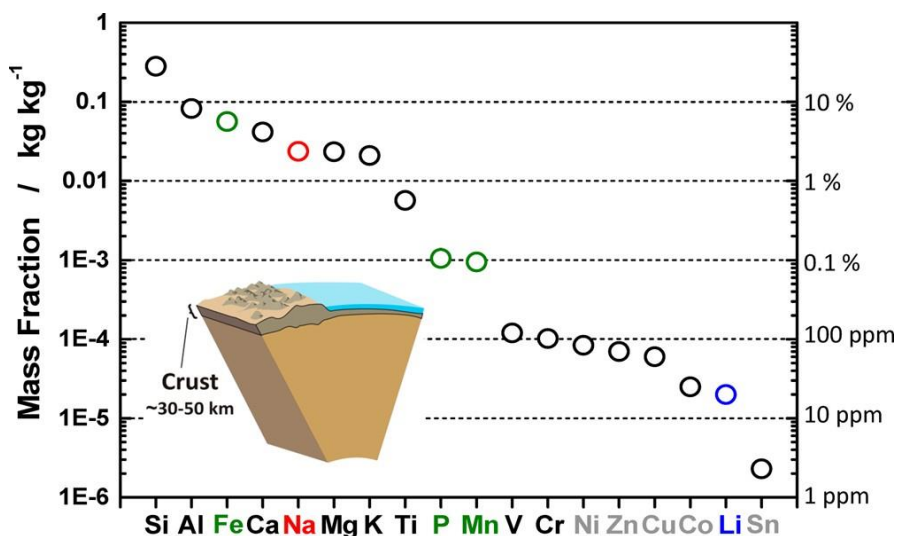
Figure 1-7. Metal elemental abundance in the Earth's Crust from by reference.[77]

1.6.3 Main components of a batteries

A battery consists of several cells. A cell is composed of three main parts which are the positive electrode, a negative electrode and a separator soaked with a liquid or solid separating the two parts called the electrolyte. Both electrodes are made from two different materials, otherwise no current would flow. The separator plays the role of an insulator to avoid a short-circuit between both

electrodes. The electrolyte is composed of an equal amount of cations and anions; hence it is electrically neutral. A cation has a lack of electrons, whereas an anion has an abundance of electrons. In this chapter we are looking at liquid electrolytes which consist of sodium cation salts dissolved in an ionic liquid, and this electrolyte is compared to sodium salt dissolved in a common organic solvent.

1.6.4 How do rechargeable batteries store and release energy?

Discharge principle: once the charged battery is connected to an electric circuit, the battery will start her discharge by the release of her stored energy and produces an electrical current for whichever needs (turning on a laptop computer for instance). This phenomenon is caused by a chemical reaction that takes place in the electrolyte. In fact, the Na^+ cations contained in the electrolyte will flow from the negative electrode to the electrode which has an abundance of electron, the positive electrode; while the electrons (as carriers of the negative electric charge) will flow from the positive to the negative electrode via the outer circuit. The electrolyte with the separator acts as an insulator in which the electrons cannot go through. The battery is fully discharged when all the Na-ions have moved to the positive electrode. Electric current is therefore created by this perpetual movement of electric charge.

Charge principle: The battery is this time connected to an external generator. The Na-ions will flow from the positive to the negative electrode in the electrolyte, whereas the electrons will flow from the positive to the negative electrode *via* the outer circuit. The battery is fully charged when all the Na-ions have moved to the negative electrode.

After many cycles, the electrolytes gradually decomposed that will lower the battery power. When the electrolyte has decomposed, the battery cannot produce positive ions as well as electrons for the outer circuit and the battery would go flat.
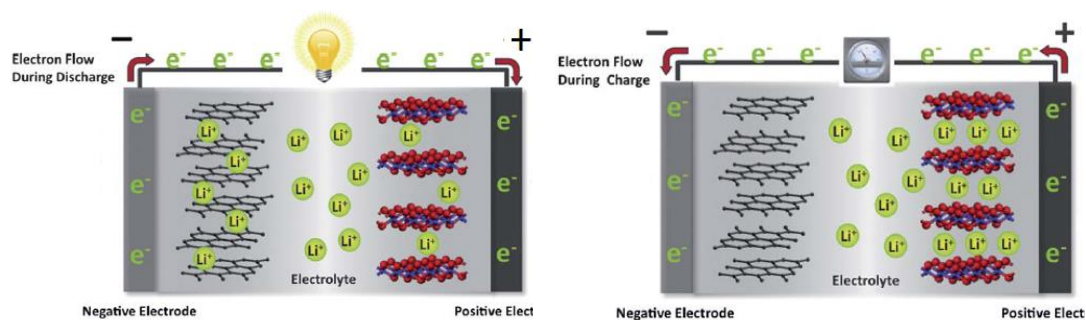
Figure 1-8: On the left, a schematic illustration is shown of a Li-ion cell in use during the discharge process (same as Na-ion cell discharge process). On the right, a schematic illustration of Li-ion cell in use during the charge process (same as Na-ion cell charge process) is shown from reference. [66]

1.6.5 Intercalation process in graphite and hard-carbon negative electrode

The electrode performance is classified by looking at the reaction mechanism in the intercalation/ de-intercalation processes. The intercalation process, also called insertion or sodiation process is the ability of the Na-ions (or Li-ions in the case of LIBs) to be inserted into the electrode. In contrast, the de-intercalation process, also called extraction or desodiation process, is the ability of the Na-ions to move out of the electrode.

When the SIBs are discharging, Na-ions are extracted from the negative electrode and inserted into the positive electrode, whereas during the charging, Na-ions are extracted from the positive electrode and inserted into the negative electrode. The electrode performances can be measured by looking at the gravimetric and volumetric capacity.

Nowadays, graphite is the most used material for negative electrodes in LIBs due to its high gravimetric and volumetric capacity, delivering a reversible capacity of 360 mAh·g^{-1}.[65] Graphite is a crystalline form of carbon, which consists of a layered structure that allows Li$^+$ insertion/extraction.

However, graphite was found to be electrochemically less active in the case of Na-insertion due to the ionic radius of the Na$^+$, which is twice as large (1.02 A) than the ionic radius of Li$^+$ (0.76 A). In fact, this causes graphite expansion and results in a much smaller energy density than in the case of graphite used in LIBs.

Unlike graphite, a much higher amount of Na$^+$ was found to reversibly insert into hard carbon (HC) as negative electrode in Na cells. Hard carbon is a disordered

24

structure (in contrast to graphite), which consists of two domains: carbon layers (as graphene, which consist of a combination of single graphite sheets) and micropores (nanosized pores) formed between them.[65] The structure of HC is specific to the source of hydrocarbon polymer precursors to HC, such as sugar, charcoal, coconut shells, phenol-formaldehyde resins or cellulose, and also to the synthesis conditions such as the carbonization temperature.[78]

So far, a commercialised hard-carbon, Carbotron P(J) (from Kureha Corporation),[79,80] prepared from a petroleum pitch has been used in the Komaba group where researchers found relevant improvements for SIBs using propylene carbonate (PC) as electrolyte. The initial capacity retention of HC-P(J) negative electrodes tested as half-cells was found to be 250 mAh·g^{-1} in 1 mol·L^{-1}-NaPF$_6$_PC solution. However, HC can also be prepared in a "greener" way by using a cheaper hydrocarbon source.

Therefore, in this work, HC was synthesis from sucrose, which is a cheap and earth abundant feedstock, and which also results in a higher reversible capacity of 300 mAh·g^{-1} for Na-coin cells using 1M-NaClO$_4$ in a 30:70 EC/DEC (ethylene carbonate/diethyl carbonate) electrolyte compared to 560 mAh·g^{-1} for Lithium coin cells using 1M-LiPF$_6$ in EC/DEC electrolyte.[81]

1.6.6   Safety issues

1.6.6.1   Li-ion batteries
Li-ion batteries are known for the best electrochemical performance as rechargeable devices, however, there are still some critical issues regarding their safety. In the table below, a number of severe accidents due to Li-ion batteries have been reported.

Table 1-5. Accidents caused by Lithium-ions batteries in the past few years, inspired by reference.[68]

Date	Country	Device catching fire or overheating	Fire causes
1 October 2013	US	Tesla car	Mechanical abuse conditions
16 January 2013	Japan	Boeing 787	Overheating lithium batteries
7 January 2013	Japan	Boeing 787-8	Electrolyte leaking, overheating
18 July 2011	China	EV bus	Overheated LiFePO4 batteries
11 April 2011	China	EV taxi	16Ah LiFePO4 battery
3 September 2010	Dubai	A Boeing B747-400F cargo plane	Overheating lithium batteries
26 Avril 2010		2700 laptop batteries done in 2006 has been recalled by Acer	Overheating and fire hazards
March 2010	Japan	Two iPod nano music player	Overheating lithium batteries
January 2010	China	Two EV buses	Overheated LiFePO4
July 2009	China	Cargo plane	Spontaneous combustion
21 June 2008	Japan	Laptop	overheating lithium batteries
June 2008	Japan	Honda HEV	Overheated LiFePO4
2006 to present		Mobile phones (>10000)	Short-circuit, overheating

Figure 1-9: Photo of a laptop computer going into fire caused by the overheating of its Li-ion battery.

Concerns with the safety of Li-ion batteries are mainly due to the self-accelerated degradation of Li-ion battery called "thermal runaway".[82] This degradation can appear during overcharge, over-discharge or short-circuits which will produce an overheating which is much higher than manufacturer ratings. In fact, a chain of exothermal reactions happens when the critical temperature is reached, and will increase the cells' temperature even more, and therefore the reaction kinetics of the self-degradation of Li-ion batteries can lead to fire or explosion. Currently, overcharging is the most important safety issue for Li-ion batteries that needs to be prevented. Overcharging is defined has "a state when electricity

flow is forced through the cell after its designed capacity is already full", [68] and is already a well understood process.

Another main issue is the formation of dendritic lithium, which leads to internal short circuits of LIBs. The lithium dendrite is an agglomeration of the lithium-ions that will grow on the negative electrode surface, instead of being intercalated within the negative electrode as it is shown on Figure 1-10 below. Dendrites will pass through the separator allowing a connection between the positive and negative electrode, leading to short-circuits.
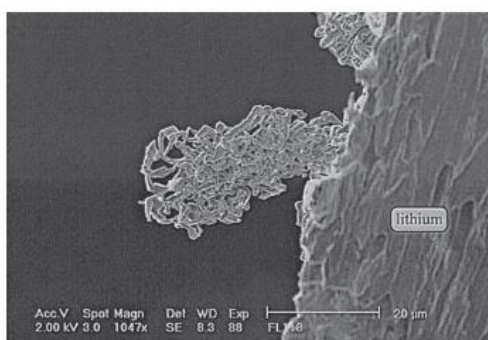
Figure 1-10 : Lithium dendrite formed on the anode surface of $LiMn_2O_4$/Li battery after first charge at 1C from reference. [83]

Currently, one area of research is focused on alternative ways to control the internal voltage (V), temperature (T), pressure (P) and current (I). A desired feature of batteries would be an internal protection mechanism by improving the safety on components such as the positive and negative electrodes, current collector and electrolytes.

1.6.6.2   Na-ion batteries

All those concerns found for LIBs are relevant to SIBs and need to be taken into account before any further investigations. Furthermore, sodium metal as well as all other alkali metals are known to be extremely reactive with water, and therefore with the water contained in the air. It is therefore very important to manipulate SIBs into an environment of inert atmosphere such as an Argon-filled glovebox. It is obviously very important to make sure the produced cells used under normal atmosphere will be safely made to have no contact with air. Therefore, a lot of the current research goes into investigating new negative electrodes but also new safer electrolytes such as ionic liquids.[65]

1.6.6.3 Electrolytes

Ionic liquid-based electrolytes are an obvious choice for the same reasons that these are useful in lithium devices i.e., large electrochemical windows, low volatility and high thermal stability. To date, there are only very few publications detailing IL electrolytes studied for these emerging applications.[84-91] However, it is clear from this emerging work that ILs may offer the same advantages as electrolytes for sodium based battery systems as they do for lithium,[92-98] however, SEI related transport phenomena will not be identical, which require further studies to explore.

Furthermore, the flammability of conventional alkyl carbonate electrolytes hinders the integration of large-scale lithium-ion batteries in transportation and grid storage applications.[85] Therefore, room temperature ionic liquids (RTILs) have emerged as potential replacements for these alkyl carbonates in terms of safety and toxicity. However, in order to achieve high energy density batteries, there is an urgent need for further improvement of RTILs before being applied in commercial products.

1.7 Conclusion and scientific approaches

In this work, three imidazolium-based carboxylate ILs (for n= 2, 4 and 8) have been investigated in combination with pure water as binary mixture. A milky solution is observed while mixing water and the $[C_2MIm][C_7H_{15}CO_2]$ that show the presence of a potential emulsion or very strong aggregation; whereas a clear solution is observed while mixing water and $[C_2MIm][CH_3CO_2]$ that show a weaker potential of strong aggregation.

This result is in accordance with the work published by Anouti *et al.*, and Hall *et al.*, explained previously in this introductory chapter. In fact, alkyl-carboxylates in binary mixtures with solvents are well known in the world of surfactants, as well as pure imidazolium alkyl-carboxylate anion ILs which are known as self-organising structures due to the Van der Waals forces between the cations and the anion as well as anion-anion interactions.

After this *present chapter* on the generality of the main parts investigated in this whole work, the *second chapter* will describe the IL synthesis used for this whole work as well as their characterizations via ^1H ,^{13}C NMR and mass spectroscopy (MS).

Then, the *third chapter* will show a full study of the IL in binary mixtures with water in terms of their macroscopic properties that includes the following properties: density, viscosity, conductivity and thermal properties; that will lead into more specific properties which are the volumetric and transport properties of those mixture, to then conclude by an IL classification according to the Walden rule. This chapter will give information on the intramolecular interaction of the mixtures.

To complete the above study, the *fourth chapter* will investigate the microscopic properties on the IL-water binary mixtures by using first a ^1H, ^{13}C and 2D-(^1H/^{13}C) HSQC-NMR-spectroscopy study, and then an X-ray and neutron scattering study; which combined, have revealed some important information thanks to the intra and intermolecular interactions between (cation–anion), (individual ion–water), and (IL ions pair–water) in solution. In the literature, it is known that the study of the chemical shift variation using ^1H and ^{13}C-NMR

spectroscopy can give a good understanding of the intermolecular interactions regarding the nature of the interactions but also their strength, as well as the specific atoms involved in those kinds of interactions. In this way, it should help to understand how to design specific IL-electrolytes in regards to their need for (i.e., metal-ion battery electrolytes, solar cell electrolytes, heat transfer fluids etc.) by tuning both the IL cation and anion with specific functional group and by choosing the appropriate IL-solvent concentrations.

The experimental data of the macro and microscopic properties of the known 1-ethyl-3-methylimidazolium acetate, $[C_2MIm][CH_3CO_2]$, was also compared to the literature in order to make sure the experimental methods carried out for the two other ILs (the butanoate and octanoate anion) were corrects.

The fifth and sixth chapters, will then show two separate applications of ILs:

The *fifth chapter* will show a first application of the IL solutions studied in Chapters 2, 3 and 4. Those solutions will be used in the *in-situ* synthesis of copper(II) oxide nanoparticles, which has been carried out using a copper complex as precursors dissolved in those IL solutions. In order to understand the metal oxide nanoparticles formation, the interactions between the ionic liquids with the copper precursors were studied combining with the previous understanding found in chapter 3 and 4. In this way, a better understanding of the metal oxide nanoparticle formation should allow in the future to gain better control over shape, morphology and size of the materials formed. This novel nanofluid could then be used for heat transfer fluids in car industry or as a catalyst.

The *sixth chapter* will show the use of new ionic liquid solutions as electrolytes for safer sodium-ion batteries. These novel ionic liquids electrolytes should lead to safer batteries as they offer several advantages such as non-volatility, non-flammability and large electrochemical windows and therefore good long-term stability. The main objective of this project carried out in Tokyo is to improve safety of Na-ion batteries by using novel functionalized ILs as electrolytes. To finish, the *seventh Chapter* will give a short overview of the outcomes of this work as well as some perspective on future works.

Chapter 2 _ Synthesis and Characterisation of 1-ethyl-3-methylimidazolium carboxylates

2.1 Introduction

Synthesis of ILs have been well described in the literature. Seddon *et al.*, have particularly lead to a better knowledge in regards to IL synthesis and purification.[4]

Ionic liquid can be prepared following three different methods known as quaternisation, metathesis and direct combination of halide salt with metal halide. The last two are the most current synthesis since it gives almost always straight-full reaction in shorter reaction times at lower reaction temperature.

According to Brehm *et al.*, ionic liquid 1-ethyl-3-methylimidazolium acetate, referred as $[C_2MIm][CH_3CO_2]$, can be considered an enzyme-friendly co-solvent for biocatalysis as well as a good solvent for strongly hydrogen bonding materials such as cellulose or chitin and has significant ability to capture CO2.

2.2 Materials

The reagents used for the synthesis of ILs were supplied by Alfa Aesar [1-methyl-imidazole (99%)], Sigma Aldrich (diethylsulfate (98%), strontium hydroxide octahydrate (95%), butyric acid (99%), octanoic acid (99%)) and Riedel de Haen (acetic acid (99-100%)). To study the physical properties, 1-ethyl-3-methilimidazolium hydrosulfate (99%) and 1-ethyl-3-methylimidazolium acetate (95%) have been purchased from Io-li-tec. To carry out the neutron scattering experiment, the deuterated reagents were purchased from QMX laboratories (acetic acid-d_4 (98 atom % D) and octanoic acid-d_{16} (98 atom% D)). Pure water was used for the mixtures.

2.3 Imidazolium based cations and carboxylate based anions ionic liquids synthesis and characterisation

For each of the three imidazolium-based alkyl-carboxylate ionic liquids; 1-ethyl-3-methylimidazolium acetate, $[C_2MIm][CH_3CO_2]$, 1-ethyl-3-methylimidazolium butanoate, $[C_2MIm][C_3H_7CO_2]$, and 1-ethyl-3-methyl imidazolium octanoate, $[C_2MIm][C_7H_{15}CO_2]$; the four following steps have been undertaken:

The first step corresponds to the synthesis of 1-ethyl-3-methylimidazolium ethylsulfate, $[C_2MIm][EtSO_4]$, which is a result of the reaction of 1-methylimidazole and diethyl sulfate as it was well described previously by colleagues.[99]
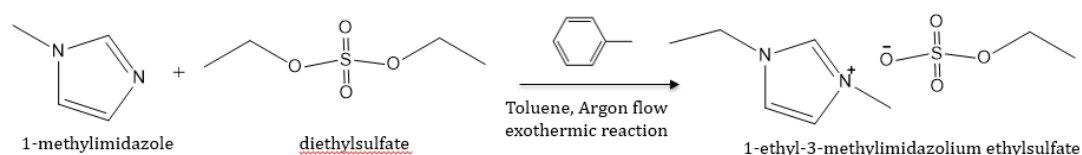
Figure 2-1. First step: IL-synthesis precursor

The second step consists of the synthesis of 1-ethyl-3-methylimidazolium hydrosulfate, $[C_2MIm][HSO_4]$, obtained from the hydrolysis of the $[C_2MIm][EtSO_4]$ IL precursor made from the first step as it was reported previously by Jacquemin *et al.*.[100]
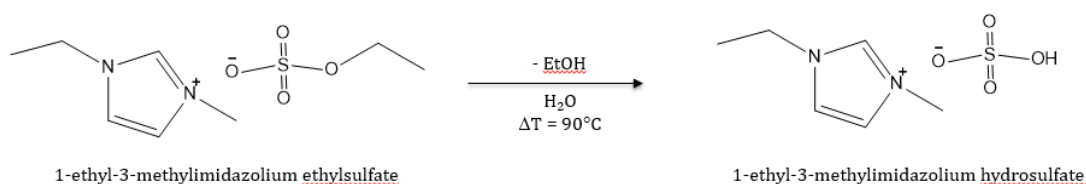
Figure 2-2. Second step: IL-synthesis by hydrolysis.

The third step involved the hydroxide metathesis of $[C_2MIm][HSO_4]$ (synthesis in the second step) into the 1-ethyl-3-methylimidazolium hydroxide, $[C_2MIm][OH]$ using strontium hydroxide, which forms the insoluble $SrSO_4$ that precipitates and can be filtered off.[101]
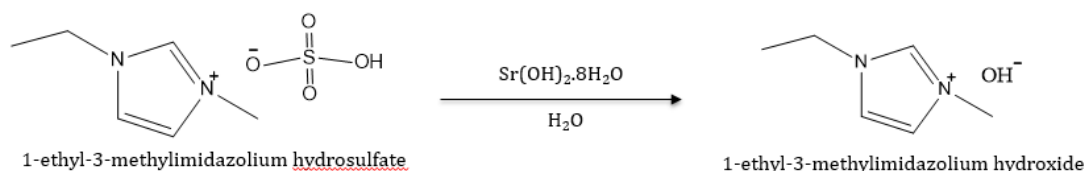
Figure 2-3. Third step: IL-synthesis by hydroxide metathesis.

In the last step, the respective 1-ethyl-3-methylimidazolium acetate, butanoate and octanoate can be synthesised by simple addition of the respective acid (fourth step a, b, c).[101]
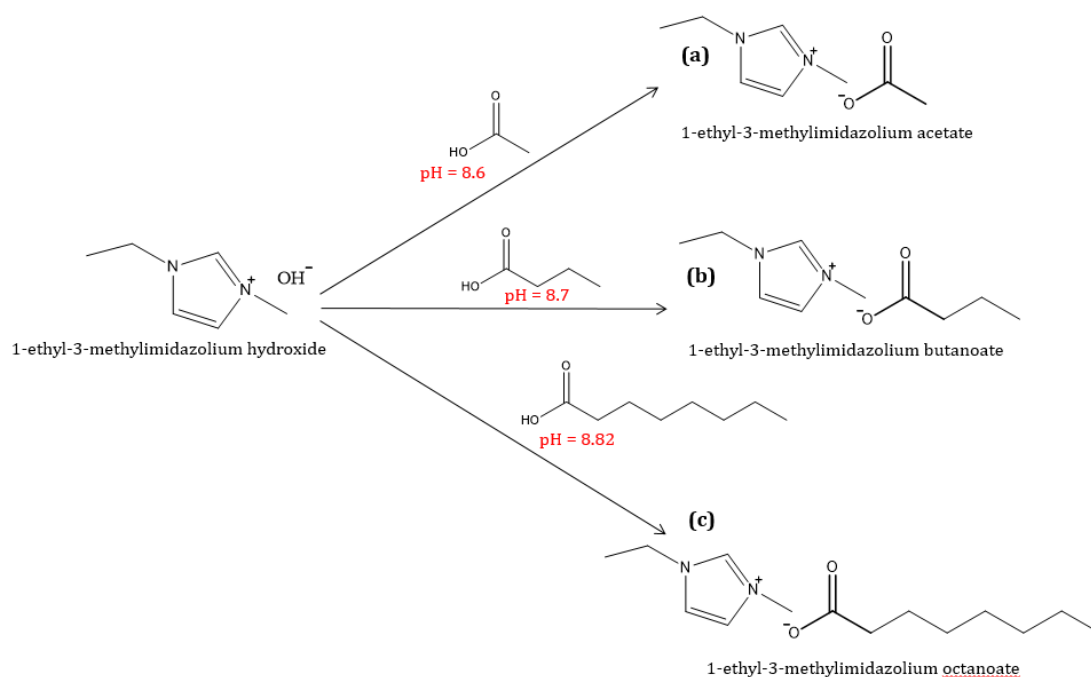
Figure 2-4. Fourth step: 1-ethyl-3-methylimidazolium acetate **(a)**, 1-ethyl-3-methylimidazolium butanoate **(b)** and 1-ethyl-3-methylimidazolium octanoate **(c)** IL-synthesis.

All synthesised ILs were characterised using ^{1}H and ^{13}C-NMR spectroscopy using a Bruker Spectrospin 300 Ultrashield™.

For the characterization of the macroscopic properties in Chapter 3, the synthesis of the three ILs was carried out starting from the [C$_2$MIm][HSO$_4$] purchased from Io-li-tec and then followed by the strontium hydroxide method. However, to study the microscopic properties in Chapter 4, the three ILs where prepared from the starting materials diethyl sulfate and 1-methyl-imidazole, which was then

followed by water hydrolysis as described in more detail below in order to have better control of the starting materials and to obtain very pure ILs.

2.3.1 First step in the synthesis of 1-ethyl-3-methylimidazolium ethyl sulfate, [C₂MIm][EtSO₄]

1-methyl imidazole (17.6 mL, 0.221 mol) was taken up with a plastic syringe of 5 mL and slowly added into a 250 mL 3 neck round-bottom flask. To prevent an exothermic reaction, 100 mL of toluene was added to the mixture. The round-bottom flask was stocked in an ice-bath and a magnetic stirrer was applied. A condenser was then inserted to the round-bottom flask, where nitrogen was purged over the sample to create an inert atmosphere. At the same time, a dropping funnel with diethyl sulfate (29 mL, 0.221 mol) was added to the round-bottom flask. Diethyl sulfate was then added dropwise to the solution (exothermic reaction). Then the solution was left stirring at RT for 2h. Two phases were obtained; the upper phase containing the organic phase was removed, and the lower phase containing the IL was washed with toluene. The IL was then washed with ethyl acetate followed by a rotary evaporator at 75 °C for 1 h and overnight high vacuum at 70°C, resulting in a colourless viscous liquid [ES-MS +ve mode: 111.0909 ([cation]+ calc, 111.0922); -ve mode: 124.9899 ([anion]- calc, 124.9909)]. **δH(300MHz, D₂O)(ppm)** 8.63 (1H, s, NC**H**NC₂H₅), 7.43 (1H, s, NC**H**CHN), 7.36 (1H, s, NCHC**H**N), 4.18 (2H, q, N(C**H₂**)CH₃), 4.02 (2H, q, H₃C-C**H₂**-OSO₃), 3.83 (3H, s, NC**H₃**), 1.43 (3H, s, O₂C(C**H₃**)), 1.36 (3H, t, N(CH₂)C**H₃**), 1.21 (3H, t, **H₃**C-CH₂-OSO₃). **δC(75.4 MHz, D₂O) (ppm)** 135.96, 123.89, 122.29, 65.96, 45.19, 32.02, 14.90, 14.67.

2.3.2 Second step synthesis of 1-ethyl-3-methylimidazolium hydrosulfate, [C₂MIm][HSO₄]

The hydrolysis of [C$_2$MIm][EtSO$_4$] to [C$_2$MIm][HSO$_4$], was carried out following the synthesis process described in a work published by Jacquemin *et al.,* in QUILL.[100]

1 eq of [C$_2$MIm][EtHSO$_4$] mixed with >3 eq of distillated water were left stirring in an open vessel supported by a condenser for two weeks at 150°C. Few drops of sulfuric acid were necessary to speed up the kinetics of the reaction. Some water was added when needed. The kinetic reaction was followed by proton and carbon NMR spectroscopy. *Note: for 70 g of [C$_2$MIm][EtHSO$_4$] to start with, three weeks were necessary to complete the reaction and 6 drops of sulfuric acids were added in total during the reaction. It allows having a very pure IL with no halogen involved at all since the starting materials do not have any.* **δH(300 MHz, D$_2$O)(ppm)** 8.57 (1H, s, NC**H**NC$_2$H$_5$), 7.35 (1H, s, NC**H**CHN), 7.29 (1H, s, NCHC**H**N), 4.11 (2H, q, N(C**H$_2$**)CH$_3$), 3.76 (3H, s, NC**H$_3$**),1.36 (3H, t, N(CH$_2$)C**H$_3$**). **δC(75.4 MHz, D$_2$O) (ppm)** 135.91, 123.82, 122.22, 45.11, 35.96, 14.84.

2.3.3 Third step synthesis of 1-ethyl-3-methylimidazolium hydroxide, [C₂MIm]OH

Strontium hydroxide octahydrate (1.2 eq) was dissolved in hot distillated water (100 °C, large excess) in a round-bottomed hydroxide metathesis flask (1 L) and stirred at 100 °C for 30 min. 1-Ethyl-3-methylimidazolium hydrogensulfate made previously (1 eq) was combined with water (excess) in a beaker, stirred and added to the hot solution of strontium hydroxide octahydrate. Directly upon combination, a white precipitate was formed. The flask was removed from the heat and left to stir briefly and was allowed to cool to room temperature (6 h). The solution was cooled further (4 °C, 12 h). The white precipitate was removed *via* vacuum filtration of the mixture (P4 glass sintered funnel with Dicalite filter aid) and a second time using a 1.2 μm glass microfibre filter.

Note: A 1.2 μm glass microfibre filter is very important here sinces there would be very small particles of precipitate and also because the IL may dissolve normal filter paper. Make this part of the experimentat part, not as a separate note

2.3.4 Fourth step (a) synthesis of 1-ethyl-3-methylimidazolium acetate, [C₂MIm][CH₃CO₂]

Acetic acid (1 eq) was combined with an excess of H_2O and was added slowly to the aqueous solution of [C₂MIm]OH (1 eq). The solution was stirred briefly then reduced in volume *in vacuo* (rotary evaporator; 70 °C). When most of the water had been removed, ethanol was added (99 %, large excess) in order to precipitate out any additional solid, and left to settle (4 °C, 12 h). Additional precipitate was removed *via* vacuum filtration using a 1.2 μm glass microfibre filter. The solvent was completely removed *in vacuo* (rotary evaporator; 70 °C) and the flask containing the liquid was transferred to a high vacuum line (80 °C; 3 days) leaving a golden viscous liquid (90%). **δH(300MHz, D₂O)(ppm)** 8.58 (1H, s, NC**H**NC₂H₅), 7.34 (1H, s, NC**H**CHN), 7.30 (1H, s, NCHC**H**N), 4.07 (2H, q, N(C**H₂**)CH₃), 3.75 (3H, s, NC**H₃**), 1.77 (3H, s, O₂C(C**H₃**)), 1.36 (3H, t, N(CH₂)C**H₃**). **δC(75.4 MHz, D₂O) (ppm)** 181.18, 136.31, 123.61, 122.20, 44.85, 35.77, 23.45, 14.81.

2.3.5 Fourth step (b) synthesis of 1-ethyl-3-methylimidazolium butanoate, [C₂MIm][C₃H₇CO₂]

Butanoic acid (1 eq) was added slowly, drop-wise, to the colourless solution of [C₂MIm]OH obtained previously (1 eq) until a pH of 8.7 was obtained using a Mettler Toledo MP220 pH meter. Ethanol (99 %, large excess) was then added to help azeotropic distillation of water. The solution was reduced in volume *in vacuo* (rotary evaporator; 70 °C); when most of the water had been removed, ethanol was added (99 %, excess) in order to precipitate out any additional solid, left to settle (4 °C, 12 h). Additional precipitate was removed *via* vacuum filtration using a 1.2 μm glass microfibre filter. The solution was again reduced in volume *in vacuo* (rotary evaporator; 70 °C). If precipitate was observed it was removed again *via* vacuum filtration using a 1.2 μm glass microfibre filter. Additional absolute ethanol (small excess) was added and the solvent was completely removed *in vacuo* (rotary evaporator; 70 °C) and the flask containing the liquid was transferred to a high vacuum line (80 °C; 3 days), leaving a golden viscous liquid (94%). **δH(300MHz, D₂O)(ppm)** 8.59 (1H, s, NC**H**NC₂H₅), 7.35 (1H, s, NC**H**CHN), 7.31 (1H, s, NCHC**H**N), 4.07 (2H, q, N(C**H₂**)CH₃), 3.76 (3H, s, NC**H₃**), 2.01 (2H, s, O₂C(C**H₂**)(CH₂)CH₃, 1.41 (5H, m, O₂C(CH₂)(C**H₂**)CH₃), 0.75 (3H, ,

N(CH$_2$)CH$_3$). **δC(75.4 MHz, D$_2$O) (ppm)** 184.21, 135.90, 123.79, 121.82, 45.11, 39.90, 35.70, 19.70, 14.82, 13.75.

2.3.6 Fourth step (c) synthesis of 1-ethyl-3-methylimidazolium octanoate, [C$_2$MIm][C$_7$H$_{15}$CO$_2$]

Octanoic acid (1eq) was added slowly, drop wise, to the colourless solution of [C$_2$MIm]OH (1 eq) obtained previously in step 3, until a pH of 8.82 was reach using a Mettler Toledo MP220 pH meter. Ethanol (99 %, large excess) was then added to help azeotropic distillation of water. The solution was reduced in volume *in vacuo* (rotary evaporator; 70 °C); when most of the water had been removed, ethanol was added (99 %, large excess) in order to precipitate out any additional solid, left to settle (4 °C, 12h). Additional precipitate was removed *via* vacuum filtration using a 1.2 μm glass microfibre filter. The solution was again reduced in volume *in vacuo* (rotary evaporator; 70 °C). Precipitate was observed and additional precipitate was removed *via* vacuum filtration using a 1.2 μm glass microfibre filter. The solution was reduced in volume *in vacuo* (rotary evaporator; 70 °C). Additional absolute ethanol (65 cm^3) was added and the solvent was completely removed *in vacuo* (rotary evaporator; 70 °C) and the flask containing the liquid was transferred to a high vacuum line (80 °C; 3 days), leaving a golden viscous liquid (33 g, 70 %).

δH (300MHz, D$_2$O) (ppm) 8.62 (1H, s, NC**H**NC$_2$H$_5$), 7.37 (1H, s, NC**H**CHN), 7.33 (1H, s, NCH**CH**N), 4.09 (2H, q, N(C**H$_2$**)CH$_3$), 3.77 (3H, s, NC**H$_3$**), 2.02 (2H, t, O$_2$C(C**H$_2$**)), 1.38 (5H, t, O$_2$C(CH$_2$)$_4$(C**H$_2$**) (C**H$_2$**) C**H$_3$**), 1.14 (8H, s, O$_2$C(CH$_2$)(C**H$_2$**)$_4$(C**H$_3$**)), 0.71 (3H, t, N(CH$_2$)C**H$_3$**). **δC(75.4 MHz, D$_2$O) (ppm)** 184.32, 135.47, 123.85, 122.28, 45.15, 38.07, 35.96, 31.50, 29.20, 28.73, 26.35, 22.43, 14.75, 13.83.

2.4 Ionic liquids deuterated synthesis and characterisation used for Neutron and X-ray Diffraction experiments in Chapter 4

2.4.1 Synthesis of 1-ethyl-3-methylimidazolium acetate for neutron diffraction measurements

In this part, the same protocol used to synthesis the 1-ethyl-3-methylimidazolium acetate as described previously (see 2.4.4 batch) was carried out. Both, protiated and deuterated mixtures were prepared in the same way. Thus, only a table with the quantities of reagents will be described.

2.4.1.1 *1-ethyl-3-methylimidazolium acetate fully protiated, [C₂MIm][CH₃CO₂]-PP*

Table 2-1: Table of reagent for $[C_2MIm][CH_3CO_2]$-PP synthesis for the first solution

Solution 1	M (g/mol)	n (mol)	m(g)	d	V(mL)
[C₂MIm][HSO₄]	208	1 eq, 0.072 mol	15	N/A	N/A
Acetic acid	60	1 eq, 0.072 mol	4.30	1.0499	4.3

Table 2-2: Table of reagent for $[C_2MIm][CH_3CO_2]$-PP synthesis for the solution 2

Solution 2	M (g/mol)	n (mol)	m(g)	d	V(mL)
[C₂MIm][HSO₄]	208	1 eq, 0.072 mol	15	N/A	N/A
Acetic acid	60	1 eq, 0.072	4.33	1.0499	4.12

Elementary analysis: CHNS found C: 52.96%, H: 8.58%, N: 15.71%. This should also give the calc values ES-MS: +ve mode: 111.0919 ([cation]+ calc, 111.0922); -ve mode: 229.1176 ([anion]- calc, 229.1188).

2.4.1.2 1-ethyl-3-methylimidazolium acetate protiated cation and deuterated anion, [C₂MIm][CH₃CO₂]-PD

Table 2-3: Table of reagents for [C₂MIm][CH₃CO₂]-PD synthesis for the solution 3.

Solution 3	M (g/mol)	n (mol)	m(g)	d	V(mL)
[C₂MIm][HSO₄]	208	1 eq, 0.06 mol	12.4	N/A	N/A
Acetic acid-d₄	62.06	1 eq, 0.06 mol	3.6	1.0499	3.4

Elementary analysis: ES-MS (MeCN) +ve mode: 111.0913 ([cation]+ calc, 111.0922)

2.4.2 Synthesis of 1-ethyl-3-methylimidazolium octanoate for neutron diffraction

In this part, the same protocol was used to synthesise the 1-ethyl-3-methylimidazolium octanoate described previously (see 2.4.6 batch). Only protiated/protiated and protiated/deuterated mixtures were prepared in the same way. Thus, only a table with the quantities of the reagents will be described. The deuterated/protiated and deuterated/deuterated samples have to be prepared using [C₂MIM] Br as precursor.

2.4.2.1 1-ethyl-3-methylimidazolium octanoate fully protiated, [C₂MIm][C₇H₁₅CO₂] PP

Table 2-4: Table of reagent for [C₂MIm][C₇H₁₅CO₂] PP synthesis for the solution 4

Solution 4	M (g/mol)	n (mol)	m(g)	d	V(mL)
[C₂MIm][HSO₄]	208	1eq, 0.061mol	12.6	N/A	N/A
Octanoic acid	144	1eq, 0.061 mol	8.74	0.91	9.6

Elementary analysis: CHNS found C : 63.09ù, H : 10.58%, N : 10.87%, give calc values ES-MS: (MeCN) +ve mode: 111.0891 ([cation]+ calc, 111.0922); -ve mode: 143.1038 ([anion]- calc, 143.1072).

2.4.2.2 1-ethyl-3-methylimidazolium octanoate protiated cation and deuterated anion, [C₂MIm][C₇H₁₅CO₂]-PD

Table 2-5: Table of reagent for $[C_2MIm][C_7H_{15}CO_2]$-PD synthesis for the solution 5.

Solution 5	M (g/mol)	n (mol)	m(g)	d	V(mL)
[C₂MIm][HSO₄]	208	1eq, 0.053 mol	11	N/A	N/A
Octanoic acid-d₁₆	158.3	1eq, 0.053 mol	8.4	0.91	8

Elementary analysis: ES-MS: (MeCN) +ve mode: 111.0915 ([cation]+ calc, 111.0922); -ve mode: 158.1982 ([anion]- calc, 158.2014).

2.4.3 Synthesis of 1-ethyl-3-methylimidazolium-d₁₁ octanoate for deuterated/protiated and deuterated/deuterated mixtures for neutron diffraction analysis

According to Hardacre et al.,[102] the synthesis of 1-ethyl-3-methylimidazolium-d₁₁ was synthesised by making the precursors 1-methylimidazole-d₆, 1-ethyl-3-methylimidazolium-d₁₁ bromide, 1-ethyl-3-methylimidazolium-d₁₁ hydrogensulfate, and then 1-ethyl-3-methylimidazolium-d₁₁ hydroxide, respectively, in order to produce 1-ethyl-3-methylimidazolium-d₁₁ octanoate. In one case the octanoate anion will be protiated and in another fully deuterated.

2.4.3.1 1-methylimidazole-d₆ synthesis

Four autoclaves of 20 mL were used for this experiment. Each batches were containing the four respective mixtures as shown in Table 2-6 and were dissolved in 1,4-dioxane. The ruthenium (III) chloride hydrate (RuCl₃·xH₂O) and Tri(butyl)phosphite (TBP) were used as a catalyst. The mixtures were then left stirred at 600 rpm at 200 °C for five consecutive days. The reactor 1 containing the solution 1 did not seal very well and so the solvent evaporated and the product decomposed. Thus, the 3 other solutions were then merged together, and then filtrated to remove the RuCl₃ solid. The filtrate was also washed with 1,4 dioxane. The rotary evaporatory was used to remove 1,4 dioxane at 50 °C. This reaction has unfortunately less than 40% yield. A Kugelrohr distillation was used

to separate the liquids following the boiling point of each compound as seen in the Table 2-7. A colourless liquid of [MIm]-d_6 was obtained (6 g, 40%).

Table 2-6: synthesis of 1-methylimidazole-d_6 for the solution 10.

Solution 10	Solution 1	Solution 2	Solution 3	Solution 4
Imidazole-d_4	3.4613 g	3.75 g	3.7531 g	3.7697 g
Tri(butyl)phosphite	0.865 g	0.865 g	0.865 g	0.865 g
RuCl$_3$	0.19 g	0.19 g	0.19 g	0.19 g
MeOH-d_4	7.53 g	7.5381 g	7.53 g	7.5175 g

Table 2-7: Boiling point of reagents.

Compounds 'name	BP°C
Imidazole-d_4	256 °C
Methylimidazole-d_6 *(product wanted)*	198 °C
Tri(butyl)phosphite	125 °C

2.4.3.2   1-ethyl-3-methylimidazolium-d_{11} bromide, [C$_2$MIm-d_{11}]Br

In a 100 mL two-neck round-bottom flask surrounded by a close condenser, [MIm]-d6 (3.5 g, 0.04 mol) was dissolved in acetonitrile-d_3. Then, under nitrogen, bromoethane-d_5 (5 g, 0.044 mol) was added slowly to the previous mixture. The reaction was left stirred in a closed vessel at 65 °C under nitrogen overnight. The solvent was removed *via* rotary evaporator at 65 °C maximum and then high vacuum overnight. No solid was formed but a viscous yellow pale product was obtained. The product was purified according to Nockemann *et al.*[103]

Remark: Do not heat under vacuum more than 70 °C otherwise the [C$_2$MIm]Br will decompose.

Table 2-8. Table of reagent for [C$_2$MIm-d$_{11}$]Br

Solution 11	M (g/mol)	n (mol)	m(g) /V(mL)
1-methyl-imidazole-d$_6$	88.14	1 eq, 0.04	3.5 g
Bromoethane-d$_5$	114	1.1 eq, 0.044	5 g
Acetonitrile-d$_3$	65	excess	8 mL

2.4.3.3 1-ethyl-3-methylimidazolium hydrosulfate deuterated, [C$_2$MIm-d$_{11}$][HSO$_4$]

1 eq H$_2$SO$_4$ was added to 1 eq [C2MIM-d$_{11}$] Br under vacuum using a sodium hydroxide solution to trap the HBr gas. This precursor was then used to make to [C$_2$MIM-d$_{11}$] octanoate protiated in one case and deuterated in another by sample addition of the respective acid in stoichiometric quantities.

2.4.3.4 1-ethyl-3-methylimidazolium octanoate deuterated cation and protiated anion, [C$_2$MIm][C$_7$H$_{15}$CO$_2$]-DP

Table 2-9: Table of reagent for [C$_2$MIm][C$_7$H$_{15}$CO$_2$]-DP synthesis for the solution 6.

Solution 6	M (g/mol)	n (mol)	m(g)	d	V(mL)
[C$_2$MIm][HSO$_4$-d$_{11}$]	219.23	1 eq, 0.003 mol	0.657	N/A	N/A
Octanoic acid	144	1 eq, 0.003 mol	0.455	0.91	0.5

Elementary analysis: ES-MS: (MeCN)   +ve mode: 119.1409([cation]+ calc, 122.1612); -ve mode: 143.1045 ([anion]- calc, 143.1072).

2.4.3.5   1-ethyl-3-methylimidazolium octanoate deuterated cation and anion, [C$_2$MIm][C$_7$H$_{15}$CO$_2$]-DD

Table 2-10: Table of reagent for [C$_2$MIm][C$_7$H$_{15}$CO$_2$]-DD synthesis for the solution 7.

Solution 7	M (g/mol)	n (mol)	m(g)	d	V(mL)
[C$_2$MIm][HSO$_4$·d$_{11}$]	219.23	1 eq, 0.06 mol	1.71	N/A	N/A
Octanoic acid-d$_{16}$	158.3	1 eq, 0.0078 mol	1.24	0.91	1.36

<u>Elementary analysis</u>: ES-MS: (MeCN) +ve mode: 119.1409([cation]+ calc, 122.1612); -ve mode: 158.1979 ([anion]- calc, 158.2014).

2.5 Conclusion

By mixing those present ILs with water, some precious information was observed shown on Figure 2-5, which has driven this study to explore in more detail this phenomenon by looking at the macroscopic properties as well as the microscopic properties of those range of IL in their neat and binary mixture with water (cf. Chapter 3 and 4). Those studies were used to explore their properties for further applications such as nanoparticle formation (cf. Chapter 5).

As it is seen on Figure 2-5 below, $[C_2MIm][CH_3CO_2]$-IL stay a clear solution after the addition of water; whereas $[C_2MIm][C_7H_{15}CO_2]$-IL looks like an unclear, creamy and whitish dispersion that looks like an emulsion.
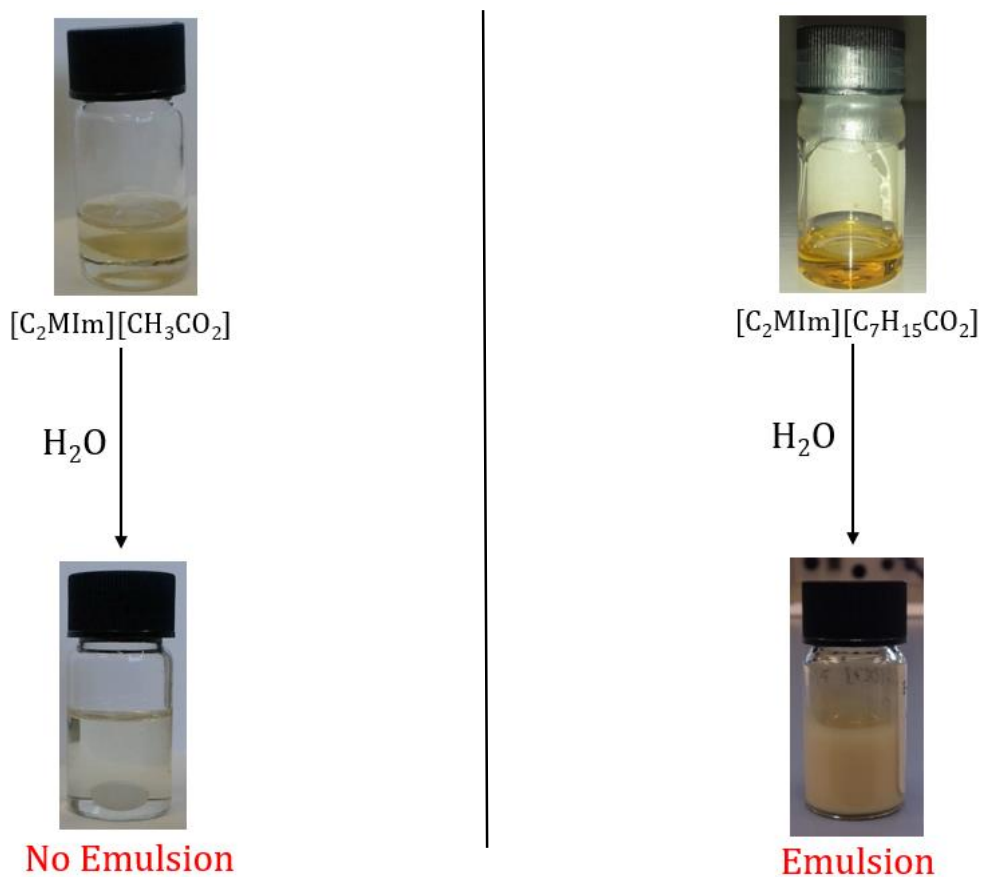
Figure 2-5. Experimental photo showing the two ILs, $[C_2MIm][CH_3CO_2]$ and $[C_2MIm][C_7H_{15}CO_2]$ in their pure state and then mixed with water.

Chapter 3 _ Macroscopic properties of ionic liquid and water binary mixtures

3.1 Introduction

In this chapter, the macroscopic properties of pure ionic liquids described in chapter 2 and their mixtures with water are presented. Herein, their physical properties are used to probe their interaction in solution, by looking at their appearance, texture, color, melting point, boiling point, density, mutual solubility, polarity, conductivity, viscosity, *etc.* More specifically, this study was focused on their thermal properties which includes solid-liquid phase transitions and decomposition temperatures, their volumetric properties thanks to density data, as well as, their transport properties based on experimental viscosity and conductivity data. Data collected herein are in fact very important with regards to not only from a fundamental point of view but also with respect to industrial needs since density and viscosity data are essential prior to develop any industrial process

The aim of this chapter is to understand the interaction changes by adding water in selected alkyl-carboxylate-based ILs (acetate, butanoate and octanoate), which drives the overall IL/water structures in solution. Furthermore, as explained in the introduction chapter, the water is the main impurity in these ILs since it is very hard to remove all its content in carboxylate-based ILs coming from their synthesis process driven by the high hygroscopic character of these ILs. Additionally, it was also proven in chapter 5 that the presence of water is requested to lead to nanoparticle formation in those ILs. Therefore, the water level dependence on the physical properties of selected ILs was investigated as a function of composition and temperature at 0.1 MPa.

In this present work, the above mentioned properties were studied for the pure $[C_2MIm][CH_3CO_2]$, $[C_2MIm][C_3H_7CO_2]$, $[C_2MIm][C_7H_{15}CO_2]$, as well as, their mixtures with water over the whole composition range. The temperature dependence on these properties was also studied from 293.15 K to 363.15 K at 0.1 MPa. Collected density data were then used to calculate the excess molar

volume for all binary mixtures to gain a deeper understanding on the interaction in solution between ILs and water. Furthermore, the combination of the density data with experimental viscosity and conductivity values led to determine the ionicity of investigated mixtures thanks to the Walden rule.[104,105]

This chapter describes these relevant thermodynamic properties which is divided into four sections involving the studies of their thermal, volumetric, transport and IL-ionicity properties.

3.2 Thermal properties of 1-ethyl-3-methylimidazolium alkyl-carboxylate

The thermal behaviour of the three ILs in mixture with water was investigated for each composition by differential scanning calorimetry (DSC) from 180 K to 390 K at 5 K·min^{-1}. This experiment was repeated through 2/3 cycles and the resulting collections of DSC traces for the investigated mixtures are presented in

Figure 3-1, Figure 3-2 and Figure 3-3. The DSC trace observed for each pure IL reveals only a glass transition temperature, T_g, close to 205 K in the case of the $[C_2MIm][C_3H_7CO_2]$ and $[C_2MIm][C_7H_{15}CO_2]$ as no feature is observed for the dried $[C_2MIm][CH_3CO_2]$ in the investigated temperature range.

However, when this particular IL is quickly cooled and no freezing transition is observed, the IL is expected to undergo supercooling into the glassy state. In other words, dried ILs are liquid at temperature higher than 210 K. More surprisingly, no feature change is observed by adding water into these ILs for their IL compositions higher than 0.1 in mole fraction units demonstrating in fact the strong interaction between water and these ILs.

However, in the case of the $[C_2MIm][CH_3CO_2]$ solution at x_{IL} = 0.1, a sharp exothermic crystallization peak (T_f = 210 K) is observed during the second cooling measurement while the associated melting transition is firstly observed at lower temperature (T_m = 200 K) which may be attributed to a clear change on the solid-liquid transition driven by water molecules in solutions. Similarly, in the case of the $[C_2MIm][C_3H_7CO_2]$ solution at x_{IL} = 0.05, two endothermic peaks were observed during the heating scans at 230 K and 245 K which may be attributed

to the eutectic and melting transition temperatures, respectively; while a clear exothermic crystallization peak (T_f = 210 K) is observed during the cooling showing in fact a quite important subcooling effect for such mixture. Interestingly, in the case of the $[C_2MIm][C_3H_7CO_2]$ solution at $x_{IL} < 0.5$ no glass transition is observed in the investigated temperature range which may be also attributed to strong interaction between water molecules and this IL when water is in excess in the solution. These feature changes are in fact related to DSC traces expected in the case of the pure water, which is mainly driven by a melting temperature at 273.15 K.
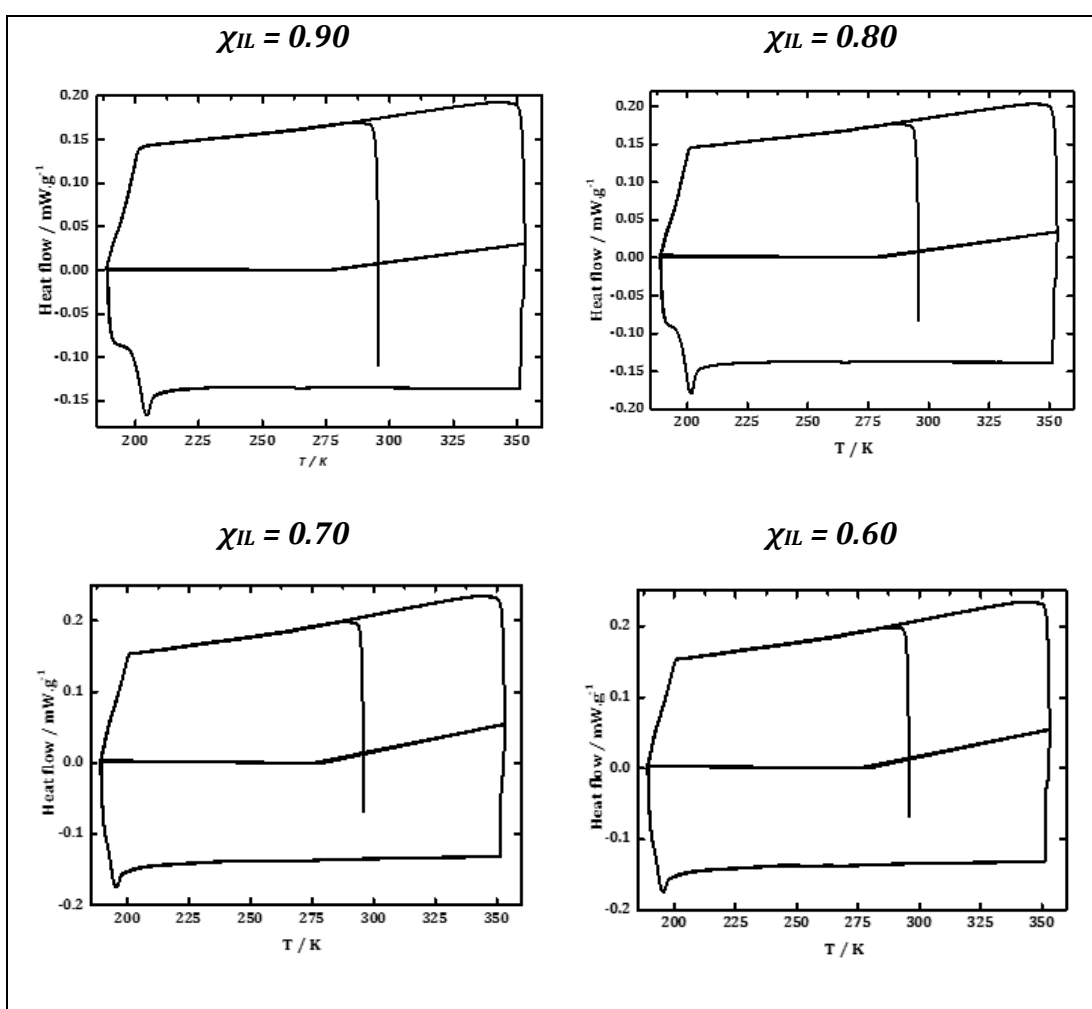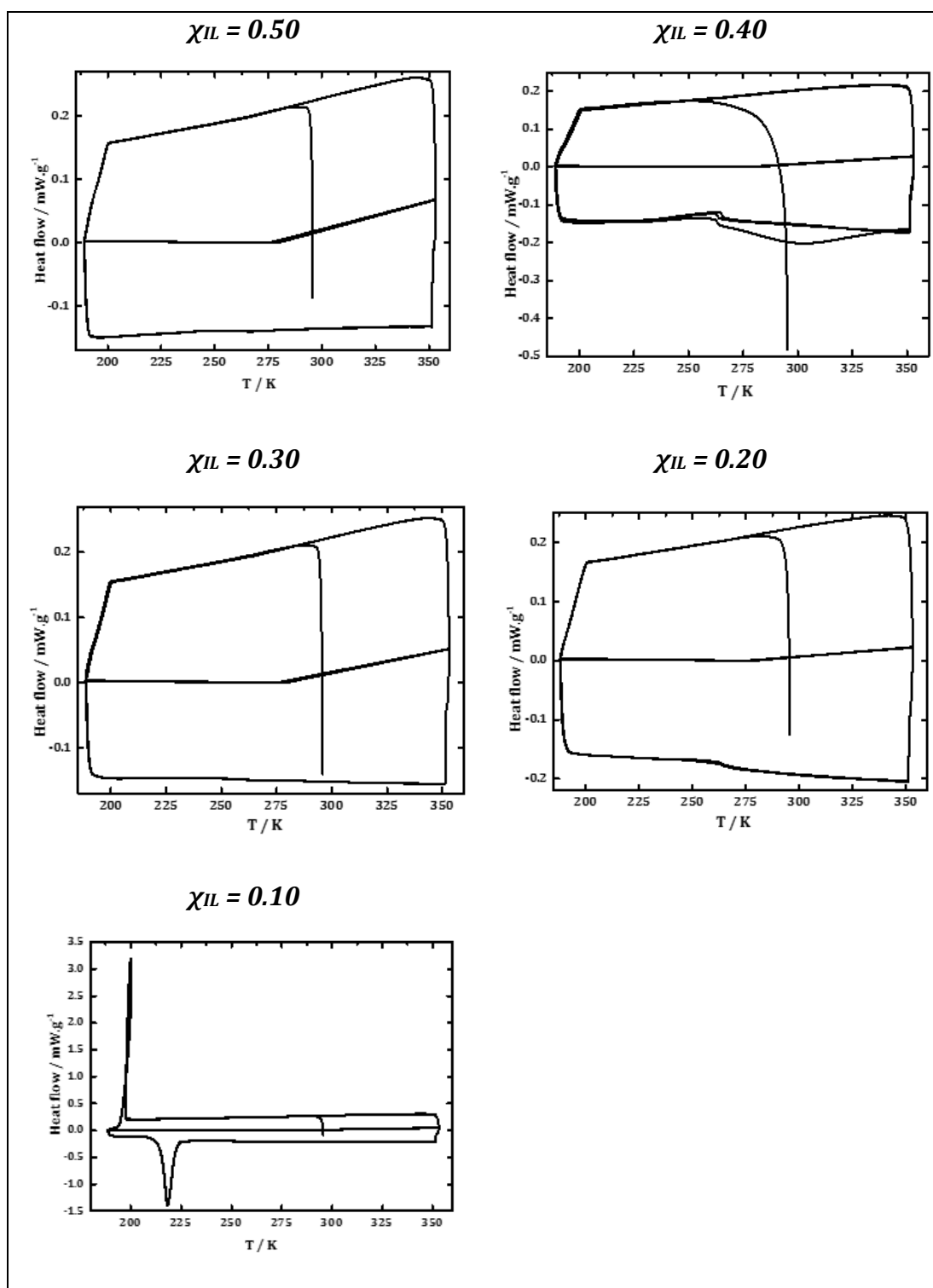
Figure 3-1. DSC traces for the $[C_2MIm][CH_3CO_2]$ + water binary mixture for IL mole fraction composition, χ_{IL} = 0.1 to 0.9.
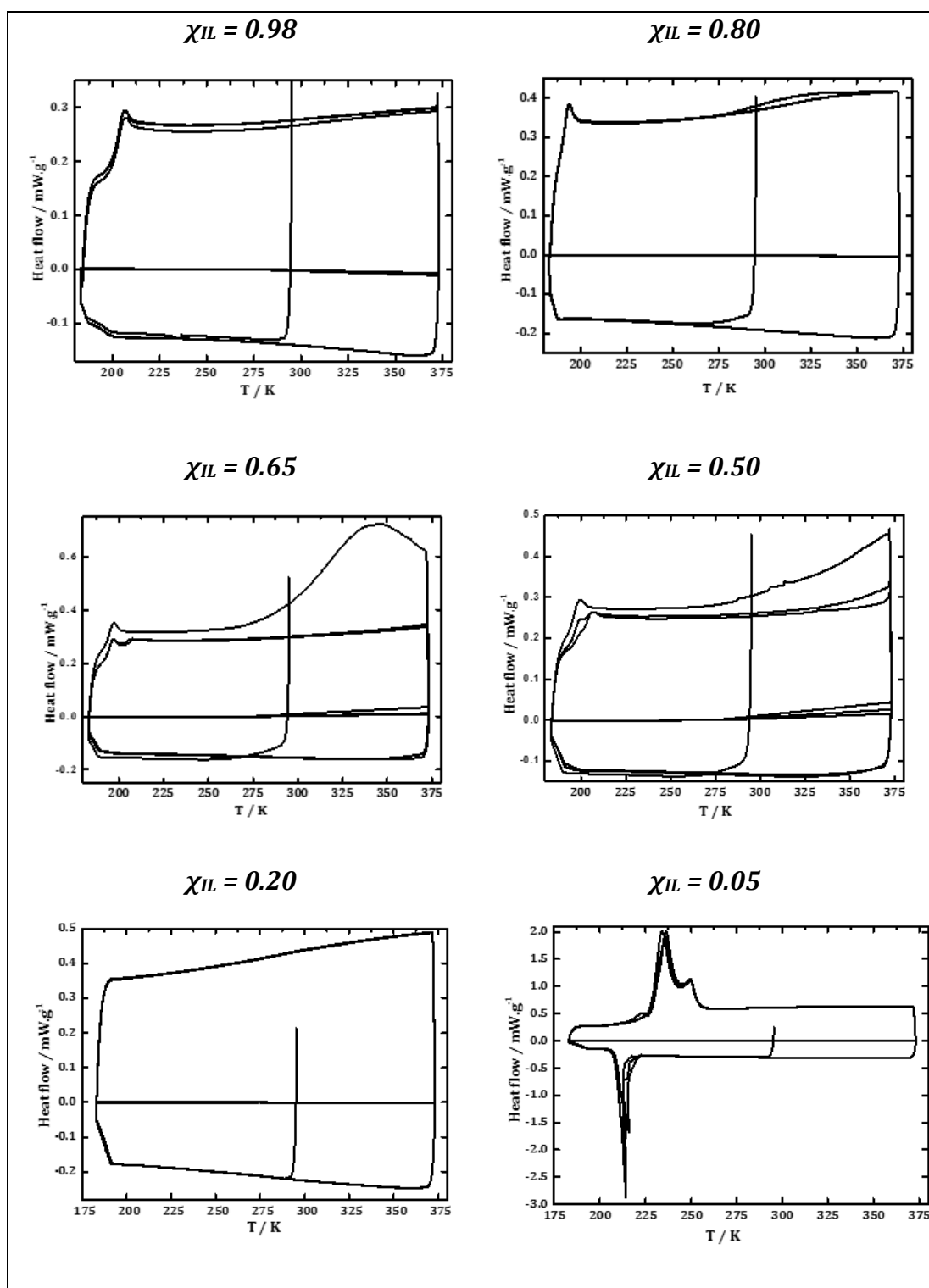
Figure 3-2. DSC traces for the $[C_2MIm][C_3H_7CO_2]$ + water binary mixture for IL mole fraction composition, χ_{IL} = 0.05 to 0.98.
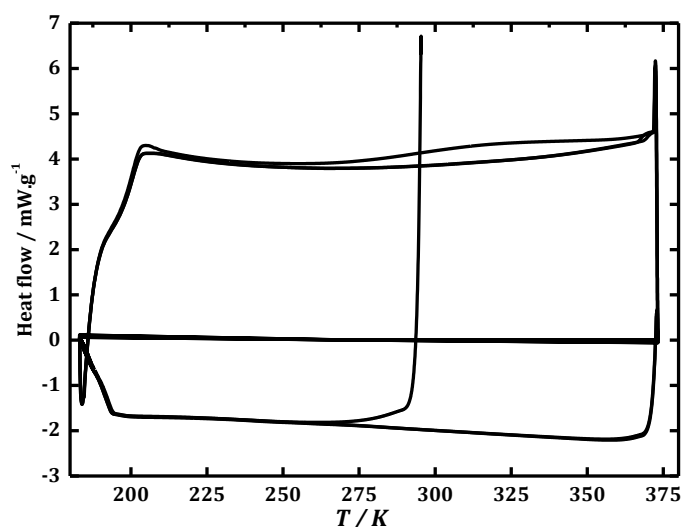
Figure 3-3. DSC traces for the [C₂MIm][C₇H₁₅CO₂] + water binary mixture for the IL mole fraction composition, χ_{IL} = 0.80.

To further investigate the thermal properties, a TGA analysis of each IL in a range of compositions has been carried out to determine the decomposition temperature, T_{dec}, as a function of the composition and IL structure as displayed in Figure 3-4. According to the Figure 3-4, whatever the IL structure, it appears that for all aqueous mixtures highly concentrated in the ILs (*i.e.* x_{IL} > 0.5), T_{dec} are in the range of (480 to 498) K without any feature due to the presence of free water, except for a slight decrease in the wt% due to the increase of the volatility of such solutions with the water level (see Figure 3-4a yellow curve *vs.* red one, for example).

Indeed, in the case of those solutions containing the [C₂MIm][CH₃CO₂], the [C₂MIm][C₃H₇CO₂] or the [C₂MIm][C₇H₁₅CO₂] (Figure 3-4 (a), (b) or (c), respectively), T_{dec}, are in range of (488 to 498) K; (480 to 494) K; or (484 to 490) K, respectively. From those solutions (*i.e.* with x_{IL} > 0.5), the higher is the temperature, the higher is the water concentration in the solution. Therefore, increasing the water concentration in those IL-rich mixtures seems to increase the decomposition temperature of the solution. This unexpected result may be related to strong water and ion interactions and by the absence of free water in solution. However, by increasing the water content in solution (*i.e.* when water is the driving solvent, x_{IL} < 0.5), all solutions show two distinct T_{dec}, which could be

52

attributed to the presence of free water (1st decomposition) and (IL + water) solvated species (2nd decomposition).

Interestingly, whatever the IL structure, it may be observed in Figure 3-4 that the 2nd decomposition temperature is in the range of those observed for highly IL concentrated solutions. For example, for compositions at χ_{IL} = 0.20, the solutions start to lose some free water (about 40 wt% in the case of the acetate solution) at an onset temperature close to 350 K prior to observed the final decomposition of the solutions (onset temperatures are in the range of 478 K to 491 K for the three investigated ILs solution at x_{IL} = 0.2).

Similarly, for compositions at χ_{IL} = 0.05, the solutions start to lose some water (approximatively 50 wt%) at an onset temperature close to 330 K, prior to observed the final decomposition of the solutions (onset temperatures are in the range of 490 K to 498 K for the three investigated ILs solution at x_{IL} = 0.05). By depicting all TGA results, for all samples with x_{IL} < 0.5, it appears that approximatively (10, 8, 6) wt% of the overall water is strongly associated to these ILs while (90, 92, 94) wt% of water molecules seem to be less interacting with the ions in solutions (*i.e.* corresponding to a mole fraction of solvated water molecule close to x_{water} = 0.5 in each case) for the acetate, butanoate and octanoate-ILs, respectively.

Therefore, increasing the alkyl-chain length of the anion does not seem to affect the main ILs decomposition temperature strongly (IL + solvated water molecules) since all solutions display the same final onset temperature. In other words, whatever the alkyl chain length of the carboxylate anion, the water environment (especially at xIL > 0.5) seems to be similar for investigated solutions, which may be related to analogous types of water-ions interactions.
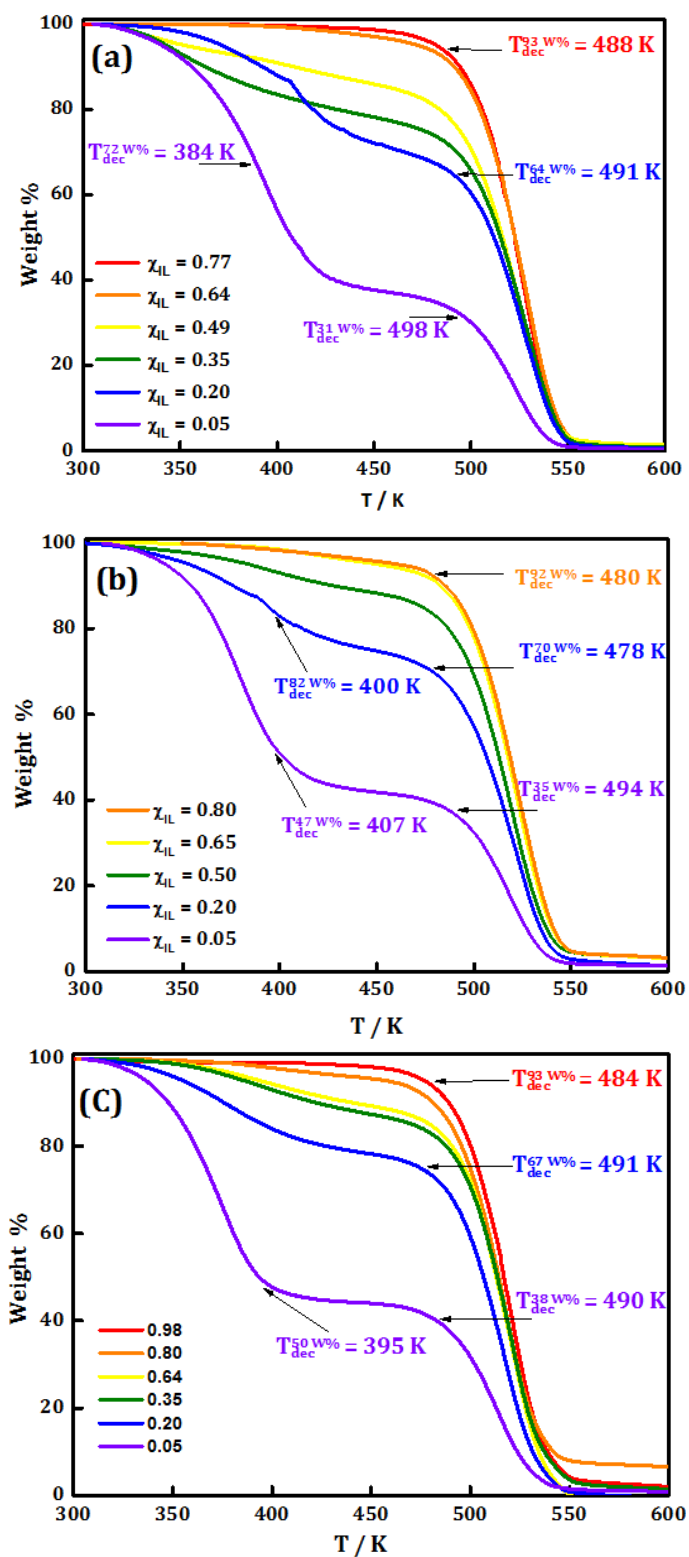
Figure 3-4. TGA curves of [C₂MIm][CH₃CO₂] (a), [C₂MIm][C₃H₇CO₂] (b), [C₂MIm][C₇H₁₅CO₂] (c) as a function of ionic liquid composition, χ_{IL} .

3.3 Effect of water on volumetric properties of 1-ethyl-3-methylimidazolium alkyl-carboxylate

In this section a volumetric study was carried out for the three pure ILs and their mixture with water as a function of the composition and temperature at 0.1 MPa. First of all, the density of all investigated compositions as a function of the temperature is spread out to further determine the excess molar volumes, as well as derived properties such as the apparent and partial molar volumes. The aim of this study is to evaluate the effect of the presence of water into selected ILs to gain an understanding of interactions in solutions.

3.3.1 Density data

The density of the three pure ILs and of the aqueous solutions of 1-ethyl-3-methylimidazolium alkyl-carboxylate, ($[C_2MIm][C_nH_nCO_2] + H_2O$) for ($n = 1, 3$ and 7) binary mixtures was measured as a function of the temperature from 293.15 K to 363.15 K over the whole composition range expressed in IL mole fraction; χ_{IL}. The obtained results are listed in Table 3-1. Due to the very hygroscopic nature of these ILs, water is still present in the dried ILs and therefore the remaining water level, determined by Karl-Fisher titration (cf. Chapter 1) was taken into account to determine the real IL mole fraction of each composition made. These mixtures were prepared in a dried nitrogen-glovebox to avoid any water contamination from the air (cf. experimental part).

Table 3-1. Experimental density, ρ, data of ([C$_2$MIm][CH$_3$CO$_2$] + H$_2$O), ([C$_2$MIm][C$_3$H$_7$CO$_2$] + H$_2$O), and ([C$_2$MIm][C$_7$H$_{15}$CO$_2$] + H$_2$O) binary mixtures as a function of the ionic liquid mole fraction, χ_{IL}, for a temperature range from (293.15 to 363.15) K at 0.1 MPa.

T/K	293.15	298.15	303.15	313.15	323.15	333.15	343.15	353.15	363.15
χ_{IL}				([C$_2$MIm][CH$_3$CO$_2$] + H$_2$O), ρ/g·cm^{-3}					
0.00	0.9982	0.9970	0.9956	0.9922	0.9880	0.9832	0.9778	0.9718	0.9654
0.05	1.0426	1.0403	1.0378	1.0325	1.0269	1.0210	1.0143	1.0037	/
0.19	1.1019	1.0988	1.0955	1.0886	1.0818	1.0749	1.0679	1.0608	1.0536
0.33	1.1099	1.1068	1.1037	1.0972	1.0908	1.0844	1.0780	1.0714	1.0648
0.47	1.1086	1.1056	1.1025	1.0962	1.0902	1.0841	1.0780	1.0718	1.0656
0.62	1.1066	1.1036	1.1005	1.0942	1.0882	1.0821	1.0761	1.0701	1.0641
0.77	1.1046	1.1015	1.0983	1.0920	1.0859	1.0799	1.0739	1.0680	1.0620
0.89	1.1031	1.0999	1.0968	1.0905	1.0844	1.0784	1.0724	1.0665	1.0606
1.00	1.0999	1.0968	1.0936	1.0872	1.0810	1.0748	1.0687	1.0626	1.0567
				([C$_2$MIm][C$_3$H$_7$CO$_2$] + H$_2$O), ρ/g·cm^{-3}					
0.00	0.9982	0.9970	0.9956	0.9922	0.9880	0.9832	0.9778	0.9718	0.9654
0.05	1.0450	1.0421	1.0391	1.0328	1.0263	1.0196	1.0126	1.0053	0.9971
0.20	1.0784	1.0752	1.0718	1.0649	1.0581	1.0512	1.0441	1.0370	1.0299
0.50	1.0760	1.0730	1.0699	1.0634	1.0572	1.0509	1.0446	1.0383	1.0320
0.65	1.0720	1.0694	1.0663	1.0600	1.0538	1.0476	1.0415	1.0354	1.0292
0.80	1.0701	1.0670	1.0638	1.0575	1.0514	1.0453	1.0392	1.0331	1.0271
1.00	1.0640	1.0610	1.0579	1.0514	1.0452	1.0390	1.0329	1.0269	1.0209
				([C$_2$MIm][C$_7$H$_{15}$CO$_2$] + H$_2$O), ρ/g·cm^{-3}					
0.00	0.9982	0.9970	0.9956	0.9922	0.9880	0.9832	0.9778	0.9718	0.9654
0.05	1.0142	1.0115	1.0086	1.0025	0.9963	0.9897	0.9833	0.9732	0.9691
0.20	1.0219	1.0186	1.0152	1.0084	1.0017	0.9949	0.9879	0.9807	0.9729
0.35	1.0184	1.0153	1.0121	1.0055	0.9990	0.9925	0.9859	0.9794	0.9728
0.50	1.0140	1.0110	1.0078	1.0014	0.9950	0.9887	0.9824	0.9761	0.9698
0.64	1.0104	1.0075	1.0044	0.9980	0.9918	0.9856	0.9795	0.9733	0.9671
0.80	1.0072	1.0044	1.0013	0.9951	0.9889	0.9827	0.9766	0.9705	0.9644
1.00	1.0053	1.0022	0.9991	0.9928	0.9866	0.9804	0.9743	0.9682	0.9622

*The density values of the pure water were taken from the literature.[106,107]

3.3.1.1 *Comparison of density data with the literature of dried [C$_2$MIm][CH$_3$CO$_2$]*

There is no data available in the literature on the physical properties of dried and binary mixtures with water for the [C$_2$MIm][C$_3$H$_7$CO$_2$] and [C$_2$MIm][C$_7$H$_{15}$CO$_2$], to date. However, several research groups have already published volumetric data of the dried [C$_2$MIm][CH$_3$CO$_2$] IL and its mixture with water.[107-113] Therefore, it is interesting to evaluate the accuracy of all combined data (from this actual work and others). A deviation graph (δ) is presented in Figure 3-5 to depict the standard deviations (Eq. 7) between the density data of the pure IL presented in

this work ($\rho^{Cal.}$) with those from the literature ($\rho^{lit.}$) as a function of the temperature.

(Eq. 7)

$$\delta = 100 \, \frac{\rho^{lit.} - \rho^{cal.}}{\rho^{cal.}},$$
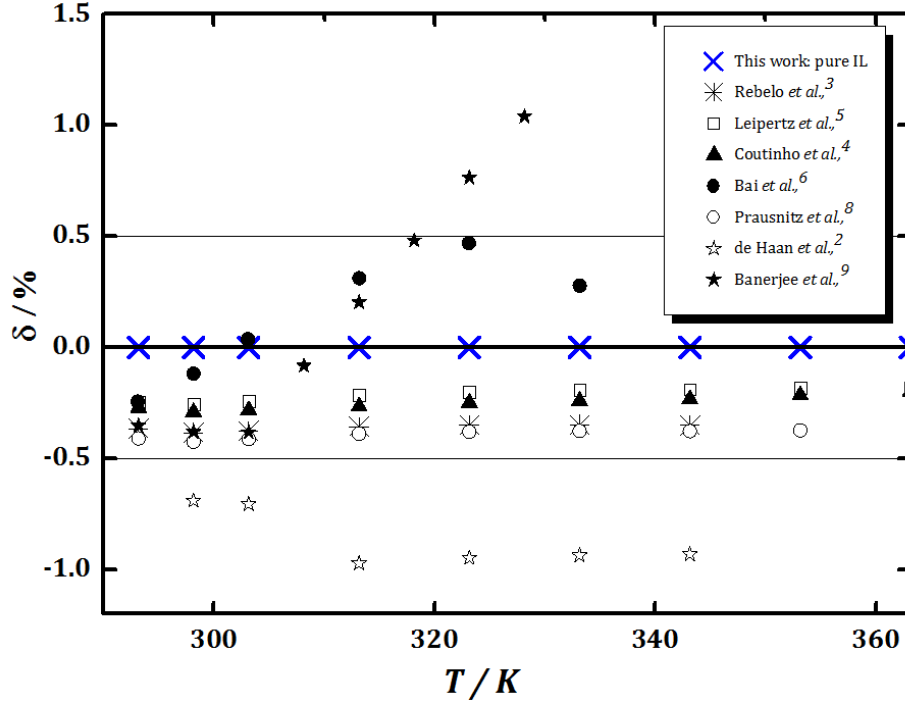
Figure 3-5. Comparison of the experimental density data from this work with those from the literature in the case of the dried [C₂MIm][CH₃CO₂] as a function of temperature at 0.1MPa.[107-113]

As shown in Figure 3-5, large deviations close to + 1 % and to - 1% were observed with data published by Banerjee *et al.*,[114] (⋆) and de Haan *et al.*,[107] (☆), respectively. However, our data are in better agreement with other literature data within an accuracy close to +/- 0.5 %, as already reported in the case of other hydrophilic / hygroscopic ILs.[115] As explained previously in Chapter-2 and as claimed by Jacquemin *et al.*,[116,117] such deviations can be attributed to two groups of errors: i) the apparatus; and ii) the impurities present in ILs.[116,117] Where the overall uncertainty must be determined by taking into account not only the uncertainty of each instruments used (balance, Karl-Fisher and densitometer), as well as, the errors associated to experimental works (*i.e.* sample left in contact with air, calibration of each equipment), but more importantly from the impurities left in the dried IL coming from their synthesis, while different synthesis routes and purification methods used could lead to different impurities

and in fact affect the overall purity of the "pure" ILs. Therefore, it can be concluded that data presented during this work are in agreement with the literature data published by Rebelo *et al.,*[108] Leipertz *et al.,*[110] Coutinho *et al.,*[109] Bai *et al.,*[111] and Praunitz *et al.*[113]

3.3.1.2 *Density of the dried IL and binary mixture with water as a function of the temperature*

According to the data reported in Table 3-1 and as expected from the literature, it appears that the density of the pure ILs increases by decreasing the anion alkyl-chain length and the overall trend follows this order, whatever the temperature is set to:

$\rho([C_2MIm][CH_3CO_2]) > \rho([C_2MIm][C_3H_7CO_2]) > \rho([C_2MIm][C_7H_{15}CO_2])$

For example, at 293.15 K, their density is (1.0999, 1.0701 and 1.0053) $g \cdot cm^{-3}$, respectively. Furthermore, as shown in Figure 3-6, Figure 3-7 and Figure 3-8, whatever the composition and IL structure, their density decreases linearly with the temperature. This shows that all mixtures are getting lighter (less dense) by increasing the temperature, as expected. In fact, density data of each mixture were then fitted by using a linear relationship as a function of temperature (Eq. 8).[118]

(Eq. 8)

$$\rho_i = \sum_{i=0}^{1} b_i \cdot T^i \ ,$$

$\rho;$ represents the density of the solution, $b_i;$ the linear fitting coefficients of the density, and $T^i;$ the temperature, i being the IL mole fraction.

As shown in Figure 3-6, Figure 3-7 and Figure 3-8, the density data of the pure ILs as well as their mixture with water are, generally, higher than the density of the pure water (red line in each Figure). In other words, the pure ILs are denser than pure water over the whole temperature range studied, except in the case of the [C_2MIm][C_7H_{15}CO_2] when the temperature is higher than 320 K. This behaviour may be related to the difference on the thermal expansion coefficient between this IL and water.
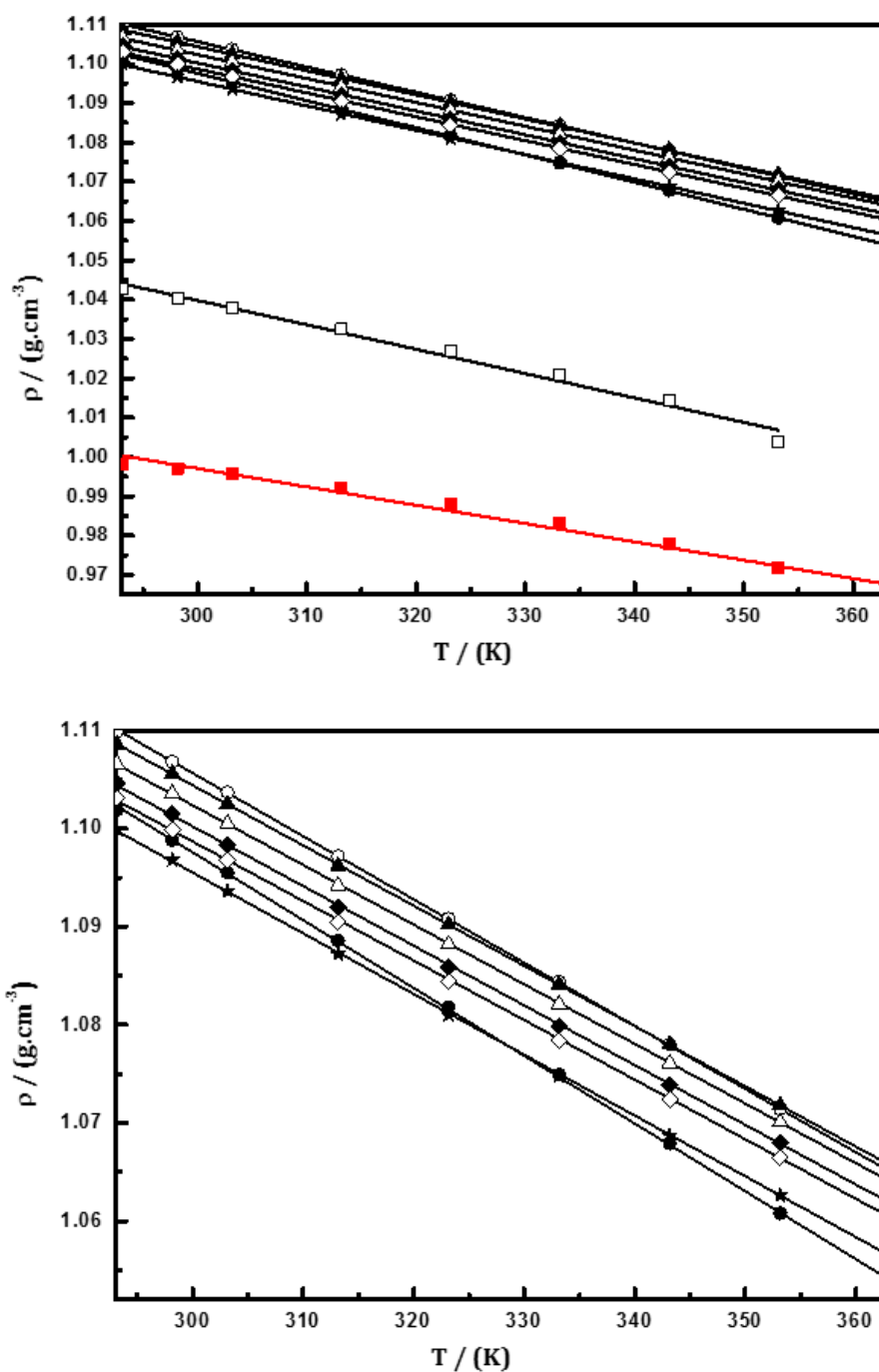
Figure 3-6. Density data, ρ, of the ($[C_2MIm][CH_3CO_2]$ + H_2O) binary mixture as a function of the temperature and 0.1 MPa at χ_{IL}: ■, 0.00; □, 0.05; ●, 0.19; ○, 0.33; ▲, 0.47; △, 0.62; ◆, 0.77; ◇, 0.89; ★, 1.00. The top figure includes all compositions, whereas the bottom figure shows a zoom on some compositions only. The lines represent linear type fitting of the experimental data with parameters reported in Table 3-2.
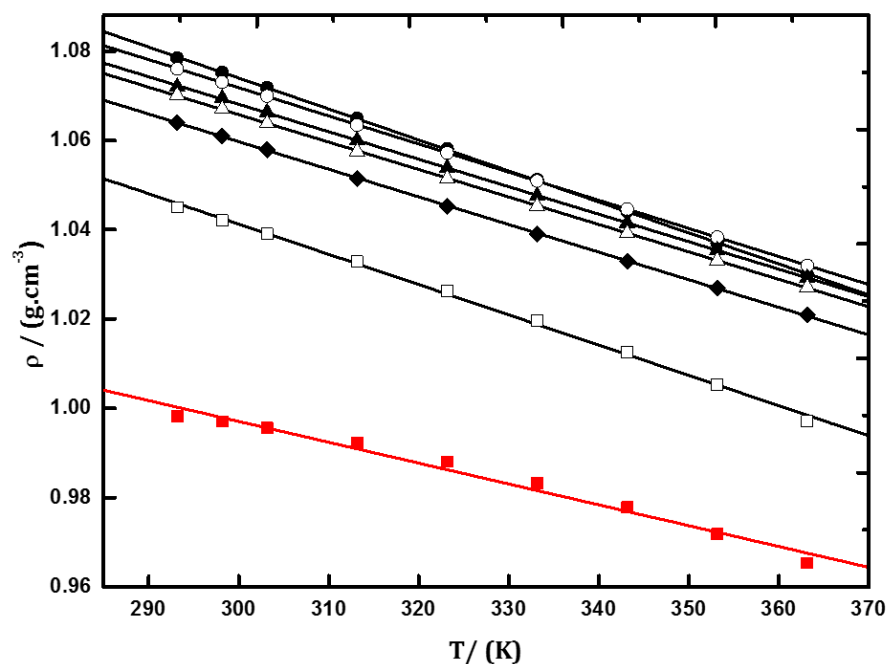
Figure 3-7. Density data, ρ, of the ($[C_2MIm][C_3H_7CO_2]$ + H_2O) binary mixture as a function of the temperature and 0.1 MPa at χ_{IL}: ■, 0.00; □, 0.05; ●, 0.20; ○, 0.50; ▲, 0.65; △, 0.80; ◆, 1.00. The lines represent linear type fitting of the experimental data with parameters reported in Table 3-2.
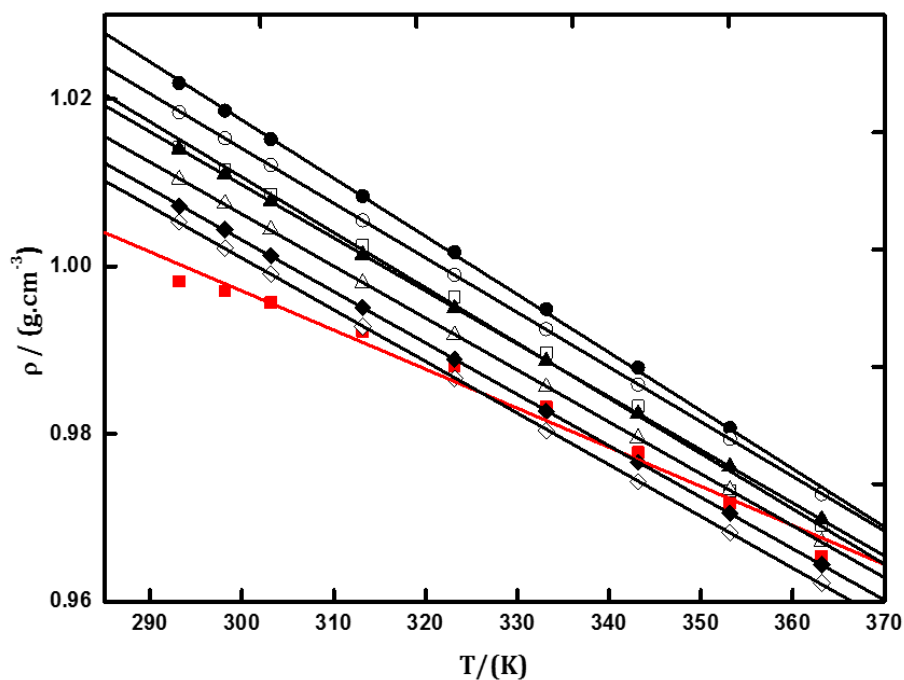
Figure 3-8. Density data, ρ, of the ($[C_2MIm][C_7H_{15}CO_2]$ + H_2O) binary mixture as a function of the temperature and 0.1 MPa at χ_{IL}: ■, 0.00; □, 0.05; ●, 0.20; ○, 0.35; ▲, 0.50; △, 0.65; ◆, 0.80; ◇, 1.00. The lines represent linear type fitting of the experimental data with parameters reported in Table 3-2.

Table 3-2. Linear fitting coefficients b_i of the density of the ([C_2MIm][CH_3CO_2] + H_2O), ([C_2MIm][$C_3H_7CO_2$] + H_2O), and ([C_2MIm][$C_7H_{15}CO_2$] + H_2O) binary mixture as a function of the temperature calculated from experimental data provided in Table 3-1 using the equation 1 along with their standard deviations (eq. 9).

χ_{IL}	b_0/ g·cm^{-3}	$10^4 \times b_1$/ g·cm^{-3}·K^{-1}	$10^4 \times \sigma$/ g·cm^{-3}	χ_{IL}	b_0/ g·cm^{-3}	$10^4 \times b_1$/ g·cm^{-3}·K^{-1}	$10^4 \times \sigma$/ g·cm^{-3}	χ_{IL}	b_0/ g·cm^{-3}	$10^4 \times b_1$/ g·cm^{-3}·K^{-1}	$10^4 \times \sigma$/ g·cm^{-3}
([C_2MIm][CH_3CO_2] + H_2O)				([C_2MIm][$C_3H_7CO_2$] + H_2O)				([C_2MIm][$C_7H_{15}CO_2$] + H_2O)			
0.00	1.1371	-4.6669	16.19	0.00	1.1370	-4.6669	16.2	0.00	1.1371	-4.6669	16.2
0.05	1.2258	-6.1993	16.86	0.05	1.2445	-6.7760	8.1	0.05	1.2087	-6.6030	12.0
0.19	1.3048	-6.9087	2.48	0.20	1.2820	-6.9360	2.0	0.20	1.2256	-6.9393	4.0
0.33	1.2988	-6.4400	1.20	0.50	1.2607	-6.2983	0.7	0.35	1.2098	-6.5253	0.7
0.47	1.2885	-6.1373	0.68	0.65	1.2527	-6.1540	1.5	0.50	1.1997	-6.3307	0.6
0.62	1.2847	-6.0783	1.13	0.80	1.2501	-6.1450	1.2	0.65	1.1923	-6.2023	0.9
0.77	1.2827	-6.0827	1.90	1.00	1.2452	-6.1827	1.8	0.80	1.1874	-6.1430	0.9
0.89	1.2808	-6.0697	1.97					1.00	1.1861	-6.1703	1.1
1.00	1.2812	-6.1903	1.82								

(Eq. 9)

$$\sigma = \left(\frac{\sum (\rho_i^{exp} - \rho_i^{cal})^2}{n - v} \right)^{0.5}$$

Where σ; represents the standard deviation, n; the number of experimental points, v; the number of adjustable parameters.

3.3.1.3 Density of the dried ILs and binary mixtures with water as a function of the composition

As reported in Table 3-1 and shown in Figure 3-9, Figure 3-10 and Figure 3-11, whatever the temperature and IL structure, the density data seem to follow a logarithmic trend as a function of the IL mole fraction. In other words, the maximum of density is not observed for any pure component as it is generally observed in the case of the densities of IL-based binary mixtures. However, this feature was already observed in the case of protic ionic liquid-based binary mixtures when they are mixed with different organic solvents or water.[119] This behaviour could be associated to specific changes on their cohesive energy driven by interactions changes in solution when these ILs are mixed with a co-solvent, which may be also attributed to the formation of an emulsion.[119] By fitting each density dataset as the function of IL mole fraction by using a logarithmic-type function, it appears that this maximum is generally observed for an IL mole fraction between 0.1 and 0.4. Furthermore, as shown in Figure 3-9, Figure 3-10

and Figure 3-11, for all temperatures investigated, density maxima are shifting towards lower IL mole fraction by increasing the anion alkyl chain length while each IL density maximum seems to be temperature independent. More interestingly, the density deviations between each IL density maximum with the respect of density values of pure components seem to increase by increasing the anion alkyl chain length, which may be associated to more specific interactions changes in solution by increasing the van der Waals forces (from acetate to octanoate).
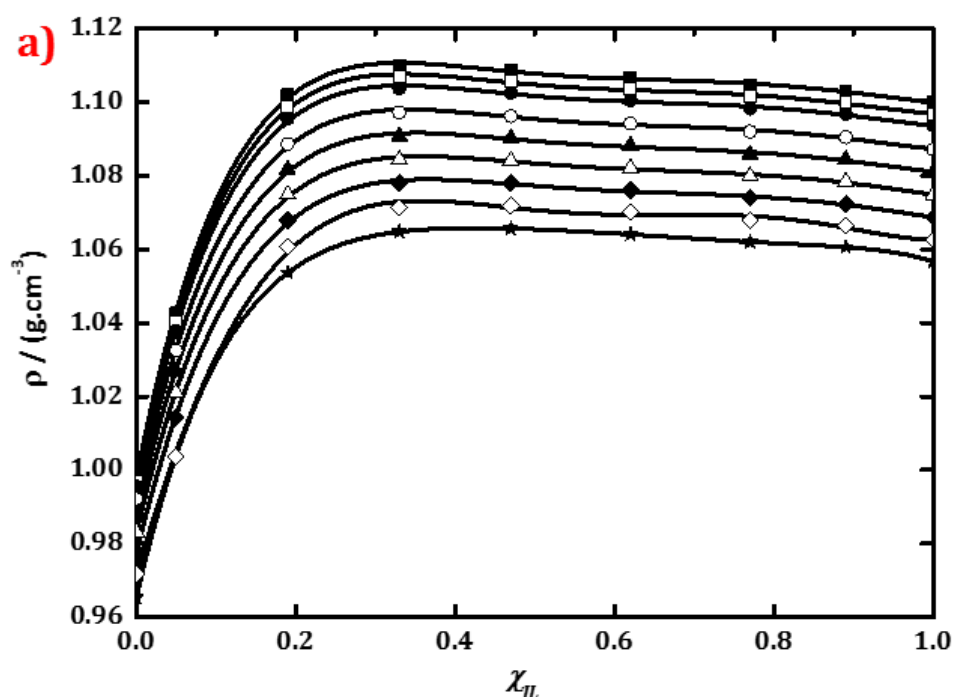
Figure 3-9. Density data for ($[C_2MIm][CH_3CO_2]$ + H_2O) binary mixture as a function of $[C_2MIm][CH_3CO_2]$ mole fraction, χ_{IL}, at 0.1MPa; ■, T = 293.15 K; □, T = 298.15 K; ●, T = 303.15 K; ○, T = 313.15 K; ▲, T = 323.15 K; △, T = 333.15 K; ◆, T = 343.15 K; ◇, T = 353.15 K; ★ T = 363.15 K.
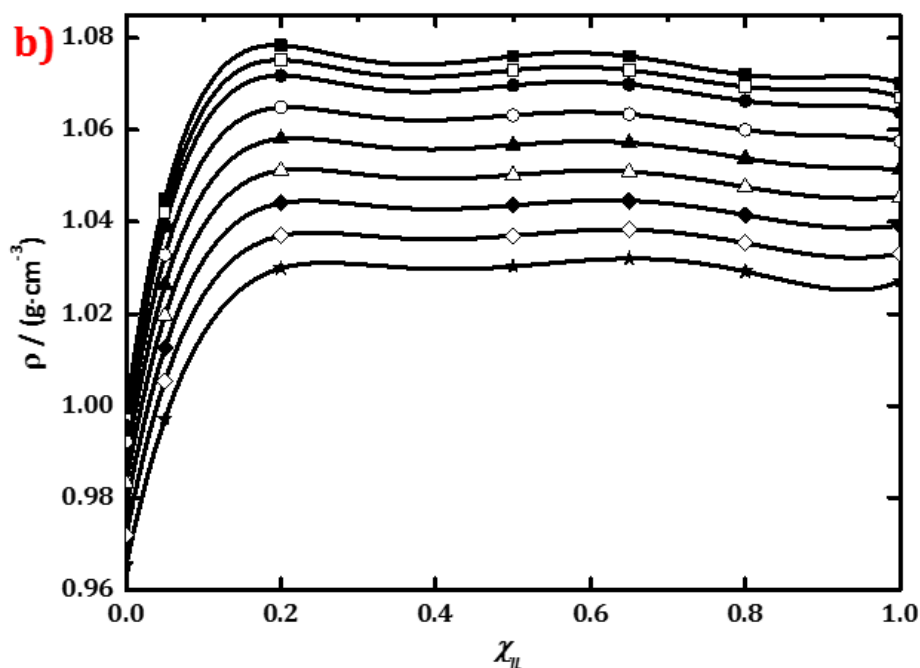
Figure 3-10. Density data for ($[C_2MIm][C_3H_7CO_2]$ + H_2O) binary mixture as a function of $[C_2MIm][C_3H_7CO_2]$ mole fraction, χ_{IL}, at 0.1MPa; ■, T = 293.15 K; □, T = 298.15 K; ●, T = 303.15 K; ○, T = 313.15 K; ▲, T = 323.15 K; △, T = 333.15 K; ◆, T = 343.15 K; ◇, T = 353.15 K; ★ T = 363.15 K.
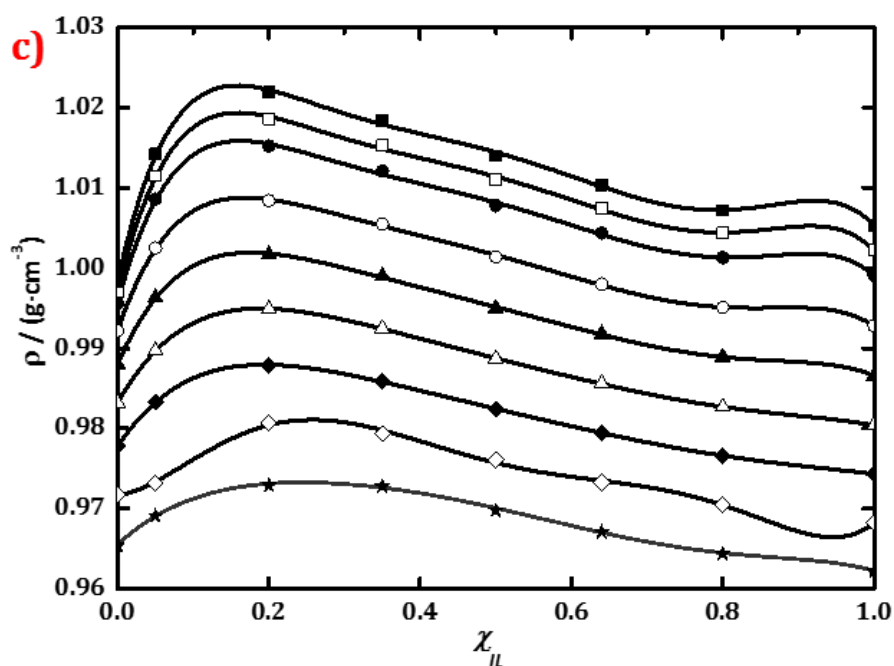
Figure 3-11. Density data for ($[C_2MIm][C_7H_{15}CO_2]$ + H_2O) binary mixture as a function of $[C_2MIm][C_7H_{15}CO_2]$ mole fraction, χ_{IL}, at 0.1MPa; ■, T = 293.15 K; □, T = 298.15 K; ●, T = 303.15 K; ○, T = 313.15 K; ▲, T = 323.15 K; △, T = 333.15 K; ◆, T = 343.15 K; ◇, T = 353.15 K; ★ T = 363.15 K.

63

To highlight this effect, it is also interesting to compare the three IL densities in their whole composition range at a specific temperature as shown in Figure 3-12 for datasets measured at 298.15 K. It is clear from this figure that, the shorter is the anion alkyl chain length, the higher will be the density values for the whole composition range and the lower will be the difference between the maximum and the density of the corresponding pure IL. Hence at any composition, density values follow the same trend as reported in the case of the pure ILs:

$\rho([C_2MIm][CH_3CO_2]) > \rho([C_2MIm][C_3H_7CO_2]) > \rho([C_2MIm][C_7H_{15}CO_2])$.
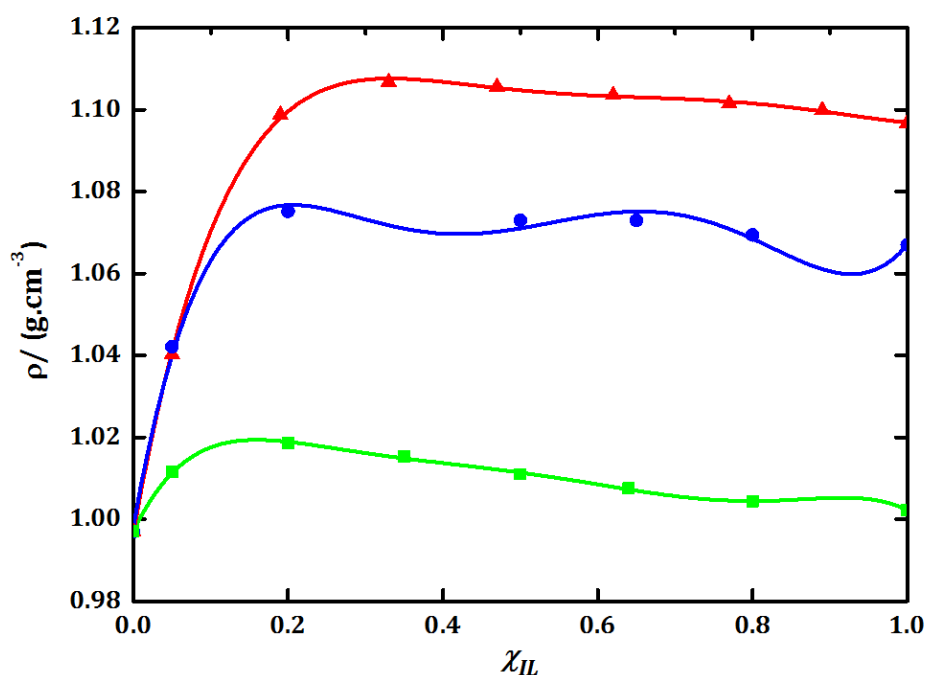
Figure 3-12. Density data at 298 K for ($[C_2MIm][C_nH_nCO_2]$ + H_2O) binary mixtures as a function of IL mole fraction, χ_{IL}: ▲, $[C_2MIm][CH_3CO_2]$; ●, $[C_2MIm][C_3H_7CO_2]$; ■, $[C_2MIm][C_7H_{15}CO_2]$ at 0.1MPa.

According to the above-mentioned results, it is also interesting to establish a link between the density and the structure of the IL, which may be probed by the molar mass of the ions reported in Table 3-3.

Table 3-3. Molar mass of each ion (M_{ions} / g·mol^{-1}).

Cations	M_{cation} / g·mol^{-1}	Anions	M_{anion} / g·mol^{-1}
		$CH_3CO_2^-$	59.04
C_2MIm^+	111.17	$C_3H_7CO_2^-$	87.09
		$C_7H_{15}CO_2^-$	143.20

Hence, smallest is the molar mass of the anion, denser is the solution as already confirmed through the density of the pure ILs.

3.3.2   Excess molar volume, V^E

In thermodynamics, the volume is known as an extensive parameter. This means that the volume depends of the state and the quantity of molecules of the system. Physical properties of IL in binary mixture with either solvent or another IL are in large investigation since those materials can be used in various applied area (such as electrolytes, catalyst etc.).[32] In order to understand and interpret the nature of the interactions between the molecules present in the mixture, the excess properties of liquid mixtures can provide important information which may be related to spectroscopic data provided in Chapter 4. The excess molar volume (V^E) is used to study the deviation behaviour of a mixture regarding its ideal state as follows (Eq. 10).[120]

(Eq. 10)

$$V^E = V_m - V_m^{Ideal} \, ,$$

Where

(Eq. 11)

$$V_m^{Ideal} = \sum_{i=1}^{N} \chi_i \cdot V_i^0 ,$$

V_m is the molar volume, V_i^0 is the molar volume of the pure constituent i, and χ_i it mole fraction in solution.

The molar volume (V_m) of a fluid represents the volume occupied by one mole of a substance at a given temperature and pressure.

(Eq. 12)

$$V_m = \frac{M}{\rho},$$

Where (M /g.mol^{-1}) is the molar mass of the fluid and (ρ /g.cm^{-3}) its density.

Excess molar volumes, V^E , reported in Table 3-4, were calculated from the density data (Table 3-1) as the function of the composition according to (Eq. 13):

(Eq. 13)

$$V^{\mathrm{E}} = \frac{1}{\rho_m} \sum_{i=0}^{N} \chi_i . M_i - \sum_{i=0}^{N} \frac{\chi_i . M_i}{\rho_i},$$

ρ_m represents the density of the mixture, χ_i the mole fraction, M_i /(g.mol^{-1}) the molar mass and ρ_i the density of the pure component i.

This mathematical equation (Eq. 13), can be rewritten as follows in the case of our binary mixtures (Eq. 14):

(Eq. 14)

$$V^{\mathrm{E}} = \left[\frac{(\chi_{IL} . M_{IL} + \chi_{water} . M_{water})}{\rho_m}\right] - \left[\frac{\chi_{IL} . M_{IL}}{\rho_{IL}} + \frac{\chi_{water} . M_{water}}{\rho_{water}}\right],$$

Where IL represents the IL compound, $water$ represents the water molecules, and m the mixture.

All V^E data were then fitted as a function of the IL composition by using the third order of the Redlich-Kister type fitting equation:

(Eq. 15)

$$V^E = \chi_{water}(1 - \chi_{water}) \sum_{n=1} A_n (1 - 2\chi_{water})^{n-1},$$

for n = 3:

(Eq. 16)

$$V^E = \chi_{water}(1 - \chi_{water})[(A_1(1 - 2\chi_{water})^0 + (A_2(1 - 2\chi_{water})^1 + (A_3(1 - 2\chi_{water})^2 + (A_2(1 - 2\chi_{water})^3],$$

Where A_1, A_2 and A_3 are the adjustable parameters determined from the correlation of all datasets.

All V_m and V^E calculated data along with the parameters of the Redlich-Kister type fitting equation are displayed in Appendices B to E.

3.3.2.1 Comparison of the excess molar volume data, V^E, with the literature of ([C$_2$MIm][CH$_3$CO$_2$]+ H$_2$O) binary mixtures

The ([C$_2$MIm][CH$_3$CO$_2$]+ H$_2$O) binary mixtures are already known in the literature in terms of density properties.[107,111,121] However, no density data was reported to date in the case of the binary mixtures containing the [C$_2$MIm][C$_3$H$_7$CO$_2$] and

[C$_2$MIm][C$_7$H$_{15}$CO$_2$]. Therefore, before analysing our data, it is important to confirm the method used here to determine, fit and draw V^E. It was only possible to compare the present V^E data of this work with the dataset published by de Haan *et al.* as shown in Figure 3-13.[107] However, in the case of the Schubert *et al.*, it was not possible to extract the density raw data into their excess molar volume since no density data was reported in the case of the pure IL. [121]

Figure 3-13 shows the comparison of our V^E data with those published by de Haan *et al.*.[107] Both datasets are following very similar trend, *i.e.* both curves show negatives data within the same order of magnitude whatever the composition investigated, reflecting in fact the accuracy of our V^E dataset even if large deviations were observed between both density datasets (see Figure 3-12). This is due to the nature of the excess properties equation which is in fact a subtraction of molar volumes taken from density data, error on density datasets are generally less pronounced by calculating then excess properties if such errors remain constant during the whole measurements. Furthermore, both datasets were then fitted with the same Redlich-Kister type fitting equation to highlight that the V^E maxima located at around χ_{IL} = 0.3 in both cases.
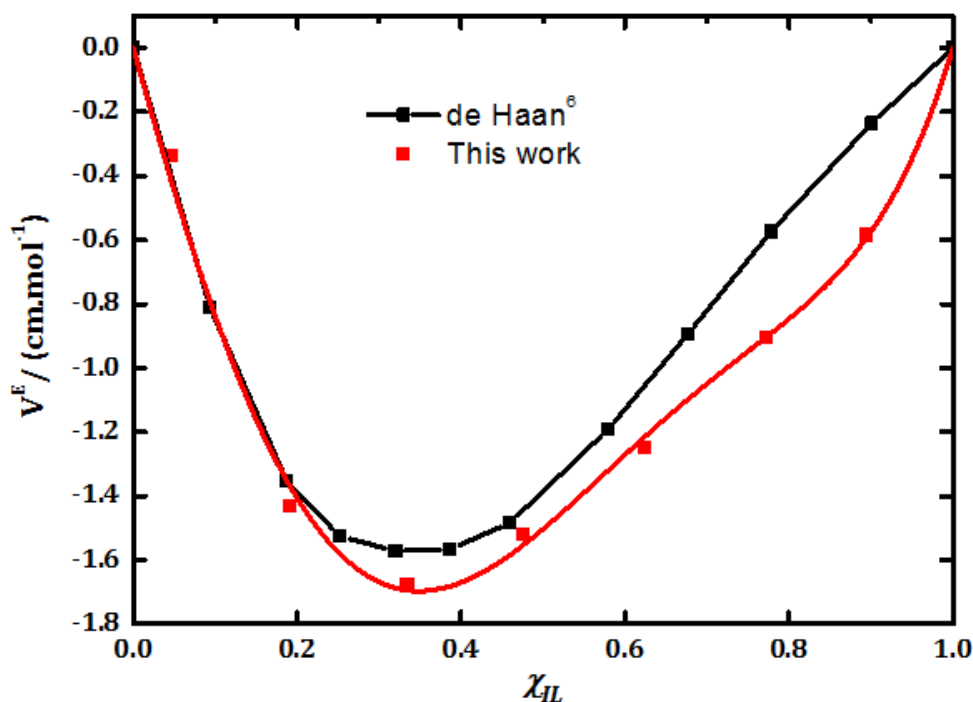
Figure 3-13. Comparison of the excess molar volume V^E for ([C$_2$MIm][CH$_3$CO$_2$]+H$_2$O) binary mixtures taken at 298.15 K as a function of [C$_2$MIm][CH$_3$CO$_2$] mole fraction composition, χ_{IL}, at

0.1MPa; with ■ represents the work of de Haan et al. (lines represent a guide for this eyes),[107] and ■ represents data from this work (lines represent the 3rd order Redlich Kister type fitting).

3.3.2.2   *VE of the binary mixtures in function of the composition*

All excess molar volume data calculated from the density raw data (Table 3-1) for all investigated mixtures and temperatures are reported in the Appendix C. From these data, it was then possible to plot the calculated V^E data and then fot them with the third order of the Redlich-Kister equation. The graphs underneath show the variation of the V^E data as the function of the composition from (293.15 to 263.15) K.
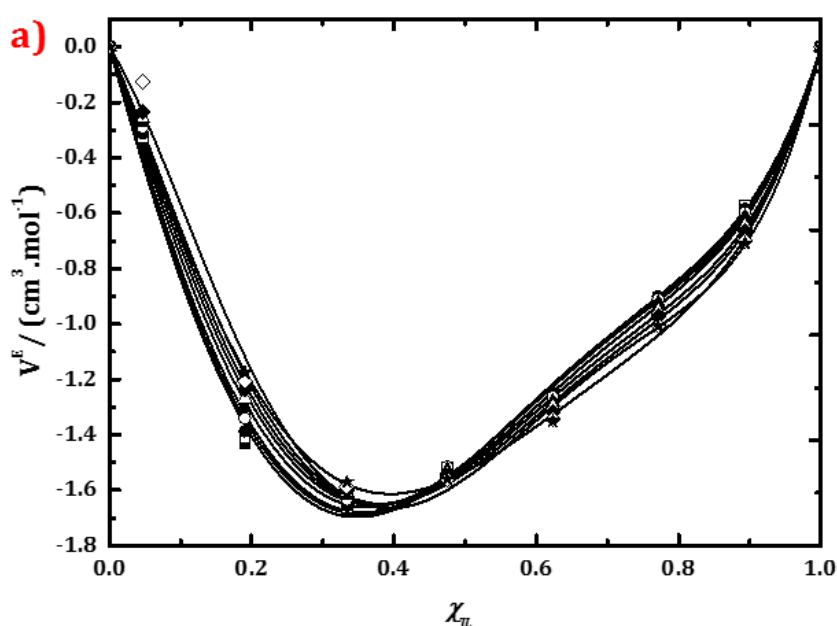
Figure 3-14. Excess molar volume V^E for ($[C_2MIm][CH_3CO_2]$ + H_2O) binary mixture as a function of $[C_2MIm][CH_3CO_2]$ mole fraction, χIL, at 0.1 MPa and at ■, T = 293.15 K; □, T = 298.15 K; ●, T

Figure 3-15. Excess molar volume V^E for ([C$_2$MIm][C$_3$H$_7$CO$_2$] + H$_2$O) binary mixture as a function of [C$_2$MIm][C$_3$H$_7$CO$_2$] mole fraction, χIL , at 0.1 MPa and at ■, T = 293.15 K; □, T = 298.15 K; ●, T = 303.15 K; ○, T = 313.15 K; ▲, T = 323.15 K; △, T = 333.15 K; ◆, T = 343.15 K; ◇, T = 353.15 K; ★ T = 363.15 K. Lines represent the 3rd order Redlich Kister type fitting.
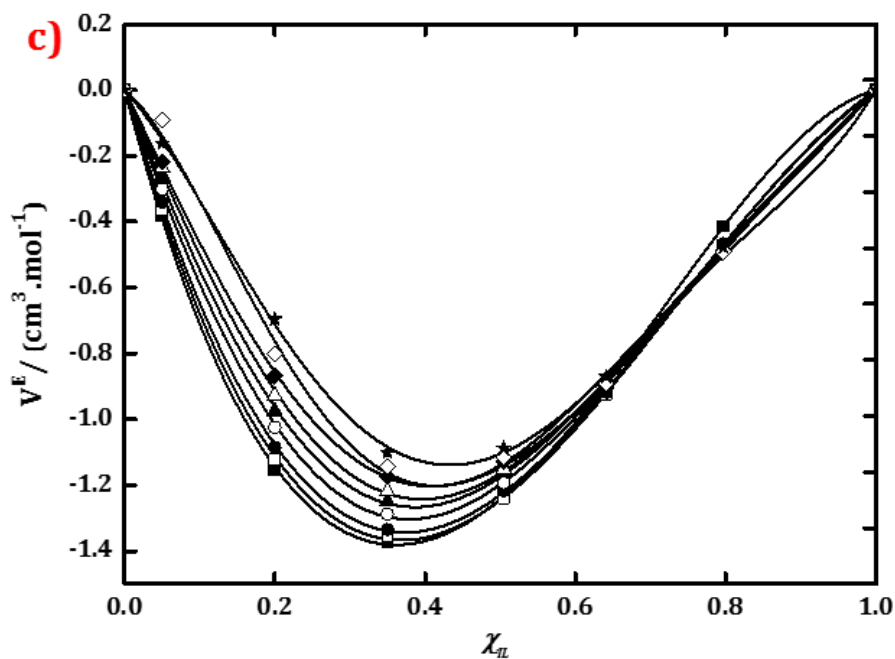
Figure 3-16. Excess molar volume V^E for ([C$_2$MIm][C$_7$H$_{15}$CO$_2$] + H$_2$O) binary mixture as a function of [C$_2$MIm][CH$_3$CO$_2$] mole fraction, χIL , at 0.1 MPa and at ■, T = 293.15 K; □, T = 298.15 K; ●, T = 303.15 K; ○, T = 313.15 K; ▲, T = 323.15 K; △, T = 333.15 K; ◆, T = 343.15 K; ◇, T = 353.15 K; ★ T = 363.15. Lines represent the 3rd order Redlich Kister type fitting.

When $V^E >0$ is observed for a given system, this means that hydrogen-bonds break up, allowing volume dilatations of the solution.[118,122] However, in the case of the three binary systems containing an alkyl-carboxylate-based IL mixed with water, V^E show negative values throughout their whole composition range (Figure 3-14, Figure 3-15 and Figure 3-16). This indicates an increase of interactions between the ions in solution and water molecules, observed by a volume contraction ($V^E <0$) between (293.15 and 363.15) K.

This confirms the presence of strong intermolecular interactions due to hydrogen bonds between water and those ILs. Those interactions are stronger than the hydrogen bonds formed between *water-water* molecules and IL ions.[118,123] Furthermore, V^E becomes less negative by increasing the temperature. To highlight such behaviour, for each system the V^E maximum at the two extreme temperatures studied was reported in Table 3-4. This table clearly shows also a shift of the V^E maxima in term of IL mole fraction composition, χ_{IL}.

Table 3-4. V^E maxima and the corresponding IL mole fraction, χ_{IL}, for the three ILs studied.

Binary mixture	T /K	V^E maxima	χ_{IL}
(a) $[C_2MIm][CH_3CO_2] + H_2O$	293.15	-1.697	0.34
	363.15	-1.613	0.39
(b) $[C_2MIm][C_3H_7CO_2] + H_2O$	293.15	-1.686	0.33
	363.15	-1.555	0.45
(c) $[C_2MIm][C_7H_{15}CO_2] + H_2O$	293.15	-1.382	0.36
	363.15	-1.139	0.42

The molecular association becomes maximal when V^E is at its maximum at approximately $\chi_{IL} = 0.35$ at 293.15 K and 0.40 at 363.15 K for the three IL-based solutions. This means that at those specific temperature and composition, χ_{IL}, there are strong *anion-water* / cation-water interactions in solution.

Another interesting fact already reported elsewhere, was the addition of water into those type of ILs producing heat that reveals an exothermic reaction for the three ILs studied.[123] This is due to a reaction between water and the anion to form carboxylic acids formed from the carboxylate anion precursor as it was reported previously from our group.[124] The graph underneath show V^E curves for the three ILs at 298.15 K:
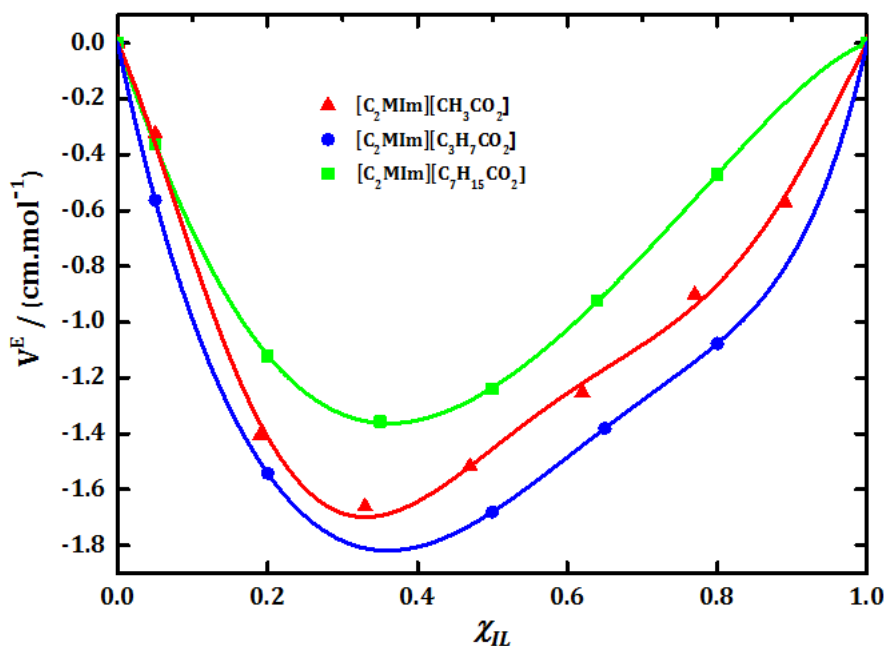
Figure 3-17. Excess molar volume V^E at 298.15 K for ($[C_2MIm][C_nH_nCO_2]$ + H_2O) binary mixtures as a function of $[C_2MIm][C_nH_nCO_2]$ mole fraction, χ_{IL}, at 0.1MPa; ▲, $[C_2MIm][CH_3CO_2]$; ●, $[C_2MIm][C_3H_7CO_2]$; ■, $[C_2MIm][C_7H_{15}CO_2]$. Lines represent the Redlich Kister of the third order.

By comparing all three ILs in terms of V^E, it is interesting to note that the $[C_2MIm][C_7H_{15}CO_2]$ gets less negative V^E values than the two other binary systems. This is due to its long alkyl chain which increases the van der Waals forces in the mixture. These result can be associated to a stronger self-organisation due to van der Waals forces which are intensely present in the case of the octanoate-anion as already stated above with the respect of the density values.

However, there is a strong hydrogen bonding network for all three ILs due to the *water-cation* interaction already well-known in the literature,[125] and also with the carboxylate function, since oxygen atoms are very electronegative atoms and will form easily hydrogen bonds with hydrogens from water molecules. This tend along with the variation of the density with the IL composition seem to indicate a possible formation of an emulsion in the case of the $[C_2MIm][C_7H_{15}CO_2]$ mixed with water. However, more investigation needs to be done in order to prove this relevant fact.

3.3.2.3 *Excess molar entropy of the binary systems, S^E*

Entropy is the thermodynamic function, *S*, that describes randomness and disorder of molecules in a given system. It is based on the number of different arrangements available to them in term of space and energy. For instance, molecules in a solid phase have only a strict and rigid position; whereas gas molecules can move and expand as freely as possible. Thus, gas molecules have the highest positional entropy, since positional entropy depends on the number of available configurations or arrangements in space.[126] The binary system studied here are in the liquid phase and therefore it is interesting to study the excess entropy, *S^E*, of all three systems in order to get a better idea on their molecule disorders.

However, the molar volume, *V_m*, expressed in nm³ of the pure components and their mixtures are involved in the excess entropy equation and therefore needs to be firstly determined. Based on the experimental density, the molar volume, *V_m* can be calculated in nm³ by using the equation below:

(Eq. 17)

$$V_m = \frac{\chi_1 M_1 + \chi_2 M_2}{N_a \cdot \rho},$$

Where *χ_1* and *χ_2* are, respectively, the mole fraction of the IL and water; *M_1* and *M_2* are, respectively, the molar mass of IL and water; *N_a* and *ρ* are, respectively, the Avogadro's constant and the density of the binary mixture.

The molar volume values, *V_m*, of pure components and their mixtures expressed in cm³·mol⁻¹ and in nm³ are reported in Appendix D. The variation of excess standard entropy, *S^E*, at T = 298.15 K was calculated as follow:

(Eq. 18)

$$S^E = S^\circ_m - S^\circ_{id.},$$

(Eq. 19)

$$S^\circ_{id.} = \chi_{IL} \cdot S^\circ_{IL} - \chi_{H2O} \cdot S^\circ_{H2O},$$

where *χ_i* and S°_i are, respectively, the mole fraction and the standard entropy of component *i, id.* means the ideal system.

According to Glasser,[127] the standard entropy, $S°$, can be calculated knowing the molar volume of a component at T = 298.15 K by using (Eq. 20):

(Eq. 20)

$$S°(298.15\ K)/(J \cdot K^{-1} \cdot mol^{-1}) = 1246.5\ x\ (V_m/nm^3) + 29.5,$$

This equation is used to calculate $S°_m$, $S°_{H2O}$, $S°_{IL}$ and $S°_{id}$

The values of Real, $S^°_m$, ideal, $S^°_{id.}$, and excess, S^E standard entropy of the ([C₂MIm][CₙHₙCO₂] + H₂O) binary mixtures as a function of [C₂MIm][CₙHₙCO₂] mole fraction, χ_{IL}, at T = 298.15 K and 0.1 MPa were reported in Table 3-5.

Table 3-5. Real, $S^°_m$, ideal, $S^°_{id.}$, and excess, S^E standard entropy of the ([C₂MIm][CₙHₙCO₂] + H₂O) binary mixture as a function of [C₂MIm][CₙHₙCO₂] mole fraction, χ_{IL}, at T = 298.15 K and 0.1 MPa calculated from (Eq. 18), (Eq. 19) and (Eq. 20) above using V_m expressed in nm³ from Appendix D.

χ_{IL}	$S^°_m$ / J·K⁻¹·mol⁻¹	$S^°_{id.}$ */ J·K⁻¹·mol⁻¹	S^E / J·K⁻¹·mol⁻¹
	For ([C₂MIm][CH₃CO₂] + H₂O)		
0.00	66.86	66.86	0
0.05	79.39	80.06	-0.67
0.19	117.99	120.90	-2.91
0.33	158.19	161.63	-3.44
0.47	198.50	201.64	-3.14
0.62	241.17	243.76	-2.59
0.77	283.95	285.82	-1.87
0.89	319.23	320.42	-1.18
1.00	350.67	350.67	0.00
	For ([C₂MIm][C₃H₇CO₂] + H₂O)		
0.00	66.86	66.86	0.00
0.05	83.91	85.07	-1.17
0.20	133.06	136.25	-3.19
0.36	189.48	192.73	-3.25
0.50	236.80	240.28	-3.48
0.65	291.14	294.00	-2.86
0.80	342.15	344.37	-2.23
1.00	415.72	415.72	0.00
	For ([C₂MIm][C₇H₁₅CO₂] + H₂O)		
0.00	66.86	66.86	0.00
0.05	90.51	91.26	-0.75
0.20	161.98	164.30	-2.32
0.35	234.78	237.58	-2.81
0.50	310.60	313.16	-2.56
0.64	377.75	379.66	-1.91
0.80	454.81	455.78	-0.97
1.00	554.78	554.78	0.00

The standard entropies of the pure ILs, S°_{IL}, are $(350.7, 415.7, 554.8)$ J$\cdot$ K$^{-1}\cdot$ mol^{-1} in this respective order:

S°[C₂MIm][CH₃CO₂] < S°[C₂MIm] [C₃H₇CO₂] < S°[C₂MIm][C₇H₁₅CO₂]

Generally, the standard entropy increase with the molecular weight as there are more possible arrangements of atoms in space for larger, more complex molecules, which increases the number of possible microstates. Hence from the above results, the $[C_2MIm][C_7H_{15}CO_2]$ system has the highest positive value of standard entropy 554.8 J K^{-1} Mol^{-1} and has therefore a better thermodynamic self-organisation than the$[C_2MIm][C_3H_7CO_2]$ and $[C_2MIm][CH_3CO_2]$ system studied here. And the standard entropy of the mixtures, S°_m, increases for all three ILs with the variation of IL mole fraction, $\chi_{IL} = (0$ to $1)$.

The graph of the variation of the excess standard entropy, S^E, as a function of IL mole fraction, χ_{IL}, at 298.15 K for the three ILs is shown in Figure 3-18 along with the Redlich-Kister coefficients displayed in Appendix E.
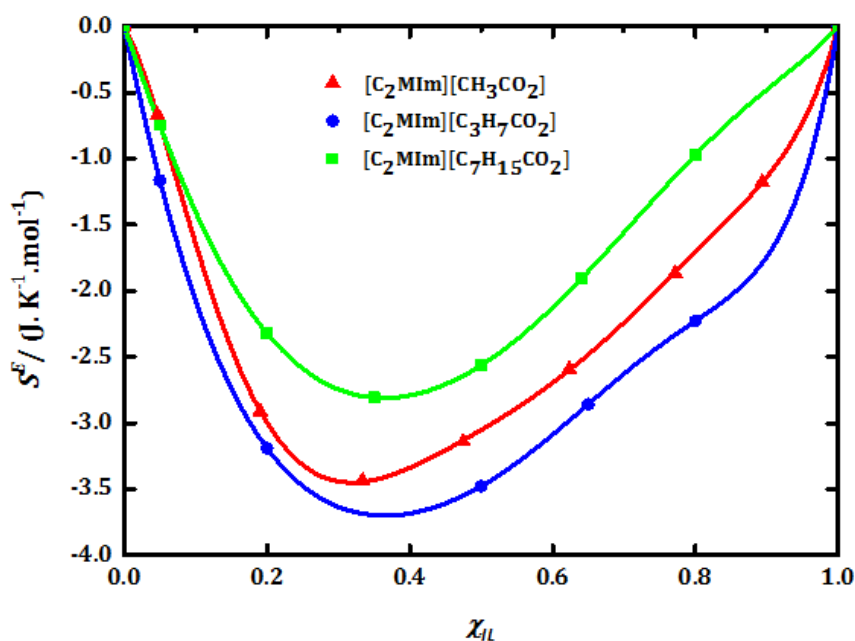
Figure 3-18. Excess standard entropy, S^{E}, of the $([C_2MIm][C_nH_nCO_2] + H_2O)$ binary mixture as a function of $[C_2MIm][C_nH_nCO_2]$ mole fraction, $\chi_{IL,}$ for: ▲, $([C_2MIm][CH_3CO_2] + H_2O)$; ●, $([C_2MIm][C_3H_7CO_2] + H_2O)$; ■, $([C_2MIm][C_7H_{15}CO_2] + H_2O)$, at T = 298.15 K and 0.1 MPa. The line represents the Redlich-Kister-type fitting equation generated by using data from the Appendix E.

The excess standard entropy data, S^E, for all three IL solutions are negative, that can be linked to the fact that the real disorder of ([C$_2$MIm][C$_n$H$_n$CO$_2$] + H$_2$O) (for n = 1,2,3) is lower than that expected from the ideality rule. Those results can then be linked to a volume contraction due to the addition of water into those ILs which increases the overall order in the solution. In fact, S^E maximum are found at χ_{IL} = 0.30 in the case of the [C$_2$MIm][CH$_3$CO$_2$] solution, and at χ_{IL} = 0.36 for the two other solutions, which are in agreement with the V^E maximum determined at 298.15 K.

3.3.3   Apparent and partial molar volumes

From the previously calculated excess molar volume, V^E, it is then possible to calculate the apparent and the partial molar volumes in the aim to extract information of each component at infinite dilution.

As reported Pires *et al.*,[118] the apparent molar volumes, $V_{\phi,i}$, of a component in a binary mixture is defined as:

(Eq. 21)

For the IL $$V_{\phi,IL} = V_{m,IL} + \frac{V^E}{\chi_{IL}},$$

(Eq. 22)

For water $$V_{\phi,water} = V_{m,water} + \frac{V^E}{\chi_{water}},$$

Where $V_{m,IL}$ and $V_{m,water}$ are the molar volume of the pure IL and water component, χ_{IL} and χ_{water} are the mole fraction of IL and water component in the binary mixture, respectively.

Then the partial molar volumes at infinite dilution can be calculated as follows:

(Eq. 23)

$$\overline{V}_{m,1} = V_{m,1} + \frac{V^E}{\chi_1} + \chi_1(1 - \chi_1)\left[\frac{\partial(V^E/\chi_1)}{\chi_1}\right],$$

Where $\overline{V}_{m,1}$ are the partial molar volume and $V_{m,1}$ the molar volume of the component 1 (IL or water in the present case).

The variation of the apparent molar volume, $V_{\phi,i}$, and partial molar volume, $\overline{V}_{m,1}$, of the ILs and water as a function of composition and temperature are reported in the Appendices F and G. From those values it is then possible to determine by

graphical extrapolation the infinite dilution values,$V_{m,i}^{\infty}$, for both $V_{\phi,i}$ and $\overline{V}_{m,1}$ when $\chi_i = 0$ for each temperature investigated. Then the molar volume, $V_{m,i}$,of each pure component (IL and water) has been compared to $V_{\phi,i}$ and $\overline{V}_{m,1}$ values at infinite dilution, by checking that $V_{\phi,i}^{\infty} = \overline{V}_{m,i}^{\infty}$. Based on the results reported in the Table 3-6, it appears that for all IL solutions $V_{m,pure} > (V_{\phi,i}^{\infty} = \overline{V}_{m,i}^{\infty})$, which means that a water/IL molecule has a smaller volume in the IL/water solutions than expected from their pure state.

This conveys to the fact that strong interactions are present between water and those three ILs studied. Therefore, the IL/water behaviour at infinite dilution can be seen as follow:

> ➢ When one mole of water is added into the pure ILs at infinite dilution condition, the volume occupied by this mole of water is lower than that expected (i.e. 18 cm^3 at 293.15 K), and reaches 10 cm^3 in the case of the [C$_2$MIm][CH$_3$CO$_2$], 11 cm^3 for the [C$_2$MIm][C$_3$H$_7$CO$_2$] and 14 cm^3 for the [C$_2$MIm][C$_7$H$_{15}$CO$_2$].

> ➢ When one mole of IL is added into the pure water at infinite dilution conditions, the volume occupied by a mole of [C$_2$MIm][C$_n$H$_n$CO$_2$] is lower than that expected (154 cm^3, 186 cm^3 and 253 cm^3 for the actetate, butanoate and octanoate, respectively), and reaches a value close to 148 cm^3, 173 cm^3 and 244 cm^3 for the actetate, butanoate and octanoate, respectively.

Thus, by mixing those ILs with water, it is clear that there is a volume contraction of those binary systems since the volume calculated at infinite dilutions are all lower than the volume in their pure state. This explained the negative values of V^E found previously that also conveys to a volume contraction due to strong formation of hydrogen bonding in solution.

Table 3-6. Partial molar volumes at infinite dilution, for [C$_2$MIm][C$_n$H$_n$CO$_2$], $\overline{V}_{m,IL}^{\infty}$, and for H$_2$O, $\overline{V}_{m,water}^{\infty}$, and molar volumes, $V_{m,i}$, of the pure ILs and water as a function of temperature from (293.15 to 263.15) K at 0.1 MPa.

T/K	$\overline{V}_{m,IL}^{\infty}$ /(cm^3·mol^{-1})	$V_{m,IL}$ /(cm^3·mol^{-1})	$\overline{V}_{m,water}^{\infty}$ /(cm^3·mol^{-1})	$V_{m,water}$ /(cm^3·mol^{-1})
For ([C$_2$MIm][CH$_3$CO$_2$] + H$_2$O)				
293.15	148.99	154.75	10.21	18.03
323.15	153.34	157.45	9.47	18.21
363.15	157.05	161.07	7.38	18.64
For ([C$_2$MIm][C$_3$H$_7$CO$_2$] + H$_2$O)				
293.15	173.96	186.09	11.01	18.03
323.15	181.05	189.43	14.55	18.21
363.15	188.33	193.94	14.29	18.64
For ([C$_2$MIm][C$_7$H$_{15}$CO$_2$] + H$_2$O)				
293.15	244.94	253.03	17.04	18.03
323.15	252.73	257.82	17.22	18.21
363.15	261.27	264.36	16.89	18.64

Regarding the impact of the alkyl-chain length of the anion in terms of volume taken by either the IL or the water molecules at infinite dilution, it is clear that water molecules take more space in the case of the [C$_2$MIm][C$_7$H$_{15}$CO$_2$] than in the two other ILs. Furthermore, its volume decreases by decreasing the anion alkyl chain length to become closer to the ideality in the case of the octanoate IL. For instance, at 323.15 K, its volume is close to (9, 14 and 17) cm^3 for [C$_2$MIm][CH$_3$CO$_2$], [C$_2$MIm][C$_3$H$_7$CO$_2$] and [C$_2$MIm][C$_7$H$_{15}$CO$_2$], respectively.

This is due to the fact that the Coulombic forces are higher in the case of the [C$_2$MIm][CH$_3$CO$_2$]; whereas these are much weaker than those expected in the case of the butanoate or octanoate ILs. The intermolecular interactions between the cation and the anion in the pure [C$_2$MIm][C$_7$H$_{15}$CO$_2$] are in fact weaker than those expected in the [C$_2$MIm][CH$_3$CO$_2$] due to a large increase of the van der Waals forces, while such interactions are well balanced in the case of the butanoate sample. This in fact can be associated to the free volume in pure ILs, which tends to increase by increasing the alkyl chain length of the anion, allowing for more spaces and possible arrangements of water molecules in solution, increasing then number of possible microstates, as expected from entropy data reported above. In

other words, the probability to find similar water-IL complexes in solution decreases by increasing the alkyl chain-length of the alkyl-carboxylate-based ILs. This behaviour could be related to the fact that water molecules will be more strongly localised in the 3D space in the case of the octanoate solution through the formation of emulsion like state increasing in fact the overall entropy of the system.

3.4 Effect of water on transport properties of $[C_2MIm][C_nH_nCO_2]$

This section is devoted on the transport properties for the three pure ILs and their binary mixtures with water. The aim of this study is to probe the impact of water addition into these ILs by looking at transport behaviours of their mixtures to extract additional information on their interactions in solution, which may be associated to volumetric data to finally determine their ionicity. For a better clarity this section was divided in two parts. The first part presents the viscosity data for all compositions as a function of the temperature to gain understanding on interactions in solution through the calculation of the viscosity deviation, as well as, the excess Gibbs energy. The second part describes the conductivity data at 298.15 K as a function of the composition measured for the three binary mixtures, as well as, the ionicity of each electrolytic solution.

3.4.1 Viscosity measurements, η, of the $([C_2MIm][C_nH_nCO_2]$ + water) binary mixture as a function of temperature and composition

Generally, most of ILs have been found to be more viscous than traditional organic solvents and water and those ones can be called Newtonian fluids.[128,129] Therefore, from a practical point of view, it is necessary to study the viscosities of a these new materials as well as, their mixture with a co-solvent to decrease the overall viscosity of the solution. In this study it is in fact important to compare the viscosities of the three pure $[C_2MIm][C_nH_nCO_2]$ ILs and their mixture with water to be then able to select the composition which will have the strongest molecular interactions and therefore a better aggregation behaviour to eventually lead to a better uniformed metal oxide nanoparticles in solution (see Chapter 5).

The viscosity of the pure ILs and their mixtures with pure water was investigated from (293.15 to 363.15) K over the whole composition range as shown in the Table 3-7.

Table 3-7. Viscosity, η (/mPa·s), data of ([C₂MIm][CₙHₙCO₂] + H₂O) binary mixtures as a function of [C₂MIm][CₙHₙCO₂] mole fraction, χ_{IL}, for a temperature range from (293.15 to 363.15) K at 0.1 MPa.

T/K	293.15	298.15	303.15	323.15	328.15	333.15	343.15	348.15	353.15	363.15
χ_{IL}				For ([C₂MIm][CH₃CO₂] + H₂O)						
0.00	1.00	0.89	0.80	0.55	0.51	0.47	0.40	0.41	0.36	0.32
0.05	4.49	3.84	3.34	2.16	1.98	1.83	1.59	1.40	1.33	1.26
0.20	36.26	27.75	21.84	10.29	8.86	7.72	6.04	4.89	4.45	4.07
0.35	55.78	41.56	31.92	13.94	11.83	10.17	7.77	6.15	5.54	4.07
0.49	64.30	47.80	36.49	15.21	12.72	10.77	7.98	6.14	5.45	4.87
0.64	72.36	54.24	41.74	17.91	15.08	12.85	9.64	7.49	6.68	6.00
0.77	180.50	129.38	95.53	35.73	29.22	24.24	17.31	12.88	11.26	9.92
0.90	188.85	136.73	101.89	39.26	32.31	26.95	19.44	16.77	14.60	11.34
1.00	198.89	141.84	103.79	36.57	29.37	23.91	16.43	11.77	10.09	8.73
χ_{IL}				For ([C₂MIm][C₃H₇CO₂] + H₂O)						
0.00	1.00	0.89	0.80	0.55	0.51	0.47	0.40	0.41	0.36	0.32
0.05	5.66	4.05	3.57	3.06	3.01	2.98	2.93	2.89	2.88	2.86
0.20	26.75	20.75	16.51	8.00	6.92	6.05	4.77	3.88	3.53	3.23
0.36	62.00	52.81	39.96	16.52	13.85	11.77	8.79	6.83	6.10	5.48
0.50	111.70	87.05	65.89	26.38	21.83	18.29	13.27	10.00	8.79	7.78
0.65	151.00	121.75	90.15	33.77	27.59	22.85	16.26	12.05	10.51	9.24
0.80	214.90	167.40	122.86	43.63	35.09	28.60	19.69	14.12	12.11	10.48
0.89	285.22	218.04	168.17	64.49	51.68	41.69	27.65	18.77	15.59	13.02
1.00	386.19	290.68	220.85	80.12	63.40	50.52	32.72	21.72	17.85	14.74
χ_{IL}				For ([C₂MIm][C₇H₁₅CO₂] + H₂O)						
0.00	12.93	10.62	8.81	6.23	4.55	3.42	2.63	2.07	1.66	1.35
0.20	95.98	71.07	53.76	32.50	20.91	14.16	10.01	7.34	5.55	4.31
0.35	194.76	140.92	104.42	60.99	38.17	25.28	17.54	12.66	9.45	7.26
0.50	327.98	237.58	175.59	101.14	61.93	39.92	26.88	18.79	13.57	10.08
0.54	416.50	300.09	220.78	76.95	61.31	49.44	33.23	23.21	19.64	16.75
0.62	490.88	362.84	270.89	92.12	71.81	56.40	35.53	22.97	18.64	15.22
0.77	700.82	486.57	346.53	109.76	85.94	68.24	44.69	30.57	25.66	21.71
0.91	711.60	529.76	398.25	138.93	108.93	86.04	54.79	44.16	35.80	23.94

*The viscosity values of the pure water were taken from the literature.[106,107]

3.4.1.1 Scientific approach

For several fluids, experimental viscosity values can be, normally, adjusted using the conventional Arrhenius equation (eq. 24). However, it appears that the temperature dependence of ILs on the viscosity exhibits generally a non-

Arrhenius behaviour, which could then be correctly fitted by using the Vogel-Tamman-Fulcher (VTF) equation (Eq. 25). In fact, the experimental viscosities were fitted using the conventional Arrhenius and VTF equations, where then both calculated values were compared with the experimental values using two different Deviation statistics' law: the Average Absolute Relative Deviation (AARD%)(Eq. 26) and the Root-Mean-Square-Deviation (RMSD%)(Eq. 27).

The experimental data were fitted in the aim to reduce the AARD% or RMSD%, and have shown that AARD% methods is the appropriate one to use since measured viscosity values are generally larger than 1 mPa.s. After changing both equations into the Napierian logarithm (ln) as shown in the equations below, it is possible to find the unknown parameters ηo, Ea/R and Bn by using the Linest function in Excel and then the Solver function to find the value of T_0. The Solver function has to be first installed on the Excel software (easy process).

(Eq. 24)

- Arrhenius equation*: $\quad \eta = \eta o \times e^{\left(\frac{Ea}{R} \times \frac{1}{To}\right)}$,

$$Transformed\ into\ logarithm\ function \quad \ln(\eta) = \ln(\eta o) + \frac{Ea}{R} \times \frac{1}{To}$$

(Eq. 25)

- VTF equation*: $\quad \eta = \eta o \times e^{\left(\frac{Bn}{T-To}\right)}$,

$$Transformed\ into\ Logarithm\ function \quad \ln(\eta) = \ln(\eta o) + \frac{Bn}{T-To}$$

*Where 1/To and 1/(T-T0) are the *x* variable.

To use the Linest function, at least six excel cells (2 columns, 3 rows) have to be selected before writing the Linest function in the top insert function cell. Two variables would then be selected with the Linest function; η_{exp} , $1/T_0$, for Arrhenius and $1/(T-T_0)$ for VTF equation. For instance, the Linest Arrhenius function would be wrote in this manner: [Linest(J3:J18,K3:K18,,1)], where [J3:J18] are the cells representing $\ln(\eta_{exp})$, (K3:K18) representing (1/T) values, and 1 is the true Boolean function. The results will appear by pressing [ctrl+shift+enter] instead of simply press [Enter] ([F2] is used to change the variables within the Linest function when needed). The first cell in the first

column is in fact ln(ηo) and therefore ηo can be calculated from the exponential function : exp(ln(ηo))= ηo. The first cell of the second column gives the constant [E_a/R] for Arrhenius and B_n for the VTF equation. Then the viscosity can be calculated theoretically by using those new variables into the equation listed above.

The calculated viscosities can then be compared with the experimental viscosities *via* deviation statistic rules. Indeed, deviation being a measure of the difference between the experimental and calculated values, there are several ways to calculate the deviation of a set of measurements.

The chosen deviation law would be the one with a percentage closest to 0% that would be ran using the Solver function. The RMSD% (Root-mean-square-deviation) and the AARD% (Average-absolute-relative-deviation) have been investigated here in order to determine which of the conventional equation should be the most accurate regarding the fit of the experimental data.

The RMSD% and the AARD% are calculated by the used of two different equations that would fit better for either bigger or smaller values. Therefore, it is essential to check which of those two deviation equations are fitting the best the results. There are lots of statistic laws other than those two, however, in physical chemistry, most of the papers are published using one of those two conventional statistic laws.[130,131]

In more detail, the RMSD% and the AARD% represent the sample standard deviation of the different predicted and observed values, allowing aggregating the magnitude of the errors of all the predicted values compared to the observed values into a single predictive value in percentage. It is known as a good measure of accuracy for a specific variable (but not between variable as it is scale-dependant).

- The Average Absolute Relative Deviation in percentage (AARD%):

(Eq. 26)

$$AARD\% = \frac{100}{N}\left(\sum_{i=0}^{n}\frac{|x'_i - x_i|}{x_i}\right),$$

- The Root-Mean-Square-Deviation in percentage (RMSD%):

(Eq. 27)

$$RMSD\ \% = 100\sqrt{\frac{\sum_{i=1}^{N}(x_i - x'_i)^2}{N-2}},$$

where x_i represents the experimental values and x'_i represents the calculated values

To finish, the solver function is used to make the two final values AARD% and the RMSD% closer as possible to zero%. Solver function is going to try all the possibilities to reduce those two values by minimalizing the T_o values for both equations. T_o being linked to two other variables η_o, Ea/R for the Arrhenius function and η_o, Bn for the VTF function (variables calculated by the Linest function). From this method, the best calculated viscosity parameters would be chosen allowing the best fitting of the experimental viscosity values.

3.4.1.2 *Comparison of viscosity data with the literature of dried [C₂MIm][CH₃CO₂]*

A deviation graph (δ) is presented in Figure 3-19 to present the standard deviation between the viscosity data reported during this work ($\eta^{Cal.}$) (See Table 3-1) with those from the literature ($\eta^{lit.}$) as a function of the temperature, by using the following equation:

(Eq. 28)

$$\delta = 100\ \frac{\eta^{lit.} - \eta^{cal.}}{\eta^{cal.}},$$
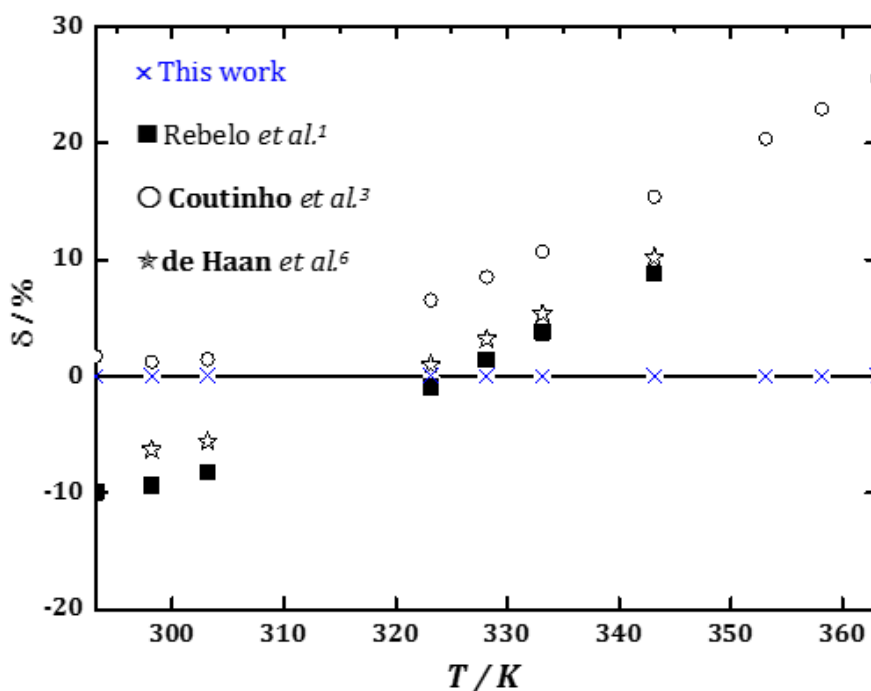
Figure 3-19. Comparison of the experimental viscosity data of the $[C_2MIm][CH_3CO_2]$ from this work with those from the literature as a function of temperature at 0.1MPa. [107,108,110]

In Figure 3-19, data from Bai *et al.*[111] were not taken into account since the standard deviation from their viscosity data with those presented herein (or from other datasets from the literature) was very large (*i.e.* from -50 % to 180 %) which seems completely out of the normal range expected normally for other ILs. Indeed, it has been reported that deviation can be up to 20% therefore all data are in this range and can be considered.[115]

3.4.1.3 *Viscosity of the pure ILs in function of the temperature*

The Figure 3-20 shows the viscosity data of the pure $[C_2MIm][CH_3CO_2]$, $[C_2MIm][C_3H_7CO_2]$, $[C_2MIm][C_7H_{15}CO_2]$ as a function of the temperature from (293.15 to 363.15) K. As expected, the viscosity decreases exponentially with the temperature. For example, the viscosity of the pure $[C_2MIm][CH_3CO_2]$ is decreasing from (198.89 to 8.73) mPa·s from (293.15 to 363.15) K.

However, the viscosity values increase significantly by increasing the number of carbon on the alkyl chain length of the anion. For instance, at 293.15 K, the viscosity of the pure $[C_2MIm][CH_3CO_2]$, $[C_2MIm][C_3H_7CO_2]$ and $[C_2MIm][C_7H_{15}CO_2]$ are (198.9, 386.2 and 711.6) mPa·s, respectively. This is in

agreement with the respective molecular weight of the ILs reported in Table 3-3, since heavier is the molecule, viscous it should be.
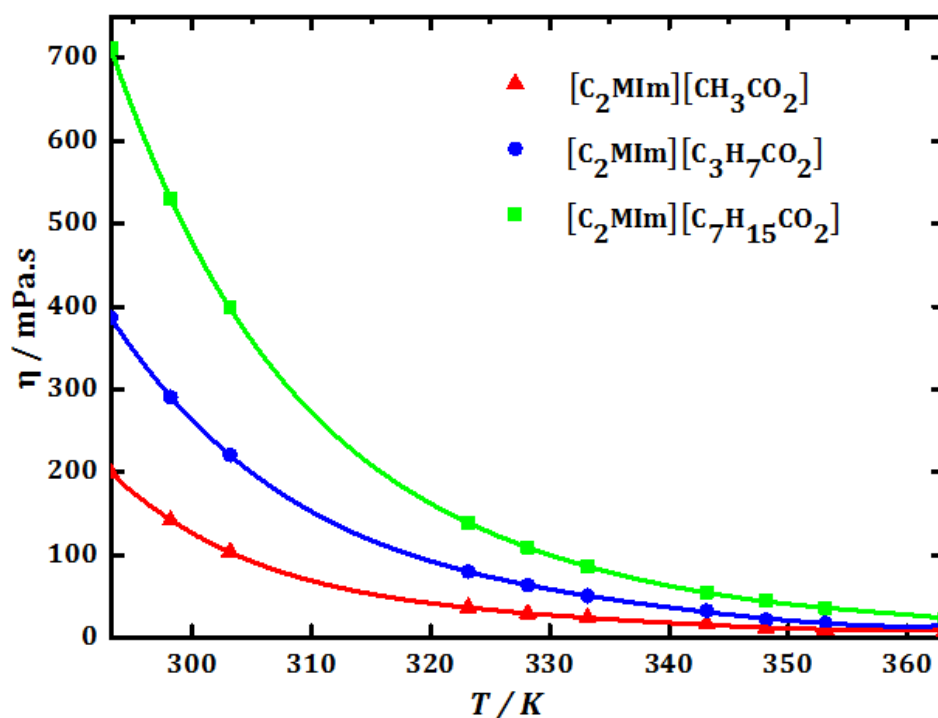
Figure 3-20. Viscosity data, η, of the pure ILs as a function of the temperature from (293.15 to 363.15) K for χ_{IL}: ▲, [C₂MIm][CH₃CO₂]; ●, [C₂MIm][C₃H₇CO₂]; ■, [C₂MIm][C₇H₁₅CO₂] at 0.1MPa.

3.4.1.4 *Viscosity of the binary mixture as a function of the temperature*

It is also interesting to study the IL behaviour in term of viscosity when adding pure water to those pure ILs. The Figure 3-21, Figure 3-22 and Figure 3-23 show the viscosity of the selected binary mixtures as a function of the temperature at different compositions ranging from 0 to 1 in IL mole fraction units. At any composition, all solutions show a decrease in viscosity data with the temperature. Also, by increasing the water concentration in the solution, an automatically decrease on its viscosity is observed. This is an expected result since water viscosity values are lower than 1 mPa·s over the whole temperature range covered during this work.[106,107]

In the case of the [C₂MIm][CH₃CO₂], a dramatic drop of the viscosity values is observed between x_{IL} = 0.64 and 0.77. Those results are showing that the presence of water below χ_{IL} < 0.77 in this specific IL decreases considerably the viscosity of the solution. This could indicate a strong dissociation between the

cation and the anion at those specific compositions due to the increase in the water concentration, or due to a stronger hydrogen bonding network formation between water and the IL-anion. However, the viscosity of the two other IL-based solutions is decreasing much more regularly with no dramatic viscosity gap between each composition.
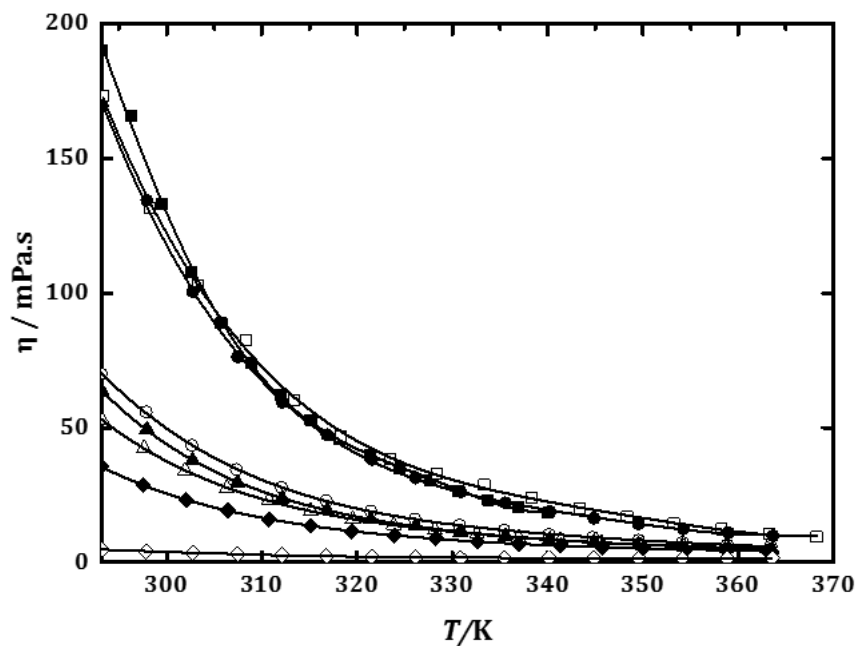
Figure 3-21. Viscosity data, η, of the ([C$_2$MIm][CH$_3$CO$_2$] + H$_2$O) binary mixture as a function of the temperature from (293.15 to 363.15) K and 0.1MPa at χ_{IL} =: ■, 1.00; □, 0.90; ●, 0.77; ○, 0.64; ▲, 0.49; △, 0.35; ◆, 0.20; ◇, 0.05. The lines represent the VTF fitting of the experimental data with parameters reported in Appendix H.
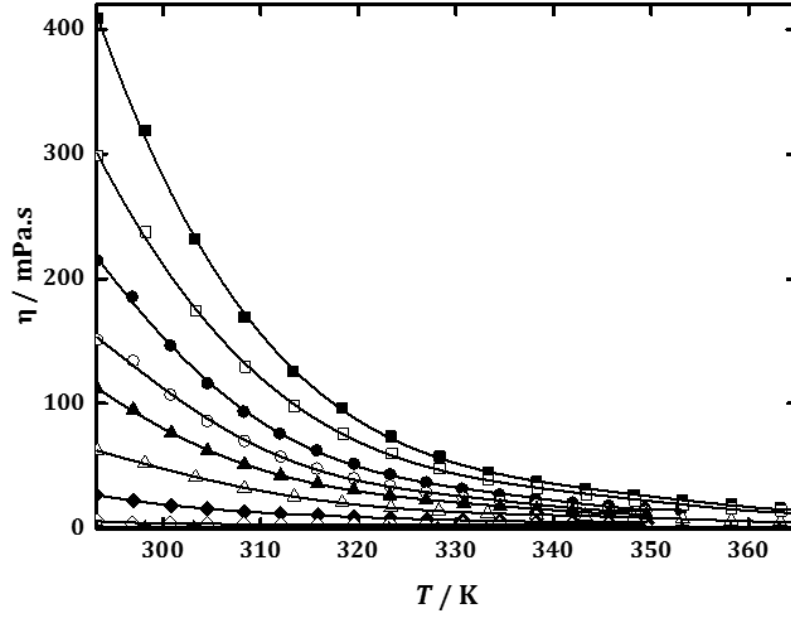
Figure 3-22. Viscosity data, ɳ, of the ([C₂MIm][C₃H₇CO₂] + H₂O) binary mixture as a function of the temperature from (293.15 to 363.15) K and 0.1MPa at χ_{IL} =: ■, 1.00; □, 0.88; ●, 0.80; ○, 0.65; ▲, 0.50; △, 0.36; ◆, 0.20; ◇, 0.05; ★, 0. The lines represent the polynomial fitting of the experimental data with parameters reported in Appendice.
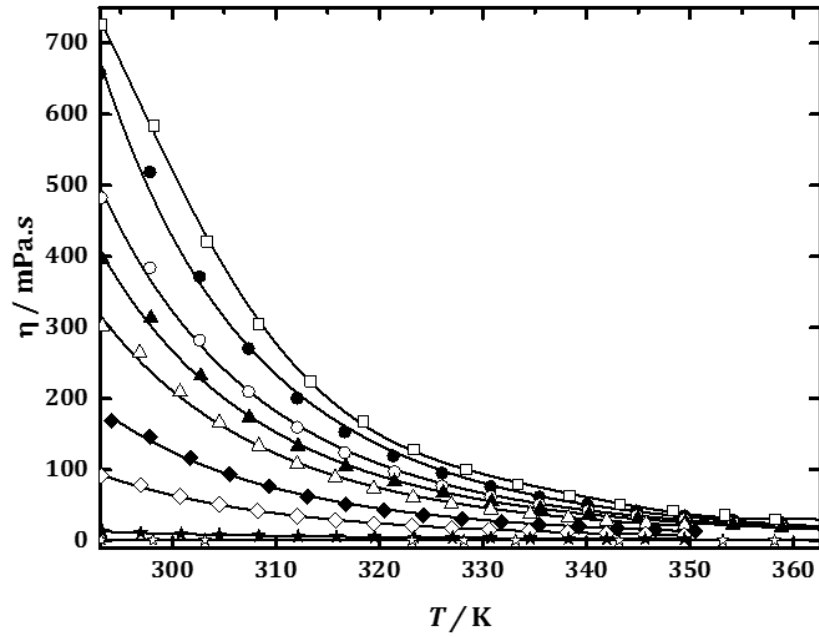
Figure 3-23. Viscosity data, ɳ, of the ([C₂MIm][C₇H₁₅CO₂] + H₂O) binary mixture as a function of the temperature from (293.15 to 363.15) K and 0.1MPa at χ_{IL} =: ■, 1.00; □, 0.91; ●, 0.77; ○, 0.62; ▲, 0.54; △, 0.50; ◆, 0.35; ◇, 0.20; ★, 0.05; ⋆, 0.00. The lines represent the VTF fitting of the experimental data with parameters reported in Appendice.

3.4.1.5 Viscosity of the binary mixture as a function of the composition

The change on the viscosity when adding pure water to those pure ILs has also been drawn as a function of the composition for different temperatures. Figure 3-24, Figure 3-25 and Figure 3-26 show such behaviour as a function of the IL mole fraction, χ_{IL}, at (293.15, 298.15, 303.15, 323.15, 328.15, 333.15, 343.15, 348.15, 353.15 and 363.15) K.
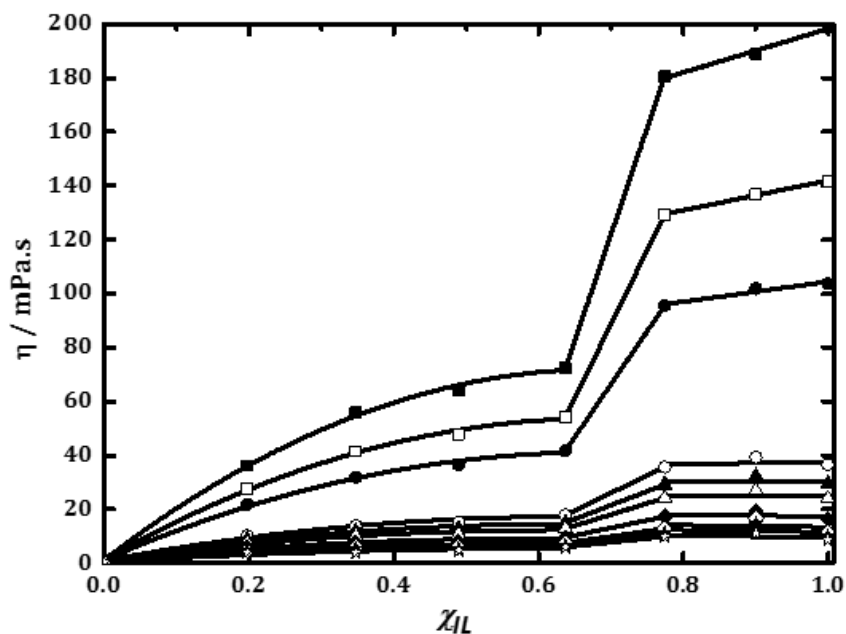
Figure 3-24. Viscosity data, η, of the ([C$_2$MIm][CH$_3$CO$_2$] + H$_2$O) binary mixture as a function of the [C$_2$MIm][CH$_3$CO$_2$] mole fraction, χ_{IL} at: ■, 293.15 K; □, 298.15 K; ●, 303.15 K; ○, 323.15 K; ▲, 328.15 K; △, 333.15 K; ◆, 343.15 K; ◇, 348.15 K; ★, 353.15 K; ✶, 363.15 K at 0.1MPa. The lines represent the polynomial fitting of the experimental data with parameters reported in. Appendix H.
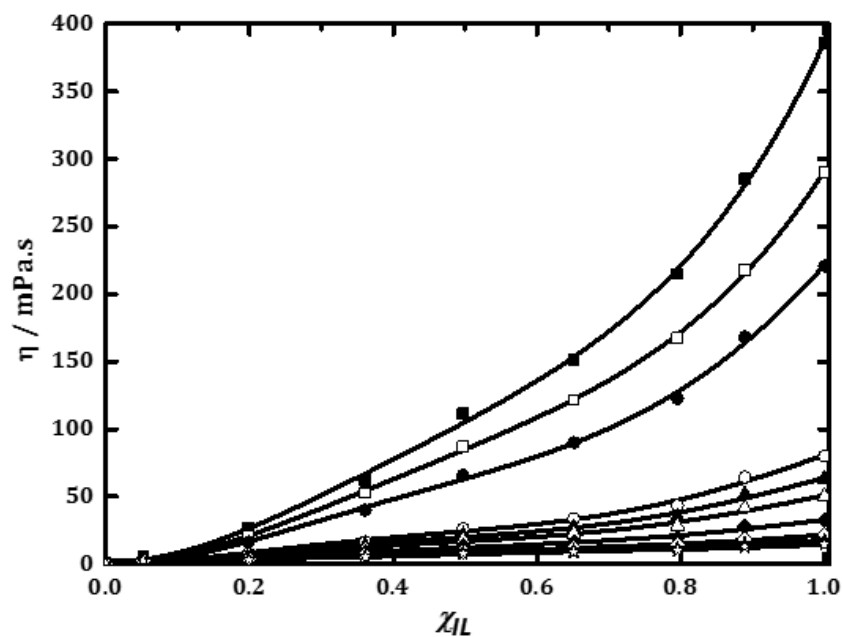
Figure 3-25. Viscosity data, η, of the ([C₂MIm][C₃H₇CO₂] + H₂O) binary mixture as a function of the [C₂MIm][C₃H₇CO₂] mole fraction, χ_{IL} at: ■, 293.15 K; □, 298.15 K; ●, 303.15 K; ○, 323.15 K; ▲, 328.15 K; △, 333.15 K; ◆, 343.15 K; ◇, 348.15 K; ★, 353.15 K; ✶363.15 K at 0.1MPa. The lines represent the polynomial fitting of the experimental data with parameters reported in Appendix H.
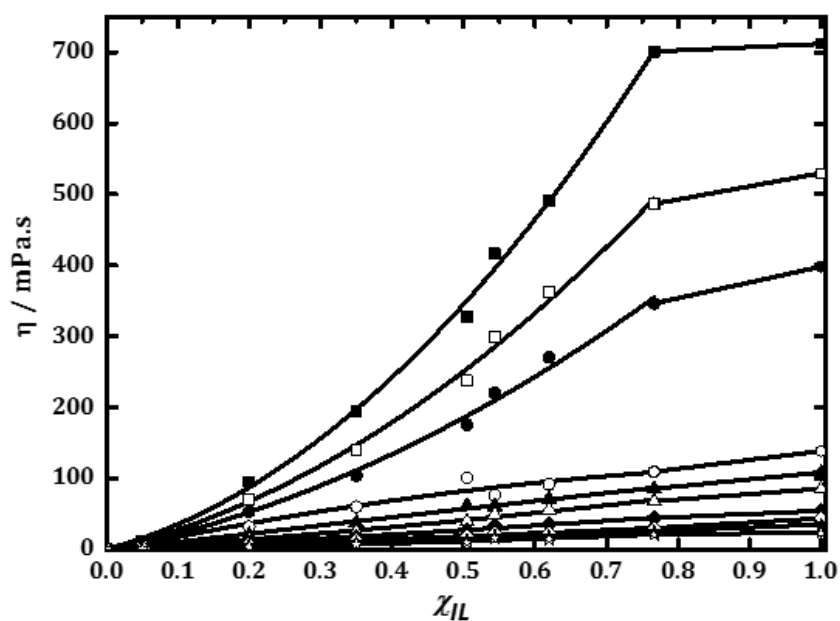
Figure 3-26. Viscosity data, η, of the ([C₂MIm][C₇H₁₅CO₂] + H₂O) binary mixture as a function of the [C₂MIm][C₇H₁₅CO₂] mole fraction, χ_{IL} at: ■, 293.15 K; □, 298.15 K; ●, 303.15 K; ○, 323.15 K; ▲, 328.15 K; △, 333.15 K; ◆, 343.15 K; ◇, 348.15 K; ★, 353.15 K; ✶363.15 K at 0.1MPa. The lines represent the polynomial fitting of the experimental data with parameters reported in Appendix H.

Again, a dramatic drop of the viscosity is obtained in the case of the [C$_2$MIm][CH$_3$CO$_2$] solutions between 0.64 and 0.77 in IL mole fraction. In fact, it is known that ILs and particularly the pure [C$_2$MIm][CH$_3$CO$_2$] has very strong Coulombic interactions between the cation and the anion.[23] The acetate anion is small and polar and has been proven to form hydrogen bonds with its 1-ethyl-3-methylimidazolium cation.

According to Brehm *et al*, there are formation of carbenes and acetic acid in the pure [C$_2$MIm][CH$_3$CO$_2$] which is caused by the strong hydrogen bonding abilities of the acetate anion to abstract a hydrogen atom of the cation to reform the acetic acid.[23] However, when adding pure water to the pure IL, there would be a new hydrogen-bonding network formed, specifically between the oxygen atoms from the carboxylate anion and the hydrogen from the water molecules. This will prevent the formation of carbene, and will lead to weakening the Coulomb interactions between these ions and thus decrease the viscosity of the solution.[23]

However, the formation of acetic acid from the reaction between the water and the anion to form hydroxide anion and the carboxylic acid is inherent and this may increase while increasing the water concentration, especially below χ_{IL} = 0.77, as it is observed here.

However, the Coulombic interactions are stronger in the case of the [C$_2$MIm][CH$_3$CO$_2$] compared to the two other ILs. Indeed, both cation and anion are closer to each other due to the very short alkyl chain on the anion. This is why viscosity will tend to decrease more regularly for the two other ILs while increasing the water concentration instead of dropping suddenly, perhaps due to a lower probability to have a reaction between larger carboxylate and water.

Although, there is an exothermic reaction observed for the three mixtures since it was possible to feel heat after mixing water to it; the formation of butanoic and octanoic acid does not seem to affect the respective solutions as much as for the [C$_2$MIm][CH$_3$CO$_2$] mixture. Unfortunately, this information has not been studied in this work and only assumptions can be made. For instance, it could be due to a pH difference that could lead more easily to the formation of acids.

3.4.1.6 Viscosity deviations from ideality, Δη, of the binary mixture as a function of the composition

To go further, the viscosity deviation from ideality, $\Delta\eta$, was then calculated according to the following equation:

(Eq. 29)

$$\Delta\eta = \eta + (\chi_{IL}\eta_{IL} + \chi_{water}\eta_{water}),$$

Where$\Delta\eta$, represents the viscosity deviation, χ_{IL} and χ_{water} the mole fraction of the respective IL and water solutions, η_{IL} and η_{water} the viscosity of the pure respective components.

Only one graph from the calculated values is shown in this part since the graphs are not the main focus to understand the meaning of those values. In fact, the table below shows $\Delta\eta$ as a function of the IL mole fraction composition and the temperature from (293.15 to 363.15) K.

Table 3-8. Viscosity deviations from the ideality, Δη (/mPa.s) of ([C$_2$MIm][C$_n$H$_n$CO$_2$] + H$_2$O) binary mixture as a function of [C$_2$MIM][C$_n$H$_n$CO$_2$] mole fraction, χ_{IL}, for a temperature range from (293.15 to 363.15) K at 0.1 MPa.

T/K	293.15	298.15	303.15	323.15	328.15	333.15	343.15	348.15	353.15	363.15
χ_{IL}				For ([C$_2$MIm][CH$_3$CO$_2$] + H$_2$O)						
0.00	0	0	0	0	0	0	0	0	0	0
0.05	-6.41	-4.10	-2.60	-0.19	0.03	0.19	0.38	0.42	0.49	0.52
0.20	-3.82	-0.98	0.70	2.63	2.65	2.62	2.47	2.24	2.17	2.09
0.35	-14.01	-8.33	-4.68	0.88	1.29	1.55	1.79	1.80	1.80	0.83
0.49	-33.53	-22.06	-14.70	-2.96	-1.91	-1.17	-0.26	0.17	0.33	0.44
0.64	-54.70	-36.44	-24.67	-5.58	-3.82	-2.55	-0.98	-0.15	0.12	0.33
0.77	26.34	19.39	15.02	7.30	6.38	5.63	4.50	3.68	3.37	3.10
0.90	9.75	8.99	8.40	6.30	5.82	5.38	4.61	6.14	5.48	3.45
1.00	0	0	0	0	0	0	0	0	0	0
χ_{IL}				For ([C$_2$MIm][C$_3$H$_7$CO$_2$] + H$_2$O)						
0.00	0	0	0	0	0	0	0	0	0	0
0.05	-15.45	-11.97	-8.72	-1.65	-0.78	-0.11	0.84	1.37	1.60	1.79
0.20	-50.86	-37.78	-28.06	-8.38	-6.10	-4.37	-2.06	-0.77	-0.31	0.05
0.36	-77.98	-52.64	-40.24	-12.74	-9.35	-6.76	-3.27	-1.26	-0.57	-0.04
0.50	-80.78	-57.90	-44.30	-13.72	-9.94	-7.06	-3.19	-1.00	-0.26	0.29
0.65	-100.80	-67.82	-53.92	-18.59	-13.87	-10.20	-5.18	-2.24	-1.24	-0.48
0.80	-92.52	-64.02	-52.99	-20.22	-15.44	-11.68	-6.42	-3.24	-2.16	-1.32
0.89	-58.29	-40.53	-28.30	-6.82	-4.75	-3.28	-1.48	-0.59	-0.32	-0.13
1.00	0	0	0	0	0	0	0	0	0	0
χ_{IL}				For ([C$_2$MIm][C$_7$H$_{15}$CO$_2$] + H$_2$O)						
0.00	0	0	0	0	0	0	0	0	0	0
0.05	-23.60	-16.71	-11.86	-1.24	-1.38	-1.33	-0.49	-0.53	-0.47	-0.15
0.20	-46.92	-35.43	-26.41	4.32	-1.25	-3.39	-1.25	-1.81	-1.88	-0.73
0.35	-54.89	-45.03	-35.44	12.02	-0.28	-5.13	-1.89	-3.05	-3.31	-1.33
0.50	-31.73	-30.28	-25.84	30.74	6.68	-3.75	-0.98	-3.70	-4.67	-2.16
0.54	29.36	11.81	4.01	1.21	1.88	2.47	3.27	-0.97	0.03	3.60
0.62	49.73	34.37	23.91	5.86	4.14	2.93	1.43	-4.53	-3.67	0.27
0.77	155.14	80.29	41.09	3.15	2.32	2.18	2.59	-3.37	-1.87	3.29
1.00	0	0	0	0	0	0	0	0	0	0

In the case of the [C$_2$MIm][C$_3$H$_7$CO$_2$], all $\Delta\eta$ values are negative at all temperature studied, over the entire composition range. Furthermore, $\Delta\eta$ values increase by decreasing the temperature, and become almost ideal for temperature superior to 348.15 K. $\Delta\eta$ maxima are found at all temperature around χ_{IL} = 0.7. According to Eyring and Pires,[118,132] a negative viscosity deviation is characteristic of mixtures having no strong ionic specific interactions as could be expected idealy and in this case could be attributed to the strong dissociation of the *cation-anion* through new hydrogen bonds environment caused by the insertion of water in solution.
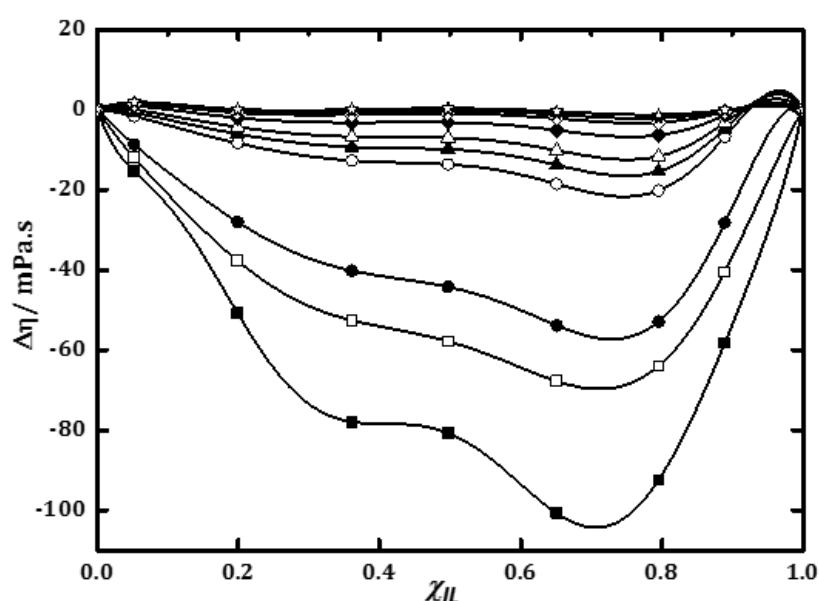
Figure 3-27. Viscosity deviations, $\Delta\eta$, of the ideality of the ([C$_2$MIm][C$_3$H$_7$CO$_2$] + H$_2$O) binary mixture as a function of the [C$_2$MIm][C$_3$H$_7$CO$_2$] mole fraction χ_{IL}, at: ■, 293.15 K; □, 298.15 K; ●, 303.15 K; ○, 323.15 K; ▲, 328.15 K; △, 333.15 K; ◆, 343.15 K; ◇, 348.15 K; ★, 353.15 K; ✳, 363.15 K at 0.1MPa. The lines represent the Redlich-Kister-type fittings with the parameters reported in Table 21.

However, [C$_2$MIm][CH$_3$CO$_2$] and [C$_2$MIm][C$_7$H$_{15}$CO$_2$] solutions behave differently. Indeed, [C$_2$MIm][CH$_3$CO$_2$] seems to have an ideal behaviour with a $\Delta\eta{\sim}0$ for temperatures higher than 323 K, as similarly observed in the case of the solutions containing the [C$_2$MIm][C$_7$H$_{15}$CO$_2$] for temperatures higher than 348 K. Then, the [C$_2$MIm][CH$_3$CO$_2$] solution has a similar behaviour than that observed with the [C$_2$MIm][C$_3$H$_7$CO$_2$] where $\Delta\eta < 0$ only from composition from 0 to 0.64 in IL mole fraction units for temperature below 323 K; whereas the [C$_2$MIm][C$_7$H$_{15}$CO$_2$] mixture has negative values from 0 to 0.5 in IL mole fraction for temperature

below 343 K. Furthermore, positive values are also found from composition χ_{IL} (0.77 to 1) and χ_{IL} (0.54 to 1) at the same temperatures for $[C_2MIm][CH_3CO_2]$ and $[C_2MIm][C_7H_{15}CO_2]$, respectively. A summary of those results is displayed in the Table 3-9.

Table 3-9. Viscosity deviation from ideality, $\Delta\eta$ (/mPa.s), behaviour of the acetate and $[C_2MIm][C_7H_{15}CO_2]$.

$\Delta\eta$	$[C_2MIm][CH_3CO_2]$		$[C_2MIm][C_7H_{15}CO_2]$	
$\Delta\eta \sim 0$	$\chi_{IL} = 0$ to 1	$T(K) \geq 323$ K	$\chi_{IL} = 0$ to 1	$T(K) \geq 348$ K
$\Delta\eta < 0$	$\chi_{IL} = 0$ to 0.64	$T(K) < 323$ K	$\chi_{IL} = 0$ to 0.50	$T(K) < 343$ K
$\Delta\eta > 0$	$\chi_{IL} = 0.77$ to 1	$T(K) < 323$ K	$\chi_{IL} = 0.54$ to 1	$T(K) < 343$ K

Those results clearly correlate with the viscosity behaviour discussed previously. There are strong specific interactions above 0.77 in IL mole fraction for the $[C_2MIm][CH_3CO_2]$ and above 0.54 in IL mole fraction in the case of the $[C_2MIm][C_7H_{15}CO_2]$; whereas weaker specific interactions are found for x_{IL} below 0.64 and 0.50 for $[C_2MIm][CH_3CO_2]$ and $[C_2MIm][C_7H_{15}CO_2]$, respectively. In fact, in both cases, water is intensively present in solutions and the hydrogen bonds between the ions and water increase.

However, according to Brehm *et al.*,[23] the acetate anion forms stronger hydrogen bonds with the imidazolium cation than with water and this could be why there is such a difference of viscosity deviation from this specific solution as the cation-anion interactions must decrease by increasing the alkyl chain length on the anion.

In fact, even there are more hydrogen bonds formed while the water concentration increases, this would still be present as weaker sign than the strong *cation-anion* hydrogen bonds that explained this sudden change of viscosity deviation sign observed in the case of the acetate mixture. While in the case of the octanoate solutions, changes of the sign could be attributed to the entropy results as such solution seems to be driven by the formation of emulsion.

3.4.1.7 Excess Gibbs energy

On the basis of the theory of absolute reaction rates,[118,133,134] the excess Gibbs energy, ΔG^{E*}, of activation of viscous flow were calculated by using the following equation:

(Eq. 30)

$$\frac{\Delta G^{E*}}{RT} = \left[\ln\left(\frac{\eta V_m}{\eta_2 V_{m,2}}\right) - \chi_1 \ln\left(\frac{\eta_1 V_{m,1}}{\eta_2 V_{m,2}}\right) \right],$$

Where V_m, $V_{m,1}$ and $V_{m,2}$ are the molar volumes of the binary mixture and of the pure components 1 (IL) and 2 (water), respectively.

The calculated values and fitting parameters of ΔG^{E*} are reported in the appendix K and shaped into graphs in function of the IL composition for the three ILs as seen in Figure 3-28, Figure 3-29 and Figure 3-30.
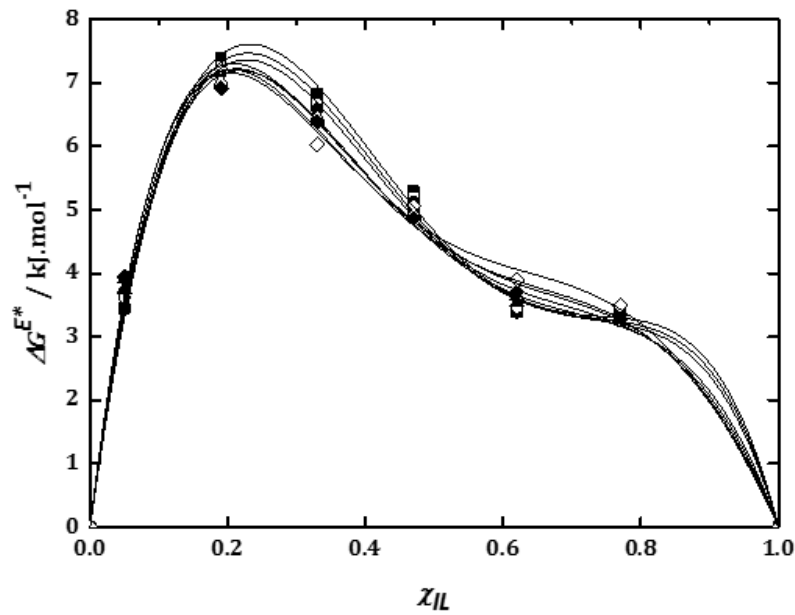
Figure 3-28. Excess Gibbs energy of activation of viscous flow, ΔG^{E*}, for ($[C_2MIm][CH_3CO_2] + H_2O$) as a function of IL mole fraction, χ_{IL}, at: ■, 293.15 K; □, 298.15 K; ●, 303.15 K; ○, 323.15 K; ▲, 333.15 K; △, 343.15 K; ◆, 353.15 K; ◇, 363.15 K; at 0.1MPa.
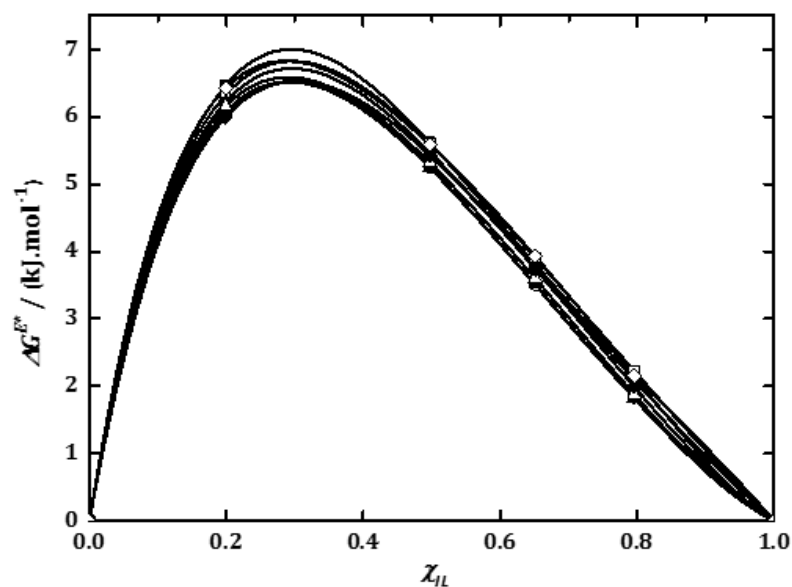
Figure 3-29. Excess Gibbs energy of activation of viscous flow, ΔG^{E*}, for ([C$_2$MIm][C$_3$H$_7$CO$_2$] + H$_2$O) as a function of IL mole fraction, χ_{IL}, at:■, 293.15 K; □, 298.15 K; ●, 303.15 K; ○, 323.15 K; ▲, 333.15 K; △, 343.15 K; ◆, 353.15 K; ◇, 363.15 K; at 0.1MPa.
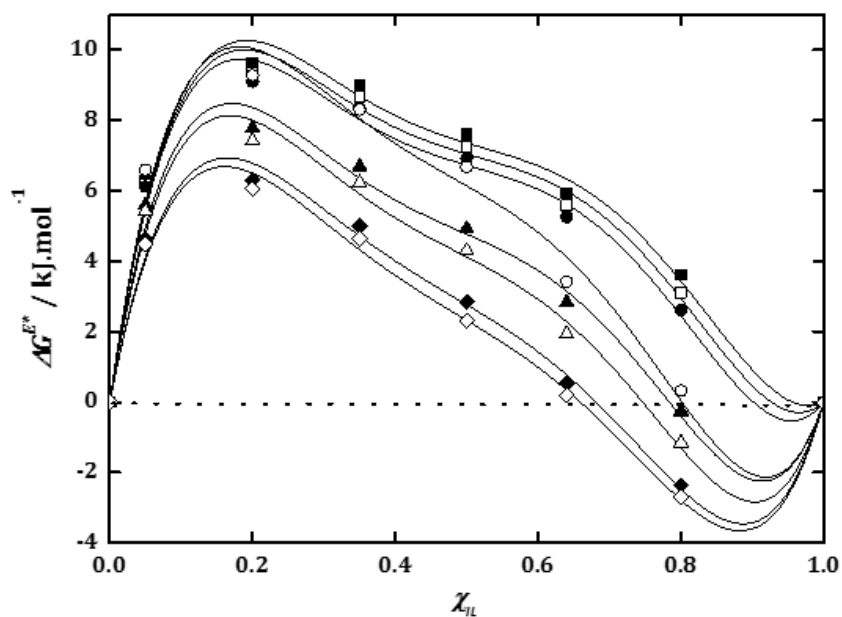
Figure 3-30. Excess Gibbs energy of activation of viscous flow, ΔG^{E*}, for ([C$_2$MIm][C$_7$H$_{15}$CO$_2$] + H$_2$O) as a function of IL mole fraction, χ_{IL}, at: ■, 293.15 K; □, 298.15 K;●, 303.15 K; ○, 323.15 K; ▲, 333.15 K; △, 343.15 K; ◆, 353.15 K; ◇, 363.15 K; at 0.1MPa. The lines represent the Redlich-Kister-type fittings with the parameters reported in Appendix K.

The data show positive values of ΔG^{E*} for the three ILs over the whole composition, except in the case of the octanoate samples at temperatures higher than 323 K and compositions in IL higher than 0.8 in mole fraction units. In fact, ΔG^{E*} data decrease while the temperature increases in the case of the

[C$_2$MIm][C$_7$H$_{15}$CO$_2$]; although the temperature does not seem to affect strongly either [C$_2$MIm][CH$_3$CO$_2$] and [C$_2$MIm][C$_3$H$_7$CO$_2$] solutions.

Furthermore, ΔG^{E*} maxima are found around 0.25, 0.35 and 0.2 in IL mole fraction for the respective [C$_2$MIm][CH$_3$CO$_2$], [C$_2$MIm][C$_3$H$_7$CO$_2$] and [C$_2$MIm][C$_7$H$_{15}$CO$_2$] solutions. According to Kapadi *et al.*, positive values indicate the specific interaction leading to complex formation through intermolecular hydrogen bonding interaction between unlike molecules (IL + water) compared to like molecules (IL + IL or water + water).[135] while in the case of the octanoate solution at x_{IL} > 0.8, due to the increase of Van der Waals interaction in solution, interactions between alike molecules are more pronounced (see Figure 3-30), this could be related to the possible formation of an emulsion as state previously.

3.4.2 Conductivity measurements of the ([C$_2$MIm][C$_n$H$_n$CO$_2$] + Water) binary mixture as a function of composition

The conductivity of an IL is an important property to be consider for the design of future electrolytes. Generally, the ionic conductivity of ILs is governed by their molecular weight, viscosity, density and ion size.[136]

3.4.2.1 Comparison of conductivity data with the literature of dried [C$_2$MIm][CH$_3$CO$_2$]

Only few conductivity data of the pure [C$_2$MIm][CH$_3$CO$_2$] are available in the literature, to date.[107,110,111] However, no data was found for the [C$_2$MIm][C$_3$H$_7$CO$_2$] nor the [C$_2$MIm][C$_7$H$_{15}$CO$_2$], to date. Herein, the conductivity of [C$_2$MIm][CH$_3$CO$_2$] at 298.15 K was found to be close to 2.77 mS.cm^{-1}.

Such a value matches very well with data reported in the literature, as for example Feng et al.,[111] found a conductivity of 2.54 mS.cm^{-1}, while de Haan et al.,[107] reported a value close to 2.33 mS.cm^{-1} at 298.15 K. All those values are much closed to each other and the difference can be due to the impurities in the IL, or from the uncertainty instruments used.[116,117]

3.4.2.2 Conductivity of the binary mixture in function of the composition

The conductivity of the pure ILs and of ([C$_2$MIm][C$_n$H$_n$CO$_2$] + H$_2$O) mixtures was measured as a function of the composition at 298.15 K. The data are listed in the Table 3-10 below and are displayed in the following figure:
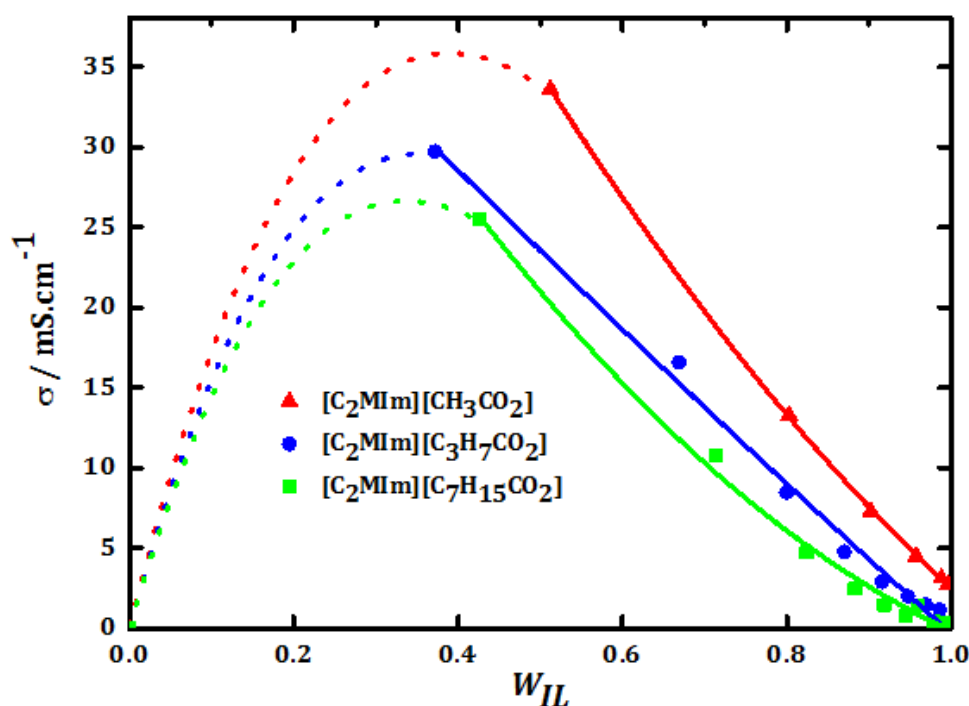
Figure 3-31. Conductivity, σ, data at 298.15 K of ([C$_2$MIm][C$_n$H$_n$CO$_2$] + H$_2$O) binary mixture as a function of [C$_2$mim][C$_n$H$_n$CO$_2$] mass fraction composition, W_{IL}, for: ▲, ([C$_2$MIm] [CH$_3$CO$_2$] + H$_2$O); ●, ([C$_2$MIm] [C$_3$H$_7$CO$_2$] + H$_2$O); ■, ([C$_2$MIm] [C$_7$H$_{15}$CO$_2$] + H$_2$O) at 0.1MPa. The dashed lines represent an extrapolation of the straight lines fits via a polynomial function.

No experimental data has been measured below 0.4-0.5 in IL mass fraction, because all compositions were made in regards to the IL mole fraction, and then, while transferring the composition into mass ratios, it has shown a lack of information below 0.4 IL mass fraction. Therefore, the data were extrapolated until 0 (dashed lines on the graph) using a polynomial function; whereas the experimental data were directly fitted (solid lines) using another polynomial function.

In Figure 3-31, the conductivity of ILs solutions shows a decrease when increasing the alkyl-chain length on the anion. In fact, the pure IL shows a conductivity of (2.77, 1.19, 0.32) mS·cm^{-1} for the pure [C$_2$MIm][CH$_3$CO$_2$], [C$_2$MIm][C$_3$H$_7$CO$_2$] and [C$_2$MIm][C$_7$H$_{15}$CO$_2$] ILs, respectively. This suggest that the transport of the ions in those ILs is perhaps more dependent on their viscosity as it may be extrapolated from the Stokes-Einstein Law. In fact, it appears that a decrease of the alkyl chain length on the anion increase the conductivity and decreases the viscosity. However, for all solutions, a clear conductivity increase

is observed by adding water in solution, which may be related to the expected cation-anion dissociation by adding water in solution.

Table 3-10. Conductivity, σ, data of ([C$_2$MIm][C$_n$H$_n$CO$_2$] + H$_2$O) binary mixture as a function of [C$_2$MIm][C$_n$H$_n$CO$_2$] mole fraction composition, χ_{IL}, at 298.15 K and 0.1 MPa.

[C$_2$MIm][CH$_3$CO$_2$]			[C$_2$MIm][C$_3$H$_7$CO$_2$]			[C$_2$MIm][C$_7$H$_{15}$CO$_2$]		
T = 298.15 K								
χ_{IL}	w_{IL}	σ/mS·cm^{-1}	χ_{IL}	w_{IL}	σ/mS·cm^{-1}	χ_{IL}	w_{IL}	σ/mS·cm^{-1}
0.96	0.99	2.77	0.87	0.99	1.19	0.95	0.99	0.32
0.89	0.98	3.15	0.74	0.97	1.49	0.86	0.98	0.39
0.70	0.95	4.49	0.62	0.95	2.01	0.77	0.97	0.48
0.49	0.90	7.31	0.50	0.92	2.92	0.63	0.96	0.83
0.30	0.80	13.28	0.38	0.87	4.78	0.44	0.92	1.46
0.10	0.51	33.60	0.27	0.80	8.48	0.35	0.88	2.49
0.00	0.00	0.00	0.15	0.67	16.58	0.25	0.82	4.72
			0.05	0.37	29.70	0.15	0.72	10.78
			0.00	0.00	0.00	0.05	0.43	25.50
						0.00	0.00	0.00

*Pure water used for this study was found with 0.00325 mS.cm^{-1}

Coadou *et al*,[137] have made the distinction clear between these two transport properties (viscosity & conductivity). They explained that the viscosity measured experimentally is a macroscopic property, which is related to the cohesive energy of the solution. And that the conductivity seems to be more strongly affected by the structure (volume), interaction (packing), and the mobility of ions in the solution. Therefore, one way to investigate the relationship between the viscosity (also called fluidity) and the conductivity (also called resistivity) of the IL solutions is driven by the determination of their iconicity using the Walden plot.[137]

3.5 Walden rule and ionicity

In this last section, the pure IL and the mixtures with water were investigated with regards to their ionicity according to the Walden rule. Walden has established the so-called *Walden rule* in order to classify ILs via their ionicity through their specific viscosity and molar conductivity properties.[104,138,139] Indeed the classical Walden Plot is used to discuss the relationship between the molar conductivity (resistivity) and the viscosity (fluidity) of a mixture to determine the ionicity of the system studied.[105,140] Walden product (W) is represented as follow:

(Eq. 31)

$$W = \Lambda_m \cdot \eta,$$

Where Λ_m represents the molar conductivity, η the viscosity and W is a constant that represents the ionicity.

In the pure IL, the molar conductivity, Λ_m, (S·cm²·mol⁻¹) can be expressed depending on the molar volume, V_m, (cm³.mol⁻¹), and the conductivity, σ (S.cm⁻¹), as follow:

(Eq. 32)

$$\Lambda_m = V_m \cdot \sigma \ \text{(S·cm}^2\text{·mol}^{-1}\text{)},$$

However, in the case of the IL + water binary mixture, since the overall molar volume, V_m, (cm³.mol⁻¹), of the solution is taken into account all species (ions and water), and as the molar conductivity must be calculated using solely the ions concentration in solution, (C_{ions}, mol.cm⁻³), the following equation must be used:

(Eq. 33)

$$\Lambda_m = \frac{\sigma}{C_{ions}} \ \text{(S·cm}^2\text{·mol}^{-1}\text{)},$$

Since the conductivity data were investigated at only one temperature; 298.15 K; the molar conductivity Λ_m, (S·cm²·mol⁻¹) data must be taken at the same temperature for all its parameters involved (density and conductivity).

The IL concentration, C_{ions}, was calculated regarding the density data taken at 298.15 K and the mass of each compounds taken for each composition as reported in the following equation:

(Eq. 34)

$$C_{IL} = \frac{n_{IL}}{V_{Total}} = \frac{m_{IL}}{M_{IL}} \times \frac{\rho_{mixture}}{(m_{IL}+m_{water})},$$

Since

$$n_{IL} = \frac{m_{IL}}{M_{IL}} \qquad \text{And} \qquad V_{Total} = \frac{(m_{IL}+m_{water})}{\rho_{mixture}}$$

Then, the calculated concentration was plotted as a function of the IL mole fraction, χ_{IL} and fitted using a polynomial function as reported for the three ILs in the Table 3-11. The viscosity data were fitted as the function of the composition by using a similar methodology. Once having all the data needed, the molar conductivity, Λ_m, (S·cm^2·mol^{-1}) as well as the fluidity, $(\frac{1}{\eta})$, was then calculated as shown in Table 3-12.

Table 3-11. Fitting equations of concentration, C_{ions} (mol.cm^{-3}) and viscosity, η (mPa.s), of the [C$_2$MIm][CH$_3$CO$_2$], [C$_2$MIm][C$_3$H$_7$CO$_2$] and [C$_2$MIm][C$_7$H$_{15}$CO$_2$].

	Fitting equations of ions concentration, C_{ions}/mol.cm^{-3}, and viscosity, η /mPa.s
[C$_2$MIm] [CH$_3$CO$_2$]	C_{ions} (χ_{IL} = 0 - 1) = 0.0751x^5 - 0.2293x^4 + 0.26747x^3 – 0.1511x^2 + 0.0443x + 7.0733.10^{-5} η (χ_{IL} = 0 – 0.64) = -111.17x^2 + 152.8884x + 1.23884 η (χ_{IL} = 0.64- 0.77) = 548.4812x – 295.1446 η (χ_{IL} = 0.77 – 1) = 55.47355x + 86.55457
[C$_2$MIm] [C$_3$H$_7$CO$_2$]	C_{ions} (χ_{IL} = 0 - 1) = -0.2364x6 + 0.7654x5 - 0.9831x4 + 0.6434x3 - 0.2314x2 + 0.0473x + 4.10^{-6} H (χ_{IL} = 0 - 1) = -2811.9x6 + 8841.8x5 - 9705.5x4 + 4448.6x3 - 582.54x2 + 99.632x + 0.5699
[C$_2$MIm] [C$_7$H$_{15}$CO$_2$]	C_{ions} (χ_{IL} = 0 - 1) = 0.03544x^5 – 0.10837x^4 + 0.12846x^3 - 0.07489x^2 + 0.02259x + 7.4026.10^{-4} η (χ_{IL} = 0 – 0.77) = 529.6075x^2 + 239.26572x – 1.03123 η (χ_{IL} = 0.77 - 1) = 185.002x + 344.76144

Table 3-12. Experimental conductivity data, σ (S/cm) and calculated data of the viscosity, η (Poise), concentration, C_{ions} (mol.cm^{-3}), and the independent variable Log$_{10}$ $(\frac{1}{\eta})$ and Log$_{10}$ $(\frac{\sigma}{C})$ used for the Walden plot.

χ_{IL}	σ (S/cm)	η (Poise)	C_{ions} (mol.cm^{-3})	Log$_{10}$ $(\frac{1}{\eta})$	Log$_{10}$ $(\frac{\sigma}{C})$
			$[C_2MIm][CH_3CO_2]$		
0.10	$3.36.10^{-2}$	0.154	$3.23.10^{-3}$	0.812	1.016
0.30	$1.33.10^{-2}$	0.372	$5.31.10^{-3}$	0.430	0.398
0.49	$7.31.10^{-3}$	0.496	$5.87.10^{-3}$	0.304	0.095
0.70	$4.49.10^{-3}$	0.912	$6.34.10^{-3}$	0.040	-0.150
0.90	$3.15.10^{-3}$	1.363	$6.40.10^{-3}$	-0.135	-0.308
1.00	$2.77.10^{-3}$	1.400	$6.42.10^{-3}$	-0.146	-0.365
			$[C_2MIm][C_3H_7CO_2]$		
0.05	$2.97.10^{-2}$	0.047	$1.89.10^{-3}$	1.331	1.196
0.16	$1.66.10^{-2}$	0.137	$3.67.10^{-3}$	0.862	0.655
0.27	$8.52.10^{-3}$	0.317	$4.33.10^{-3}$	0.499	0.294
0.38	$4.71.10^{-3}$	0.571	$4.72.10^{-3}$	0.243	0.000
0.50	$2.97.10^{-3}$	0.856	$5.00.10^{-3}$	0.067	-0.226
0.62	$1.97.10^{-3}$	1.149	$5.15.10^{-3}$	-0.060	-0.417
0.74	$1.49.10^{-3}$	1.473	$5.24.10^{3}$	-0.168	-0.545
1.00	$1.19.10^{-3}$	2.004	$5.25.10^{-3}$	-0.302	-0.645
			$[C_2MIm][C_7H_{15}CO_2]$		
0.05	$2.55.10^{-2}$	0.125	$1.71.10^{-3}$	1.173	0.901
0.15	$1.08.10^{-2}$	0.469	$2.83.10^{-3}$	0.581	0.329
0.25	$4.72.10^{-3}$	0.918	$3.33.10^{-3}$	0.152	0.037
0.35	$2.49.10^{-3}$	1.462	$3.54.10^{-3}$	-0.152	-0.165
0.44	$1.46.10^{-3}$	2.095	$3.65.10^{-3}$	-0.398	-0.321
0.55	$8.29.10^{-4}$	2.889	$3.75.10^{-3}$	-0.655	-0.461
0.63	$4.81.10^{-4}$	4.928	$3.88.10^{-3}$	-0.906	-0.693
0.77	$3.92.10^{-4}$	6.001	$3.88.10^{-3}$	-0.995	-0.778
1.00	$3.22.10^{-4}$	6.996	$3.90.10^{-3}$	-1.084	-0.845

The Walden equation can be rewritten and plotted as follows, where $\log_{10}(\Lambda_m)$ corresponds to the ordinate and $\log_{10}(\frac{1}{\eta})$ corresponds to the abscissa as it is presented in Figure 3-32 for the three ILs studied:

(Eq. 35)

$$\log_{10}(\Lambda_m) = \log_{10}(W) + \log_{10}(\frac{1}{\eta}),$$

The Figure 3-32 shows the Walden plot of the molar conductivity, Λ_m of the ($[C_2MIm][C_nH_nCO_2]$ + H_2O) binary mixture as a function of composition, χ_{IL} at 298.15 K and 0.1 MPa.
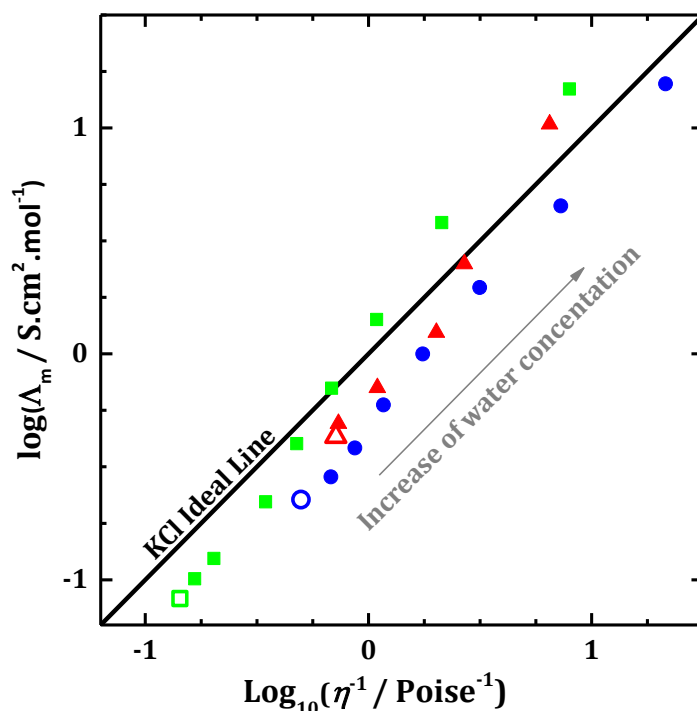
Figure 3-32. Walden plot of the molar conductivity, Λ_m of the ([C$_2$MIm][C$_n$H$_n$CO$_2$] + H$_2$O) binary mixture as a function of composition χ_{IL} at 298.15 K and 0.1 MPa, with $\triangle$, the pure [C$_2$MIm][CH$_3$CO$_2$]; $\blacktriangle$, ([C$_2$MIm][CH$_3$CO$_2$] + H$_2$O); $\bigcirc$, the pure [C$_2$MIm][C$_3$H$_7$CO$_2$]; $\bullet$, ([C$_2$MIm][C$_3$H$_7$CO$_2$] + H$_2$O); $\square$, the pure [C$_2$MIm][C$_7$H$_{15}$CO$_2$] and $\blacksquare$, ([C$_2$MIm][C$_7$H$_{15}$CO$_2$] + H$_2$O).

The specific points on the graph were calculated using the correlation parameters of the fitting equations for concentration and viscosity at the same experimental conductivity compositions. The fitting equations are found in the Table 3-11 of this section. The solid line in Figure 3-32 represents the ideal line for ionic mobility established by using data for an aqueous solution of KCl at 0.01 mol.dm^{-3}, which is a strong electrolyte where all ions are known to be fully dissociated and equally mobile in solution.[141,142]

From the "*Classical*" Walden rule, the Walden product (*W*) can be understood to a degree of dissociation, which is directly linked to the ions dissociation once in solution. From (Eq. 31), *W* can be extracted using the (Eq. 35), which is a linear function type (*y = b + ax*) where *a = 1*. The Walden product of the pure IL (*W*) were found by applying the *Classical* Walden rule using (Eq. 31). However, in the case of the IL in mixture with water, the specific point does not seem to be a parallel line to the KCl ideal line. In their case, *a ≠ 1*, and therefore the "*Fractional*"

Walden rule has to be applied, which involves the presence of a new coefficient α, that gives the shift of W' compared to the KCl Ideal line:

(Eq. 36)

$$W' = \Lambda_m \cdot \eta^{\alpha},$$

(Eq. 37)

$$\log_{10}(\Lambda_m) = \log_{10}(W') + \alpha \cdot \log_{10}(\frac{1}{\eta}),$$

Where α is an additional exponent fitting parameter, and W' is the "Walden product" of the fractional Walden rule.

Hence, the Walden product of IL mixtures with water (W') was found by fitting the Walden plot with a linear function type ($y = b + ax$), where b is the intercepts and is represented by $\log_{10}(W'/S.cm^2.mol^{-1})$ ranging from (-0.32 and 0.04), and a represents the coefficient α (i.e. slopes) ranging from (1.15 and 1.41), according to (Eq. 37). This allows to get W' value for each IL solutions. The Walden product W and W' are displayed in percentage (%) in Table 3-13.

If the Walden plots are on the ideal line, this means that the dissociation constant is equal to 1 and therefore, that the IL is completely dissociated and can act as a very good electrolyte. However, if the points are below 10 % of the Ideal Line, ILs are qualified of poor ILs with poor electrolyte behaviour.[143] The KCl ideal line shows 100 % of its ions dissociated in solutions, which means the absence of ion-pairs in solution as expected in the case of the very high diluted KCl solutions, where ions are all solvated by the solvent molecules. According to Coadou *et al*, all solutions having a Walden product inferior to 100 % may indicate a slight tendency for the formation of ion-pairs in solution. Such a behaviour has already been reported for several ILs.[141]

Thus, for a Walden product (W or W') inferior to 100 %, it is possible to calculate the number of ion-pairs in solution of IL (displays in Table 3-13), by simply looking at the difference between them two:

(Eq. 38)

$$\text{Number of ion-pairs (\%) = } 100 - W^{()},$$

Table 3-13. Walden products of the pure ILs (*W*) and of the IL solutions (*W'*) as well as the number of ions pairs found in both solutions, displayed at 298.15 K and 0.1mPa.

Walden products	[C$_2$MIm] [CH$_3$CO$_2$]	[C$_2$MIm] [C$_3$H$_7$CO$_2$]	[C$_2$MIm] [C$_7$H$_{15}$CO$_2$]
W (%)	60	45	58
Nb of ion pairs (%)	40	55	42
W' (%)	158	48	91
Nb of ion pairs (%)	none	52	9

In the pure ILs, the *classical* Walden products (*W)* show data inferior to the KCl ideal line and thus inferior to 100 %, with (60, 45 and 58) % for the pure ILs [C$_2$MIm][CH$_3$CO$_2$], [C$_2$MIm][C$_3$H$_7$CO$_2$] and [C$_2$MIm][C$_7$H$_{15}$CO$_2$], respectively at 298.15 K and 0.1 MPa. This is in agreement with the literature, where most of the time pure ILs are mainly constituted of ions-pairs, which increase their character neutral and make them less-conductive. [137,144]

However, for the same kind of cation, much better ionicity values were determined for the 1-ethyl-3-methylimidazolium tetrafluoroborate, [C$_2$MIm][BF$_4$], at 96 %,[141] the 1-butyl-3-methylimidazolium tertrafluoroborate, [C$_4$MIm][BF$_4$], at 64 %;[142] whereas the 1-butyl-1-methylpyrrolidium, [C$_4$mpyrr][TFSI], exhibits a ionicity of 72 %.[145] Two other studies have revealed the ionicity of hydrophobic ILs of some pure ether functionalised sulfonium bis(trifluoromethyl)sulfonylimide. They have found a decrease of the ionicity due to the increases of the degree of asymmetry and functionalization within the alkyl chain of the cation with a ionicity ranging from 30 % and 56 %.[137,144]

However, in mixtures with water, their Walden products (W') increases through the fractional Walden rule from (158, 48 and 91) % for [C$_2$MIm][CH$_3$CO$_2$], [C$_2$MIm][C$_3$H$_7$CO$_2$] and [C$_2$MIm][C$_7$H$_{15}$CO$_2$] solutions, respectively, at 298.15 K and 0.1 mPa. IL having a Walden product superior to 100 % are called "superionic", which means they have a better potential electrolyte behaviour than KCl Ideal solution. The number of ion-pairs is also decreasing, becoming almost inexistent in the case of [C$_2$MIm][CH$_3$CO$_2$] (none) and [C$_2$MIm][C$_7$H$_{15}$CO$_2$] (9 %) solutions.

For [C$_2$MIm][C$_3$H$_7$CO$_2$], W' shows data inferior to the KCl ideal line along its whole composition. However, [C$_2$MIm][CH$_3$CO$_2$] and [C$_2$MIm][C$_7$H$_{15}$CO$_2$] show data superior or equal to the KCl ideal line from χ_{IL}(0.3 to 0.05) and χ_{IL}(0.44 to 0.05) respectively; whereas above those compositions to their pure systems, they exhibit data inferior to the KCl ideal line. This could actually explain the high value of their W'.

Those results are in accordance with the volumetric and transport properties studies. In fact, the excess molar volumes, V^E, have shown negative values that prove a volume contraction between water and IL with maxima around $\chi_{IL} = 0.35$ for the three ILs. Stronger values were found for [C$_2$MIm][CH$_3$CO$_2$] and [C$_2$MIm][C$_7$H$_{15}$CO$_2$]. This has shown that at those ILs composition, there are an increase of hydrogen bonds. Furthermore, the deviation viscosities, $\Delta\eta$, have shown negative data for $\chi_{IL} < (0.64$ and $0.50)$ for the respective [C$_2$MIm][CH$_3$CO$_2$] and [C$_2$MIm][C$_7$H$_{15}$CO$_2$]; whereas for [C$_2$MIm][C$_3$H$_7$CO$_2$], it has shown negative data for the whole composition range.

This demonstrates the non-strong specific interaction found when $\Delta\eta < 0$, which supports the idea of a dissociation between the ion-pairs (*cation-anion*) due to the insertion of water. In fact, water is known to breakdown the hydrogen-bonds in the *cation-anion* network.

This explained why W' is found under the KCl ideal line for the less dilutes solutions; while it is found on or above the KCl line for the [C$_2$MIm][CH$_3$CO$_2$] and [C$_2$MIm][C$_7$H$_{15}$CO$_2$] for the other more diluted solutions. In addition, the excess Gibbs energy,ΔG^{E*}, have revealed positive data for the whole composition of the three ILs with a maxima found at $\chi_{IL} = (0.25, 0.35$ and $0.2)$ for the respective [C$_2$MIm][CH$_3$CO$_2$], [C$_2$MIm][C$_3$H$_7$CO$_2$], and [C$_2$MIm][C$_7$H$_{15}$CO$_2$] IL solutions. According to Kapadi *et al.*,[135] those values also prove that positive values indicate the specific interaction leading to complex formation through intermolecular hydrogen bonding interaction between unlike molecules compared to like molecules.

Furthermore, the addition of water in those ILs show that W, will not remind constant in function of the composition and therefore the *fractional* Walden rule

had to be used instead of using the classical one. Water has shown to give far better ionic character of the solution since it increases the number of dissociated-ions into water. In another words, water helps to breakdown the interactions between ion-pairs leaving free ions in solutions and thus giving a better conductivity of the solution.

Those data should give a better IL-electrolyte behaviour with an increase of the temperature. Unfortunately, the temperature dependency cannot be checked since the conductivity was only investigated at 298.15 K.

3.6 Conclusions

These ILs exhibit good thermal stability, low melting points, and good volumetric and transport properties. Furthermore, they can be classified as "good" ILs with ionicities ranging from 45 to 60 % in the pure system, and from 48 to 158 % in their binary mixtures with water.

The volumetric properties of the 1-ethyl-2-methylimidazolium alkyl-carboxylate ILs in binary mixtures with water have shown a volume contraction for all mixtures. This has proven the formation of a new hydrogen-bond network between the water molecules and the anion leading to the breakdown of the already existing hydrogen-bonding network present in the pure IL between the cation and the anion. The hydrogen-bonding network between water molecules and anions has been found to be stronger at about (χ_{IL} = 0.35).

Furthermore, the transport properties study of those mixtures have revealed a change of behaviour from χ_{IL} < 0.64 for the [C_2MIm][CH_3CO_2] and the [C_2MIm][$C_7H_{15}CO_2$] with regards to the viscosity data. From those compositions the dissociation between the cation and the anion due to water insertion is becoming stronger. However, [C_2MIm][$C_3H_7CO_2$] has no dramatic change and seems to have a gradual and weaker *cation-anion* dissociation compared to the two other IL systems. Those results were supported by the excess Gibbs energy,ΔG^{E*}, which have shown positive values for all three systems studied with maxima of χ_{IL} ranging between (0.2 and 0.35). This is in accordance with the volumetric properties that also show extreme IL-water behaviour at those compositions.

In fact, the *Fractional* Walden rule has shown that about 50 % of ion-pairs are presents in those pure ILs; whereas almost none ion-pairs are found for the $[C_2MIm][CH_3CO_2]$ and $[C_2MIm][C_7H_{15}CO_2]$ solutions with water. An ideal electrolyte behaviour is found for $\chi_{IL} \leq 0.3$ and 0.44 for those two respective ILs. For those two later systems, water has led to increase their ionic character by increasing dramatically their number of dissociated-ions due to the breakdown of interactions between ion-pairs leading to a better conductivity of the solutions. However, the ionicity of $[C_2MIm][C_3H_7CO_2]$ hasn't been much improved by the addition of water since it keeps to the almost same number of ion-pairs after dilution of the pure IL.

The non-tendency due to the alkyl-chain length on the anion is probably due to the fact that eight carbons lead to a better aggregation behaviour in water and that at only four carbons it doesn't aggregate as well. Regarding the acetate-anion, its ion-pairs dissociation will be easier due to its shorter alkyl-chain length.

3.7 Experimental part

3.7.1 Preparation of [C₂MIm][CₙHₙCO₂]and water mixtures

Binary mixtures containing each respective IL ([C_2MIm]$^+$ cation combined with the acetate or butanoate or octanoate anion) and pure water, H_2O, were prepared by mass, based on their mole ratio, with an accuracy of $\pm 1 \cdot 10^{-4}$ g using an AnD-HR-120 balance. All mixtures have been prepared in a Nitrogen-glovebox in order to avoid any additional moisture in the sample. The exposure to the air was then only up to a minute. A Karl-Fisher titration was run for each IL in order to determine its initial water content using a Metrohm 899 Coulometer, 803^{Ti} Stand. This water level was then taking into account when determining the real water level in each solution. (cf. Chapter 1, section 1.2.3).

3.7.2 Thermal properties

Differential scanning calorimetry (DSC) was using a DSCQ2000 with a RSC90 cooling system and Tzero aluminium, Lemetic pan and lid, sample purge flow 50mL/min. And the thermal gravimetric analysis (TGA) was using TGAQ5000, platinium pans, Sample purge flow of 25mL/min. DSC and TGA samples were prepared from the solution used for density and viscosity and were sealed within the N_2-glovebox in order to avoid any moisture from the air.

3.7.3 Density measurements

The densities were measured using a density meter, Mettler Toledo DM40 for each IL, as a function of temperature from 293.15 K to 363.15 K, and then a last measurement was done at 293.15 K to look at the effect of the temperature on the density for each sample. This final verification was done to verify that the composition was not changed by increasing the temperature due to water evaporation. Seven solutions were then measured from each IL ranging between 0.0 and 1.0 in IL-mole fraction composition while the density of pure water was taken from the literature. [106,107]

3.7.4 Viscosity measurements

The viscosities were measured using the Malvern Bohlin Gemini 150 rheometer with a conic-plate system. Pure ILs and investigated mixtures were measured as a function of temperature from 293.15 K to 363.15 K. Seven solutions were

measured from each IL ranging between 0.0 and 1.0 in IL-mole fraction composition while the density of pure water was taken from the literature. [106,107]

3.7.5 Conductivity measurements

Conductivity measurements have been carrying out on the HACH-Lange, Senslon™ + EC71 on the three pure ILs and their mixtures with water.

The probe of the conductimeter was emerged into a glass tube containing around 3 mL of product and then closed with parafilm inside the N_2-glovebox to avoid any further contact with air. (The conductimeter used had a particularity to have a detachable probe). Then the probe was reconnected to the conductimeter itself connected to a water circulator allowing to have the same temperature for each measurement. The temperature was found for each measurement at 298.15 K. Each ratio was measured separately. Therefore, ten solutions were measured from each IL following the IL mole fraction below: 0.00, 0.05, 0.15, 0.25, 0.35, 0.45, 0.55, 0.65, 0.75, 0.85, 0.95. In total, about 30 samples were measured for each respective IL solution.

Chapter 4 _ Microscopic properties of ionic liquid and water binary mixtures

4.1 NMR-Spectroscopy study introduction

4.1.1 Imidazolium cation IL in binary mixture with a solvent

This study aims to understand the intermolecular interactions of imidazolium IL cations and their carboxylate IL anions in the presence of water. A short review on the 'imidazolium IL cation/molecular solvent' interactions *via* ^{1}H-NMR spectroscopy is reported below in Table 4-1 and

Table 4-2. So far, Marekha *et al.* have shown that imidazolium ring hydrogen atoms of an IL/solvent mixture have been found to have different strengths of hydrogen bonding interactions depending on the IL-anion and the solvent concentration used.[44] In order to focus this literature review, only the imidazolium ring hydrogen atoms have been considered regarding the impact of the anion and solvent on an imidazolium cation.
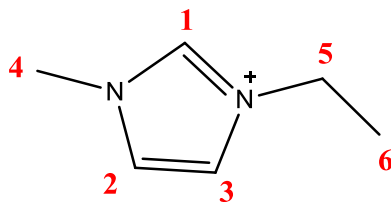
Figure 4-1. Imidazolium cation numbered

Table 4-1. Positive chemical shifts, $\Delta\delta_H(x)$ of the imidazolium ring hydrogen atoms H1, H2/H3 and chemical shifts behaviour of H4 found in the literature influenced by the IL-anion and by the increase of the solvent concentration, ordered in function of the imidazolium cation alkyl chain length.

Cation	Anion	Solvent	$\Delta\delta_H$(H1)	$\Delta\delta_H$(H2/H3)	$\Delta\delta_H$(H4)	Ref
[C$_2$MIm]	[TFSI]	DMSO	>0	>0	>0	[146]
[C$_2$MIm]	[TFSI]	CH$_3$OH	>0	>0	≥0	[146,147]
[C$_2$MIm]	[TFSI]	CH$_3$CN	>0	>0	>0	[146]
[C$_2$MIm]	[TFSI]	H$_2$O	>0	>0	>0	[148]
[C$_2$MIm]	[TFSI]	(CH$_3$)$_2$CO	>0	>0	>0	[149]
[C$_2$MIm]	[TfO]	(CH$_3$)$_2$CO	>0	>0	<0	[149]
[C$_2$MIm]	[NfO]	(CH$_3$)$_2$CO	>0	>0	>0	[149]
[C$_4$MIm]	[BF$_4$]	(CH$_2$OH)$_2$	>0	>0	>0	[150]
[C$_8$MIm]	[BF$_4$]	(CH$_2$OH)$_2$	>0	>0	>0	[150]

Table 4-2. Negative chemical shifts, $\Delta\delta_H(x)$ of the imidazolium ring hydrogen atoms H1 and chemical shifts behaviour of H2/H3 and H4 found in the literature influenced by the IL-anion and by the increase of the solvent concentration, ordered in function of the imidazolium cation alkyl chain length.

Cation	Anion	Solvent	$\Delta\delta_H$(H1)	$\Delta\delta_H$(H2/H3)	$\Delta\delta_H$(H4)	Ref
[C$_1$MIm]	[CH$_3$SO$_4$]	H$_2$O	<0	<0	<0	[151]
[C$_2$MIm]	[C$_2$H$_5$SO$_4$]	D$_2$O	<0	<0	>0	[38]
[C$_2$MIm]	Cl	CH$_3$CN	<0	<0	<0	[147]
[C$_2$MIm]	[CF$_3$CO$_2$]	(CH$_3$)$_2$CO	<0	<0	>0	[149]
[C$_2$MIm]	[C$_3$F$_8$CO$_2$]	(CH$_3$)$_2$CO	<0	<0	<0	[149]
[C$_2$MIm]	[CH$_3$CO$_2$]	(CH$_3$)$_2$CO	<0	<0	<0	[149]
[C$_2$MIm]	[CH$_3$CO$_2$]	H$_2$O	<0	>0	≤0	[28]
[C$_4$MIm]	[CH$_3$SO$_3$]	H$_2$O	<0	<0	<0	[151]
[C$_4$MIm]	[C$_8$H$_{17}$SO$_4$]	(CH$_2$OH)$_2$	<0	<0	>0	[150]
[C$_4$MIm]	[PF6]	(CH$_3$)$_2$CO	≤0	<0	<0	[44]
[C$_4$MIm]	[TfO]	(CH$_3$)$_2$CO	<0	<0	<0	[44]
[C$_4$MIm]	[TFSI]	(CH$_3$)$_2$CO	≤0	<0	<0	[44]
[C$_4$MIm]	[BF$_4$]	(CH$_3$)$_2$CO	<0	<0	<0	[44]
[C$_4$MIm]	[BF$_4$]	H$_2$O	<0	<0	<0	[24,152-154]
[C$_4$MIm]	Cl	H$_2$O	<0	<0	>0	[24,153,155]
[C$_4$MIm]	Br	H$_2$O	<0	<0	<0	[24]
[C$_4$MIm]	I	H$_2$O	<0	<0	<0	[24]
[C$_4$MIm]	Cl	DMSO	<0	>0	N/A	[155]
[C$_4$MIm]	[CF$_3$CO$_2$]	H$_2$O	<0	<0	<0	[41]
[C$_4$MIm]	[CF$_3$CO$_2$]	CH$_3$OH	<0	>0	>0	[41]
[C$_6$MIm]	Br	H$_2$O	<0	<0	<0	[156]
[C$_6$MIm]	Cl	H$_2$O	<0	<0	<0	[151]
[C$_8$MIm]	Br	H$_2$O	<0	<0	<0	[156]
[C$_8$MIm]	Cl	H$_2$O	<0	<0	<0	[153]
[C$_{12}$MIm]	[NO$_3$]	H$_2$O	<0	<0	≤0	[157]
[C$_{12}$MIm]	[NO$_3$]	C$_6$H$_6$	<0	<0	≤0	[157]
[C$_{12}$MIm]	[TFSI]	C$_6$H$_6$	<0	<0	<0	[158]

According to two Tables above, for the imidazolium ring hydrogen atoms, mainly *negative values* of the relative chemical shift are observed when the *anions are basic*, such as for halides, substituted sulfonates, RSO_3^-, sulfates, RSO_4^-, carboxylates, RCO_2^-, and tetrafluoroborate, BF_4^-, based ILs. Overall, the study of chemical shift variations in IL-solvent mixtures from the literature cited above have also shown that significant changes occurr for low IL contents in IL/water mixtures, especially when $x_{IL} < 0.1\text{-}0.2$. This is due to the fact that at high dilution, the IL is either dissociated into individual ions or into ion pairs or even small aggregates. Thus, in such conditions the IL can be compared to a conventional electrolyte which is known to have strong interplay between ion-ion and ion-molecular interactions.

According to Marekha *et al.,* and to the above Table 4-1 and

Table 4-2, three main effects are observed to explain such chemical shift variations.[44]

- ❖ The first effect is in the case of *weak interactions between the IL cation and anion.* For this kind of IL, after dilution with an appropriate solvent, it forms small aggregate units or even full dissociation of both, cation and anion. This dissociation will increase with the dilution coefficient and will result in a small increase of the chemical shift (≤ 0.05ppm) observed on the ^{1}H-NMR spectroscopy due to a *downfield* shift of the hydrogen atoms. [147-149,157-161]

- ❖ The second effect is in the case of the *presence of hydrogen bonds in the IL* between the imidazolium ring hydrogen atoms and between the adjacent alkyl hydrogen atoms with the electronegative atoms of the anions. When a solvent is added to this kind of IL, an *upfield* of the imidazolium ring hydrogen atoms will be observed on the ^{1}H-NMR spectroscopy. [162-164]

- ❖ Thirdly, the mixture of *IL cations with a polar molecular solvent* will form hydrogen bonds with donor atoms of the solvent; such as oxygen atoms for alcohols and DMSO. This would result in a *downfield* shift of the imidazolium ring hydrogen atoms as well as the adjacent alkyl hydrogen atoms. [39,146,165]

114

A conclusion from those three effects on the imidazolium ring hydrogen atoms can be drawn as follows. When $\Delta\delta_i(x) > 0$, hydrogen bonds formed from the IL-solvent mixture are stronger than those formed between the IL cation and anion; whereas when $\Delta\delta_i(x) < 0$, the interionic hydrogen bonds formed between the cation and the anion IL are stronger than those formed between the IL-cation and the solvent. However, in the case of ILs with highly basic anions, this would result in large negative values $\Delta\delta_i(x) << 0$ due to the formation of very strong interionic hydrogen bonds and therefore weaker hydrogen bonds between the IL-cation and solvent.

4.1.2 Interaction behavior of the imidazolium cation and acetate anion binary mixture with solvent

So far, five articles have been reported in the literature to describe the interaction behaviour of the 1-ethyl-3-methylimidazolium acetate ionic liquid in water binary mixture using NMR spectroscopy.[25,28,125,166,167] In addition, two more publications have characterised this type of IL with a change on the imidazolium alkyl chain length or solvent.[168,169] The Table 4-3 below gives an overview of these papers regarding their IL and solvent used.

Table 4-3. Imidazolium cation and carboxylate anion binary mixture with solvent studied via NMR spectroscopy in the literature.

Imidazolium cation	Carboxylate Anion	Solvent	Ref
[C$_2$MIm]	[CH$_3$CO$_2$]	H$_2$O	25,28,166
[C$_2$MIm]	[CH$_3$CO$_2$]	D$_2$O	125,167
[C$_4$MIm]	[CH$_3$CO$_2$]	D$_2$O	167,168
[C$_6$MIm]	[CH$_3$CO$_2$]	D$_2$O	167,170
[C$_8$MIm]	[CH$_3$CO$_2$]	D$_2$O	167
[C$_2$MIm]	[CH$_3$CO$_2$]	DMSO	169
[C$_2$MIm]	[CH$_3$CO$_2$]	D$_6$-DMSO	125
[C$_2$MIm]	[CH$_3$CO$_2$]	CD$_3$OD	125
[C$_2$MIm]	[CH$_3$CO$_2$]	CD$_3$CN	125
[C$_2$MIm]	[CH$_3$CO$_2$]	D$_6$-DMSO	125
[C$_2$MIm]	[CH$_3$CO$_2$]	CD$_3$COCD$_3$	125
[C$_2$MIm]	[CH$_3$CO$_2$]	C$_6$D$_6$	125
[C$_2$MIm]	[CH$_3$CO$_2$]	CDCl$_3$	125
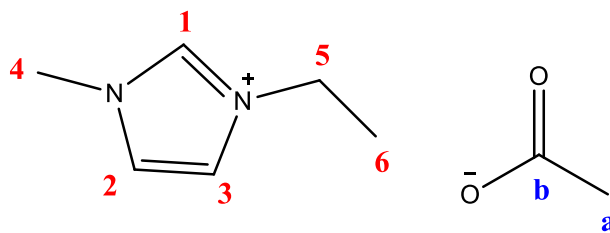
Figure 4-2. Chemical structure of [C$_2$MIm][CH$_3$CO$_2$], 1-ethyl-3-methyl-imidazolium acetate with the proton and carbon resonances labelled (1 to b).

4.1.3 Interaction behavior [C$_2$MIm][CH$_3$CO$_2$] and water binary mixture

Hall *et al.* have shown in their work that acetate anions form strong hydrogen bonds with water.[28,125,167] Therefore, when the water concentration increases in the IL solution, the imidazolium ring hydrogen atoms have negative relative chemical shift values corresponding to an upfield shift from the imidazolium ring hydrogen atoms. This is indicating a decrease of the interionic interaction between the anion and the cation and shows an increase of the hydrogen bonding between the IL-anion and water. In addition, the water molecules are also showing a negative relative chemical shift value corresponding to an upfield shift. In fact, by increasing the water concentration in the IL solutions, the water molecules have stronger interactions with the IL anion than with other water molecules.

In complementary work, Allen *et al* have used NMR spin relaxation and exchange spectroscopy methods to characterise the molecular interactions in the [C$_2$Mim][CH$_3$CO$_2$]-water binary mixtures.[166] In this study, NMR relaxometry techniques are used to describe the effect of water concentration on the mobility of IL molecules as well as the interactions of [C$_2$Mim][CH$_3$CO$_2$] with water. Their results have showed an increase in hydrogen bonding at 0.43 mole fraction of water in the [C$_2$Mim][CH$_3$CO$_2$]-water binary mixtures, which can be associated to the extremely basic environment that offer [C$_2$Mim][CH$_3$CO$_2$] IL. In fact neat [C$_2$Mim][CH$_3$CO$_2$] is known to be very basic and adding water to it would slightly decrease its basicity while remaining basic as shown in the

Table 4-4.

Table 4-4. Impact of the water concentration in $[C_2Mim][CH_3CO_2]$ IL in term of pH.

χ_{IL}	W_{H2O}	pH
1	0 %	14.2
0.5	10 %	12.5
0.30	25 %	10.9

In addition Chen *et al.*, are the only authors to characterise the NMR shifts of the hydrogen bonds between the cation and the anion of $[C_2Mim][CH_3CO_2]$ IL when this IL is extremely diluted with water: H1 (42%), H3 (24%), H4 (22%), H4 (6%), H5 (5%) and H6 (1%) (Those values were obtained by the difference of H-bonds between water/H and anion/H based on the relative chemical shift of ^{1}H-NMR).[25] To obtain those precise values, they first observed the chemical shift of the binary mixture using ^{1}H and ^{13}C spectroscopy as summarised in the Table 4-5 below.

Table 4-5. H and C relative chemical shifts $\Delta\delta_i(x)$, of position 1 to a, and their total amount of hydrogen bonding with water in term of strength.

H & C positions	$\Delta\delta_H(x)$	$\Delta\delta_C(x)$	H-bonds interaction with anion	H-bonds interaction with water	Total amount of H-bonds
1, 2, 3	<0	<0	Decrease strongly	Increase weakly	Reduce strongly
4, 5	<0	>0	Decrease strongly	Increase weakly	Reduce weakly
6, a	>0	<0	Decrease weakly	Increase strongly	Reduce dramatically

According to the Table 4-5 above, for H and C cation ring (1, 2, 3), the addition of water will show a decrease in H and C chemical shift which conveys that the electron-density of the H/C(1,2,3) of the pure IL increases after dilution. By adding water to the IL, the total quantity of hydrogen bonds will reduces, since because the H-bond interaction between the anion/(H and C position 1,2,3) will strongly decrease, whereas the interaction water/(H and C position 1,2,3) will weakly increase. For the alkyl carbons adjacent to nitrogen (4,5), same conclusion as above where drawn, but with weaker strength and quantity of interactions.

To complement their work, they used 2D-NMR [1]H-^{1}H NOESY which has provided valable information. All protons in the pure $[C_2MIm][CH_3CO_2]$ are all interacting with each other; whereas at high dilution of the $[C_2MIm][CH_3CO_2]$ IL with water

at χ_{IL} = 0.5 mol%, the IL is not fully dissociated. In fact, there are still weak Van der Waals forces present between the Ha and H4 position as reported in their paper shown in the figure below.
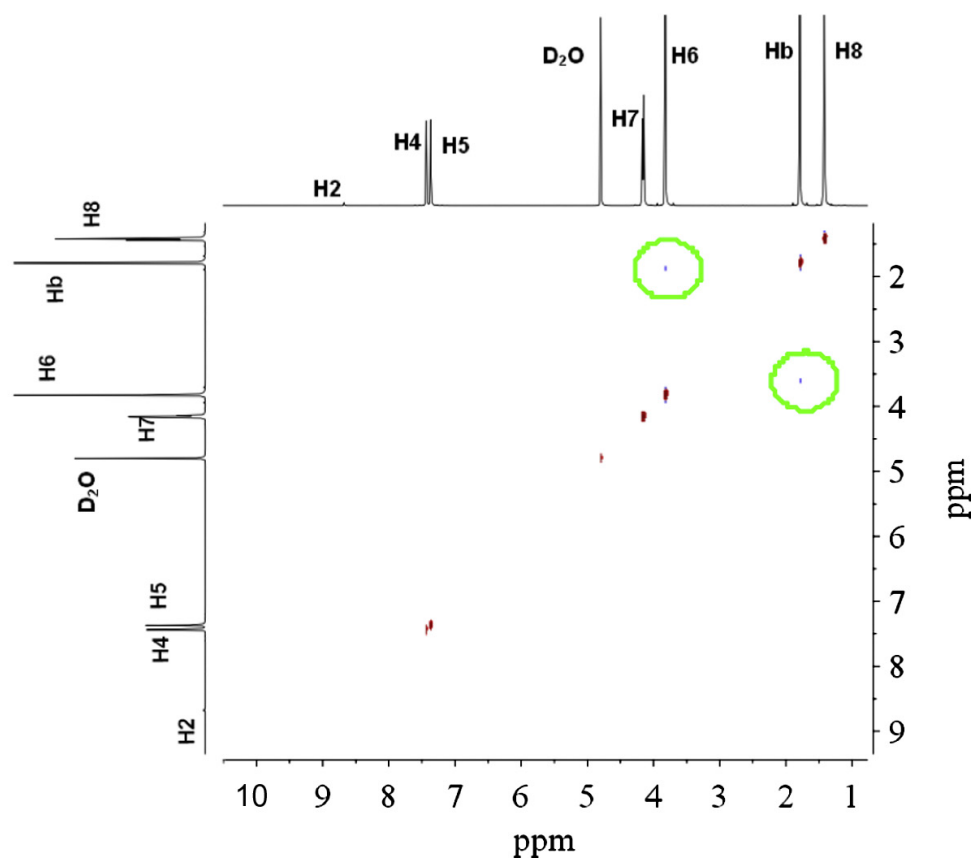
Figure 4-3. 2D ^{1}H-^{1}H NOESY NMR spectra of 0.5 mol% [C$_2$MIm][CH$_3$CO$_2$] in D$_2$O solution from Chen et al., 2015. [25] Where H6 is called H4 in this chapter and Hb is called Ha.

Thus, there are still ion-pairs in the highly diluted [C$_2$MIm][CH$_3$CO$_2$] solution. This is due to the fact that there is stronger intermolecular interaction of H-bonds in the [C$_2$MIm][CH$_3$CO$_2$] cations/anions than for other ILs.[171,172] Indeed the number of hydrogen-bonded ion-pairs in ILs increased as follows; [C$_2$MIm][CH$_3$CO$_2$] > [C$_2$MIm][X$_2$] (X$_2$= BF$_4$, PF$_6$) > [C$_2$MIm][X$_1$] (X$_1$ = Br, Cl) which supports the importance of the higher basicity of the acetate anion, which therefore has higher hygroscopicity than other ILs and thus absorbs very easily water from the moisture air .[25] The state of hydrophilic and hydrophobic behaviour of ILs in aqueous solutions in term of associative or dissociative cation/anion IL is summarized in Table 4-6. Hence the basicity and acidity of the anion play an important role and can help to predict the interaction behaviour between the cation and anion after the addition of a molecular solvent.

Table 4-6. State of hydrophilic and hydrophobic ILs in aqueous solutions referred from Yee and Chen.[25,173]

Characteristic	Ionic liquid	Effect of water on cation/anion IL interaction
Hydrophobic	$[C_nMIm][TFSI]$ (n = 2,4,6)	Associative
Moderate hydrophilic	$[C_2MIm][CH_3CH_2SO_4]$	Hydration behavior
Hydrophilic	$[C_2MIm][Cl]$	Fully dissociative
Hydrophilic	$[C_2MIm][CH_3CO_2]$	Not fully dissociative[25] (weak *van der* Waals force between H4/Ha)

At high dilution, the acetate anion will be hydrated most compared to the cation, due to its higher hydrophilicity. Hence it becomes unable to form hydrogen bonding with the proton of the cation. A schematic summary of the behaviour between the $[C_2MIm][CH_3CO_2]$ cation and anion of the IL in the extremely diluted water solution (0.5mol%) is reported below by Chen *et al.*[25]
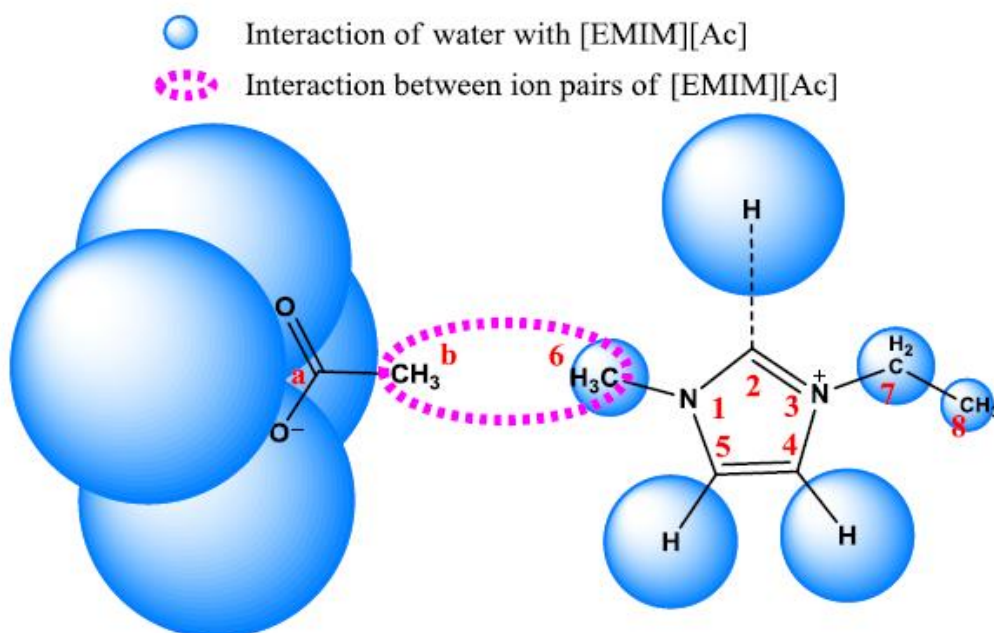
Figure 4-4. Model of ions pairs of $[C_2MIm][CH_3CO_2]$ in the extremely diluted water solution (0.5 mol%) proposed by Chen et al., 2015.[25] The strength of hydrogen-bonding interaction between water and the corresponding atoms is associated to the size of the blue circles.

4.1.4 Influence of the imidazolium cation alkyl chain length

Chen *et al.,* have studied the interaction mechanism of imidazolium-based ILs with acetate anions and water throughout the whole concentration range via ^{1}H-NMR spectroscopy. They were investigating the influence of the alkyl chain length in the imidazolium cation in term of hydrogen bonding by studying the cations [C$_2$MIm]+, [C$_4$MIm]+, [C$_6$MIm]+, [C$_8$MIm]+ for the ionic liquids, all with the acetate anion.[167]

As a result, both cation–anion and water/IL interaction strengths are in the following order according to the order regarding the alkyl chain lengths of the cations: [C$_2$MIm] **>** [C$_4$MIm] **>** [C$_6$MIm] **>** [C$_8$MIm]. This order is linked to the fact that the alkyl chain lengths of the imidazolium cation is hydrophobic and the longer is the alkyl chain, the more hydrophobic will be the cation; whereas the acetate is hydrophilic effect.

In addition, imidazolium cation with longer alkyl chain lengths exhibit stronger Van der Waals forces between the chains, which tends to form some degree of order in the liquid. Hence, water can more easily attack the [C$_2$MIm][CH$_3$CO$_2$] IL which has the less aggregation due to its shorter alkyl chain length, and therefore has a more hydrophilic and less hydrophobic character than the other ILs with longer alkyl chain lengths.

Thus, [C$_2$MIm][CH$_3$CO$_2$] IL is the most disturbed by water, and the IL that shows the stronger interactions for the cation and the anion compared to longer alkyl chain lengths at the imidazolium cation.

4.1.5 Influence of the use of non-aqueous molecular solvents

Chen *et al.,* have also been looking at the hydrogen-bonding interaction between [C$_2$MIm][CH$_3$CO$_2$] and seven solvents: deuterated water, D$_2$O, deuterated dimethylsulfoxide, D$_6$-DMSO, deuterated methanol, CD$_3$OD, deuterated acetonitrile, CD$_3$CN, deuterated acetone, CD$_3$COCD$_3$, deuterated benzene, C$_6$D$_6$, and deuterated chloroform, CDCl$_3$.[167] The whole composition of each binary system was investigated by the chemical shits in the ^{1}H NMR. Overall,

the H-bonds between the cation and the anion decreases, while the H-bonds between the IL and solvent increases while adding water to the neat IL. However, the decrease of H-bonds between the cation and the anion of $[C_2MIm][CH_3CO_2]$ IL is stronger than the increase of H-bonds of H1, H2 and H3 with water and methanol; however, it is weaker in acetonitrile and dimethyl sulfoxide.[167] The table below is showing the protic characteristic of each solvent and their dielectric constants.

Table 4-7. Solvent dielectric constant from polar to non-polar solvent.

Class of solvent	Solvent name	Solvent formula	Dielectric constant
Polar protic solvent	Water	H_2O	80
	Methanol	CH_3OD	33
Polar aprotic solvent	Dimethyl sulfoxide	DMSO	47
	Acetonitrile	CH_3CN	37
	Acetone	CH_3COCH_3	21
Non-polar solvent	Chloroform	$CHCl_3$	4.8
	Benzene	C_6H_6	2.4

As shown in the above table, water and methanol are polar protic solvents which means they already possess hydrogen bonding in their system (O-H or N-H bonds) and therefore they can form new hydrogen bonding by acting as hydrogen bonding donor / acceptor. However, acetonitrile and dimethyl sulfoxide are polar aprotic solvents, which therefore can't act as hydrogen bonding donors (no O-H or N-H bonds). These solvents dissolve charged species easily due to the high polarity and their hydrogen acceptor properties.

4.2 Microscopic properties of IL and water binary mixtures *via* NMR-spectroscopy

NMR chemical shifts were determined *using* ^1H and ^{13}C NMR-spectroscopy. For each composition of $[C_2MIm][C_nH_nCO_2]$/water mixture, proton and carbon spectra were measured in a range of temperatures between 300K to 345K. To determine the chemical shifts of each atom at each composition, each spectrum was arranged using the DMSO peak seen from the capillary tube which was fixed at 2.56 ppm for all spectra, in order to have the same reference for each and be able to compare each other on the same scale. This method follows several other NMR studies on imidazolium based-IL, which are detailed in the introduction chapter.

Then the change in position of each peaks on the addition of water was determined using the chemical shift δ_i of the pure IL as reference. The chemical shift at the composition was subtracted from the chemical shift $\delta_{pure\ IL}$ reference, as it is shown in (Eq. 39) below. This change is called absolute chemical shift and is noted as $\Delta\delta_i$.

(Eq. 39)

$$\Delta\delta_i = \delta_{mixture} - \delta_{pure\ IL}$$

$\Delta\delta_i$ being the absolute chemical shift taken from the distance between the chemical shift δ_i of a mixture composition and the chemical shift of the pure IL for each peaks.

The data is also shown as graphs using only the chemical shift for the mixture at 5 mol% IL in water and of the pure IL as shown (Eq. 40) and (Eq. 41),since this provides direct information about the water effect on the IL at high dilution.

(Eq. 40)

$$Absolute\ change = \delta_{5mol\%IL} - \delta_{pure\ IL}$$

(Eq. 41)

$$Relative\ change = (\delta_{5mol\%IL} - \delta_{pure\ IL})/\ \delta_{pure\ IL}$$

With $\delta 1$ representing the shift data for the mixture of 5% IL in water and $\delta 2$ representing the shift data for the pure IL.

4.2.1   Cation/anion interactions of the pure ILs

By analysing the chemical shifts of the pure IL, it is possible to evaluate which of the three ionic liquids studied in this work has the strongest cation/anion interactions. Indeed, the chemical shift of the proton in position 1 reveals a stronger interaction with the anion in the following order: $[C_2MIm][CH_3CO_2]$ (δ_{H1}=10.27ppm) < $[C_2MIm][C_3H_7CO_2]$ (δ_{H1}=10.37ppm) < $[C_2MIm][C_7H_{15}CO_2]$ (δ_{H1}=10.43ppm) detailed in the Table 4-8. In fact, as it was explained in the introduction chapter, the higher the chemical shift value, the stronger are the interactions from the atom targeted with its environment (intra- or inter-molecular interactions).

From those observed values, there is clearly a downfield shift of H1 observable while increasing the alkyl carbon chain length of the anion. However, there is no difference in terms of the strength of interaction at the proton in position 2(δ_{H3} ~8.23 ppm) and 3 (δ_{H3} ~8.05 ppm). This means that H1 is the only proton from the imidazolium ring affected by the alkyl chain length of the anion.

The carbon chemical shift confirmed the stronger interactions between cation and anion for the octanaote-IL system, which has a larger chemical shift for the peak corresponding to the COO$^-$ group of the anion; $[C_2MIm][CH_3CO_2]$ (δ_C ~173.95 ppm) < $[C_2MIm][C_3H_7CO_2]$ (δ_C ~175.96 ppm) < $[C_2MIm][C_7H_{15}CO_2]$ (δ_C ~175.43 ppm). The three carbons from the cation ring show the same chemical shifts and therefore there seems to be no influence of the anion alkyl chain lengths on the strength of interactions.
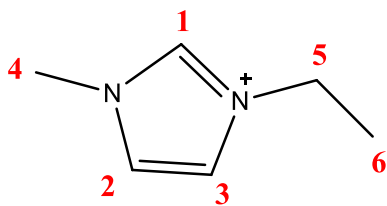
Figure 4-5. Imidazolium cation numbered

Table 4-8. Imidazolium ring chemical shifts of H1, H2, H3 and C_{COO-}, C1, C2, C3 for $[C_2MIm][CH_3CO_2]$, $[C_2MIm][C_3H_7CO_2]$ and $[C_2MIm][C_3H_7CO_2]$.

(in ppm)	$[C_2MIm][CH_3CO_2]$	$[C_2MIm][C_3H_7CO_2]$	$[C_2MIm][C_3H_7CO_2]$
δH1	10.27	10.37	10.43
δH2	8.23	8.23	8.24
δH3	8.05	8.03	8.06
δC$_{COO-}$	173.95	175.96	175.43
δC1	137.35	137.64	136.98
δC2	123.12	123.20	122.47
δC3	121.68	121.85	121.10

4.2.2 Interactions of $[C_2MIm][CH_3CO_2]$ with water

In the following parts, the interaction between anion/water, water/water and cation/anion, will be described for each IL. Below, the chemical structure of the $[C_2MIm][CH_3CO_2]$-IL is drawn (Figure 4-6). The imidazolium cation is labelled from 1 to 6 (in red) and the anion from a to b (in blue). Those labels will be used to refer to the proton (H) or carbon (C) positions studied.
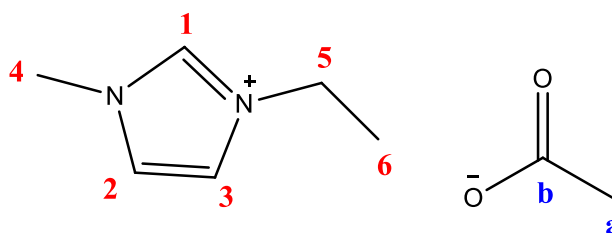
Figure 4-6. Chemical structure labelling for $[C_2MIm][CH_3CO_2]$, 1-ethyl-3-methyl-imidazolium acetate.

By directly comparing the spectra of the pure $[C_2MIm][CH_3CO_2]$-IL and the most diluted IL-solution at 5 mol% IL fraction, it is clear that water molecules are changing the interactions in the pure IL, as it is shown in the Figure 4-7 below. An upfield shift is clearly observed for H1, H2 and H3 of the imidazolium ring, while a downfield shift is observed for H6 and Ha of the methyl group, which has the longest distance to the more electronegative atoms N or O. Those results were already observed, as it was detailed in the above review and in the introduction chapter.[25,28,125,166,167] Thus, it is worth investigating the water effect on this IL in more detail to first support these results according to the literature and then

apply the same strategy to investigate the influence of the alkyl chain lengths of the anion with water.
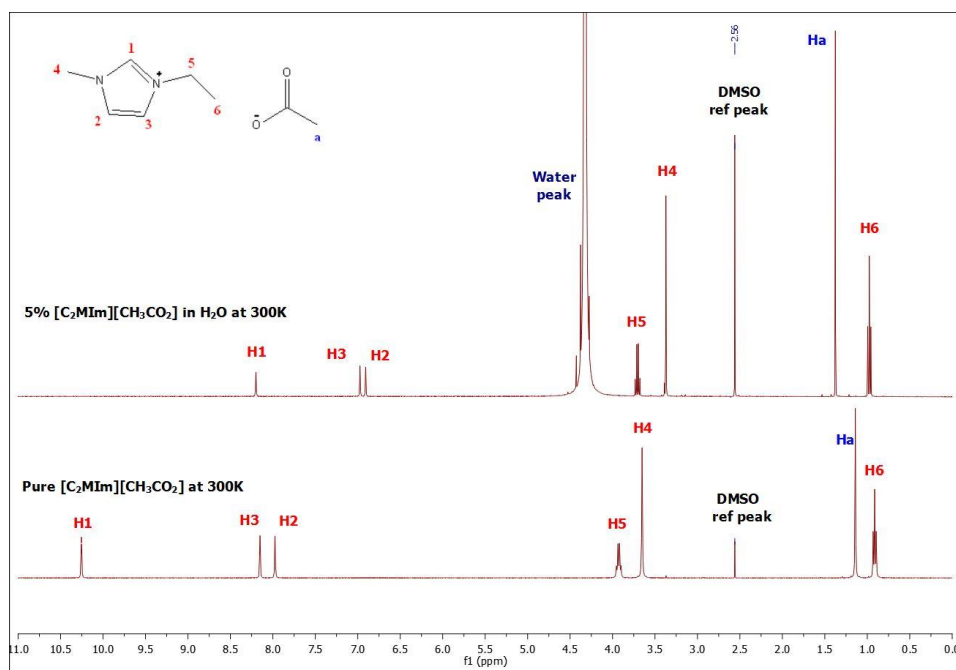
Figure 4-7. ¹H NMR spectrum of pure [C₂MIm][CH₃CO₂] (down) and 5% mole fraction of [C₂MIm][CH₃CO₂] in H₂O (up) using a DMSO capillary at 300K.
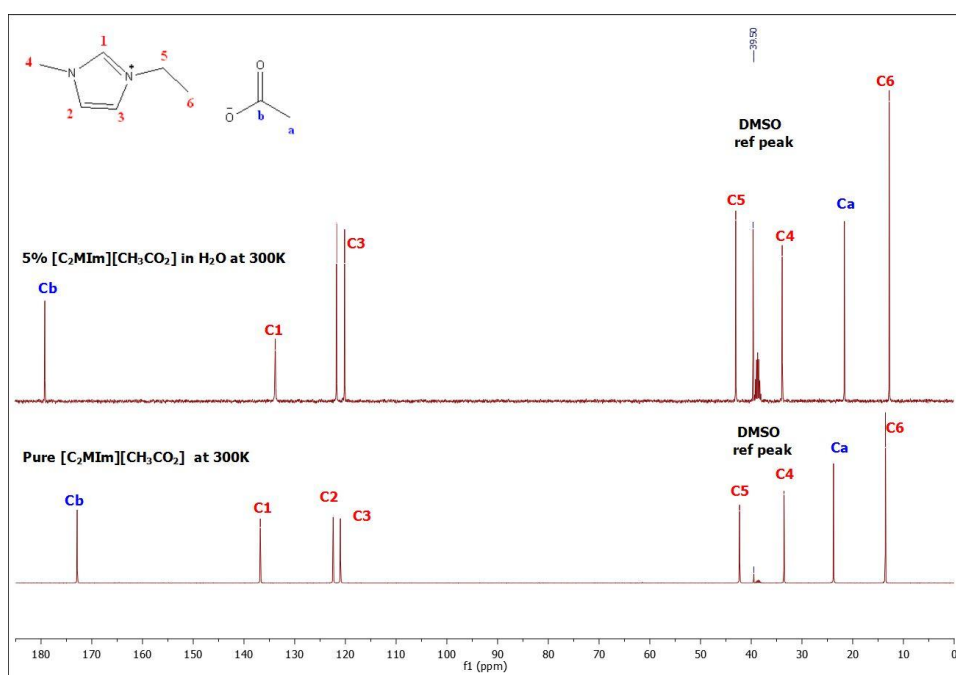
Figure 4-8. ¹³C NMR spectrum of pure [C₂MIm][CH₃CO₂] (down) and 5% mole fraction of [C₂MIm][CH₃CO₂] in H₂O (up) using a DMSO capillary at 300K.

4.2.2.1 ^{1}H and ^{13}C-NMR chemical shifts at each composition

The two graphs below are showing the ^{1}H and ^{13}C-NMR chemical shifts of IL and water binary mixtures in function of the ionic liquid mole fraction. In total, seven mixtures were analysed and are represented by a filled-circle in the graphs in

Figure 4-9. All circles are connected to each other with a non-statistical line as a guide for the eye.
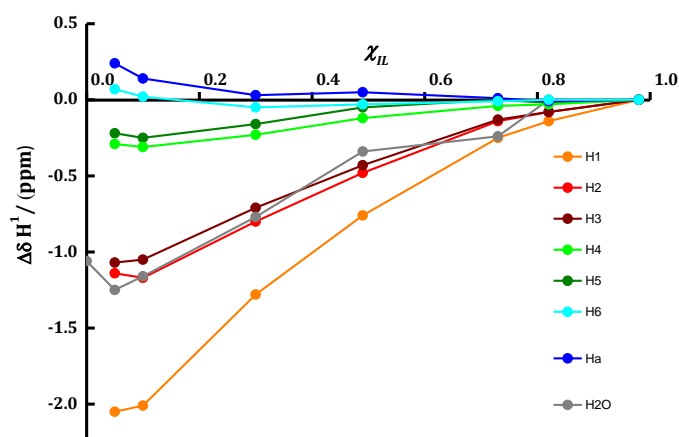
Figure 4-9. $\Delta\delta^1$H at 300K versus mole fraction of ionic liquid for the various [C$_2$MIm][CH$_3$CO$_2$] resonances (1 to a) (FIG. 1); H1 (orange), H2 (red), H3 (wine), H4 (green), H5 (olive), H6 (Cyan), Ha (blue), and water resonance; H$_2$O (grey). The lines are only a guide for the eye.

Figure 4-10. $\Delta\delta^{13}C$ at 300K versus mole fraction of ionic liquid for the various $[C_2MIm][CH_3CO_2]$ resonances (1 to b) (FIG. 1); C1 (orange), C2 (red), C3 (wine), C4 (green), C5 (olive), C6 (Cyan), Ha (blue), Hb (royal). The lines are given as a guide to the eye.

4.2.2.1.1 Cation imidazolium ring (1-2-3)

In this part, the proton H1, H2 and H3 and carbon C1, C2 and C3 of the cation imidazolium ring will be investigated shown in the two

Figure 4-9 and Figure 4-10. All protons and carbons have negative values for their $\Delta\delta$, corresponding to an upfield shift. This shows that the addition of water perturbs the dry $[C_2MIm][CH_3CO_2]$ hydrogen bonding network. The greatest shift is found for the H1 and C1 position (orange lines), which is known to have the most acidic proton on the imidazolium ring.[28] This is in agreement with the literature, where it was found that water molecules are in competition with the IL-anions to be positioned close to position 1.

Furthermore, hydrogen bonds formed between water molecules and position 1 of the IL-cations are much weaker than the one formed between the IL-anion and position 1. However, upon the addition of water, the acetate-anion will leave the ring proton cation, while strong hydrogen bonds will form between the water-anion and water/cation, which leads to an upfield shift.[23] This is confirmed by Cb which is the anion carbon links to the two oxygen atoms (very electro negative atoms). In fact, Cb has a very strong downfield shift while adding water to the dry IL, which shows that acetate anion prefers water molecules to position 1 of the ring cation at high dilution.

4.2.2.1.2   Alkyl adjacent to nitrogen cation atoms (4-5)

In the case of the two alkyl groups adjacent to the nitrogen cation atoms, H4 and H5, seem to exhibit a slight upfield shift after the addition of water. It is becoming more significant from the IL composition at $\square\square$= 0.3. However, it is not as significant than the protons ring discussed earlier. It is also in disagreement with work published by Ries *et al.,* although it is difficult to compare the data, since their graphs are in function of the mass fraction and not in function of the mole fraction as it is reported in this section.[28] However, C4 and C5 are not affected at all by the addition of water, since their shifts stay constant and around zero.

4.2.2.1.3   Methyl groups of both anion and cation alkyl chain length (6-a)

Both methyl groups on both of the alkyl chains of the acetate anion and ethyl-imidazolium cation have both a small downfield shift for H6 and Ha as it was also found in the literature,[28] whereas there is a small upfield shift for C6 and Ca. Therefore, water doesn't seem to interact much with this part of the IL.

4.2.2.1.4   Water molecules behavior

While increasing the water content of the IL, the water peak shows a strong upfield shift. This can be explained because water molecules prefer bonds to the proton in position 1 of the ring cation and also to the anion rather than with other water molecules. Thus, water-water hydrogen bonds are weaker than water-cation and water-anion hydrogen bonds, and it is expected to see a strong upfield shift of the water peak.

4.2.2.2 Absolute and relative change of ^1H & ^{13}C-NMR for pure [C₂MIm][CH₃CO₂] with and without dilution

The four graphs below are showing the absolute and relative change of ^1H and ^{13}C-NMR between the pure [C₂MIm][CH₃CO₂] and its mixtures at high dilution (5% IL mole fraction). In this way it is easier to define the influence of water on each proton and carbon on the molecule since the driest solution is compared to the most diluted solution. Negative and positive values are discussed regarding specific proton and carbon atoms of the system.
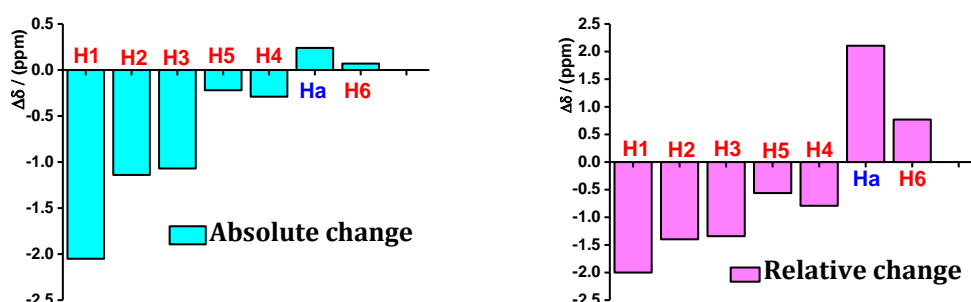
Figure 4-11. Relative change (bottom) and absolute chemical shift change (up) of ^1H NMR spectra for 5% mole fraction of [C₂MIm][CH₃CO₂] in H₂O referred with the pure [C₂MIm][CH₃CO₂] at 300K.
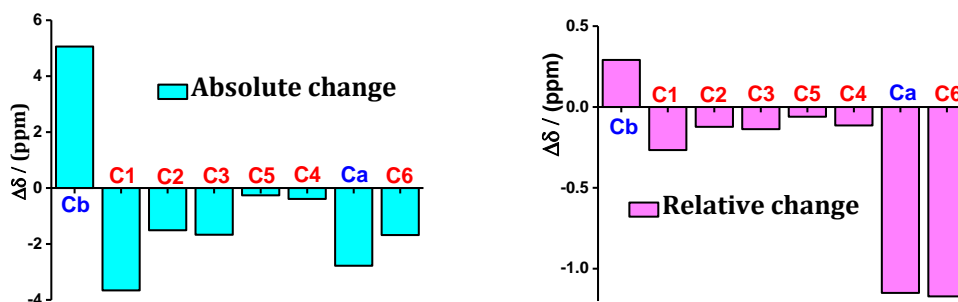
Figure 4-12. Relative change (bottom) and absolute chemical shift change (up) of ^{13}C NMR spectra for 5% mole fraction of [C₂MIm][CH₃CO₂] in H₂O referred with the pure [C₂MIm][CH₃CO₂] at 300K.

4.2.2.2.1 Cation imidazolium ring (1-2-3)

The decrease in the relative and absolute chemical shift in the cation ring (1, 2, 3) of [C₂MIm][CH₃CO₂] suggests that the electron-density of H1, H2, H3, C1, C2 and C3 of the pure [C₂MIm][CH₃CO₂] increases after dilution with water. The electron-density is a measure of probability of an electron which is present at a specific location, around the atom and its bonds. As it was explained by Mu *et al.*, the

overall hydrogen bonding strengths decreases.[25] In fact, after dilution of the IL with water, there is a strong increase in number of hydrogen bonds of water/C123H and a decrease of the hydrogen bonds of anion/C123H. However, hydrogen bonds of anion/C123H being much stronger than hydrogen bonds of water/C123H, negative values are displayed.

4.2.2.2.2 *Alkyl adjacent to nitrogen cation atoms (4-5)*

In the case of the two alkyl groups adjacent to nitrogen atoms, the relative and absolute chemical shift decrease slightly in the case of H4, H5 and C4, C5. The latter suggests that the electron-density of those atoms is increasing while diluting the dry IL with water. However, it doesn't affect those atoms as much as the ring atoms, since their values is near to zero. Mu *et al.* explained those results by a reduction of the total hydrogen bonds due to the increase of hydrogen bonds in water/C67H and the decrease of hydrogen bonds in anion/ C67H.[25]

4.2.2.2.3 *Methyl groups of both anion and cation alkyl chain length (6-a)*

More interestingly, the methyl groups which were found at the largest distance from the cation ring (position 6) and the anion (position a) show an increase in the chemical shift for H6 and Ha, while a decrease is observed for C6 and Ca. This suggests that the dilution of the dry IL with water creates a decrease of the electron-density of H6, Ha, and an increase of the electron-density for C6, Ca. According to Mu *et al.,* there is a serious decrease of the total hydrogen bonds with those concerned atoms observed. This fact is due to the new hydrogen-bonding network formed after dilution of the pure IL between water molecules and C6aH atoms, and due to the decrease in hydrogen bonds present in the pure IL between anion/C6aH. Here, hydrogen bonds between anion/C6aH are weaker than the ones formed between water/C6aH.[25]

4.2.3 Interaction of [C₂MIm][C₃H₇CO₂] with water

In the following parts, the interaction between anion/water, water/water and cation/anion, will be described for each IL. Below, the chemical structure of the [C₂MIm][C₃H₇CO₂]-IL is shown (Figure 4-13). The imidazolium cation is labelled from 1 to 6 (in red) and the anion from a to d (in blue). Those labels will be used to refer to either the proton (H) or carbon (C) position studied.
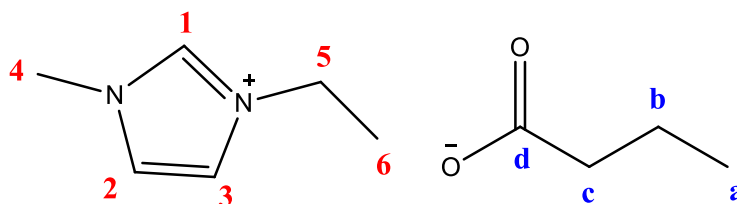

Figure 4-13. Chemical structure of [C₂MIm][C₃H₇CO₂], 1-ethyl-3-methyl-imidazolium butanaote with the carbon resonances labelled (1 to d).

It was possible to dilute the IL and still see a signal in the NMR up to a concentration of 1 mol% of IL in water. The comparison of the ^{1}H and ^{13}C-NMR spectra of the pure [C₂MIm][C₃H₇CO₂]-IL and its highly diluted mixtures at 1 mol% can be seen below.
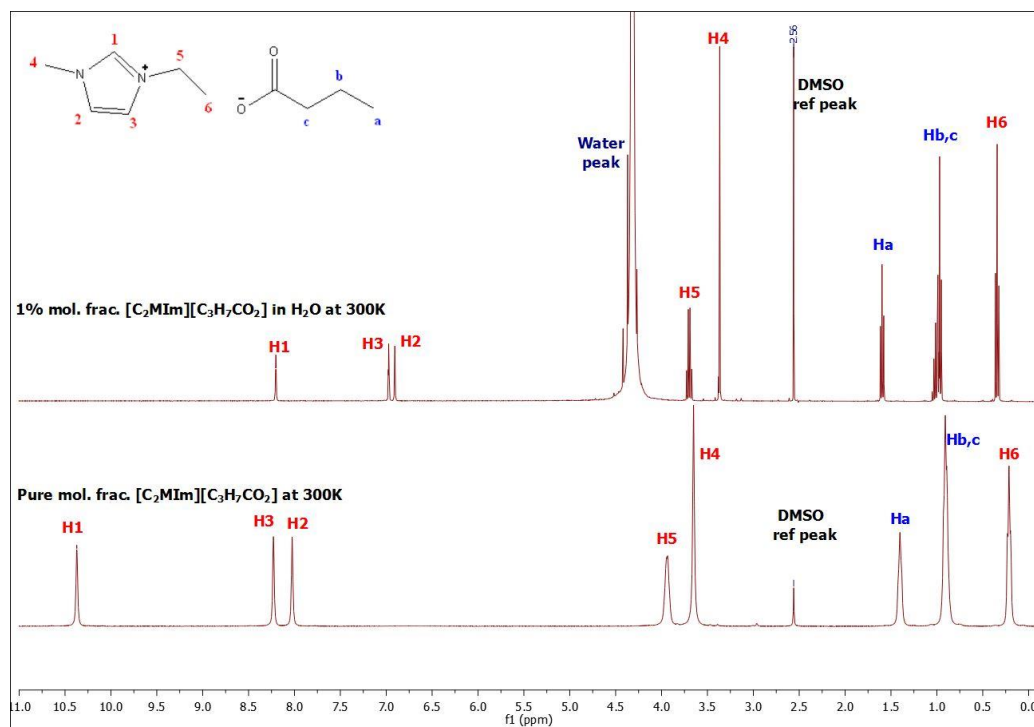
Figure 4-14. ^{1}H NMR spectrum of pure [C₂MIm][C₃H₇CO₂] (down) and 1% mole fraction of [C₂MIm] [C₃H₇CO₂] in H₂O (up), using DMSO capillary at 300K.
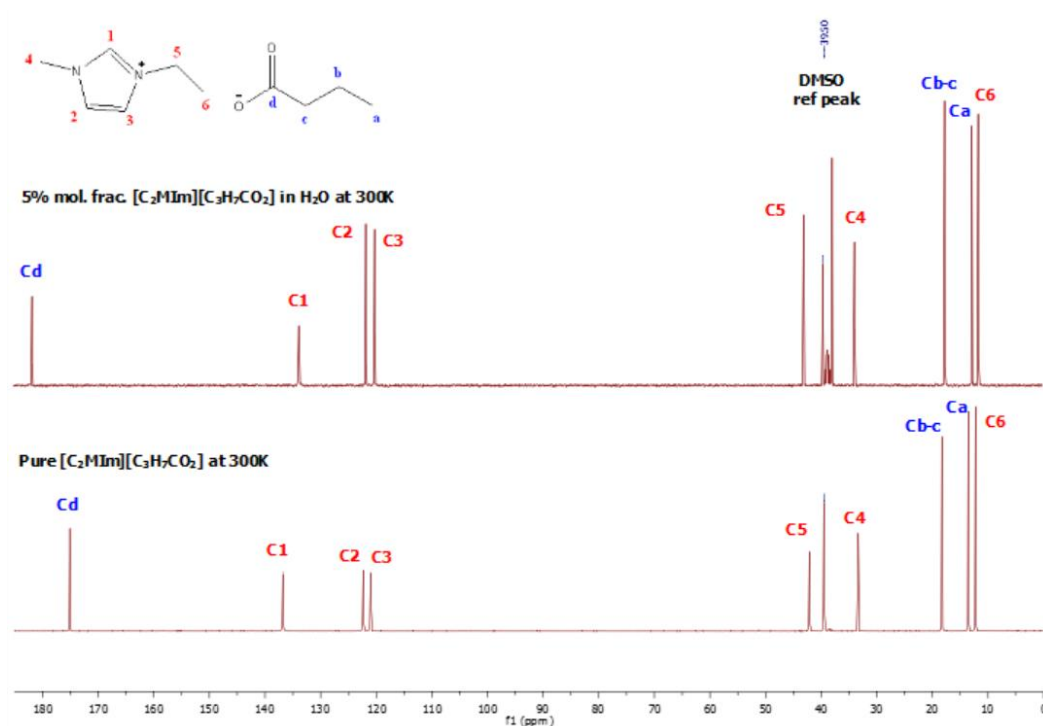
Figure 4-15. ^{13}C NMR spectrum of pure [C$_2$MIm][C$_3$H$_7$CO$_2$] (down) and 5% mole fraction of [C$_2$MIm] [C$_3$H$_7$CO$_2$] in H$_2$O (up), using DMSO capillary at 300K.

4.2.3.1 ^{1}H and ^{13}C-NMR chemical shifts at each composition

The two graphs below are showing the ^{1}H and ^{13}C-NMR chemical shifts of the IL and water binary mixtures in function of the ionic liquid mole fraction, as shown previously.
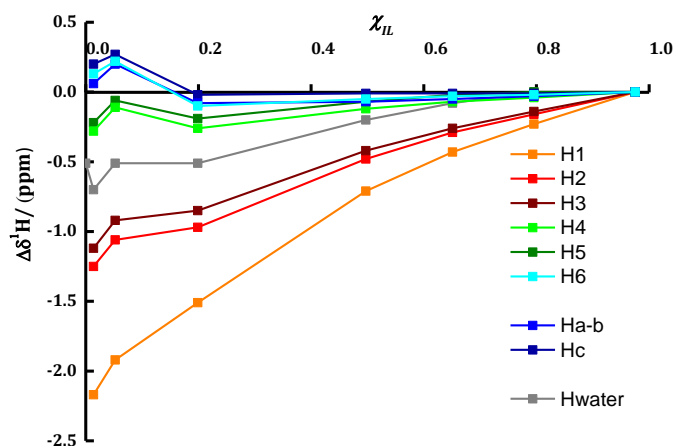
Figure 4-16. $\Delta\delta^1$H at 300K versus mole fraction of ionic liquid for the various [C$_2$MIm][C$_3$H$_7$CO$_2$] resonances (1 to c) (FIG. 12),); H1 (orange), H2 (red), H3 (wine), H4 (green), H5 (olive), H6 (Cyan), Ha-b (blue), Hc (royal), and water resonance; H$_2$O (grey). The lines are given as a guide to the eye.
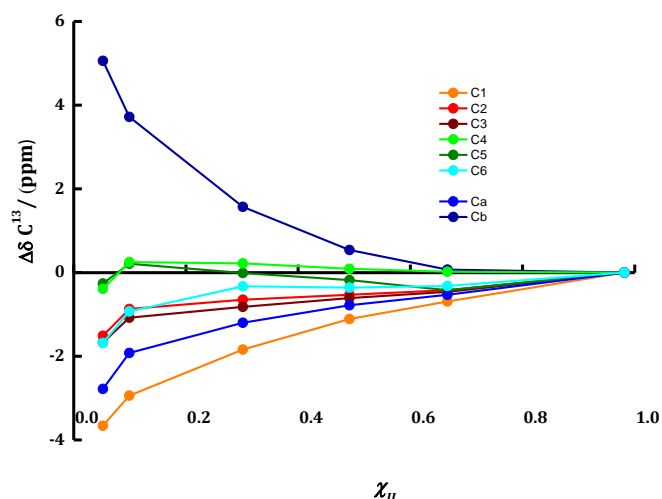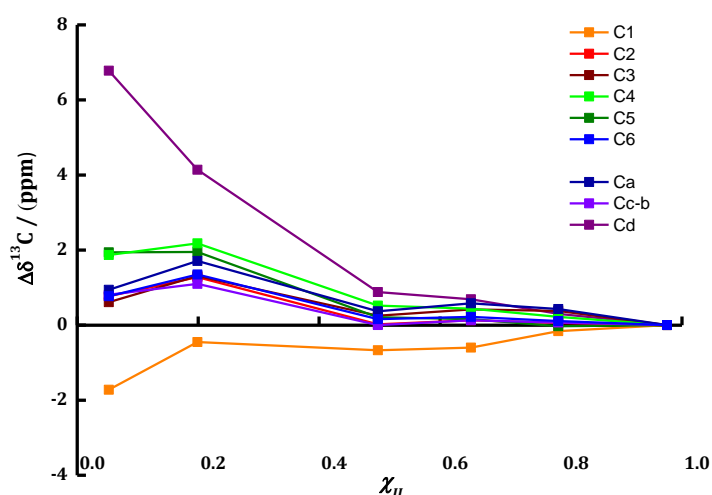
Figure 4-17. $\Delta\delta^{13}C$ at 300K versus mole fraction of ionic liquid for the various $[C_2MIm][C_3H_7CO_2]$ resonances (1 to d) (FIG. 17), C1 (orange), C2 (red), C3 (wine), C4 (green), C5 (olive), C6 (Cyan), Ca (blue), Cb (royal), Cc (violet), Cd (purple),. The lines are given as a guide to the eye.

4.2.3.1.1 Cation imidazolium ring (1-2-3)

As for the acetate anion, the protons of the cation imidazolium ring (H1, H2, H3) have negative values of their $\Delta\delta$, corresponding to an upfield shift. Again, $\Delta\delta$ is very strong in the case of H1 for the same reason explained for the acetate anion. In fact, when the water concentration increases, the butanoate-anion will leave the ring proton cation, while strong hydrogen bonds will form between the water-anion and water/cation.

This is confirmed by Cd (similar carbon than Cb on the acetate anion) that has a strong downfield shift, which shows that butanoate anions prefer water molecules to position 1 of the ring cation at high dilution, as it was also found for the acetate anion.

However, for C1, C2 and C3 an upfield shift is found only for the pure IL to a 20 mol% mole IL fraction, while it turns into a downfield shift from 20 to 5 mol%. This may indicate that both cation and anion are becoming fully dissociated in the case of the butanoate anion from 20 mol% to more diluted solutions.

134

4.2.3.1.2 Alkyl adjacent to nitrogen cation atoms (4-5)

In the case of the alkyl groups adjacent to the nitrogen cation atoms, H4 and H5 seem to show a slight upfield shift due to the addition of water. However, a downfield shift is observed for C4 and C5, with a very strong downfield shift for C4, the methyl group just beside the nitrogen ring atom. Therefore, when adding water to the pure $[C_2MIm][C_3H_7CO_2]$, a new hydrogen bonding network is formed between water/C4; whereas this part was not affected by water in the case of the acetate anion-IL.

4.2.3.1.3 Methyl groups of both anion and cation alkyl chain length (6-a)

Both methyl groups of the butanoate anion and the ethyl part of the cation show only a weak downfield shift for H6, Ha, and for C6, Ca; a weak upfield shift from the pure to 20 mol% IL mole fraction was observed, while it turns into a downfield shift from 20 to 5 mol%. Therefore, water doesn't seem to interact much with this part of the IL.

4.2.3.1.4 Water molecules behavior

Increasing the water concentration within the pure IL displays a strong upfield shift of the water peak for the same reasons as explained for the acetate system.

The four graphs below are showing the absolute and relative change of ^1H and ^{13}C-NMR between the pure $[C_2MIm][C_3H_7CO_2]$ and its mixtures at high dilution (1% IL mole fraction). Negative and positive values regarding specific proton and carbon atoms of the system can be discussed in the same way as for the acetate system.
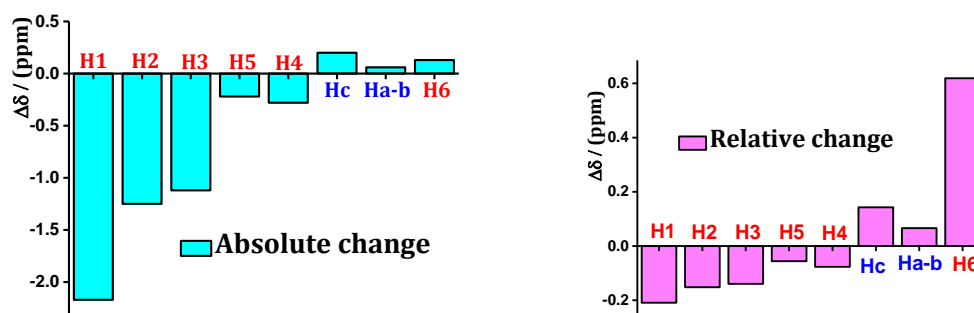
Figure 4-18. Relative change (bottom) and Absolute chemical shift change (up) of ^1H NMR spectra for 1% mole fraction of $[C_2MIm][C_3H_7CO_2]$ in H_2O referred with the pure $[C_2MIm][C_3H_7CO_2]$ at 300K.
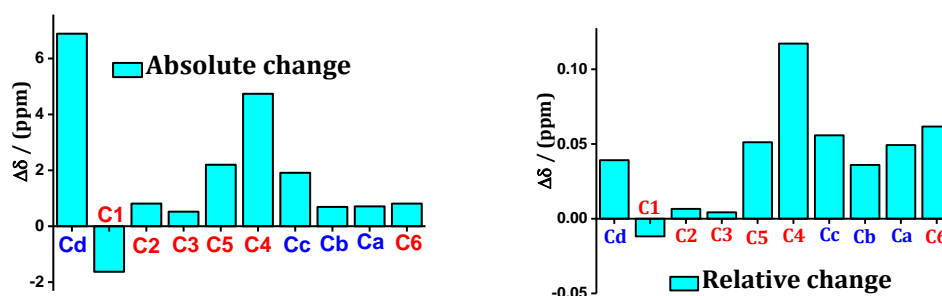
Figure 4-19. Relative change (bottom) and Absolute chemical shift change (up) of ^{13}C NMR spectra for 5% mole fraction of $[C_2MIm][C_3H_7CO_2]$ in H_2O referred with the pure $[C_2MIm][C_3H_7CO_2]$ at 300K.

4.2.3.2.1 Cation imidazolium ring (1-2-3)

The decrease in the relative and absolute chemical shift in the cationic ring (1, 2, 3) of $[C_2MIm][C_3H_7CO_2]$ suggests that the electron-density of H1, H2, H3 and C1 increases after dilution with water in comparison to the pure $[C_2MIm][C_3H_7CO_2]$. The same is observed for the acetate system; position 1 of the system is the one

showing the most significant change. However, a weak increase is found for C2 and C3 in both, relative and absolute chemical shifts (upfield or downfield?), which suggests a slight increase of their electron-density.

4.2.3.2.2 *Alkyl adjacent to nitrogen cation atoms (4-5)*

For the two alkyl groups adjacent to nitrogen atoms, it was found that the relative and absolute chemical shifts decrease slightly in the case of H4, H5, while these increase strongly for C4, C5. This suggests that the electron-density of H4, H5 increases slightly with the dilution of the pure IL; while it decreases strongly for C4, C5.

4.2.3.2.3 *Methyl groups of both anion and cation alkyl chain length (6-a)*

Furthermore, the methyl groups found at the longest distance from the cation ring (position 6) and the anion (position a) show a strong increase of the relative and absolute chemical shift of both, the proton and carbon, especially for the H6 position. This suggests a decrease of the electron-density of H6, Ha, C6, Ca atoms.

4.2.4 Interactions of [C₂MIm][C₇H₁₅CO₂] with water

In the following parts, the interaction between anion/water, water/water and cation/anion, will be described for each of the $[C_2MIm]^+$ based ILs. Below, i the chemical structure of the $[C_2MIm][C_7H_{15}CO_2]$-IL is shown (Figure 4-20). The imidazolium cation is labelled from 1 to 6 (in red) and the anion from a to h (in blue). Those labels will be used to refer to either the proton (H) or the carbon (C) position studied.
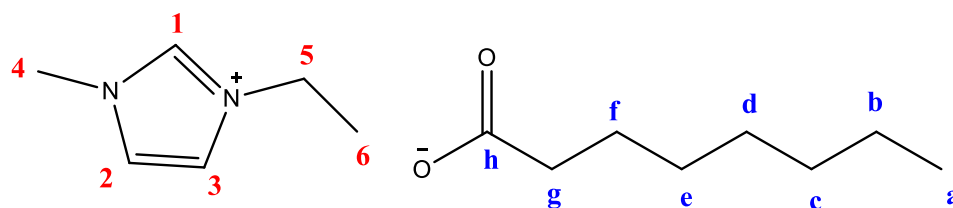
Figure 4-20. Chemical structure of $[C_2MIm][C_7H_{15}CO_2]$, 1-ethyl-3-methyl-imidazolium octanoate with the carbon resonances labelled (1 to h).
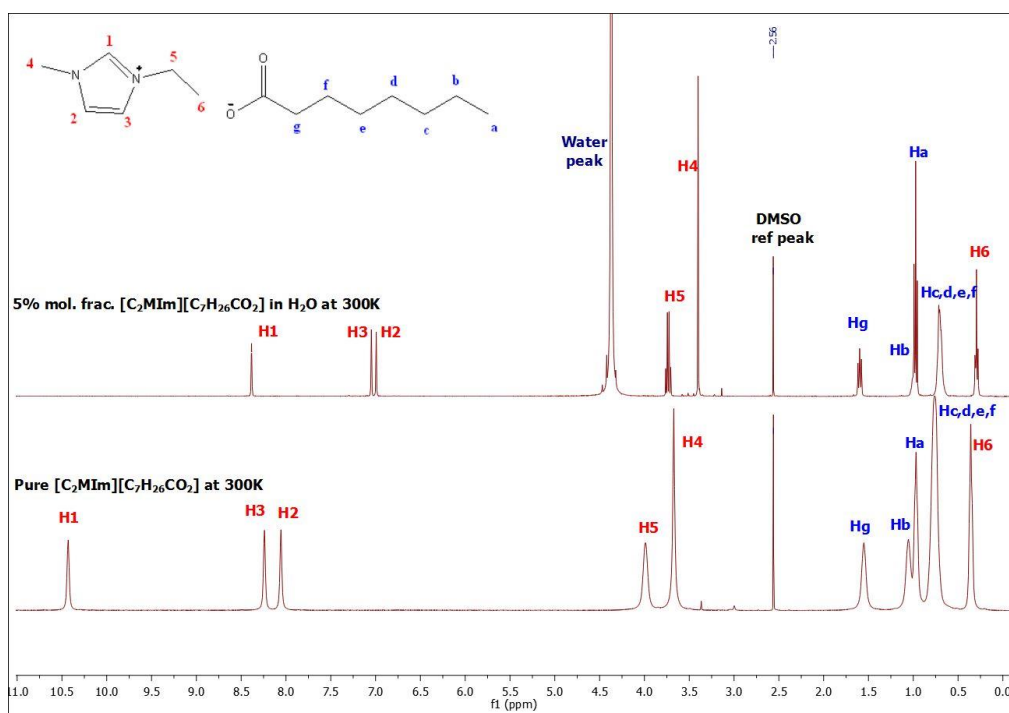
Figure 4-21. ¹H NMR spectrum of pure $[C_2MIm][C_7H_{15}CO_2]$, (down) and 5% mole fraction of $[C_2MIm][C_7H_{15}CO_2]$, in H_2O (up), using DMSO capillary at 300K.
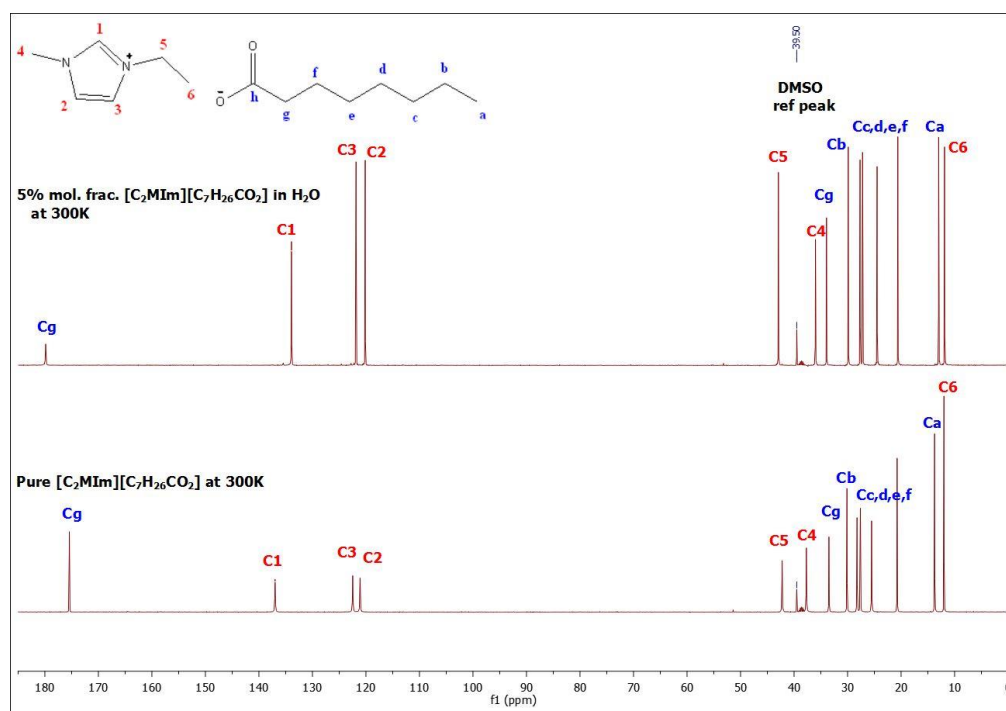
Figure 4-22. ^{13}C NMR spectrum of pure [C$_2$MIm][C$_7$H$_{15}$CO$_2$], (down) and 5% mole fraction of [C$_2$MIm][C$_7$H$_{15}$CO$_2$], in H$_2$O (up), using DMSO capillary at 300K.

4.2.4.1 ^{1}H and ^{13}C-NMR chemical shifts at each composition

The two graphs below are showing the ^{1}H and ^{13}C-NMR chemical shifts of IL and water binary mixtures in function of the ionic liquid mole fraction, as it was described for the ILs with acetate and butanoate anions.
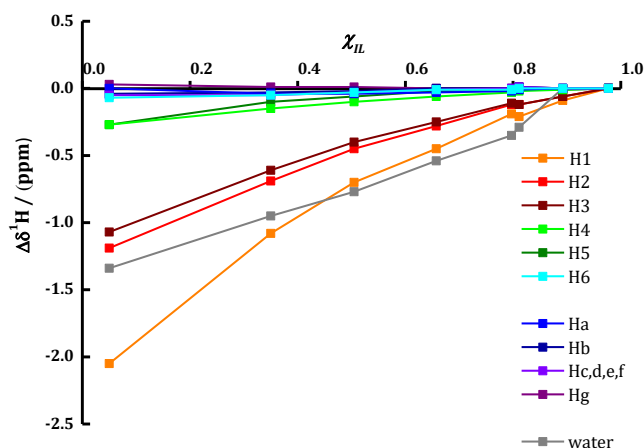
Figure 4-23. Δδ^{1}H at 300K versus mole fraction of ionic liquid for the various [C$_2$MIm][C$_7$H$_{15}$CO$_2$], resonances (1 to g) (FIG. 21); H1 (orange), H2 (red), H3 (wine), H4 (green), H5 (olive), H6 (Cyan), Ha (blue), Hb (royal), Hc,d,e,f (violet), Hg (purple) and water resonance; H$_2$O (grey). The lines are given as a guide to the eye.

139
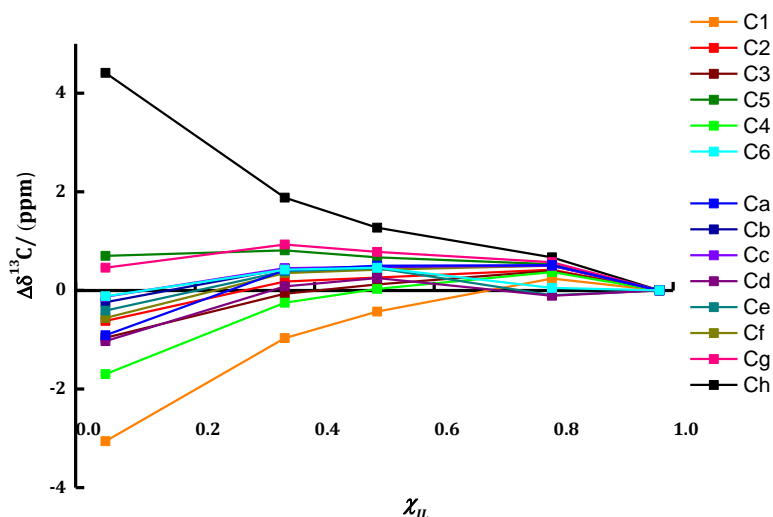
Figure 4-24. $\Delta\delta^{13}C$ at 300K versus mole fraction of ionic liquid for the various $[C_2MIm][C_7H_{15}CO_2]$, resonances (1 to h) (FIG. 25); C1 (orange), C2 (red), C3 (wine), C4 (green), C5 (olive), C6 (Cyan), Ca (blue), Cb (royal), Cc (violet), Cd (purple), Ce (dark-cyan), Cf (dark yellow), Cg (pink), Ch (black). The lines are given as a guide to the eye.

4.2.4.1.1 Cation imidazolium ring (1-2-3)

The protons of the cation imidazolium ring (H1, H2, H3 and C1) have negative values of their $\Delta\delta$, corresponding to an upfield shift. Again, $\Delta\delta$ is very strong in the case of H1 for the same reason as explained for the acetate anion.

In fact, when the water concentration increases, the octanoate-anion will leave the ring proton cation, while strong hydrogen bonds will form between the water-anion and water/cation. This is confirmed by Ch (similar atom than Cb on the acetate anion) that has a strong downfield shift, which shows that octanoate-anions prefer water molecules to position 1 of the ring cation at high dilution as it was also found for the acetate anion.

However, a small downfield shift is found for C2 that was never found for both, acetate and butanoate, where both were upfield shifts for C2.

4.2.4.1.2 Alkyl adjacent to nitrogen cation atoms (4-5)

In the case of the alkyl groups adjacent to the nitrogen cation atoms, H4, C4 and H5 seem to show a slight upfield shift after the addition of water. However, there

is a downfield shift found for the C5 and C4 atoms, whereas there is an upfield shift for C4 from a mole fraction (IL) of 0.30 to more diluted solutions.

4.2.4.1.3 Methyl groups of both anion and cation alkyl chain length (6-a)

Both, the alkyl group of the octanoate anion and the ethyl/methyl part of the cation are not affected by the addition of water since no shift are observed. C6 seems also not to be significantly affected by the water addition, since no significant shift is observed, as well as for Ca.

4.2.4.1.4 Water molecules behavior

However, the more water molecules are found in the IL solutions the stronger is the upfield shift. This shows that water will interact strongly with some parts of the IL, such as position 1. However, water doesn't interact strongly with position *a* like it is seen for the acetate anion. But water create strong hydrogen bonds with Ch.

4.2.4.2 *Absolute and Relative change of ^1H & ^{13}C-NMR for [C₂MIm][C₇H₁₅CO₂] with and without dilution*

The four graphs below are showing the absolute and relative change of ^1H and ^{13}C-NMR between the pure [C₂MIm][C₇H₁₅CO₂] and its mixture at high dilution (5% IL mole fraction). Negative and positive values would be discussed regarding specific proton and carbon atoms of the system in the same way as for the acetate and butanoate system.
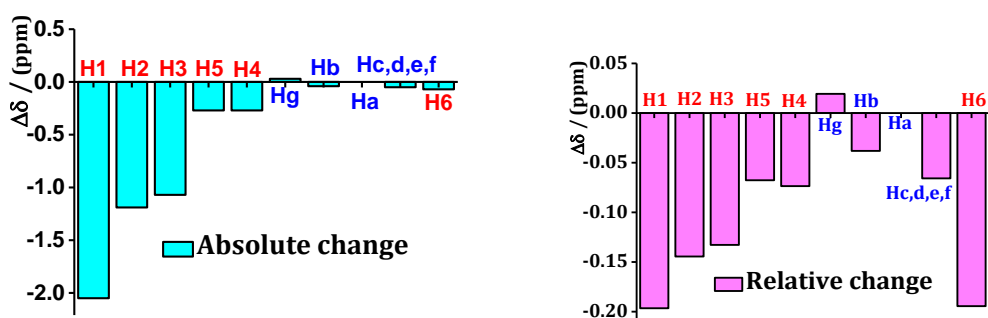
Figure 4-25. Relative change (bottom) and Absolute chemical shift change (up) of ^1H NMR spectra for 5% mole fraction of [C₂MIm][C₇H₁₅CO₂], in H₂O referred with the pure [C₂MIm][C₇H₁₅CO₂], at 300K.
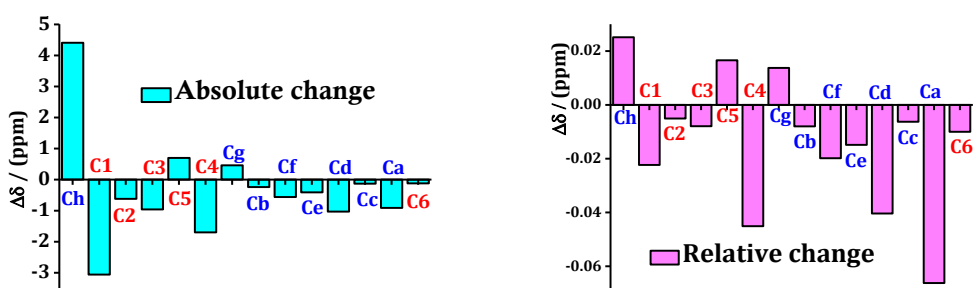
Figure 4-26. Relative change (bottom) and Absolute chemical shift change (up) of ^{13}C NMR spectra for 5% mole fraction of [C₂MIm][C₇H₁₅CO₂], in H₂O referred with the pure [C₂MIm][C₇H₁₅CO₂], at 300K.

4.2.4.2.1 Cation imidazolium ring (1-2-3)

The decrease in the relative and absolute chemical shift in the cation ring (1, 2, 3) of $[C_2MIm][C_7H_{15}CO_2]$ suggests that the electron-density of H1, H2, H3 and C1,C2,C3 of the pure $[C_2MIm][C_7H_{15}CO_2]$ increases after dilution with water. Same as for the acetate system; position 1 of the system is the one having the most significant change.

4.2.4.2.2 Alkyl adjacent to nitrogen cation atoms (4-5)

In the case of the two alkyl groups adjacent to the nitrogen ring atoms, the relative and absolute chemical shift decreases significantly in the case of H4, H5 as well as for C5; whereas it increases strongly for C4. This suggests that the electron-density of H4, H5 , C5 increases slightly with the dilution of the pure IL; while decrease strongly for C4.

4.2.4.2.3 Methyl groups of both anion and cation alkyl chain length (6-a)

Furthermore, the methyl groups found at the longest distance from the cation ring (position 6) and the anion (position a) show a slight increase of the relative and absolute chemical shift of both proton and carbon for H6 and C6 atoms. This suggests a decrease of the electron-density of H6 and C6 atoms.

However, for Ha no shift is observed since its value remains at near zero before and after dilution with water, whereas Ca exhibits a very strong increase of its relative and absolute chemical shift that also suggests a decrease of its electron-density.

4.2.5 Influence of water on the three ILs

A comparison of the water peak for the three ILs is displayed in the graph below. From this graph it is clear that the water peak shows an upfield shift (negative values) for all three ILs, which suggests a strong solvation of ions in presence of water. In fact, the more water is added to the IL, the stronger is the upfield shift. The octanoate-anion is the one which has higher water upfield shift due to its polar headgroup that creates a hydrophobic effect and which exhibits the strongest interaction with water. The latter is supported by the X-ray data in the next part of this chapter.
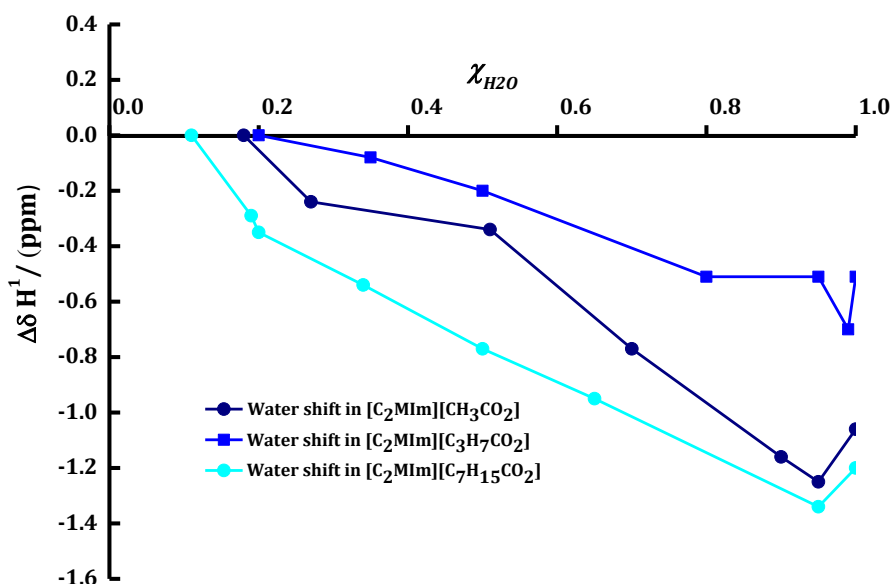
Figure 4-27. $\Delta\delta^1 H$ at 300K versus mole fraction of pure water of the water peak in the respective IL, [C$_2$MIm][CH$_3$CO$_2$] (royal), [C$_2$MIm][C$_3$H$_7$CO$_2$] (blue), [C$_2$MIm][C$_7$H$_{15}$CO$_2$] (cyan).The lines are given as a guide to the eye.

4.2.6 Influence of the anion alkyl chain length in water solutions

Targeting some main atoms, it was possible to draw some interesting comparison between all three carboxylate-ILs to allow a better understanding on the impact of the anion alkyl chain length on the hydrogen bond network. First of all, the main shifted position H1 in the imidazolium ring will be investigated. Then, the carbon linked to the two oxygens in the carboxylate anion and the last methyl group at the end of the anion alkyl chain. And to finish the methyl group

linked to one nitrogen of the imidazolium ring cation. OK, same discussion here as just before.

4.2.6.1   Imidazolium ring H1

The graph in Figure 4-28 below shows the H1 atom shifts in the three IL solutions with water at different composition. Water definitely disturbs the hydrogen bonding network between the anion and the cation at this position. Indeed, water will compete to form hydrogen bonds with H1 atoms in all cases.

However, the upfield shift of H1 found while increasing the water concentration is of the same strength in all three solutions of the ILs. Therefore, the length of the anion alkyl chain has no impact regarding this position and water will interfere in the same way for all three ILs, although the anion alkyl chain length is of different length.
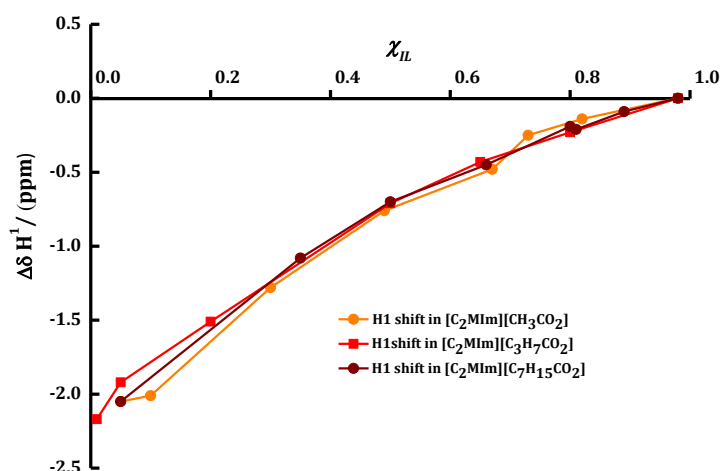
Figure 4-28. $\Delta\delta^1H$ at 300K versus IL mole fraction of H1 atoms from the ring cation in the respective IL, [C$_2$MIm][CH$_3$CO$_2$] (wine), [C$_2$MIm][C$_3$H$_7$CO$_2$] (red), [C$_2$MIm][C$_7$H$_{15}$CO$_2$] (orange).The lines are given as a guide to the eye.

4.2.6.2   Carboxylate anion, position of Cb, Cd and Ch

The graph in Figure 4-29 below shows the carbon shifts linked the carboxylate-function from the three IL solutions with water at different compositions. All three solutions show a strong downfield shift when the water concentration increases. Indeed, the carboxylate carbon is linked to two electronegative oxygen

atoms, and when the water concentration increases, water molecules form hydrogen bonds with the two oxygen atoms of the carboxylate anion. This will lower the electron density at the carboxylate group and therefore deshields its chemical shift value (will have a higher value). Therefore, when adding water to the three IL solutions this will consequently increase their shift values (i.e. Cb pure $[C_2MIm][CH_3CO_2]$ = 173.95 ppm, *vs* Cd in 5 mol% $[C_2MIm][CH_3CO_2]$ = 179.01 ppm).Furthermore, below 0.2 mol% of IL in solutions, water is hardly present in solutions and almost all water molecules are creating hydrogen bonds with the two oxygen atoms of the carboxylate anion. The deshieding will be stronger in the case of the acetate anion, that is probably due to an inductive effect (+I) from the long alkyl chains.
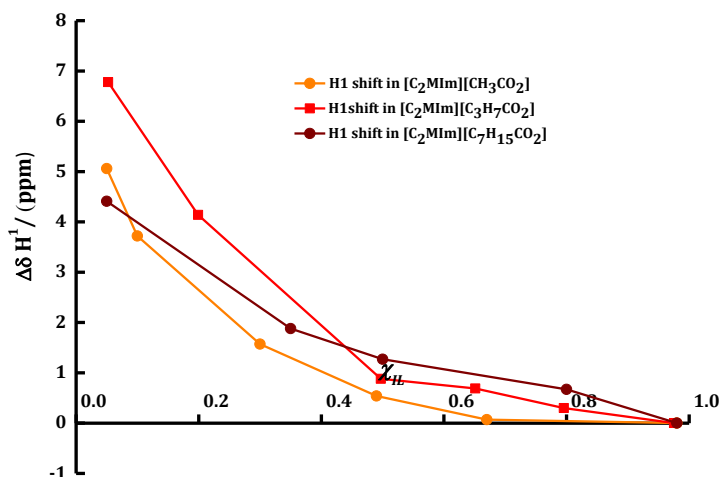
Figure 4-29. $\Delta\delta^{13}C$ at 300K versus IL mole fraction of Cb, Cd and Ch atoms from the carboxylate anion in the respective IL, $[C_2MIm][CH_3CO_2]$ (wine), $[C_2MIm][C_3H_7CO_2]$ (rouge), $[C_2MIm][C_7H_{15}CO_2]$ (orange). The lines are given as a guide to the eye.

4.2.6.3 Imidazolium cation methyl group, C4

The graph in Figure 4-30 below shows the carbon methyl group link to the nitrogen ring cation; C4 from the three IL solutions with water at different composition. The shift behaviour is dramatically different in the case of the butanoate anion, where a strong downfield shift is observed when increasing the water concentration in its IL solution. In the contrary, water doesn't show any

interaction with the position as in the case of the acetate anion, and shows a strong upfield shift from around 0.3 mol% IL in the case of octanaote-anion.
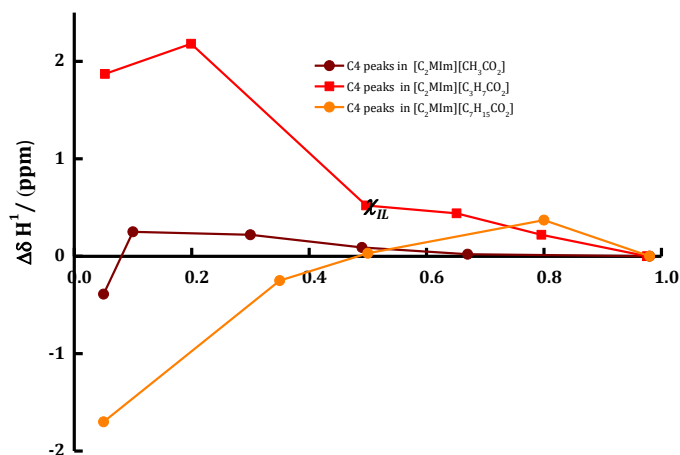
Figure 4-30. $\Delta\delta^{13}C$ at 300K versus IL mole fraction of C4 atoms from the ring cation in the respective IL, $[C_2MIm][CH_3CO_2]$ (wine), $[C_2MIm][C_3H_7CO_2]$ (rouge), $[C_2MIm][C_7H_{15}CO_2]$ (orange).The lines are given as a guide to the eye.

4.2.7   Influence of the temperature

The impact of the temperature in term of interaction was investigated from 300 to 343 K in proton and carbon NMR spectroscopy. However, no significant data were found regarding a change in temperature. The change in temperature from 300 to 343 K in the pure IL and 5 mol% of IL solutions can be found in the appendix L to O.

4.2.8   Conclusion

To conclude, at high dilution (5 mol% of IL solutions); H1, H2, H3 atoms from the ring cation, as well as Cb, Cd, Ch from the carbon carboxylate-anion are getting disturbed in the same way by water addition, even though the anion alkyl chain lengths are different. However, Ca atoms, the last methyl group of all three ILs is disturb by water only in the case of acetate anion, showing that longer anion alkyl chain length (>3) have already a strong self-organisation of hydrogen bond which is harder to disturb for the anions with longer chains. To finish, at high dilutions, all three ILs seems to be fully dissociated, losing their structured hydrogen bond network.

4.3 Intra-and-inter-molecular interactions of IL and water binary mixtures using X-Ray and neutron scatterings

In this work, a series of 1-ethyl-3-methylimidazolium alkanoate (n=2,4 and 8) ILs has been analysed in their neat state and in binary mixture with water, using X-ray scattering, using both, Small Angle X-Ray Scattering (SAXS) (range 0.2 to 1.6 nm^{-1}) and Wide Angle X-Ray Scattering (WAXS) (range 1.6 to 20 nm^{-1}). No pre-peaks were observed at very low Q, whereas two dominant contributions of correlation lengths were present at higher Q in the pure and binary mixtures.

4.3.1 Neutron and X-Ray Instruments

All experiments were carry out at at the Institut Laue-langevin (ILL) in Grenoble in France for the neutron scattering and the European Synchrotron Radiation Facility (ESRF) for the X-Ray scattering.
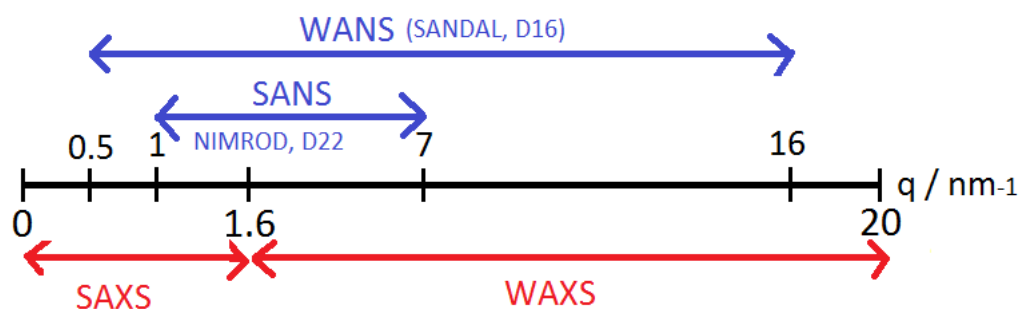
Figure 4-31 : Neutron (blue) and X-ray (red) Scale used for each instruments in this study*.

Legend:

WANS = *Wide Angle Neutron Scattering*

SANS = *Small Angle Neutron Scattering*

WAXS = *Wide Angle X-ray Scattering*

SAXS = *Small Angle X-ray Scattering*

Table 4-9 : Instruments location and name used in this study.

	UK (Didcot)	France (Grenoble)
Neutron pulse name:	**ISIS**	**ILL = Institut Laue-langevin**
SANS, instrument name	NIMROD	D22
WANS, instrument name	SANDAL	D16
X-Ray pulse name:	**STFC (Science & Technology Facilities Council)**	**ESFR (European Synchrotron Radiation Facility)**
SAXS, WAXS, instruments name	*Not used*	D2AM-BM02

These instruments employ diffraction techniques to probe the structure of materials, which can yield information regarding the correlation lengths of intra- and inter-molecular distances. Diffraction data are collected in Q space, as it was reported in the Chapter 1.

Q can easily be converted to real space according to Bragg's law and Q space equation that allows to calculate the inter and intra-molecular disctances.

(Eq. 42)

$$Q \ (/nm^{-1}) = 2\pi \ /d(/nm^{-1})$$

In order to get the absolute intensity ($/cm^{-1}$) of each value, the sample intensities have to be substracted by the intensity of the empty capilary (e) and divided by the capilary diameter (d).

(Eq. 43)

$$\text{Absolute Intensity } (/cm^{-1}) = [I(Q) - I_e(Q)] \ / \ d \ (/cm)$$

Low Q values represent large distances between similar patterns (supramolecular organisations, objects, etc.) and inter-molecular interactions, namely Van der Waals interactions; whereas high Q ones represent small distances, namely intra-molecular interactions and seen as covalent interactions.

4.3.2 Influence of water on the ionic liquid organisation in function of the anion alkyl chain length using X-Ray source

In this section, Wide Angles X-Ray Scattering (WAXS) in the range of 1.6 to 20 nm^{-1} and Small Angles X-Ray Scattering (SAXS) in the range of 0.2 to 1.6 nm^{-1} were used at the European Synchrotron Radiation Facility (ESRF) on the D2AM-BM02 instrument in Grenoble in France, where two significant contributions were observed in the solutions of ILs.

The pure systems which include pure water, and the three ILs [C_2MIm][CH_3CO_2], [C_2MIm][$C_3H_7CO_2$] and [C_2MIm][$C_7H_{15}CO_2$] were first investigated separately to figure out their organisation in their neat form using WAXS. Then, the binary mixtures of IL and water in their entire composition (χ_{IL} = 0.1 to 1) were analysed to obtain information on the role of water in the IL structure and organisation using SAXS and WAXS.

4.3.2.1 Pure systems

Since the systems studied include water and ionic liquid mixtures, it is important to identify the pure water pattern before investigating the pure ILs and then their binary mixtures with water.

The WAXS scattering pattern of pure water presented below shows no relevant correlation lengths at low Q. This means that water molecules have no structured pattern while being on their own in terms of inter-molecular interactions; even though there are lots of hydrogen bonds between hydrogen atoms from one water molecule to oxygen atoms from another water molecule (H---O bond).

However, a high intensity correlation is displayed at 19.963 nm^{-1}, which shows very strong intra-molecular interactions due to strong covalent bonds (H-O-H bonds). This principal peak was also observed at around 20 nm^{-1} using either X-ray or neutron sources.[174,175]
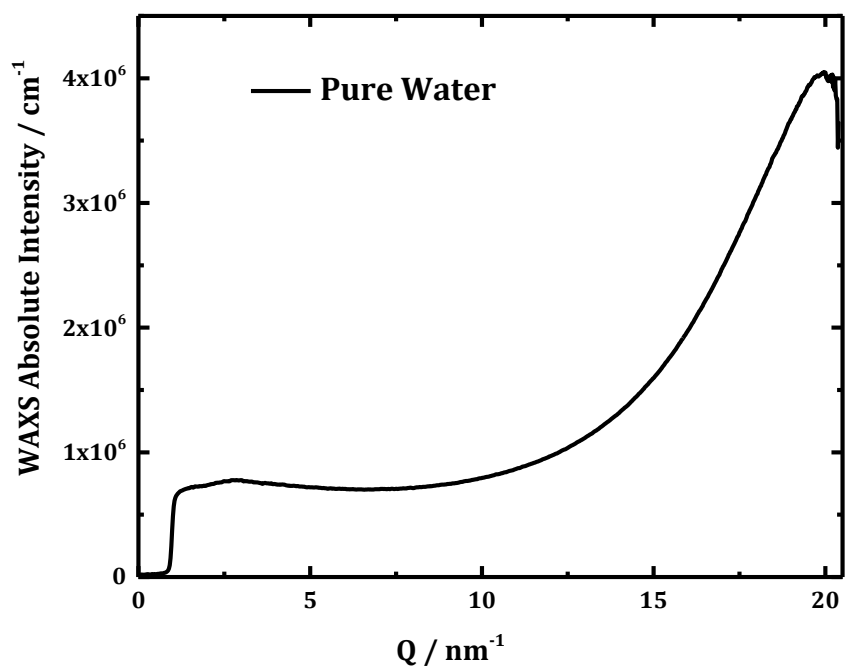
Figure 4-32. WAXS diffraction pattern of the pure water.
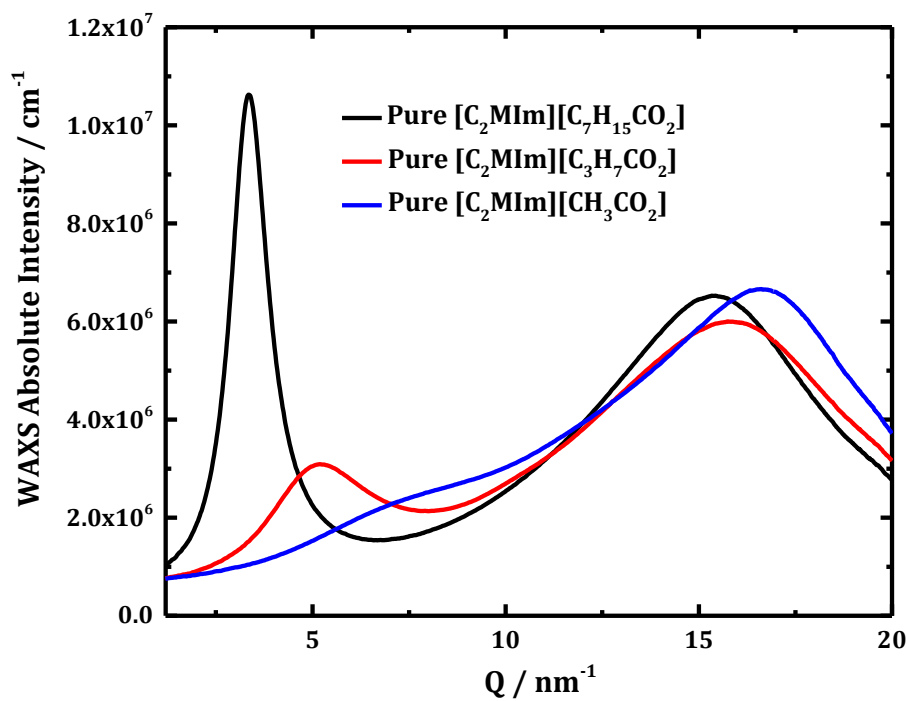
Figure 4-33. WAXS diffraction patterns of the pure ILs, with $[C_2MIm][CH_3CO_2]$ (blue), $[C_2MIm][C_3H_7CO_2]$ (red), and $[C_2MIm][C_7H_{15}CO_2]$ (back).

The three purest ILs ($\chi_{IL} \geq 9$) have been compared to each other on the above WAXS diffraction patterns. The pure [C_2MIm][CH_3CO_2] is showing only one significant contributions (group of several correlations lengths) at 16.62 nm^{-1}. On the contrary pure [C_2MIm][$C_3H_7CO_2$] and pure [C_2MIm][$C_7H_{15}CO_2$] are showing two significant pre-peaks at (5.2 and 3.34) nm^{-1} respectively, and two contributions at (15.75 and 15.43) nm^{-1} respectively.

Those two latter ILs indicate their self-organisation in their neat systems. The differences are seen in q with different positions, lower in the case of the [C_2MIm][$C_7H_{15}CO_2$] than for the [C_2MIm][$C_3H_7CO_2$] respective anions, and in the intensity of the pre-peaks (low Q) which is much more higher in the case of the [C_2MIm][$C_7H_{15}CO_2$] than for the [C_2MIm][$C_3H_7CO_2$] respective anions. The shift toward higher Q in the second contributions show shorter intra-molecular interactions when the anion alkyl chain length is getting shorter.

Since the [C_2MIm][CH_3CO_2] does not show any relevant pre-peaks between 3 and 6 nm^{-1}, and the intensity of this pre-peak is increasing with longer carbon chain lengths, this reveals that this pre-peak at low Q is showing the inter-molecular interactions from the anion alkyl-chain length and its cation. The second contribution seen at high Q is on the contrary showing the intra-molecular interaction between the anion and the cation. Those two contributions have been seen and reported in case of ILs.[29,30]

4.3.2.2   *Ionic liquid and water binary systems*

Small Angles X-Ray Scattering (SAXS) and Wide Angles X-Ray Scattering (WAXS) was performed for the whole composition of the three ILs solutions with water at 25 and 50°C.

4.3.2.2.1   *Inter-molecular interactions using SAXS*

In this section, Small Angles X-Ray Scattering (SAXS) in the range of 0.2 to 1.6 nm^{-1} was used at the European Synchrotron Radiation facility (ESFR) on the D2AM-BM02 instrument in Grenoble in France.

At low Q (range 0.2-1.6 nm^{-1}) it is expected to gain information on the system studied in term of inter-molecular interactions. Here, all the diffraction patterns

of the three ILs weren't showing any correlation lengths that could relate to strong inter-molecular interactions due to addition of water within the pure IL. It is an unexpected result since it has been shown previously in the literature that alkylammonium alkanoate ILs for n [3,4 + 4,3] show two significant correlation lengths at low Q that have been assigned to mesoscopic organisation due to nanoscale segregation.[30]

4.3.2.2.2 Intra and inter-molecular interactions using WAXS

In Figure 4-34 below shows the WAXS diffraction patterns of all three ILs in binary mixture with water measured at 25°C in their all composition from χ_{IL}=0.1 to 1.
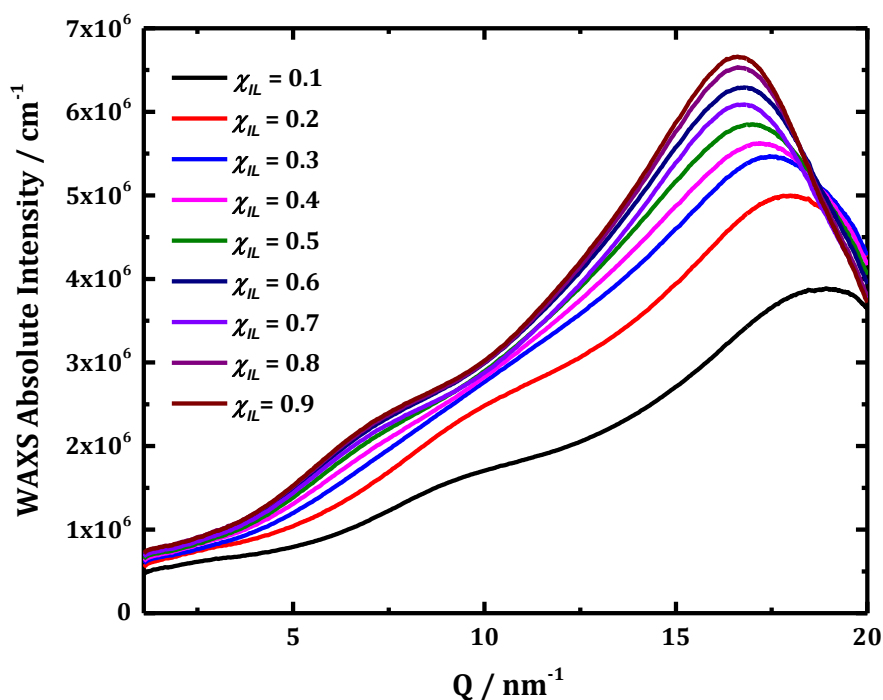
Figure 4-34. [C$_2$MIm][CH$_3$CO$_2$] and water binary mixtures from 0.1 to 1 at 25°C

[C$_2$MIm][CH$_3$CO$_2$] seems to have a better intra-molecular structuration when no water is added to the pure system since the diffraction patterns is showing higher intensity and sharper curves at χ_{IL} = 0.9. When adding water to the pure [C$_2$MIm][CH$_3$CO$_2$], the WAXS diffraction patterns show a decrease in the intensities, as well as a shift towards higher Q. The shift and the decrease of intensity is dramatically observed for χ_{IL}=0.2 and 0.1, thus for the two most

153

diluted samples. Indeed the Q values for the pure IL (χ_{IL}=0.9) and the most diluted mixture (χ_{IL} = 0.1) is 16.62 nm^{-1} and 18.93 nm^{-1} respectively, which shows a significant shift of 2.31 nm^{-1}. In this system the pure and binary system of [C$_2$MIm][CH$_3$CO$_2$], and water doesn't seem to have a strong inter-molecular structure.

Conversely, [C$_2$MIm][C$_3$H$_7$CO$_2$] in binary mixture with water present a structurations' improvement from χ_{IL} = 0.9 to 0.4 since higher intensities at those compositions are displayed. However, the highest intensity is observed for the composition χ_{IL} = 0.7 followed by the one at χ_{IL} = 0.8. This is very significant from the pre-peaks (around 5 nm^{-1}), where no pre-peak is defined at the lower IL concentration for χ_{IL} = 0.1. Under this condition, at high dilution, the IL seems to loose its entire self-organisation. For the second contribution (around 16 nm^{-1}) the Q values have no significant change going from 15.2 to 16.2 nm^{-1} from composition χ_{IL} = 1 to 0.6 respectively; while a dramatic shift is observed from composition χ_{IL} = 0.5 to 0.1 with Q values going from 16.3 to 18.5 nm^{-1}.
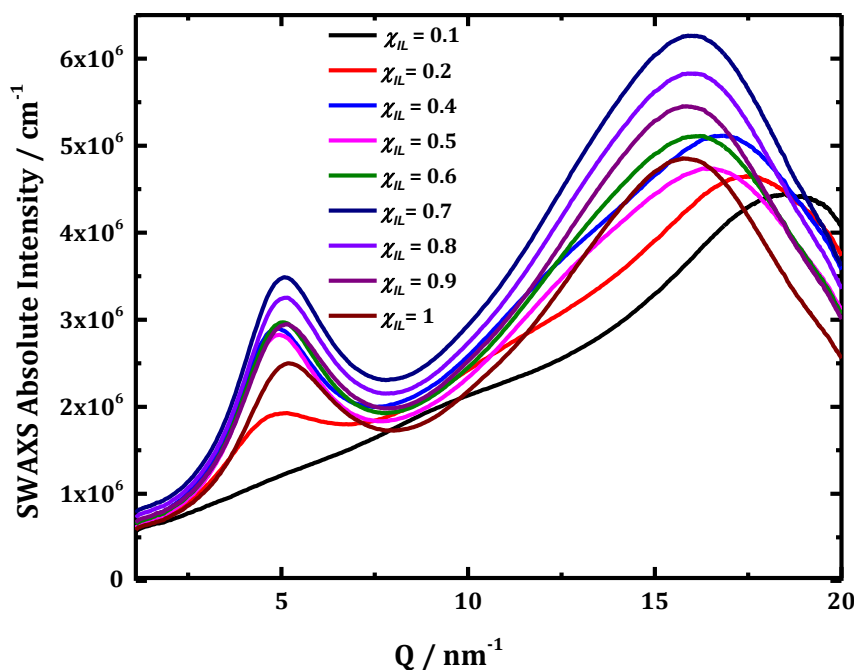
Figure 4-35. [C$_2$MIm][C$_3$H$_7$CO$_2$] and water binary mixtures from 0.1 to 1 at 25℃.

Here the pre-peak has a lower intensity than the second contribution in the [C$_2$MIm][C$_3$H$_7$CO$_2$] IL system and is also lower than [C$_2$MIm][C$_7$H$_{15}$CO$_2$]. However, it can be clearly seen that this IL starts to have an organized structure from χ_{IL}= 0.6 on, whereas below χ_{IL}= 0.6 the IL seems to loose completely its intra-molecular organisation, mostly at high dilution at χ_{IL}= 0.2 ad 0.1.

In the case of [C$_2$MIm][C$_7$H$_{15}$CO$_2$], the presence of water, following the pre-peaks (around 3 nm^{-1}) seems to seriously promote its organisation since the intensity of the pre-peaks increases from χ_{IL} = 1 to 0.2. A compelling shift from high Q to the low Q is also observed when adding water to the pure IL from χ_{IL} = 1 to 0.2. However, the shift is even more distinct towards low Q at composition χ_{IL} = 0.1, while its intensity dramatically decreases.

Since it is observed in the second contribution lengths (around 15 nm^{-1}), diluting the IL to a composition lower than a mole fraction of 0.2 of IL (χ_{IL} < 0.2) seems to significantly disturb the whole systems. Indeed, the intensity is heavily lower at χ_{IL} = 0.1 and its Q value is shifting towards high Q to 16.8 nm^{-1}. However, no relevant shift is observed for the whole composition from χ_{IL} = 0.2 to 1 with a contribution lengths going from 15.8 to 15.4 nm^{-1} respectively.

The pre-peak reveals a more organised structure of the binary mixture at high dilution (χ_{IL} ≤ 0.2), whereas the second contribution shows a decrease of its intra-molecular organisation while increasing the water concentration in the pure IL. Therefore, the pre-peak shows interactions between the alkyl chain length and the water, whereas the second contribution only shows the interaction between the cation and the anion, since the water does not change significantly the value of the second contribution (no compelling shifts observed). Water only affects the cation-anion interactions at high dilution (χ_{IL} ≤ 0.1), where the IL becomes dissociated into individual ions.

155
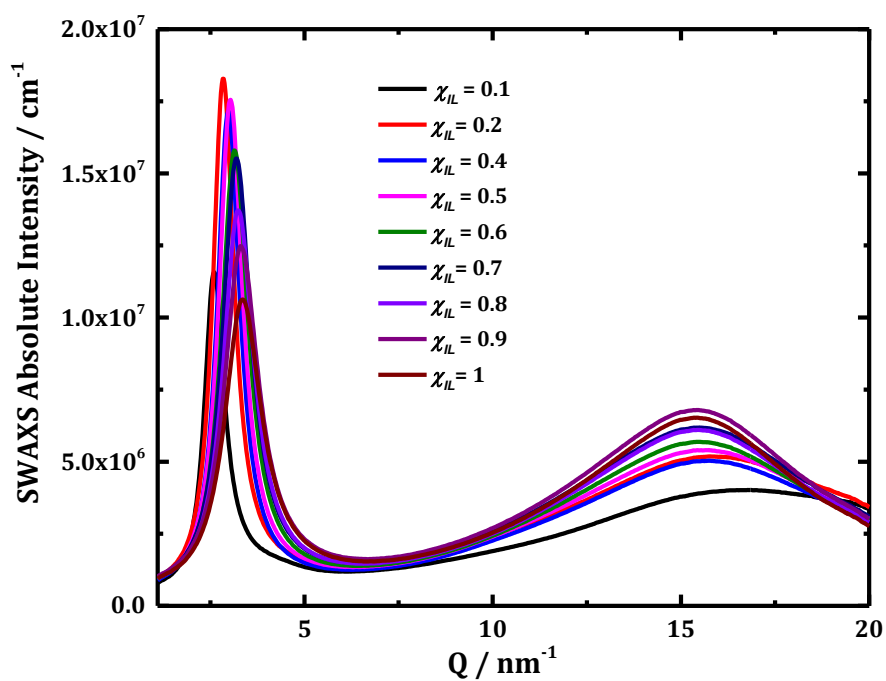
Figure 4-36. [C₂MIm][C₇H₁₅CO₂] and water binary mixtures from 0.1 to 1 at 25°C.
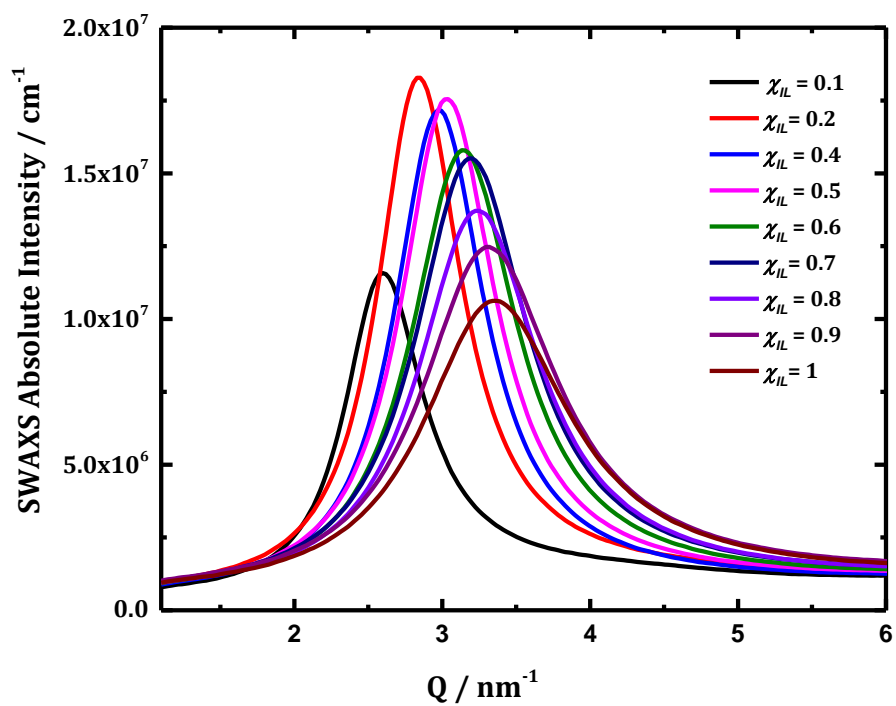
Figure 4-37. ZOOM [C₂MIm][C₇H₁₅CO₂] and water binary mixtures from 0.1 to 1 at 25°C.

4.3.3 Impact of the anion alkyl chain length

The effect of water addition on the three distinct scattering pattern of the ionic liquids [C$_2$MIm][CH$_3$CO$_2$], [C$_2$MIm][C$_3$H$_7$CO$_2$] and [C$_2$MIm][C$_7$H$_{15}$CO$_2$] is shown Figure 4-38 and Figure 4-39 where the Q position of the pre-peaks and the high Q contributions are plotted versus the ionic liquid mole fraction χ_{IL}.
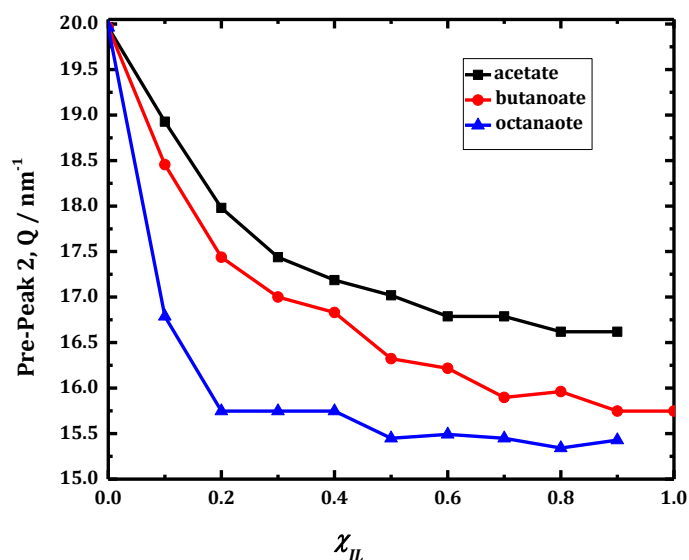
Figure 4-38. Position of the second contribution values for [C$_2$MIm][CH$_3$CO$_2$] (black), [C$_2$MIm][C$_3$H$_7$CO$_2$] (red) and [C$_2$MIm][C$_7$H$_{15}$CO$_2$] (blue), vs. IL mole fraction, χ_{IL}.
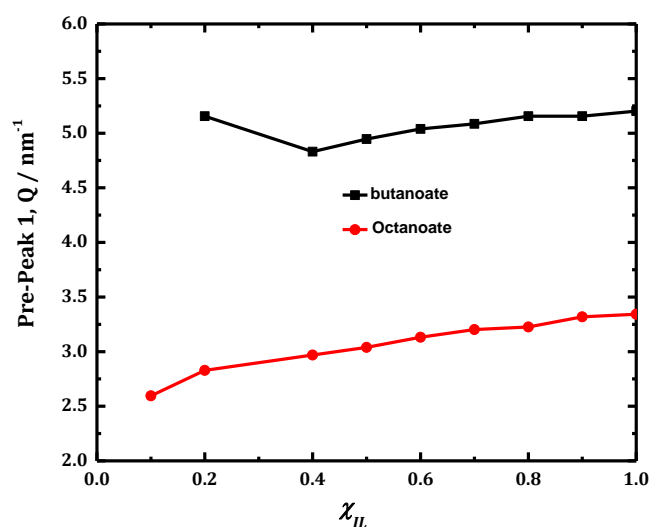
Figure 4-39. Position of the pre-peak Q values for [C$_2$MIm][C$_3$H$_7$CO$_2$] (black) and [C$_2$MIm][C$_7$H$_{15}$CO$_2$] (red), vs. IL mole fraction, χ_{IL}.

In the second contribution (around 16 nm^{-1}), (Figure 4-38) the intensity is about the same for the three pure ILs, which means that the intra-molecular interactions are not affected by the size of the anion alkyl chain length. However, the shorter the anion alkyl chain length, the higher is the Q value; respectively, the Q values show 15.43 nm^{-1} (d = 0.41 nm), 15.75 nm^{-1} (d = 0.40 nm) and 16.62 nm^{-1} (d = 0.38 nm) for the pure [C$_2$MIm][C$_7$H$_{15}$CO$_2$], [C$_2$MIm][C$_3$H$_7$CO$_2$] and [C$_2$MIm][CH$_3$CO$_2$] ILs. In terms the of intra-molecular distances, these are shorter (higher Q value) for shorter anion alkyl chain lengths, which is in agreement with the anion structure. This peak has been assigned to represent the ion-ion contact.[30]

When the concentration of water increases, a shift of the second contribution towards high Q is observed. This is showing that IL structural distances with water are getting shorter while the water concentration is increasing. Indeed, the principal peak of pure water is around 20 nm^{-1},[174,175] and therefore, by mixing the pure IL with pure water it is expected that the Q value would move towards the pure water Q value.

Concerning the pre-peak (around 4 nm^{-1}), (Figure 4-39) the intensity increases and the peaks move towards low Q values while the number of carbons in the anion alkyl chain increases. In fact, in the pure [C$_2$MIm][C$_3$H$_7$CO$_2$] and [C$_2$MIm][C$_7$H$_{15}$CO$_2$]-IL, the respective Q values of the pre-peak are 5.20 nm^{-1} (d = 1.21 nm) and 3.34 nm^{-1} (d = 1.88 nm). The [C$_7$H$_{15}$CO$_2$]$^-$ anion shows much stronger inter-molecular interactions than the [C$_3$H$_7$CO$_2$]$^-$ anion due to the increase of *van der Waals* forces from its longer carbon chain length (n=8). Indeed, there a strong hydrophobic interaction in the alkyl chain in the case of the [C$_7$H$_{15}$CO$_2$]$^-$ anion that display a serious self-organisation of this latter compared to the [C$_3$H$_7$CO$_2$]$^-$ anion in which the intensity of this pre-peak is much lower and also less defined.

However, there are no pre-peaks in the case of the [CH$_3$CO$_2$]$^-$ anion. This peak has been assigned to be associated with the total number of carbon atoms present in the cation and the anion.[30] Furthermore, by increasing the water concentration in those ILs, the Q value are moving toward lower Q for both [C$_3$H$_7$CO$_2$]$^-$ and

[C7H15CO2]- anion. Water seems to enhance the IL organization until a certain limit; for the [C3H7CO2]- anion, $\chi_{IL} \geq 0.4$ and for the [C7H15CO2]- anion, $\chi_{IL} \geq 0.4$

Table 4-10. Pre-peak and second contribution values (nm-1) from binary mixture with water for all three ILs; [C2MIm][CH3CO2], [C2MIm][C3H7CO2] and [C2MIm][C7H15CO2] for their composition in IL mole fraction (χ_{IL}) from 0 to 0.95.

IL	[C2MIm][CH3CO2]		[C2MIm][C3H7CO2]		[C2MIm][C7H15CO2]	
χ_{IL}	Pre-peak Q (nm-1)	Second contribution Q (nm-1)	Pre-peak Q (nm-1)	Second contribution Q (nm-1)	Pre-peak Q (nm-1)	Second contribution Q (nm-1)
0.0		19.963	none	19.963	none	19.963
0.1		18.927	none	18.455	2.596	16.788
0.2		17.979	5.155	17.438	2.829	15.748
0.3		17.438	/	/	2.969	15.748
0.4		17.187	4.831	16.83	3.039	15.748
0.5	none	17.019	4.947	16.323	3.132	15.449
0.6		16.788	5.039	16.217	3.202	15.492
0.7		16.788	5.086	15.898	3.225	15.449
0.8		16.620	5.155	15.962	3.319	15.342
0.9		16.620	5.155	15.750	3.342	15.430
0.95		/	5.202	15.750	/	/

4.3.4 Influence of the temperature on the octanoate anion organisation using neutron source

In this section, Wide Angle Neutron Scattering (WANS) in the range between 0.5 to 16 nm-1 and Small Angle Neutron Scattering (SANS) in the range of 1 to 7 nm-1 were used at the Institut Laue-langevin (ILL) on the respective D16 and D22 instruments in Grenoble, France.

Only [C2MIm][C7H15CO2] was investigated due to its interesting self-organisation. In this part, the influence of the temperature in its self-organisation with water for a binary mixture of 0.25 mole fraction of IL and 0.75 mole fraction of water was studied. Results reveal only information on the pre-peaks studied previously, which allows an investigation in more detail on the inter-molecular interactions of the [C2MIm][C7H15CO2] system. Two distinct instruments using both a neutron source were used and both have confirmed the same IL behavior as it is explained below.

4.3.4.1 Using Wide Angle Neutron Scattering (WANS)

The WANS pattern is showing Q values from 0.5 to 16 nm^{-1} in comparison to WAXS that shows Q values from 1.6 to 20 nm^{-1}. Therefore, the second contribution is hardly visible here due to low contrasts of scattering length densities. However, the significant pre-peak that was observed with WAXS is clearly visible here and will be discussed.

4.3.4.1.1 Pure [C₂MIm][C₇H₁₅CO₂] ionic liquid

In this study, different forms of the pure $[C_2MIm][C_7H_{15}CO_2]$ were investigated using the protiated cation (P) with its protiated (P) or deuterated (D) anion. The ILs will be noted as PP or PD, the first letter being the cation and the second the anion. In fact, it is interesting to look at both PP and PD structure in order to keep the one which has the most contrast while being scattered by a neutron source.

From the graph underneath, the pre-peak for both the pure $[C_2MIm][C_7H_{15}CO_2]$-PP and -PD is both at 3.19 nm^{-1} but the peak is more obvious for the -PD than for the -PP mixture. Therefore, the pure -PD WANS pattern will be taken as a reference to compare the IL-mixtures with water. The pre-peak Q value is slightly different than the one from the pure WAXS pattern found at 3.34 nm^{-1}. This is because the WAXS pattern was measured for a dryer sample than the one used in WANS.
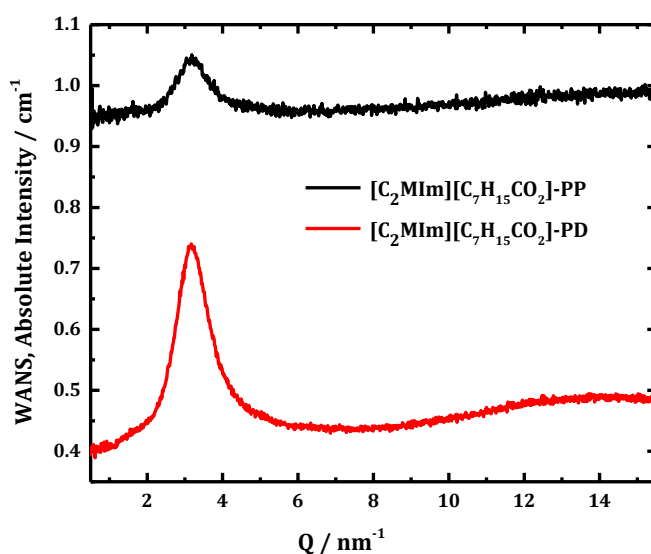
Figure 4-40. WANS pattern for $[C_2MIm][C_7H_{15}CO_2]$-PP (black) and -PD (red).

It is also interesting to note that there is negligible influence of temperature in the neat IL in the range measured. Indeed, on the graph below no shift of the pre-peak is observed between 15 and 45 °C for the pure $[C_2MIm][C_7H_{15}CO_2]$-PD. The only difference comes from to the intensity, which is slightly higher at 15 °C, which means there is more inter-molecular interactions at 15 °C than above 20 °C. Therefore, a comparaison of IL solutions at 15 °C will be investigated to have the most contrast possible.
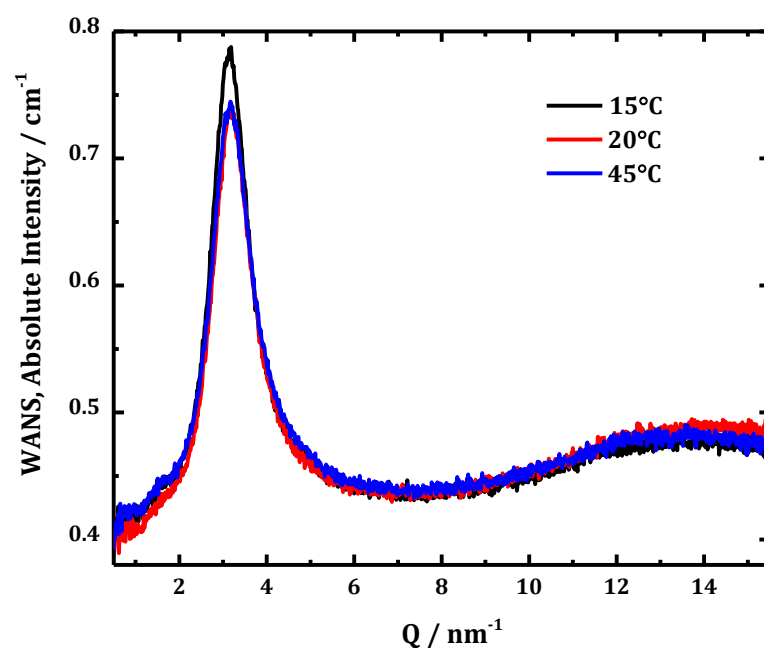
Figure 4-41. WANS pattern for the pure $[C_2MIm][C_7H_{15}CO_2]$-PD at 15°C (Black), 20°C (red) and 45°C (blue).

4.3.4.1.2 *Binary mixture of $[C_2MIm][C_7H_{15}CO_2]$ and water at 15°C*

To gain a better contrast of the IL solutions, the pure $[C_2MIm][C_7H_{15}CO_2]$-PP and -PD were mixed with either H_2O or D_2O using a 0.25 mole fraction of IL and a 0.75 mole fraction of water.

Table 4-11. $[C_2MIm][C_7H_{15}CO_2]$ mixture with water in regards to protiated (P) or deuterated (D) state used in this study.

$[C_2MIm][C_7H_{15}CO_2]$	Water state
PP	H_2O
PP	D_2O
PD	H_2O
PD	D_2O

A significant shift of the pre-peak toward smaller Q ($/nm^{-1}$) at 2.78 nm^{-1} (vs 3.19 nm^{-1} for the pure $[C_2MIm][C_7H_{15}CO_2]$ is observed for all mixtures. This means that there is an increase of *van der Waals* forces in the inter-molecular region when adding water to the pure $[C_2MIm][C_7H_{15}CO_2]$. In addition, the intensity is higher for the sample PD/H_2O which has the strongest contrast due to it's deuterated and protionated mixtures (pink curve on Figure 4-42).
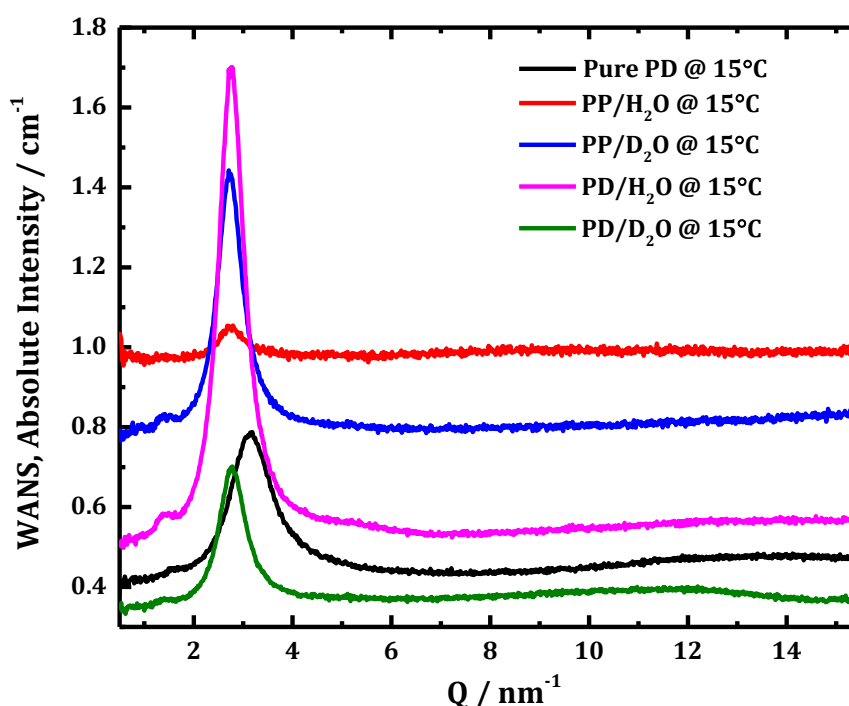
Figure 4-42. Comparison of the WANS pattern of the pure $[C_2MIm][C_7H_{15}CO_2]$-PD (black) and its mixture with water at 15℃ for the structure PP/H_2O (red), PP/D_2O (blue), PD/H_2O (pink) and PD/D_2O (green).

4.3.4.1.3 Impact of the temperature for the [C₂MIm][C₇H₁₅CO₂] binary mixture with water

The Q values of the pre-peak stay the same from 15 to 20 °C, whereas there is a small shift towards larger Q at 2.79 nm^{-1} (vs 2.78 nm^{-1} at 15 and 20°C), while increasing the temperature of the binary mixture to 45 °C. The shift is very small, whereas there is a significant decrease of the intensity at 45 °C, which shows that the inter-molecular interactions are getting weaker at higher temperature.
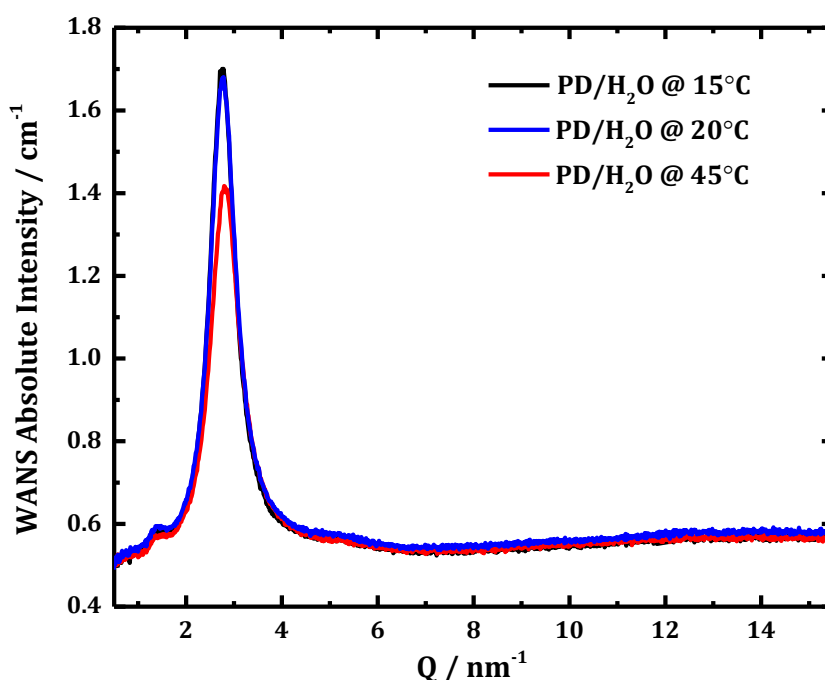
Figure 4-43. Comparison of the WANS pattern of the binary mixture with water of [C₂MIm][C₇H₁₅CO₂]-PD and H₂O at 15°C (black), 20°C (blue) and 45°C (red).

4.3.4.2 Using Small Angle Neutron Scattering (SANS)

In this section the above results found with WANS will also be confirmed using SANS looking the influence of water and temperature on the structure of the [C₂MIm][C₇H₁₅CO₂] binary mixture with water.

4.3.4.2.1 Influence of water on the structure of [C₂MIm][C₇H₁₅CO₂] structure

Below, the SANS patterns of the pure [C₂MIm][C₇H₁₅CO₂] fully protiated (PP) and of its mixture with water at 15°C is shown. When adding water to the pure IL, a significant shift of the pre-peak towards low Q is clearly visible from the two

patterns below (with pre-peak Q values of pure IL and binary mixture respectively; 3.16 nm^{-1} (d = 1.99 nm) and 2.78 nm^{-1} (d = 2.26 nm)). This shift reveals stronger and longer inter-molecular interactions between the cation and the anion due to the addition of water. These results show that water strongly interacts with the IL and strengthens its self-organisation.
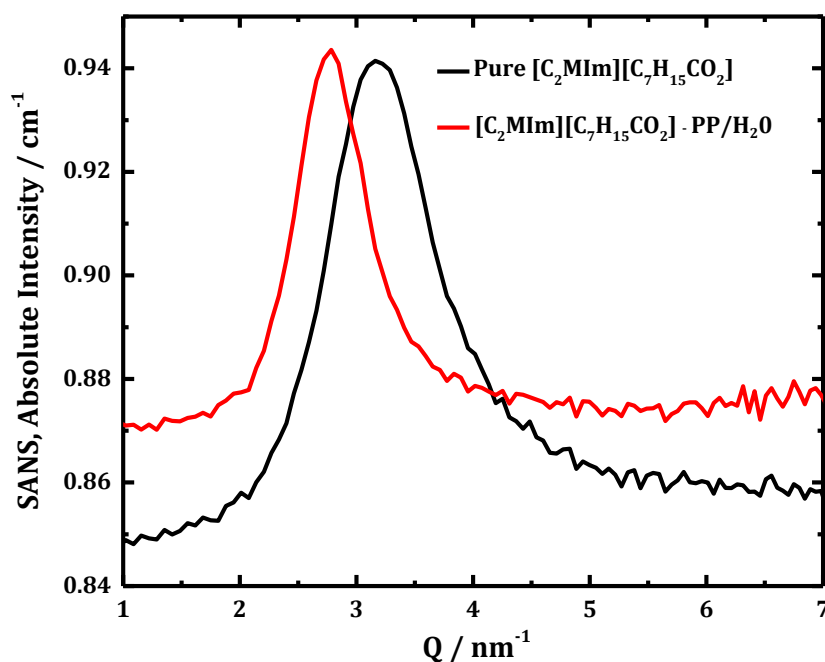
Figure 4-44. SANS pattern of the pure $[C_2MIm][C_7H_{15}CO_2]$-PP (black) and in binary mixture with protiated water (red) at 15°C.

4.3.4.2.2 Influence of temperature on the $[C_2MIm][C_7H_{15}CO_2]$ in binary mixture with water

The SANS pattern underneath is showing the $[C_2MIm][C_7H_{15}CO_2]$-PP in a binary mixture with protiated water at 15°C, 35 °C, 45 °C and 15 °C. The same sample was used throughout the whole experiment where the temperature was gradually increased from 15 to 45 °C, and then was cooled back to 15 °C. A shift of the pre-peak towards higher Q is observed while increasing the temperature to 35 °C with Q values of 2.78 nm^{-1} at 15 °C, and 2.85 nm^{-1} at 35 and 45 °C.
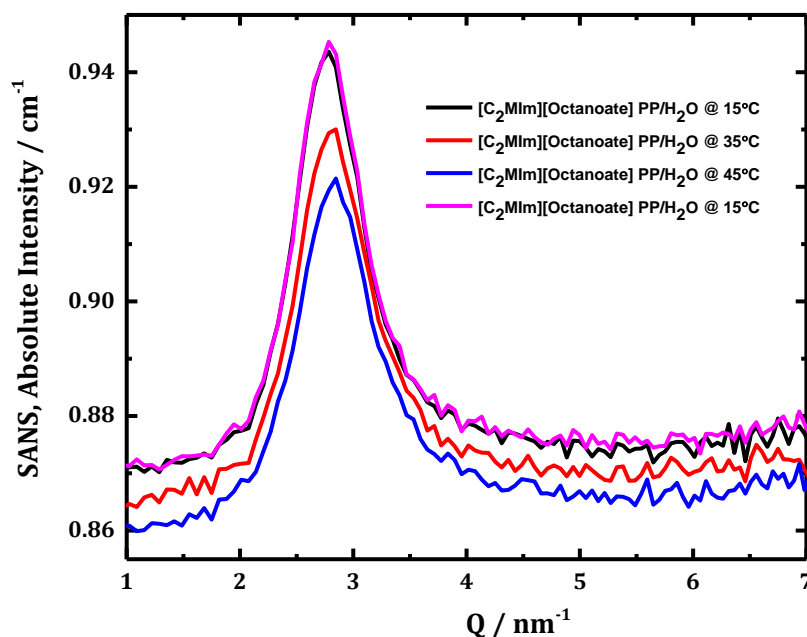
Figure 4-45. SANS pattern of $[C_2MIm][C_7H_{15}CO_2]$-PP in binary mixture with protiated water at 15 ℃ (black), 35 ℃ (red), 45 ℃ (blue) and again to 15 ℃ (pink).

An increase in temperature weakens the inter-molecular organisation and therefore increases its entropy.

However, those diffraction patterns are showing that the organisation of IL /water and pure IL is stable as there is no significant Q shift when varying the temperature from 15 to 45 ℃. In addition, the process seems reversible as going from 15 to 45 ℃ and then going back to 15 ℃ giving exactly the same pattern than the first one taken at 15 ℃ with the same Q value of 2.78 nm^{-1}.

This result is important, as it shows that the liquid structure can slightly change when varying the temperature but won't destroyed its interaction behaviour, and that It is a reversible mechanism similar to the one found for the phase equilibrium of the pure water; which means that inter-molecular interactions are not destroyed after a change of temperature but are only getting weaker or stronger.

4.3.5 Conclusions

The pre-peak at about 4 nm^{-1} was observed in all instruments, WAXS, WANS and SANS; whereas the second contribution at around 16 nm^{-1} was mainly observed by WAXS. In fact, WAXS was set up with a higher range, and therefore it was the only instrument that could discern this peak at high Q.

The pre-peak was assigned as low Q to show inter-molecular interactions; whereas the second contribution was assigned as high Q to show intra-molecular interactions.

The intra-molecular interactions in the pure ILs are getting shorter while the anion alkyl chain length decreases, which is seen by a shift towards higher Q on the neat IL systems. However, when adding water to the pure ILs, the intra-molecular interactions are getting even shorter, which can be observed by the shift towards higher Q. An explanation for this observation is that water forces the cation/anion intra-molecular interactions to be closer to each other by competing for this position with the IL.

Unlike inter-molecular interactions, which are are only visible for the butanoate and octanaote-IL systems, and which are much stronger when the anion alkyl chain length increases. Furthermore, adding water to the pure ILs seems to enhance their structural organisation since the pre-peak is moving towards lower Q with high intensities. However, the ILs are only showing these features of organisation until a certain limit of the mole fraction of the added water is exceeded ($\chi_{IL} \leq 0.4$ for the $[C_3H_7CO_2]^-$ anion and $\chi_{IL} \leq 0.2$ for the $[C_7H_{15}CO_2]^-$ anion).

In addition, WANS and SANS have shown no significant change of the $[C_2MIm][C_7H_{15}CO_2]$-IL structure in the temperature range between 15 to 45°C. Only the inter-molecular interactions are getting stronger while the temperature decreases, which is commonly observed in other systems; clearly seen in the case of the pure water with its solid state at low temperature due to stronger inter-molecular interactions, and its vapour state at high temperature due to weaker intra-molecular interactions.

4.4 Experimental parts

4.4.1 NMR-spectroscopy measurements

For each IL composition, 14 measurements have been run on a Bruker Topsin 2.1 Ultrashield 400plus, 400MHz spectroscopy, including ^1H, ^{13}C and HSQC (2D-^1H/^{13}C)-NMR spectroscopy at a range of temperature (from 300 to 343K). Each IL mixture was prepared in a nitrogen-glovebox using neat sample with a capillary tube of 0.9 ratio of D_6-DMSO and 0.1 ratio of H_6-DMSO in order to have the same reference peak in each sample.*Note: For each measure, the initial water content found within each pure ionic liquid (by using the Karl-Fisher) was taking into account to calculate the real mole and mass ratio of each sample.*

4.4.2 X-ray and neutron measurements

4.4.2.1 Samples' preparation

The mixtures were prepared under Nitrogen glovebox with the ratio and weight of each compound detailed below.

Table 4-12: $[C_2MIm][CH_3CO_2]$, $[C_2MIm][C_3H_7CO_2]$ and $[C_2MIm][C_7H_{15}CO_2]$ ionic liquids and water binary mixture composition used for X-ray measurement (SAXS and WAXS).

$[C_2MIm][CH_3CO_2]$ + H_2O			$[C_2MIm][C_3H_7CO_2]$ + H_2O			$[C_2MIm][C_7H_{15}CO_2]$ + H_2O		
χ_{IL}	m_{IL} (g)	m_{H2O} (g)	χ_{IL}	m_{IL} (g)	m_{H2O} (g)	χ_{IL}	m_{IL} (g)	m_{H2O} (g)
0	0.0000	0.5000	0	0.0000	0.5000	0	0.0000	0.5000
0.1	0.2574	0.2454	0.1	0.2790	0.2336	0.1	0.3025	0.1945
0.2	0.3533	0.1493	0.2	0.3619	0.1325	0.2	0.3908	0.1090
0.3	0.4027	0.0933	0.3	0.4129	0.0952	0.3	0.4244	0.0723
0.4	0.4369	0.0666	0.4	0.4435	0.0675	0.4	0.4480	0.0583
0.5	0.4472	0.0520	0.5	0.4598	0.0457	0.5	0.4730	0.0303
0.6	0.4715	0.0293	0.6	0. 4712	0.0233	0.6	0.4830	0.0220
0.7	0.4809	0.0184	0.7	0.4848	0.0170	0.7	0.4905	0.0130
0.8	0.4837	0.0169	0.8	0.4876	0.0129	0.8	0.4938	0.0074
0.9	0.4968	0.0050	0.9	0.4972	0.0056	0.9	0.5000	0.0000
1	0.5000	0.0000	1	0.5000	0.0000	1	/	/

The samples analysed via SANS and WANS were composed of 0.25 mole fraction of dried ionic liquid and 0.75 mole fraction of pure water.

4.4.2.2 Small- and Wide-Angle X-ray Scattering (SWAXS)

SWAXS measurements were performed at the ESRF (European Synchrotron Radiation Facility, Grenoble, France in June 2015) on the BM02-D2AM beamline. The incident photon energy was tuned to 11 keV which corresponds to a wavelength of $\lambda= 1.12$ Å. A two-dimensional detector, a CDD camera developed by Princeton, presently Ropper Scientific, was used.

Two different distances between the sample and the detector were used to cover magnitudes of the scattering vector modulus (q) from 0.06 to 20 nm^{-1}. The corresponding Bragg distances were from 0.3 to 100 nm. The magnitude of the scattering vector is defined as $q=(4\pi/\lambda)\sin\theta$, where θ is half of the scattering angle and λ is the wave length. In the short geometry, the distance from the sample to the detector was 16 cm, which covers the q range from 1.1 to 20.4 nm^{-1}. In the long geometry, the distance from the sample to the detector was 164cm, which covers the q range from 0.06 to 1.56 nm^{-1}. The intensity curves measured by the long geometry were scaled to the absolute intensities with the aid of a laboratory-calibrated Lupolen sample. The data measured with the short geometry were merged to the long measurements by matching of the data in the region 1.1-1.56 nm^{-1}.

The scattered intensities were recorded during 20 or 50 s for SAXS, and 5, 10 or 20 s for WAXS. The corrections of primary data were carried out using the software Bm2Img available on the beamline: (i) the dark current (i.e. non-illuminated camera), (ii) the flat field response (i.e. homogeneously illuminated camera), and (iii) the tapper distortion. The standard silver behenate was used for the q-range calibration. 2D images were converted into radial averages over the image center to yield the scattered intensity I vs the scattering vector q. As an additional correction, the contribution of the empty cell was subtracted to the scattering intensity of the studied samples. Quartz capillaries (2 mm in diameter with a wall thickness of 0.01 mm) from Hilgenberg were used as sample containers.

The local contact was Cyrille Rochas.

4.4.2.3 Small-Angle Neutron Scattering (SANS)

Small-angle neutron scattering (SANS) experiments were performed at the Laue Langevin Institut (ILL, Grenoble, France in August 2016) on the D16 spectrometer. The neutron wavelength was fixed at 4.55 Å using a monochromator. A 2D gas-filled detector settled at 950 mm from the sample position (1-mm-thick quartz cell) was moved at four different angles on a goniometer arm in order to cover a q-vector range between $0.049 < q$ (Å^{-1}) < 1.57 with a reasonable overlap (2.5°) that allows a good concatenation of the scattering data. A standard H_2O normalization, detector noise, empty cell, and incoherent scattering corrections were applied to display the scattering intensity $I(q)$ in absolute units (cm^{-1}).

Chapter 5 _ Application of ionothermal synthesis of copper oxide nanoparticles

5.1 Introduction

Nanofluids are nano-scaled colloidal suspensions consisting of solid particles, rods, fibers or tubes dispersed in different base fluids such as water, ethylene gycol, glycerol, engine oil or again, ionic liquids.[48,49] The production and characterisation of the latter dispersions, using ionic liquids as base fluids, will be the purpose of this study. Indeed, metal oxide nanomaterials dispersed in ionic liquids can also be called nanofluids.[176] They can be made easily *in-situ,* where ionic liquids play an important role in the formation and stabilisation of these nanomaterials, as it was explained in Chapter 1. Those materials can be used as solvents and catalyst, in heat transfer, as magnetic fluids, lubricants and luminescent materials, for the conservation of artworks, novel electrolytes for batteries and in solar cell, or in medical equipments.[177-181]

Swadzba-Kwasny *et al.*, have recently demonstrated,[176] that carboxylate based ionic liquids, in the presence of water, can be used for the *in-situ* synthesis of copper(II) oxide nanoparticles; starting from a simple copper(II) acetate precursor dissolved in the IL. This results in the formation of highly stable nanofluids (dispersions of CuO nanoparticles in the IL). In this paper, a simple, inexpensive and reproducible manner to produce stable IL-nanofluid was studied. Using copper oxide nanoparticles allows for an increase of the thermal conductivity of the liquid.

In this study, two IL-nanofluids were prepared by alternating magnetic stirring and ultrasound bath at 50°C, using copper(II) acetate hydrate in 1-butyl-3-methylimidazolium acetate [C_4mim][CH_3CO_2], and in Trioctyl(dodecyl) phosphonium acetate [P_{88812}][CH_3CO_2] respectively. Both samples were then heated to 120°C and dried overnight under high vacuum. The products were

characterised by different methods as reported in Table 5-1 ; whereas the particles were analysed as shown in

Table 5-2.

Table 5-1. Methods used to characterise the nanofluids.

^{13}C NMR and DSC	To follow the formation of the NPs formed
TEM, XPS	To study the NP structure, size and shape
IR, UV-Vis, TGA, DSC and densitometry	To study the precursor species and physical properties of the IL-nanofluids.

Table 5-2: Results of the characterisation of the nanofluids.

XPS analysis:	Indicates that a mixed valent copper(I,II) oxide has formed in [C_4mim][CH_3CO_2] and a copper(II) oxide has been formed in [P_{88812}][CH_3CO_2].
TEM:	Shows particle size diameters of 50 nm in [P_{88812}][CH_3CO_2] and clusters below 1 nm for [C_4mim][CH_3CO_2]
UV-Vis spectroscopy:	Cu(OAc)$_2$ in [C_4mim][CH_3CO_2] is blue at RT, green at 70 C and deep red liquid at 120 °C

Heating-up to 120 °C enables a fast reaction rate and prevents thermal decomposition of the acetate-based IL. The two different modes of agitation used (stirring and ultrasound) are known to decrease the size of the formed nanoparticles and reduces aggregation, and will therefore be used in this study.

This study has helped to gain information on the influence of the cation on the formation of copper oxide NPs. Indeed, [C_4mim][CH_3CO_2] is known to be hydrophilic, aromatic and able to coordinate as a carbene to metals; whereas [P_{88812}][CH_3CO_2] is known to be hydrophobic, aliphatic and non-coordinating. Those basic anions are acting as a base and stabilising agent, allowing for the preparation of stable NPs dispersions in ILs (nanofluids). Therefore, this study reported a facile method for the *in situ* synthesis of stable copper (II) oxide NPs and copper(I, II) oxide clusters in acetate-based ILs, the final product (CuO or Cu$_x$O(I, II)) depending on the cation of the IL chosen.

In parallel, this present study (see Chapter 3 and 4) and others,[182,183] has also demonstrated that binary mixtures of water and octanoate-based ILs form stable emulsions, *a contrario* of those based on the acetate anion, resulting in a strong reorganisation of the IL structure in the presence of water. This structural organisation may then explain the ability to this IL family to form highly stable nanofluids.

Those studies have shown a very strong self-organised structure in the case of the pure octanaoate anion, as well as on its solutions with water. However, for all three ILs, water dissociated most of the ion-pairs of the IL from about 0.35 IL mole fraction (see, Chapter 3 and 4). The ability to this IL family to be used as anionic surfactant will be investigated in this chapter in regards to the nanoparticle formation.

In fact, despite their importance, carboxylate-based IL structures and their interactions with metallic precursors, such as copper(II) acetate and copper(II) octanoate, have not been studied previously. This project aims to examine in greater details the interactions of these three carboxylates: acetate, butanoate and octanoate based ionic liquids with water in the presence of copper(II) acetate, butanoate and octanoate precursors to understand then the influence of interaction changes on the formation of CuO particles in ionic liquids media. The formation of copper(II) oxide nano-dispersions in these ionic liquids can be used as a model-system for more complex systems that also give evidence for nanoparticle formation, such as rare earth oxides.

This work is based on the hypothesis that there is a link between the IL/water structure, the structure of the polar domains where the polar precursors are located, and the resulting morphology of the nanomaterials.

5.2 Aims and outlook

The aim of this work was to produce new stable IL-nanofluids and gain a better understanding in the change of the metal salt precursor in term of morphology and size of the nanoparticles.

In this work, copper oxide nanoparticles (CuO-NPs) were synthesis *in-situ* in ionic liquid by simply dissolving the respective copper(II) carboxylate precursor with its respective ionic liquid. The ionic liquid anion is being the same as the metal anions in order to produce copper oxide.

In this new study the impact of the water into copper(II) carboxylate dissolution in IL was studied, as well as the impact on the morphology (shape and size) of the copper oxide NPs by increasing the carbon chain length of the anion from 2, 4 and 8 carbons and also by increasing the amount of water into the reaction.

First of all, the solubility of copper-salt precursors with water was investigated in order to pointed out the importance of using IL as both solvent and reagent in the nanofluids formation. Then the copper salt was analysed by single crystal in order to gain a better understanding on their basic structure before they are turning into copper oxide NPs.

The thermal properties as well as the physical properties of the new nanofluid solutions were measured (density, viscosity and conductivity) in order to fully characterised those new materials and discuss any point in term of future applications.

Furthermore, UV-VIS spectroscopy, Transmission Electron Microscope (TEM) analysis, and X-Ray diffraction experiment have given a unique insight into the liquid structure of each solution. From those investigations, it was possible to understand the resulting differences in the nanomaterial morphology, as well as on the formation mechanisms of nanomaterials in ILs.

5.3 Choice of ionic liquids and reaction conditions

5.3.1 Synthesis of nanofluids

Nanofluids can be made *via* a ionothermal process, a method that has been previously used by our group.[176] In a ionothermal reaction, all reactants are dissolved in an ionic liquid, and subsequent heating of the whole system at ambient pressure initiates the reaction, whereby the ambient pressure is maintained due to the non-volatile nature of ionic-liquids.[184]

In this thesis, copper oxide nanoparticles are made firstly by mixing an ionic liquid with a metal precursor and a small amount of water at 50°C in order to dissolve the metal precursor into the ionic liquid. Then the solution is heated to 120 °C for about 30 minutes, were the formation of copper oxide nanoparticles has been observed in our previous work.[176] The experiment has shown that reaching at least 30 minutes of heating at 120°C was very necessary to make sure the transformation of copper salt into nanoparticles occurs.

The reaction time was found to be dependend on the concentration of the reagent used. For instance, the higher the copper salt concentration or the more water was present in the solution, the longer the solutions had to be heated at 120 °C in order to keep a deep red colour of the solution at room temperature. If the solution, once cooled back to room temperature didn't show a deep red colour, this meant that the entire synthesis didn't occur and the solution had to be left longer at 120°C. Sometimes, the solutions were heated overnight at 120°C and no decomposition was found. However, the solution had to be very well stirred using magnetic stirring.

The solutions can be kept under argon or nitrogen as a nanofluid solution where the nanoparticles are dispersed in the ionic liquid. The detailed synthesis is provided in the experimental part of this chapter. In this work, it was not possible to quantify the yield of the reaction since it is not possible to separate the NPs from the IL, which has led to some difficulties in the analysis and characterisation. In Figure 5-1 below the process is summarised. It has been found that an intermediate is formed between 80-90 °C. The latter can be isolated by

crystallisation from concentrated solutions and be studied by single crystal diffraction as it is described in the following part of this section.
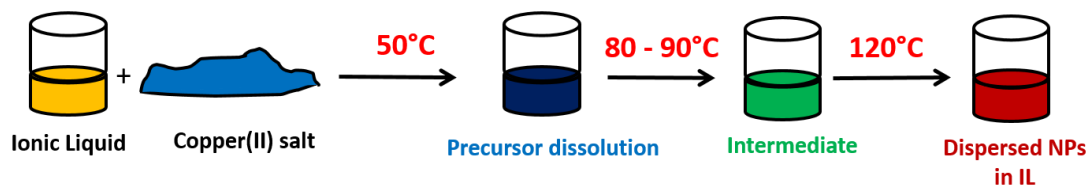
Figure 5-1. Nanofluid formation via a ionothermal process.
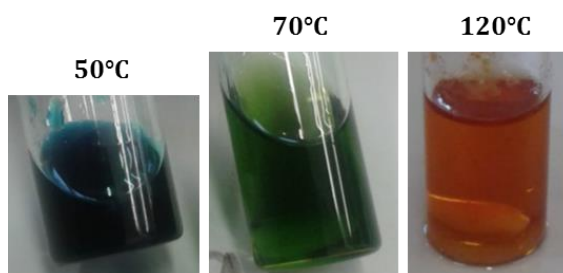
Figure 5-2. Experimental photo showing the colour changes from the copper(II) octanoate precursor to the nanofluid formation.

The full equilibrated equation of the synthesis of CuO from copper(II) acetate in $[C_2MIm][CH_3CO_2]$ involved the presence of water as follows:

(Eq. 44)

$$2[C_2MIm][CH_3CO_2] + Cu_2(CH_3CO_2)_4.2H_2O \xrightarrow{50°C}$$
$$[C_2MIm]_2[Cu_2(CH_3CO_2)_4(OH)_2] + CH_3CO_2H \xrightarrow{120°C}$$
$$2CuO + 2[C_2MIm][C_nH_nCO_2] + 4(CH_3CO_2H)$$
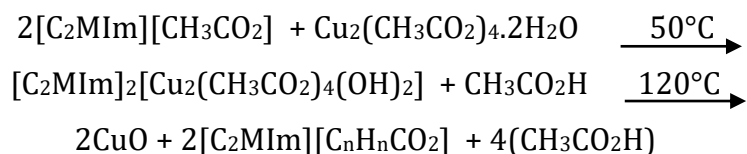
However, the full equilibrated equation of the synthesis of CuO from copper(II) butanoate and octanoate in their respective ILs is different and also involved the presence of water as follows (water is already initially present in their IL, but one drop on water were always added):

(Eq. 45)

$$2[C_2MIm][C_nH_nCO_2] + Cu_2(C_nH_nCO_2)_4 + 2H_2O \xrightarrow{50°C}$$
$$[C_2MIm]_2[Cu_2(C_nH_nCO_2)_4] + 2H_2O \xrightarrow{120°C}$$
$$2CuO + 2[C_2MIm][C_nH_nCO_2] + 4(C_nH_nCO_2H)$$

176
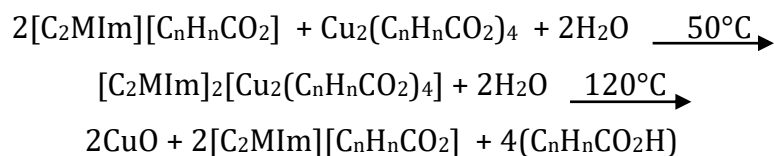
The function of the water in these reactions is as a co-solvent providing the basicity from the acetate anions, but also as a reagent and the source of the oxygen. The molecular weight and density of the reagents used in this study are found in Table 5-3.

Table 5-3. Molecular weight, M (g/mol) and density (g.cm^{-3}) of pure water, 1-ethyl-3-methylimidazolium carboxylate and copper(II) carboxylate reagent used.

Reagents used	M (g.mol^{-1})	Density (g.cm^{-3})
Pure water	18.02	0.9970
$[C_2MIm][CH_3CO_2]$	170.21	1.0968
$[C_2MIm][C_3H_7CO_2]$	198.26	1.0670
$[C_2MIm][C_7H_{15}CO_2]$	254.37	1.0022
$Cu(CH_3CO_2)_2$	199.65	1.882
$Cu(C_3H_7CO_2)_2$	237.74	2.773
$Cu(C_7H_{15}CO_2)_2$	349.95	N/A

$[C_2MIm][CH_3CO_2]$

50°C $Cu_2(CH_3CO_2)_4 \cdot 2H_2O$

$[C_2MIm]_2[Cu_2(CH_3CO_2)_4(OH)_2]$
$+ CH_3CO_2H$
Solution

$[C_2MIm][C_7H_{15}CO_2]$

50°C $Cu_2(C_7H_{15}CO_2)_4$
$+$
H_2O

$[C_2MIm]_2[Cu_2(C_7H_{15}CO_2)_4]$
$+ 2H_2O$
Dispersion
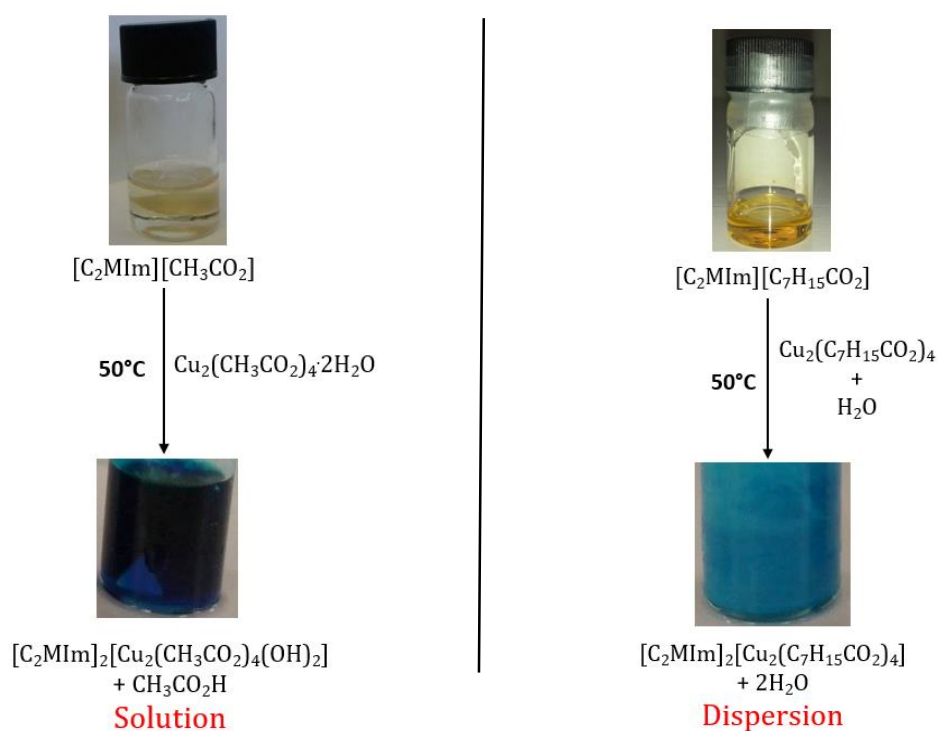
Figure 5-3. Photo taken before and after introduction and mixture of the copper salt in its respective IL, using copper(II) acetate (left) and copper(II) octanoate (right).

5.3.2   Solubility of copper(II) carboxylate in water

To demonstrate that the ILs are required for the highly concentrated solutions of copper(II) carboxylate precursors, a solubility test was carried out.

Copper(II) acetate is known to be very soluble in water, however, when increasing the carbon chain length of the copper(II) carboxylate, it was found to be almost impossible to dissolve the new compound into water as described in the experiment below:

The preparation of a saturated solution of copper(II) salts was carried out using 100 mg of copper(II) salts in 3 mL of water. Only a small amount was able to dissolve. The solution was then filtrated to remove the copper which hasn't dissolved and the solution was analysed by a copper elementary analysis (for 1 ppm = 1 mg/L) using AAS. As a result, 14.11 mg (4705 ppm) of copper(II) butanoate were found in the filtrate solution, whereas 16.06 mg of copper(II) octanoate were found.

Thereby, Copper(II) carboxylate salts were shown to not dissolve completely in water when the alkyl chain length of the anion reaches 4 carbons and above. This is due to the fact that longer carbon chain length on the carboxylate would make the compound more hydrophobic than for compounds with shorter chains such as the acetate chain (2 carbons only).

5.3.3   Solubility and species of copper(II) salts in carboxylate ionic liquids

In this part, the copper salts followed by the copper salts dissolved in their respective ILs were recrystallized (cf, experimental part) and analysed by single crystal in order to gain a better understanding on their basic structure before they are turning into copper oxide NPs.

Single-crystal X-ray Diffraction is a non-destructive analytical method that provides deep information about the internal lattice of crystalline substances. It includes the unit cell dimension, bond-lengths, bond-angles, and detail of the site-ordering. The data generated from the X-ray analysis are interpreted and refined to obtain the crystal structure.[185] More detailed on X-ray diffraction have been described in Chapter 1.

5.3.3.1 Copper(II) acetate dihydrate at room temperature

Copper(II) acetate dihydrate dissolves well in acetate ionic liquids. As known for aqueous species, the copper(II) acetate adopts a paddle-wheel structure, $[Cu_2(CH_3CO_2)_4(H_2O)_2]$, as shown in Figure 5-2.[186-188]
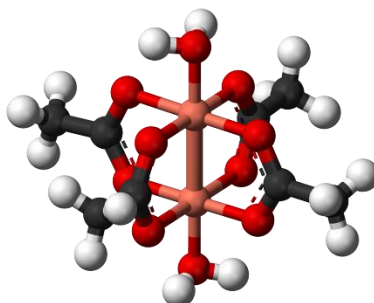
Figure 5-4. Paddle-wheel structure of copper(II) acetate dihydrate, $[Cu_2(CH_3CO_2)_4(H_2O)_2]$. Atoms: Cu (pink), O (red), C (black) and H (white).[187]

However, in ionic liquids such as $[C_2MIm][CH_3CO_2]$, there are a vast excess of acetate anions present, and upon heating it has been observed that the coordinating water molecules of the paddle-wheel structure are removed by coordinating acetate groups. As an example, the structure of a coordination polymer with bridging acetate anions could be isolated and has been reported by Köckerling and co-workers, see Figure 5-5 (top).[189] In our group, Shihui Zhang (MPhil thesis) has isolated the compound $[C_4MIm][Cu_2(CH_3CO_2)_5]$, which is a coordination polymer crystallised from a concentrated solution of copper(II) acetate in the ionic liquid $[C_4MIm][CH_3CO_2]$, see Figure 5-5 (bottom). A reaction equation is given below in (Eq. 46):

(Eq. 46)

$$[C_4MIm][CH_3CO_2] + 2[Cu(CH_3CO_2)_2 \cdot H_2O] \longrightarrow [C_4MIm][Cu_2(CH_3CO_2)_5]$$
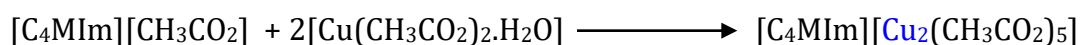
However, this is obviously a solid state species, and evidence has been found (EXAFS, unpublished results of Shihui Zhang *et al.*) that in the solution it can be assumed that the paddle-wheel structures are present with partially substituted acetate coordination in the axial position.
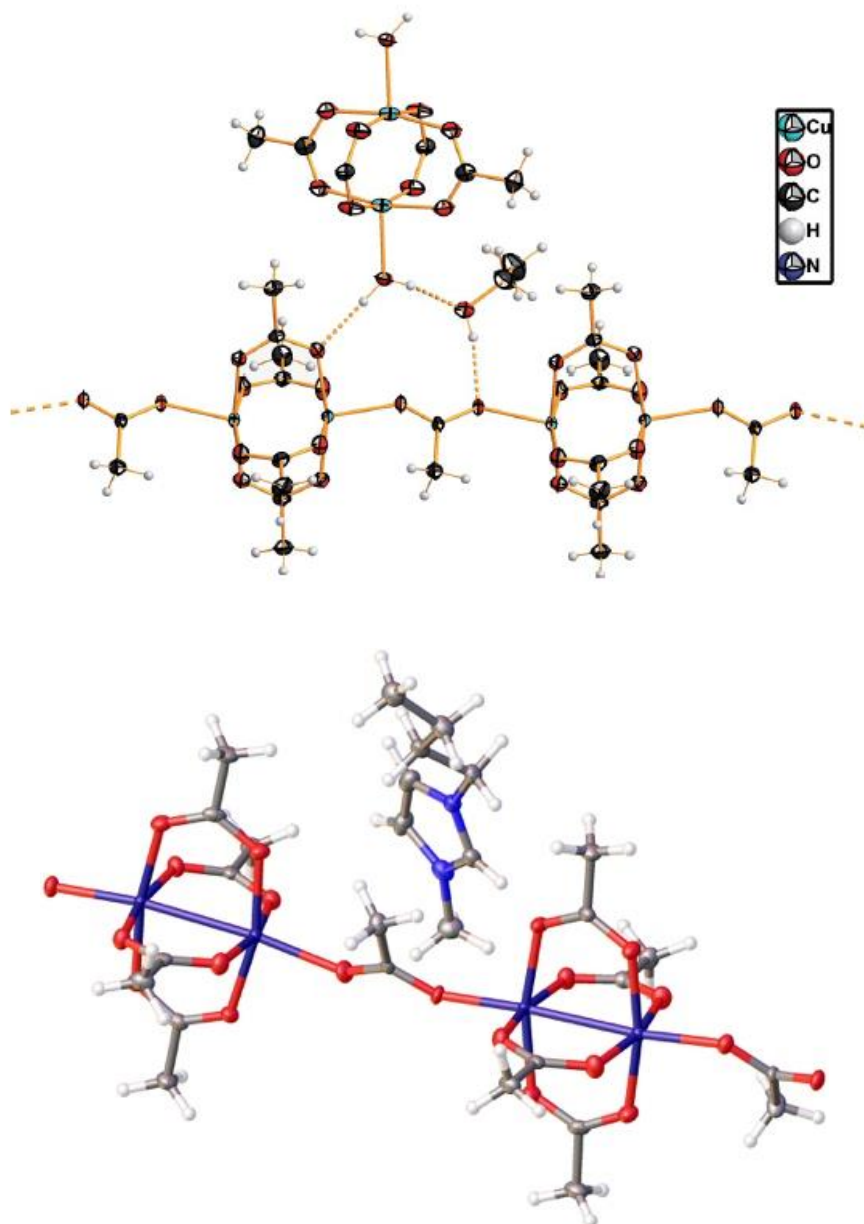
Figure 5-5. Coordination polymer (C₄MIm)[Cu₂(CH₃CO₂)₅]·[Cu(CH₃CO₂)₂(H₂O)]₂·C₂H₅OH obtained from a solution of Cu₂(CH₃CO₂)₄(H₂O)₂ in the ionic liquid [C₄MIm][CH₃CO₂] in the presence of ethanol (top),[189] and the structure of [C₄MIm][Cu₂(CH₃CO₂)₅], crystallised from the pure concentrated ionic liquid solution (bottom).

5.3.3.2 Copper(II) acetate dihydrate at 80°C

Swazba-Kwasny *et al.*, reported on the formation of a $[C_2MIm][Cu_3(CH_3CO_2)_5(H_2O)(OH)_2].H_2O$, which is formed by heating a solution of $Cu_2(CH_3CO_2)_4(H_2O)_2$ in the ionic liquid $[C_2MIm][CH_3CO_2]$ to 80°C by crystallising the compound by slow cooling to RT.[176] The occurrence of the bridging hydroxyl group has been explained by the basicity of the acetate ionic liquid and the presence of a small amount of water coming from the coordinated H_2O in the copper(II) acetate dihydrate. The structure of $[C_2MIm][Cu_3(CH_3CO_2)_5(H_2O)(OH)_2]·H_2O$ consists of triangles of copper coordinated to a shared OH^- group and bridged by acetate groups in mono- and bidentate mode and can be seen in Figure 5-6. These trimeric hydroxy-clusters are then interlinked by acetate bridging to form a 1-dimensional coordination polymer. A reaction equation is given below in (Eq. 47):

(Eq. 47)

$[C_2MIm][CH_3CO_2]$ + $2[Cu(CH_3CO_2)_2.H_2O]$

$\longrightarrow$ $[C_2MIm][Cu_3(CH_3CO_2)_5(H_2O)(OH)_2].H_2O$
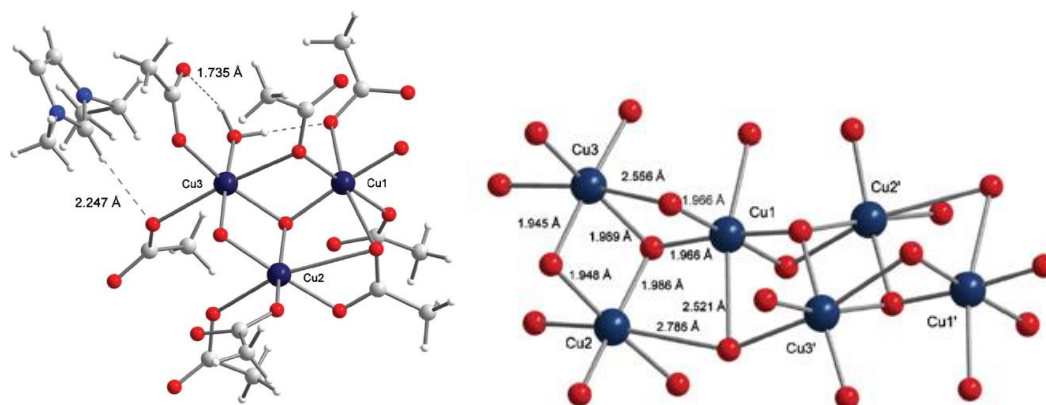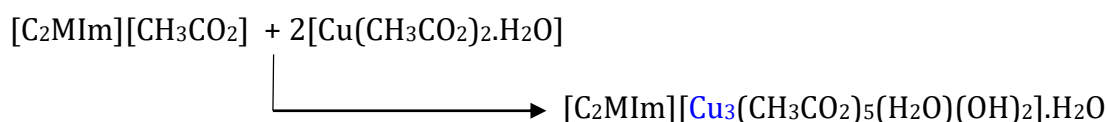
Figure 5-6. Structure of $[C_2MIm][Cu_3(CH_3CO_2)_5(H_2O)(OH)_2].H_2O$, formed by heating a solution of $Cu_2(CH_3CO_2)_4(H_2O)_2$ in the ionic liquid $[C_2MIm][CH_3CO_2]$ to 80°C and crystallising the compound by slow cooling.[176]

5.3.3.3 Copper(II) butanoate at room temperature

In this thesis, the dissolution and species of copper(II) butanoate and octanoate in the respective ionic liquids was also investigated. Therefore, these compounds, $Cu(C_3H_7CO_2)_2$ and $Cu(C_7H_{15}CO_2)_2$ were synthesised and characterised.

Thereby, copper(II) butanoate could be crystallised from methanol and the crystal structure was determined. The crystal structure is shown in Figure 5-7 and consists of a paddle-wheel structural, however, rather than having isolated dimers as in the structure of the corresponding copper(II) acetate, this structure features a polymeric structure with the bridging carboxylates also bridging to the neighbouring dimers. This results in a 1-dimensional coordination polymer. This structure has not been reported previously. Figure 5-8 is showing the packing in the crystal structure of $Cu_2(C_3H_7CO_2)_4$.
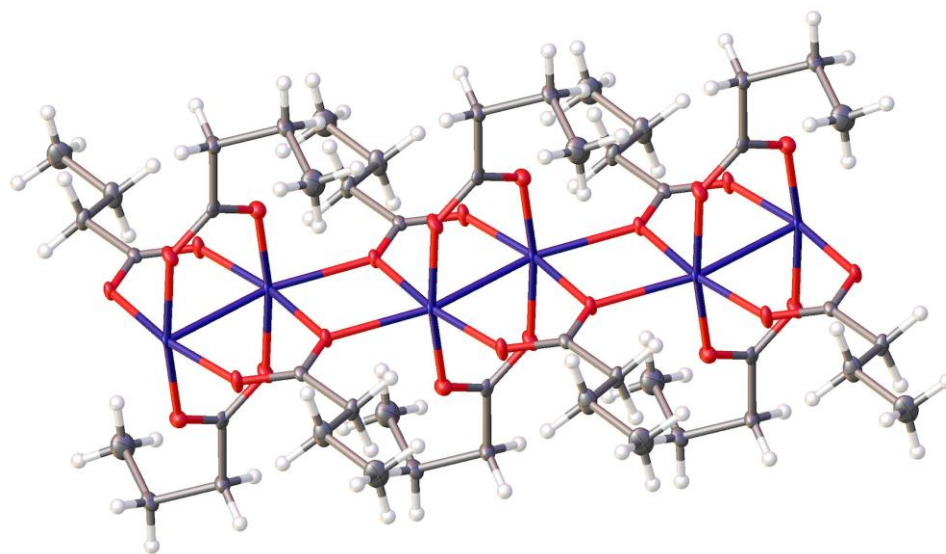
Figure 5-7. Crystal structure of copper(II) butanoate, $Cu_2(C_3H_7CO_2)_4$.
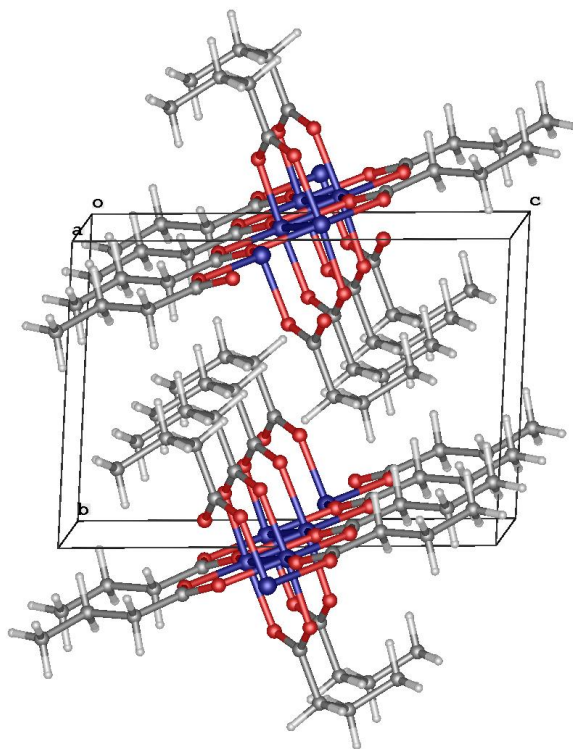
Figure 5-8. 1-D coordination polymer packing in the crystal structure of $Cu_2(C_3H_7CO_2)_4$.

Table 5-4. Crystal Data for $Cu(C_3H_7CO_2)_2$.

Empirical formula	$CuC_8H_{14}O_4$
Formula weight	237.74 g/mol
Temperature/K	293(2)
Crystal system	triclinic
Space group	P-1
a/Å	5.15600(12)
b/Å	8.6547(3)
c/Å	11.5154(3)
α/°	93.614(2)
β/°	93.5413(19)
γ/°	102.710(2)
Volume/Å³	498.76(2)
Z	9
ρ_{calc}g/cm³	2.773
μ/mm⁻¹	10.582
F(000)	396.0
Radiation	CuKα (λ = 1.54184)
2Θ range for data collection/°	10.52 to 145.44
Index ranges	-6 ≤ h ≤ 6, -10 ≤ k ≤ 10, -14 ≤ l ≤ 14
Reflections collected	9209
Independent reflections	1969 [R_{int} = 0.0299, R_{sigma} = 0.0182]
Data/restraints/parameters	1969/0/120
Goodness-of-fit on F²	1.050
Final R indexes [I>=2σ (I)]	R_1 = 0.0246, wR_2 = 0.0648
Final R indexes [all data]	R_1 = 0.0247, wR_2 = 0.0649
Largest diff. peak/hole / e Å⁻³	0.36/-0.50

However, after dissolving the $Cu(C_3H_7CO_2)_2$ in the ionic liquid $[C_2MIm][C_3H_7CO_2]$, a highly concentrated solution was prepared, and from this sample a crystalline product was obtained. The crystal structure of this compound was determined, and the compound turned out to be $[C_2MIm]_2[Cu(C_3H_7CO_2)_4]$ as show the Figure 5-9. This structure consists of $[C_2MIm]^+$ cations and isolated $[Cu(C_3H_7CO_2)_4]^-$ anions. This is a remarkable result, since the corresponding acetate structures always contain the paddle-wheel motif. The copper(II) $[Cu(C_3H_7CO_2)_4]^-$ anions are showing a square-planar coordination with four monodentately coordinating butanoate groups. Figure 5-10 is showing the packing in the crystal structure of $[C_2MIm]_2[Cu(C_3H_7CO_2)_4]$. The copper centres are packing along the *c* axis, however, the distance between the copper metal centres is very large. A reaction equation is given below in (Eq. 48):

(Eq. 48)

$[C_2MIm][C_3H_7CO_2] + Cu(C_3H_7CO_2)_2 \longrightarrow [C_2MIm]_2[Cu(C_3H_7CO_2)_4]$
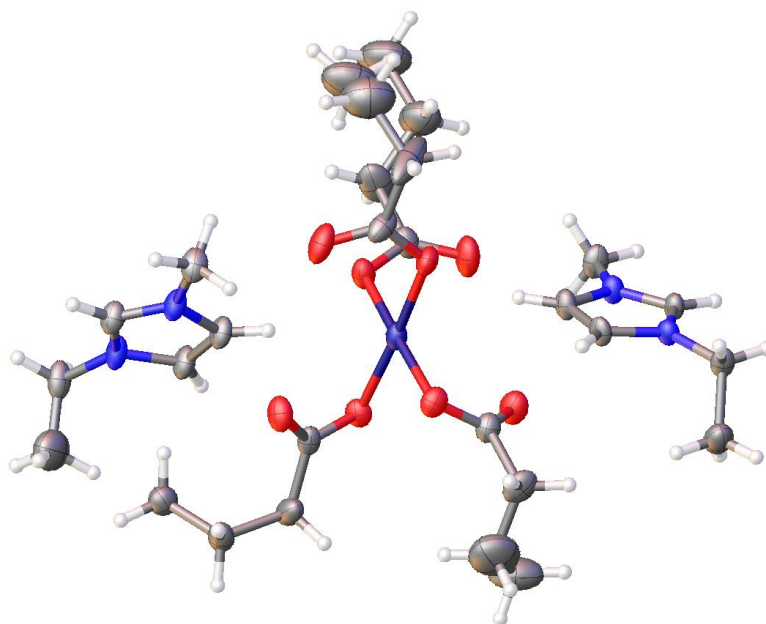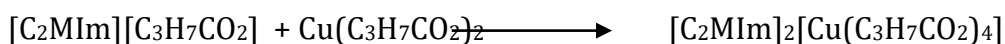
Figure 5-9. Structure of $[C_2MIm]_2[Cu(C_3H_7CO_2)_4]$, formed by heating a solution of $Cu(C_3H_7CO_2)_2$ in the ionic liquid $[C_2MIm][C_3H_7CO_2]$ to 80°C and crystallising the compound by slow cooling.
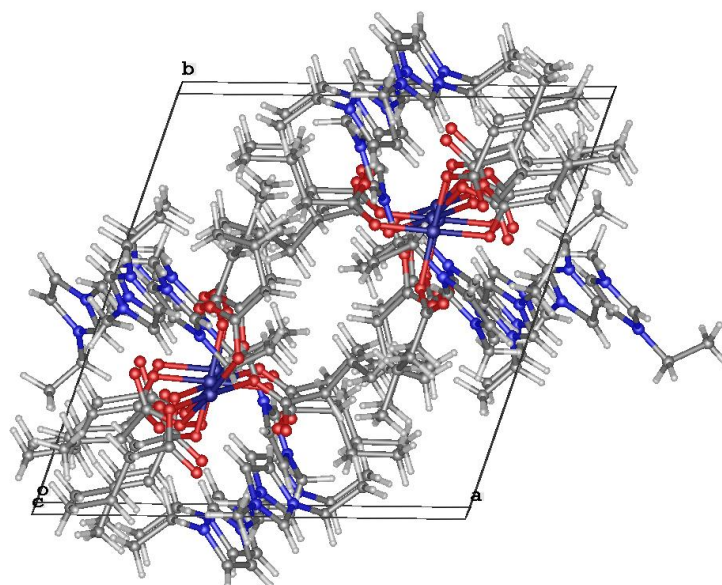
Figure 5-10. Square-planar coordination packing in the crystal structure of [C₂MIm]₂[Cu(C₃H₇CO₂)₄].

Table 5-5. Crystal data for [C₂MIm]₂[Cu(C₃H₇CO₂)₄].

Empirical formula	$CuC_{20}H_{39}N_2O_2$
Formula weight	403.08 g/mol
Temperature/K	100.00(10)
Crystal system	triclinic
Space group	P-1
a/Å	14.3866(6)
b/Å	15.9472(9)
c/Å	17.1521(8)
α/°	65.732(5)
β/°	77.128(4)
γ/°	67.803(5)
Volume/Å³	3310.9(3)
Z	14
ρ_{calc}g/cm³	2.994
μ/mm⁻¹	9.875
F(000)	2898.0
Radiation	Cu Kα (λ = 1.54184)
2Θ range for data collection/°	8.4 to 145.24
Index ranges	-17 ≤ h ≤ 14, -18 ≤ k ≤ 19, -20 ≤ l ≤ 20
Reflections collected	22643
Independent reflections	12772 [R_{int} = 0.0375, R_{sigma} = 0.0573]
Data/restraints/parameters	12772/0/755
Goodness-of-fit on F²	1.722
Final R indexes [I>=2σ (I)]	R_1 = 0.0821, wR_2 = 0.2502
Final R indexes [all data]	R_1 = 0.1011, wR_2 = 0.2625
Largest diff. peak/hole / e Å⁻³	2.51/-0.92

5.3.3.4   Copper(II) octanoate at room temperature

Copper(II) octanoate was synthesis and characterised, however it was not possible to recrytallise the compound in methanol or any other solvent. Surprisingly, a similar structure was obtained after dissolving $Cu(C_7H_{15}CO_2)_2$ in the ionic liquid $[C_2MIm][C_7H_{15}CO_2]$, where a highly concentrated solution was prepared, and from this sample also a crystalline product was obtained.

The crystal structure of this compound was determined, and the compound turned out to be $[C_2MIm]_2[Cu(C_7H_{15}CO_2)_4]$ as show in Figure 5-11. Similarly to the butanoate, this structure consists of $[C_2MIm]+$ cations and isolated $[Cu(C_7H_{15}CO_2)_4]^-$ anions. The copper(II) $[Cu(C_7H_{15}CO_2)_4]^-$ anions are showing a square-planar coordination with four monodentately coordinating octanoate groups. Figure 5-12 is showing the packing in the crystal structure of $[C_2MIm]_2[Cu(C_7H_{15}CO_2)_4]$. The copper centres and the cations are packing within one layer of the structure, separated by layers of the long alkyl chains arranged into another layer. A reaction equation is given below in (Eq. 49).

(Eq. 49)

$$[C_2MIm][C_7H_{15}CO_2] + Cu(C_7H_{15}CO_2)_2 \longrightarrow [C_2MIm]_2[Cu(C_7H_{15}CO_2)_4]$$
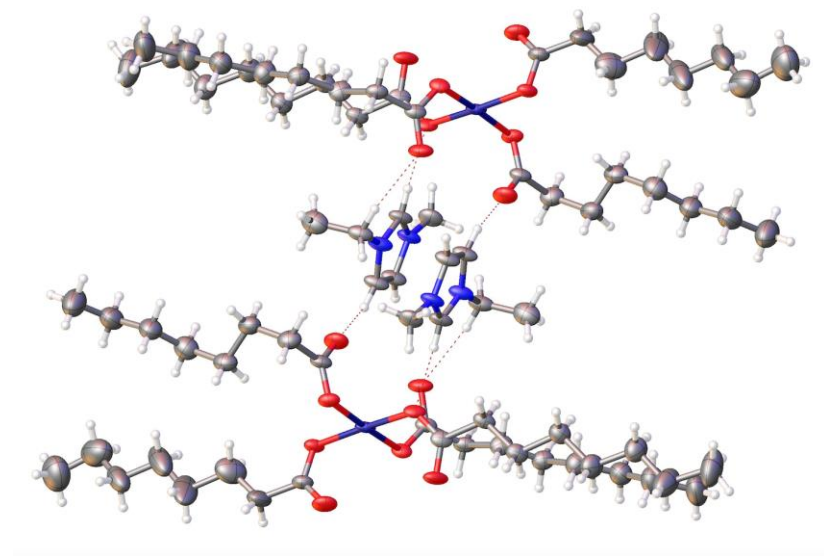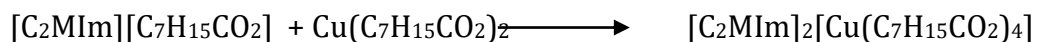
Figure 5-11. Structure of $[C_2MIm]_2[Cu(C_7H_{15}CO_2)_4]$ formed by heating a solution of $Cu(C_7H_{15}CO_2)_2$ in the ionic liquid $[C_2MIm][C_7H_{15}CO_2]$ to 80°C and crystallising the compound by slow cooling.
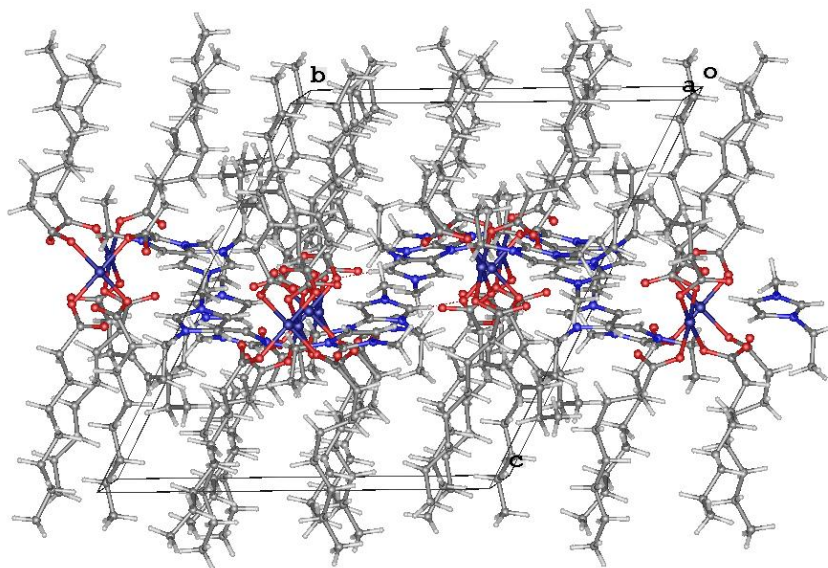
Figure 5-12. square-planar coordination packing in the crystal structure of [C₂MIm]₂[Cu(C₇H₁₅CO₂)₄].

Table 5-6. Crystal Data for [C₂MIm]₂[Cu(C₇H₁₅CO₂)₄].

Empirical formula	$CuC_{38}H_{71}N_2O_2$
Formula weight	651.53 g/mol
Temperature/K	99.9(2)
Crystal system	triclinic
Space group	P-1
a/Å	17.1050(4)
b/Å	17.4308(6)
c/Å	18.9701(6)
α/°	63.412(3)
β/°	86.315(2)
γ/°	76.256(3)
Volume/Å³	4907.3(3)
Z	2
ρ_{calc} g/cm³	1.161
μ/mm⁻¹	1.027
F(000)	1864.0
Crystal size/mm³	0.259 × 0.1593 × 0.1484
Radiation	CuKα (λ = 1.54184)
2Θ range for data collection/°	9.982 to 133.198
Index ranges	-20 ≤ h ≤ 20, -20 ≤ k ≤ 18, -22 ≤ l ≤ 22
Reflections collected	84986
Independent reflections	17300 [R_{int} = 0.0553, R_{sigma} = 0.0392]
Data/restraints/parameters	17300/0/1044
Goodness-of-fit on F²	1.098
Final R indexes [I>=2σ (I)]	R_1 = 0.1030, wR_2 = 0.2630
Final R indexes [all data]	R_1 = 0.1186, wR_2 = 0.2727
Largest diff. peak/hole / e Å⁻³	1.76/-1.17

5.3.3.5   *Conclusion*

Copper(II) acetate dehydrate, $[Cu_2(CH_3CO_2)_4(H_2O)_2]$, is a known paddle-wheel isolated structure of two atoms of copper linked to each other and surrounded by four acetate anion and two water molecules. Unlike isolated structure found in the acetate anion, Copper(II) butanoate, $Cu_2(C_3H_7CO_2)_4$ show a 1-D coordination polymer paddle-wheel. Unfortunately, it was not possible to crystallised Copper(II) octanoate due to the long alkyl chain length of the carboxylate.

When those copper(II) salts are dissolved at room temperature in their respective ILs, $[C_4MIm][C_nH_nCO_2]$, different types of crustal structure are found , which will depend on the temperature of dissolution as well as the alkyl chain length of the anion.

Indeed, Copper(II) acetate dehydrate forms a coordination polymer paddle-wheel structure of $[C_4MIm][Cu_2(CH_3CO_2)_5]$. This structure has replaced water molecules by acetate anion highly present in solution which has allowed polymer formation instead of isolated structured. However, when heated at 80°C, it forms a 1-D coordination polymers of trimeric hydroxyl-clusters structure, $[C_2MIm][Cu_3(CH_3CO_2)_5(H_2O)(OH)_2] \cdot H_2O$. This time there are three Copper atoms linked to each other instead of two. However, Copper(II) butanoate and octanoate forms a square-planar coordination with four monodentately coordinating anion groups.

These data would help to gain more understanding in the copper oxide nanofluid formation.

5.4 Characterisation of copper oxide nanoparticles and the influence of the presence of water

In this section, the nanoparticles are first of all characterised using X-Ray Photoelectron Spectroscopy (XPS) analysis in order to determine the copper oxidation state(s). Then, the particle morphology will be discussed with regards to role of the water concentration using Transmission Electron Microscopy (TEM). Finally, the physical properties of the ternary mixtures were investigated in order to fully characterise the nanofluids.

The composition used to synthesis CuO-NPs are shown in Table 5-9. The solution S1 to S6 where the molar and mass ratio were calculated as reported in the Chapter 1, where the water content present after drying the IL was taken into account. However, the water content already present in the copper salt wasn't taken into account in this work.

Table 5-7. Composition used to synthesis CuO-NPs from the different copper(II) carboxylate precursors.

Copper(II) precursor used	Copper salts solutions	Nanofluid solutions	Molar ratio IL : Cu(II) : H$_2$O	Mass ratio IL : Cu(II) : H$_2$O	W % in the dried IL
Copper(II) acetate	S1	S13	89 : 5 : 6	93 : 6 : 0	0.78 %
	S2	S14	57 : 6 : 37	89 : 8 : 3	
	S3	S15	50 : 5 : 45	82 : 10 : 8	
Copper(II) butanoate	S7	S10	90 : 4 : 6	94 : 4 : 0	0.45 %
	S8	S11	70 : 4 : 26	90 : 7 : 3	
	S9	S12	50 : 4 : 46	84 : 9 : 7	
Copper(II) octanoate	S4	S16	90 : 4 : 6	95 : 5 : 0	0.17 %
	S5	S17	70 : 4 : 26	91 : 7 : 2	
	S6	S18	35 : 2 : 63	83 : 7 : 10	

* In red are highlighted the composition with no water, except the water content left in the dried IL.

189

5.4.1 XPS analysis of copper oxide

In this section, the use of the NIST X-Ray Photoelectron Spectroscopy (XPS) Database has been very helpful since it gives easy access to the energies of many photoelectron and Auger-electron spectral lines.[190] The binding energy of Cu $2p_{3/2}$ is known to give a peak at around 933 eV and weak satellite features at 945 eV for Cu(I); whereas it is known to give a peak at around 933.5 eV with strong satellite peaks at 943 eV for Copper(II). The XPS analysis of copper metal, (I) and (II) is reported from the database in the Figure 5-13.
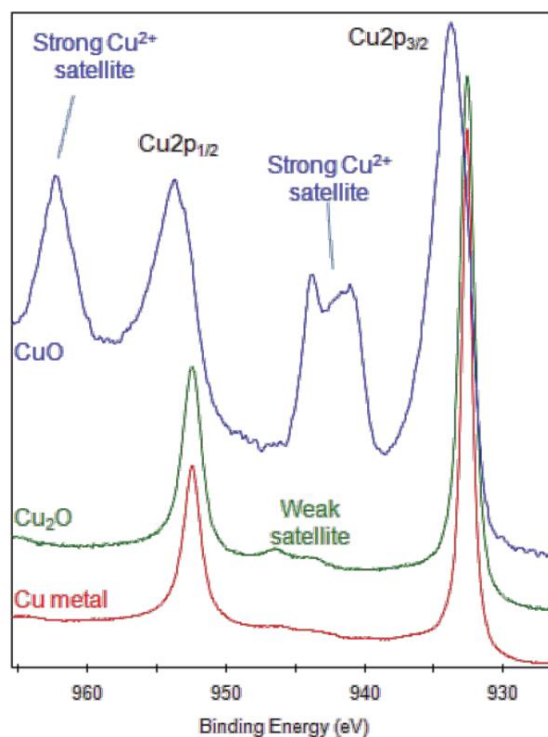
Figure 5-13. XPS spectra for Cu $2p_{3/2}$ spectra lines of copper(O) (in red), Copper(I) oxide (in green) and copper(II) oxide (in blue) from the NIST X-Ray Photoelectron Spectroscopy Database.[190]

5.4.1.1 Nanofluids from a copper(II) acetate precursor

IL-nanofluids made from copper(II) acetate and [C$_4$MIm][CH$_3$CO$_2$] were previously analysed using XPS in the work of Nockemann *et al.*, where a mixed valent copper(I,II) oxide was found.[176] The binding energy value was found at 932.3 eV assigned to the Cu(I) state; while 933.1 eV and 940 eV was assigned to the Cu(II) state. The Figure 5-14-a below represents their XPS analysis. The Figure 5-14-b represents CuO in [P$_{88812}$][CH$_3$CO$_2$].
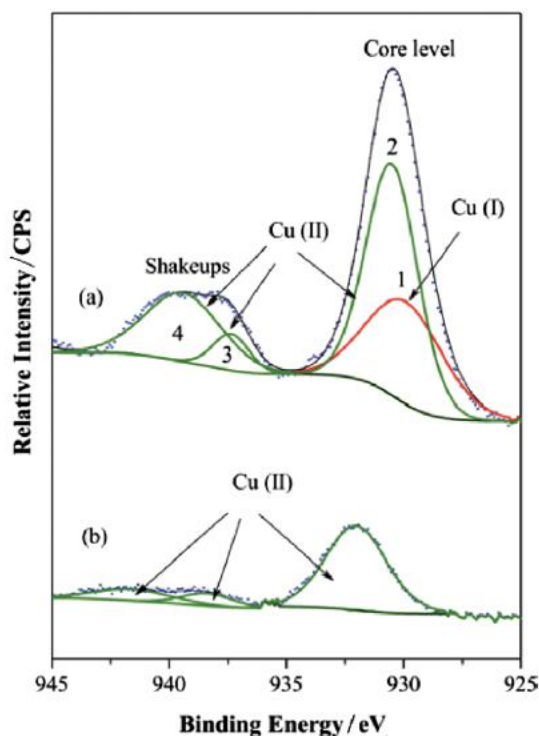
Figure 5-14. XPS spectra for Cu $2p_{3/2}$ spectra lines of nanofluids from copper(II) acetate using: (a)$[C_4MIm][CH_3CO_2]$ and b)$[P_{88812}][CH_3CO_2]$. Peak 1 represents copper(I) and peaks 2-4 represent copper(II).[176]

5.4.1.2 Nanofluids from copper(II) butanoate and octanoate precursors

In this section the nanofluid solutions made from copper(II) butanoate and copper(II) octanoate precursors in their respective ILs were analysed using XPS in order to determine the formation of copper oxide and the oxidation states of the metal. The binding energies were normalised using the C 1s at 284.8 eV and are shown for all atoms in Table 5-8. The spectra obtained are shown in Figure 5-15. Since the nanofluid solutions are very sensible to air (as reported in the synthesis section), samples were prepared in an Argon-glovebox, then stocked in a desiccator filled with Argon and the sample were placed into the XPS instrument under the presence of an Argon flux.

However, the sample measured is so small (drop size) that it was difficult to recognized a present reaction with air or not. Also, the beam wouldn't go further than a few nm into the surface sample, which means that only the surface in contact with atmosphere would be analysed and if a reaction had occurred with air, only this material would be analysed. This fact could unfortunately have altered the presence of CuO in solution and could have lead to Cu_2O instead.

191
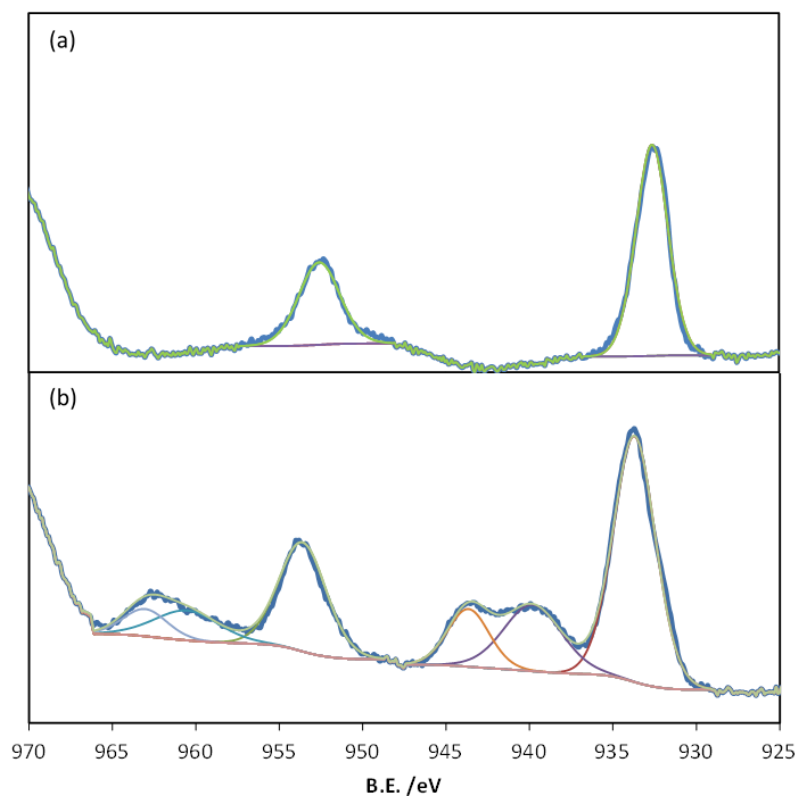
Figure 5-15. XPS spectra normalised for Cu $2p_{3/2}$ spectra lines of nanoparticles in: (a) [C_2MIm][$C_7H_{15}CO_2$] and (b) [C_2MIm][$C_3H_7CO_2$].

Table 5-8. Binding energy of the atoms found in the nanofluid solutions from copper(II) bunatoate (b) and octanoate (a) precursors in their respective IL. The main peaks to determine copper oxide state are in red colour.

	Octanoate (a)		Butanoate (b)	
Cu 2p 3/2	932.6	866.9	933.7	1321.4
Cu 2p 3/2	/	/	939.8	485.2
Cu 2p 3/2	/	/	943.7	299.5
N 1s	401.4	5338.9	401.5	6492.6
N 1s	399.1	1680.9	/	/
O 1s	533.4	8661.1	532.2	13192.3
O 1s	532.1	11444.2	530.1	4840.3
O 1s	530.0	2978.8	/	/
C 1s	286.1	21204.1	286.2	20073.3
C 1s	284.8	16502.2	284.8	16618.5

Elucidation of the Cu oxidation state from Cu 2p XPS is difficult as the binding energies for the oxidation states are very similar. However, the spectra in Figure 5-15 do give some information: in sample (a) there are not any satellite or shake

192

down peaks; whereas in the sample (b) there are (around 940 eV). According to the NIST X-Ray Photoelectron Spectroscopy (XPS) Database, satellite peaks only come from Cu(I) (very weak/ small satellites) or Cu(II) (strong satellites).[190] Thus, there is a definite difference between sample (a) and (b), where (a) can only be Cu(I) and (b) has to have Cu(II) in it but you cannot rule out the presence of Cu(I).

Therefore, nanofluids made from copper(II) butanoate are containing copper(I) oxide nanoparticles; whereas nanofluids made from copper(II) octanoate are mainly containing copper(II) oxides nanoparticles. However, nanofluids made from copper(II) acetate are containing a mixed valent of Copper(I,II) oxide.

5.4.2 Impact of Water on the size distribution of the CuO nanoparticles *via* TEM analysis

The presence of water is indispensable to the CuO-NPs formation as it was shown in the (Eq. 44) and (Eq. 45) of this chapter. Chapter 3 and 4 has also shown the role of water in binary mixture using same ILs as for the CuO-NPs synthesis. From those results, water seems to reorganise the ILs until a limit of concentration and then to fully or partly dissociate into a $[C_2MIm]^+$ cation and the $[C_nH_nCO_2]^-$ anion at higher concentration.

In this part, the impact of water on the CuO-NPs formation was investigated by using Transmission Electron Microscopy (TEM), by determination of the size distribution and shape of CuO-NPs for different composition of the ternary mixtures. However, it was not possible to add more than 0.65 water mole fraction in solution without getting a precipitate or to dissolve all the copper salt. And it was not possible to include less than 0.3 IL mole fraction in the solution for the same reasons.

The composition used to synthesise CuO-NPs are shown in Table 5-9. The molar and mass ratio were calculated as reported in Chapter 1, where the water content present after drying the IL was taking into account. However, water content already present in the copper salt wasn't taken into account in this work.

Table 5-9. Composition used to synthesis CuO-NPs from the different copper(II) carboxylate precursors.

Copper(II) precursor used	Solution name	Molar ratio IL : Cu$^{(II)}$: H$_2$O	Mass ratio IL : Cu$^{(II)}$: H$_2$O	W % in the dried IL
Copper(II) acetate	S1	89 : 5 : 6	93 : 6 : 0	0.78 %
	S2	57 : 6 : 37	89 : 8 : 3	
Copper(II) butanoate	S3	90 : 4 : 6	94 : 4 : 0	0.45 %
	S4	70 : 4 : 26	90 : 7 : 3	
	S5	50 : 4 : 46	84 : 9 : 7	
Copper(II) octanoate	S6	90 : 4 : 6	95 : 5 : 0	0.17 %
	S7	70 : 4 : 26	91 : 7 : 2	
	S8	35 : 2 : 63	83 : 7 : 10	

* In red are highlighted the composition with no water, except the water content left in the dried IL.

TEM images of synthesised copper oxide nanostructures, following by their size distribution are presented below in function of their respective copper salt and IL precursors. The water concentration will be discussed. The size distribution of the TEM images were measured using ImageJ free program.[191,192]

5.4.2.1 *CuO-NPs from copper(II) acetate precursor*

In this first part, solutions of copper oxide NPs were synthesised from a copper(II) acetate precursor in [C$_2$MIm][CH$_3$CO$_2$] at two different molar ratios, as reported in Table 5-9, in order to study the impact of water on the NPs size.
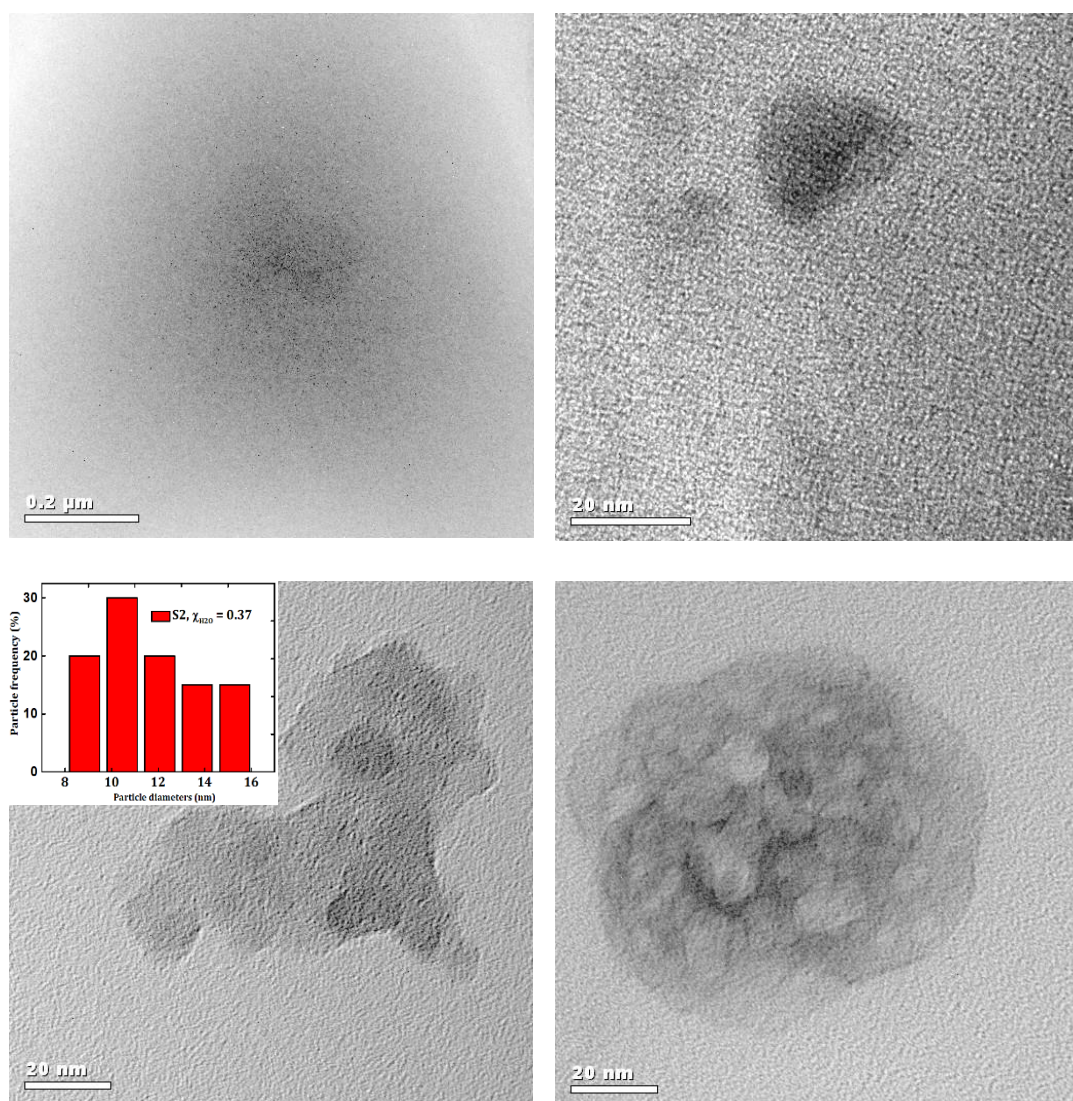
Figure 5-16. TEM images of copper(I,II), oxide clusters synthesised in [C$_2$MIm][CH$_3$CO$_2$] and copper(II) acetate precursor for S1 (top two images), and S2 with its size distribution diagram (bottom two images).

The solution, S1, only shows very small dots smaller than 10 nm, where those particle have been isolated and be analysed with the TEM instruments in

[C$_2$MIm][CH$_3$CO$_2$] as seen in the two images on top of Figure 5-16. This solution only contains 0.78 % of the water content left in the dried IL. Thus, it contains sufficient amount of water to produce CuO as reported in (Eq. 44). This result is in accordance to the work published by our group elsewhere,[176] where they could only see barely-visible mixed-oxidation state clusters of copper(I,II) oxide as seen in the following TEM images reported in Figure 5-17:
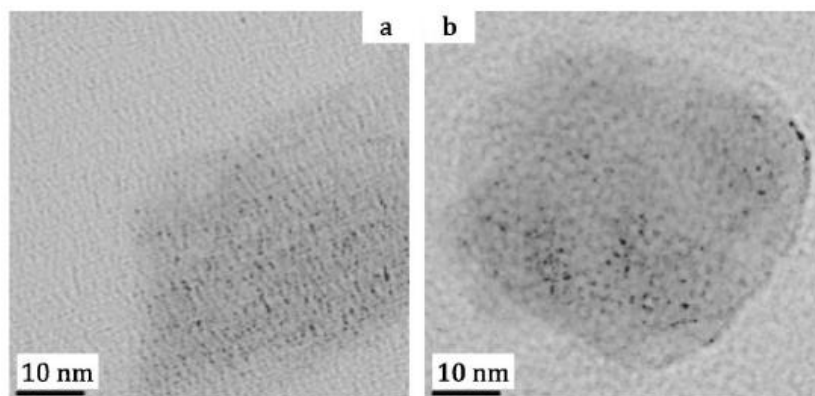
Figure 5-17. TEM images of copper(I,II) oxide clusters synthesised in [C$_4$MIm][CH$_3$CO$_2$] and using copper(II) acetate precursor from the work published by Nockemann *et al.*[176]

However, when increasing the water concentration to 25 % mole ratio, the solution, S2, displayed particle diameters in the range of 9 -15 nm and do not seem to go below 9 nm. The size distribution of the CuO-NPs is shown in Figure 5-16 (bottom).

5.4.2.2 *CuO-NPs from copper(II) butanoate precursor*

In this second part, solutions of copper oxide NPs were synthesised from a copper(II) butanoate precursor in [C$_2$MIm][C$_3$H$_7$CO$_2$] at three different molar ratios, as reported in Table 5-9, in order to study the impact of water and the chain length of the anion on the NP size.

The first solution, S3, shows TEM images at two different reaction-times from a solution that only contained 0.45 % of the water content left in the dried IL. The first part shows the reaction at an intermediate stage (Figure 5-18) and the second one at the final stage of the reaction (Figure 5-20).

196

The NP growth was only observed at this composition by pure incident. In fact, after the full dissolution of copper salt, the solution (S3) was only heated for 20 minutes at 120°C instead of more than 30 minutes. The solution was given a deep red colour as it was expected to do. However, when the solution went back to room temperature, it turned to a greenish colour (almost like its intermediate state). As it was explained previously in the CuO synthesis, the whole reaction did not occur, and the TEM images are showing very large aggregation of square and spherical CuO-NPs in ranges of [100 – 400] nm (Figure 5-18 and Figure 5-19). This is in agreement with the crystallography and UV-VIS study that show different copper coordination state depending on the temperature.
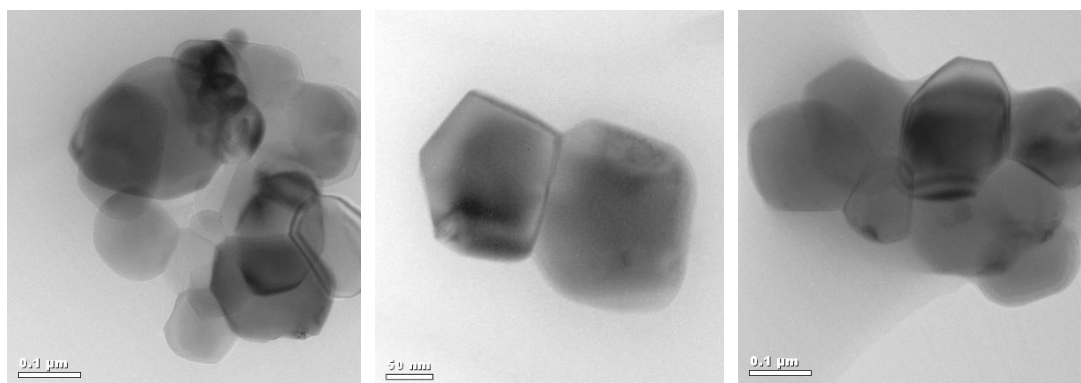
Figure 5-18. TEM images of copper oxide nanoparticles synthesised in [C_2MIm][$C_3H_7CO_2$] and copper(II) butanoate precursor for S3 at a reaction time of only 20 minutes heated at 120°C.
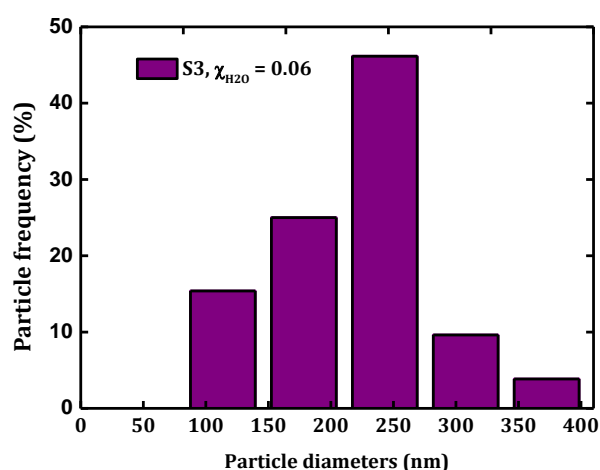
Figure 5-19. Particle frequency (%) in function of the particle diameters (nm) from CuO synthesised from Solution S3 at a reaction time of only 20 minutes heated at 120°C.

However, after more than 30 minutes of heating, the solution shows much smaller and spherical particle diameters in a range of [18 - 57] nm, with a maximum frequency between a range of 37 – 51 nm (Figure 5-20). They are also much bigger that for the CuO synthesised from copper(II) acetate.
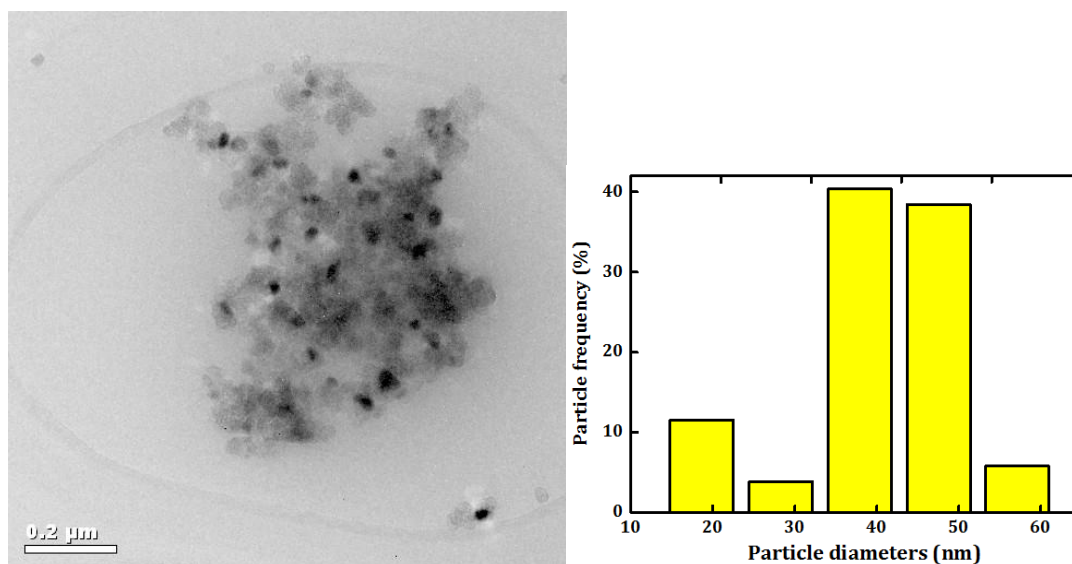
Figure 5-20. TEM images of copper oxide nanoparticles synthesised in $[C_2MIm][C_3H_7CO_2]$ and copper(II) butanoate precursor at a complete reaction time (left), and the particle frequency (%) in function of the particle diameters (nm) from CuO synthesised (right) from S3.

This time, the water concentration was increased to firstly a 26 % mole ratio, where the TEM images and the size distribution diagram, displayed in Figure 5-21, show particle range diameters of 24 to 51 nm, with a maximum frequency between 24 and 40 nm. Water concentration was then increased to 46 % mole ratio, where the TEM images and the size distribution diagram in Figure 5-22 follow, show particle ranges diameters of 11 to 51 nm, with a maximum frequency between 11 and 26 nm.
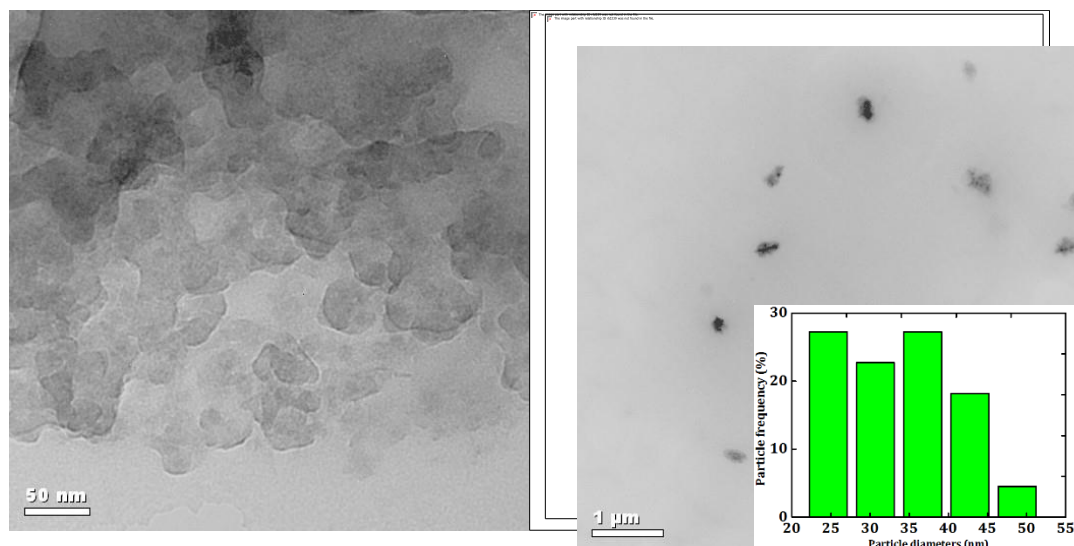
Figure 5-21. TEM images of copper oxide nanoparticles synthesised in [C$_2$MIm][C$_3$H$_7$CO$_2$] and copper(II) butanoate precursor for S4 at a complete reaction time and the particle frequency (%) in function of the particle diameters (nm) from CuO synthesised from Solution S4.
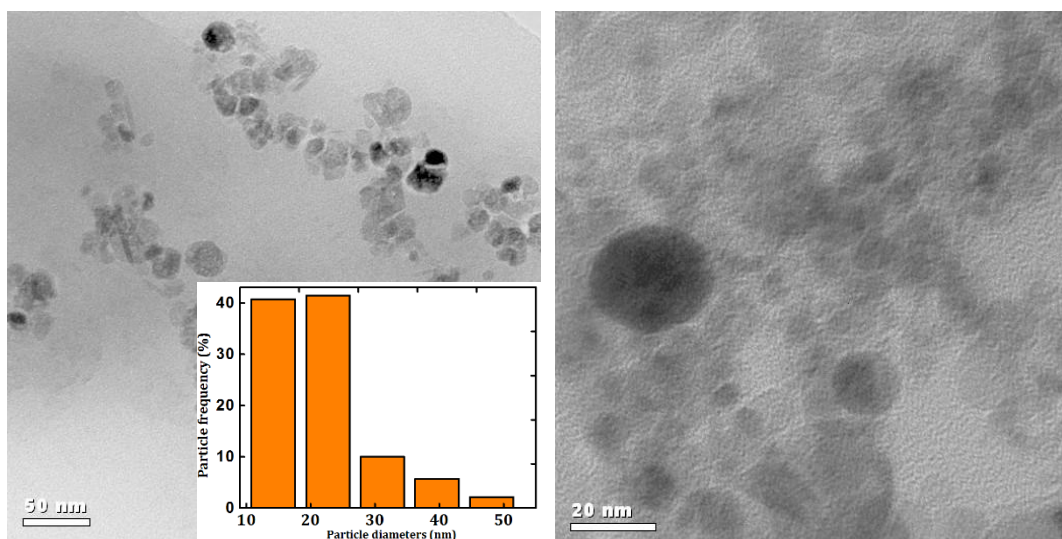
Figure 5-22. TEM images of copper oxide nanoparticles synthesised in [C$_2$MIm][C$_3$H$_7$CO$_2$] and copper(II) butanoate precursor at a complete reaction time, and particle frequency (%) in function of the particle diameters (nm) from CuO synthesised from Solution S5.

A summary of all CuO-NPs syntheses from the copper(II) butanoate are displayed in the Figure 5-23. From those results it seems that the water concentration does not influence the size distribution of the nanoparticles formed, since these are all in a range of 10-61 nm.
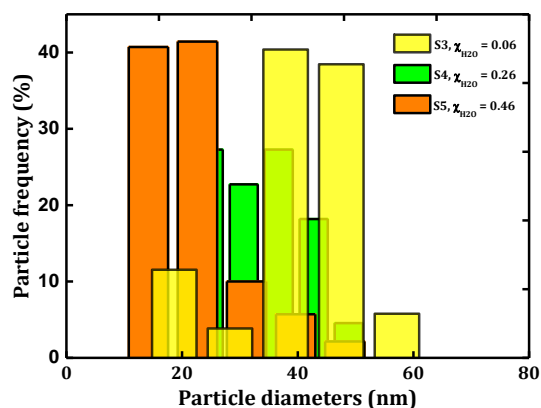
Figure 5-23. Particle frequency (%) in function of the particle diameters (nm) from CuO synthesised from Solution S3, S4 and S5.

5.4.2.3 *CuO-NPs from copper(II) octanoate precursor*

In this third part, solutions of copper oxide NPs were synthesised from a copper(II) octanoate precursor in $[C_2MIm][C_7H_{15}CO_2]$ at three different molar ratios, as reported in Table 5-9, in order to study the impact of water on the NPs size. The solution, S6, shows TEM images from a solution that only contained 0.17 % of the water content left in the dried IL (Figure 5-24). The particle diameters are in a range of 10 - 21 nm with a maximum frequency at 14 nm. They are much smaller and packed than for the CuO synthesised from copper(II) butanoate.
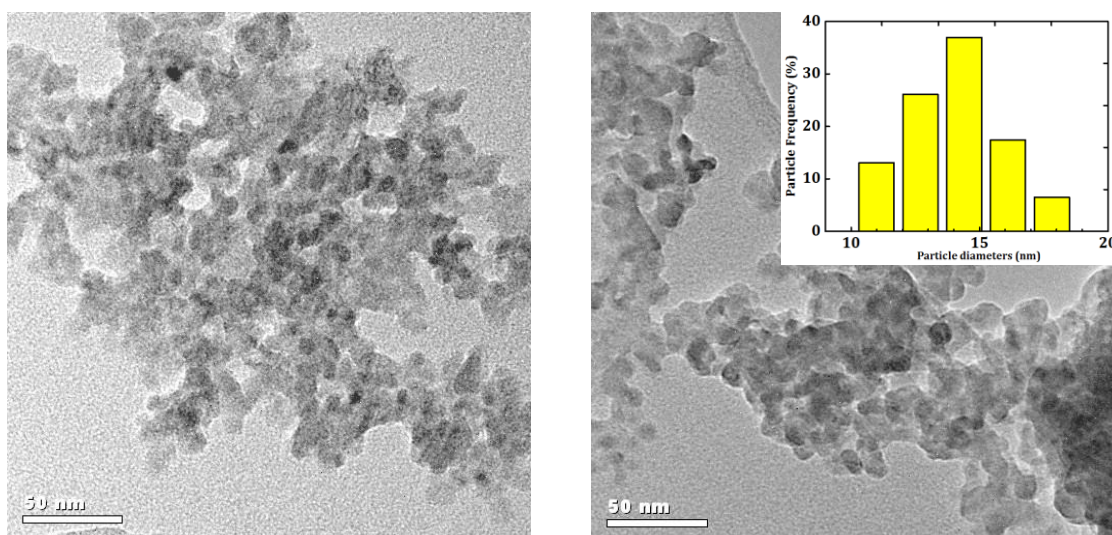
Figure 5-24. TEM images of copper oxide nanoparticles synthesised in $[C_2MIm][C_7H_{15}CO_2]$ and copper(II) octanoate precursor at a complete reaction time, and particle frequency (%) in function of the particle diameters (nm) from CuO synthesised from Solution S6.

200

Furthermore, by increasing the water concentration to 26 % mole ratios, the TEM images and the size distribution diagram in Figure 5-25 and Figure 5-26, show particle ranges diameters of 7 to 23 nm, with a maximum frequency at 7 nm. And then increasing the water concentration to 63 % mole fraction, the TEM images and the size distribution diagram in Figure 5-25 show particle ranges diameters of 10 to 25 nm, with a maximum frequency around 20 nm.
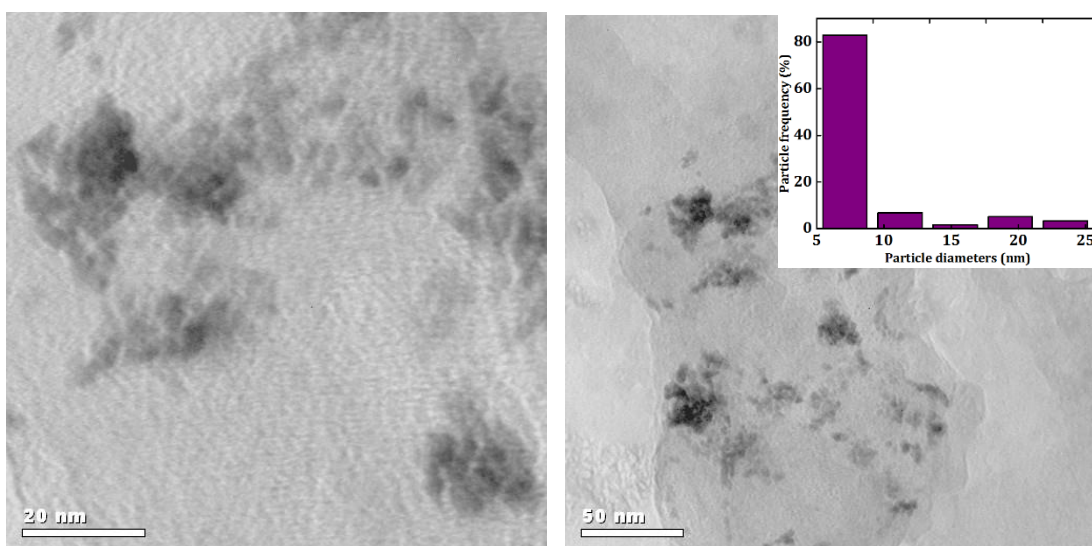
Figure 5-25. TEM images of copper oxide nanoparticles synthesised in [C₂MIm][C₇H₁₅CO₂] and copper(II) octanoate precursor at a complete reaction time, and particle frequency (%) in function of the particle diameters (nm) from CuO synthesised from Solution S7.
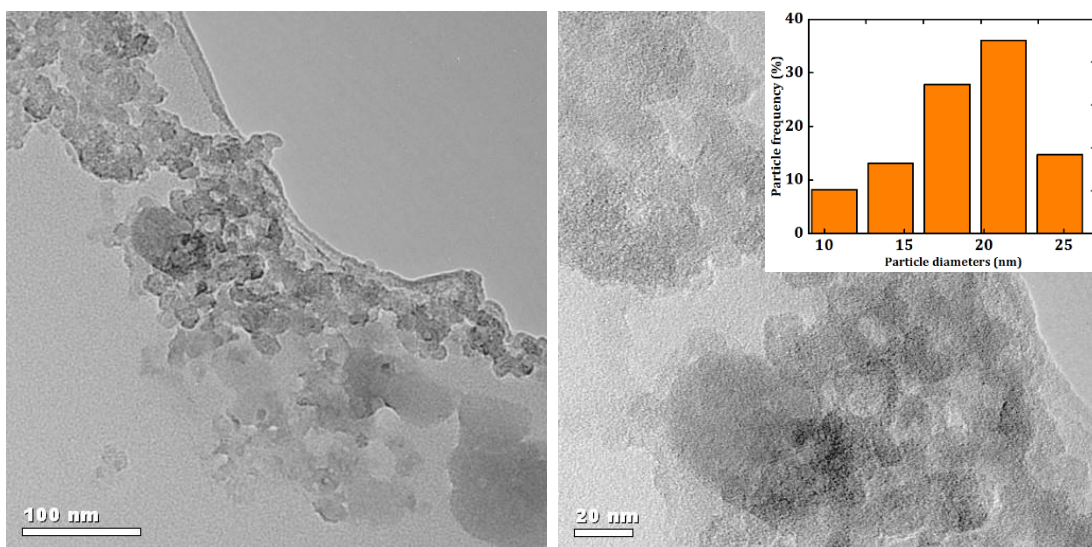
Figure 5-26. TEM images of copper oxide nanoparticles synthesised in [C₂MIm][C₇H₁₅CO₂] and copper(II) octanoate precursor at a complete reaction time, and particle frequency (%) in function of the particle diameters (nm) from CuO synthesised from Solution S8.

A summary of all CuO-NPs syntheses from the copper(II) octanoate is displayed in the Figure 5-27. From those results it seems that water concentration doesn't influence the size distribution of the nanoparticles formed since these are all in a range of 10 - 25 nm.
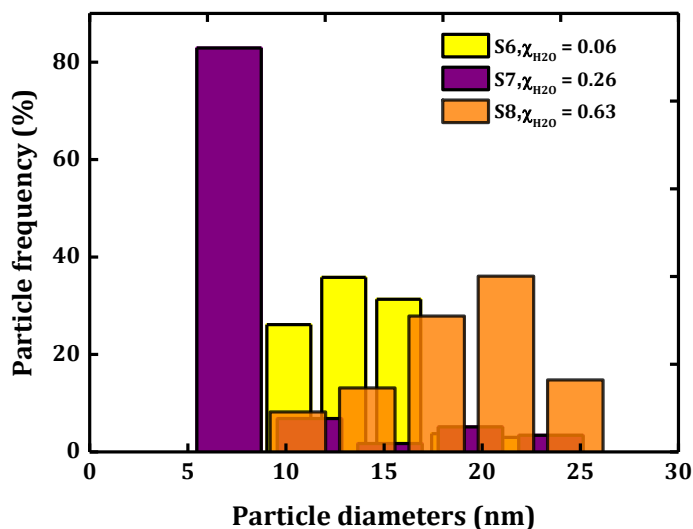
Figure 5-27. Particle frequency (%) in function of the particle diameters (nm) from CuO synthesised from Solutions S6, S7 and S8.

5.4.2.4 *Influence of the alkyl-chain length from the carboxylate precursor on the CuO-NPs*

From the previous results, it is possible to gain a better understanding on the impact of water on the NP size as well as on the impact of the alkyl-chain length on the copper salt and respective IL. First of all, the water concentration does not seem to have a huge influence with regards to the particle size diameters (until a certain limit since above 65% mole fraction the solution will precipitate). It was then possible to combine all particle diameter data from each respective copper salt precursor, in order to look at the influence of the alkyl-chain length of the respective anion precursor.

The results are shown in Figure 5-28, where CuO-NPs synthesised from copper(II) acetate display a maximum frequency at about 10 nm (S1 was not taking into account in this graph since the particle were too small to count); CuO-

NPs synthesised from copper(II) butanoate display a maximum frequency at about 45 nm; and CuO-NPs synthesised from copper(II) octanoate display a maximum frequency at about 15 nm.
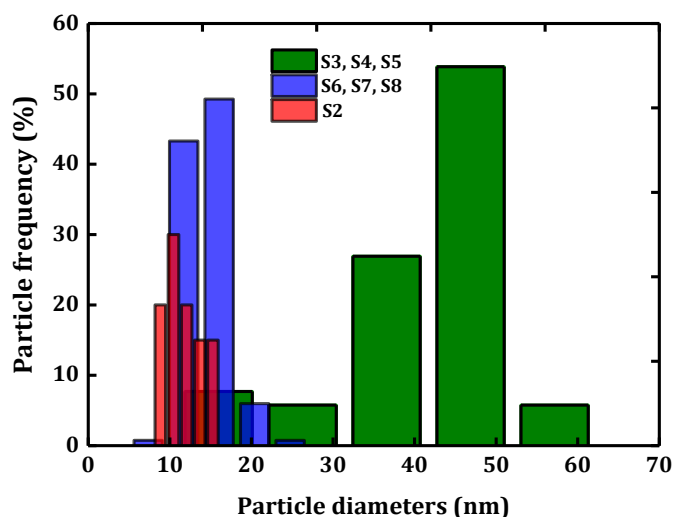
Figure 5-28. Particle frequency (%) in function of the particle diameters (nm) from CuO synthesised from all solutions with copper(II) acetate (red), butanoate (green), and octanoate (blue). *Only S1 has not been taking into account since particles were too small.

Since the particle diameter frequencies are overlapping in Figure 5-28, the CuO particle diameters were also displayed in function of the number of carbons on the alkyl-chain length of the copper salt precursors.
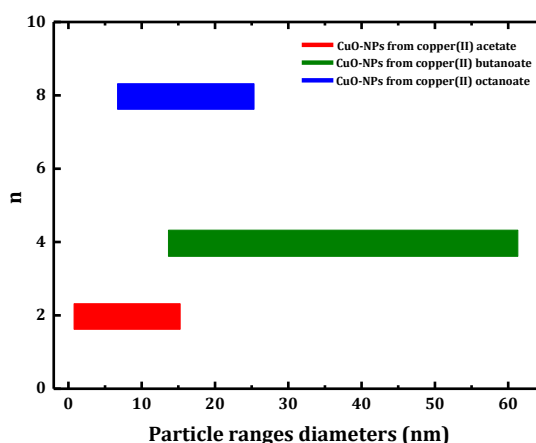
Figure 5-29. Number of carbon, n, of the copper(II) carboxylate precursor in function of the CuO particle ranges diameters.

The ranges of the particle diameters were then displayed and compared with the work published by Nockemann *et al.*, in Table 5-10 and Table 5-11.[176]

Table 5-10. Particle range diameters for different type of IL-cation from this work and elsewhere.[176]

Cations	Anion	Characteristic	Particles range diameters
$[P_{66614}]^+$		Hydrophobic	NPs < 50 nm[176]
$[C_4MIm]^+, n = 4$	$[CH_3CO_2]$ n = 2	Hydrophilic	Cluster < 0.5nm[176]
$[C_2MIm]^+, n = 2$		Hydrophilic	$d_p = [5 - 20]$ nm (this work)

Table 5-11. Particle range diameters for different type of IL-anion from this work.

Cation	Anions	Characteristic	Particles range diameters
	$[CH_3CO_2]$ n= 2	Hydrophilic	$d_p = [1 - 15]$ nm
$[C_2MIm]^+$ n = 2	$[C_3H_7CO_2]$ n = 4	Hydrophobic +	$d_p = [14 - 61]$ nm
	$[C_7H_{15}CO_2]$ n = 8	Hydrophobic +++	$d_p = [7 - 25]$ nm

In conclusion, the formation of the particles is resulting in certain size distributions, and are influenced by either the IL-cation (proven in our previous work) or the IL-anion (proved in this present work). Here, we demonstrated that changing the structure of the IL, e.g. changing the anion from acetate to an octanoate, also changes the morphology of the resulting nanomaterials. This is an important result, since the control over the morphology of transition metal oxides is very challenging and the concept could then be transferable to other metal oxides such as Fe, Mn, Co, Ni, but also to lanthanide oxides.

5.4.3 Physical properties of copper precursors in ionic liquid before/after turning into nanofluids

The solutions were analysed after the copper salts were dissolved at 50°C in their respective ILs, and after the same solutions had turned into nanofluids at 120°C. Three ternary mixture solutions for each copper salt precursor were investigated in order to characterise and gain more understanding on the role of water in the *in-situ* nanoparticle synthesis. The compositions used were made in the same way as described in the previous part for the TEM analysis at same ratio shown in Table 5-7.

Table 5-12. Composition used to synthesis CuO-NPs from the different copper(II) carboxylate precursors.

Copper(II) precursor used	Copper salts solutions	Nanofluid solutions	Molar ratio IL : Cu$^{(II)}$: H$_2$O	Mass ratio IL : Cu$^{(II)}$: H$_2$O	W % in the dried IL
Copper(II) acetate	S1	S13	89 : 5 : 6	93 : 6 : 0	0.78 %
	S2	S14	57 : 6 : 37	89 : 8 : 3	
	S3	S15	50 : 5 : 45	82 : 10 : 8	
Copper(II) butanoate	S7	S10	90 : 4 : 6	94 : 4 : 0	0.45 %
	S8	S11	70 : 4 : 26	90 : 7 : 3	
	S9	S12	50 : 4 : 46	84 : 9 : 7	
Copper(II) octanoate	S4	S16	90 : 4 : 6	95 : 5 : 0	0.17 %
	S5	S17	70 : 4 : 26	91 : 7 : 2	
	S6	S18	35 : 2 : 63	83 : 7 : 10	

* In red are highlighted the composition with no water, except the water content left in the dried IL.

5.4.3.1 Temperature decomposition

Thermal properties of neat ILs, dissolved copper salt solutions at 50°C and prepared nanofluid solutions, as well as the water content of the tested samples, are shown in Table 5-13 and displayed in Figure 5-30.

Table 5-13. Values of decomposition temperature, Tdec (/K), of the pure ionic liquids and their ternary solution before and after NPs formation.

	T_{dec} / K	H_2O content/ wt%
[C$_2$MIm][CH$_3$CO$_2$]	488	
S1	482	0.78 %
S13	487	
[C$_2$MIm][C$_3$H$_7$CO$_2$]	480	
S7	474	0.45 %
S10	471	
[C$_2$MIm][C$_7$H$_{15}$CO$_2$]	484	
S4	484	0.17 %
S16	478	
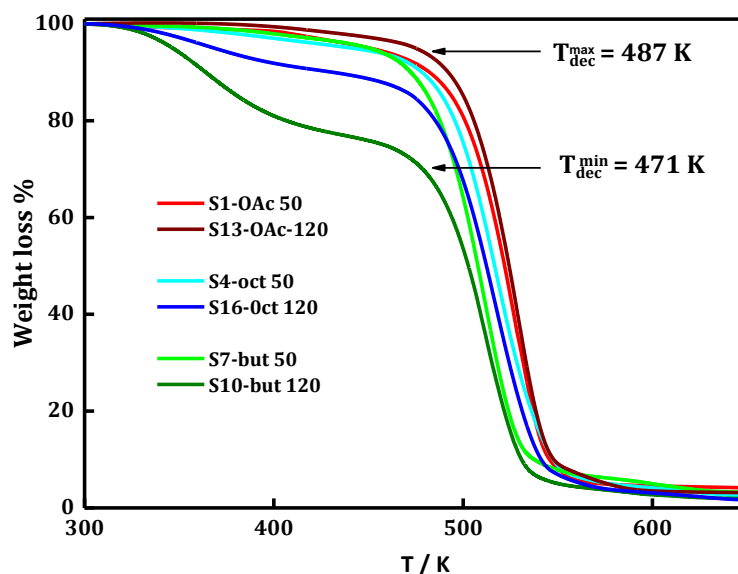
Figure 5-30. TGA curves of copper(II) acetate solutions (1,2,3) and nanofluids solutions (13, 14, 15) for a ranges of water composition ternary mixture

The presence of copper salt and copper oxide-NPs only slightly affected the decomposition temperatures, and, as reported by Nockemann *et al.*,[176] this effect is too small to have any practical significance.

5.4.3.2 Density

The density of the three pure $[C_2MIm][C_nH_nCO_2]$-ILs and of the copper salt solutions before and after nanoparticle formation was measured as a function of the temperature from (20 to 90)°C at different water mole fraction composition, χ_{H2O}, from 0 to 0.63. The results are listed in Table 3-1 and Table 5-15.

Table 5-14. Experimental density, ρ, measurements of copper salt ternary mixture after dissolution at 50°C as a function of water mole fraction composition, χ_{H2O}, for a temperature range from (20 to 90)°C at 0.1 MPa.

T/K	20	25	30	40	50	60	70	80	90
χ_{H2O}				from copper(II) acetate solutions, ρ/g·cm^{-3}					
0.00	1.0999	1.0968	1.0936	1.0872	1.081	1.0748	1.0687	1.0626	1.0567
0.06	/	1.1255	1.1222	1.1155	1.109	1.1026	1.0963	1.0899	1.0832
0.37	1.1402	1.137	1.1336	1.1263	1.1197	1.1132	1.1068	1.1002	1.0934
0.45	1.153	1.1498	1.1465	1.1398	1.1333	1.1268	1.1202	1.1133	1.1061
				from copper(II) butanoate solutions, ρ/g·cm^{-3}					
0.00	1.0640	1.0610	1.0579	1.0514	1.0452	1.0390	1.0329	1.0269	1.0209
0.06	1.0762	1.073	1.0698	1.0632	1.0567	1.0503	1.044	1.0376	1.031
0.26	1.0824	1.0793	1.0761	1.0695	1.0631	1.0566	1.0501	1.0434	1.0362
0.46	1.0926	1.0893	1.086	1.0792	1.0725	1.0657	1.0588	1.0515	1.0438
				from copper(II) octanoate solutions, ρ/g·cm^{-3}					
0.00	1.0053	1.0022	0.9991	0.9928	0.9866	0.9804	0.9743	0.9682	0.9622
0.06	1.0117	1.009	1.0061	0.9998	0.9937	0.9875	0.9812	0.9748	0.9683
0.26	1.016	1.0133	1.0102	1.0037	0.9973	0.9909	0.9844	0.9779	0.9713
0.63	1.0255	1.0226	1.0194	1.0126	1.0059	0.9992	0.9925	0.9855	0.9783

Table 5-15. Experimental density, ρ, measurements of nanofluid ternary mixture after full reaction at 120°C as a function of water mole fraction composition, χ_{H2O}, for a temperature range from (20 to 90)°C at 0.1 MPa.

T/K	20	25	30	40	50	60	70	80	90
X_{H2O}				from copper(II) acetate solutions, ρ/g·cm^{-3}					
0.06	1.1245	1.1209	1.1173	1.1099	1.1022	1.0952	1.0883	1.0815	1.0748
0.37	1.1319	1.1284	1.1251	1.1184	1.1118	1.1053	1.0987	1.0921	1.0851
0.45	1.1399	1.1367	1.1332	1.1262	1.1193	1.1122	1.1044	1.0926	n/A
				from copper(II) butanoate solutions, ρ/g·cm^{-3}					
0.06	1.0721	1.0688	1.0656	1.059	1.0525	1.0462	1.0399	1.0336	1.0273
0.26	1.0769	1.0738	1.0705	1.0638	1.0573	1.0508	1.0443	1.0379	1.0314
0.46	1.0854	1.0824	1.079	1.0721	1.0653	1.0584	1.0515	1.0444	1.0369
				from copper(II) octanoate solutions, ρ/g·cm^{-3}					
0.06	1.0103	1.0072	1.0040	0.9975	0.9910	0.9845	0.9779	0.9714	0.9646
0.26	1.0120	1.0086	1.0050	0.9978	0.9905	0.9828	0.9753	0.9693	0.9617
0.63	1.0170	1.0140	1.0108	1.0042	0.9977	0.9911	0.9844	0.9772	0.9693

The Figure 5-31, Figure 5-32 and Figure 5-33, show the density data in function of the temperature. The experimental densities, ρ/ g cm^{-3}, were correlated with temperature, T/°C using a linear regression, according to (Eq. 50), where the correlation parameters are shown in Table 5-16.

(Eq. 50)

$$\rho = \sum_{i=0}^{1} b_i \cdot T^i$$

ρ; represents the density of the ionic liquid, b_i; the linear fitting coefficients of the density, and T^i; the temperature.
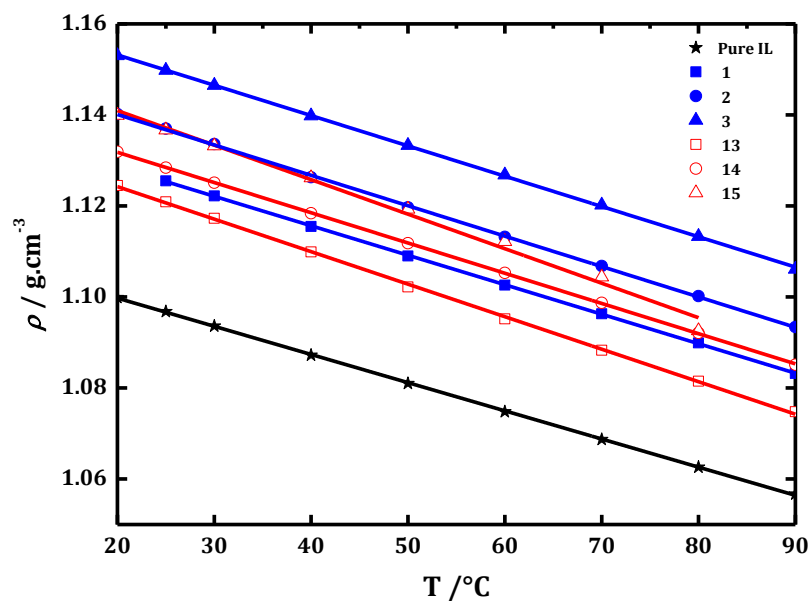
Figure 5-31. Density measurements, ρ, of the copper(II) acetate ternary mixture as a function of the temperature and 0.1 MPa at χ_{H2O}: $\star$, pure [C$_2$MIm][CH$_3$CO$_2$]; $\blacksquare$, S1; $\square$, S13; $\bullet$, S2; $\circ$, S14; $\blacktriangle$, S3; $\triangle$, S15. The lines represent linear type fitting of the experimental data with parameters reported in Table 5-16.
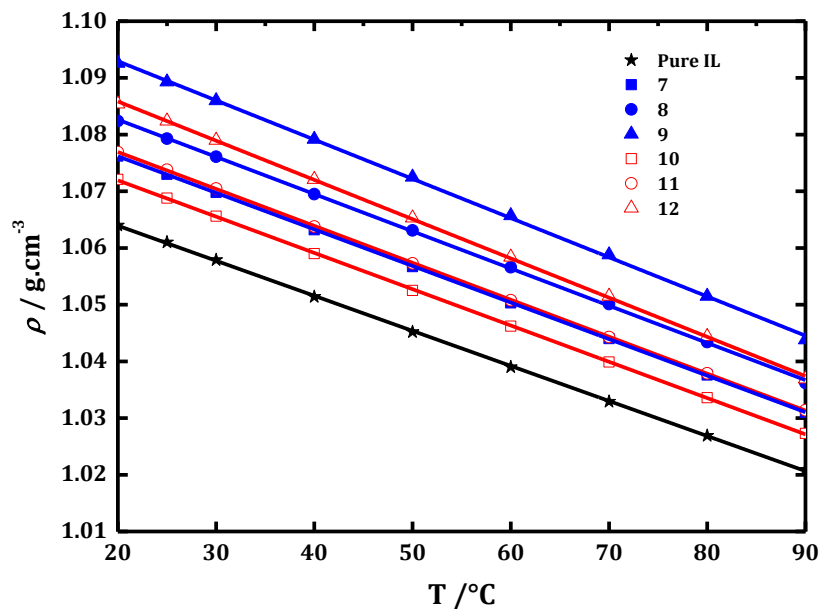
Figure 5-32. Density measurements, ρ, of the copper(II) butanoate ternary mixture as a function of the temperature and 0.1 MPa at χ_{H2O}: $\star$, pure [C$_2$MIm][C$_3$H$_7$CO$_2$]; $\blacksquare$, S7; $\square$, S10; $\bullet$, S8; $\circ$, S11; $\blacktriangle$, S9; $\triangle$, S12. The lines represent linear type fitting of the experimental data with parameters reported in Table 5-16.
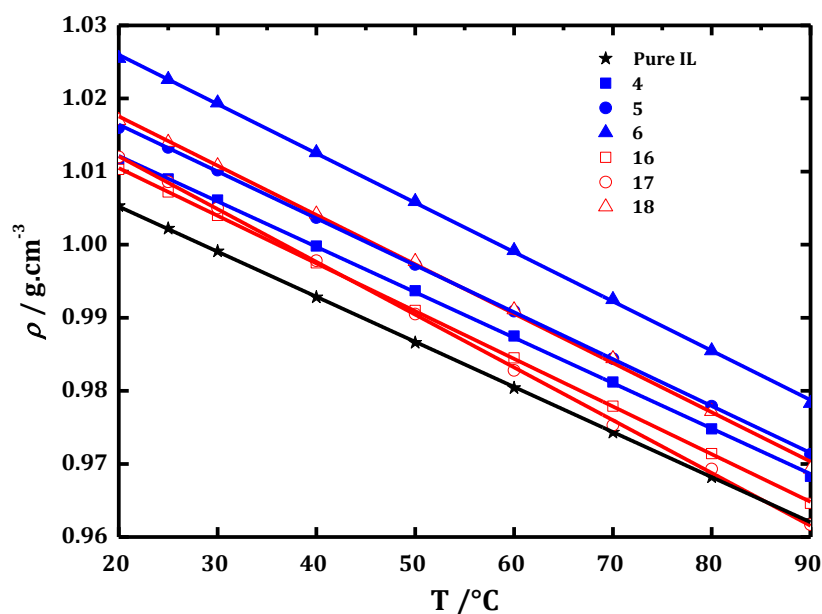
Figure 5-33. Density measurements, ρ, of the copper(II) octanoate ternary mixture as a function of the temperature and 0.1 MPa at χ_{H2O}: ★, pure [C$_2$MIm][C$_7$H$_{15}$CO$_2$]; ■, S4; □, S16; ●, S5; ○, S17; ▲, S6; △, S18. The lines represent linear type fitting of the experimental data with parameters reported in Table 5-16.

All solutions containing copper salt or the nanofluids have higher density than their respective pure ILs. However, when the solutions are turning into CuO-NPs, the densities are lower than their precursor solution. This proves a change of coordination of the copper. As it was observed, the nanofluid solutions were always more fluid than the solutions before reaction. Surprisingly, the density of the copper salt and nanofluid solutions were getting closer to the density of the pure ILs when the anion alkyl chain length increased. This is probably due to the amount of single copper atoms which are in larger proportion in the solution of copper(II) acetate than in the two other ones.

Table 5-16. Linear fitting coefficients b_i of the density of the ternary mixtures as a function of the temperature calculated from experimental data provided in Table 5-14 and Table 5-15 using the equation 1 along with their standard deviations (eq. 2).

χ_{H2O}	$b_0/$ g·cm^{-3}	$10^4 \times b_1/$ g·cm^{-3}·K^{-1}	$10^4 \times \sigma/$ g·cm^{-3}	χ_{H2O}	$b_0/$ g·cm^{-3}	$10^4 \times b_1/$ g·cm^{-3}·K^{-1}	$10^4 \times \sigma/$ g·cm^{-3}	χ_{H2O}	$b_0/$ g·cm^{-3}	$10^4 \times b_1/$ g·cm^{-3}·K^{-1}	$10^4 \times \sigma/$ g·cm^{-3}
Copper(II) acetate				**Copper(II) butanoate**				**Copper(II) octanoate**			
Pure	1.1121	-0.0006	0.0008	Pure	1.0763	-0.0006	0.0008	Pure	1.0176	-0.0006	0.0005
S1	1.1416	-0.0006	0.0008	S7	1.0891	-0.0006	0.0004	S4	1.0246	-0.0006	0.0012
S2	1.1535	-0.0007	0.0012	S8	1.0958	-0.0007	0.0012	S5	1.0293	-0.0006	0.0010
S3	1.1665	-0.0007	0.00020	S9	1.1068	-0.0007	0.0019	S6	1.0395	-0.0007	0.0014
S13	1.1385	-0.0007	0.0019	S10	1.0847	-0.0006	0.0007	S16	1.0235	-0.0007	0.0006
S14	1.1451	-0.0007	0.0006	S11	1.0900	-0.0007	0.0004	S17	1.0265	-0.0007	0.0018
S15	1.1561	-0.0008	0.00141	S12	1.0997	-0.0007	0.0014	S18	1.0311	-0.0007	0.0026

$$\sigma = \left(\frac{\sum (\rho_i^{exp} - \rho_i^{cal})^2}{n - v} \right)^{0.5}$$

σ; represents the standard deviation, n; the number of experimental points, v; the number of adjustable parameters.

5.4.3.3 Viscosity

The viscosities of the three pure [C$_2$MIm][C$_n$H$_n$CO$_2$]-ILs and of the copper salt solutions before and after nanoparticle formation were measured as a function of the temperature from 20 to 100°C at different water mole fraction composition, χ_{H2O}, from 0 to 0.63. The experimental data are listed in and were fitted using a polynomial function since the data did not follow the Arrhenius Law (for t it was not possible to fit the data using the VTF fitting).

Increasing the water concentration only decreases the viscosity. Thus, only the solution with the lower water content is shown here in Figure 5-34. The nanofluid solutions show less viscous solutions than their pure IL, apart from the solution made with copper(II) acetate precursor that show higher viscosity data.

However, the nanofluid solution made with copper(II) octanoate precursor shows much higher viscosity than the nanofluid solution made with a copper(II) butanoate precursor. This could explain the higher presence and smallest diameters of the CuO-NPs formed in the copper(II) octanoate precursor solution.

211

Indeed, viscosity has already been shown to play an important role in the formation and stability of NP formation.
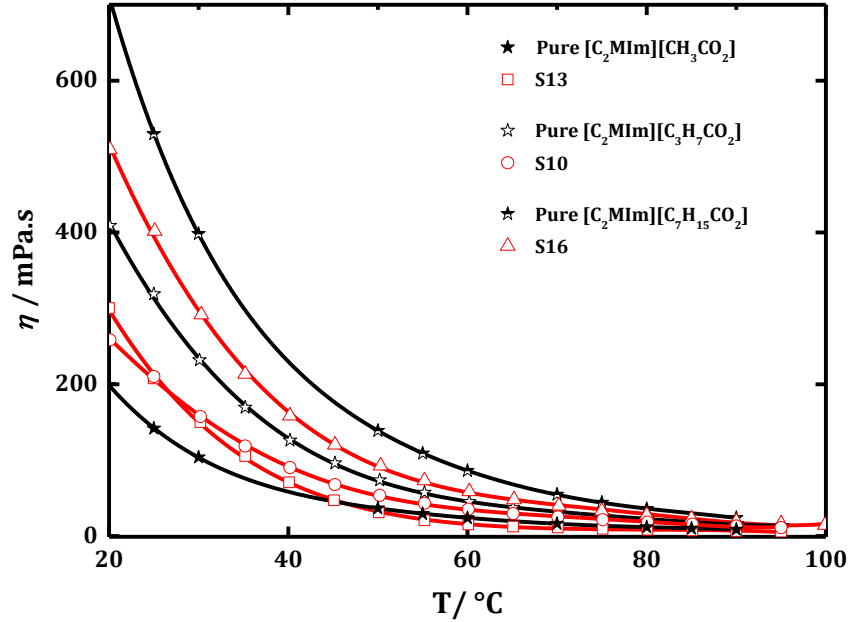
Figure 5-34. Viscosity, η, of the pure ILs as a function of the temperature from (20 to 100) °C for $\chi_{IL:}$ ★(full), [C₂MIm][CH₃CO₂]; ★(empty), [C₂MIm][C₃H₇CO₂]; ★(half-full), [C₂MIm][C₇H₁₅CO₂] and for the nanofluid solution from: □, copper(II) acetate precursor (S13); ○, copper(II) butanoate precursor (S13); △, copper(II) octanoate precursor (S13); at 0.1MPa.

Table 5-17. Experimental Viscosities, η, of the nanofluid solutions as a function of temperature from (20 to 100) °C at 0.1 MPa.

S13		S10		S16	
T(°C)	η exp(mPa.s)	T(°C)	η exp(mPa.s)	T(°C)	η exp(mPa.s)
20	300.4	20.1	258.4	20.1	509.1
25	207.6	25	210.1	25.1	401.7
30.2	150.1	30.2	157.3	30.3	291.7
35.2	105.3	35.2	118.6	35.2	213.4
40.1	70.63	40.2	90.25	40.2	158.5
45.1	47.07	45.2	67.82	45.2	120.2
50.1	31.01	50.2	53.48	50.3	92.62
55.2	20.7	55.2	43.03	55.2	73.14
60.1	15.1	60.1	35.28	60.2	58.68
65.1	12.46	65.1	29.59	65.2	47.97
70.1	11.12	70.1	24.99	70.2	39.7
75.1	9.475	75.1	21.4	75	33.03
80.1	8.25	80.1	18.36	80	27.28
85.1	7.293	85.1	15.58	85	22.86
90	6.493	90	13.13	90	19.13
95	5.749	95	11.08	95	16.36

Table 5-18. Polynomial fitting parameters for the viscosity as a function of temperature from (20 to 100) °C at 0.1 MPa. The pure IL data can be found in Table 3-7 of Chapter-3.

T(K)	S13	S10	S16
A_0	9.80E+02	5.22E+02	1.29E+03
A_1	-5.30E+01	-1.25E+01	-5.09E+01
A_2	1.19E+00	-1.61E-01	6.36E-01
A_3	-1.38E-02	8.33E-03	3.38E-05
A_4	8.41E-05	-9.56E-05	-5.24E-05
A_5	-2.14E-07	3.58E-07	2.67E-07

5.4.3.4 Conductivity

The conductivities of the pure IL and of the copper salt ternary mixture before and after it turned into NPs were measured as a function of the water composition at only one temperature; 298.15 K. The data are listed in the Table 5-19 below:

Table 5-19. Experimental Conductivity, σ, measurements of the nanofluid solutions as a function of temperature from (20 to 100) °C at 0.1 MPa.

Copper(II) precursor used	Copper salts solutions	σ/mS·cm^{-1}	Nanofluid solutions	σ/mS·cm^{-1}
[C$_2$MIm][CH$_3$CO$_2$]	/	2.77	/	/
Copper(II) acetate	S1	2.14	S13	2.79
	S2	2.79	S14	3.79
	S3	4	S15	5.86
[C$_2$MIm][C$_3$H$_7$CO$_2$]	/	1.19	/	/
Copper(II) butanoate	S7	0.78	S10	1.08
	S8	1.15	S11	1.7
	S9	3.89	S12	5.06
[C$_2$MIm][C$_7$H$_{15}$CO$_2$]	/	0.32	/	/
Copper(II) octanoate	S4	0.19	S16	0.28
	S5	0.33	S17	0.43
	S6	1.594	S18	1.08

*Pure water used for this study was found with 0.00325 mS.cm^{-1}

213

Those results are very interesting. First of all, when increasing the water concentration to its maximum (around 0.60 water mole ratio) in the copper solution before and after it turned into NPs, the conductivities of the new solutions are much higher than the conductivity of their pure respective ILs. For instance, in the solution S3 and S15 show a conductivity of 4 and 5.86 mS·cm^{-1}; whereas the pure [C$_2$MIm][CH$_3$CO$_2$]- IL displays a conductivity of only 2.77 mS·cm^{-1}. It is even more spectacular in solution S12 made from the copper(II) butanoate, where the conductivity increases five time more than in its pure IL.

However, even if water concentration did not affect the particle size of the CuO-NPs formed (as reported in the TEM analysis of this section), water seems to considerably increase the conductivity of the nanofluid. This is a very interesting observation since similar solution could be made using appropriate reagent to increase the conductivity of electrolytes for instance.

Another very interesting fact is that changing the copper salt coordination to CuO-NPs increases the conductivity of the new solution. It is in accordance with the literature where most of the time NPs has been found to increase the conductivity of the system.

Furthermore, the conductivity dramatically decreases while increasing the alkyl-chain length on the carboxylate anion. Therefore, the copper(II) octanoate seems to make better shaped NPs as seen in the TEM analysis; however, it would not be a good electrolyte in comparison of the nanofluids synthesised from copper(II) acetate.

5.5 Study of formation of Copper oxide nanoparticles

5.5.1 UV-Vis spectroscopy

Before investigating the copper(II) salt solutions in IL with UV-Vis spectroscopy, some preliminary work was carried out. The determination of the limit of copper(II) acetate in water was first investigated, to determine the most suitable copper concentration that was kept for all solutions investigated in this work.

Then copper(II) acetate solutions in their respective ILs were investigated at different temperatures and compared with previous results from our group. Similar work was carried out for copper(II) octanoate. These measurements were carried out with the help of Clarisse Bloyet (Master student). Plasmon resonance is a well-known characteristic of NPs formation. It has been seen in lots of studies of NPs in UV-VIS spectra, mostly in Gold nanoparticles.[193-196]

5.5.1.1 Determination of the limit of copper(II) salt

At room temperature, solutions of copper(II) acetate hydrate is known to show typical absorption band at 370 and 690 nm, where the limit of concentration of copper(II) acetate was found at 10^{-3} M.[197] The reported UV-Vis spectra of copper(II) acetate in acetic acid at different concentration is shown in Figure 5-35.
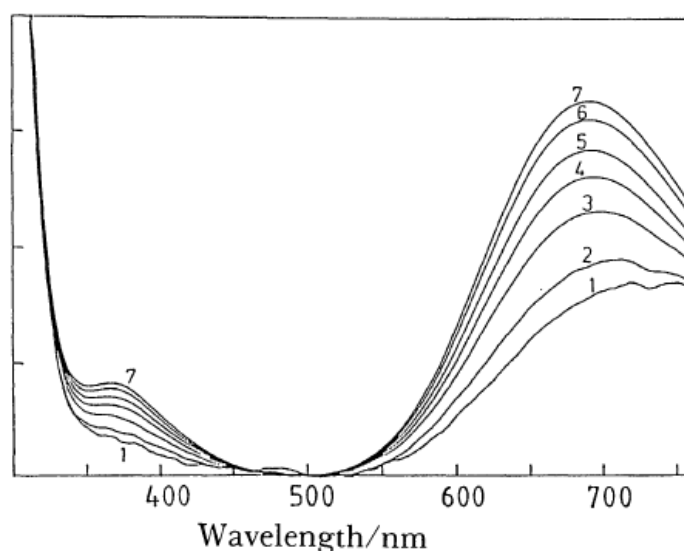
Figure 5-35. Absorption spectra of Copper(II) acetate in acetic acid at various copper(II) concentration: 1, 1.08; 2, 2.15; 3, 5.37; 4, 10.1; 5, 21.2; 6, 51.4; 7, 98.1x10^{-5} M from Kikuchi *et al.*[197]

The experiment was repeated by dissolving copper(II) acetate in water at various concentration. The limit concentration was found at 5.10^{-3} M as seen in Figure 5-36. This copper(II) concentration was kept for all future copper(II) salt solutions to be investigated using UV-Vis spectroscopy.
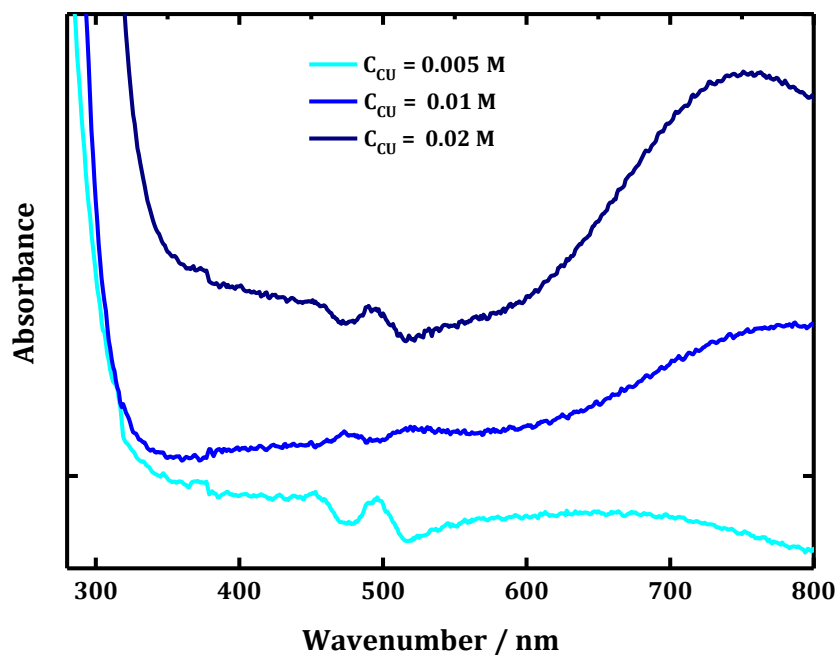
Figure 5-36. Absorption spectra of Copper(II) acetate in water at various copper(II) concentration: 0.005 (cyan), 0.01 (blue) and 0.02M (dark blue).

5.5.1.2 *Copper(II) acetate hydrate in [C₄MIm][CH₃CO₂]*

At room temperature, a solution of copper(II) acetate hydrate in [C$_2$MIm][CH$_3$CO$_2$] was given a blue colour solution, with an absorption band at about 600 nm Figure 5-38. The same type of solution using [C$_4$MIm]$^+$ cation instead of [C$_2$MIm]$^+$ cation, was investigated by Swadzba-Kwasny *et al.*, where an absorption band was found at 630 nm Figure 5-37.[176]

The solution was then heated carefully to about 70°C where the colour changed to green, with an absorption band at about 540 nm. In our previous work, a broad band was found at about 700 nm.[176] The green colour can only be observed for a few minutes, after watching the temperature increases carefully. Further heating to 120°C resulted in a deep red solution, exhibiting an absorption maximum at 460 nm, whereas the absorption bands was found at 530 nm in our previous

216

work.[176] Our results are in accordance to our previous group and could then be carried out for other copper(II) salt solutions.
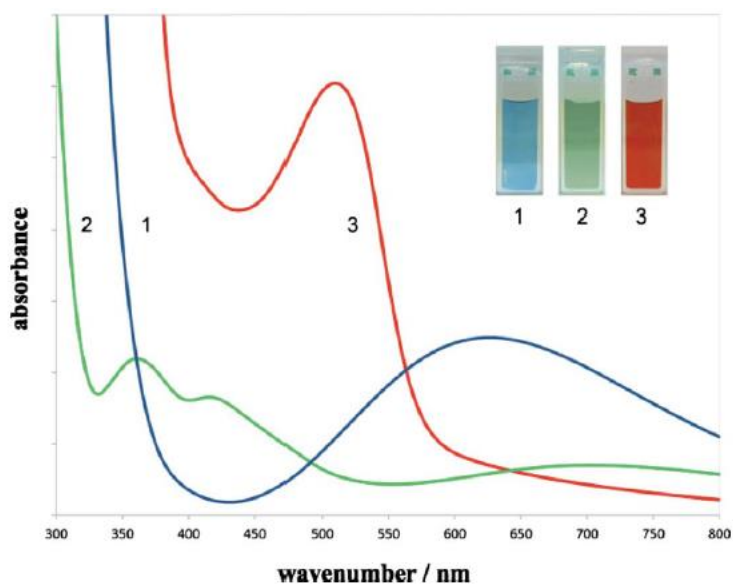
Figure 5-37. Colour changes observed during the synthesis of nanofluids with copper(II) acetate in [C$_4$MIm][CH$_3$CO$_2$] from Swadzba-Kwasny *et al.*[176] The photos are in accordance to the UV-VIS spectra.
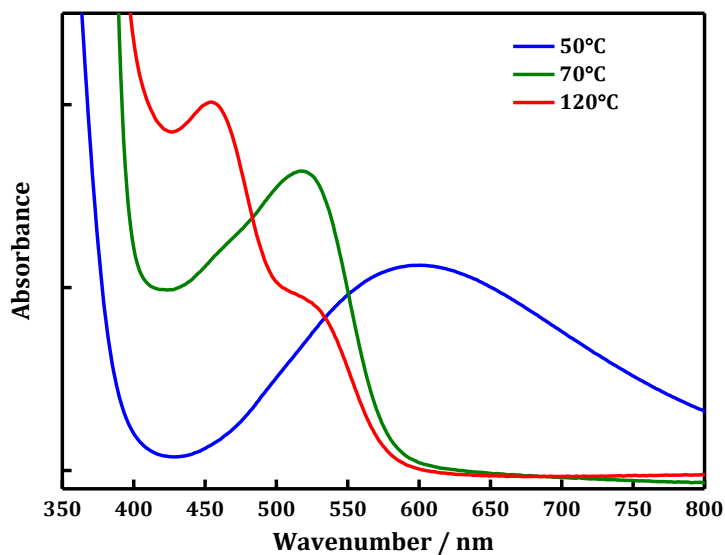
Figure 5-38. Colour changes observed during the synthesis of nanofluids with copper(II) acetate in [C$_2$MIm][CH$_3$CO$_2$]. The blue spectrum represents the solution at 50°C; the green spectrum, the solution at 70°C; and the red spectrum, the solution at 120°C.

The processes of the nanofluid formation can be explained as follows:[176]

The first step shows a partial dehydration of the solution copper(II) species. The second step include decomposition of the solution species, along with a partial reduction of the copper(II) to (I), which occurs due to simultaneous formation of carbenes in the basic solutions. At this stage, the intermediate species is very unstable since the green colour is very temperature dependant and has shown different absorption bands in this work and the previous work. This could be due to either particle growth or to a coordination change of the copper molecule. As it was shown in the crystallisation section of this chapter, this is definitely due to a coordination change of the copper molecule, where copper structure had two distinct coordination depending on the temperature. The formation of the partially dehydrated species was found to be the rate-limiting step that was followed by a rapid decomposition according to DSC preliminary tests.

Furthermore, plasmon band is found for the red line at 460 nm, which is typical of the nanoparticle formation. However, it seems that there are still some compounds from the previous coordination (green line) at 540 nm, which is not present in our previous work. Probably because the reaction time was too short to achieve a complete nanoparticle formation

5.5.1.3   Copper(II) octanoate hydrate in [C$_2$MIm][C$_7$H$_{15}$CO$_2$]

At room temperature, a solution of copper(II) octanoate in [C$_2$MIm][C$_7$H$_{15}$CO$_2$] was given a blue colour solution, with an absorption band at about 425 nm (Figure 5-39). The solution was then heated carefully to about 70°C where the colour changed to green, with an absorption band at about 425 nm. Same as for the copper(II) acetate, the green colour can only be observed for a few minutes, after watching the temperature being increased carefully.

Further heating to 120 °C resulted in a deep red solution, exhibiting an absorption maximum at 445 nm. The solution was then heated to 150 °C, showing a black colour that is due to the decomposition of the solution. A plasmon band is also found for the red line, which is typical from the nanoparticle formation. Even the shape is not as well defined than a typical plasmon band, and the TEM proves the presence of NPs in the [C$_2$MIm][C$_7$H$_{15}$CO$_2$] IL.
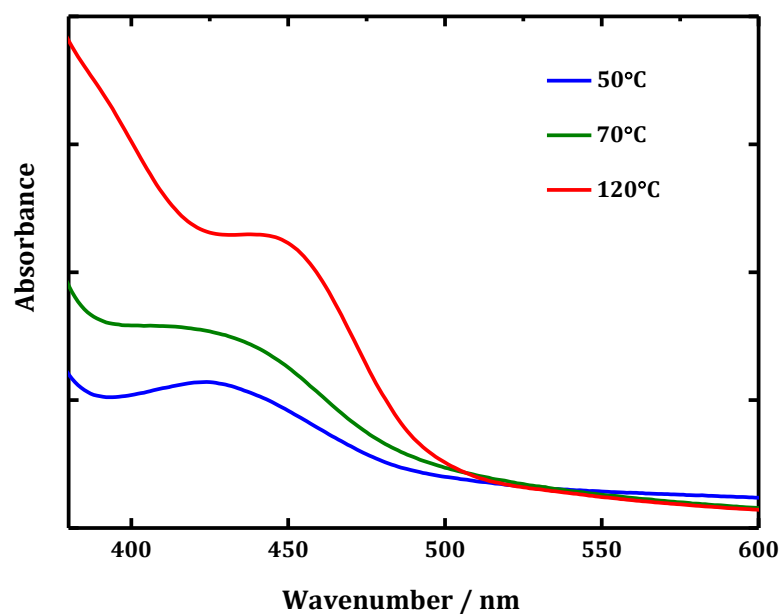
Figure 5-39. Colour changes observed during the synthesis of nanofluids with copper(II) octanoate in $[C_2MIm][C_7H_{15}CO_2]$. The blue spectrum represents the solution at 50°C; the green spectrum, the solution at 70°C; and the red spectrum, the solution at 120°C.
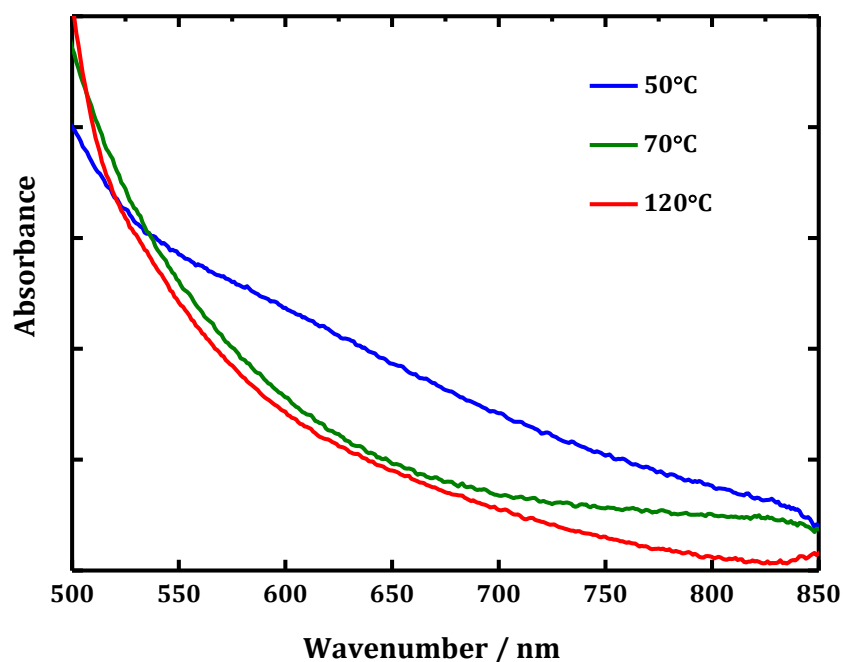
Figure 5-40. ZOOM of Figure 5-39: Colour changes observed during the synthesis of nanofluids with copper(II) octanoate in $[C_2MIm][C_7H_{15}CO_2]$. The blue spectrum represents the solution at 50°C; the green spectrum, the solution at 70°C; and the red spectrum, the solution at 120°C.

5.5.1.4 Conclusion

Copper salt solutions in their respective ILs containing the same anions were showing different absorption bands, depending on the temperature the solutions have been heated to. For all solutions, nanofluids were observed at the highest absorbance, exhibiting a plasmon band typical for the presence of nanoparticles.

5.5.2 Small and Wide Angle X-Ray Scattering

To go further, Small Angle X-Ray Scattering (SAXS) (range 0.2 to 1.6 nm^{-1}) and Wide Angle X-Ray Scattering (WAXS) (range 1.6 to 20 nm^{-1}) experiment has given a unique insight into the liquid structure of each solution. All experiments were carry out at at the Institut Laue-langevin (ILL) in Grenoble in France for the neutron scattering and the European Synchrotron Radiation Facility (ESRF) for the X-Ray scattering. The work done in Chapter 4 was used to compared the ternary mixture of copper with the neat IL respective solutions. No significant pre-peaks were observed at very low Q, whereas two dominant contributions of correlation lengths were present at higher Q in the pure and binary mixtures.

First of all, it was not possible to dissolve the copper precursor below 0.3 ionic liquid mole fraction. Thus, only three main compositions were analysed as described in Table 5-20 below. One experiment was using no water except the small water content already present in solutions (w_{H2O} < 0.001 weight fraction) contained in the dry IL and the copper precursor, a second composition using the less molar fraction of IL possible to use that contain 0.65 water molar fraction, and the last composition containing almost equal amounts of water and IL (0.50 IL molar fraction and 0.45 water molar fraction). For all composition, 0.05 copper precursor molar fraction was constantly used. This value was the maximum of copper precursor that could be dissolved completely and that could be visible via X-Ray source.

Table 5-20. Ternary mixtures of IL, water and copper precursor composition using all 0.05 copper precursor molar fraction, analysed via X-Ray.

χ_{IL}	χ_{H2O}
0.30	0.65
0.50	0.45
0.95	0.00

Firstly, the minimum concentration of IL needed to make *in-situ* CuO-NPs has been confirmed using SAXS. Then, the parts further will tend to understand the influence of temperature, water and anion alkyl chain length in the nanoparticle solutions using WAXS.

5.5.2.1 *Determination of the minimum IL-concentration to make CuO-NPs*

To determine the minimum IL-concentration required to make *in-situ* CuO-NPs, each composition was sealed in a sample container before the solution had turned into nanoparticles. In this way it was possible to follow the kinetics of the reaction of *in-situ* CuO-NPs. In fact, before the NPs formation takes place, the ternary mixture has to be first well dissolved at 50°C for few hours. It's only when heated at 120°C that nanoparticles would be formed. Therefore, the SAXS pattern of each composition was compared for the spectra taken at 50°C (only for the ternary mixture dissolution), at 120 °C and with its respective pure IL taken at 50°C.

When no change of pattern was exhibited for the same mixture taken at 50 °C and at 120 °C, it was concluded that the *in-situ* NPs formation of copper oxide didn't occur. The lower the IL-concentration and the shorter the alkyl chain lengths in the solution, the lower were the chances to obtain NPs in the solution. This fact was also confirmed by the colour of the respective solutions which is expected to be reddish when the NPs formation had occurred, and blue when no reaction had occurred. This is the case, because the solution has not proceeded from the first state of simple dissolution at 50°C, or would become again greenish when the particles were stocked in an intermediate state (the intermediate state is discussed in the Crystallography part of this Chapter).

However, for the case of the $[C_2MIm][CH_3CO_2]$, the ternary mixture processed at 50 and at 120 °C exhibited a completely disorganised SAXS pattern for all three compositions ($\chi_{IL} = 0.95$, 0.50 and 0.30). This is probably due to the fact that $[C_2MIm][CH_3CO_2]$ is not a well-structured IL and below 4 carbons in the anion carboxylate chain, the NPs are like cluster and not NPs like it is observed via TEM for the $[C_2MIm][C_3H_7CO_2]$ and $[C_2MIm][C_7H_{15}CO_2]$. Therefore, it is normal to see no particular peak at low Q for this specific IL.
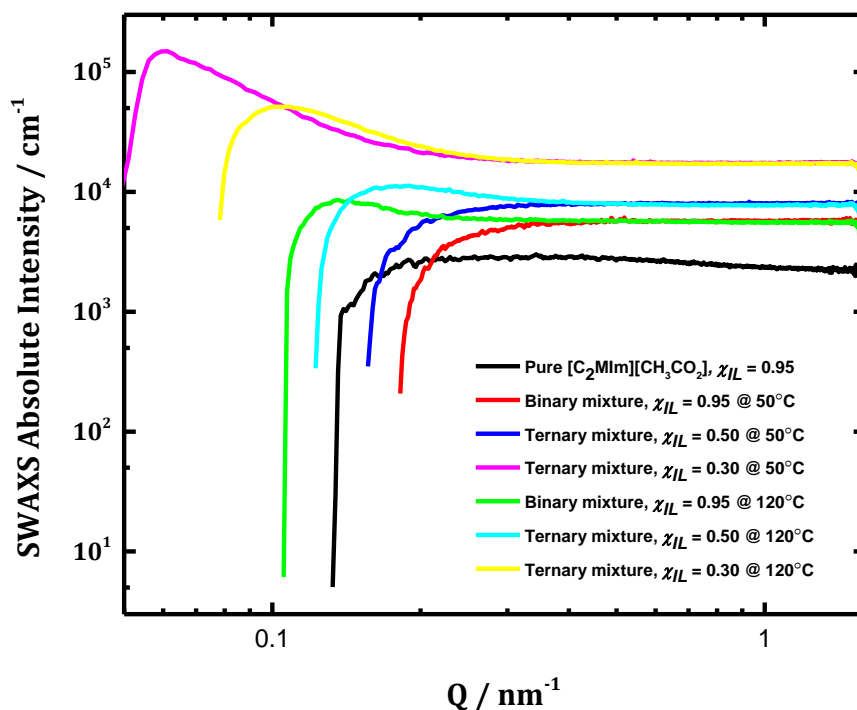
Figure 5-41. SAXS patterns of the pure [C$_2$MIm][CH$_3$CO$_2$] (black), and its binary and ternary mixtures with water and copper(II) acetate precursor at 50°C for the composition χ_{IL} = 0.95 (red), χ_{IL} = 0.50 (blue) and χ_{IL} = 0.30 (pink), and its ternary mixture at 120°C for the composition χ_{IL} = 0.95 (green), χ_{IL} = 0.50 (cyan) and χ_{IL} = 0.30 (yellow).

Furthermore, in the case of [C$_2$MIm][C$_3$H$_7$CO$_2$], the NP formation doesn't seem to happen for a composition of χ_{IL} = 0.3 at 120 °C. Indeed, the SAXS patterns at 120 °C of composition 0.95 and 0.50 IL mole fractions formed a q^{-2} slope, which means that they are structural solutions. Unlike their respective composition taken at 50 °C, which formed a q^{-3} slope, which means that their solutions stay homogenous at this temperature and therefore no NPs are formed. However, a totally different figure is found for the composition of 0.3 IL mole fractions taken at 50 and 120 °C. Indeed, they both have very similar SAXS patterns with both a q^{-3} slope. Therefore, it seems that no reaction happens with this copper carboxylate precursor (n = 4) for a composition below 0.3 mole fraction of IL.

Surprisingly, the ternary mixtures of [C$_2$MIm][C$_7$H$_{15}$CO$_2$] show a q^{-2} slope for all three compositions (χ_{IL} = 0.95, 0.50 and 0,30) at 50°C, and show a q^{-3} slope for all three compositions at 120 °C. Therefore, the formation of NPs seems to happen in any composition of IL/water in the case of copper carboxylate precursor (n =

8). This is probably due to the already well-organised IL structure in the pure IL system and even more organised while mixed with water for $\chi_{IL} \geq 0.2$ as seen in the Chapter 4. $[C_2MIm][C_3H_7CO_2]$ results are in accordance with this hypothesis as no NPs seems to be forms for a mixture of $\chi_{IL} = 0.3$, and it was seen in the previous chapter that it is a well-organised structure for a binary mixture with water at $\chi_{IL} \geq 0.4$. Therefore, copper oxide seems to have allocated places when the system is much more organised than when it is not organised.
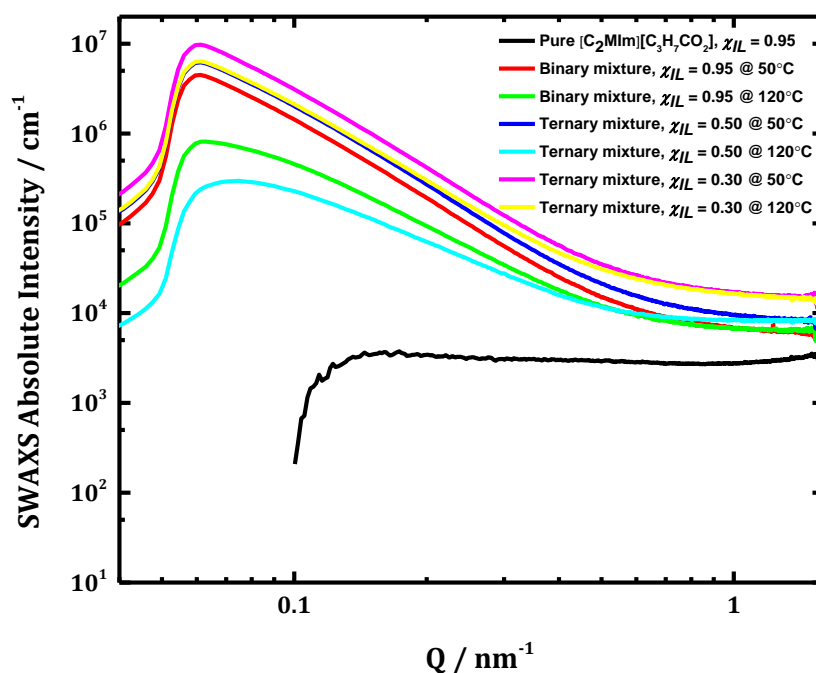
Figure 5-42. SAXS patterns of the pure $[C_2MIm][C_3H_7CO_2]$ (black), and its binary and ternary mixtures with water and copper(II) butanoate precursor at 50°C for the composition $\chi_{IL} = 0.95$ (red), $\chi_{IL} = 0.50$ (blue) and $\chi_{IL} = 0.30$ (pink), and its ternary mixture at 120°C for the composition $\chi_{IL} = 0.95$ (green), $\chi_{IL} = 0.50$ (cyan) and $\chi_{IL} = 0.30$ (yellow).
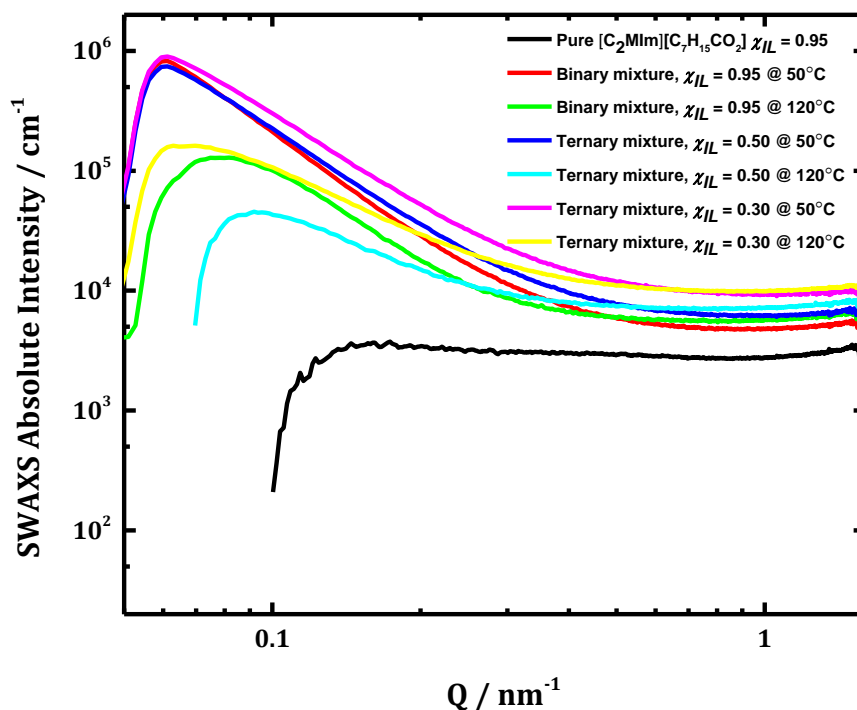
Figure 5-43. SAXS patterns of the pure $[C_2MIm][C_7H_{15}CO_2]$ (black), and its binary and ternary mixtures with water and copper(II) octanoate precursor at 50°C for the composition $\chi_{IL} = 0.95$ (red), $\chi_{IL} = 0.50$ (blue) and $\chi_{IL} = 0.30$ (pink), and its ternary mixture at 120°C for the composition $\chi_{IL} = 0.95$ (green), $\chi_{IL} = 0.50$ (cyan) and $\chi_{IL} = 0.30$ (yellow).

5.5.2.2 NPs' formation in function of the temperature

Previously in this chapter, heating of a solution of an IL and a copper precursor to 120 °C has been shown to produce NPs of copper oxides (Cf. TEM, XPS results). However, only the crystallography part of this Chapter has allowed to discover an intermediate at around 80 °C. For further information, to get a better understanding on the NPs formation between 50 °C and 120 °C, a deeper study of the *in-situ* NPs formation has been followed using SWAXS instrument from the range of 1.6 to 20 nm^{-1}. Each sample of ternary mixtures was first well dissolved at 50°C and then stored in a sample container. Each solution was kept into their own container during the whole experiment into the SWAXS instrument. The NPs formation was thus follow up *in-situ via* a SWAXS pattern taken every 10 °C starting from 25 to 130 °C. In this way it was possible to look at differences of

pattern between temperatures. Underneath are only shown the two relevant patterns needed to support the presence of NPs in solution after heating to 120°C.

SWAXS patterns for the three compositions studied and for all three ILs are showed underneath. A color-coded was used to represents same composition taken at 50 and 120°C.

So far, the results have shown higher intensities of each predominant peaks for mixtures taken at 50°C than their same composition taken at 120°C. Furthermore, increasing water concentration in those ternary mixture will also increase the intensity of both Q values. However, their Q values are all much higher than their pure respective ILs SWAXS patterns (show in the part below).

More interestingly, for all IL at all three compositions, significant shifts towards low Q is observed from 50 to 120°C for the second contribution; whereas no significant shifts are observed for the pre-peak. This means that intramolecular distances between the anion and cation IL are getting longer when NPs are formed into the solutions (cf. Chapter 1). This could be due the fact that NPs are intercalated into the IL and therefore increase the space between the anion and the cation.

However, SWAXS patterns for $[C_2MIm][C_7H_{15}CO_2]$ show very repetitive pattern for all compositions compared to the acetate and butanoate-anion that doesn't have a repetitive pathway for all composition. This shows that even at high water concentration, the $[C_7H_{15}CO_2]^-$ anion solutions keep a very well-organised structure that allow CuO-NPs to intercalate in the same way at any composition.
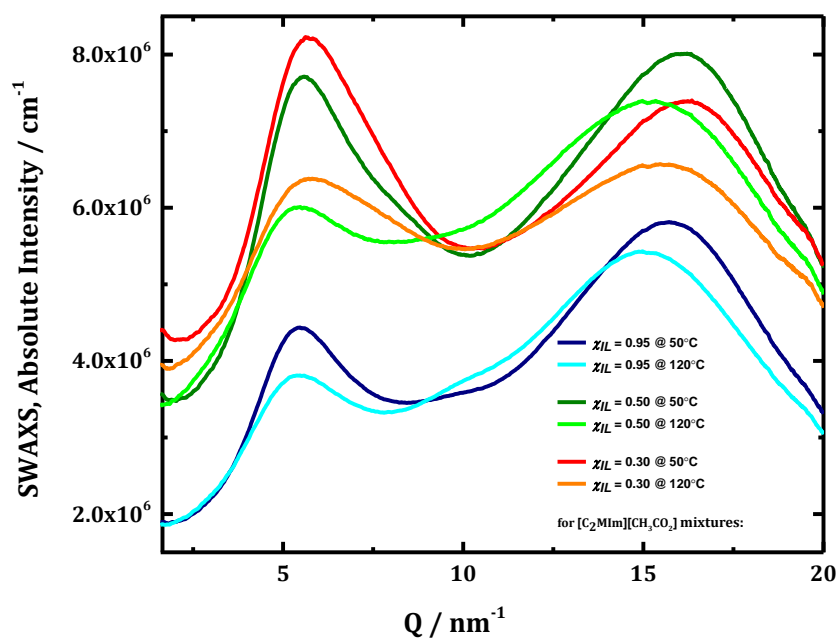
Figure 5-44. SWAXS patterns of [C$_2$MIm][CH$_3$CO$_2$] in binary and ternary mixtures with water and copper(II) acetate at 50°C for the composition χ_{IL} = 0.95 (Blue), χ_{IL} = 0.50 (green) and χ_{IL} = 0.30 (red), and at 120°C for the composition χ_{IL} = 0.95 (cyan), χ_{IL} = 0.50 (green) and χ_{IL} = 0.30 (orange).
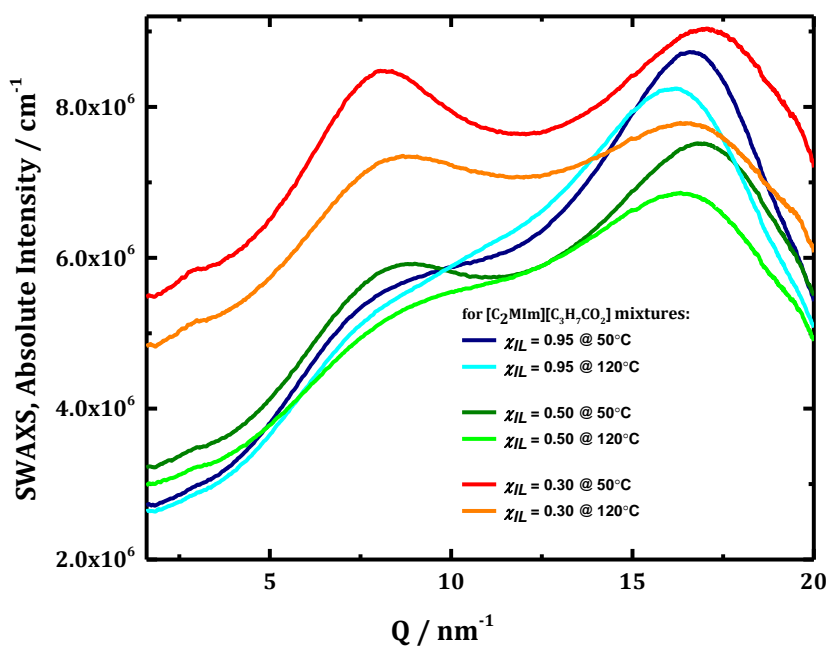
Figure 5-45. SWAXS patterns of [C$_2$MIm][C$_3$H$_7$CO$_2$] in binary and ternary mixtures with water and copper(II) butanoate at 50°C for the composition χ_{IL} = 0.95 (Blue), χ_{IL} = 0.50 (green) and χ_{IL} = 0.30 (red), and at 120°C for the composition χ_{IL} = 0.95 (cyan), χ_{IL} = 0.50 (green) and χ_{IL} = 0.30 (orange).
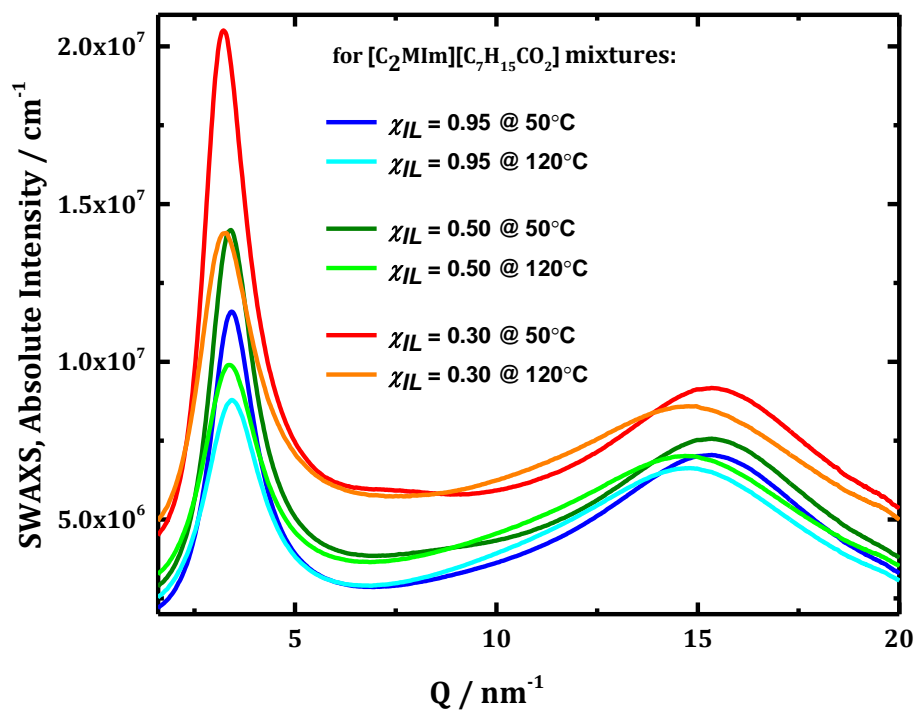
Figure 5-46. SWAXS patterns of [C2MIm][C7H15CO2] in binary and ternary mixtures with water and copper(II) octanoate at 50°C for the composition χ_{IL} = 0.95 (Blue), χ_{IL} = 0.50 (green) and χ_{IL} = 0.30 (red), and at 120°C for the composition χ_{IL} = 0.95 (cyan), χ_{IL} = 0.50 (green) and χ_{IL} = 0.30 (orange).

5.5.2.3 *Influence of water in the NPs formation*

In this part, SWAXS was used to study the influence of water in the NPs formation from the range of 1.6 to 20 nm^{-1}. The ternary mixtures of the three main compositions (χ_{IL} = 0.95, 0.50 and 0.30) at 120°C were plotted in the same graph for each respective IL and compared to its own pure IL in order to look at the impact of the water concentration in the NPs formation.

Table 5-21. Pre-peak and second contribution values (nm^{-1}) from pure ILs and their ternary mixtures with water and copper(II) carboxylate for all three ILs; [C$_2$MIm][CH$_3$CO$_2$], [C$_2$MIm][C$_3$H$_7$CO$_2$] and [C$_2$MIm][C$_7$H$_{15}$CO$_2$] for their composition in IL mole fraction (χ_{IL}) from 0 to 1.

IL	[C$_2$MIm][CH$_3$CO$_2$]		[C$_2$MIm][C$_3$H$_7$CO$_2$]		[C$_2$MIm][C$_7$H$_{15}$CO$_2$]	
χ_{IL}	Pre-peak Q (nm^{-1})	Second contribution Q (nm^{-1})	Pre-peak Q (nm^{-1})	Second contribution Q (nm^{-1})	Pre-peak Q (nm^{-1})	Second contribution Q (nm^{-1})
0	/	19.963	/	19.963	/	19.963
0.3	5.803	15.470	8.672	16.323	3.295	14.782
0.5	5.480	15.342	$\simeq 7.000$	16.323	3.342	14.674
0.95	5.456	14.976	$\simeq 6.500$	16.217	3.435	14.761
1	/	16.620	$\simeq 5.200$	15.750	3.34	15.430

Pure [C$_2$MIm][CH$_3$CO$_2$] and binary mixtures with water show only a contribution at around 16.62 nm^{-1} as seen in Chapter 4. However, when adding copper(II) acetate precursor to the solution, the WAXS patterns at 120°C shows another pre-peak at around 5.50 nm^{-1} for all three ternary compositions. Thus [C$_2$MIm][CH$_3$CO$_2$] seems to get more structured after the addition and formation of CuO-NPs due to formation of coulombic interactions.
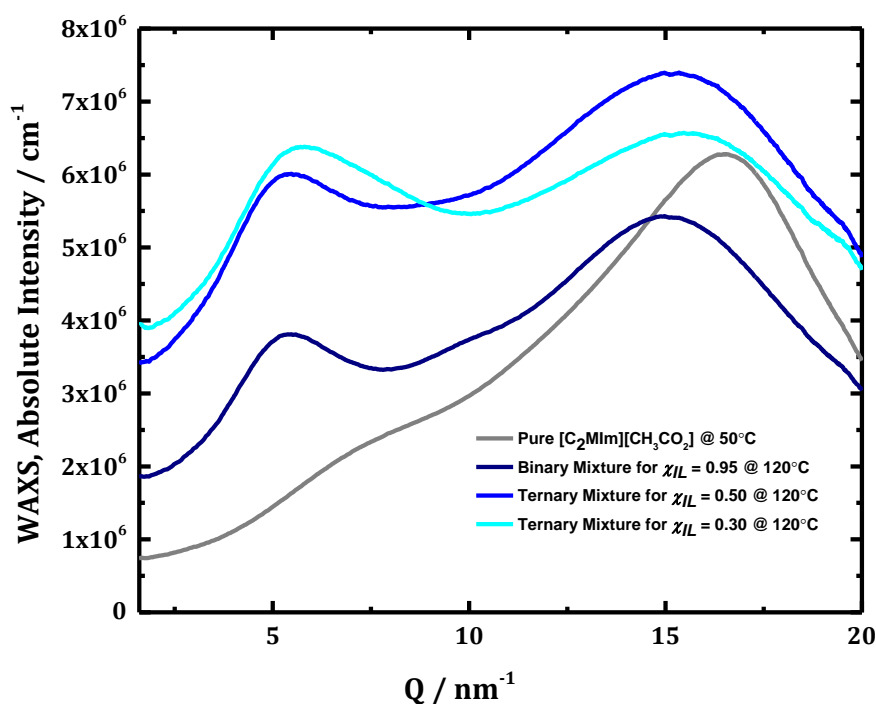
Figure 5-47. SWAXS patterns of the pure [C$_2$MIm][CH$_3$CO$_2$] (grey), and its binary and ternary mixtures with water and copper(II) acetate precursor at 120°C for the composition χ_{IL} = 0.95 (navy), χ_{IL} = 0.50 (blue) and χ_{IL} = 0.30 (cyan).

However, $[C_2MIm][C_3H_7CO_2]$ pure and in binary mixtures with water show already two pre-peaks at around same Q values than for the acetate (5.20 and 15.43 nm^{-1}). Unlike $[C_2MIm][CH_3CO_2]$, $[C_2MIm][C_3H_7CO_2]$ gets significantly disordered after the formation of CuO-NPs compared to its pure IL structure. Indeed, the first pre-peak seems to disappear since only a smooth bump is observed for composition 0.5 and 0.95 IL mole fractions. However, much higher intensity and better-defined first pre-peak is still observed at composition 0.3 IL mole fractions.
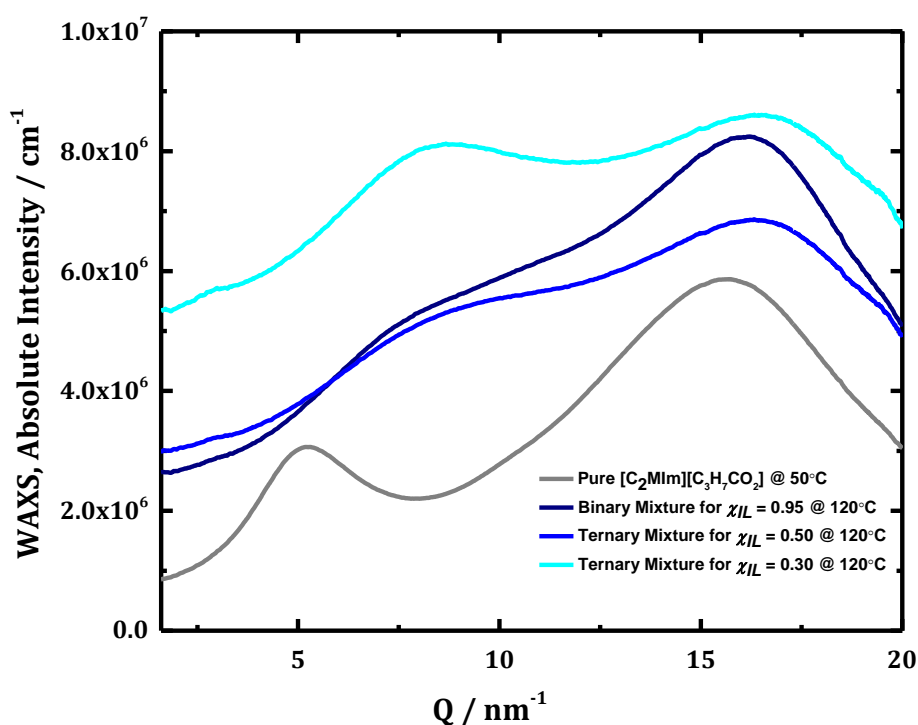
Figure 5-48. SWAXS patterns of the pure $[C_2MIm][C_3H_7CO_2]$ (grey), and its binary and ternary mixtures with water and copper(II) butanoate precursor at 120°C for the composition $\chi_{IL} = 0.95$ (navy), $\chi_{IL} = 0.50$ (blue) and $\chi_{IL} = 0.30$ (cyan).

In the contrary, the $[C_2MIm][C_7H_{15}CO_2]$ stays structured before and after the formation of CuO-NPs due to its hydrophobic character and its strong Van der Waals interactions.

The second contribution at high Q (near 15 nm^{-1}) is a significant peak found in ILs regarding their cation/anion interactions. In the case of $[C_2MIm][C_7H_{15}CO_2]$ this peak is significantly shifted after the formation of CuO-

NPs. This shows that in all type of solutions presented here, CuO-NPs will fit where there is space and therefore will be formed more instantly in the case of the [C$_2$MIm][C$_7$H$_{15}$CO$_2$] due to its very well-organised structured, that forces the NPs to fit at the same place every time. Probably the octanoate-anions form a capping layer on the surface of the NPs that disturbs the structure of the IL.
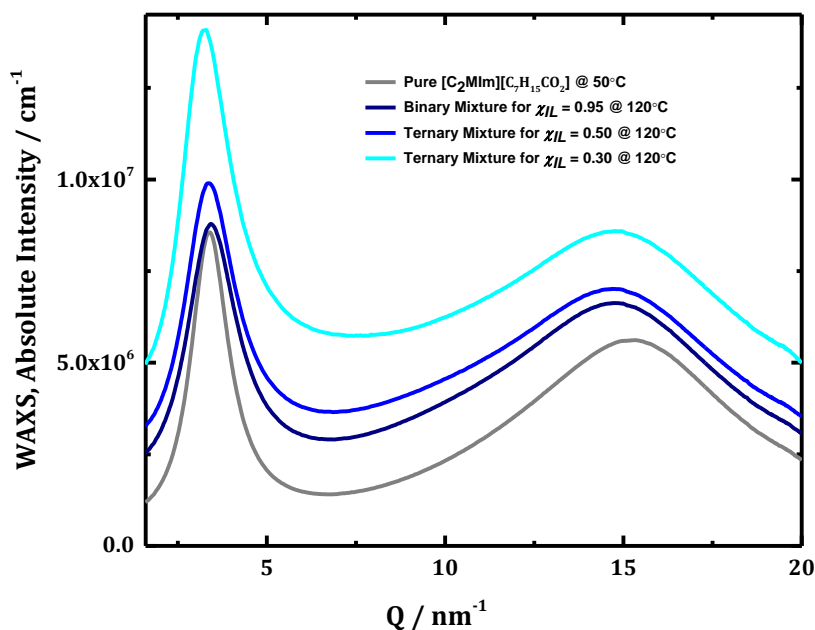
Figure 5-49. SWAXS patterns of the pure [C$_2$MIm][C$_7$H$_{15}$CO$_2$] (grey), and its binary and ternary mixtures with water and copper(II) octanoate precursor at 120°C for the composition χ_{IL} = 0.95 (navy), χ_{IL} = 0.50 (blue) and χ_{IL} = 0.30 (cyan).

5.5.2.4 *Influence of the anion alkyl chain length IL in the NPs solutions*

In this part, SWAXS was also used to study the influence of the anion alkyl chain length in the NP formation in the range of 1.6 to 20 nm^{-1} at 120°C. The ternary mixtures of the three respective ILs were plotted in the same graph for each respective composition (χ_{IL} = 0.95, 0.50 and 0.30) in order to look at the impact of the alkyl chain length in the NPs formation.

[C$_2$MIm][C$_7$H$_{15}$CO$_2$] has a strong anion/cation organisation compared to the [C$_2$MIm][CH$_3$CO$_2$] and [C$_2$MIm][C$_3$H$_7$CO$_2$], since its intramolecular interactions are stronger and well-structured.

To conclude, those three graphs underneath show that the effect of the concentration in IL/water doesn't seem to dramatically affect the structure of the

231

solution in presence of CuO-NPs. In fact, the two main pre-peaks don't change significantly for each IL solution. However, here it has been proven that anion alkyl chain length superior or equal to 8 carbons have significant self-organisation that seems to be not been disturbed by any changes either in terms of temperature, water and IL concentrations, or even by the addition of a metal precursor or nanoparticles.
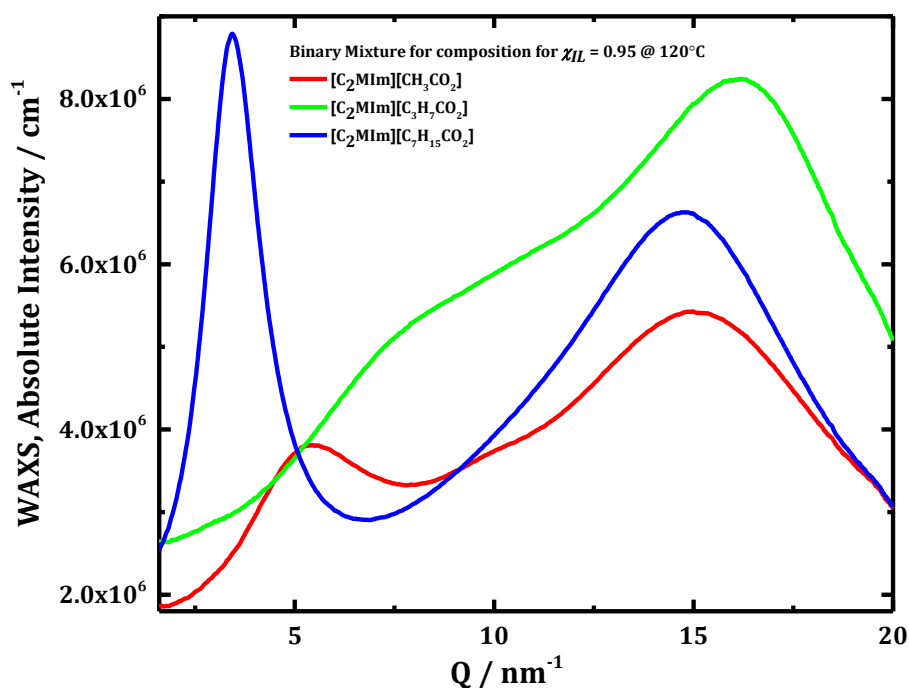
Figure 5-50. SWAXS patterns at the composition χ_{IL} = 0.95 of the binary mixtures with water and copper(II) carboxylate precursor at 120°C of [C₂MIm][CH₃CO₂] (red), [C₂MIm][C₃H₇CO₂] (green), [C₂MIm][C₇H₁₅CO₂] (blue).
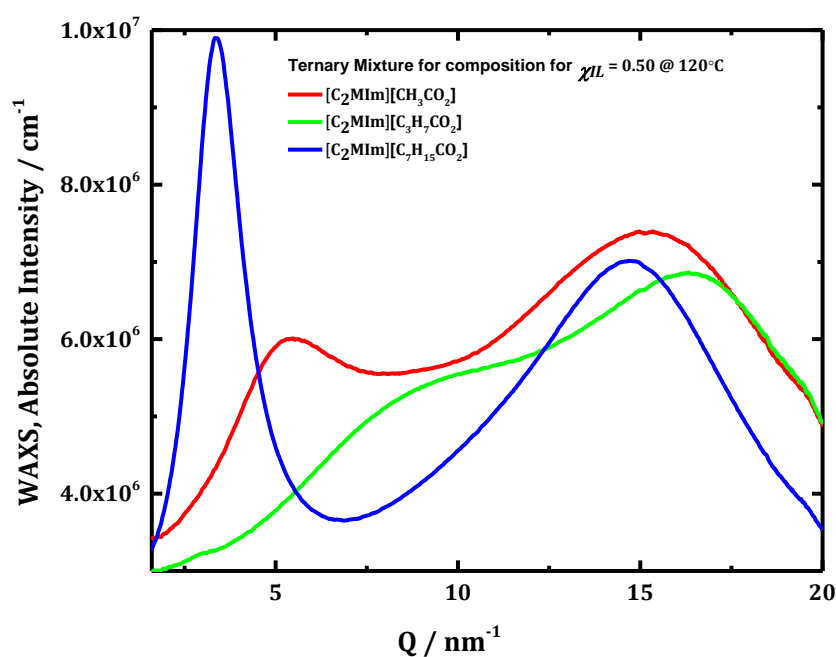
Figure 5-51. SWAXS patterns at the composition χ_{IL} = 0.50 of the ternary mixtures with water and copper(II) carboxylate precursor at 120°C of [C₂MIm][CH₃CO₂] (red), [C₂MIm][C₃H₇CO₂] (green), [C₂MIm][C₇H₁₅CO₂] (blue).
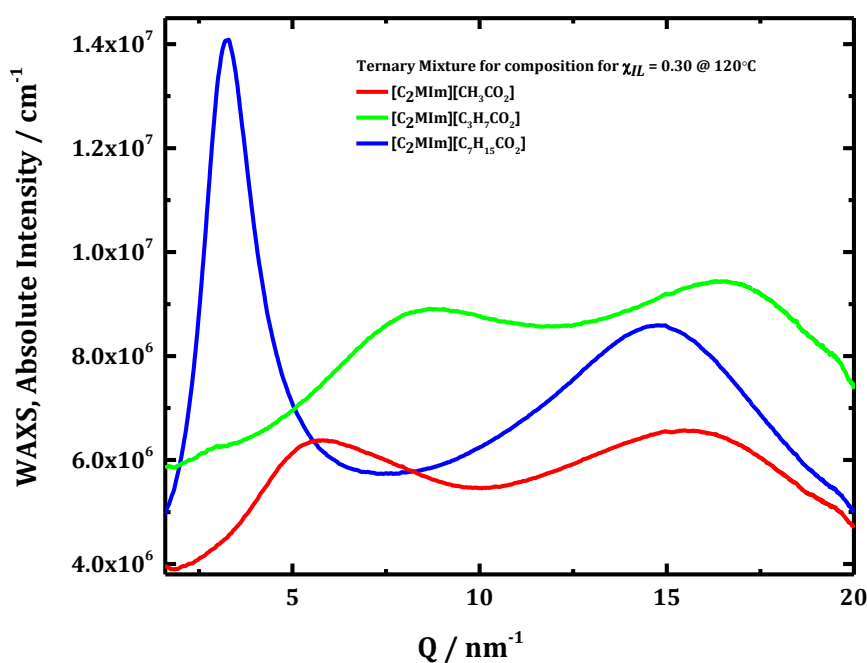
Figure 5-52. SWAXS patterns at the composition χ_{IL} = 0.30 of the ternary mixtures with water and copper(II) carboxylate precursor at 120°C of [C₂MIm][CH₃CO₂] (red), [C₂MIm][C₃H₇CO₂] (green), [C₂MIm][C₇H₁₅CO₂] (blue).

5.5.2.5 Conclusions

NP formation of copper oxide was studied in solutions containing a mixture of ILs, copper precursors (χ_{Cu} = 0.05) and water with regards to three specific compositions (χ_{IL} = 0.95, 0.50 and 0.30).

The NPs formation does not seem to occur for compositions ≤ 0.30 in the case of the [C$_2$MIm][C$_3$H$_7$CO$_2$]; whereas all composition seems to have led to NPs formation in the case of the [C$_2$MIm][C$_7$H$_{15}$CO$_2$] solutions. However, no evidence was found in the case of [C$_2$MIm][CH$_3$CO$_2$], since clusters of sub-nano size and not NPs are observed for IL-solutions of anion alkyl chain length below 4 carbons (cf, TEM results).

However, in the intramolecular domain, there is significant evidence of a change of the IL-structure while NPs are formed. In fact, the same solutions were measured at 50 and 120°C and compared regarding their SWAXS patterns. Intramolecular distances are getting longer after the formation of NPs has occurred, since NPs seems to have found free places between the anion and the cation.

The self-organised structure of the [C$_2$MIm][C$_7$H$_{15}$CO$_2$] was revealed by repetitive patterns found for all composition, which allow NPs to intercalate in the same free space at any composition. The well-defined structure of the [C$_7$H$_{15}$CO$_2$]$^-$ anion is due to its hydrophobic character and its strong Van der Waals interactions.

Adding a copper salt precursor or CuO-NPs has shown to restructure the acetate-anion solutions, since a new pre-peak is occurred. However, it seems to completely de-organise the [C$_3$H$_7$CO$_2$]$^-$ anion, since the pre-peaks tend to disappear. As explained above, the addition of copper in the [C$_2$MIm][C$_7$H$_{15}$CO$_2$] does not disturb its self-organisation.

Increasing the water concentration has beenshown to strengthen the interactions in all cases, since the intensities (of what??) is getting higher for all solutions. (higher is the intensity, higher are the intra-or-inter-molecular interaction of a system studied), However, the change in concentration of the solutions doesn't

affect the structure since the main correlation lengths stay around the same values.

Furthermore, the impossibility to determine the size of the NPs using SAXS and WAXS can be explained as follow. In fact, the NP formation produces by-products, such as water and carboxylic acid, coming from the copper salt precursor. The addition of the by-products and the presence of so many kind of interactions (*cation/anion, cation/water, anion/water, copper/water, copper/ cation and copper/anion*) have very much disturbed the whole system, making it almost impossible to determine the exact size of the NPs formed.

5.6 Conclusions

In this chapter, it has been proven that using ionothermal synthesis of copper(II) carboxylates in their respective ILs leads to either cluster or NPs formation of CuO. In fact, the basic anions are acting as a base and stabilising agent, allowing the preparation of stable NP dispersions in ILs (nanofluids).

The particles have resulted in very small CuO-NPs in the case of the copper(II) octanoate precursor with ranges of [10 - 25] nm, as well as for the copper(II) acetate precursor with ranges of [1-15] nm; whereas it has shown bigger CuO-NPs in the case of copper(II) butanoate precursor with ranges of [10-61] nm. The very small NPs from the copper(II) octanoate precursor can be explained by the high viscosity of the solution which should help to produce the NPs slowly and therefore in a more uniform shape as well as smaller size.

It has been shown, that the water concentration does not specifically influence the NPs size demonstrated by TEM analysis and the SWAXS study. However, it significantly improved the physical properties of the nanofluid formed; such as conductivity data. In fact, diluting the pure IL would lead to almost complete dissociation of both anion-cation in the case of the $[C_2MIm][CH_3CO_2]$ and $[C_2MIm][C_7H_{15}CO_2]$ (cf. Chapter-3, Walden plot).

By combining all this data, it was possible to suggest a mechanism of CuO-NPs formation in the case of the copper(II) octanoate precursor solutions. Since water addition in the ILs tend to dissociate both cation and anion, it may form water shell surrounded by a $[C_7H_{15}CO_2]^-$ anion shell of the IL. The CuO-NPs would then be formed within the water shell as described in Figure 5-53 and Figure 5-54. It was also difficult to find NPs with the TEM since the NPs where formed only inside the water shell, leaving then free spaces with no NPs, as it is schematised in Figure 5-55.

This can be explained by van der Waals forces which are essential for well-organised solutions, and which are more present in the $[C_2MIm][C_7H_{15}CO_2]$ than the two other ILs due to presence of the long alkyl-chains.

However, the particles from the copper(II) butanoate precursor would lead to bigger CuO-NPs that could be due to a larger water shell or a non-existent water-shell. In fact, the $[C_2MIm][C_3H_7CO_2]$-IL is not as well-structured and could leave more free space for the copper salt. This could then leave more free spaces for the CuO-NPs to grow larger. However, in the case of the $[C_2MIm][CH_3CO_2]$-IL, there is no organisation observed for the pure IL (cf, Chapter-4,WAXS part), whereas there is an improved of the solution organisation after addition of copper salt and NPs formation. This could explain why only clusters or very small CuO-NPs are found in this latter.
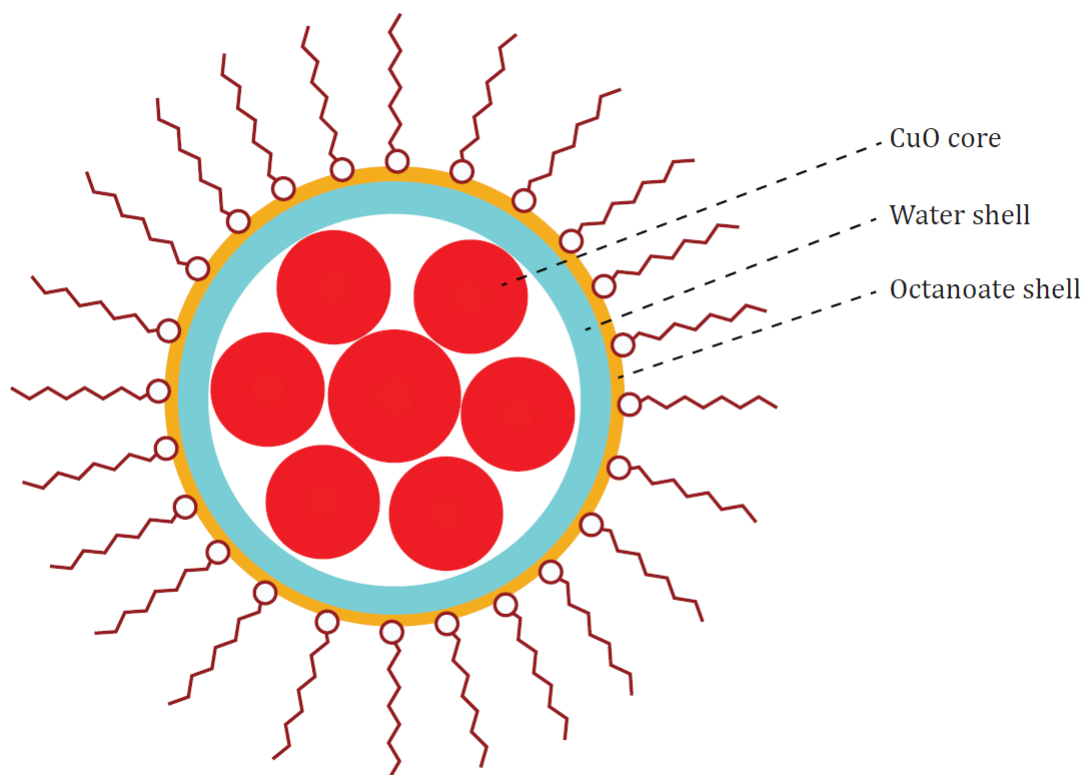
Figure 5-53. Schematic view of the CuO-NPs formation in the $[C_2MIm][C_7H_{15}CO_2]$ IL and water mixture for one aggregation structure.
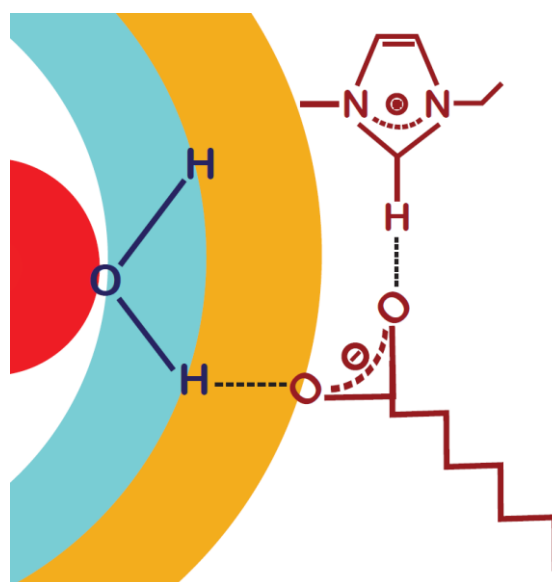
Figure 5-54. Zoom of Figure 5-53 in regards to the interaction involved in both shell between $[C_2MIm][C_7H_{15}CO_2]$ IL and water molecules.
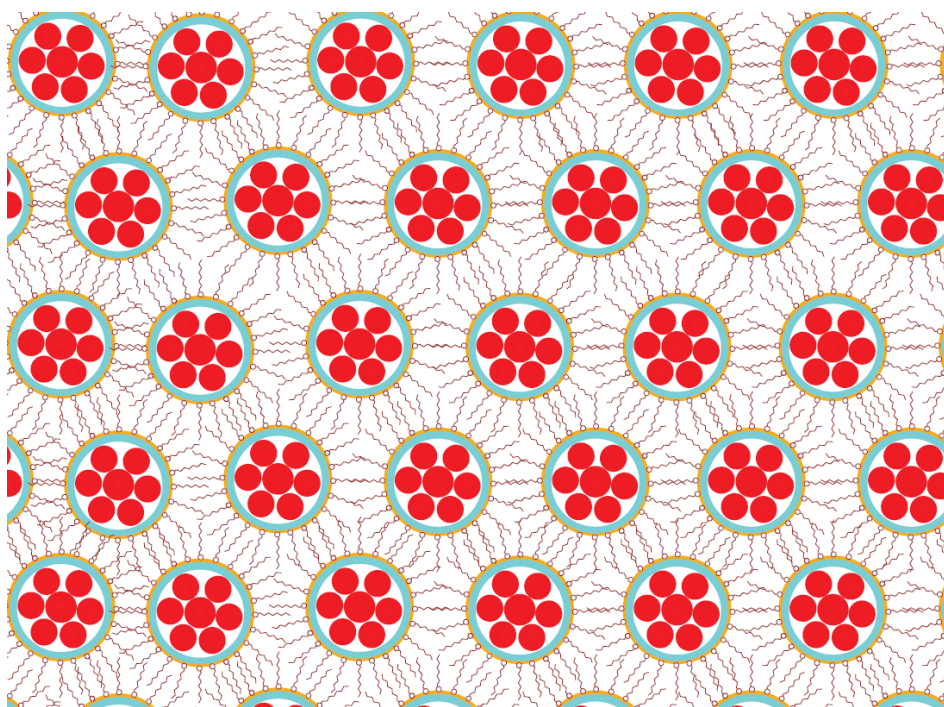
Figure 5-55. Schematic view of the CuO-NPs formation in the [C_2MIm][$C_7H_{15}CO_2$] IL and water mixture for the whole aggregation.

5.7 Experimental part

5.7.1 IL-nanofluids synthesis

The synthesis was prepared as elsewhere.[176]

The nanofluid solutions were prepared in a sealed 5 mL glass vials by mixing copper(II) carboxylate and a drop of pure water in its corresponding IL precursor under an Argon-glovebox. The maximum of copper salt that could be entirely dissolved in IL was found at 0.05 mole fraction. Then the solutions were heated at 50 °C in order to allow full dissociation of the copper salt by alternating magnetic stirring and sonication in an ultrasound bath. The solutions were exhibiting a deep blue colour. Once all the salt was completely dissolved, solutions were heated at 120 °C in an oil bath for at least 30 minutes under magnetic stirring. The nanoparticles formation was only happening when solutions were giving a deep red colour. The red solutions were found less viscous than the blue solutions. The red solutions had to be store in a desiccator and could only be opened in a nitrogen or argon-filled glovebox, since the nanofluid solutions are sensitive to air (becoming back in presence of air).

5.7.2 Single Crystal analysis measurements

Crystallography. The frames were integrated using the Bruker SAINT software package. Using a narrow-frame algorithm. Data were corrected for absorption effects using the numerical method with SADABS. A suitable crystal of each [C_2MIm][$C_nH_nCO_2$] IL was selected and measured on a four-circle diffractometer Kappa APEX II(Bruker AXS) with CCD detector and graphite-monochromated Mo Kα radiation. The crystal was kept at 200.15 K during data collection. Using Olex2, the structure was solved by direct methods using the ShelXS structure solution program and refined by full-matrix least-squares on F2 using the ShelXL program package.

Crystal Data. $Cu_2(C_3H_7CO_2)_4$, (M = 237.74 g/mol): triclinic, space group P-1 (no. 2), a = 5.15600(12) Å, b = 8.6547(3) Å, c = 11.5154(3) Å, α = 93.614(2)°, β = 93.5413(19)°, γ = 102.710(2)°, V = 498.76(2) Å^3, Z = 9, T = 293(2) K, μ(CuKα) = 10.582 mm^{-1}, $Dcalc$ = 2.773 g/cm^3, 9209 reflections measured (10.52° ≤ 2Θ ≤

145.44°), 1969 unique (R_{int} = 0.0299, R_{sigma} = 0.0182) which were used in all calculations. The final R_1 was 0.0246 (>2sigma(I)) and wR_2 was 0.0649 (all data).

Crystal Data. [C_2MIm]$_2$[$Cu(C_3H_7CO_2)_4$], (M =403.08 g/mol): triclinic, space group P-1 (no. 2), a = 14.3866(6) Å, b = 15.9472(9) Å, c = 17.1521(8) Å, α = 65.732(5)°, β = 77.128(4)°, γ = 67.803(5)°, V = 3310.9(3) Å^3, Z = 14, T = 100.00(10) K, μ(Cu Kα) = 9.875 mm^{-1}, $Dcalc$ = 2.994 g/cm^3, 22643 reflections measured (8.4° ≤ 2Θ ≤ 145.24°), 12772 unique (R_{int} = 0.0375, R_{sigma} = 0.0573) which were used in all calculations. The final R_1 was 0.0821 (>2sigma(I)) and wR_2 was 0.2625 (all data).

Crystal Data. [C_2MIm]$_2$[$Cu(C_7H_{15}CO_2)_4$], (M =651.53 g/mol): triclinic, space group P-1 (no. 2), a = 17.1050(4) Å, b = 17.4308(6) Å, c = 18.9701(6) Å, α = 63.412(3)°, β = 86.315(2)°, γ = 76.256(3)°, V = 4907.3(3) Å^3, Z = 2, T = 99.9(2) K, μ(CuKα) = 1.027 mm^{-1}, $Dcalc$ = 1.161 g/cm^3, 84986 reflections measured (9.982° ≤ 2Θ ≤ 133.198°), 17300 unique (R_{int} = 0.0553, R_{sigma} = 0.0392) which were used in all calculations. The final R_1 was 0.1030 (I > 2σ(I)) and wR_2 was 0.2727 (all data).

Synthesis. Single crystals of $Cu_2(C_3H_7CO_2)_4$, [C_2MIm]$_2$[$Cu(C_3H_7CO_2)_4$] and [C_2MIm]$_2$[$Cu(C_7H_{15}CO_2)_4$] were a suitable crystal was selected and place on a diffractometer. The crystal was kept at 293(2) K during data collection. Using Olex2,[198] the structure was solved with the ShelXS structure solution program using Direct Methods[199] and refined with the ShelXL refinement package using Least Squares minimisation.[200]

5.7.3 Photoluminescence measurements

Photoluminescence measurements were recorded on an Edinburgh Instruments FLSP920 UV–Vis–NIR spectrofluorimeter, using a 450 W xenon lamp as the steady-state excitation source, a Hamamatsu R928P PMT photomultiplier working at −22°C for the visible range, and a Hamamatsu R5509-72 photomultiplier operating at −80°C for the NIR range.

An appropriate amount of Copper(II) salt (5.10^{-3} M) was dissolved in the respective IL. The solutions were dissolved at 50°C. A small sample of the solutions was then transferred into a closed Quartz capillary (2 mm in diameter with a wall thickness of 0.01 mm) from Hilgenberg and analysed with the UV-Vis

instruments. Then the closed capillaries were heated at 70, 90 and 120°C where a UV-Vis spectrum was taken after each of those temperature in order to investigate *in-situ* the nanofluid synthesis.

5.7.4 TEM measurements

Transmission Electron Microscope (TEM) images were acquired in bright field TEM, using a Tecnai 200 kV F20 Transmission Electron Microscope with a Field Emission Gun. The samples were prepared by diluting a drop of the nanofluid solution in dichloromethane (DCM), and left few minutes in an ultrasonic bath. A few drops of sample were then pipetted onto an Agar holey carbon film copper TEM grids, and washed with DCM. The prepared grid was set aside for *ca.* 20 min prior to inserting it into the microscope, in order to allow the solvent to evaporate. Images were taken with a Gatan CCD digital camera attached to the microscope.

5.7.5 XPS measurements

The XPS spectra were obtained using a Kratos AXIS Ultra DLD XPS spectrometer using monochromated Al Kα X-rays and a hemispherical analyser with a pass energy of 160 eV. The samples were prepared in an Argon-glovebox, then stocked in a desiccator full with Argon and the sample were then placed into the XPS instrument under the presence of an Argon flux. The IL-nanofluid samples were mounted on conducting copper tape and the binding energies were normalised to the C1s at 284.8 eV. Background subtraction was performed using a Shirley background and Casa XPS.[201]

5.7.6 SAXS/SANS measurements

SAXS and WAXS measurements were used as explained in Chapter 4. However, each samples were analysed first at 25, 50, 60, 70, 80, 90, 100, 110, 120 and 131.5°C in order to follow the *in-situ* formation of the nanoparticles. Each samples were prepared in an Argon-glovebox to avoid any moisture with water. The respective ionic liquid was first mixed with water and stirred using a magnetic stirring bar. Then the respective carboxylate was added and stirred using a magnetic stirring bar in a close vessel at 50°C using an oil bath. A small sample of the solution was then transferred quickly outside the glovebox to a small container; a Quartz capillary (2 mm in diameter with a wall thickness of 0.01 mm)

from Hilgenberg. The table below show the respective mass taken for each composition. It was not possible to dissolve the copper precursor below 0.3 ionic liquid mole fraction.

TABLE 5-22. $[C_2MIm][CH_3CO_2]$, $[C_2MIm][C_3H_7CO_2]$ and $[C_2MIm][C_7H_{15}CO_2]$ ionic liquids, water and copper carboxylate (n= 2, 4 and 8) ternary mixture compositions used for X-ray measurement (SAXS and WAXS).

		$[C_2MIm][CH_3CO_2]$			$[C_2MIm][C_3H_7CO_2]$			$[C_2MIm][C_7H_{15}CO_2]$		
		m_{IL}	m_{Cu}	m_{H2O}	m_{IL}	m_{Cu}	m_{H2O}	m_{IL}	m_{Cu}	m_{H2O}
χ_{IL}	χ_{H2O}	(mg)	(mg)	(mg)	(mg)	(mg)	(mg)	(mg)	(mg)	(mg)
0.30	0.65	359.4	68.3	78.3	354.4	74.3	64.6	360.5	855	50
0.50	0.45	415.2	46.7	36.5	416.0	53.0	34.5	430.3	56.1	8.9
0.95	0.00	478.2	27.7	0	469.5	30.1	0	463.0	33.5	0

Chapter 6 _ Development of Novel Nonflammable Ionic Liquid Electrolytes for Safer Sodium-ion Batteries

6.1 Introduction

In this chapter, a second application of new ionic liquid solutions was investigated as electrolytes for sodium-ion batteries. This had the aim to provide safer electrolytes, since these offer several advantages over conventional electrolytes such as non-volatility, non-flammability and large electrochemical windows, which results in better long-term stability. The ILs name used in all publications and the one used in this chapter are reported in the three table below:

Table 6-1. Comparison of IL cations abbreviations used in publications and this chapter

ILs Cation names	Abbreviations used in this report	Abbreviations used in publications
N-butyl-N-methylpyrrolidinium	[Pyrr$_{14}$]	[C$_4$mpyr] or [BMP]
N-propyl-N-methylpyrrolidinium	[Pyrr$_{13}$]	[C$_3$C$_1$pyrr]
N,N,-diethyl-N-methoxyethyl	[Pyrr$_{22(201)}$]	[DEME]

Table 6-2. Comparison of IL anion abbreviations

ILs Anions names	Abbreviations used in this report	Abbreviations used in publications
Bis(fluorosulfonyl)imide or amide	[FSI]	[FSA]
Bis[(trifluoromethyl)sulfonyl]imide or amide	[TFSI]	[TFSI] or [NTf$_2$]

Table 6-3. IL cations abbreviations

Ionic liquids cation used in this study	Abbreviations used
1-(2-methoxyethyl)-1 methylpyrrolidinium	[Pyrr$_{1(201)}$]
Dimethyl(2-methoxyethyl)sulfonium	[S$_{11(201)}$]
Dimethyl 1-butyl sulfonium	[S$_{114}$]
1-Butyl-1-methylazepanium	[Aze$_{14}$]
1-Butyl-1-methylpiperidinium	[Pip$_{14}$]

6.1.1 A short review on IL-based electrolytes tested for Na-ion batteries

Many families of IL-based-electrolytes have been studied for Lithium-ion batteries. The most used cations are imidazolium and pyrrolidinium, whereas the most used anions are [TFSI]$^-$ and [FSI]$^-$. Those two cations are easy to tune by changing the length, the number and the functionality of the alkyl chains. Further the synthesis of those combined cations and anions is fairly easy and provides high purity and yields. From the literature, scientists are mainly using the [TFSI]$^-$ anion as it is shown in Table 6-4 below. In fact, [TFSI]$^-$ anion has great physical properties comparable to common organic electrolyte used for Metal-ion batteries such as high thermal stability and low.

In addition, ILs-based with the [TFSI]$^-$ anion are cheaper to make or to buy than the one with the [FSI]$^-$ anion. Moreover, a recent study has shown that FSI anion is more suitable than the [TFSI]$^-$ anion due to its lighter molecular weight and therefore is lower viscosity. Indeed [TFSI]$^-$ anion tend to decompose easily after a certain time of cycling or at high temperature.[91] This is due to the extra carbon chain length that decomposed leaving free fluorine atoms.

The best capacity has been found for a polymer electrolyte based on [Pyrr$_{14}$][TFSI] tested with LiFePO$_4$/Li$_4$Ti$_5$O$_{12}$ electrode at 20 °C and 40 °C that provided 550 and 450 mAh·g^{-1} respectively [28]. The [Pyrr$_{13}$][FSI] tested with Li electrode at 30 °C can also be highlighted for its 350 mAh·g^{-1} [202]. However, only little ILs-based electrolytes have been tested for Na-ion batteries. Below are showed a recorded up to date of all those publications. Research has been carried out from 2012 to 2015. The ILs capacity data has been ranged in function of the temperature. Table 6-4 is showing the cycling performance of the ILs-based electrolyte tested in half-cell negative electrodes, and Table 6-5 and

Table 6-6 in the half-cell positive electrodes.

Table 6-4. Cycling performances of half-cell negative electrode in Na-ion batteries containing ionic liquids as electrolytes.

Ionic Liquids	Salts	Negative electrode	T (°C)	Cycle number	Discharge Capacity, First cycle (mAh·g⁻¹)	Discharge Capacity after x cycles (mAh·g⁻¹)	C-rate	Ref
[Pyrr$_{13}$][FSI]	1M-NaFSI	HC	90°C	500	/	230	1000 mA	[25]
[Pyrr$_{13}$][FSI]	1M-NaFSI	HC		500				[25]
[Pyrr$_{13}$][FSI]	1M-NaFSI	HC	90°C	500	/	229	200 mA	[73]
			90°C		277	274	20 mA	
[Pyrr$_{13}$][FSI]	10:90-NaFSI	HC	90°C	40	/	260	50 mA	[94]
NaFSI/KFSI	56:44	Na/Sn	90°C	30	729	121	0.619 mA·cm^{-2}	[203]
[Pyrr$_{13}$][FSI]	1MNaFSI	HC	25°C	500	/	25	1000 mA	[73]
[Pyrr$_{13}$][FSI]	1M-NaFSI	HC	25°C	500	/	50	200 mA	[73]
[Pyrr$_3$][FSI]	1M-NaFSI	HC	25°C	500	/	25	20 mA	[73]

Table 6-5. Cycling performances of half-cell positive electrode in Na-ion batteries containing [Pyrr$_{13}$][FSI]- based electrolytes

Ionic Liquids	Salts	Positive electrode	T (C)	Cycle number	Discharge Capacity after x cycles (mAh·g^{-1})	C-rate	Ref
[Pyrr$_{13}$][FSI]	1M-NaFSI	Na/NaCrO$_2$	90°C	500	118	100mA	[91]
[Pyrr$_{13}$][FSI]	0.4M-NaFSI	Na/NaCrO$_2$	90°C	40	96	500mA	[204]
[Pyrr$_{13}$][FSI]	0.4M-NaFSI	Na/NaCrO$_2$	90°C	40	76	200mA	[204]
[Pyrr$_{13}$][FSI]	0.25MNaFSI	Na/NaCrO$_2$	90°C	40	123	20 mA	[204]
[Pyrr$_{13}$][FSI]	1M-NaFSI	Na/Na$_2$FeP$_2$O$_7$	90°C	300	94	100mA	[205]
[Pyrr$_{13}$][FSI]	1M-NaFSI	Na/Na$_2$FeP$_2$O$_7$	90°C	300	94	20 mA	[205]
[Pyrr$_{13}$][FSI]	1M-NaFSI	Na/Na$_2$FeP$_2$O$_7$	90°C	300	94	10 mA	[205]
[Pyrr$_{13}$][FSI]	NaFSI (2:8)	Na/NaCrO$_2$	80°C	100	106	20 mA	[206]
[Pyrr$_{13}$][FSI]	NaFSI (2:8)	Na/NaCrO$_2$	80°C	100	62	500mA	[206]
[Pyrr$_{13}$][FSI]	1M-NaFSI	Na/Na$_2$FeP$_2$O$_7$	75°C	300	94	20 mA	[205]
[Pyrr$_{13}$][FSI]	1M-NaFSI	Na/Na$_2$FeP$_2$O$_7$	50°C	300	90	100mA	[205]
[Pyrr$_{13}$][FSI]	1M-NaFSI	Na/Na$_2$FeP$_2$O$_7$	50°C	300	94	20 mA	[205]
[Pyrr$_{13}$][FSI]	0.25MNaFSI	Na/NaCrO$_2$	25°C	35	117	20 mA	[204]
[Pyrr$_{13}$][FSI]	NaFSI (2:8)	Na/NaCrO$_2$	25°C	100	92	20 mA	[206]
[Pyrr$_{13}$][FSI]	1M-NaFSI	Na/Na$_2$FeP$_2$O$_7$	25°C	300	77	100mA	[205]
[Pyrr$_{13}$][FSI]	1M-NaFSI	Na/Na$_2$FeP$_2$O$_7$	25°C	300	90	20 mA	[205]
[Pyrr$_{13}$][FSI]	1M-NaFSI	Na/Na$_2$FeP$_2$O$_7$	25°C	300	90	10 mA	[205]
[Pyrr$_{13}$][FSI]	1M-NaFSI	Na/NaCrO$_2$	20°C	500	21	100mA	[207]

.

Table 6-6. Cycling performances of half-cell positive electrode in Na-ion batteries containing [Pyrr$_{14}$][TFSI]-based electrolytes

Ionic Liquids	Salts	Positive electrode	T (C)	Cycle number	Discharge Capacity after x cycles (mAh·g^{-1})	C-rate	Ref
[Pyrr$_{14}$][TFSI]	1M-NaBF$_4$	Na/NaCrO$_2$	75°C	100	125	0.05C	[208]
[Pyrr$_{14}$][TFSI]	1M-NaClO$_4$	Na/Na$_{0.44}$MnO$_2$	75°C	100	115	0.05C	[209]
[Pyrr$_{14}$][TFSI]	1M-NaBF$_4$	Na/NaCrO$_2$	50°C	100	125	0.05C	[208]
[Pyrr$_{14}$][TFSI]	1M-NaClO$_4$	Na/NaCrO$_2$	50°C	100	125	0.05C	[208]
[Pyrr$_{14}$][TFSI]	1M-NaPF$_6$	Na/NaCrO$_2$	50°C	100	120	0.05C	[208]
[Pyrr$_{14}$][TFSI]	0.1M-NaTFSI	Na/NaFePO$_4$	50°C	100	110	0.05C	[210]
[Pyrr$_{14}$][TFSI]	0.25M-NaTFSI	Na/NaFePO$_4$	50°C	100	/	0.05C	[210]
[Pyrr$_{14}$][TFSI]	0.5M-NaTFSI	Na/NaFePO$_4$	50°C	100	125	0.05C	[210]
[Pyrr$_{14}$][TFSI]	1M-NaTFSI	Na/NaFePO$_4$	50°C	100	120	0.05C	[210]
[Pyrr$_{14}$][TFSI]	1M-NaBF$_4$	Na/NaCrO$_2$	25°C	100	92	0.05C	[208]
[Pyrr$_{14}$][TFSI]	1M-NaClO$_4$	Na/NaCrO$_2$	25°C	100	79	0.05C	[208]
[Pyrr$_{14}$][TFSI]	1M-NaPF$_6$	Na/NaCrO$_2$	25°C	100	44	0.05C	[208]
[Pyrr$_{14}$][TFSI]	0.1M-NaTFSI	Na/NaFePO$_4$	25°C	100	46	0.05C	[210]
[Pyrr$_{14}$][TFSI]	0.25M-NaTFSI	Na/NaFePO$_4$	25°C	100	51	0.05C	[210]
[Pyrr$_{14}$][TFSI]	0.5M-NaTFSI	Na/NaFePO$_4$	25°C	100	56	0.05C	[210]
[Pyrr$_{14}$][TFSI]	1M-NaTFSI	Na/NaFePO$_4$	25°C	100	48	0.05C	[210]
[Pyrr$_{14}$][TFSI]	1M-NaBF$_4$	Na/Na$_{0.44}$MnO$_2$	25°C	100	84	0.05C	[209]
[Pyrr$_{14}$][TFSI]	1M-NaClO4	Na/Na$_{0.44}$MnO$_2$	25°C	100	97	0.05C	[209]
[Pyrr$_{14}$][TFSI]	1M-NaTFSI	Na/Na$_{0.44}$MnO$_2$	25°C	100	92	0.05C	[209]
[Pyrr$_{14}$][TFSI]	1M-NaPF6	Na/Na$_{0.44}$MnO$_2$	25°C	100	38	0.05C	[209]

Table 6-7. Cycling performances of half-cell positive electrode in Na-ion batteries containing a mixed IL-electrolytes.

Ionic Liquids	Salts	Positive electrode	T (C)	Cycle number	Discharge Capacity after x cycles (mAh·g^{-1})	C-rate	Ref
NaTFSI/CsTFSI	10:90	Na/NaCrO$_2$	150 °C	10	83.4	10 mA	[211]
NaTFSI/CsTFSI	10:90	Na/NaCrO$_2$	150 °C	50	66.4	66.4mA	[211]
NaFSI/KFSI	56:44	Na/NaCrO$_2$	80 °C	100	69	15mA	[212]

In the literature, only two main ILs have been studying for their electrochemical performance: [Pyrr$_{13}$][FSI] and [Pyrr$_{14}$][TFSI]. These works came from mainly two main groups, one based in Taiwan; Dr N. Wongittharom and C.H. Wang *et al.* [208,210] and one based in Japan; Dr T. Nohira and Prof. R. Hagiwara *et al.*[204-207,211,212]. Others groups in Italy and Germany have been looking at the physical properties of different IL-based electrolytes without testing their electrical performance [93,97,213,214].

From those two above tables, it is clear that the electrochemical performance for positive half-cell electrodes has been studied in more detail than for negative half-cell electrodes. This is due to the fact that electrochemical performance for negative electrodes in Na-ion batteries are still very challenging to test compared to positive electrodes. This is why this chapter based on negative electrodes is very interesting as only few data on negative electrodes can be found in the literature.

However, according to the work of C. Ding *et al.*[73], the charge-discharge performance of only one HC/ NaCrO$_2$ as sodium-ion full cell has been investigated at 90 °C. In this work, they obtained for the first cycle a charge capacity and a discharge capacity of 326 mAh·g^{-1} and 263 mAh·g^{-1} respectively and a reversible capacity after further cycles of 260 mAh·g^{-1}. Those values are higher than the HC/NaNi$_{0.5}$Mn$_{0.5}$O$_2$ using ester alkyls carbonates solvent-based electrolyte as it was reported from Prof. Shinichi Komaba and co-worker [215]. This is showing that IL-based electrolytes are promising and safe electrolytes for SIBs and are worth further investigations.

From Table 6-5 and

Table 6-6, it is clearly outstanding that a temperature higher than 50 °C will improve the capacities of the materials. Nevertheless, it seems that at room temperature it is better to use a salt concentration between 0.5 and 0.25 M as showed the work. Indeed, for 25 °C, a concentration of 0.1, 0.25, 0.5 and 1 M of NaTFSI salt will respectively give a capacity of 46, 51, 56 and 48 mAh·g^{-1}, whereas at 50 °C, the capacities will increase their values by 55-65%. [210]

6.2 Aims and objectives

In this study, a series of seven ILs based on pyrrolidinium, piperidinium, azepanium, and sulfonium cations bearing the bistrifluormethanesulfonimide (TFSI) anion were synthesised and characterised at Queen's University Belfast. Their synthesis as well as their physicochemical properties such as density, viscosity and conductivity, along with thermal properties including phase transition behaviour and decomposition temperature were measured by Sinead Murphy, a PhD candidate from QUB. Therefore, those specific results would not be shown in this work. Understanding the structure-property relationship of the ILs will however facilitate the improvement of electrolytes for deployment in SIBs.

At the Tokyo University of Science, I investigated the electrochemical performance of those IL-based electrolytes mixed with sodium bis(fluorosulfonyl)imide (NaFSI) salt in half Na-ion coin cells. Cyclability, coulombic efficiency and capacity retention have been investigated in order to define the best IL-electrolyte for Na-ion batteries or at least find a trend in the change of the IL-cation.
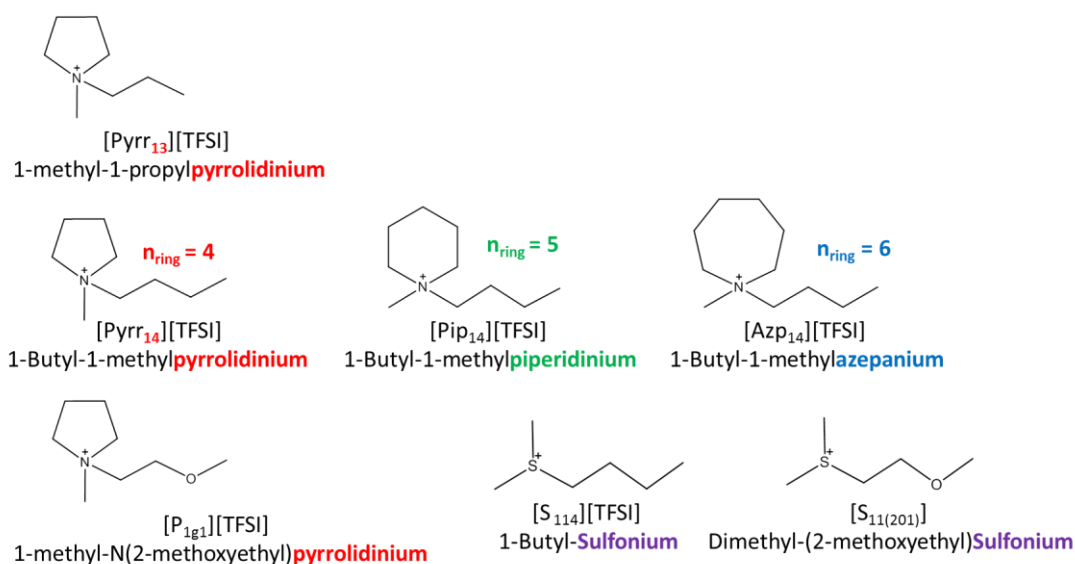
Figure 6-1. Cations of TFSI anion-based ionic liquids used as electrolyte for SIBs.
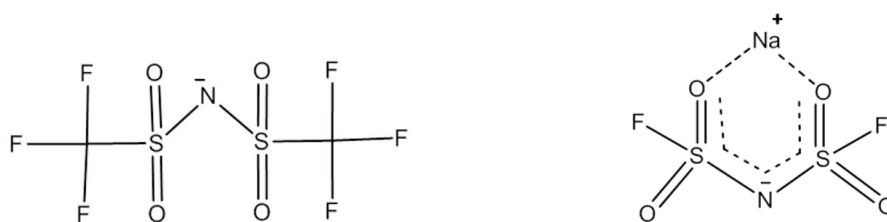
Figure 6-2. TFSI IL-anion structure, bis[(trifluoromethyl)sulphonyl]imide (left) and the NaFSI salt, sodium bis(fluorosulfonyl)imide salt (right) used to make the IL-based electrolytes.

The new electrolytes were made using NaFSI salt dissolved in each of the seven ILs. The reactivity with sodium metal of each IL-based electrolyte was then tested in an argon-glovebox to avoid reactions between the new IL-based electrolytes and the sodium-metal used as a reference electrode while making the new coin-cells. Sodium-metal is known to be extremely reactive with water and air, that may lead to explosion as it was explained in the introduction chapter, and it is known that removing water completely from ILs can be challenging.

The experiments have shown different kinds of reactivity, and from those results, two different batches of electrolytes were prepared for the whole study. The first group of electrolytes was made using a solution of ILs with with 0.25 mol·L^{-1} of NaFSI salt dissolved, whereas a second group of electrolytes was investigated using a ternary mixture of ILs, and propylene carbonate (PC) as an additive in a 50:50 mass ratio with 0.3 mol·L^{-1} of NaFSI salt. This choice will be explained later in the next part.

Hard-carbon (HC) was synthesised derived from sucrose carbonised (use the British spelling throughout) at 1300 °C and a HC/sodium polyacrylate (PANa)-binder was prepared. In this study, the binder was fixed to a PANa-binder, which is, to the best of our knowledge, the most suitable for the Na-ion battery.[215]

Then a sodium half coin-cells for the HC negative electrode or $Na_{2/3}Ni_{1/3}Mn_{2/3}O_2$ positive electrode was assembled with Na-metal as the reference electrode. It was found that vacuum assembly is the best method to dispose the IL electrolyte into the Na-ion battery, as it will allow the IL-electrolyte to penetrate properly into the glass fibre separator and therefore allow a better connection between both electrodes.

The method of fabrication of coin-cells was firstly validated by using a commercial electrolyte (1 M-NaPF$_6$ in EC/DEC). Only then, IL-based electrolytes were tested with Na-cells for galvanostatic charge-discharge. Furthermore, analysis of the surface electrodes before and after cycling was carried out using X-ray photoelectron spectroscopy in order to investigate the electrode and electrolyte decomposition.

On the other hand, a study of the interaction between IL and NaFSI salt electrolyte was undertaken. Generally, a good electrolyte for energy storage needs to exhibit only weak interactions between Na$^+$ and the IL, as well as having a low viscosity in order to allow free mobility of the Na$^+$. In fact, during the charge and the discharge of a battery, Na$^+$ won't be able to reach both electrodes if these are not able to move easily due to strong interactions with other ions. In this last case, there will be a low conductivity, and thus a weak capacity of the coin cell. It is therefore very important to understand how the salt interacts with the IL in order to acquire better electrolytes for SIBs.

6.3 Results and discussion on the electrochemical performance of IL-based electrolytes in Na-ion cells

6.3.1 Dissolution of the NaFSI salt into ILs

Two different batches of electrolytes were prepared for the whole study. The first group of electrolytes was made using a solution of ILs with 0.25 mol·L^{-1} of the NaFSI salt dissolved (0.25 mol·L^{-1} was taken as the limit of solubility found in the [Pyrr$_{14}$][TFSI] and was carry out for all the other IL-based electrolytes).

Only three ILs were tested for galvanostatic charge-discharge; [Pyrr$_{1(201)}$][TFSI], [Pyrr$_{14}$][TFSI], [Pyrr$_{13}$][TFSI]. The other ILs were not tested in this group of electrolyte due to a higher percentage of water determined by Karl-Fischer titration. Regarding safety issues, it was not possible to test the electrolytes having a water content higher than 60ppm.

Therefore, a new group of electrolytes was investigated using a ternary mixture of ILs and propylene carbonate (PC) in a 50:50 mass ratio with 0.3 mol·L^{-1} of NaFSI salt. Based on reports by Kühnel et al.,[216] it was found that using ILs as an additive could increase the electrochemical performance of metal-ion batteries and also lead to improved safety. The presence of ILs in the mixture is known to lower the kinetics of PC evaporation, and therefore reduces the corrosion process of the copper current collector. Also, it would reduce the water content by half which is initially found in the pure IL solution, which makes the new IL-based electrolytes solution sufficiently safe to be tested for Na-cells.

In this group, five ILs were chosen as IL-based electrolytes: [Azp$_{14}$][TFSI], [Pip$_{14}$][TFSI], [Pyrr$_{14}$][TFSI], [S$_{11(201)}$] [TFSI], [S$_{114}$][TFSI]. As a reference, the electrolyte solution of 1 mol·L^{-1} NaFSI in PC was also investigated and the electrochemical performances were compared with the pure [Pyrr$_{14}$][TFSI] that was tested in the first group of electrolytes.

Only for [Azp$_{14}$][TFSI], it was found to be impossible to dissolve the NaFSI salt, since a precipitate was formed. Therefore, no further investigations were carried

out with this IL. This is probably due to a precipitation caused by mixing TFSI and FSI anions between the ILs, and the salts which were not miscible due the large ring of the azepanium cation (n=6).

6.3.2 Electrochemical performance of the HC half-cell negative electrodes

Before investigating the new IL-based electrolytes, it was important to validate the coin cell making process first of the HC-synthesis from sucrose negative electrode using a known electrolyte. In this work, HC as the negative electrode was combined with a 1 mol·L^{-1} of NaPF$_6$ in EC/DEC electrolyte that was used as a reference to validate the coin cell making process and also to validate the synthesis of the freshly made HC from sucrose according to the literature procedures.[81,217] Only then, the new IL-based electrolytes were tested in a Na-cell.

In the first part, electrolytes were tested with the HC-negative electrode, where Na coin cells were assembled with sodium metal and a sucrose hard-carbon negative electrode. Each cell was cycled at room temperature and tested for galvanostatic charge-discharge at 12.5 mA·g^{-1} between 0.0 and 2.0 V *vs.* Na$^+$/Na. In the second part, only the best electrolytes tested for the HC-s negative electrode were tested for Na$_{2/3}$Ni$_{1/3}$Mn$_{2/3}$O$_2$ positive electrode materials, whereas each coin-cell was tested in a galvanostatic charge-discharge test at 12.5 mA·g^{-1} between 2.0 and 4.1 V *vs.* Na$^+$/Na.

From the electrochemical performances of those new IL-based electrolytes, their charge-discharge curves were drawn, as well as the capacity retention and coulombic efficiency in order to get a better understanding on the electrochemical performance of ILs based electrolyte compared to common solvent electrolytes.

6.3.2.1 *Material validation of the hard carbon electrode made from sucrose tested in the Na-cell*

Some ILs are known to be "greener" than most of the common solvents due to their very low volatility and their high boiling point, and in this work these will be used as electrolytes. The negative HC electrode would be prepared from a sucrose hydrocarbon source; sucrose being very cheap and abundant. However, the quality of this material (so-called HC-s) is very much dependent on the

synthetic conditions, thus it was necessary to test the new materials as negative electrodes with common solvent before starting the actual work with the new IL-based electrolytes. In the literature, several reports have shown the impact of the carbonisation temperature during HC synthesis from sucrose. [81,218,219] The best results so far have shown a reversible capacity of 300 mAh·g^{-1} for the Na-coin cell using 1 M-NaClO$_4$ in 30:70 EC/DEC electrolyte [81].

In order to validate the use of the new HC-s made from sucrose in the application of future Na-coin cells using new IL-based electrolyte, half-cells were used by using a HC-s/PANa binder (95:5) negative electrode with the Na metal reference in the 1 M-NaPF$_6$_EC/DEC electrolyte prepared in an argon glovebox, and then the electrochemical performance was measured for the freshly made coin cells. The charge-discharge cycles were all constant with a discharge capacity of 300 mAh·g^{-1}. The capacity retention was found at around 300 mAh·g^{-1}, which was in accordance with the literature and the coulombic efficiency, which was close to 99.5% after the first cycle. Figure 6-3 and Figure 6-4 below are showing the reliability of the new synthesised materials, as these give similar results to the ones found in the literature.[81,217] From those results, it was possible to carry out tests on new Na-coin cells using IL-based electrolytes with HC negative electrodes as it is shown in the following.
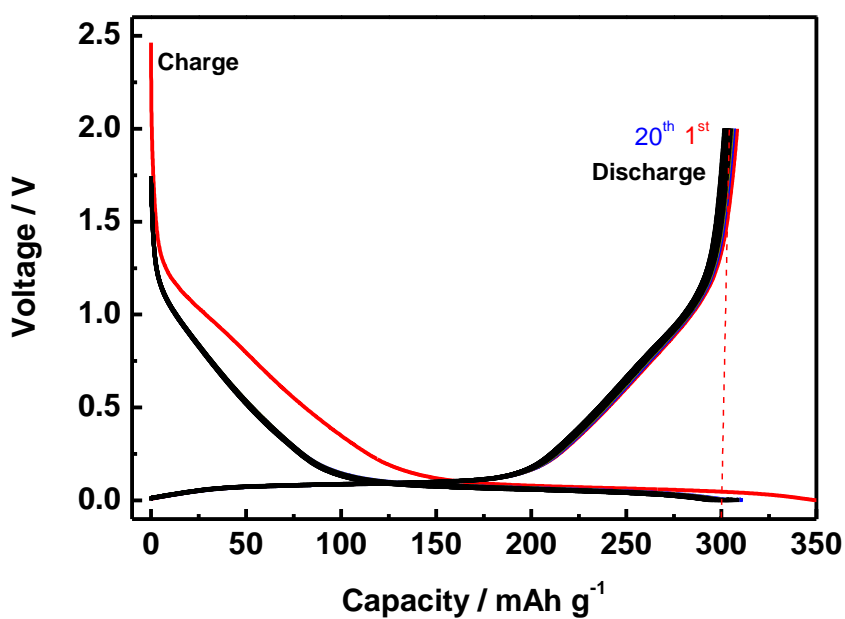
Figure 6-3. Charge-discharge capacity of electrodes of hard-carbon, derived from sucrose carbonized at 1300 °C, at a rate of 13 mA·g^{-1} in 1 mol·dm^{-3} NaPF$_6$ dissolved in EC:DEC (50:50 in vol%) showing a discharge capacity of 300 mAh·g^{-1}.
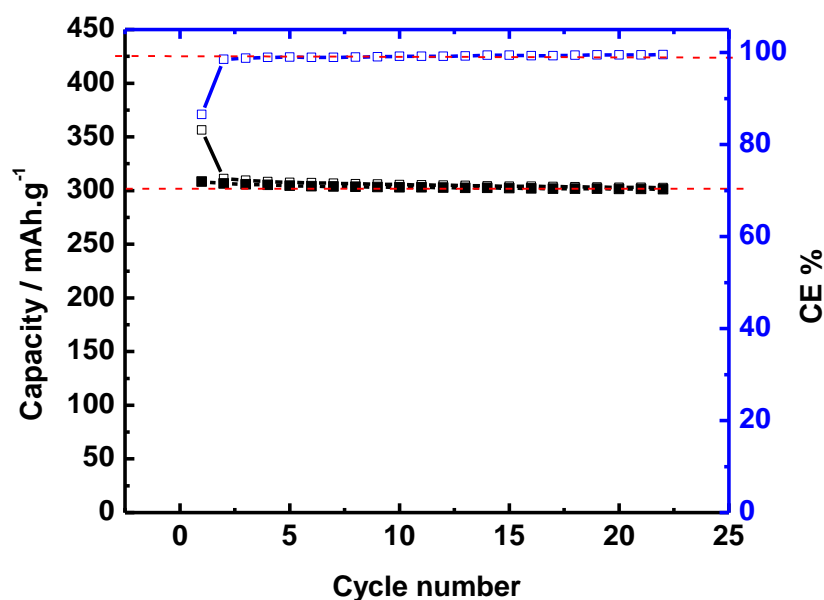
Figure 6-4. Capacity retention and coulombic efficiency of hard-carbon electrode, derived from sucrose carbonized at 1300 °C, at a rate of 13 mA·g-1 in 1 mol·dm^{-3} NaPF$_6$ dissolved in EC:DEC (50:50 in vol%) showing a capacity retention of 300 mA·g^{-1} and a coulombic efficiency close to 99.5%.

6.3.2.2 *Binary mixture electrolytes: 0.25 M-NaFSI in ILs tested with sucrose hard-carbon for Na-cells*

The first group of electrolytes was made using a unique solution of ILs dissolved with 0.25 mol·L^{-1} of NaFSI salt. In this part, different aspects of the IL cations were investigated such as the impact of an additional carbon on the alkyl chain length in the pyrrolidinium ring with n = 3 and n = 4, the influence of different functional groups between the alkyl chain and methoxyethyl group, which includes the presence of oxygen atom, the impact of the ring size by using pyrrolidinium (n = 4), piperidinium (n = 5) and azepanium (n = 6), and finally the change of the heteroatom from nitrogen to sulphur. An overall conclusion will outline the advantages and disadvantages in the use of binary or ternary mixture of electrolytes in the application of Na-cells.

Only [Pyrr$_{13}$][TFSI], [Pyrr$_{14}$][TFSI], and [Pyrr$_{1(201)}$][TFSI] were found to be stable in the presence of the sodium metal, and therefore were directly tested as electrolytes for the Na cells. *(Note, [Pyrr$_{14}$][TFSI] was tested in both groups as a reference from two different batches).* The full names and physical properties of the three ILs study in this part are shown in the Table 6-8 below. The three ILs were mixed separately with 0.25 mol·L^{-1} NaFSI salt in an argon-glovebox to produce the new IL-based electrolytes.

The electrochemical performances of these electrolytes were tested in half-cells composed of HC-s (synthesised from sucrose) as the negative electrode. The three ILs investigated here are composed of the same type of cations which include the pyrrolidinium ring (n=4). They differ in their functional groups which includes either an increase in the alkyl chain length or the addition of an oxygen as part of the chain.

Table 6-8. Ionic liquid cations and anions used in the first group of electrolytes, and their physical properties as pure ILs.

IL cation	IL anion	Viscosity (mPa.s) at 25 °C	Conductivity (mS.cm⁻¹) at 25 °C
[Pyrr$_{13}$] 1-methyl-1-propylpyrrolidinium		26.0	3.9
	[TFSI] bistrifluormethanesulfonimide		
[Pyrr$_{14}$] 1-Butyl-1-methylpyrrolidinium		59.0	2.7
[Pyrr$_{1(201)}$]		53.0	3.7
1-methyl-N(2-methoxyethyl)pyrrolidinium			

6.3.2.2.1 Influence of the cation chain length (n = 3, 4) on pyrrolidinium cation

In Figure 6-5, the charge-discharge of [Pyrr$_{13}$][TFSI] and [Pyrr$_{14}$][TFSI] based electrolytes during the first and second cycle was compared. The discharge capacity of [Pyrr$_{13}$][TFSI] was found to be 122 and 134 mAh·g⁻¹ at the first and the second cycle, respectively, while the discharge capacity of [Pyrr$_{14}$][TFSI] was found to be 107 and 116 mAh·g⁻¹ at the first and the second cycle, respectively. From those results it is clear that the capacity improved in both cases after the first cycle.

In the first cycle, the discharge capacity of [Pyrr$_{13}$][TFSI] and [Pyrr$_{14}$][TFSI] was found to be 122 and 107 mAh·g⁻¹, respectively. This shows that the capacity rose when the alkyl chain length is decreased by one carbon. Indeed, the highest capacity was found for the [Pyrr$_{13}$][TFSI]-based electrolyte, probably due to its lighter molecular weight (408.38 g.mol⁻¹) and mainly due to its low viscosity, which is two times lower than the viscosity of [Pyrr$_{14}$][TFSI]; 26.0 mPa·s. In fact, Na⁺ will flow much easier with an electrolyte having a low viscosity as it was explained in the introduction part [220]. During charge and discharge of a battery, Na⁺ ions would not be able to reach both electrodes due to strong interactions with other atoms. This result shows clearly that the increase of the alkyl chain length in the pyrrolidinium cation would tend to lead to a decrease of the capacity of the Na-cell

However, the coulombic efficiency stabilized after the third cycle at around 94.3% and 99.1% for [Pyrr$_{13}$][TFSI] and [Pyrr$_{14}$][TFSI], respectively. This shows that

despite of [Pyrr$_{13}$][TFSI] having the higher discharge capacity, it is not the most stable electrolytes.
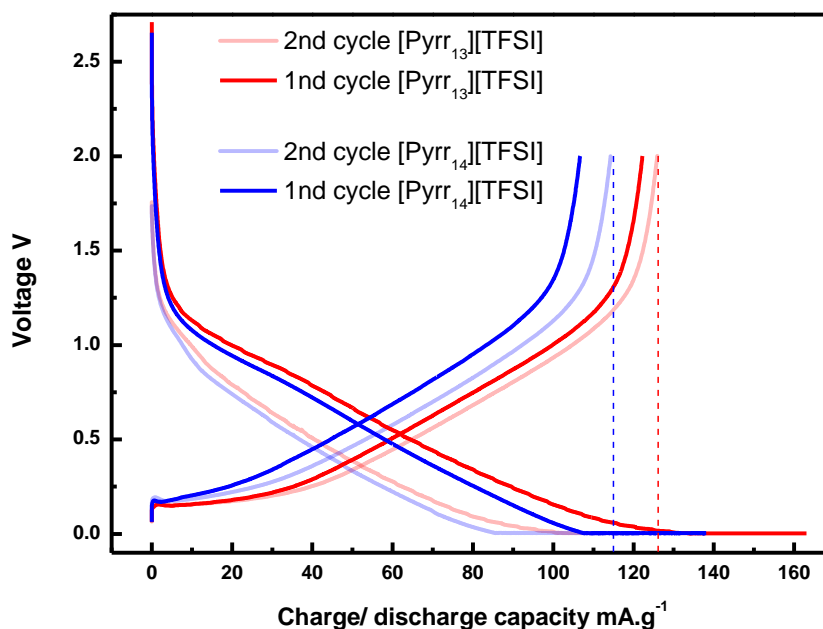
Figure 6-5. Comparison of the charge/ discharge capacities in the 1st and 2nd cycle of [Pyrr$_{13}$][TFSI] (red) and [Pyrr$_{14}$][TFSI] (Blue).
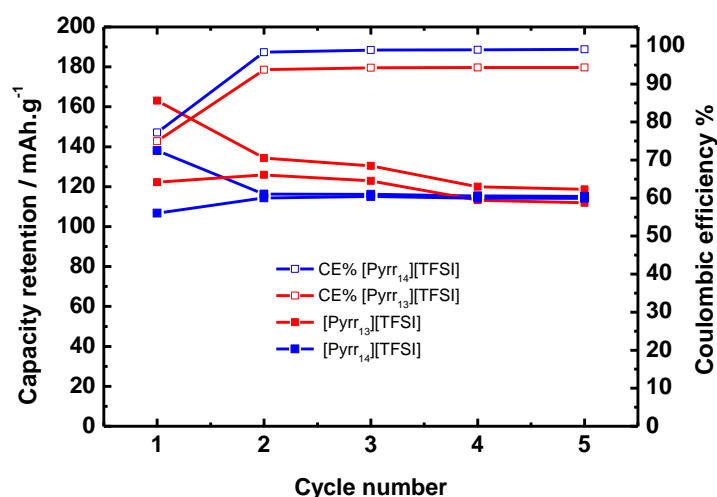
Figure 6-6. Charge and discharge capacity retention of [Pyrr$_{13}$][TFSI] (red) and [Pyrr$_{14}$][TFSI] (blue) electrolytes and comparison of the coulombic efficiency of [Pyrr$_{13}$][TFSI] (red-white) and [Pyrr$_{14}$][TFSI] (blue-white).

Moreover, the starting potential of each discharge was found at 61 and 63 mV in [Pyrr13][TFSI] and [Pyrr14][TFSI], respectively, while these should not be higher than 10 mV in the ester alkyl carbonate based electrolytes. This could be caused by a high polarization in the Na-cell based on IL electrolyte, probably due to the decomposition of the TFSI IL-anion. This typically causes irreversible decomposition at the negatively polarized hard-carbon electrode.

6.3.2.2.2 Influence of additional functional group on pyrrolidinium cation

The first cycle shows a discharge capacity of [Pyrr1(201)][TFSI] and [Pyrr14][TFSI] of 79 and 107 mAh·g^{-1}, respectively. Those results show a serious capacity drop when an oxygen is added to the alkyl chain.

In addition, the [Pyrr1(201)][TFSI]–based electrolyte was found to decompose after the 10th cycle, as shown in Figure 6-7. Furthermore, its discharge starting potential was found at 114 mV, which is almost twice the value of the two other IL-based electrolytes. This value is in a very critical range of high polarization which will cause serious issues for Na-cell. Therefore, for these reasons, and due to its low capacity and high polarization, this IL was excluded for the rest of this study.
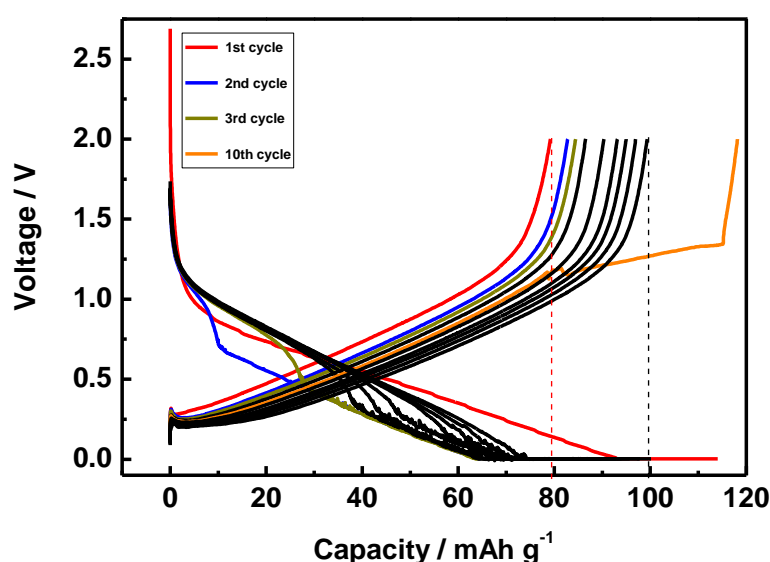
Figure 6-7. Charge/discharge capacity of the 10th first cycles of 0.25M-NaFSI in [Pyrr 1(201)][TFSI] electrolyte in HC negative Na-cell showing the cycling decomposition from the 10th cycle.

Among those three IL cations, it was shown that the pyrrolidinium ring is potentially suitable for Na-cells. However, it was shown that the electrochemical performances of the Na-cells were higher for a pyrrolidinium cation having an alkyl chain functional group instead of a methoxyethyl functional group. The methoxyethyl functional group seems to complicate the system in the Na-cell, since the cells have shown cycle decomposition after the 10th cycle, whereas it did not show any decomposition for the alkyl chain functional group.

Future investigations should be done on the electrolyte decomposition as well as the electrode before and after cycling disorder, in order to understand what is happening during the cycling process. NMR and XPS may be useful tools to further investigate this issue. This would allow to study SEI (solid electrolyte interphase) formation as well as dendrite formation on the surface of the electrode, which could cause short-circuits.

The binary mixtures have shown that the pyrrolidinium ring is potentially suitable for Na-cells. All the three electrolytes made with the pyrrolidinium cation as the ILs [Pyrr$_{13}$][TFSI], [Pyrr$_{14}$][TFSI], and [Pyrr$_{1(201)}$][TFSI], were able to make several electrochemical cycles. However, it was shown that the electrochemical performances of the Na-cell were higher for a pyrrolidinium cation having an alkyl chain functional group instead of a methoxyethyl functional group.

6.3.2.3 *Ternary mixture electrolytes: 0.3 M-NaFSI in IL/PC (1:1) ILs tested in sucrose hard-carbon for Na-cell*

The second group of electrolytes was investigated using a ternary mixture of IL and PC in 50:50 mass ratio with 0.3 mol·L^{-1} of NaFSI salt dissolved in an argon glovebox. The four following ILs, [Pip$_{14}$][TFSI], [Pyrr$_{14}$][TFSI], [S$_{114}$][TFSI] and [S$_{11(201)}$][TFSI], were investigated. The full names and physical properties of the three ILs are shown in Table 6-9 below. The electrochemical performances were tested with the HC/PANa electrode.

Table 6-9. Ionic liquid cations and anions used in the second group of electrolytes and their physical properties as pure ILs.

IL cation	IL anion	Viscosity (mPa.s) at 25 °C	Conductivity mS.cm^{-1} at 25 °C
[Pip$_{14}$]		121.2	1.04
1-Butyl-1-methylpiperidinium			
[Pyrr$_{14}$]		58.8	2.72
1-Butyl-1-methylpyrrolidinium			
[S$_{114}$]	[TFSI] bistrifluormethanesulfonimide	82.8	2.48
1-Butyl-Sulfonium			
[S$_{11(201)}$]		53.0	4.04
Dimethyl-(2-methoxyethyl)Sulfonium			

6.3.2.3.1 *Influence of the cation ring size (n= 4 to 6)*

In this part, the influence of an additional carbon in the ring of the cation was investigated. Pyrrolidinium (n = 4), piperidinium (n = 5) and Azepanium (n = 6) were studied. First of all, Azepanium-based ILs, [Azp$_{14}$][TFSI], were found not to allow dissolution of the salt NaFSI. Hence, no further experiments were carried out with this IL. Therefore, no conclusion can be drawn regarding the electrochemical performance of azepanium.

However, it was possible to study the electrochemical performance of both, pyrrolidinium (n = 4) and piperidinium (n = 5) cations. In fact, the [Pip$_{14}$][TFSI] and [Pyrr$_{14}$][TFSI] as IL-based electrolytes were suitable for long-term cycles since no decomposition was observed. A comparison in the 2nd cycle of the two IL based electrolytes, [Pip$_{14}$][TFSI] and [Pyrr$_{14}$][TFSI], is shown in Figure 6-8 where the respective discharge capacity of 130 and 120 mAh·g^{-1} was observed. In

addition, the capacity retention of both [Pip$_{14}$][TFSI] and [Pyrr$_{14}$][TFSI] electrolytes shows a respective value of 136 and 124 mAh·g^{-1}. Those results show that the increase by one carbon in the cation ring slightly increases the capacity of the cell. In addition, the coulombic efficiency for all electrolytes after 35 cycles is about 99.7%. This is showing a good stability of those electrolytes and makes them suitable candidates as as safer electrolytes for SIBs.

Besides, high polarization due to IL-based electrolytes is still an issue in this part, as it was explained for the first group of electrolyte. Here, the starting potential of each discharge cycle was found to be 83 and 85 mV in [Pip$_{14}$][TFSI] and [Pyrr$_{14}$][TFSI], respectively, instead of being lower that 10 mV.
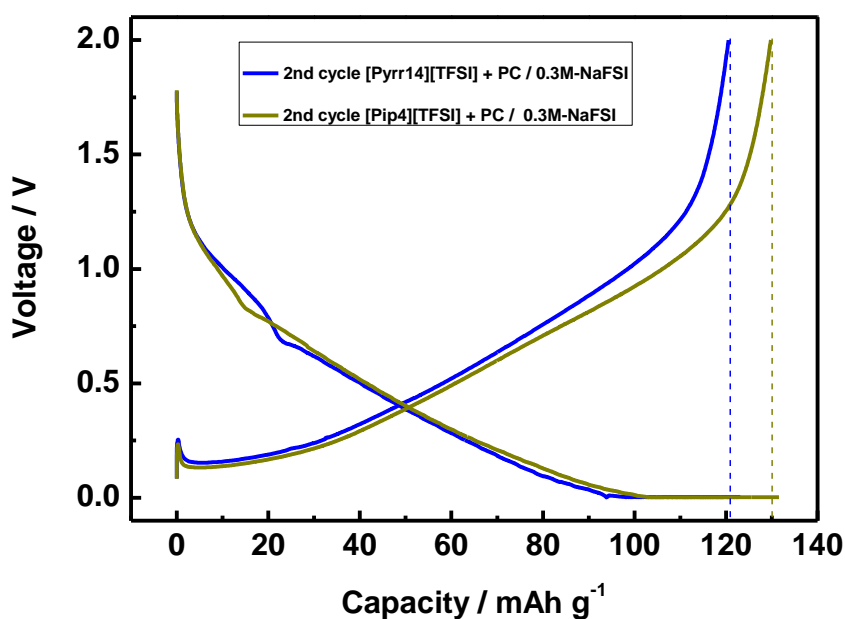
Figure 6-8. Comparison of the charge/ discharge capacities in the 2nd cycle of [Pyrr$_{14}$][TFSI] (blue) and [Pip$_{14}$][TFSI] (green) electrolytes.
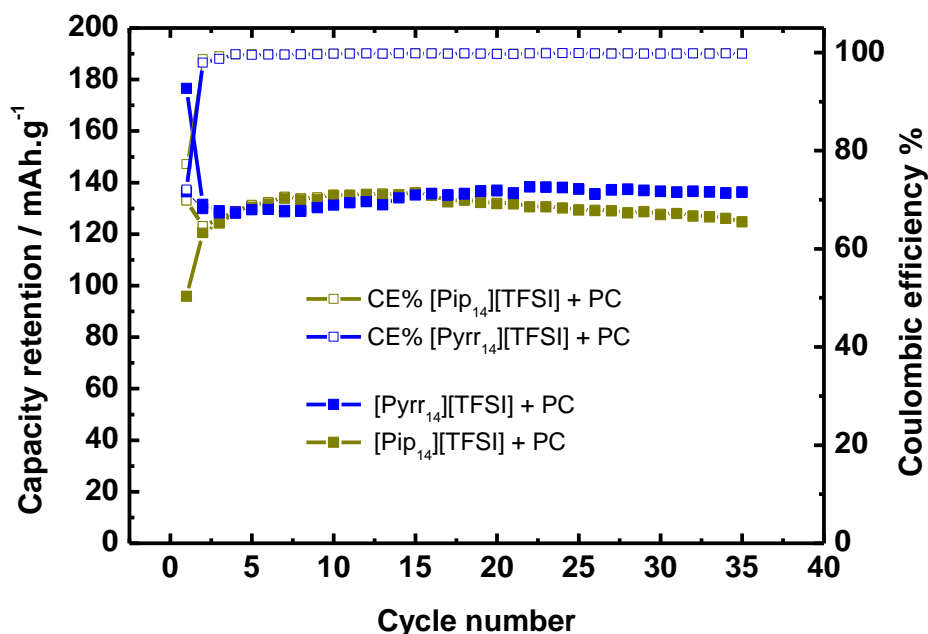
Figure 6-9. Comparison of the capacity retention and coulombic efficiency of [Pyrr14][TFSI] (blue) and [Pip14][TFSI] (green) electrolytes.

6.3.2.3.2 Influence of an additional functional group on the sulfonium cation

In this part, two sulfonium-based ILs were studied. Dimethyl-1-butyl-sulfonium, [S114][TFSI], contains only alkyl chains as functional groups, whereas dimethyl-(2-methoxyethyl)sulfonium [S11(201)] has an additional methoxyethyl functional group.

The discharge capacity of the second cycle of [S114][TFSI] shows a value of 135 mAh·g^{-1} with a capacity retention of 131 mAh·g^{-1} and a coulombic efficiency of about 99.7% after 35 cycles that show a good electrochemical performance and good stability compared to our previous electrolytes. Again, high polarisation was observed at 71 mV instead of 10 mV that could hinder Na$^+$ insertion into the HC-s.
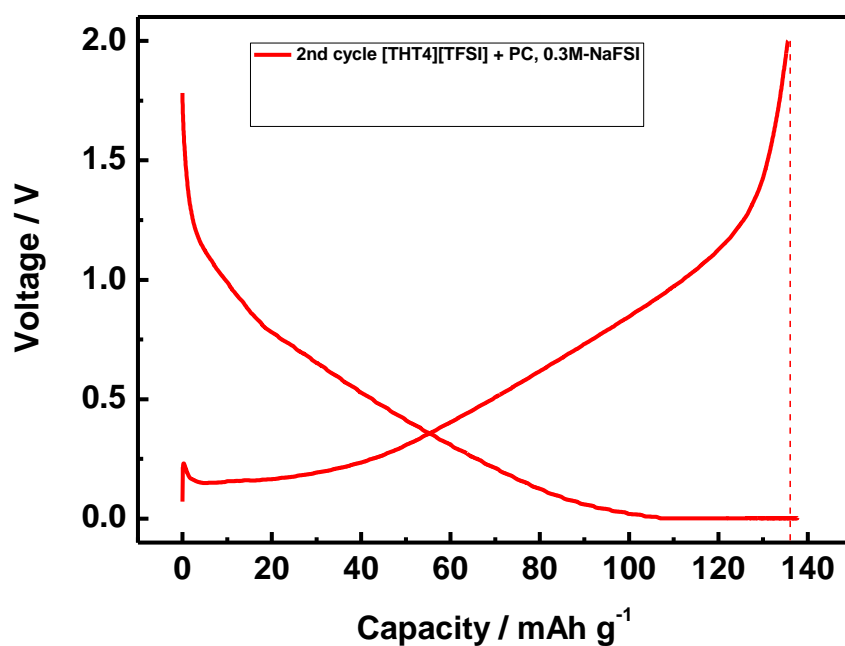
Figure 6-10. 2nd cycle Charge/ discharge curve of HC in 0.25 mol·L^{-1} NaFSI in [S$_{114}$][TFSI].
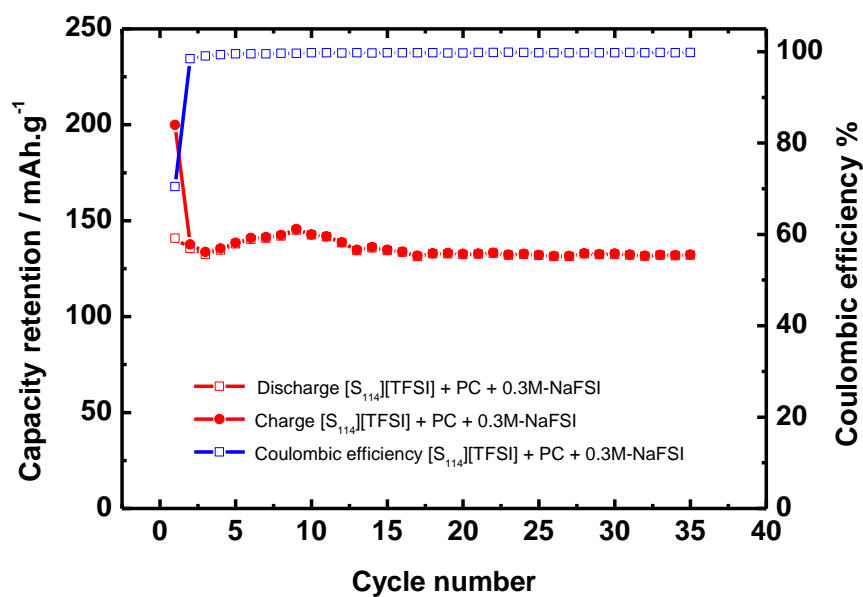
Figure 6-11. Capacity retention (red) and coulombic efficiency (blue) of [S$_{114}$][TFSI] ternary electrolyte with PC and 0.3M-NaFSI.

However, [S$_{11(201)}$] was found to decompose after six cycles having a very low charge/discharge capacity (lower than 50 mAh·g^{-1}). A yellow colour due to the

decomposition of the IL was observed after opening the coin cell confirming those results as show the Figure 6-12. Therefore, this IL was excluded from the study.
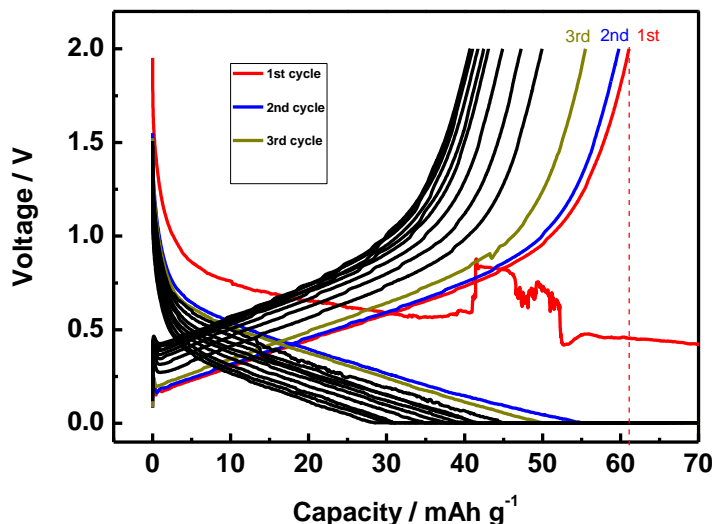
Figure 6-12. Open coin cell showing the [Pyrr$_{1(201)}$][TFSI] decomposition to a yellow colour instead of staying colourless.

Figure 6-13. Charge/discharge capacities of 0.3M-NaFSI in [Pyrr1(201)][TFSI]/PC electrolyte in HC negative Na-cell showing the cycling decomposition and a decrease of the discharge capacity starting from the fist cycle at only 60 mA·g^{-1} and down to only 30 mA·g^{-1} at the 10th cycle.

The ternary mixtures have shown that the piperidinium ring cation (n = 5) results in a higher electrochemical performance than the pyrrolidinium ring cation (n = 4). However, the sulfonium cation has shown slightly higher electrochemical performance in terms of discharge capacity than the piperidinium Na-cell. Furthermore, high polarisation during discharge is found for all ternary mixtures and could lead to further issues regarding their electrochemical performance in Na-cell. However, the sulfonium cation has the lowest polarisation (71 mV vs 85 mV), which could make sulfonium cations better electrolytes for further investigations of the Na-cell.

Nevertheless, methoxyethyl functional group including in sulfonium cation [S$_{11(201)}$][TFSI] has failed the electrochemical performance test in Na-cells, as well as it has failed it for the pyrrolidinium cation [Pyrr$_{1(201)}$][TFSI], which was investigated in the previous test in the binary mixtures. Therefore, it seems that the methoxyethyl functional group doesn't work well in the Na-cell due to the presence of oxygen. This could be due to a breakdown of the alkyl chain

containing oxygen that could release volatile compounds and therefore become corrosive until a short-circuit occurs.

Again, as a future work, it will be interesting to find out what is happening in those two cells; whether it is caused by the electrolyte degradation, or by an incompatibility with HC negative electrode.

Among those results, PC-electrolytes without IL still have a discharge capacity more than twice as high as for the ternary mixture electrolytes. 1 mol·L^{-1} NaFSI in the PC electrolyte has been found with a discharge capacity of 310 mAh·g^{-1} and with a coulombic efficiency close to 100% from the second cycle, as shown in Figure 6-14. This expected result is found due to the high viscosity characteristic of the ILs compared to the very low viscosity of PC (2.5 mPa.s @25 °C). A higher viscosity is indeed known to lower the transfer of Na$^+$ atoms from the positive and negative electrode during the charge/discharge of the cell and therefore reduces the capacity of the cell. However, each IL has a constant coulombic efficiency close to 100 % from the 2nd cycle even after 35 cycles that shows that the ILs are able to be stable during long term cycling comparable to standard solvents used as electrolyte for SIBs.
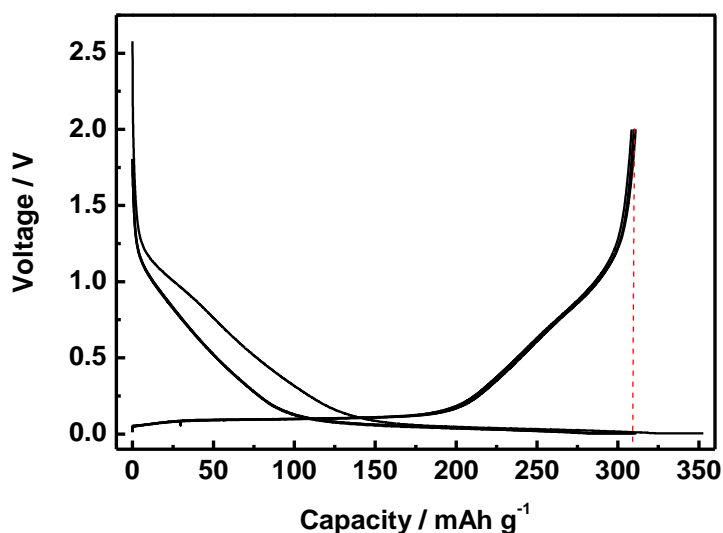
Figure 6-14. Charge-discharge capacity of 1 mol dm^{-3} NaPF$_6$ dissolved in PC electrolyte tested forHC-s negative electrodes, at a rate of 13 mA·g^{-1}.

6.3.2.4 *Influence of the addition of PC co-solvent (1:1 weight%) in the pyrrolidinium cation*

The [Pyrr13][TFSI] and [Pyrr14][TFSI] ILs were found to have a similar charge/discharge cycling behaviour than that of IL/PC mixtures discussed previously. Furthermore, when we compare the results from [Pyrr14][TFSI]/PC mixture (1:1 weight%), and for those from the [Pyrr14][TFSI]-based electrolyte without PC, there is not much difference in terms of their discharge capacity at the second cycle which remained 120 and 116 mAh·g^{-1}, respectively. The graphs are shown below in Figure 6-15 and Figure 6-16. In fact, lowering the viscosity by the addition of PC should result in an increase of the capacity, however, the results do not show a significant change here. This shows that addition of common organic solvent does not always improve the capacity of the cell the way it is discussed in the literature.[78]
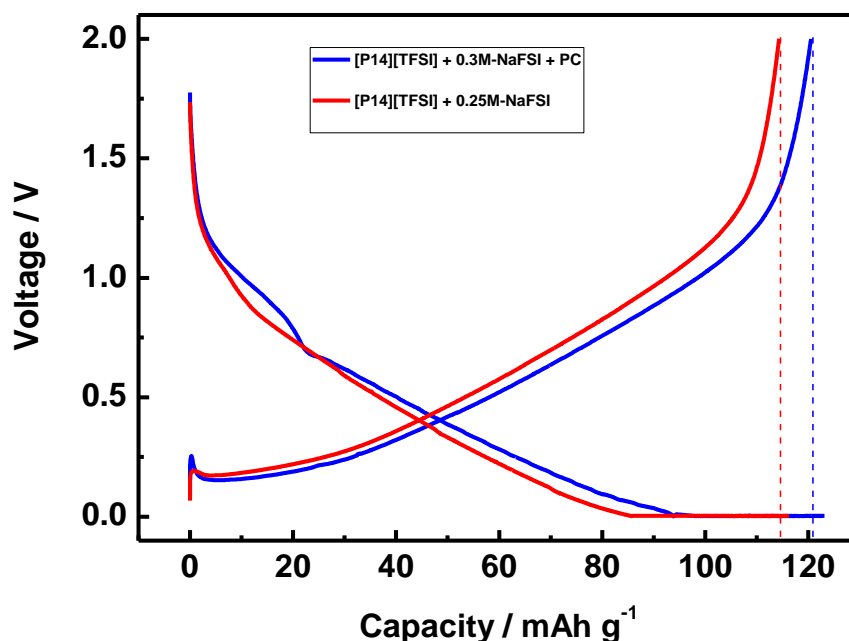
Figure 6-15. Comparison of the charge/ discharge capacities in the 2nd cycle of 0.25M-NaFSI in [Pyrr14][TFSI] electrolyte (red) and 0.3M-NaFSI in [Pyrr14][TFSI]/PC electrolyte (blue) showing a slightly higher discharge capacity in the case of the addition of PC in the IL-based electrolyte.
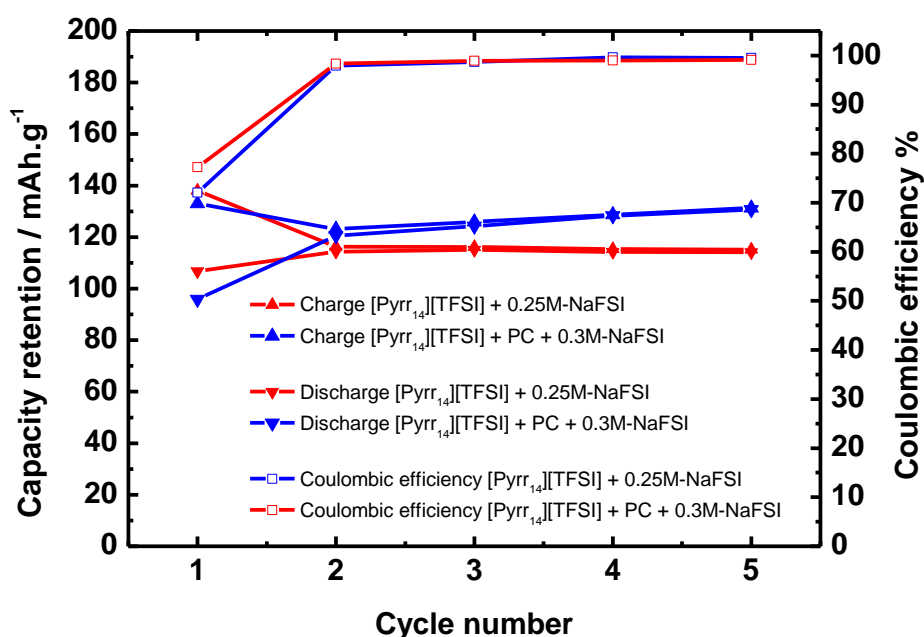
Figure 6-16. Comparison of the capacity retention and coulombic efficiency of 0.25M-NaFSI in [Pyrr$_{14}$][TFSI] electrolyte (red) and 0.3M-NaFSI in [Pyrr$_{14}$][TFSI]/PC electrolyte (blue) showing an higher capacity retention in the case of the addition of PC in the IL-based electrolyte.

6.3.3 New Ionic liquids-based electrolytes tested in Na$_{2/3}$Ni$_{1/3}$Mn$_{2/3}$O$_2$ positive electrodes for Na-cell

Among the IL-based electrolytes tested in the previous part with HC half-cells as the negative electrodes for the Na-cell, only the ones having the best capacity retention were tested with the Na$_{2/3}$Ni$_{1/3}$Mn$_{2/3}$O$_2$ half-cell positive electrode. Thus, Na coin cells were assembled with sodium metal, Na$_{2/3}$Ni$_{1/3}$Mn$_{2/3}$O$_2$ positive electrode and [Pyrr$_{13}$][TFSI], [Pyrr$_{14}$][TFSI] and ([Pip$_{14}$][TFSI]+PC) IL-based electrolytes. Their electrochemical behaviour was investigated and studied with regards to their cations while using the TFSI anion for those samples.

Table 6-10. Ionic liquid cations and anions used as based electrolytes tested in half-cell positive electrode and the physical properties of the pure ILs

IL cation	IL anion	Viscosity (mPa·s^{-1}) at 25 °C	Conductivity mS·cm^{-1} at 25 °C
[Pyrr$_{13}$] 1-methyl-1-propylpyrrolidinium		26.0	3.9
[Pyrr$_{14}$] 1-Butyl-1-methylpyrrolidinium	[TFSI] bistrifluormethanesulfonimide	59.0	2.7
[Pip$_{14}$] 1-Butyl-1-methylpiperidinium		121.0	3.7

The electrochemical performance has shown that only the [Pyrr$_{14}$][TFSI] IL-based electrolyte was found suitable in combination with the $Na_{2/3}Ni_{1/3}Mn_{2/3}O_2$ positive electrode. [Pip$_{14}$][TFSI] mixed with PC and was found to decompose after the second cycle. [Pyrr$_{13}$][TFSI] was found to exhibit a sever decrease in the retention capacity from the 7th cycle to 15th cycle on with a starting discharge capacity of 87 mAh·g^{-1} in the first cycle to 14 mAh·g^{-1} in 15th cycle.

In comparison, the [Pyrr$_{14}$][TFSI] and [Pyrr$_{13}$][TFSI] charge/discharge curves were plot together as shown in Figure 6-17. In this graph, we can clearly see a constant regularity in term of the retention capacity remaining between 83 and 85 mAh·g^{-1} for [Pyrr$_{14}$][TFSI]-based electrolytes compared to the [Pyrr$_{13}$][TFSI] electrolyte, which is decreasing severely. This could be due to a higher water content in the synthesised batch prepared from [Pyrr$_{13}$][TFSI]. Indeed, [Pyrr$_{13}$][TFSI] seems to be a more suitable electrolyte than [Pyrr$_{14}$][TFSI] if we look at its physical properties. In fact, [Pyrr$_{13}$][TFSI] is found to have a higher conductivity and a lower viscosity than its neighbour [Pyrr$_{14}$][TFSI] with a conductivity of 3.9 mS·cm^{-1} compared to 2.7 mS·cm^{-1} and a viscosity of 26.0 mPa·s^{-1} compared to 59.0 mPa·s^{-1}.
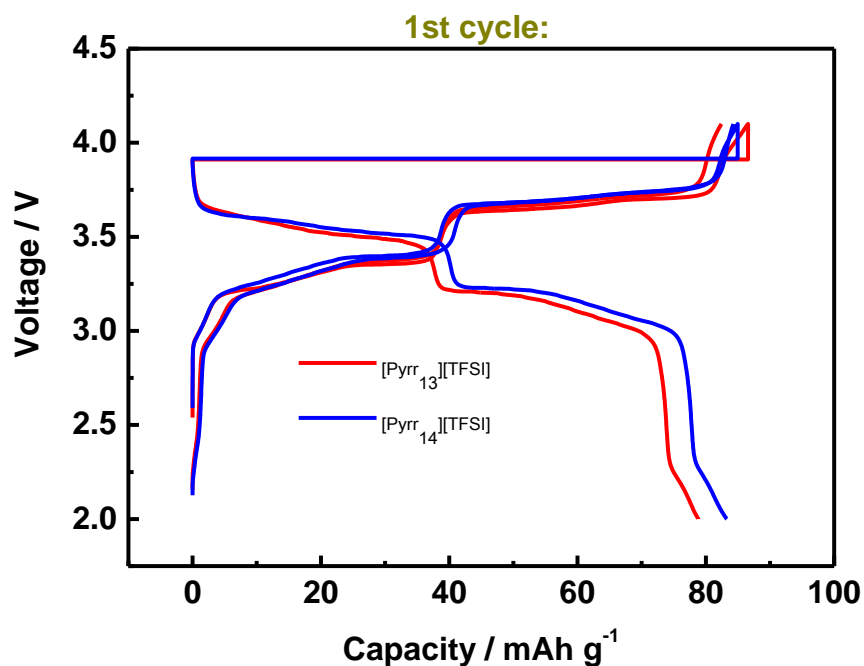
Figure 6-17. 1st cycle of the charge-discharge capacity of both electrolytes containing 0.25 mol·dm^{-3} NaFSI dissolved in (red) [Pyrr$_{13}$][TFSI] and (blue) [Pyrr$_{14}$][TFSI] ILs tested for Na$_{2/3}$Ni$_{1/3}$Mn$_{2/3}$O$_2$ positive electrodes, at a rate of 13 mA·g^{-1}.
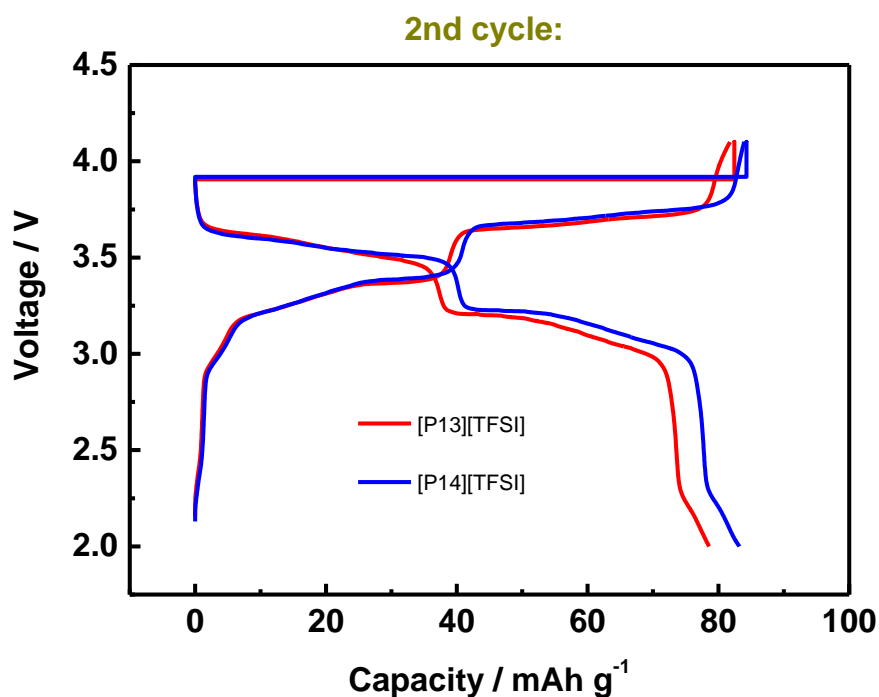
Figure 6-18: 2nd cycle of the charge-discharge capacity of both electrolytes containing 0.25 mol·dm-3 NaFSI dissolved in (red) [Pyrr$_{13}$][TFSI] and (blue) [Pyrr$_{14}$][TFSI] ILs tested for Na$_{2/3}$Ni$_{1/3}$Mn$_{2/3}$O$_2$ positive electrodes, at a rate of 13 mA·g^{-1}.

Furthermore, the coulombic efficiency of [Pyrr$_{14}$][TFSI] remains close to 100% during its 15 cycles and the charge/ discharge retention capacity is still remaining around 83 - 84 mAh·g^{-1} from its first cycle to its 15th cycle, as shown in Figure 6-19. This shows that this IL-based electrolyte could be tested in a full battery. Nevertheless, more tests are needed regarding this specific IL before it could be tested in a full battery system. It would also be very interesting to look at the effect of a different anion with [Pyrr$_{14}$] and [Pyrr$_{13}$] cation such as the FSI anion instead of the TFSI anion. The FSI anion is meant to be a promising anion compared to the TFSI anion according to the literature [91].
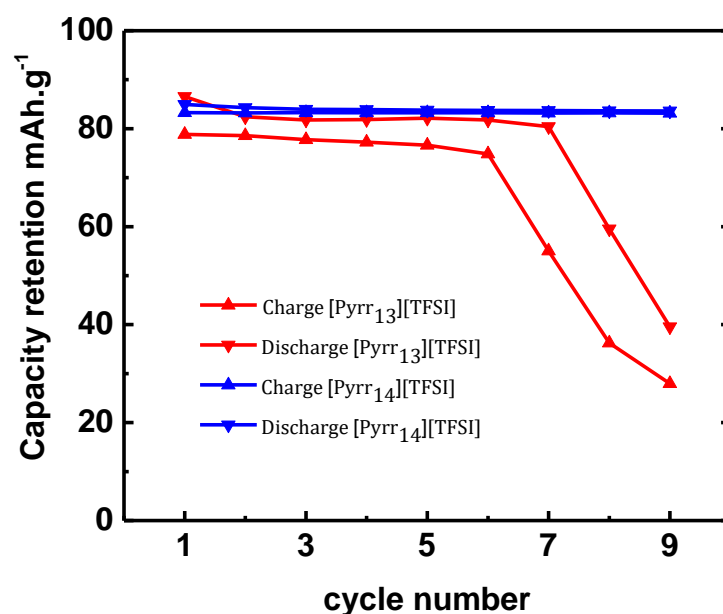
Figure 6-19. Comparison of the capacity retention of 0.25M-NaFSI in [Pyrr$_{13}$][TFSI] electrolyte (red) and 0.25M-NaFSI in [Pyrr$_{14}$][TFSI] electrolyte (blue) showing a good electrochemical behaviour for [Pyrr$_{14}$][TFSI] electrolyte and a severe decrease of the capacity retention in the case of [Pyrr$_{13}$][TFSI] electrolyte.
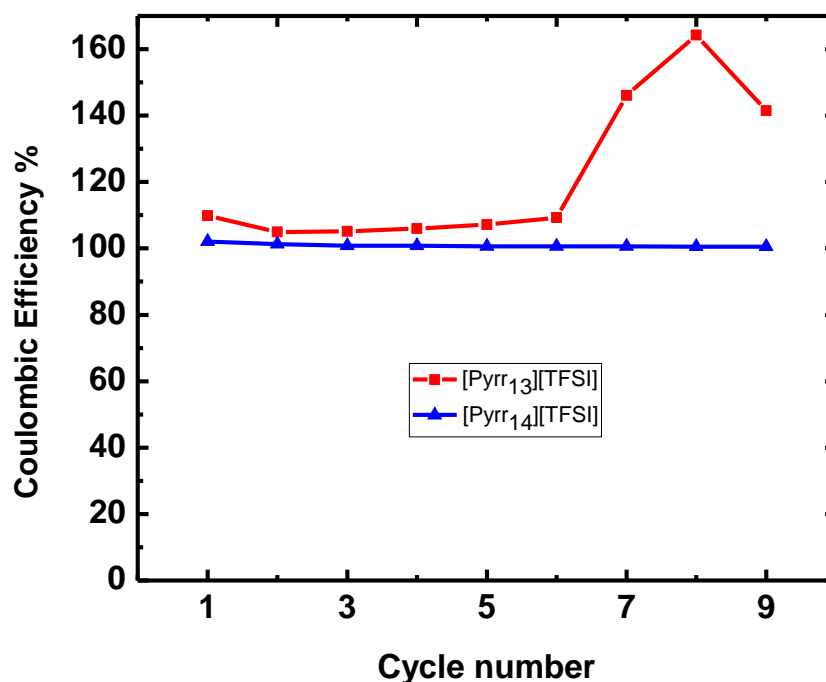
Figure 6-20. Comparison of the coulombic efficiency of 0.25M-NaFSI in [Pyrr$_{13}$][TFSI] (red) and [Pyrr$_{14}$][TFSI] (blue) electrolytes showing an abnormal electrochemical behaviour in the case of [Pyrr$_{13}$][TFSI] and a good electrochemical behaviour in the case of [Pyrr$_{14}$][TFSI].

6.3.4   Surface analysis of the electrodes before and after cycling

The decomposition of the electrolyte solution at the negative electrode appears to be a severe problem in order to realise long cycle life for battery applications. The choice of the electrolyte has a significant impact on the electrochemical behaviour as well as on the formation of the surface passivation layers of the negative electrode. In fact, during the first sodium insertion in the first cycle, it is known that the passivation layer (so-called SEI, solid electrolyte interphase) is formed due to the decomposition of the electrolyte. Therefore, in order to study the different electrode performances depending on the electrolytes, we investigated the electrode surface before and after cycling tests using XPS analysis.[221]

The XPS measurements reveal the characteristics of the surface layers for the HC pristine electrode and surface layer of the same electrode after 2 cycles. In this way, it is possible to gain deeper understanding about the SEI. In this work, only the three ionic liquids-based electrolytes that have shown good electrochemical performances were investigated during the SEI formation after the second cycles.

Table 6-11. Discharge capacity at the 2nd cycle of the three IL-based electrolytes tested for HC electrode analysis via XPS.

Ionic liquids-based electrolyte	Discharge capacity mAh.g^{-1} at the 2nd cycle
[Pyrr$_{13}$][TFSI] + 0.25M-NaFSI	134
0.5 [Pyrr$_{14}$][TFSI] +0.5 PC + 0.3M-NaFSI	121
0.5 [Pip$_{14}$][TFSI] + 0.5PC + 0.3M-NaFSI	130

The XPS spectra analyses were performed for sodium, fluoride, oxygen, nitrogen, carbon and sulphur. In this work, we only show the relevant atoms which are fluoride, carbon, nitrogen and sulphur. The XPS data are shown in Table 6-12, which summarises the XPS data by showing the change in the electrode before and after cycling in the case of three distinct IL-based electrolytes, and are described below. The pristine is showing the surface layer of a hard carbon electrode sample, analysed before it was in contact with any electrolytes and before it was measured for its electrochemical performance.
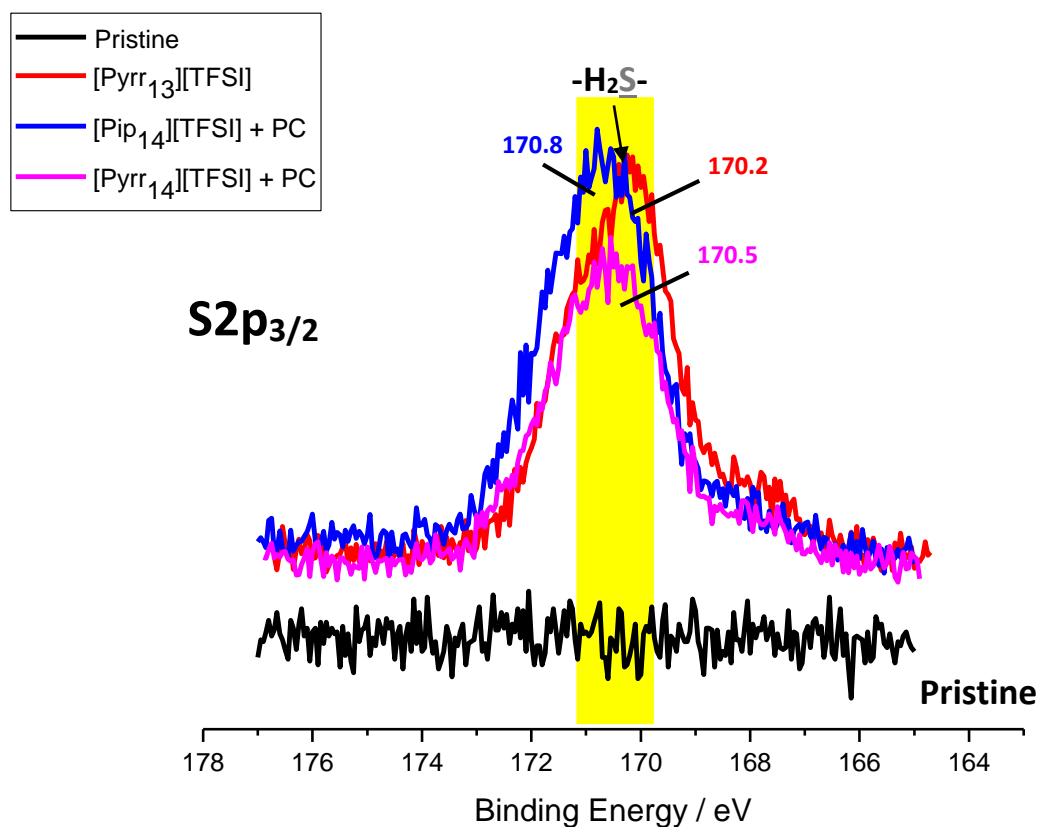
Figure 6-21. XPS spectra of the Sulfonium atoms for the hard-carbon negative electrode rested in sodium-ion half coin cell in IL-based-NaFSI solution: 1) before cycling: pristine (black line), and 2) after cycling tested with three different IL-based electrolytes: [Pyrr13][TFSI] (red line), [Pip14][TFSI]+PC (blue line), [Pyrr14][TFSI]+PC (pink line) showing the SEI-type formation depending on the electrolyte used.
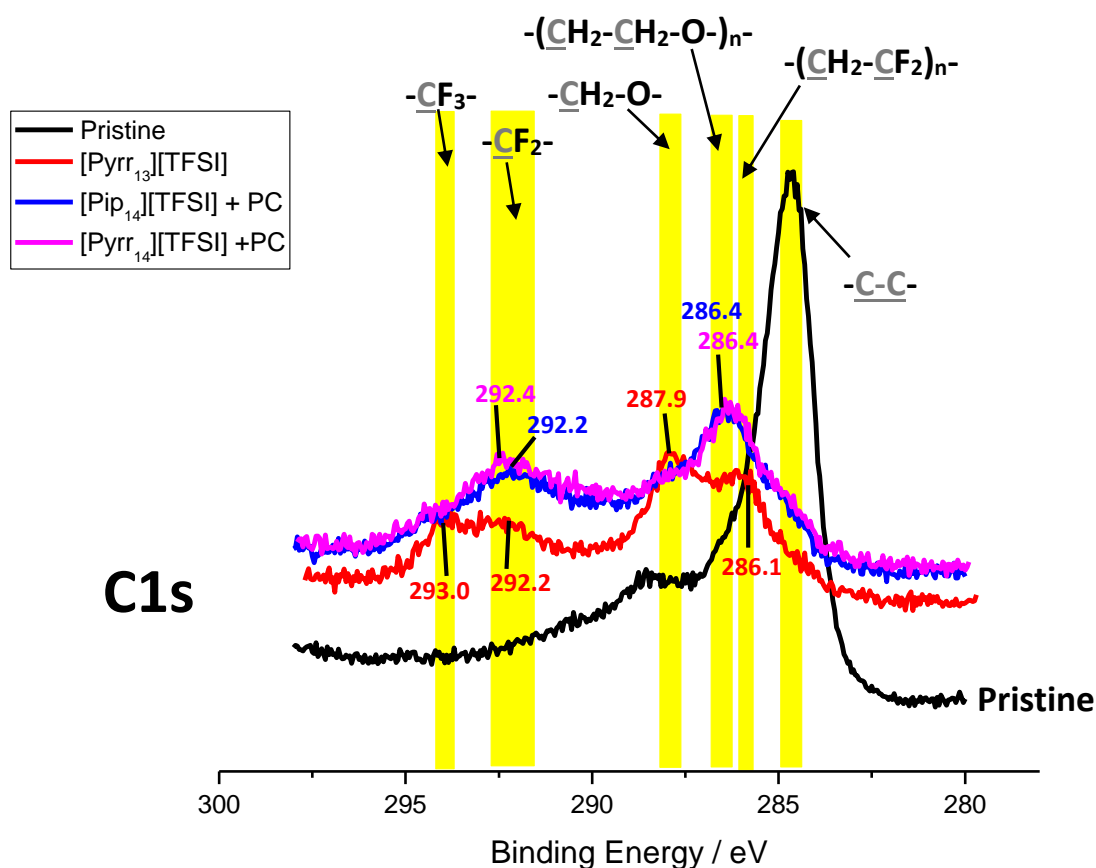
Figure 6-22. XPS spectra of the Carbon atoms for the hard-carbon negative electrode rested in sodium-ion half coin cell in IL-based-NaFSI solution: 1) before cycling: pristine (black line), and 2) after cycling tested with three different IL-based electrolytes: [Pyrr13][TFSI] (red line), [Pip14][TFSI]+PC (blue line), [Pyrr14][TFSI]+PC (pink line) showing the SEI-type formation depending on the electrolyte used.
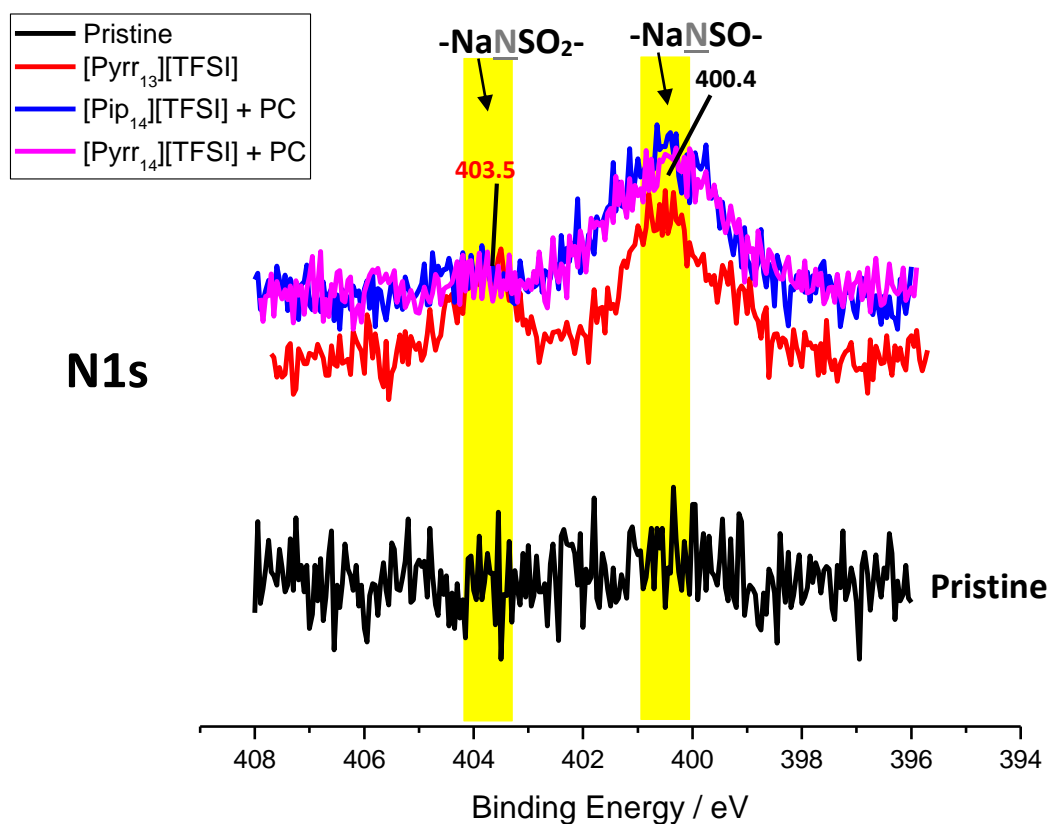
Figure 6-23. XPS spectra of the Nitrogen atoms for the hard-carbon negative electrode rested in sodium-ion half coin cell in IL-based-NaFSI solution: 1) before cycling: pristine (black line), and 2) after cycling tested with three different IL-based electrolytes: [Pyrr13][TFSI] (red line), [Pip14][TFSI]+PC (blue line), [Pyrr14][TFSI]+PC (pink line) showing the SEI-type formation depending on the electrolyte used.
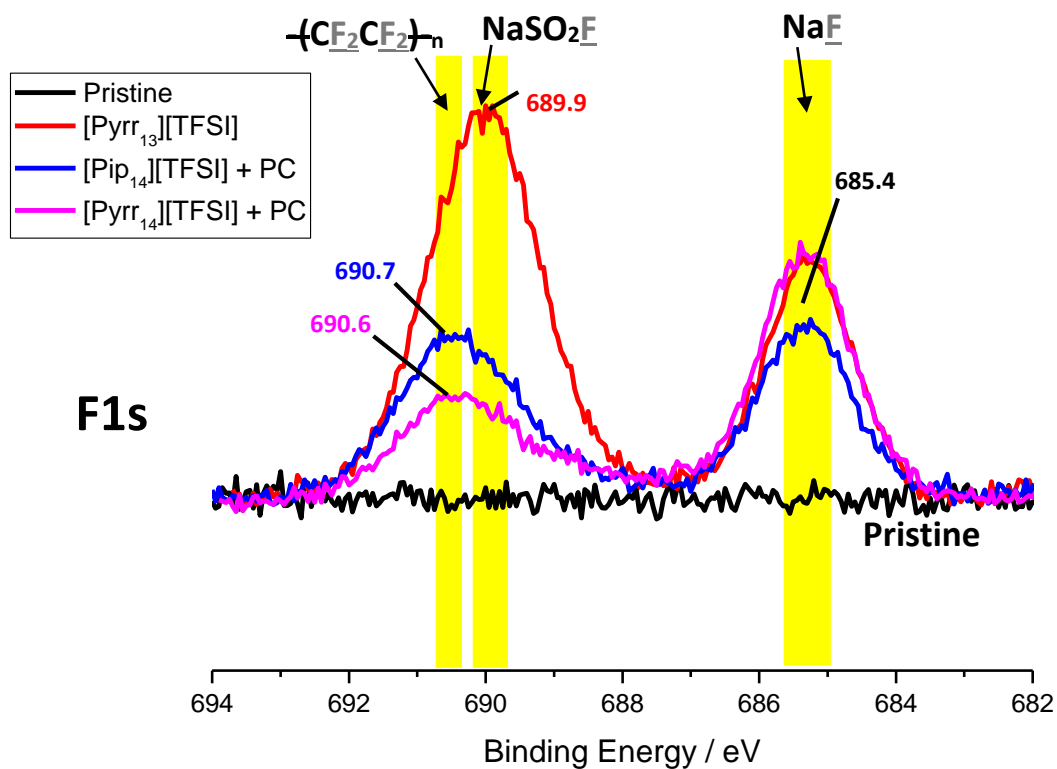
Figure 6-24. XPS spectra of the Fluoride atoms for the hard-carbon negative electrode rested in sodium-ion half coin cell in IL-based-NaFSI solution: 1) before cycling: pristine (black line), and 2) after cycling tested with three different IL-based electrolytes: [Pyrr13][TFSI] (red line), [Pip14][TFSI]+PC (blue line), [Pyrr14][TFSI]+PC (pink line) showing the SEI-type formation depending on the electrolyte used.

Table 6-12. Surface layer analysis of the hard carbon electrode via XPS; 1) before cycling: pristine (black line), and 2) after cycling tested with three different IL-based electrolytes: [Pyrr$_{13}$][TFSI] (red line), [Pip$_{14}$][TFSI]+PC (blue line), [Pyrr$_{14}$][TFSI]+PC (pink line) showing the SEI-type formation depending on the electrolyte used.

Surface layer of electrodes XPS analysis	1-Pristine (Black line)	2-[Pyrr$_{13}$][TFSI] (Red line)	2- [Pip$_{14}$][TFSI] + PC (Blue line)	2-[Pyrr$_{14}$][TFSI] + PC (Pink line)
Sulfonium: S$_2$p$_{3/2}$	none	H$_2$S	H$_2$S	H$_2$S
Carbon: C1s	-C-C-, CH$_2$O- -CH$_2$-	**-CF$_3$-,** -CF$_2$-, **-CH$_2$-O-, -(CH$_2$-CF$_2$)$_n$-**	-CF$_2$-, -(CH$_2$-CH$_2$-O)$_n$-	-CF$_2$-, -(CH$_2$-CH$_2$-O)$_n$-
Nitrogen: N1s	none	**NaNSO$_2$,** NaNSO	NaNSO	NaNSO
Fluoride: F1s	none	**NaSO$_2$F**, NaF	(CF$_2$-CF$_2$)$_n$, NaF	(CF$_2$-CF$_2$)$_n$, NaF

From Table 6-12 it is clear that an SEI has been formed after cycling. Indeed, the surface analysis of the pristine is only showing the hard carbon when it comes to the carbon atoms analysis and is showing no signal for the other atom analysis. However, there are no signals showing the presence of hard carbon on the electrode after cycling (2). This shows that all the surface layers of the HC electrodes after cycling are covered by a new SEI.

The SEI is showing the same type of signal for the electrodes that has been found using the IL/PC mixture electrolytes, whereas it is showing new signals in the case of the SEI formed on the electrodes without the PC. This shows, that the addition of PC to the IL will change the nature of the SEI. The presence of the PC decomposition is found in the carbon analysis -(CH$_2$-CH$_2$-O)$_n$-.

After cycling, we can clearly see the decomposition of the TFSI anion from the IL or from the FSI anion from the salt (it is not possible at this stage to distinguish from which one is coming from the decomposition). In the carbon analysis, the presence of -CF$_3$-, -CF$_2$-, and -(CH$_2$-CF$_2$)$_n$- is clearly showing the decomposition of the fluoride, which seems to have attached to the hard carbon of the electrode. Also, the formation of H$_2$S revealed by the sulphur analysis, contributes to support the decomposition of TFSI or the FSI anion. The decomposition is

certainly coming from the NaFSI salt due to the process of charge/discharge, which is driven by the intercalation/de-intercalation of the sodium atoms of the salt. The sodium salt intercalation is found in the fluoride analysis, which has been identified as two distinct forms: NaF (found within the three electrolytes) and $NaSO_2F$ in case of the electrolytes without PC, but also in the nitrogen analysis as $NaNSO_2$ and NaNSO. These two forms demonstrate the decomposition of the FSI salt, since on one side Na^+ is linked to the Fluoride directly, which means there is a decomposition of the FSI anion and in the other part Na^+ is linked to the nitrogen atoms. Therefore, in the SEI we can clearly see the sodium intercalation linked to the hard carbon of the electrodes under two distinct forms that show NaFSI salt decomposition (NaF) and non-decomposition ($NaNSO_2$).

The presence of $-CF_3-$ is only found in case of the electrolyte in the absence of PC. The electrolyte without PC shows then decomposition of both, IL anion and salt anion. Also, there are more different types of molecules formed on the SEI in case of the electrolyte without PC. This could explain why its electrochemical performance is less efficient than in the case of the electrolytes containing PC.

However, the SEI doesn't show any cation decomposition, therefore it seems that SEI in all the cases is formed depending on the anion salt used, which is in accordance with the known sodium intercalation/de-intercalation process, which is driving the salt forward and back. Therefore, this study has revealed the importance of SEI formation, which depends on the nature of the electrolyte used.

6.4 Conclusions and future work

The aim of this study was to investigate ILs as safer electrolytes and to evaluate the suitability of binary mixtures without the use of common organic carbonate solvents for sodium-ion batteries. However, binary mixtures with a water content below 60 ppm were found to be difficult to obtain due to the presence of ILs, which are known for issues removing their water content completely. Therefore, ternary mixtures were investigated in order to test new IL-cationic electrolytes, that couldn't be tested in binary mixture due to their water contents. In fact, the presence of PC, a well-known organic carbonate solvent, was used to decrease the water content in the final electrolyte solution where a 1:1 mass ratio of IL and PC were used and tested.

Nevertheless, ternary mixtures resulted in higher capacity retention than binary mixtures and also longer cycle life, since no decomposition was found after 35 cycles in most of the electrolyte solutions. This is probably due to the viscosity that remains lower in the ternary mixtures than in the binary mixtures due to the addition of PC, which has a viscosity at least twice as low as the pure ILs of only 25.0 mPa. It could also be due to the highest salt concentration dissolved in the ternary mixture (0.3 M vs 0.25 M). In fact, the electrochemical performance of the Na-cell should improve by the increase of Na^+ in the electrolyte.

Finally, ternary mixtures are cheaper to make than binary mixtures, since only half of their solutions contains ILs. ILs are known to be relatively expensive compounds to synthesise due to purification issues. However, binary mixtures will still be a safer alternative to ternary mixture due to the absence of organic carbonate solvents, which are flammable and volatile. In this sense, further investigations should be undertaken to find the best IL-based electrolyte for Na-cells. For instance, the anionic part should be investigated with the same cation to find trends for the use of a certain anion in combination with a certain cation.

New functional groups could also be tested using pyrrolidinium, piperidinium and sulfonium cations in order to design the best IL-based electrolytes for Na-cells. Those results have already shown promising results that could definitely

lead to a future generation of electrolytes for Na-cells leading to a better design of the IL.

The graph below summarises the ionic liquid cation trend as electrolyte for hard-carbon negative electrodes tested in the sodium-ion half coin cell. All the anions are TFSI anions, the bis[(trifluoromethyl)sulphonyl]imide.

In this graph, we can see the influence of the functional group on the pyrrolidinium cation where it shows better capacity retention for the 1-Butyl-1-methylpyrrolidinium cation, [Pyrr$_{14}$], than for the [Pyrr$_{13}$] and the [Pyrr$_{1(201)}$]. In the second part we can see the influence of the addition of PC on the IL electrolyte, which shows better capacity retention for the piperidinium cation, [Pip$_{14}$], than for the [Pyrr$_{14}$] cation and the sulfonium cation, [S$_{114}$]. In addition, this shows that a larger ring size (n = 5) shows better capacity retention than a smaller ring size (n = 4).

Finally, it was also possible to compare the effects of the addition of PC to the IL-electrolyte. However, there is not much difference in terms of capacity retention in the case of [Pyrr$_{14}$] with or without PC, although the results are slightly higher with the addition of PC into the IL electrolyte.

Capacity retention (mAh·g⁻¹) vs IL cations fonctional group

Legend: [Pyrr1(201)] [Pyrr13] [Pyrr14] [Pyrr14]' (n=4) + PC [Pip14] (n=5) + PC [S114] + PC
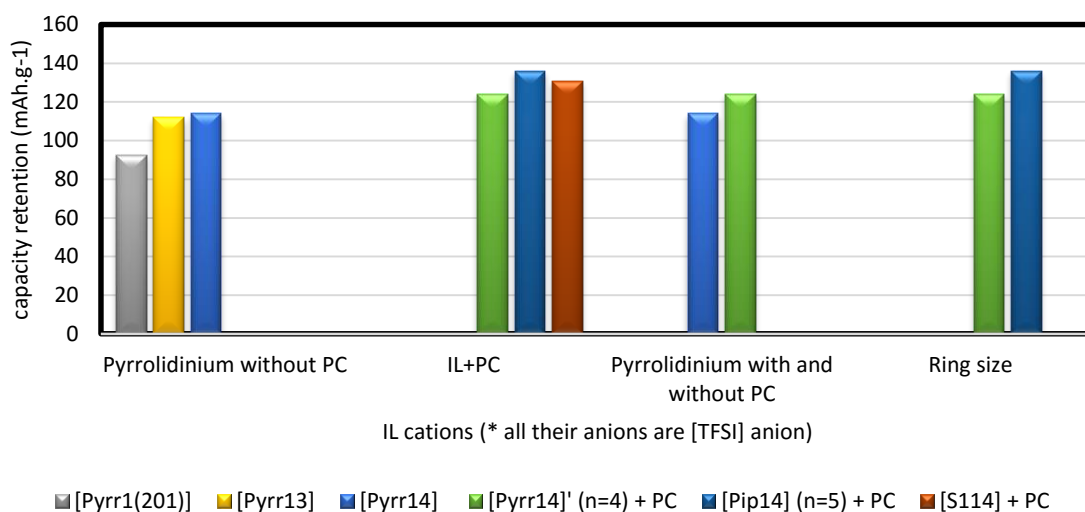
Figure 6-25. Graph summarizing the IL cation tendency vs the discharge capacity performed in Sodium-ion coin cell for hard carbon negative electrode with NaFSI salt. The first group is showing the impact of a functional group on the pyrrolidinium cation, the second group is showing the effect of PC on three different cations, the third group is showing the effect of PC on the pyrrolidinium group, and then the last group is showing the impact of the cation ring size for n=4 and n=5.

Besides, high polarization due to IL-based electrolytes is still an issue for Na-cells in this part, as it was explained for the first group of electrolyte. Here, the starting potential of each discharge was found to be 71, 83, and 85 mV in [S$_{114}$][TFSI], [Pip$_{14}$][TFSI] and [Pyrr$_{14}$][TFSI], respectively. Those results were found to be higher than for the first group of electrolytes in [Pyrr$_{13}$][TFSI] and [Pyrr$_{14}$][TFSI], which could lead to the conclusion that those two cations seem more suitable for the Na cell than [S$_{114}$][TFSI] and [Pip$_{14}$][TFSI].

6.5 Experimental part

6.5.1 IL-based electrolytes synthesis

ILs were all synthesised, characterised, and sealed within an argon-glovebox and sent to TUS by airmail where they were stored in a glovebox filled with argon. Electrolytes were then prepared in the same argon-glovebox by adding either 0.3 mol/L^{-1} of NaFSI salt into an IL/PC mixture (1:1 mass ratio) or 0.25 mol/L^{-1} of NaFSI salt into pure ionic liquids. The molecular weight taken for NaFSI salt was 203.3 g/mol. The synthesis of the ILs as well as their characterization using NMR-spectroscopy were carried out by Sinead Murphy, a PhD candidate from QUB, and won't therefore be included in this work.

Table 6-13. Experimental data for the first group of electrolyte solutions: 0.3 mol·L^{-1} NaFSI salt in IL with PC mixture (1:1 mass ratio) (1st batches).

Electrolytes name (1st Batches)	M_{IL} (g/mol)	IL (g)	PC (g)	NaFSI salt (mg)	[NaFSI] (mol·L^{-1})	Error
[Azp$_{14}$][TFSI]	450.89	0.8154	0.1846	60.99	0.3	0.001
[Pip$_{14}$][TFSI]	436.86	0.8106	0.1894	60.99	0.3	0.001
[Pyrr$_{14}$][TFSI]	422.83	0.8055	0.8055	60.99	0.3	0.001
[S$_{11(201)}$)] [TFSI]	401.37	0.7972	0.7972	60.99	0.3	0.001
[S$_{114}$][TFSI]	399.4	0.7964	0.7964	60.99	0.3	0.001

Table 6-14. Experimental data for the first group of electrolyte solutions: 0.3 mol·L^{-1} NaFSI salt in IL with PC mixture (1:1 mass ratio) (2nd batches) and the PC 1 mol·L^{-1}-NaFSI reference electrolytes.

Electrolytes name (2nd Batches)	M_{IL} (g/mol)	IL (g)	PC (g)	NaFSI salt (mg)	[NaFSI] (mol·L^{-1})	Error
[Pip$_{14}$][TFSI]	436.86	0.992	0.9938	122.88	0.3	0.019
[Pyrr$_{14}$][TFSI]	422.83	0.995	0.99063	125	0.3	0.036
[S$_{11(201)}$)] [TFSI]	401.37	0.74763	0.74886	60.65	0.3	0.002
[S$_{114}$][TFSI]	399.4	0.994	0.993	122	0.3	0.012
PC reference	/	/	2	406.6	1	0.005

Table 6-15. Experimental data for the second group of electrolyte solutions: 0.25 mol·L^{-1} NaFSI salt in IL.

Electrolytes name (3rd Batches)	M_{IL} (g/mol)	IL (mL)	NaFSI salt (mg)	[NaFSI] (mol·L^{-1})	Error
[Pyrr$_{1(201)}$][TFSI]	424.40	4	200	0.25	0.011
[Pyrr$_{14}$][TFSI]	422.83	4	200	0.25	0.011
[Pyrr$_{13}$][TFSI]	408.38	4	200	0.25	0.011

6.5.2 Electrode synthesis

6.5.2.1 Synthesis of hard carbon (HC) from sucrose

Hard carbon was prepared by a two-step process from sucrose source material. Sucrose was dehydrated at 180℃ in air, after precursors derived from sucrose were prepared in a horizontal tube furnace with a heating rate of 5°C·min^{-1} and held at a carbonisation/pyrolysis temperature by controlling the temperature at 1300°C for 1 hour under argon atmosphere.

To finish, the product consisting of black tiny crystals of pure hard-carbon was crushed for about 40 min until it becomes a very fine black powder with no shiny parts anymore.
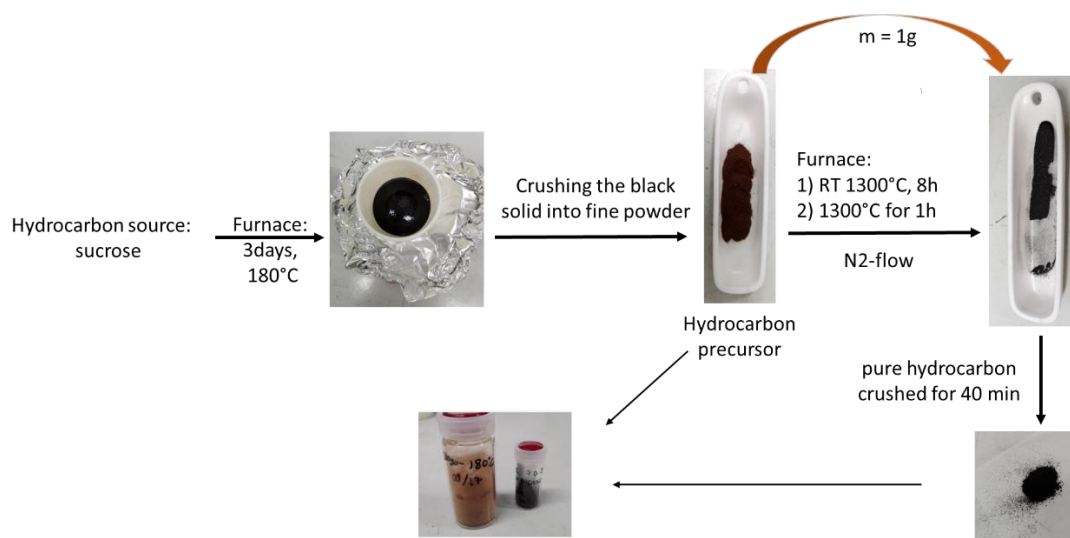
Figure 6-26. Schematic representation of the synthesis of HC from sucrose.

6.5.2.2 HC/PaNA-binder (95:5 mass ratio) negative electrode synthesis

Aluminium foil was cut and cleaned with ethanol and then dried in an oven at 70 °C while HC/PANa-binder mixtures were prepared. A total of 0.1 g of mixture including 0.095 g of HC synthesized from sucrose and 0.005 g of PANa-binder were prepared for each preparation allowing to make about 7 electrodes. Before adding water to the mixture, the previous copper foil was left flat on a clean glass support, ready to collect the future electrode mixture. In a bowl grinder, 50 μL of water was added for three consecutive times to 0.005 g of PANa-binder.

It has to be ensured that no solid state of the binder left. The mixture should only look homogenous and elastic. Then, 0.095 g of HC were synthesized from sucrose and then added to the PANa mixture, and 50 μL of water were added two times to this mixture (during the process of adding water, the mixture was concentrated with a small spatula to the middle of the grinder each time before adding a new batch of 0.05 mL of water to make sure there was no more solid state in the mixture).

The mixture is ready when moved aside; it is taking a few second to come back to its initial position. The mixture is then assembled into a straight line on the clean alumina foil and processed along the foil into a homogeneous layer. The batch of

electrode is then dried to 70°C in an oven for about 30 min and then dried under high vacuum at 150°C covered by a drilled aluminium foil to avoid contamination by other materials.

6.5.3 Coin cells materials and assembly

6.5.3.1 Coin cells materials

The half cells for electrochemical measurements were conducted by using 2032-type coin-cells, in which synthesised hard carbon as the negative electrode was investigated in combination with sodium metal (Kanto Chemical, Co., Ltd.), and with the ionic liquid electrolytes that have been synthesised at Queen's University Belfast in UK. A glass fibre separator (ADVATEC®) was used to separate both electrodes.
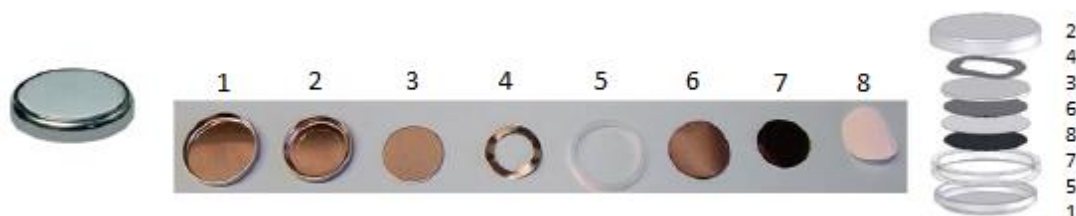
Figure 6-27. Half coin cell materials assembly from bottom to top: Bottom casing (1), gasket (5), hard carbon negative electrode (7), glass fibre separator (8), Sodium-metal electrode (6), stainless steel spacer (3), spring (4) and top casing (2).

6.5.3.2 Coin cell preparations

Each metallic parts of the battery were cleaned with acetone, whereas the plastic parts were cleaned with ethanol, and these were both sonicated in a beaker full of solvent for 15 minutes. Both parts were then dried under a fumehood for 24 hours and then placed into an oven at 70 °C for 24 hours.

6.5.3.3 Coin cells assembling

First of all, the top casing (2) and the spring (4) were assembled together by using an electric current of 2.5-3 V. Then, the hard carbon (HC) negative electrode supported by copper foil was weighed out in order to calculate the exact weight of the pure HC on the electrode. Then, the rest of the coin cells were assembled as follows in a glovebox filled with argon, since sodium-metal cannot be manipulated in a wet environment.

The HC negative electrode (7) was placed in the middle of the bottom casing (1), the copper foil facing the bottom casing to allow electrons from the solution to

flow through the bottom to top casing. 50 μL of ionic liquid-based electrolyte were placed at the top of the HC negative electrode and left 5 minutes under high vacuum at -50 PA in the vacuum chamber of the glovebox. Then, the glass fibre separator (previously dried under vacuum at 70 °C) was placed on top of the HC negative electrode soaked with IL electrolytes using plastic tweezers (on had to make sure the electrode does not move from the centre of the coin cell and doesn't touch the external border of the bottom casing, otherwise a short-circuit could occur after the parts assembly). The gasket was then superposed to the bottom casing, holding the separator in the right place. Another 200 μL of IL-based electrolyte was then added on top of the separator.

While the electrolyte was being soaked by the separator, Na-metal was cut by using metallic tweezers to manipulate the Na-metal. It was checked that the sodium electrode was shiny, very thin and all flat. The sodium metal electrode was then placed in the centre of the top of the separator soaked with the IL-based electrolyte (ensured that it is on top of the HC negative electrode, where again no electrodes should be touching the external casings).

In order to facilitate this process, the bottom coin cell was hold by plastic tweezers while the Na-metal was added using metallic tweezers. Finally, the two assembled sprinsg and top casings were added, and the half-cell was sealed within the glovebox using a crumping machine for coin cells. The half-cell was then cleaned using DMC as a solvent to remove any excess of electrolytes.

6.5.4 Galvanostatic charge/discharge cycling tests

Galvanostatic charge/discharge cycling tests were carried out in Na half cells that were assembled with sodium metal as the reference electrode and a sucrose hard-carbon negative electrode or $Na_{2/3}Ni_{1/3}Mn_{2/3}O_2$ positive electrode as working electrode using a battery cycler (TOSCAT-2100, Toyo System Co., Ltd.).

The hard-carbon material that was used as the negative electrode was cycled at room temperature with six IL-based electrolytes and each coin-cell was tested for galvanostatic charge-discharge at 12.5 mA·g^{-1} between 0.0 and 2.0 V vs. Na$^+$/Na.

$Na_{2/3}Ni_{1/3}Mn_{2/3}O_2$ material as the positive electrode was cycled at room temperature with three IL-based electrolytes and each coin-cell was tested for galvanostatic charge-discharge at 12.5 mA·g^{-1} between 2.0 and 4.1 V vs. Na^+/Na.

6.5.5 XPS-Surface analysis of the electrodes

Each coin cell was open in the Argon-glovebox, where each electrode was carefully isolated and washed for 2 seconds with the DCM solvent. The electrodes were then dried for a few minutes inside of the glovebox and then the sample was left to dry for 4-5 hours under high vacuum without exposing it to the air. Surface analysis was carried out using the soft X-ray photoelectron spectrometer (SOXPES) (JEOL, Model JPS-9010MC).

Chapter 7 _ Conclusions

The main part of this work was to investigate a connection between the IL-anion-variations in the IL solutions of 1-ethyl-2-methylimidazolium alkyl-carboxylates, [C$_2$MIm][C$_n$H$_n$CO$_2$], in binary mixtures with water. In fact, alkyl carboxylates are known compounds to have surfactant behaviour. Although it was not possible to attribute all their properties to their surfactant behaviour, however it was possible to see very strong aggregation behaviour while increasing the alkyl chain length of the carboxylate IL-anion using the [C$_2$MIm][CH$_3$CO$_2$], [C$_2$MIm][C$_3$H$_7$CO$_2$] and [C$_2$MIm][C$_7$H$_{15}$CO$_2$]-ILs. The very strong aggregation behavior in the [C$_2$MIm][C$_7$H$_{15}$CO$_2$] mixed with water was actually visible experimentally.

The aggregation behaviour of the [C$_2$MIm][C$_n$H$_n$CO$_2$]-ILs were thus investigated in their neat structure as well as in binary mixtures with water using a wide range of techniques. The macroscopic properties of those ILs have shown an increase of their hydrogen bonding networks in the presence of water due to a volume contraction while mixing the two compounds; as well as good transport properties. It was also possible to calculate the number of ion-pairs left in solution after dilution with water using the Walden rule. However, when increasing the water concentration, [C$_2$MIm][C$_3$H$_7$CO$_2$] has shown neutral behaviour with regards to its ionicity; whereas [C$_2$MIm][CH$_3$CO$_2$], and [C$_2$MIm][C$_7$H$_{15}$CO$_2$]-ILs have shown a very high ionicity behaviour with only a few ion-pairs left in solution at high dilution.

Those results were supported using NMR-spectroscopy by studying the chemical shifts of the pure ILs in binary mixtures with water. Indeed, for the three ILs, the imidazolium ring proton and carbon atoms were disturbed in the same way by the addition of water and were therefore not dependant on the anion's carboxylate chain lengths. In addition, at high dilution (5 mol% of IL), the three ILs have shown a full dissociation of both cation and anion due to a loss of their initial hydrogen bond network.

Furthermore, a SAXS study was performed on the mixtures in order to lead to more accurate information regarding the intra- and inter-molecular interactions within the pure ILs and the binary mixtures. An increase in water concentration was manifested by a decrease of the intra-molecular interactions between the cation and the anion that is supported by the NMR-spectroscopy study and the ionicity data, that have shown an almost full dissociation of the ions in solution. Furthermore, $[C_2MIm][C_7H_{15}CO_2]$ was the only IL exhibiting a significant organisation, where very defined peaks were observed specific to the inter-molecular interactions. This can be explained by the Van der Waals forces which are essential for well-organised solutions, and which are significantly more present in $[C_2MIm][C_7H_{15}CO_2]$ than in the two other ILs due to the long alkyl-chain. All those results have therefore confirmed the aggregation behaviour of the octanoate-anion in its pure state as well as in mixtures with water. Some future work could be done to investigate the surfactant effect by using surface tension for instance. Also, dynamic light scattering (DLS) was tried, but did not give conclusive results due to the wide structure of both cation and anion which completely disturbed the results.

In this study, IL/water binary mixtures were used to explore the properties characteristic to $[C_2MIm][C_nH_nCO_2]$-ILs for further applications such as nanoparticle formation (cf. Chapter 5). In fact, the basic anions are known to act as a base and stabilising agent, allowing the preparation of stable NPs dispersions in ILs (so-called nanofluids). Copper oxide nanoparticles (CuO-NPs) were then synthesised *in-situ* in an $[C_2MIm][C_nH_nCO_2]$-IL, using its respective copper(II) carboxylate. Further heating to 120°C has shown the colour of the solution changing from blue to red, which was due to a change of the copper salt coordination and nano-particle formation. These changes upon temperature changes were firstly observed by crystallography and UV-VIS spectroscopy. The particle sizes and characterisation were then preformed using TEM, SAXS and XPS analysis.

The results have shown that the use of different anion chain lengths definitely has led to a different range of particle sizes. For instance, the copper(II) acetate precursor results in the formation of CuO(I,II) clusters or CuO-NPs in the ranges

of [1-15] nm depending on its imidazolium-based cation used. However, very small CuO-NPs in the range of [10 - 25] nm were formed using copper(II) octanoate precursor; whereas it has been shown that larger CuO-NPs in the case of copper(II) butanoate precursor in the ranges of [10-61] nm were obtained. The very small particles obtained from the copper(II) octanoate precursor are probably related to the high viscosity found in $[C_2MIm][C_7H_{15}CO_2]$-IL, which is much higher than for the two other ones, which leads to slower mass transport in the IL.

A very interesting fact with regards to the effect of water studied previously on the binary mixtures, is that the CuO particle sizes were showing a non-dependency on the water concentration. However, it was not possible to add more than 0.65 IL mole fraction without getting a precipitate instead of the NPs. However, an increase of water concentration, as well as transforming the copper salt solution into a nanofluid solution has been shown to increase the physical properties such as conductivity and viscosity. Furthermore, from all the data found on the $[C_2MIm][C_nH_nCO_2]$-ILs in binary mixtures with water and in ternary mixtures with copper salt or as a nanofluid solution, it was possible to draw a mechanism of the CuO-NPs formation in the case of the three ILs, especially for $[C_2MIm][C_7H_{15}CO_2]$ in which better NPs size and better aggregation behaviour was found.

In the future, it would be very interesting to use different types of imidazolium-based cations as well as different anion-ILs. In addition, new metal salts should be tested in order to look at the metal influence of the NPs morphology. However, those nanofluids have not been tested in applied chemistry and therefore need to be further investigated. Those nanofluids as well as novel nanofluids using the same cheap and straightforward synthetic routes that could be used for applications such as catalysts, heat transfer fluids or electrolytes for solar cell.

Furthermore, since the effect of the anion-IL with imidazolium-based cations was studied with regards to their binary mixtures with water and with regards to the CuO-NPs formation, it was also interesting to evaluate the impact of the cation-variation for a different type of application. In fact, the use of ILs and solvent binary mixtures is under investigation, since it improves some of the physical

properties of the IL. However, those ILs have shown a very hygroscopic behaviour and can therefore not being use in all types of application such as electrolytes for metal-ion batteries.

By receiving a JSPS-fellowship, this has allowed me to test some of my materials in Tokyo for three months, in order to investigate ILs as safer electrolytes and to evaluate the suitability of binary mixtures without the use of common organic carbonate solvents for sodium-ion batteries. Therefore, a new range of ILs was tested, based on the bis[(trifluoromethyl)sulphonyl]imide anion (TFSI$^-$) using pyrrolidinium, piperidinium, azepanium, and sulfonium cations as pure and in binary mixture with propylene carbonate (PC) solvent. The electrochemical performance of those IL-based electrolytes mixed with sodium bis(fluorosulfonyl)imide (NaFSI) salt in half Na-ion coin cells were investigated using cyclability, coulombic efficiency and capacity retention in order to define a trend in the change of the IL-cation for Na-ion battery electrolytes.

In conclusion, ternary mixtures with PC had shown higher capacity than binary mixtures as well as longer cycle life due to lowest viscosity found with the addition of PC, and larger ring size cations have shown greater capacity. For future work, it would be very interesting to test new IL-anions based of FSI$^-$ anion and not TFSI. In fact, the FSI$^-$ anion has recently shown better results for metal-ion battery electrolytes.

Furthermore, it would be interesting to test new electrolytes using nanofluids with Aluminia-NPs. In fact, aluminium oxide has been found to be a relevant compound to investigate with regards to conductivity improvement. The synthesis presented in this work could then be tuned in order to find an appropriate IL suitable for NPs as well as electrolytes for metal-ion batteries.

Uncategorized References

(1)   Walden, P. *Bull. Acad. Imper. Sci. (St. Petersburg)* **1914**, *405*.

(2)   Niedermeyer, H.; Hallett, J. P.; Villar-Garcia, I. J.; Hunt, P. A.; Welton, T. Mixtures of ionic liquids. *Chemical Society Reviews* **2012**, *41*, 7780-7802.

(3)   Austen Angell, C.; Ansari, Y.; Zhao, Z. Ionic Liquids: Past, present and future. *Faraday Discuss.* **2012**, *154*, 9-27.

(4)   Seddon, K. R.; Stark, A.; Torres, M.-J. Influence of chloride, water, and organic solvents on the physical properties of ionic liquids. *Pure and Applied Chemistry* **2000**, *72*.

(5)   D.Freudenmann, S. W., M. Wolff, C. Feldmann. *Angew. Chem. Int. Ed* **2011**, *50*.

(6)   J. D. Holbrey, A. E. V., S. K. Spear, W. M. Reichert, R. P. Swatloski, G. A. Broker and   R. D. Roger. Mercury(II) partitioning from aqueous solutions with a new, hydrophobic ethylene-glycol functionalized bis-imidazolium ionic liquid. *Green Chem.* **2003**, *5*.

(7)   M. Abai, M. P. A., A. Hassan, J. D. Holbrey, Y. Kuah, P. Nockemann, A. A. Oliferenko, N. V. Plechkova, S. Rafeen, A. A. Rahman, R. Ramli, S. M. Shariff, K. R. Seddon, G. Srinivasan and Y. Zoub An ionic liquid process for mercury removal from natural gas. *Dalton Trans.* **2015**, *44*.

(8)   S. Werner, M. H., and P. Wasserscheid. Ionic Liquids in Chemical Engineering. *Annual Review of Chemical and Biomolecular Engineering* **2010**, *1*.

(9)   Plechkova, N. V.; Seddon, K. R. Applications of ionic liquids in the chemical industry. *Chem Soc Rev* **2008**, *37*, 123-150.

(10)   Good Titration Practice™ in Karl Fischer Titration. Mettler Toledo; pp 104.

(11)   BUNSEN, R. W. *Liebigs Ann. Chem. 86* **1853**, *86*.

(12)   Chaban, V. V.; Voroshylova, I. V.; Kalugin, O. N.; Prezhdo, O. V. Acetonitrile boosts conductivity of imidazolium ionic liquids. *J Phys Chem B* **2012**, *116*, 7719-7727.

(13)   Couadou, E.; Jacquemin, J.; Galiano, H.; Hardacre, C.; Anouti, M. A comparative   study   on   the   thermophysical   properties   for   two bis[(trifluoromethyl)sulfonyl]imide-based ionic liquids containing the trimethyl-sulfonium or the trimethyl-ammonium cation in molecular solvents. *J Phys Chem B* **2013**, *117*, 1389-1402.

(14)   Kalugin, O. N.; Voroshylova, I. V.; Riabchunova, A. V.; Lukinova, E. V.; Chaban, V. V. Conductometric study of binary systems based on ionic liquids and acetonitrile in a wide concentration range. *Electrochimica Acta* **2013**, *105*, 188-199.

(15)   Voroshylova, I. V.; Smaga, S. R.; Lukinova, E. V.; Chaban, V. V.; Kalugin, O. N. Conductivity and association of imidazolium and pyridinium based ionic liquids in methanol. *Journal of Molecular Liquids* **2015**, *203*, 7-15.

(16)   Arellano, I. H. J.; Guarino, J. G.; Paredes, F. U.; Arco, S. D. Thermal stability and moisture uptake of 1-alkyl-3-methylimidazolium bromide. *Journal of Thermal Analysis and Calorimetry* **2010**, *103*, 725-730.

(17)   Cao, Y.; Chen, Y.; Lu, L.; Xue, Z.; Mu, T. Water Sorption in Functionalized Ionic Liquids: Kinetics and Intermolecular Interactions. *Industrial & Engineering Chemistry Research* **2013**, *52*, 2073-2083.

(18)   Cao, Y.; Chen, Y.; Sun, X.; Zhang, Z.; Mu, T. Water sorption in ionic liquids: kinetics, mechanisms and hydrophilicity. *Phys Chem Chem Phys* **2012**, *14*, 12252-12262.

(19)   Cao, Y.; Sun, X.; Chen, Y.; Mu, T. Water Sorption in Amino Acid Ionic Liquids: Kinetic, Mechanism, and Correlations between Hygroscopicity and Solvatochromic Parameters. *ACS Sustainable Chemistry & Engineering* **2014**, *2*, 138-148.

(20)   Francesco, F. D.; Calisi, N.; Creatini, M.; Melai, B.; Salvo, P.; Chiappe, C. Water sorption by anhydrous ionic liquids. *Green Chemistry* **2011**, *13*, 1712.

(21)   L. Cammarata, S. G. K., P. A. Salter and T. Welton. Molecular states of water in room temperature ionic liquids. *Phys. Chem. Chem. Phys.* **2001**, *3*.

(22)   Meriem Anouti, J. J., Aurélien Boisset, Johan Jacquemin, Magaly Caillon-Caravanier, Daniel Lemordant. Aggregation behavior in water of new imidazolium and pyrrolidinium alkycarboxylates protic ionic liquids. *Journal of Colloid and Interface Science* **2009**, *340*.

(23)   Brehm, M.; Weber, H.; Pensado, A. S.; Stark, A.; Kirchner, B. Proton transfer and polarity changes in ionic liquid-water mixtures: a perspective on hydrogen bonds from ab initio molecular dynamics at the example of 1-ethyl-3-methylimidazolium acetate-water mixtures--part 1. *Phys Chem Chem Phys* **2012**, *14*, 5030-5044.

(24)   Cha, S.; Ao, M.; Sung, W.; Moon, B.; Ahlstrom, B.; Johansson, P.; Ouchi, Y.; Kim, D. Structures of ionic liquid-water mixtures investigated by IR and NMR spectroscopy. *Phys Chem Chem Phys* **2014**, *16*, 9591-9601.

(25)   Chen, Y.; Li, S.; Xue, Z.; Hao, M.; Mu, T. Quantifying the hydrogen-bonding interaction between cation and anion of pure [EMIM][Ac] and evidencing the ion pairs existence in its extremely diluted water solution: Via 13C, 1H, 15N and 2D NMR. *Journal of Molecular Structure* **2015**, *1079*, 120-129.

(26)   D. T. Bowron, C. D. A., L. F. Gladden, C. Hardacre, J. D. Holbrey,; M. C. Lagunas, J. M., ‡ M. D. Mantle, C. L. Mullan, and T. G. A. Youngs. Structure and Dynamics of 1-Ethyl-3-methylimidazolium Acetate via Molecular Dynamics

and Neutron Diffraction. *J. Phys. Chem. B* **2010**, *114*.

(27)   Ding, Z.-D.; Chi, Z.; Gu, W.-X.; Gu, S.-M.; Wang, H.-J. Theoretical and experimental investigation of the interactions between [emim]Ac and water molecules. *Journal of Molecular Structure* **2012**, *1015*, 147-155.

(28)   Hall, C. A.; Le, K. A.; Rudaz, C.; Radhi, A.; Lovell, C. S.; Damion, R. A.; Budtova, T.; Ries, M. E. Macroscopic and microscopic study of 1-ethyl-3-methyl-imidazolium acetate-water mixtures. *J Phys Chem B* **2012**, *116*, 12810-12818.

(29)   Martinelli, A.; Marechal, M.; Ostlund, A.; Cambedouzou, J. Insights into the interplay between molecular structure and diffusional motion in 1-alkyl-3-methylimidazolium ionic liquids: a combined PFG NMR and X-ray scattering study. *Phys Chem Chem Phys* **2013**, *15*, 5510-5517.

(30)   Salma, U.; Ballirano, P.; Usula, M.; Caminiti, R.; Plechkova, N. V.; Seddon, K. R.; Gontrani, L. A new insight into the nanostructure of alkylammonium alkanoates based ionic liquids in water. *Phys Chem Chem Phys* **2016**, *18*, 11497-11502.

(31)   C. Hardacre; J. D. Holbrey; M. Nieuwenhuyzen; Youngs, T. G. A. Structure and Solvation in Ionic

Liquids. *Acc. Chem. Res.* **2007**, *40*.

(32)   Vasile I. Parvulescu, a. C. H. Catalysis in Ionic Liquids. *Chem. Rev.* **2007**, *107, No. 6*.

(33)   What is NMR? http://chem.ch.huji.ac.il/nmr/whatisnmr/whatisnmr.html.

(34)   Nuclear Magnetic Resonance Spectroscopy. https://www2.chemistry.msu.edu/faculty/reusch/virttxtjml/spectrpy/nmr/nmr1.htm.

(35)   Hesse-Ertelt, S.; Heinze, T.; Kosan, B.; Schwikal, K.; Meister, F. Solvent Effects on the NMR Chemical Shifts of Imidazolium-Based Ionic Liquids and Cellulose Therein. *Macromolecular Symposia* **2010**, *294*, 75-89.

(36)   Lungwitz, R.; Spange, S. A hydrogen bond accepting (HBA) scale for anions, including room temperature ionic liquids. *New Journal of Chemistry* **2008**, *32*, 392.

(37)   Lungwitz, R.; Spange, S. Determination of hydrogen-bond-accepting and -donating abilities of ionic liquids with halogeno complex anions by means of 1H NMR spectroscopy. *Chemphyschem* **2012**, *13*, 1910-1916.

(38)   Qing-Guo Zhang, N.-N. W., and Zhi-Wu Yu. The Hydrogen Bonding Interactions between the Ionic Liquid 1-Ethyl-3-Methylimidazolium Ethyl Sulfate and Water. *J. Phys. Chem. B* **2010**, *114*.

(39)   Ruiz, E.; Ferro, V. R.; Palomar, J.; Ortega, J.; Rodriguez, J. J. Interactions of ionic liquids and acetone: thermodynamic properties, quantum-chemical calculations, and NMR analysis. *J Phys Chem B* **2013**, *117*, 7388-7398.

(40)   Seddon, J. D. H. a. K. R. The phase behaviour of 1-alkyl-3-methylimidazolium tetrafluoroborates; ionic liquids and ionic liquid crystals. *J. Chem. Soc., Dalton Trans.* **1999**.

(41)   Zhang, Q. G.; Wang, N. N.; Wang, S. L.; Yu, Z. W. Hydrogen bonding behaviors of binary systems containing the ionic liquid 1-butyl-3-methylimidazolium trifluoroacetate and water/methanol. *J Phys Chem B* **2011**, *115*, 11127-11136.

(42)   ROBIN K. HARRIS, EDWIN D. BECKER, SONIA M. CABRAL DE MENEZES, ROBIN GOODFELLOW, AND PIERRE GRANGER. NMR NOMENCLATURE. NUCLEAR SPIN PROPERTIES AND CONVENTIONS FOR CHEMICAL SHIFTS (IUPAC Recommendations 2001). *Pure Appl. Chem.* **2001**, *73*.

(43)   Harris, R. K.; Becker, E. D.; Cabral De Menezes, S. M.; Granger, P.; Hoffman, R. E.; Zilm, K. W.; International Union of, P.; Applied Chemistry, P.; Biophysical Chemistry, D. Further conventions for NMR shielding and chemical shifts IUPAC recommendations 2008. *Solid State Nucl Magn Reson* **2008**, *33*, 41-56.

(44)   Marekha, B. A.; Kalugin, O. N.; Bria, M.; Idrissi, A. Probing structural patterns of ion association and solvation in mixtures of imidazolium ionic liquids with acetonitrile by means of relative (1)H and (13)C NMR chemical shifts. *Phys Chem Chem Phys* **2015**, *17*, 23183-23194.

(45)   Soper, A. K.; March 5, 2012 ed., 2012; pp 155.

(46)   H. Schnablegger, Y. S.: *The SAXS Guide, Getting acquainted with the principles*; 3rd ed.; Anton Paar GmbH: Austria, 2013.

(47)   Sivia, D. S.: *Elementary Scattering Theory for X-rau and Neutron users*; Oxford University Press: St John's College, Oxford, 2010.

(48)   Karimi-Nazarabad, M.; Goharshadi, E. K.; Entezari, M. H.; Nancarrow, P. Rheological properties of the nanofluids of tungsten oxide nanoparticles in ethylene glycol and glycerol. *Microfluidics and Nanofluidics* **2015**, *19*, 1191-1202.

(49)   Li, Y.; Zhou, J. e.; Tung, S.; Schneider, E.; Xi, S. A review on development of nanofluid preparation and characterization. *Powder Technology* **2009**, *196*, 89-101.

(50)   Liu, T.; Qin, C.; Zhu, M.; Cao, Y.; Shen, H.; Li, X. Synthesis and hydrogen storage properties of Mg-La-Al nanoparticles. *Journal of Power Sources* **2012**, *219*, 100-105.

(51)   Huynh, W. U.; Dittmer, J. J.; Alivisatos, A. P. Hybrid nanorod-polymer solar cells. *Science* **2002**, *295*, 2425-2427.

(52)   Shaalan, N. M.; Yamazaki, T.; Kikuta, T. Synthesis of metal and metal oxide nanostructures and their application for gas sensing. *Materials Chemistry and Physics* **2011**, *127*, 143-150.

(53)   Yang, S. G.; Li, T.; Gu, B. X.; Du, Y. W.; Sung, H. Y.; Hung, S. T.; Wong, C. Y.; Pakhomov, A. B. Ferromagnetism in Mn-doped CuO. *Applied Physics Letters* **2003**, *83*, 3746-3748.

(54)   Hsieh, C. T.; Chen, J. M.; Lin, H. H.; Shih, H. C. Field emission from various CuO nanostructures. *Applied Physics Letters* **2003**, *83*, 3383-3385.

(55)   Reitz, J. B.; Solomon, E. I. Propylene oxidation on copper oxide surfaces: Electronic and geometric contributions to reactivity and selectivity. *Journal of the American Chemical Society* **1998**, *120*, 11467-11478.

(56)   MacDonald, A. H. Superconductivity - Copper oxides get charged up. *Nature* **2001**, *414*, 409-410.

(57)   Patzke, G. R.; Zhou, Y.; Kontic, R.; Conrad, F. Oxide Nanomaterials: Synthetic Developments, Mechanistic Studies, and Technological Innovations. *Angewandte Chemie-International Edition* **2011**, *50*, 826-859.

(58)   Chen, F.-L.; Sun, I. W.; Wang, H. P.; Huang, C. H. Nanosize Copper Dispersed Ionic Liquids As an Electrolyte of New Dye-Sensitized Solar Cells. *Journal of Nanomaterials* **2009**.

(59)   M.Niederberger. *Acc. Chem. Res.* **2007**, *40*.

(60)   Ott, L. S.; Cline, M. L.; Deetlefs, M.; Seddon, K. R.; Finke, R. G. Nanoclusters in ionic liquids: Evidence for N-heterocyclic carbene formation from imidazolium-based ionic liquids detected by H-2 NMR. *Journal of the American Chemical Society* **2005**, *127*, 5758-5759.

(61)   Ueno, K.; Inaba, A.; Kondoh, M.; Watanabe, M. Colloidal stability of bare and polymer-grafted silica nanoparticles in ionic liquids. *Langmuir* **2008**, *24*, 5253-5259.

(62)   Wang, Y.; Yang, H. Synthesis of iron oxide nanorods and nanocubes in an imidazolium ionic liquid. *Chem Eng J* **2009**, *147*, 71-78.

(63)   Wang, Y.; Maksimuk, S.; Shen, R.; Yang, H. Synthesis of iron oxide nanoparticles using a freshly-made or recycled imidazolium-based ionic liquid. *Green Chem* **2007**, *9*, 1051-1056.

(64)   Lee, C. M.; Jeong, H. J.; Lim, S. T.; Sohn, M. H.; Kim, D. W. Synthesis of Iron Oxide Nanoparticles with Control over Shape Using Imidazolium-Based Ionic Liquids. *Acs Appl Mater Inter* **2010**, *2*, 756-759.

(65)   Yabuuchi, N.; Kubota, K.; Dahbi, M.; Komaba, S. Research development on sodium-ion batteries. *Chem Rev* **2014**, *114*, 11636-11682.

(66)   Thackeray, M. M.; Wolverton, C.; Isaacs, E. D. Electrical energy storage for transportation—approaching the limits of, and going beyond, lithium-ion batteries. *Energy & Environmental Science* **2012**, *5*, 7854.

(67)   K. Mizushima, P. C. J., P.J. Wiseman, J.B. Goodenough. LixCoO2 (0<x<-1): A new cathode material for batteries of high energy density. *Materials Research Bulletin* **1980**, *15*.

(68)   Wen, J.; Yu, Y.; Chen, C. A Review on Lithium-Ion Batteries Safety Issues: Existing Problems and Possible Solutions. *Materials Express* **2012**, *2*, 197-212.

(69)   Landi, B. J.; Ganter, M. J.; Cress, C. D.; DiLeo, R. A.; Raffaelle, R. P. Carbon nanotubes for lithium ion batteries. *Energy & Environmental Science* **2009**, *2*, 638.

(70)   Kiełczykowska, M.; Musik, I. Lithium and the application of its compounds in different fields of medicine. *Journal of Elemntology* **2012**.

(71)   Sajatovic, M.; Jenkins, J. H.; Cassidy, K. A.; Muzina, D. J. Medication treatment perceptions, concerns and expectations among depressed individuals with Type I Bipolar Disorder. *J Affect Disord* **2009**, *115*, 360-366.

(72)   Young, W. Review of lithium effects on brain and blood. *Cell Transplant* **2009**, *18*, 951-975.

(73)   Ding, C.; Nohira, T.; Hagiwara, R.; Fukunaga, A.; Sakai, S.; Nitta, K. Electrochemical performance of hard carbon negative electrodes for ionic liquid-based sodium ion batteries over a wide temperature range. *Electrochimica Acta* **2015**, *176*, 344-349.

(74)   Ellis, B. L.; Nazar, L. F. Sodium and sodium-ion energy storage batteries. *Current Opinion in Solid State and Materials Science* **2012**, *16*, 168-177.

(75)   Palomares, V.; Serras, P.; Villaluenga, I.; Hueso, K. B.; Carretero-González, J.; Rojo, T. Na-ion batteries, recent advances and present challenges to become low cost energy storage systems. *Energy & Environmental Science* **2012**, *5*, 5884.

(76)   Sawicki, M.; Shaw, L. L. Advances and challenges of sodium ion batteries as post lithium ion batteries. *RSC Adv.* **2015**, *5*, 53129-53154.

(77)	Carmichael, R. S.: *Practical handbook of physical properties of rocks and minerals*, 1990.

(78)	Irisarri, E.; Ponrouch, A.; Palacin, M. R. Review—Hard Carbon Negative Electrode Materials for Sodium-Ion Batteries. *Journal of The Electrochemical Society* **2015**, *162*, A2476-A2482.

(79)	Gotoh, K.; Maeda, M.; Nagai, A.; Goto, A.; Tansho, M.; Hashi, K.; Shimizu, T.; Ishida, H. Properties of a novel hard-carbon optimized to large size Li ion secondary battery studied by 7Li NMR. *Journal of Power Sources* **2006**, *162*, 1322-1328.

(80)	K. Shimizu, M. M., S. Morinishi, A. Nagai, A. Hoshi. Negative electrode material for nonacqueous electrolyte secondary battery of high input/output current, method for producing the same and battery employing negative electrode material

(81)	D. A. Stevens, J. R. D. High Capacity Anode Materials for Rechargeable Sodium-Ion Batteries. *Journal of The Electrochemical Society* **2000**, *147*.

(82)	Wang, Q.; Ping, P.; Zhao, X.; Chu, G.; Sun, J.; Chen, C. Thermal runaway caused fire and explosion of lithium ion battery. *Journal of Power Sources* **2012**, *208*, 210-224.

(83)	F. Orsini, A. D. P., B. Beaudoin, J.M. Tarascon, M. Trentin, N. Langenhuizen , E. De Beer , P. Notten. In situ Scanning Electron Microscopy SEM/ observation of interfaces within plastic lithium batteries. *Journal of Power Sources* **1998**, *76*.

(84)	Galiński, M.; Lewandowski, A.; Stępniak, I. Ionic liquids as electrolytes. *Electrochimica Acta* **2006**, *51*, 5567-5580.

(85)	Wong, D. H.; Thelen, J. L.; Fu, Y.; Devaux, D.; Pandya, A. A.; Battaglia, V. S.; Balsara, N. P.; DeSimone, J. M. Nonflammable perfluoropolyether-based electrolytes for lithium batteries. *Proc Natl Acad Sci U S A* **2014**, *111*, 3327-3331.

(86)	Xu, K. Nonaqueous liquid electrolytes for lithium-based rechargeable batteries, . *Chem. Rev.* **2004**, *104*.

(87)	Yang, P.; Liu, L.; Li, L.; Hou, J.; Xu, Y.; Ren, X.; An, M.; Li, N. Gel polymer electrolyte based on polyvinylidenefluoride-co-hexafluoropropylene and ionic liquid for lithium ion battery. *Electrochimica Acta* **2014**, *115*, 454-460.

(88)	Yin, K.; Zhang, Z.; Yang, L.; Hirano, S.-I. An imidazolium-based polymerized ionic liquid via novel synthetic strategy as polymer electrolytes for lithium ion batteries. *Journal of Power Sources* **2014**, *258*, 150-154.

(89)	Young, W.-S.; Kuan, W.-F.; Epps, T. H. Block copolymer electrolytes for rechargeable lithium batteries. *Journal of Polymer Science Part B: Polymer Physics* **2014**, *52*, 1-16.

(90)	Zhang, S. S. A review on electrolyte additives for lithium-ion batteries. *Journal of Power Sources* **2006**, *162*, 1379-1394.

(91)	Molina Piper, D.; Evans, T.; Leung, K.; Watkins, T.; Olson, J.; Kim, S. C.; Han, S. S.; Bhat, V.; Oh, K. H.; Buttry, D. A.; Lee, S. H. Stable silicon-ionic liquid interface for next-generation lithium-ion batteries. *Nat Commun* **2015**, *6*, 6230.

(92)	Alcántara, R.; Lavela, P.; Ortiz, G. F.; Tirado, J. L. Carbon Microspheres Obtained from Resorcinol-Formaldehyde as High-Capacity Electrodes for Sodium-Ion Batteries. *Electrochemical and Solid-State Letters* **2005**, *8*, A222.

(93)	Egashira, M.; Tanaka, T.; Yoshimoto, N.; Morita, M. Influence of Ionic Liquid Species in Non-Aqueous Electrolyte on Sodium Insertion into Hard Carbon. *Electrochemistry* **2012**, *80*, 755-758.

(94)	Fukunaga, A.; Nohira, T.; Hagiwara, R.; Numata, K.; Itani, E.; Sakai, S.; Nitta, K.; Inazawa, S. A safe and high-rate negative electrode for sodium-ion batteries: Hard carbon in NaFSA-C1C3pyrFSA ionic liquid at 363 K. *Journal of Power Sources* **2014**, *246*, 387-391.

(95)	Komaba, S.; Murata, W.; Ishikawa, T.; Yabuuchi, N.; Ozeki, T.; Nakayama, T.; Ogata, A.; Gotoh, K.; Fujiwara, K. Electrochemical Na Insertion and Solid Electrolyte

Interphase for Hard-Carbon Electrodes and Application to Na-Ion Batteries. *Advanced Functional Materials* **2011**, *21*, 3859-3867.

(96)   MacFarlane, D. R.; Tachikawa, N.; Forsyth, M.; Pringle, J. M.; Howlett, P. C.; Elliott, G. D.; Davis, J. H.; Watanabe, M.; Simon, P.; Angell, C. A. Energy applications of ionic liquids. *Energy Environ. Sci.* **2014**, *7*, 232-250.

(97)   Monti, D.; Jónsson, E.; Palacín, M. R.; Johansson, P. Ionic liquid based electrolytes for sodium-ion batteries: Na+ solvation and ionic conductivity. *Journal of Power Sources* **2014**, *245*, 630-636.

(98)   Nikitina, V. A.; Nazet, A.; Sonnleitner, T.; Buchner, R. Properties of Sodium Tetrafluoroborate Solutions in 1-Butyl-3-methylimidazolium Tetrafluoroborate Ionic Liquid. *Journal of Chemical & Engineering Data* **2012**, *57*, 3019-3025.

(99)   Holbrey, J. D.; Reichert, W. M.; Swatloski, R. P.; Broker, G. A.; Pitner, W. R.; Seddon, K. R.; Rogers, R. D. Efficient, halide free synthesis of new, low cost ionic liquids: 1,3-dialkylimidazolium salts containing methyl- and ethyl-sulfate anions. *Green Chemistry* **2002**, *4*, 407-413.

(100)   Jacquemin, J.; Goodrich, P.; Jiang, W.; Rooney, D. W.; Hardacre, C. Are alkyl sulfate-based protic and aprotic ionic liquids stable with water and alcohols? A thermodynamic approach. *J Phys Chem B* **2013**, *117*, 1938-1949.

(101)   Ferguson, J. L.; Holbrey, J. D.; Ng, S.; Plechkova, N. V.; Seddon, K. R.; Tomaszowska, A. A.; Wassell, D. F. A greener, halide-free approach to ionic liquid synthesis. *Pure and Applied Chemistry* **2011**, *84*.

(102)   Hardacre, C. H., J. D.; McMath, S. E. J. A highly efficient synthetic procedure for deuterating imidazoles and imidazolium salts. *Chemical Communications* **2001**.

(103)   Nockemann, P. B., K.; Driesen, K. P. Purification of imidazolium ionic liquids for spectroscopic applications. *Chemical Physics Letters* **2005**, *415*.

(104)   Niedermeyer, H. H., J. P.; Villar-Garcia, I. J.; Hunt, P. A.; Welton, T. . Mixtures of ionic liquids. *Chemical Society Reviews* **2012**, *41*.

(105)   Wu Xu, E. I. C., and C. Austen Angell. Ionic Liquids: Ion Mobilities, Glass Temperatures, and Fragilities. *J. Phys. Chem. B* **2003**, *107*.

(106)   Anouti, M.; Vigeant, A.; Jacquemin, J.; Brigouleix, C.; Lemordant, D. Volumetric properties, viscosity and refractive index of the protic ionic liquid, pyrrolidinium octanoate, in molecular solvents. *The Journal of Chemical Thermodynamics* **2010**, *42*, 834-845.

(107)   Quijada-Maldonado, E. v. d. B., S. Lijbers, J. H. Meindersma, G. W. de Haan, A. B. Experimental densities, dynamic viscosities and surface tensions of the ionic liquids series 1-ethyl-3-methylimidazolium acetate and dicyanamide and their binary and ternary mixtures with water and ethanol at T=(298.15 to 343.15K). *The Journal of Chemical Thermodynamics* **2012**, *51*, 51-58.

(108)   Araújo, J. M. M.; Pereiro, A. B.; Alves, F.; Marrucho, I. M.; Rebelo, L. P. N. Nucleic acid bases in 1-alkyl-3-methylimidazolium acetate ionic liquids: A thermophysical and ionic conductivity analysis. *The Journal of Chemical Thermodynamics* **2013**, *57*, 1-8.

(109)   Freire, M. G.; Teles, A. R. R.; Rocha, M. A. A.; Schröder, B.; Neves, C. M. S. S.; Carvalho, P. J.; Evtuguin, D. V.; Santos, L. M. N. B. F.; Coutinho, J. A. P. Thermophysical Characterization of Ionic Liquids Able To Dissolve Biomass. *Journal of Chemical & Engineering Data* **2011**, *56*, 4813-4822.

(110)   Fröba, A. P.; Rausch, M. H.; Krzeminski, K.; Assenbaum, D.; Wasserscheid, P.; Leipertz, A. Thermal Conductivity of Ionic Liquids: Measurement and Prediction. *International Journal of Thermophysics* **2010**, *31*, 2059-2077.

(111)   HOU Hai-Yun, H. Y.-R., WANG Sheng-Ze, BAI Bo-Feng. Preparation and Physicochemical Properties of Imidazolium Acetates and the Conductivities of Their Aqueous and Ethanol Solutions. *Acta Phys. -Chim. Sin.* **2011**, *11*.

(112)   Mark B. Shiflett, a. A. Y. Phase Behavior of Carbon Dioxide in Ionic Liquids: [emim][Acetate], [emim][Trifluoroacetate], and [emim][Acetate] + [emim][Trifluoroacetate] Mixtures. *J. Chem. Eng. Data* **2009**, *54*.

(113)   Rosenboom, J.-G.; Afzal, W.; Prausnitz, J. M. Solubilities of some organic solutes in 1-ethyl-3-methylimidazolium acetate. Chromatographic measurements and predictions from COSMO-RS. *The Journal of Chemical Thermodynamics* **2012**, *47*, 320-327.

(114)   Rabari, D.; Patel, N.; Joshipura, M.; Banerjee, T. Densities of Six Commercial Ionic Liquids: Experiments and Prediction Using a Cohesion Based Cubic Equation of State. *Journal of Chemical & Engineering Data* **2014**, *59*, 571-578.

(115)   J. Jacquemin, P. H., A. A. H. Padua and V. Majer Density and viscosity of several pure and water-saturated ionic liquids. *Green Chem.,* **2006**, *8*.

(116)   Johan Jacquemin, P. N., David W. Rooney, Margarida F. Costa Gomes, Pascale Husson, Vladimir Majer, Agilio A. H. Padua, and Christopher Hardacre. Prediction of Ionic Liquid Properties. II. Volumetric Properties as a Function of Temperature and Pressure. *J. Chem. Eng. Data* **2008**, *53*.

(117)   Johan Jacquemin, R. G., Paul Nancarrow, David W. Rooney, Margarida F. Costa Gomes, Agilio A. H. Pádua, and Christopher Hardacre. Prediction of Ionic Liquid Properties. I. Volumetric Properties as a Function of Temperature at 0.1 MPa. *J. Chem. Eng. Data* **2005**, *53*.

(118)   Pires, J.; Timperman, L.; Jacquemin, J.; Balducci, A.; Anouti, M. Density, conductivity, viscosity, and excess properties of (pyrrolidinium nitrate-based Protic Ionic Liquid+propylene carbonate) binary mixture. *The Journal of Chemical Thermodynamics* **2013**, *59*, 10-19.

(119)   M. Anouti, A. Vigeant, J. Jacquemin, C. Brigouleix, D. Lemordant. Volumetric properties, viscosity and refractive index of the protic ionic liquid, pyrrolidinium octanoate, in molecular solvents. *The Journal of Chemical Thermodynamics* **2010**, *42*.

(120)   Stec, M.; Tatarczuk, A.; Spiewak, D.; Wilk, A. Densities, Excess Molar Volumes, and Thermal Expansion Coefficients of Aqueous Aminoethylethanolamine Solutions at Temperatures from 283.15 to 343.15 K. *J Solution Chem* **2014**, *43*, 959-971.

(121)   Römich, C.; Merkel, N. C.; Valbonesi, A.; Schaber, K.; Sauer, S.; Schubert, T. J. S. Thermodynamic Properties of Binary Mixtures of Water and Room-Temperature Ionic Liquids: Vapor Pressures, Heat Capacities, Densities, and Viscosities of Water + 1-Ethyl-3-methylimidazolium Acetate and Water + Diethylmethylammonium Methane Sulfonate. *Journal of Chemical & Engineering Data* **2012**, *57*, 2258-2264.

(122)   Anouti, M.; Caillon-Caravanier, M.; Dridi, Y.; Jacquemin, J.; Hardacre, C.; Lemordant, D. Liquid densities, heat capacities, refractive index and excess quantities for {protic ionic liquids+water} binary system. *The Journal of Chemical Thermodynamics* **2009**, *41*, 799-808.

(123)   Le, K. A.; Sescousse, R.; Budtova, T. Influence of water on cellulose-EMIMAc solution properties: a viscometric study. *Cellulose* **2011**, *19*, 45-54.

(124)   S. F. R. Taylor, C. M., C. McStay, J. Jacquemin, C. Hardacre, M Mercy, R. G. Bell, N. H. de Leeuw. CO2 Capture in Wet and Dry Superbase Ionic Liquids. *Journal of Solution Chemistry* **2015**, *44*.

(125)   Chen, Y.; Cao, Y.; Sun, X.; Mu, T. Hydrogen bonding interaction between acetate-based ionic liquid 1-ethyl-3-methylimidazolium acetate and common solvents. *Journal of Molecular Liquids* **2014**, *190*, 151-158.

(126)   Lambert, D.: Entropy in General Chemistry. In *General Chemistry*; Wikibooks, Ed.; Information Technology Services department of Occidental College: Los Angeles, 2011.

(127)   Glasser, L. Lattice and phase transition thermodynamics of ionic liquids. *Thermochimica Acta* **2004**, *421*, 87-93.

(128)   Huddleston, J. G.; Visser, A. E.; Reichert, W. M.; Willauer, H. D.; Broker, G. A.; Rogers, R. D. Characterization and comparison of hydrophilic and hydrophobic room

temperature ionic liquids incorporating the imidazolium cation. *Green Chemistry* **2001**, *3*, 156-164.

(129)   K. R. Seddon, A. S., M. J. Torres,: "Viscosity and density of 1-alkyl-3-methylimidazolium ionic liquids" dans "In Clean Solvents : Alternative Media for Chemical Reactions and Processing",. In *ACS Symposium Series 819*; M. Abraham, L. M. E., Ed.; American Chemical Society: Washington DC, 2002.

(130)   M. Honarmanda, M. R. H. N., V. Pourgharib and M. Beigi. An Accurate Correlation to Estimate Saturated Molar Volume of Liquids. *Phys. Chem. Res.,* **2016**, *4*.

(131)   Lin, L.-S. L. a. C.-H. Phase Behaviors of Water + Acetic Acid + Methyl Acetate + p-Xylene Mixture at 101.32 kPa. *The Open Thermodynamics Journal* **2008**, *2*.

(132)   H. Eyring, M. S. J.: *Significant Liquid Structure*: New York, 1969.

(133)   A. Pal, H. K. Excess molar volumes and viscosities for binary liquid mixtures containing polyethers and pyrrolidin-2-one at 298.15 K. *Indian Journal of Chemistry* **2001**, *40A*.

(134)   Bearman, R. J.; Jones, P. F. Statistical Mechanical Theory of the Viscosity Coefficients of Binary Liquid Solutions. *The Journal of Chemical Physics* **1960**, *33*, 1432.

(135)   U.R. Kapadia, D. G. H., N.B. Patil, M.K. Lande, P.R. Patil Studies of viscosity and excess molar volume of binary mixtures of propane-1,2 diol with water at various temperatures. *Fluid Phase Equilibria* **2001**, *192*.

(136)   Pierre Bonhote, A.-P. D., Nicholas Papageorgiou,; Kuppuswamy Kalyanasundaram, a. M. G. t. Hydrophobic, Highly Conductive Ambient-Temperature Molten Salts. *Inorg. Chem.* **1996**, *35*.

(137)   Erwan Coadou, P. G., Alex R. Neale, Laure Timperman, Christopher Hardacre, Johan Jacquemin, and Meriem Anouti. Synthesis and Thermophysical Properties of Ether-Functionalized Sulfonium Ionic Liquids as Potential Electrolytes for Electrochemical Applications. *ChemPhysChem* **2016**, *17*.

(138)   C. A. Angell, W. X., M. Yoshizawa, A. Hayashi, J.-P. Lucas, M. Videa: *Electrochemical*

Aspects of Ionic Liquids; Wiley Interscience: New York, 2005. pp. pp. 5 –23.

(139)   Walden, P. *Bull. Acad. Imper. Sci. (St. Petersburg)* **1914**, *405*.

(140)   Masahiro Yoshizawa, W. X., and C. Austen Angell. Ionic Liquids by Proton Transfer: Vapor Pressure,

Conductivity, and the Relevance of pKa from Aqueous

Solutions. *J. AM. CHEM. SOC.* **2003**, *125*.

(141)   Christian Schreiner, S. Z., Robert Hartl, and Heiner J. Gores. Fractional Walden Rule for Ionic Liquids: Examples from Recent Measurements

and a Critique of the So-Called Ideal KCl Line for the Walden Plot. *J. Chem. Eng. Data* **2010**, *55*.

(142)   Endres, F. Physical chemistry of ionic liquids. *Phys Chem Chem Phys* **2010**, *12*, 1648.

(143)   C. A. Angell, W. X., M. Yoshizawa, A. Hayashi, J.-P. Lucas, M. Videa: *Electrochemical Aspects of Ionic Liquids*; Wiley Interscience: New York, 2005. pp. 5-23.

(144)   Shaohua Fang, L. Y., Chao Wei, Chengxin Peng, Kazuhiro Tachibana,; Kamijima, K. Low-viscosity and low-melting point asymmetric

trialkylsulfonium based ionic liquids as potential electrolytes. *Electrochemistry Communications* **2007** *9*

(145)   Douglas R. MacFarlane, M. F., Ekaterina I. Izgorodina,; Andrew P. Abbott, G. A. a. K. F. On the concept of ionicity in ionic liquids. *Phys. Chem. Chem. Phys.* **2009**, *11*.

(146)   Takamuku, T.; Hoke, H.; Idrissi, A.; Marekha, B. A.; Moreau, M.; Honda, Y.; Umecky, T.; Shimomura, T. Microscopic interactions of the imidazolium-based ionic liquid with molecular liquids depending on their electron-donicity. *Phys Chem Chem Phys* **2014**, *16*, 23627-23638.

(147)   Toshiyuki TAKAMUKU, Y. H., Kenta FUJII, and Shigeharu KITTAKA. Aggregation of Imidazolium Ionic Liquids in Molecular Liquids Studied by Small-Angle Neutron Scattering and NMR. *The Japan Society for Analytical Chemistry* **2008**, *24*.

(148)   Umecky, T.; Takamuku, T.; Matsumoto, T.; Kawai, E.; Takagi, M.; Funazukuri, T. Effects of dissolved water on Li+ solvation in 1-ethyl-3-methylimidazolium bis(trifluoromethanesulfonyl)amide ionic liquid studied by NMR. *J Phys Chem B* **2013**, *117*, 16219-16226.

(149)   Pierre Bonhote, A.-P. D., Nicholas Papageorgiou, Kuppuswamy Kalyanasundaram, and Michael Gratzel. Hydrophobic, Highly Conductive Ambient-Temperature Molten Salts. *Inorg. Chem.* **1996**, *35*.

(150)   Singh, T.; Rao, K. S.; Kumar, A. Polarity behaviour and specific interactions of imidazolium-based ionic liquids in ethylene glycol. *Chemphyschem* **2011**, *12*, 836-845.

(151)   Russo, J. W.; Hoffmann, M. M. Measurements of Surface Tension and Chemical Shift on Several Binary Mixtures of Water and Ionic Liquids and Their Comparison for Assessing Aggregation. *Journal of Chemical & Engineering Data* **2011**, *56*, 3703-3710.

(152)   Abe, H. Peculiar Concentration Dependence of H/D Exchange Reaction in 1-Butyl-3-methylimidazolium Tetrafluoroborate-D<sub>2</sub>O Mixtures. *Open Journal of Physical Chemistry* **2011**, *01*, 70-76.

(153)   Kumar, T. S. a. A. Aggregation Behavior of Ionic Liquids in Aqueous Solutions: Effect of Alkyl Chain Length, Cations, and Anions. *J. Phys. Chem. B* **2007**, *111*.

(154)   Margherita Moreno, F. C., Andrea Mele, Carlo Pasqui, and Guido Raos. Interaction of Water with the Model Ionic Liquid [bmim][BF4]: Molecular Dynamics Simulations and Comparison with NMR Data. *J. Phys. Chem. B* **2008**, *112*.

(155)   Richard C. Remsing, Z. L., Ivan Sergeyev, and Guillermo Moyna. Solvation and Aggregation of N,N′-Dialkylimidazolium Ionic Liquids: A Multinuclear NMR Spectroscopy and Molecular Dynamics Simulation Study. *J. Phys. Chem. B* **2008**, *112*.

(156)   Cesare Marincola, F.; Piras, C.; Russina, O.; Gontrani, L.; Saba, G.; Lai, A. NMR investigation of imidazolium-based ionic liquids and their aqueous mixtures. *Chemphyschem* **2012**, *13*, 1339-1346.

(157)   Takamuku, T.; Shimomura, T.; Sadakane, K.; Koga, M.; Seto, H. Aggregation of 1-dodecyl-3-methylimidazolium nitrate in water and benzene studied by SANS and 1H NMR. *Phys Chem Chem Phys* **2012**, *14*, 11070-11080.

(158)   Shimomura, T.; Takamuku, T.; Yamaguchi, T. Clusters of imidazolium-based ionic liquid in benzene solutions. *J Phys Chem B* **2011**, *115*, 8518-8527.

(159)   Dupont, J. On the Solid, Liquid and Solution Structural Organization of Imidazolium Ionic Liquids. *J. Braz. Chem. Soc.* **2004**, *15*.

(160)   Shimomura, T.; Inoue, S.; Kadohata, S.; Umecky, T.; Takamuku, T. SANS, ATR-IR, and 1D- and 2D-NMR studies of mixing states of imidazolium-based ionic liquid and aryl solvents. *Phys Chem Chem Phys* **2013**, *15*, 20565-20576.

(161)   Stassen, H. K.; Ludwig, R.; Wulf, A.; Dupont, J. Imidazolium salt ion pairs in solution. *Chemistry* **2015**, *21*, 8324-8335.

(162)   Dong, K.; Song, Y.; Liu, X.; Cheng, W.; Yao, X.; Zhang, S. Understanding structures and hydrogen bonds of ionic liquids at the electronic level. *J Phys Chem B* **2012**, *116*, 1007-1017.

(163)   Hunt, P. A.; Ashworth, C. R.; Matthews, R. P. Hydrogen bonding in ionic liquids. *Chem Soc Rev* **2015**, *44*, 1257-1288.

(164)   Tsuzuki, S.; Tokuda, H.; Mikami, M. Theoretical analysis of the hydrogen bond of imidazolium C(2)-H with anions. *Phys Chem Chem Phys* **2007**, *9*, 4780-4784.

(165)   Francesca D'Anna, M. C., Paolo Lo Meo, Serena Riela, and Renato Noto. The effect of some amines and alcohols on the organized structure of [bmim][BF4] investigated by 1H NMR spectroscopy. *Issue in Honor of Prof Nicolò Vivona, ARKIVOC* **2009**, *(viii)*.

(166)   Allen, J. J.; Bowser, S. R.; Damodaran, K. Molecular interactions in the ionic liquid emim acetate and water binary mixtures probed via NMR spin relaxation and exchange spectroscopy. *Phys Chem Chem Phys* **2014**, *16*, 8078-8085.

(167)   Chen, Y.; Cao, Y.; Zhang, Y.; Mu, T. Hydrogen bonding between acetate-based ionic liquids and water: Three types of IR absorption peaks and NMR chemical shifts change upon dilution. *Journal of Molecular Structure* **2014**, *1058*, 244-251.

(168)   Marekha, B. A.; Bria, M.; Moreau, M.; De Waele, I.; Miannay, F.-A.; Smortsova, Y.; Takamuku, T.; Kalugin, O. N.; Kiselev, M.; Idrissi, A. Intermolecular interactions in mixtures of 1-n-butyl-3-methylimidazolium acetate and water: Insights from IR, Raman, NMR spectroscopy and quantum chemistry calculations. *Journal of Molecular Liquids* **2015**, *210*, 227-237.

(169)   Radhi, A.; Le, K. A.; Ries, M. E.; Budtova, T. Macroscopic and microscopic study of 1-ethyl-3-methyl-imidazolium acetate-DMSO mixtures. *J Phys Chem B* **2015**, *119*, 1633-1640.

(170)   Thawarkar, S.; Khupse, N. D.; Kumar, A. Comparative Investigation of the Ionicity of Aprotic and Protic Ionic Liquids in Molecular Solvents by using Conductometry and NMR Spectroscopy. *Chemphyschem* **2016**, *17*, 1006-1017.

(171)   D. T. Bowron, C. D. A., L. F. Gladden, C. Hardacre, J. D. Holbrey, M. C. Lagunas, J. McGregor, M. D. Mantle, C. L. Mullan, and T. G. A. Youngs. Structure and Dynamics of 1-Ethyl-3-methylimidazolium Acetate via Molecular Dynamics and Neutron Diffraction. *J. Phys. Chem. B* **2010**, *114*.

(172)   Kun Dong, S. Z., Daxi Wang, and Xiaoqian Yao. Hydrogen Bonds in Imidazolium Ionic Liquids. *J. Phys. Chem. A* **2006**, *110*.

(173)   Yee, P.; Shah, J. K.; Maginn, E. J. State of hydrophobic and hydrophilic ionic liquids in aqueous solutions: are the ions fully dissociated? *J Phys Chem B* **2013**, *117*, 12556-12566.

(174)   Marco D'Abramo, R. C., Alfredo Di Nola, Andrea Amadei. What can we learn by comparing experimental and theoretical-computational X-ray scattering data? *Journal of Molecular Liquids* **2009**, *144*.

(175)   Teresa Head-Gordon, G. H. Water Structure from Scattering Experiments and Simulation. . *Chem. Rev.* **2002**, *102*.

(176)   Swadzba-Kwasny, M.; Chancelier, L.; Ng, S.; Manyar, H. G.; Hardacre, C.; Nockemann, P. Facile in situ synthesis of nanofluids based on ionic liquids and copper oxide clusters and nanoparticles. *Dalton Trans* **2012**, *41*, 219-227.

(177)   C.T. Hsieh, J. M. C., H.H. Lin, H.C. Shih. *Appl. Phys. Lett.* **2003**, *83*.

(178)   G.R. Patzke, Y. Z., R. Kontic and F. Conrad,. *Angew. Chem.-Int. Ed* **2011**, *50*.

(179)   J.B. Reitz, E. I. S. *J. Am. Chem. Soc.* **1998**, *120*.

(180)   MacDonald, A. *Nature* **2001**, *414*.

(181)   S.G. Yang, T. L., B.X. Gu, Y.W. Du. *Appl. Phys. Lett.* **2003**, *83*.

(182)   J. Jacquemin, M. A., D. Lemordant. *J. Chem. Eng. Data* **2011**, *56*.

(183)   M. Anouti, P.-Y. S., C. Ghimbeu, H. Galiano, D. Lemordant,. *Colloids Surf., A* **2012**, *395*.

(184)   Tyrrell, S.; Swadźba-Kwaśny, M.; Nockemann, P. Ionothermal, microwave-assisted synthesis of indium(iii) selenide. *Journal of Materials Chemistry A* **2014**, *2*, 2616.

(185)   Single-crystal   X-ray   Diffraction. http://serc.carleton.edu/research_education/geochemsheets/techniques/SXD.html.

(186)   Baudron, S. A. Dipyrrin based homo- and hetero-metallic infinite architectures. *CrystEngComm* **2010**, *12*, 2288.

(187)   Que, L.: *Physical methods in bioinorganic chemistry: spectroscopy and magnetism*; University Science Books, March 2000. pp. 345–348

(188)   Shekhah, O.; Wang, H.; Zacher, D.; Fischer, R. A.; Woll, C. Growth mechanism of metal-organic frameworks: insights into the nucleation by employing a step-by-step route. *Angew Chem Int Ed Engl* **2009**, *48*, 5038-5041.

(189)   Hinz, A.; Köckerling, M. A New Mixed-Valent Copper Cyanido Complex and a New Copper(II) Acetato Complex, Prepared with an Ionic Liquid. *Zeitschrift für anorganische und allgemeine Chemie* **2015**, *641*, 1347-1351.

(190)   NIST X-ray Photoelectron Spectroscopy Database, Version 4.1. http://srdata.nist.gov/xps/.

(191)   T. Ferreira, W. R.: ImageJ User Guide. 1.46r, I., Ed., 12; pp 198.

(192)   ImageJ, Image Processing and Analysis in Java. https://imagej.nih.gov/ij/download.html.

(193)   Y. Qin, Y. S., N. Sun, N. Zhao, M. Li, and L. Qi. Ionic Liquid-Assisted Growth of Single-Crystalline Dendritic Gold

Nanostructures with a Three-Fold Symmetry. *Chem. Mater.* **2008**, *20*.

(194)   Anouti, M.; Mirghani, A.; Jacquemin, J.; Timperman, L.; Galiano, H. Tunable gold nanoparticles shape and size in reductive and structuring media containing protic ionic liquids. *Ionics* **2013**, *19*, 1783-1790.

(195)   Corrêa, C. M.; Bizeto, M. A.; Camilo, F. F. Direct synthesis of silver nanoparticles in ionic liquid. *Journal of Nanoparticle Research* **2016**, *18*.

(196)   Khare, V.; Li, Z.; Mantion, A.; Ayi, A. A.; Sonkaria, S.; Voelkl, A.; Thünemann, A. F.; Taubert, A. Strong anion effects on gold nanoparticle formation in ionic liquids. *J. Mater. Chem.* **2010**, *20*, 1332-1339.

(197)   Y. Kikuchi, T. S. a. K. S. The Dissociation Equilibrium of the Copper(II) Acetate Dimer in Acetic Acid. *Bull. Chem. Soc. Jpn.* **1990**, *63*.

(198)   Dolomanov, O. V., Bourhis, L.J., Gildea, R.J, Howard, J.A.K. & Puschmann, H. . *J. Appl. Cryst.* **2009**, *42*.

(199)   Sheldrick, G. M. *Acta Cryst.* **2008**, *A64*.

(200)   Sheldrick, G. M. *Acta Cryst. C71* **2015**.

(201)   Shirley, D. A. High-Resolution X-Ray Photoemission Spectrum of the Valence Bands of Gold. *Physical Review B* **1972**, *5*, 4709-4714.

(202)   Shiro Seki, Y. K., Hajime Miyashiro, Yasutaka Ohno, Yuichi Mita, and Nobuyuki Terada, Patrick Charest, Abdelbast Guerfi, and Karim Zaghib. Compatibility of N-Methyl-N-propylpyrrolidinium Cation Room-Temperature Ionic Liquid Electrolytes and Graphite Electrode. *J. Phys. Chem. C* **2008**, *112*.

(203)   Yamamoto, T.; Nohira, T.; Hagiwara, R.; Fukunaga, A.; Sakai, S.; Nitta, K.; Inazawa, S. Charge–discharge behavior of tin negative electrode for a sodium secondary battery using intermediate temperature ionic liquid sodium bis(fluorosulfonyl)amide–potassium bis(fluorosulfonyl)amide. *Journal of Power Sources* **2012**, *217*, 479-484.

(204)   Ding, C.; Nohira, T.; Hagiwara, R.; Matsumoto, K.; Okamoto, Y.; Fukunaga, A.; Sakai, S.; Nitta, K.; Inazawa, S. Na[FSA]-[C3C1pyrr][FSA] ionic liquids as electrolytes for sodium secondary batteries: Effects of Na ion concentration and operation temperature. *Journal of Power Sources* **2014**, *269*, 124-128.

(205)   Chen, C.-Y.; Matsumoto, K.; Nohira, T.; Ding, C.; Yamamoto, T.; Hagiwara, R. Charge–discharge behavior of a Na2FeP2O7 positive electrode in an ionic liquid electrolyte between 253 and 363K. *Electrochimica Acta* **2014**, *133*, 583-588.

(206)   Ding, C.; Nohira, T.; Kuroda, K.; Hagiwara, R.; Fukunaga, A.; Sakai, S.; Nitta, K.; Inazawa, S. NaFSA–C1C3pyrFSA ionic liquids for sodium secondary battery operating over a wide temperature range. *Journal of Power Sources* **2013**, *238*, 296-300.

(207)   Ding, C.; Nohira, T.; Fukunaga, A.; Hagiwara, R. Charge-discharge Performance of an Ionic Liquid-based Sodium Secondary Battery in a Wide Temperature Range. *Electrochemistry* **2015**, *83*, 91-94.

(208)   Wongittharom, N.; Wang, C. H.; Wang, Y. C.; Yang, C. H.; Chang, J. K. Ionic liquid electrolytes with various sodium solutes for rechargeable Na/NaFePO4 batteries operated at elevated temperatures. *ACS Appl Mater Interfaces* **2014**, *6*, 17564-17570.

(209)   Wang, C.-H.; Yeh, Y.-W.; Wongittharom, N.; Wang, Y.-C.; Tseng, C.-J.; Lee, S.-W.; Chang, W.-S.; Chang, J.-K. Rechargeable Na/Na0.44MnO2 cells with ionic liquid electrolytes containing various sodium solutes. *Journal of Power Sources* **2015**, *274*, 1016-1023.

(210)   Wongittharom, N.; Lee, T.-C.; Wang, C.-H.; Wang, Y.-C.; Chang, J.-K. Electrochemical performance of Na/NaFePO4 sodium-ion batteries with ionic liquid electrolytes. *Journal of Materials Chemistry A* **2014**, *2*, 5655.

(211)   Nohira, T.; Ishibashi, T.; Hagiwara, R. Properties of an intermediate temperature ionic liquid NaTFSA–CsTFSA and charge–discharge properties of NaCrO2 positive electrode at 423K for a sodium secondary battery. *Journal of Power Sources* **2012**, *205*, 506-509.

(212)   Fukunaga, A.; Nohira, T.; Kozawa, Y.; Hagiwara, R.; Sakai, S.; Nitta, K.; Inazawa, S. Intermediate-temperature ionic liquid NaFSA-KFSA and its application to sodium secondary batteries. *Journal of Power Sources* **2012**, *209*, 52-56.

(213)   Mohd Noor, S. A.; Howlett, P. C.; MacFarlane, D. R.; Forsyth, M. Properties of sodium-based ionic liquid electrolytes for sodium secondary battery applications. *Electrochimica Acta* **2013**, *114*, 766-771.

(214)   Serra Moreno, J.; Maresca, G.; Panero, S.; Scrosati, B.; Appetecchi, G. B. Sodium-conducting ionic liquid-based electrolytes. *Electrochemistry Communications* **2014**, *43*, 1-4.

(215)   N. Yabuuchi; K. Shimomura; Y. Shimbe; T. Ozeki; J. Son; H. Oji; Y. Katayama; T. Miura; Komaba, S. Graphite-Silicon-Polyacrylate Negative Electrodes in Ionic Liquid Electrolyte for Safer Rechargeable Li-Ion Batteries. *Advanced Energy Materials* **2011**, *1*.

(216)   Kühnel, R. S.; Böckenfeld, N.; Passerini, S.; Winter, M.; Balducci, A. Mixtures of ionic liquid and organic carbonate as electrolyte with improved safety and performance for rechargeable lithium batteries. *Electrochimica Acta* **2011**, *56*, 4092-4099.

(217)   E.R. Buiel, A. E. G., J.R. Dahn. Model of micropore closure in hard carbon prepared from

sucrose. *Carbon 37* **1999**.

(218)   Dahn, E. B. a. J. R. Reduction of the Irreversible Capacity in Hard-Carbon Anode Materials Prepared from Sucrose for Li-Ion Batteries. *J Electrochem. Soc.* **1998**, *145*.

(219)   E.R. Buiel, A. E. G., J.R. Dahn. Model of micropore closure in hard carbon prepared from sucrose. *Carbon* **1999**, *37*.

(220)   Lewandowski, A.; Świderska-Mocek, A. Ionic liquids as electrolytes for Li-ion batteries—An overview of electrochemical studies. *Journal of Power Sources* **2009**, *194*, 601-609.

(221)   M. Dahbi, N. Y., M.Fukunishi, K. Kubota, K. Chihara, K. Tokiwa, X. Yu, H. Ushiyama, K. Yamashita, J. Son, Y. Cui, H. Oji, and S. Komaba. Black Phosphorus as a High-Capacity, High-Capability Negative Electrode for Sodium-Ion Batteries: Investigation of the Electrode/Electrolyte Interface. *Chem. Mater.* **2016**, *28(6)*.

Appendices

Appendices of Chapter 3 _ Macroscopic properties of ionic liquid and water binary mixtures

Appendix A: Redlich-Kister equations principle

V^E, α_p^E and $\Delta\eta$ values for the ([C$_2$MIm][C$_n$H$_n$CO$_2$] + H$_2$O) system from $T = 293.15$ K to 363.15 K were fitted according to the Redlich–Kister polynomial equation:

$$Y^E = \chi_1 \chi_2 \sum_{i=0}^{m} A_i (1 - 2\chi_2)^i$$

Where Y^E represents V^E, α_p^E and $\Delta\eta$, χ_1 and χ_2 the mole fraction of the components and A_i are the adjustable parameters. The optimum number of adjustable parameters was ascertained from an examination of the variation in the standard deviation σ_{Y^E}:

$$\sigma_{Y^E} = \left(\frac{\sum \left(Y^E{}_i^{\exp} - Y^E{}_i^{\text{cal}} \right)^2}{n - v} \right)^{0.5}$$

Where, n is the number of experimental points, and v is number of adjustable parameters in each case.

Appendix B: Molar volume, V_m, of ([C$_2$MIm][CH$_3$CO$_2$] + H$_2$O), ([C$_2$MIm][C$_3$H$_7$CO$_2$] + H$_2$O), and ([C$_2$MIm][C$_7$H$_{15}$CO$_2$] + H$_2$O)

Table 0-1. Molar volume, V_m, calculated from the density measurements found in Table 3-1 of ([C$_2$MIm][CH$_3$CO$_2$] + H$_2$O), ([C$_2$MIm][C$_3$H$_7$CO$_2$] + H$_2$O), and ([C$_2$MIm][C$_7$H$_{15}$CO$_2$] + H$_2$O) binary mixture as a function of the ionic liquid mole fraction composition, χ_{IL}, for a temperature range from (293.15 to 363.15) K at 0.1 MPa.

T/K	293.15	298.15	303.15	313.15	323.15	333.15	343.15	353.15	363.15
χ_{IL}				([C$_2$MIm][CH$_3$CO$_2$] + H$_2$O), V_m/$cm^3\cdot mol^{-1}$					
0.00	18.0324	18.0533	18.0787	18.1411	18.2181	18.3076	18.4090	18.5219	18.6461
0.05	24.0531	24.1062	24.1643	24.2883	24.4208	24.5619	24.7242	24.9853	/
0.19	42.6360	42.7563	42.8851	43.1569	43.4282	43.7070	43.9934	44.2879	44.5905
0.33	62.0079	62.1816	62.3563	62.7257	63.0937	63.4661	63.8429	64.2361	64.6343
0.47	81.4397	81.6607	81.8903	82.3609	82.8142	83.2802	83.7515	84.2359	84.7260
0.62	101.9988	102.2761	102.5642	103.1547	103.7235	104.3082	104.8898	105.4779	106.0726
0.77	122.6048	122.9499	123.3081	124.0195	124.7162	125.4091	126.1098	126.8064	127.5229
0.89	139.5917	139.9978	140.3935	141.2045	141.9989	142.7889	143.5878	144.3821	145.1853
1.00	154.7496	155.1869	155.6410	156.5572	157.4552	158.3635	159.2674	160.1817	161.0760
				([C$_2$MIm][C$_3$H$_7$CO$_2$] + H$_2$O), V_m/$cm^3\cdot mol^{-1}$					
0.00	18.0324	18.0533	18.0787	18.1411	18.2181	18.3076	18.4090	18.5219	18.6461
0.05	26.2163	26.2892	26.3651	26.5259	26.6939	26.8694	27.0551	27.2516	27.4757
0.20	49.8906	50.0391	50.1978	50.5231	50.8477	51.1815	51.5295	51.8824	52.2400
0.50	99.8866	100.1659	100.4561	101.0702	101.6629	102.2723	102.8891	103.5134	104.1453
0.65	126.1175	126.4242	126.7917	127.5453	128.2957	129.0550	129.8108	130.5756	131.3622
0.80	150.6308	151.0684	151.5228	152.4255	153.3099	154.2045	155.1097	156.0256	156.9370
1.00	186.0902	186.6164	187.1632	188.3203	189.4374	190.5679	191.6933	192.8133	193.9465
				([C$_2$MIm][C$_7$H$_{15}$CO$_2$] + H$_2$O), V_m/$cm^3\cdot mol^{-1}$					
0.00	18.0324	18.0533	18.0787	18.1411	18.2181	18.3076	18.4090	18.5219	18.6461
0.05	29.4009	29.4794	29.5642	29.7441	29.9292	30.1288	30.3249	30.6396	30.7692
0.20	63.8055	64.0122	64.2265	64.6597	65.0921	65.5370	66.0014	66.4860	67.0190
0.35	98.8858	99.1878	99.5014	100.1545	100.8062	101.4663	102.1456	102.8235	103.5211
0.50	135.4229	135.8248	136.2560	137.1269	138.0089	138.8883	139.7789	140.6811	141.5950
0.64	167.7908	168.2738	168.7932	169.8756	170.9375	172.0128	173.0841	174.1866	175.3033
0.80	204.9338	205.5051	206.1414	207.4257	208.7262	210.0431	211.3551	212.6835	214.0288
1.00	253.0275	253.8101	254.5977	256.2133	257.8234	259.4538	261.0782	262.7231	264.3614

Appendix C: Excess Molar volume, V^E, and RK parameters of ([C$_2$MIm][CH$_3$CO$_2$] + H$_2$O), ([C$_2$MIm][C$_3$H$_7$CO$_2$] + H$_2$O), and ([C$_2$MIm][C$_7$H$_{15}$CO$_2$] + H$_2$O)

Table 0-2. Excess Molar volume, V^E, calculated from the Molar Volume V_m found in Table 0-1 of ([C$_2$MIm][CH$_3$CO$_2$] + H$_2$O), ([C$_2$MIm][C$_3$H$_7$CO$_2$] + H$_2$O), and ([C$_2$MIm][C$_7$H$_{15}$CO$_2$] + H$_2$O) binary mixture as a function of the ionic liquid mole fraction composition, χ_{IL}, for a temperature range from (293.15 to 363.15) K at 0.1 MPa.

T/K	293.15	298.15	303.15	313.15	323.15	333.15	343.15	353.15	363.15
χ_{IL}				([C$_2$MIm][CH$_3$CO$_2$] + H$_2$O), V^E/ cm^3·mol^{-1}					
0.00	0	0	0	0	0	0	0	0	0
0.05	-0.337	-0.324	-0.311	-0.289	-0.272	-0.258	-0.235	-0.124	/
0.19	-1.427	-1.407	-1.385	-1.339	-1.301	-1.267	-1.235	-1.206	-1.174
0.33	-1.674	-1.661	-1.654	-1.633	-1.616	-1.606	-1.599	-1.586	-1.569
0.47	-1.520	-1.517	-1.517	-1.514	-1.528	-1.540	-1.551	-1.560	-1.560
0.62	-1.249	-1.253	-1.257	-1.261	-1.281	-1.296	-1.316	-1.341	-1.350
0.77	-0.905	-0.902	-0.900	-0.910	-0.923	-0.952	-0.971	-1.006	-1.008
0.89	-0.584	-0.571	-0.583	-0.598	-0.614	-0.645	-0.664	-0.699	-0.708
1.00	0	0	0	0	0	0	0	0	0
				([C$_2$MIm][C$_3$H$_7$CO$_2$] + H$_2$O), V^E/ cm^3·mol^{-1}					
0.00	0	0	0	0	0	0	0	0	0
0.05	-0.533	-0.508	-0.486	-0.442	-0.403	-0.370	-0.339	-0.308	-0.260
0.20	-1.358	-1.333	-1.305	-1.251	-1.204	-1.160	-1.115	-1.076	-1.040
0.50	-1.160	-1.158	-1.158	-1.127	-1.113	-1.095	-1.082	-1.074	-1.061
0.65	-0.647	-0.697	-0.702	-0.692	-0.676	-0.663	-0.667	-0.674	-0.660
0.80	-0.248	-0.242	-0.237	-0.229	-0.225	-0.222	-0.223	-0.225	-0.229
1.00	0	0	0	0	0	0	0	0	0
				([C$_2$MIm][C$_7$H$_{15}$CO$_2$] + H$_2$O), V^E/ cm^3·mol^{-1}					
0.00	0	0	0	0	0	0	0	0	0
0.05	-0.381	-0.362	-0.340	-0.301	-0.269	-0.236	-0.218	-0.092	-0.163
0.20	-1.155	-1.122	-1.085	-1.024	-0.975	-0.927	-0.869	-0.803	-0.696
0.35	-1.371	-1.357	-1.335	-1.288	-1.250	-1.218	-1.173	-1.144	-1.101
0.50	-1.235	-1.239	-1.217	-1.193	-1.162	-1.150	-1.130	-1.114	-1.088
0.64	-0.897	-0.923	-0.918	-0.894	-0.891	-0.894	-0.900	-0.893	-0.871
0.80	-0.413	-0.470	-0.467	-0.483	-0.481	-0.482	-0.486	-0.491	-0.477
1.00	0	0	0	0	0	0	0	0	0

Table 0-3. Redlich-Kister fitting coefficients A_i of the V^E of the ($[C_2MIm][C_nH_nCO_2]$ + H_2O) binary mixture as a function of temperature from (293.15 to 363.15) K along with their fitting deviations, σ_Y^E.

	T /K	293.15	298.15	303.15	313.15	323.15	333.15	343.15	353.15	363.15
$[C_2MIM][CH_3CO_2]$ + H_2O	A_0	-6.0121	-6.0142	-6.0157	-6.0065	-6.0527	-6.0902	-6.1445	-6.232	-6.1349
	A_1	4.3083	4.188	4.1747	4.01	3.7937	3.6273	3.4827	3.5763	2.6983
	A_2	-2.8671	-2.6115	-2.4852	-2.2458	-1.9637	-1.883	-1.6486	-1.1496	-1.9664
	A_3	-3.8519	-3.7322	-4.0519	-4.3799	-4.5422	-4.9223	-5.2764	-6.8935	-4.0800
	σ_Y^E	0.169	0.182	0.171	0.161	0.158	0.192	0.224	0.349	0.295
$[C_2MIm]$ $[C_3H_7CO_2]$ + H_2O	A_0	-6.337	-6.3925	-6.3668	-6.3659	-6.3474	-6.3318	-6.3132	-6.2781	-6.2292
	A_1	2.01	1.6298	1.4884	1.2905	1.1257	0.9705	0.7016	0.4975	0.4541
	A_2	-4.736	-4.2041	-3.8547	-3.7337	-3.5567	-3.4564	-3.2065	-2.9135	-2.8076
	A_3	0.97732	1.62892	1.71646	1.0787	0.58544	0.0978	-0.007	-0.086	-0.8626
	σ_Y^E	0.542	0.524	0.503	0.455	0.43	0.423	0.421	0.421	0.457
$[C_2MIm]$ $[C_7H_{15}CO_2]$ + H_2O	A_0	-4.9716	-4.9833	-4.9208	-4.7936	-4.7003	-4.6596	-4.5876	-4.5604	-4.4217
	A_1	3.731	3.4482	3.3538	3.2393	3.0258	2.8244	2.4	2.6951	1.9157
	A_2	0.3482	0.1623	0.3147	0.3668	0.5456	0.8533	1.1078	1.7193	2.0175
	A_3	0.311	-0.1825	-0.4137	-1.2039	-1.3869	-1.5914	-1.2759	-3.6618	-1.8266
	σ_Y^E	0.700	0.582	0.552	0.45	0.408	0.377	0.362	0.223	0.304

Appendix D: Molar volumes V_m expressed in nm3 of ([C₂MIm][CH₃CO₂] + H₂O), ([C₂MIm][C₃H₇CO₂] + H₂O), and ([C₂MIm][C₇H₁₅CO₂] + H₂O)

Table 0-4. Molar volumes V_m expressed in nm^3 of the ([C₂MIm][CₙHₙCO₂] + H₂O) binary mixture as a function of [C₂MIm][CₙHₙCO₂] mole fraction composition, χ_{IL}, for a temperature range from (293.15 to 363.15) K at 0.1 MPa calculated from experimental density data provided in Table 3-1.

T/K	293.15	298.15	303.15	313.15	323.15	333.15	343.15	353.15	363.15
χ_{IL}	For ([C₂MIm][CH₃CO₂] + H₂O), V_m/nm^3								
0	0.030	0.030	0.030	0.030	0.030	0.030	0.031	0.031	0.031
0.05	0.040	0.040	0.040	0.040	0.041	0.041	0.041	0.041	0.000
0.19	0.071	0.071	0.071	0.072	0.072	0.073	0.073	0.074	0.074
0.33	0.103	0.103	0.104	0.104	0.105	0.105	0.106	0.107	0.107
0.47	0.135	0.136	0.136	0.137	0.137	0.138	0.139	0.140	0.141
0.62	0.169	0.170	0.170	0.171	0.172	0.173	0.174	0.175	0.176
0.77	0.204	0.204	0.205	0.206	0.207	0.208	0.209	0.211	0.212
0.89	0.232	0.232	0.233	0.234	0.236	0.237	0.238	0.240	0.241
1	0.257	0.258	0.258	0.260	0.261	0.263	0.264	0.266	0.267
	For ([C₂MIm][C₃H₇CO₂] + H₂O), V_m/nm^3								
0.00	0.030	0.030	0.030	0.030	0.030	0.030	0.031	0.031	0.031
0.05	0.044	0.044	0.044	0.044	0.044	0.045	0.045	0.045	0.046
0.20	0.083	0.083	0.083	0.084	0.084	0.085	0.086	0.086	0.087
0.36	0.128	0.128	0.129	0.130	0.130	0.131	0.132	0.133	0.134
0.50	0.166	0.166	0.167	0.168	0.169	0.170	0.171	0.172	0.173
0.65	0.209	0.210	0.211	0.212	0.213	0.214	0.216	0.217	0.218
0.80	0.250	0.251	0.252	0.253	0.255	0.256	0.258	0.259	0.261
1.00	0.309	0.310	0.311	0.313	0.315	0.316	0.318	0.320	0.322
	For ([C₂MIm][C₇H₁₅CO₂] + H₂O), V_m/nm^3								
0.00	0.030	0.030	0.030	0.030	0.030	0.030	0.031	0.031	0.031
0.05	0.049	0.049	0.049	0.049	0.050	0.050	0.050	0.051	0.051
0.20	0.106	0.106	0.107	0.107	0.108	0.109	0.110	0.110	0.111
0.35	0.164	0.165	0.165	0.166	0.167	0.168	0.170	0.171	0.172
0.50	0.225	0.226	0.226	0.228	0.229	0.231	0.232	0.234	0.235
0.64	0.279	0.279	0.280	0.282	0.284	0.286	0.287	0.289	0.291
0.80	0.340	0.341	0.342	0.344	0.347	0.349	0.351	0.353	0.355
1.00	0.420	0.421	0.423	0.425	0.428	0.431	0.433	0.436	0.439

Appendix E: Redlich-Kister fitting coefficients A_i of the S^E

Table 0-5. Redlich-Kister fitting coefficients A_i of the S^E of the ($[C_2MIm][C_nH_nCO_2] + H_2O$) binary mixture as a function χ_{IL} at 298.15K and 0.1MPa.

	A_0	A_1	A_2	A_3	A_4	A_5
$[C_2MIm][CH_3CO_2] + H_2O$	-12.209	6.400	-9.305	7.794	6.607	-19.290
$[C_2MIm][C_3H_7CO_2] + H_2O$	-13.909	6.204	-4.527	0.263	-10.77	-9.960
$[C_2MIm][C_7H_{15}CO_2] + H_2O$	-10.253	6.844	0.152	2.023	-0.737	-4.212

Appendix F: Apparent molar volumes $V_{\phi,i}$, of ([C$_2$MIm][C$_n$H$_n$CO$_2$] + H$_2$O), binary mixture

Table 0-6. Apparent molar volumes, $V_{\phi,i}$, of ([C$_2$MIm][CH$_3$CO$_2$] + H$_2$O), binary mixture as a function of [C$_2$MIm][C$_3$H$_7$CO$_2$] mole fraction composition, χ_{IL}, for a temperature range from (293.15 to 363.15) K at 0.1 MPa.

T /K	293.15	298.15	303.15	313.15	323.15	333.15	343.15	353.15	363.15
χ_{IL}					$V_{\phi,IL}$ / cm^3·mol^{-1}				
0.00	/		/	/	/	/	/	/	/
0.05	148.80	149.45	150.24	151.68	152.97	154.28	155.76	159.38	/
0.19	149.68	150.11	150.79	152.09	153.24	154.55	155.77	157.45	157.69
0.33	151.28	151.71	152.26	153.35	154.37	155.48	156.52	157.84	158.42
0.47	152.10	152.56	153.03	154.00	154.94	155.89	156.83	157.77	158.79
0.62	152.92	153.40	153.81	154.71	155.62	156.48	157.35	158.06	159.34
0.77	153.99	154.45	154.86	155.72	156.59	157.41	158.24	158.89	160.17
0.89	154.62	155.07	155.47	156.33	157.18	158.01	158.85	159.57	160.68
1.00	154.75	155.19	155.64	156.56	157.46	158.36	159.27	160.18	161.08
					$V_{\phi,H2O}$ / cm^3·mol^{-1}				
1.00	/		/	/	/	/	/	/	/
0.89	14.73	14.77	14.78	14.82	14.78	14.77	14.81	15.15	14.40
0.77	16.36	16.29	16.44	16.59	16.67	16.86	17.02	17.55	16.93
0.62	15.92	15.91	15.98	16.12	16.22	16.41	16.56	16.87	16.77
0.47	15.47	15.53	15.55	15.65	15.76	15.86	15.98	16.03	16.41
0.33	15.72	15.81	15.80	15.88	16.00	16.07	16.17	16.10	16.67
0.19	16.75	16.82	16.82	16.89	17.00	17.07	17.17	17.10	17.62
0.05	18.01	18.04	18.06	18.12	18.19	18.27	18.37	18.53	/
0.00	18.03	18.05	18.08	18.14	18.22	18.31	18.41	18.52	18.65

Table 0-7. Apparent molar volumes, $V_{\phi,IL}$ of ([C$_2$MIm][C$_3$H$_7$CO$_2$] + H$_2$O), binary mixture as a function of [C$_2$MIm][C$_3$H$_7$CO$_2$] mole fraction composition, χ_{IL}, for a temperature range from (293.15 to 363.15) Kat 0.1 MPa.

T /K	293.15	298.15	303.15	313.15	323.15	333.15	343.15	353.15	363.15
χ_{IL}					$V_{\phi,IL}$ / cm^3·mol^{-1}				
0.00	/		/	/	/	/	/	/	/
0.05	175.55	176.33	177.24	179.37	181.32	183.20	184.93	186.63	188.87
0.20	179.75	180.04	180.61	182.34	183.89	185.47	186.86	188.18	189.83
0.36	183.06	183.51	184.09	185.50	186.84	188.18	189.46	190.69	192.10
0.50	183.78	184.43	185.01	186.24	187.39	188.56	189.77	190.95	192.10
0.65	185.09	185.73	186.33	187.38	188.44	189.51	190.64	191.77	192.80
0.80	185.85	186.51	187.08	188.10	189.12	190.14	191.23	192.33	193.32
1.00	186.09	186.62	187.16	188.32	189.44	190.57	191.69	192.81	193.95
					$V_{\phi,H2O}$ / cm^3·mol^{-1}				
1.00	/		/	/	/	/	/	/	/
0.89	9.01	8.80	8.84	8.91	9.00	9.10	9.13	9.25	9.54
0.77	13.74	13.23	13.15	13.45	13.74	14.05	14.15	14.25	14.74
0.62	14.87	14.83	14.84	15.11	15.32	15.56	15.75	15.93	16.22
0.47	16.07	16.25	16.36	16.48	16.63	16.77	16.99	17.20	17.36
0.33	16.74	16.98	17.10	17.15	17.23	17.32	17.50	17.69	17.74
0.19	18.43	18.58	18.65	18.66	18.70	18.76	18.87	19.00	19.06
0.05	18.57	18.59	18.60	18.63	18.67	18.73	18.81	18.90	18.98
0.00	18.03	18.05	18.08	18.14	18.22	18.31	18.41	18.52	18.65

Table 0-8. Apparent molar volumes, $V_{\phi IL}$, of ([C$_2$MIm][C$_7$H$_{15}$CO$_2$] + H$_2$O), binary mixture as a function of [C$_2$MIm][C$_7$H$_{15}$CO$_2$] mole fraction composition, χ_{IL}, for a temperature range from (293.15 to 363.15) Kat 0.1 MPa.

T /K	293.15	298.15	303.15	313.15	323.15	333.15	343.15	353.15	363.15
χ_{IL}					$V_{\phi IL}$ / cm^3·mol^{-1}				
0.00	/		/	/	/	/	/	/	/
0.05	244.99	246.37	247.63	250.26	252.54	254.85	256.76	261.41	261.17
0.20	246.44	247.81	248.86	251.17	253.12	255.04	256.85	259.67	261.08
0.35	248.73	249.83	250.73	252.70	254.49	256.27	258.02	260.17	261.62
0.50	250.91	251.76	252.59	254.25	255.95	257.64	259.40	260.98	262.84
0.64	252.47	253.16	253.93	255.45	257.05	258.68	260.39	261.71	263.71
0.80	253.48	254.11	254.85	256.31	257.87	259.47	261.11	262.41	264.30
1.00	253.03	253.81	254.60	256.21	257.82	259.45	261.08	262.72	264.36
					$V_{\phi,H2O}$ / cm^3·mol^{-1}				
1.00	/		/	/	/	/	/	/	/
0.80	15.20	15.35	15.48	15.85	16.02	16.16	16.14	17.07	16.50
0.64	15.19	15.40	15.49	15.83	15.98	16.12	16.21	16.73	16.64
0.50	15.83	15.92	16.00	16.11	16.28	16.44	16.67	16.74	17.07
0.35	16.79	16.77	16.80	16.80	16.92	17.06	17.32	17.14	17.66
0.20	17.56	17.53	17.56	17.56	17.65	17.76	17.96	17.82	18.31
0.05	18.01	18.03	18.05	18.11	18.19	18.29	18.40	18.52	18.61
0.00	18.03	18.05	18.08	18.14	18.22	18.31	18.41	18.52	18.65

Appendix G: Partial molar volumes, $\overline{V}_{m,i}$, of ([C₂MIm][CₙHₙCO₂] + H₂O), binary mixture

Table 0-9. Partial molar volumes, $\overline{V}_{m,i}$, of ([C₂MIm][CH₃CO₂] + H₂O), binary mixture as a function of [C₂MIm][CH₃CO₂] mole fraction composition, χ_{IL}, for a temperature range from (293.15 to 363.15) K at 0.1 MPa.

T /K	293.15	298.15	303.15	313.15	323.15	333.15	343.15	353.15	363.15
χ_{IL}					$\overline{V}_{m,IL}$ / cm³·mol⁻¹				
0.00	/	/	/	/	/	/	/	/	/
0.05	148.80	149.45	150.24	151.68	152.97	154.28	155.76	159.38	/
0.19	149.68	150.11	150.79	152.09	153.24	154.55	155.77	157.45	157.69
0.33	151.28	151.71	152.26	153.35	154.37	155.48	156.52	157.84	158.42
0.47	152.10	152.56	153.03	154.00	154.94	155.89	156.83	157.77	158.79
0.62	152.92	153.40	153.81	154.71	155.62	156.48	157.35	158.06	159.34
0.77	153.99	154.45	154.86	155.72	156.59	157.41	158.24	158.89	160.17
0.89	154.62	155.07	155.47	156.33	157.18	158.01	158.85	159.57	160.68
1.00	154.75	155.19	155.64	156.56	157.46	158.36	159.27	160.18	161.08
					$\overline{V}_{m,H2O}$ / cm³·mol⁻¹				
1.00	/	/		/	/	/	/	/	/
0.89	14.73	14.77	14.78	14.82	14.78	14.77	14.81	15.15	14.40
0.77	16.36	16.29	16.44	16.59	16.67	16.86	17.02	17.55	16.93
0.62	15.92	15.91	15.98	16.12	16.22	16.41	16.56	16.87	16.77
0.47	15.47	15.53	15.55	15.65	15.76	15.86	15.98	16.03	16.41
0.33	15.72	15.81	15.80	15.88	16.00	16.07	16.17	16.10	16.67
0.19	16.75	16.82	16.82	16.89	17.00	17.07	17.17	17.10	17.62
0.05	18.01	18.04	18.06	18.12	18.19	18.27	18.37	18.53	/
0.00	18.03	18.05	18.08	18.14	18.22	18.31	18.41	18.52	18.65

Table 0-10. Partial molar volumes, $\overline{V}_{m,i}$, of ([C$_2$MIm][C$_7$H$_{15}$CO$_2$] + H$_2$O), binary mixture as a function of [C$_2$MIm][C$_7$H$_{15}$CO$_2$] mole fraction composition, χ_{IL}, for a temperature range from (293.15 to 363.15) K at 0.1 MPa.

T /K	293.15	298.15	303.15	313.15	323.15	333.15	343.15	353.15	363.15
χ_{IL}	$\overline{V}_{m,IL}$ / cm³·mol⁻¹								
0.00	/	/	/	/	/	/	/	/	/
0.05	175.55	176.33	177.24	179.37	181.32	183.20	184.93	186.63	188.87
0.20	179.75	180.04	180.61	182.34	183.89	185.47	186.86	188.18	189.83
0.36	183.06	183.51	184.09	185.50	186.84	188.18	189.46	190.69	192.10
0.50	183.78	184.43	185.01	186.24	187.39	188.56	189.77	190.95	192.10
0.65	185.09	185.73	186.33	187.38	188.44	189.51	190.64	191.77	192.80
0.80	185.85	186.51	187.08	188.10	189.12	190.14	191.23	192.33	193.32
1.00	186.09	186.62	187.16	188.32	189.44	190.57	191.69	192.81	193.95
	$\overline{V}_{m,H2O}$ / cm³·mol⁻¹								
1.00	/	/		/	/	/	/	/	/
0.89	9.01	8.80	8.84	8.91	9.00	9.10	9.13	9.25	9.54
0.77	13.74	13.23	13.15	13.45	13.74	14.05	14.15	14.25	14.74
0.62	14.87	14.83	14.84	15.11	15.32	15.56	15.75	15.93	16.22
0.47	16.07	16.25	16.36	16.48	16.63	16.77	16.99	17.20	17.36
0.33	16.74	16.98	17.10	17.15	17.23	17.32	17.50	17.69	17.74
0.19	18.43	18.58	18.65	18.66	18.70	18.76	18.87	19.00	19.06
0.05	18.57	18.59	18.60	18.63	18.67	18.73	18.81	18.90	18.98
0.00	18.03	18.05	18.08	18.14	18.22	18.31	18.41	18.52	18.65

Table 0-11. Partial molar volumes, $\overline{V}_{m,i}$, of ([C$_2$MIm][C$_7$H$_{15}$CO$_2$] + H$_2$O), binary mixture as a function of [C$_2$MIm][C$_7$H$_{15}$CO$_2$] mole fraction composition, χ_{IL}, for a temperature range from (293.15 to 363.15) Kat 0.1 MPa.

T /K	293.15	298.15	303.15	313.15	323.15	333.15	343.15	353.15	363.15
χ_{IL}					$\overline{V}_{m,IL}$ / cm^3·mol^{-1}				
0.00	/	/	/	/	/	/	/	/	/
0.05	244.99	246.37	247.63	250.26	252.54	254.85	256.76	261.41	261.17
0.20	246.44	247.81	248.86	251.17	253.12	255.04	256.85	259.67	261.08
0.35	248.73	249.83	250.73	252.70	254.49	256.27	258.02	260.17	261.62
0.50	250.91	251.76	252.59	254.25	255.95	257.64	259.40	260.98	262.84
0.64	252.47	253.16	253.93	255.45	257.05	258.68	260.39	261.71	263.71
0.80	253.48	254.11	254.85	256.31	257.87	259.47	261.11	262.41	264.30
1.00	253.03	253.81	254.60	256.21	257.82	259.45	261.08	262.72	264.36
					$\overline{V}_{m,H2O}$ / cm^3·mol^{-1}				
1.00	/	/		/	/	/	/	/	/
0.80	15.20	15.35	15.48	15.85	16.02	16.16	16.14	17.07	16.50
0.64	15.19	15.40	15.49	15.83	15.98	16.12	16.21	16.73	16.64
0.50	15.83	15.92	16.00	16.11	16.28	16.44	16.67	16.74	17.07
0.35	16.79	16.77	16.80	16.80	16.92	17.06	17.32	17.14	17.66
0.20	17.56	17.53	17.56	17.56	17.65	17.76	17.96	17.82	18.31
0.05	18.01	18.03	18.05	18.11	18.19	18.29	18.40	18.52	18.61
0.00	18.03	18.05	18.08	18.14	18.22	18.31	18.41	18.52	18.65
1.00	15.20	15.35	15.48	15.85	16.02	16.16	16.14	17.07	16.50

Appendix H: VTF fitting parameters (B_η, η_0 and T_0^η) for the viscosity as a function of temperature

Table 0-12. VTF fitting parameters for the viscosity (equation 7, B_η, η_0 and T_0^η) as a function of temperature from (293.15 to 363.15) K at 0.1 MPa for each investigated IL mole fraction with the deviations of their fit σ_η for the viscosity.

([C2MIm][CH3CO2] + H2O)				([C2MIm][C3H7CO2] + H2O)				([C2MIm][C7H15CO2] + H2O)			
χIL	η^*_0 (mPa·s)	B_η (K)	T_0^η (K)	χIL	η^*_0 (mPa·s)	B_η (K)	T_0^η (K)	χIL	η^*_0 (mPa·s)	B_η (K)	T_0^η (K)
1.00	0.007	1589.0	139.0	1	6E-04	2822.1	83.3	0.91	5.001	1272.6	42.0
0.77	0.011	1503.6	137.0	0.8	0.001	2388.2	95.9	0.77	6.E-04	2848.5	87.8
0.64	0.064	874.4	168.3	0.65	0.001	2503.9	84.0	0.62	0.001	2682.2	88.5
0.49	0.068	774.6	180.1	0.5	0.008	1599.3	125.7	0.54	0.002	2438.1	96.3
0.35	0.090	737.4	177.7	0.36	0.003	1984.2	91.2	0.5	4.E-04	2998.7	70.2
0.20	0.163	544.1	192.2	0.2	0.202	446.7	201.8	0.35	9.E-04	2525.8	86.1
0.05	0.471	123.7	240.2	0.05	2.721	4.3	287.3	0.2	0.002	2132.4	99.3
0.00	0.572	-43256.6	-1.E+07	0	0.570	-2.E17	-2E25	0.05	0.021	989.4	139.6
								0	0.570	-5E+33	-1.3E+42

Appendix I: Polynomial fitting parameters for the viscosity as a function of mole fraction composition, χ_{IL}, from (293.15 to 363.15) K at 0.1 MPa

Table 0-13. Polynomial fitting parameters for the viscosity as a function of mole fraction composition, χ_{IL}, from (293.15 to 363.15) K at 0.1 MPa for each investigated IL mole fraction.

	293.15	298.15	303.15	323.15	328.15	333.15	343.15	348.15	353.15	363.15
				([C_2MIm][CH_3CO_2] + H_2O)						
A_0	-0.3	0.0	0.2	0.4	0.4	0.4	0.3	0.4	0.3	0.3
A_1	406.6	280.0	199.4	68.3	55.4	46.2	33.8	18.4	18.1	20.5
A_2	-7890.5	-5132.2	-3421.1	-805.3	-576.5	-418.6	-223.6	54.8	47.4	40.2
A_3	67717.9	44500.9	30010.9	7489.0	5462.6	4030.1	2227.2	-94.9	-139.8	-370.5
A_4	-241832.7	-160083.1	-108868.5	-28459.7	-21096.5	-15830.9	-9125.9	-745.4	-418.6	581.6
A_5	410594.0	272895.8	186442.2	49957.1	37341.6	28268.0	16645.1	2055.4	1404.7	-46.3
A_6	-329325.9	-219312.1	-150157.7	-40679.2	-30515.3	-23184.8	-13770.1	-1679.8	-1164.3	-380.5
A_7	100529.3	66992.3	45898.1	12465.9	9357.7	7113.5	4229.5	402.8	262.2	163.4
				([C_2MIm][C_3H_7CO_2] + H_2O)						
A_0	2.38	1.83	1.97	1.49	1.35	1.22	1.01	0.93	0.85	0.79
A_1	-29.25	-31.85	-53.26	-22.97	-12.24	-2.72	12.23	21.29	25.47	28.79
A_2	1063.67	922.46	1007.27	501.25	372.02	259.72	84.72	-29.65	-76.97	-115.51
A_3	-1784.74	-1586.63	-2197.60	-1304.57	-981.34	-693.00	-233.58	74.20	200.13	302.96
A_4	1259.99	1156.54	2084.57	1407.41	1065.95	755.94	254.93	-85.60	-224.04	-337.18
A_5	-124.79	-171.03	-621.13	-501.73	-381.70	-270.12	-86.24	40.79	92.61	135.07
				([C_2MIm][C_3H_7CO_2] + H_2O)						
A_0	4.93	3.01	2.47	5.02	4.10	3.63	3.78	3.51	3.33	3.41
A_1	-533.18	-285.89	-221.41	-539.43	-460.87	-425.87	-458.44	-424.77	-414.98	-437.23
A_2	13717.38	9107.05	7322.06	9981.70	8529.73	7741.23	7877.81	7123.01	6872.42	7124.30
A_3	-67087.55	-46756.75	-39101.84	-50051.11	-44697.93	-41460.89	-41878.55	-37760.41	-36545.30	-37843.47
A_4	149494.12	108719.22	93442.42	113003.31	103636.25	97278.96	97521.77	87752.70	85032.58	87870.35
A_5	-147974.69	-111950.59	-98832.58	-117388.79	-108975.49	-102775.88	-102486.22	-92196.49	-89317.66	-92029.82
A_6	53216.12	41891.68	38033.19	45514.65	42413.26	40034.33	39775.73	35828.35	34672.03	35595.91

Appendix J: Redlich-Kister fitting coefficients, A_i, of the $\Delta\eta$ of the ([C$_2$MIm][C$_n$H$_n$CO$_2$] + H$_2$O) binary mixture

Table 0-14. Redlich-Kister fitting coefficients A_i of the $\Delta\eta$ (mPa.s) of the ([C$_2$MIm][C$_n$H$_n$CO$_2$] + H$_2$O) binary mixture as a function of temperature from (293.15 to 363.15) K.

T/K	293.15	298.15	303.15	323.15	328.15	333.15	343.15	348.15	353.15	363.15
([C$_2$MIm][CH$_3$CO$_2$] + H$_2$O)										
A_0	-145.20	-95.84	-64.19	-13.55	-8.98	-5.73	-1.75	0.23	0.92	1.59
A_1	-527.88	-362.23	-255.85	-79.92	-62.51	-49.64	-32.55	-21.11	-17.82	-7.83
A_2	-489.07	-318.19	-205.35	-18.87	-1.88	10.03	24.18	32.32	33.92	-5.36
A_3	2930.73	1995.84	1399.40	422.27	326.52	255.76	162.12	89.92	73.54	59.83
A_4	6214.66	4247.34	2970.40	834.98	623.52	467.52	262.56	109.23	74.27	228.79
A_5	-1063.28	-712.53	-485.00	-110.48	-74.92	-49.26	-16.73	28.14	29.00	-33.58
A_6	-7805.96	-5317.62	-3710.49	-1044.03	-782.25	-589.40	-336.65	-95.31	-61.38	-240.97
A_7	-3158.95	-2121.86	-1468.21	-423.46	-324.55	-252.45	-158.54	-51.62	-42.67	-17.74
([C$_2$MIm][C$_3$H$_7$CO$_2$] + H$_2$O)										
A_0	-323.94	-232.17	-177.62	-55.02	-39.86	-28.29	-12.79	-4.01	-1.06	1.15
A_1	-146.37	-99.64	-76.58	-23.06	-16.63	-11.87	-5.80	-2.46	-1.59	-0.99
A_2	-948.45	-391.13	-343.96	-157.75	-127.61	-103.09	-67.08	-43.46	-34.66	-27.44
A_3	-276.51	-189.00	-343.90	-269.38	-220.78	-176.56	-105.20	-55.28	-36.51	-21.18
A_4	2313.07	491.47	326.19	70.55	52.37	40.20	24.90	14.77	10.10	5.69
A_5	286.00	273.81	576.19	465.08	377.49	297.18	166.75	75.73	40.99	12.63
A_6	-1706.59	-153.86	162.51	303.70	265.02	226.23	160.54	113.83	98.34	86.42
([C$_2$MIm][C$_7$H$_{15}$CO$_2$] + H$_2$O)										
A_0	-339.5	-477.9	-560.7	-718.2	-669.0	-625.6	-601.2	-574.8	-544.3	-518.4
A_1	716.1	342.3	62.7	-887.2	-654.9	-541.2	-569.9	-572.9	-530.1	-500.0
A_2	828.6	22.8	-426.9	-1268.4	-1043.0	-909.5	-878.5	-839.3	-780.1	-734.9
A_3	173.0	-777.3	-1165.4	-693.1	-916.9	-964.8	-839.3	-748.6	-722.9	-692.4
A_4	-319.01	-483.61	-575.45	-692.58	-663.67	-628.97	-601.73	-574.26	-545.27	-519.99
A_5	654.19	390.28	140.35	-1024.13	-706.84	-557.88	-604.31	-610.66	-561.71	-532.36
A_6	1003.52	993.86	749.70	-1737.06	-891.66	-521.88	-648.73	-696.23	-606.76	-558.03

Appendix K: Excess Gibbs energy of activation of viscous flow, ΔGE*, Redlich-Kister fitting coefficients, A_i, of the ΔGE* of the ([C₂MIm][CₙHₙCO₂] + H₂O) binary mixture

Table 0-15. Excess Gibbs energy of activation of viscous flow, ΔG^{E*}, of the ([C₂MIm][CₙHₙCO₂] + H₂O) binary mixture as a function of [C₂MIm][CₙHₙCO₂] mole fraction composition, χ_{IL} , for a temperature range from (293.15 to 363.15) Kat 0.1 MPa calculated from experimental density and viscosity data provided in Table 3-1 and Table 3-7, respectively.

T/K	293.15	298.15	303.15	323.15	333.15	343.15	353.15	363.15
χ_{IL}	([C₂MIm][CH₃CO₂] + H₂O), ΔG^{E*}/ kJ.mol⁻¹							
0	0	0	0	0	0	0	0	0
0.05	3.4487	3.4462	3.4593	3.6219	3.7498	3.9062	3.9427	/
0.19	7.3986	7.2623	7.1582	6.9711	6.9740	7.0258	6.9115	7.2149
0.33	6.8222	6.6851	6.5808	6.3997	6.4068	6.4617	6.3865	6.0203
0.47	5.2945	5.2013	5.1271	4.9721	4.9563	4.9729	4.8696	5.0646
0.62	3.4106	3.3868	3.3783	3.4534	3.5365	3.6421	3.7037	3.8918
0.77	3.3670	3.3126	3.2748	3.2412	3.2737	3.3301	3.3539	3.4874
1	0	0	0	0	0	0	0	0
χ_{IL}	([C₂MIm][C₃H₇CO₂] + H₂O), ΔG^{E*}/ kJ.mol⁻¹							
0.00	0	0	0	0	0	0	0	0
0.05	4.0758	3.6374	3.6836	4.6229	5.1773	5.7434	6.2871	6.8603
0.20	6.4678	6.3272	6.2210	6.0487	6.0732	6.1552	5.9982	6.4262
0.50	5.6191	5.5967	5.4747	5.2451	5.2498	5.3176	5.4311	5.5875
0.65	3.8113	3.9041	3.7614	3.5012	3.5136	3.5988	3.7394	3.9297
0.80	2.1872	2.2267	2.0931	1.8252	1.8181	1.8776	1.9903	2.1495
1.00	0	0	0	0	0	0	0	0
χ_{IL}	([C₂MIm][C₇H₁₅CO₂] + H₂O), ΔG^{E*}/ kJ.mol⁻¹							
0	0	0	0	0	0	0	0	0
0.05	6.2834	6.2021	6.1180	6.5899	5.5910	5.4224	4.6215	4.4796
0.2	9.6309	9.3597	9.1009	9.2786	7.7778	7.4167	6.3024	6.0479
0.35	8.9971	8.6650	8.3463	8.3077	6.6890	6.2238	5.0044	4.6519
0.5	7.6077	7.2623	6.9172	6.6735	4.9204	4.2978	2.8460	2.3068
0.64	5.9151	5.5979	5.2538	3.4161	2.8265	1.9337	0.5394	0.1957
0.8	3.6157	3.1121	2.6115	0.3304	-0.2563	-1.1496	-2.3547	-2.6974
1	0	0	0	0	0	0	0	0

Table 0-16. Redlich-Kister fitting coefficients A_i of the ΔG^{E*} of the ($[C_2MIm][C_nH_nCO_2]$ + H_2O) binary mixture as a function of temperature from (293.15 to 363.15) K.

T /K	293.15	298.15	303.15	323.15	333.15	343.15	353.15	363.15
([C$_2$MIm][CH$_3$CO$_2$] + H$_2$O),								
A_0	18.640	18.357	18.150	17.869	17.963	18.174	18.030	18.400
A_1	-24.038	-22.909	-21.899	-18.727	-17.497	-16.415	-14.925	-12.985
A_2	41.623	40.693	39.998	38.872	38.983	39.421	39.197	38.824
A_3	5.115	2.775	0.525	-7.779	-11.675	-15.585	-18.285	-21.104
([C$_2$MIm][C$_3$H$_7$CO$_2$] + H$_2$O),								
A_0	22.348	22.271	21.781	20.861	20.881	21.154	21.613	22.239
A_1	-22.178	-20.050	-20.330	-20.652	-20.475	-20.165	-19.256	-19.183
A_2	12.750	12.046	11.333	10.074	10.160	10.614	8.950	12.271
A_3	-1.209	-4.561	-4.159	-4.625	-5.584	-6.792	-5.448	-9.568
([C$_2$MIm][C$_7$H$_{15}$CO$_2$] + H$_2$O),								
A_0	29.421	28.177	26.905	24.544	19.073	16.476	11.046	9.279
A_1	-12.229	-11.969	-12.051	-23.064	-17.742	-21.043	-24.189	-24.517
A_2	37.105	33.853	30.802	19.375	16.080	12.333	6.756	6.540
A_3	-64.779	-68.575	-71.603	-80.596	-77.528	-76.144	-66.531	-66.098

Appendices of Chapter 4 _ Microscopic properties of ionic liquid and water binary mixtures

Appendix L: ^{1}H and ^{13}C-NMR Chemical shifts (δ/ppm) and the absolute chemical shifts (Δδ/ppm) of [C₂MIm][CH₃CO₂] binary mixture with water

Table 0-17. The ^{1}H-NMR Chemical Shifts (δ/ppm) and the Absolute Chemical Shifts (Δδ/ppm) of [C$_2$MIm][CH$_3$CO$_2$] binary mixture with water at different IL concentrations as a function of the ionic liquid mole fraction composition, χ_{IL} at 298.15K.

	H1	H2	H3	H5	H4	Ha	H6	H$_2$O
χ_{IL}				δ/ppm of [C$_2$MIm][CH$_3$CO$_2$] + H$_2$O				
0.00	0	0	0	0	0	0	0	4.51
0.05	8.2	7.01	6.9	3.7	3.37	1.38	0.98	4.32
0.10	8.24	6.98	6.92	3.67	3.35	1.28	0.93	4.41
0.30	8.97	7.35	7.26	3.76	3.43	1.17	0.86	4.8
0.49	9.49	7.67	7.54	3.87	3.54	1.19	0.88	5.23
0.73	10	8.01	7.84	3.92	3.62	1.15	0.9	5.33
0.82	10.11	8.07	7.89	3.9	3.63	1.13	0.91	5.57
0.98	10.25	8.15	7.97	3.92	3.66	1.14	0.91	0
χ_{IL}				$\Delta\delta$/ppm of [C$_2$MIm][CH$_3$CO$_2$] + H$_2$O				
0.00	/	/	/	/	/	/	/	-1.06
0.05	-2.05	-1.14	-1.07	-0.22	-0.29	0.24	0.07	-1.25
0.10	-2.01	-1.17	-1.05	-0.25	-0.31	0.14	0.02	-1.16
0.30	-1.28	-0.8	-0.71	-0.16	-0.23	0.03	-0.05	-0.77
0.49	-0.76	-0.48	-0.43	-0.05	-0.12	0.05	-0.03	-0.34
0.73	-0.25	-0.14	-0.13	0	-0.04	0.01	-0.01	-0.24
0.82	-0.14	-0.08	-0.08	-0.02	-0.03	-0.01	0	0
0.98	0	0	0	0	0	0	0	0

Table 0-18. The ^{13}C-NMR Chemical Shifts (δ/ppm) and the Absolute Chemical Shifts (Δδ/ppm) of [C_2MIm][CH_3CO_2] binary mixture with water at different IL concentrations as a function of the ionic liquid mole fraction composition, x_{IL} at 298.15K.

	Cb	C1	C2	C3	C5	C4	Ca	C6
x_{IL}				δ/ppm of [C_2MIm][CH_3CO_2] + H_2O				
0.05	179.01	133.69	121.61	120.01	42.91	33.75	21.4	12.66
0.10	177.67	134.41	122.25	120.6	43.38	34.39	22.26	13.41
0.30	175.52	135.51	122.47	120.86	43.16	34.36	22.98	14.01
0.49	174.49	136.24	122.59	121.07	42.99	34.23	23.40	13.98
0.67	174.02	136.66	122.70	121.22	42.75	34.16	23.65	14.02
0.98	173.95	137.35	123.12	121.68	43.17	34.14	24.18	14.34
x_{IL}				Δδ/ppm of [C_2MIm][CH_3CO_2] + H_2O				
0.05	5.06	-3.66	-1.51	-1.67	-0.26	-0.39	-2.78	-1.68
0.10	3.72	-2.94	-0.87	-1.08	0.21	0.25	-1.92	-0.93
0.30	1.57	-1.84	-0.65	-0.82	-0.01	0.22	-1.2	-0.33
0.49	0.54	-1.11	-0.53	-0.61	-0.18	0.09	-0.78	-0.36
0.67	0.07	-0.69	-0.42	-0.46	-0.42	0.02	-0.53	-0.32
0.98	0	0	0	0	0	0	0	0

Appendix M: ^1H and ^{13}C-NMR Chemical shifts (δ/ppm) and the absolute chemical shifts (Δδ/ppm) of [C₂MIm][C₃H₇CO₂] binary mixture with water

Table 0-19. The ^{1}H-NMR Chemical Shifts (δ/ppm) and the Absolute Chemical Shifts (Δδ/ppm) of [C₂MIm][C₃H₇CO₂] binary mixture with water at different IL concentrations as a function of the ionic liquid mole fraction composition, x_{IL} at 298.15K.

	H1	H2	H3	H5	H4	Hc	H(a-b)	H6	H₂O
x_{IL}					δ/ppm of [C₂MIm][C₃H₇CO₂] + H₂O				
0.00	/	/	/	/	/	/	/	/	4.51
0.01	8.2	6.98	6.91	3.71	3.37	1.6	0.97	0.34	4.32
0.05	8.45	7.17	7.11	3.87	3.54	1.67	1.11	0.43	4.51
0.20	8.86	7.26	7.18	3.74	3.39	1.38	0.83	0.11	4.51
0.50	9.66	7.75	7.61	3.86	3.53	1.39	0.84	0.16	4.82
0.65	9.94	7.94	7.77	3.91	3.58	1.39	0.86	0.18	4.94
0.80	10.14	8.07	7.89	3.93	3.61	1.39	0.88	0.19	5.02
0.98	10.37	8.23	8.03	3.93	3.65	1.4	0.91	0.21	/
x_{IL}					Δδ/ppm of [C₂MIm][C₃H₇CO₂] + H₂O				
0.00	/	/	/	/	/	/	/	/	-0.51
0.01	-2.17	-1.25	-1.12	-0.22	-0.28	0.2	0.06	0.13	-0.7
0.05	-1.92	-1.06	-0.92	-0.06	-0.11	0.27	0.2	0.22	-0.51
0.20	-1.51	-0.97	-0.85	-0.19	-0.26	-0.02	-0.08	-0.1	-0.51
0.50	-0.71	-0.48	-0.42	-0.07	-0.12	-0.01	-0.07	-0.05	-0.2
0.65	-0.43	-0.29	-0.26	-0.02	-0.07	-0.01	-0.05	-0.03	-0.08
0.80	-0.23	-0.16	-0.14	0	-0.04	-0.01	-0.03	-0.02	0
0.98	0	0	0	0	0	0	0	0	0

Table 0-20. The ^{13}C-NMR Chemical Shifts (δ/ppm) and the Absolute Chemical Shifts (Δδ/ppm) of [C$_2$MIm][C$_3$H$_7$CO$_2$] binary mixture with water at different IL concentrations as a function of the ionic liquid mole fraction composition, x_{IL} at 298.15K.

	Cd	C1	C2	C3	C5	C4	Cc-b	Ca	C6
x_{IL}				*δ/ppm of [C$_2$MIm][C$_3$H$_7$CO$_2$] + H$_2$O*					
0.05	181.85	135.01	123.01	121.15	44.19	35.15	19.03	14.12	12.94
0.20	179.21	136.28	123.52	121.85	44.20	35.46	19.32	14.89	13.52
0.50	175.95	136.06	122.26	120.79	42.46	33.80	18.22	13.55	12.33
0.65	175.76	136.13	122.37	120.96	42.41	33.72	18.35	13.76	12.39
0.80	175.37	136.57	122.30	120.92	42.22	33.50	18.29	13.61	12.28
0.98	175.07	136.73	122.24	120.54	42.25	33.28	18.22	13.18	12.17
x_{IL}				*Δδ/ppm of [C$_2$MIm][C$_3$H$_7$CO$_2$] + H$_2$O*					
0.05	0.00	0.00	0.00	0.00	0.00	0.00	0.00	0.00	0.00
0.20	-2.64	1.27	0.51	0.70	0.01	0.31	0.29	0.77	0.58
0.50	-5.90	1.05	-0.75	-0.36	-1.73	-1.35	-0.81	-0.57	-0.61
0.65	-6.09	1.12	-0.64	-0.19	-1.78	-1.43	-0.68	-0.36	-0.55
0.80	-6.48	1.56	-0.71	-0.23	-1.97	-1.65	-0.74	-0.51	-0.66
0.98	-6.78	1.72	-0.77	-0.61	-1.94	-1.87	-0.81	-0.94	-0.77

Appendix N: ^{1}H and ^{13}C-NMR Chemical shifts (δ/ppm) and the absolute chemical shifts (Δδ/ppm) of [C$_2$MIm][C$_7$H$_{15}$CO$_2$] binary mixture with water

Table 0-21. The ^{1}H-NMR Chemical Shifts (δ/ppm) and the Absolute Chemical Shifts (Δδ/ppm) of [C$_2$MIm][C$_7$H$_{15}$CO$_2$] binary mixture with water at different IL concentrations as a function of the ionic liquid mole fraction composition, x_{IL} at 298.15K.

x_{IL}	H1	H2	H3	H5	H4	Hg	Hb	Ha	Hc,d,e,f	H6	H$_2$O
					δ/ppm of [C$_2$MIm][C$_7$H$_{15}$CO$_2$]+ H$_2$O						
0.00	/	/	/	/	/	/	/	/	/	/	4.51
0.05	8.38	7.05	6.99	3.72	3.4	1.58	1.01	0.97	0.71	0.29	4.37
0.35	9.35	7.55	7.45	3.89	3.52	1.56	1.02	0.93	0.71	0.31	4.76
0.50	9.73	7.79	7.66	3.93	3.57	1.56	1.03	0.93	0.73	0.33	4.94
0.66	9.98	7.96	7.81	3.97	3.61	1.55	1.05	0.94	0.75	0.35	5.17
0.80	10.24	8.12	7.95	3.97	3.64	1.55	1.05	0.95	0.76	0.35	5.36
0.81	10.22	8.12	7.94	3.98	3.65	1.56	1.06	0.96	0.77	0.36	5.42
0.89	10.34	8.18	8	3.98	3.66	1.55	1.05	0.97	0.76	0.36	5.71
0.98	10.43	8.24	8.06	3.99	3.67	1.55	1.05	0.97	0.76	0.36	/
x_{IL}					Δδ/ppm of [C$_2$MIm][C$_7$H$_{15}$CO$_2$] + H$_2$O						
0.00	/	/	/	/	/	/	/	/	/	/	-1.2
0.05	-2.05	-1.19	-1.07	-0.27	-0.27	0.03	-0.04	0	-0.05	-0.07	-1.34
0.35	-1.08	-0.69	-0.61	-0.1	-0.15	0.01	-0.03	-0.04	-0.05	-0.05	-0.95
0.50	-0.7	-0.45	-0.4	-0.06	-0.1	0.01	-0.02	-0.04	-0.03	-0.03	-0.77
0.66	-0.45	-0.28	-0.25	-0.02	-0.06	0	0	-0.03	-0.01	-0.01	-0.54
0.80	-0.19	-0.12	-0.11	-0.02	-0.03	0	0	-0.02	0	-0.01	-0.35
0.81	-0.21	-0.12	-0.12	-0.01	-0.02	0.01	0.01	-0.01	0.01	0	-0.29
0.89	-0.09	-0.06	-0.06	-0.01	-0.01	0	0	0	0	0	0
0.98	0	0	0	0	0	0	0	0	0	0	0

Table 0-22. The ^{13}C-NMR Chemical Shifts (δ/ppm) and the Absolute Chemical Shifts ($\Delta\delta$/ppm) of [C$_2$MIm][C$_7$H$_{15}$CO$_2$] binary mixture with water at different IL concentrations as a function of the ionic liquid mole fraction composition, x_{IL} at 298.15K.

|	Ch	C1	C2	C3	C5	C4	Cg	Cb	Cf	Ce	Cd	Cc	Ca	C6
x_{IL}					δ/ppm of [C$_2$MIm][C$_7$H$_{15}$CO$_2$] + H$_2$O									
0.05	179.84	133.92	121.85	120.14	42.93	36.00	33.94	29.87	27.67	27.20	24.48	20.61	12.83	11.87
0.35	177.31	136.01	122.65	121.03	43.04	37.45	34.41	30.55	28.58	28.00	25.59	21.19	14.15	12.41
0.50	176.70	136.55	122.73	121.22	42.90	37.73	34.26	30.58	28.65	28.06	25.76	21.22	14.24	12.45
0.80	176.10	137.22	122.89	121.50	42.76	38.07	34.05	30.61	28.73	27.51	25.40	21.24	14.25	12.04
0.98	175.43	136.98	122.47	121.10	42.23	37.70	33.48	30.11	28.23	27.61	25.51	20.74	13.74	11.99
x_{IL}					$\Delta\delta$/ppm of [C$_2$MIm][C$_7$H$_{15}$CO$_2$] + H$_2$O									
0.05	4.41	-3.06	-0.62	-0.96	0.70	-1.70	0.46	-0.24	-0.56	-0.41	-1.03	-0.13	-0.91	-0.12
0.35	1.88	-0.97	0.18	-0.07	0.81	-0.25	0.93	0.44	0.35	0.39	0.08	0.45	0.41	0.42
0.50	1.27	-0.43	0.26	0.12	0.67	0.03	0.78	0.47	0.42	0.45	0.25	0.48	0.50	0.46
0.80	0.67	0.24	0.42	0.40	0.53	0.37	0.57	0.50	0.50	-0.10	-0.11	0.50	0.51	0.05
0.98	0	0	0	0	0	0	0	0	0	0	0	0	0	0
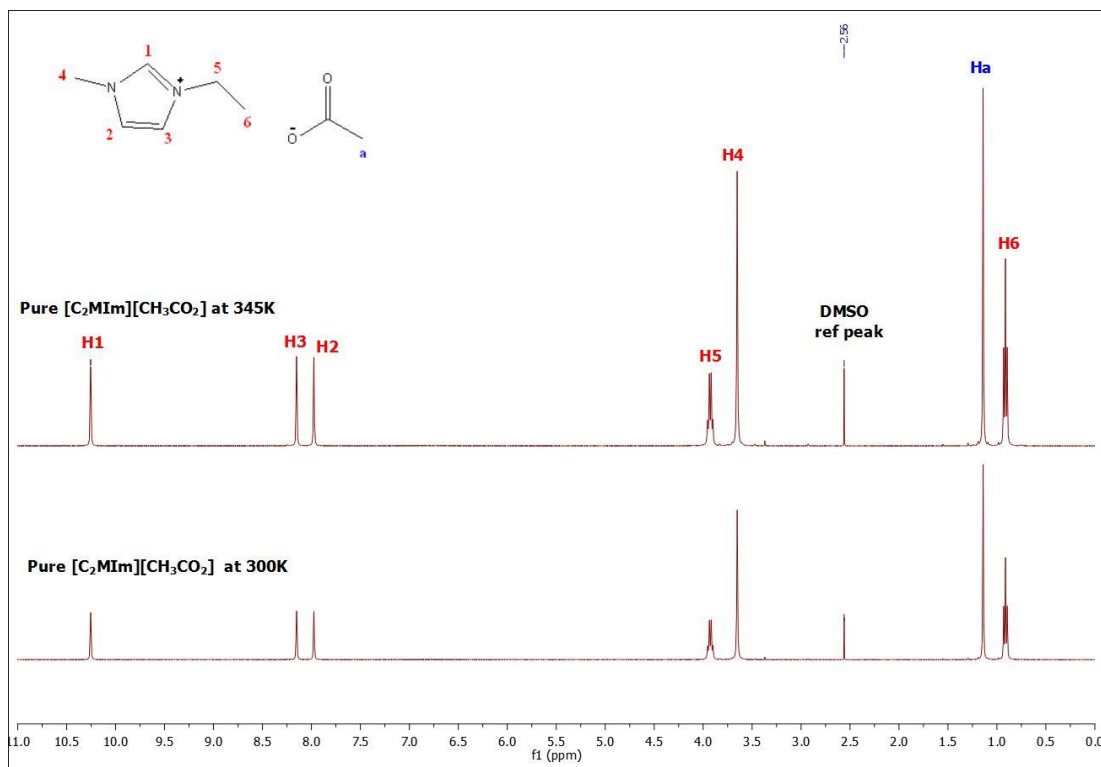
Figure 0-1. ^{1}H NMR spectrum of pure [C$_2$MIm][CH$_3$CO$_2$] at 300K (down) and at 345K (up) using DMSO capillary.
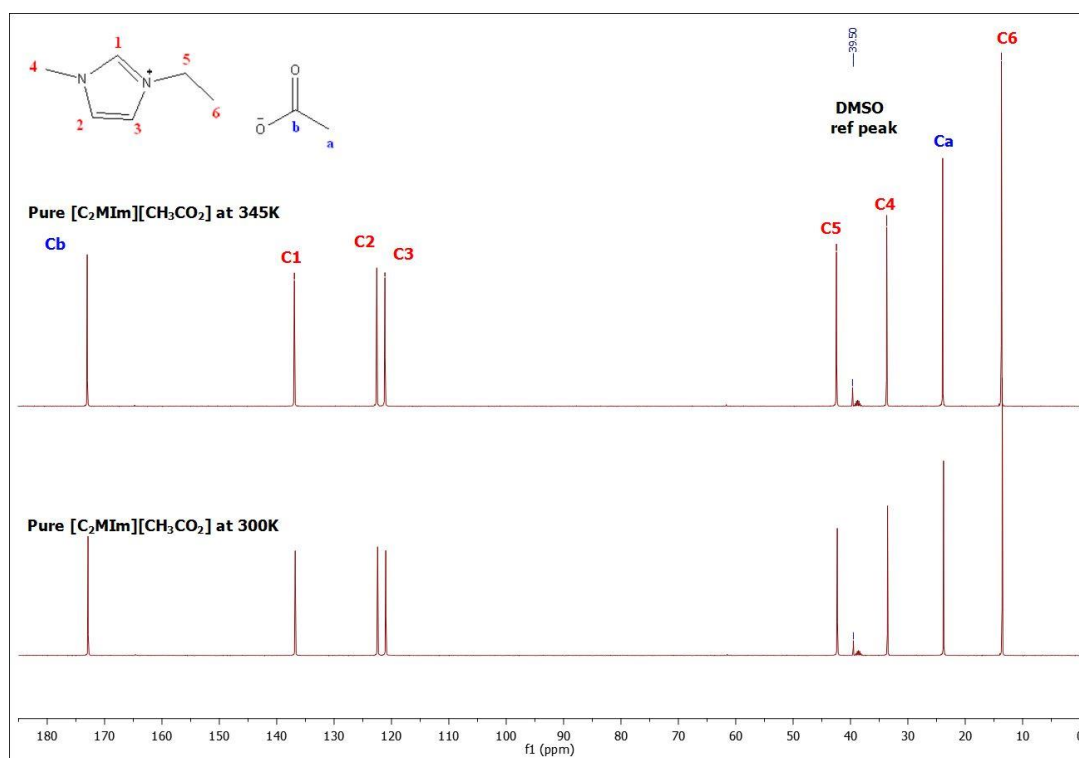
Figure 0-2. ^{13}C NMR spectrum of pure [C$_2$MIm][CH$_3$CO$_2$] at 300K (down) and 345K (up) using DMSO capillary.

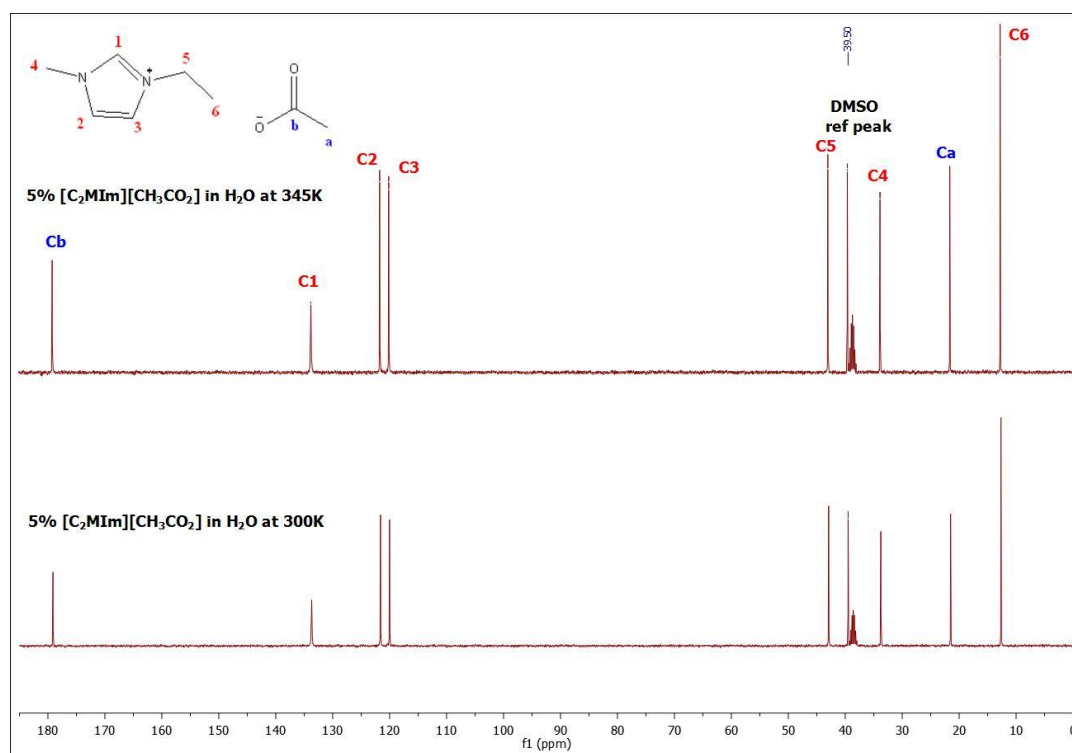Figure 0-3. ^{13}C NMR spectrum of 5% mole fraction of [C$_2$MIm][CH$_3$CO$_2$] in H$_2$O at 300K (down) and 345K (up) using DMSO capillary.